

Observatoire de Paris - PSL Research University
Unité Formation-Enseignement

MÉMOIRE D'HABILITATION À DIRIGER DES RECHERCHES

présenté par

FRANÇOIS LEVRIER

THE DYNAMICAL AND MAGNETIZED INTERSTELLAR MEDIUM

Soutenu le 21 septembre 2016 devant le jury composé de :

Mme.	Hélène SOL	Présidente
Mme	Rosine LALLEMENT	Rapporteuse
Mme	Dimitra RIGOPOULOU	Rapporteuse
M.	Martin HOUDE	Rapporteur
M.	François BOULANGER	Examineur
M.	Julien DEVRIENDT	Examineur
M.	Diego FALCETA GONÇALVES	Examineur
M.	Thomas TROLAND	Examineur

Laboratoire de Radioastronomie
École Normale Supérieure & LERMA, Observatoire de Paris, CNRS UMR 8112
24 rue Lhomond, 75231 Paris Cedex 05

Table des matières

- Curriculum Vitæ
- Liste des publications
- Dossier de synthèse
- Annexes au dossier de synthèse
 - *Polarization measurements analysis I. Impact of the full covariance matrix on the polarization fraction and angle measurements.*, L. Montier, S. Plaszczynski, F. Levrier, M. Tristram, D. Alina, I. Ristorcelli, J.-P. Bernard, *Astronomy & Astrophysics*, 574, 135, 2015
 - *Polarization measurements analysis II. Best estimators of the polarization fraction and angle.*, L. Montier, S. Plaszczynski, F. Levrier, M. Tristram, D. Alina, I. Ristorcelli, J.-P. Bernard, *Astronomy & Astrophysics*, 574, 136, 2015
 - *Planck intermediate results. XIX. An overview of the polarized thermal emission from Galactic dust.*, Planck Collaboration, *Astronomy & Astrophysics*, 576, 104, 2015
 - *Planck intermediate results. XX. Comparison of polarized thermal emission from Galactic dust with simulations of MHD turbulence.*, Planck Collaboration, *Astronomy & Astrophysics*, 576, 105, 2015
 - *Planck intermediate results. XXXV. Probing the role of the magnetic field in the formation of structure in molecular clouds.*, Planck Collaboration, *Astronomy & Astrophysics*, 586, 138, 2016
- Note d'accompagnement

Curriculum Vitæ

FRANÇOIS LEVRIER

Date of birth : August 3rd 1975

Nationality : French

Position : Maître de conférences classe normale, Section 34 of CNU (“Astronomy, astrophysics”)

Laboratory : LRA, LERMA, Ecole Normale Supérieure de Paris, Observatoire de Paris, UPMC

Work address : 24 rue Lhomond, 75231 Paris CEDEX 05

Work phone number : +33 1 44 32 39 93

Home address : 22 rue de la fidélité, 75010 Paris

Home phone number : +33 1 42 84 03 39

Mobile phone number : +33 6 82 05 57 29

e-mail address : francois.levrier@ens.fr

Positions

Since September 2008

Maître de conférences, École Normale Supérieure de Paris

August 2007 - August 2008

Post-doctoral research assistant, University of Oxford, UK, in the framework of the European FP7 program SKADS (*Square Kilometer Array Design Studies*), working with Professor Steve Rawlings.

September 2004 - June 2007 then September 2009 - June 2010

Examiner in physics (CPGE, section MPSI), Lycée Janson-de-Sailly (Paris 16^e).

September 2003 - July 2007

“Agrégé-préparateur”, Centre Interuniversitaire de préparation à l’agrégation externe de sciences physiques, option physique (ENS Paris, Universities Paris VI, Paris VII and Paris XI).

September 2000 - June 2003

Teaching assistant (“Moniteur”), University Paris VII

Academic studies

September 2000 - December 2004

Ph.D thesis at University Paris VII, under the supervision of Edith Falgarone (LERMA, ENS Paris) and François Viallefond (LERMA, Observatoire de Paris) : *Disorder and coherence in structures of the interstellar medium : statistical analysis, interferometric filtering and radiative transfer*. Mention “très honorable”. Composition of the jury : Pr. J. Bartlett, Dr. S. Guilloteau, Pr. A. Lannes, Pr. Dr. J. Stutzki, Dr. E. Falgarone, Dr. F. Viallefond.

July 2000

Successful candidate for “agrégation externe de sciences physiques, option physique” (31st).

September 1999 - June 2000

Preparation of “agrégation externe de sciences physiques, option physique”, within the “Centre Interuniversitaire de Montrouge” (ENS Paris, Universities Paris VI, Paris VII and Paris XI).

April 1999 - June 1999

Research internship at Observatoire de Paris, under the supervision of François Viallefond (LERMA, Observatoire de Paris) and Edith Falgarone (LERMA, ENS Paris) : *Studying the response of interferometers to fractal brightness distributions*.

September 1998 - June 1999

DEA (Master) “Astrophysique et techniques spatiales”, University Paris VII, mention “bien”. Graduate from Magistère Interuniversitaire de Physique.

January 1998 - June 1998

Research internship under the supervision of Trinh Xuan Thuan (University of Virginia, Charlottesville) and John Hibbard (NRAO, Charlottesville) : *The HI gas distribution and kinematics in four blue compact*

dwarf galaxies.

September 1996 - June 1998

Licence de Physique, University Paris VI, mention “assez bien”.
Maîtrise de Physique, University Paris VI, mention “bien”.

September 1996 - June 2000

Student at École Normale Supérieure de Paris (admission via the “Mathematics and Physics” competition).

September 1993 - June 1996

“Classes préparatoires aux grandes écoles” (CPGE), Lycée Condorcet (Paris).

June 1993

Baccalauréat série C (“Mathematics and Physics”), mention “bien”.

RESEARCH ACTIVITIES

My research activity within the ENS team of LERMA revolves around the structure and dynamics of interstellar gas and dust, from the most diffuse regions of the interstellar medium (ISM) to the initial stages of star formation, with an emphasis on methods related to observational simulations. This approach, which I have been developing since my doctoral work, allows to establish firmly the connection between modelling and observations, and is therefore paramount to our understanding of how the ISM works. The following paragraphs give a brief overview of some of the avenues I have explored.

■ Scientific results

- Comparison of *Planck* polarization data at 353 GHz towards molecular clouds with synthetic maps derived from numerical simulations of magnetized, turbulent ISM flows. This work, which I led within the *Planck* Collaboration (Planck Intermediate Results XX, 2015), shows that the decrease of linear polarization fraction of dust thermal emission with increasing gas column density and with increasing local dispersion of the polarization angle is basically linked to the topology of the magnetic field, at least at the scales probed by *Planck*.
- Complete analysis of the statistical bias in polarization observations, related to the non-linear relation between Stokes parameters (I, Q, U) and the usual observables which are polarization fraction and angle (p, ψ). This work led to three publications (Plaszczynski *et al.* 2014, Montier *et al.* 2015a,b), with one more currently being revised (Alina *et al.* 2016).
- Full study of the inverse problem that is the recovery of statistical properties of the interstellar magnetic field from maps of polarized submillimetre thermal dust emission. This work, in collaboration with Jérémy Neveu (now at LAL, Orsay), is based on a grid of models for the 3D dust density and the magnetic field with prescribed statistical properties, and on a maximum-likelihood analysis. It is the topic of a paper currently in preparation (Levrier *et al.* 2016).
- Analysis of relative orientations between structures of interstellar matter and the magnetic field. We note an evolution of these relative orientations as a function of column density, from a configuration in which diffuse matter filaments tend to be preferentially aligned with the magnetic field to a configuration in which this field is preferentially perpendicular to dense, self-gravitating filaments (Planck Intermediate Results XXXV, 2015).
- Construction of synthetic maps of continuum submillimetre thermal dust emission in simulations of prestellar cores (with B. Commerçon, ENS Lyon), using the ALMA (Atacama Large Millimeter Array) simulator developed by J. Pety, S. Guilloteau, and F. Guth (IRAM Grenoble). These maps allow the determination of the instrumental configurations which are best suited to estimate the magnetization level in these objects (Commerçon *et al.* 2012)..
- Construction of synthetic maps of continuum submillimetre thermal dust emission and molecular line emission in simulations of the formation and evolution of Milky-Way-like galaxies over cosmic times (work in progress in collaboration with J. Devriendt, University of Oxford).
- Simulations of the physical and chemical structure of a molecular cloud, using the Meudon PDR Code (Levrier *et al.* 2012). By considering the illumination of density profiles extracted from numerical simulations of ISM turbulent flows, I could show that abundances of several key molecular species, and

their correlations, are better reproduced when taking into account the fractal structure of the medium.

- Application of these simulations to the determination of the accuracy with which the ionization rate by cosmic rays is well determined by measurements of the column density of H_3^+ (Gerin *et al.* 2012). This work shows that usual diagnostics tend to underestimate this ionization rate.

- Statistical analysis of synthetic models of interstellar turbulence. This work (Miville-Deschênes *et al.* 2003, Levrier 2004) established the link between statistical properties of the interstellar velocity field and usual spectro-imagery observables (channel maps, intensity moment maps).

■ Participation to observational and instrumental projects

- Participation to the analysis of *Planck* polarization data at 353 GHz.

- Participation to the scientific definition of "Galactic astrophysics" aspects in space mission projects (simulation of CII [158 μm] emission in the diffuse ISM for SPICA/SAFARI; simulation of submillimetre dust emission for Millimetron and CORe++) and ground-based instrumental projects (diagnostics of interstellar turbulence with SKA, in particular).

- Participation to observational projects with ALMA to study the topology of the magnetic field at various scales, in particular in a protostellar object (HH212, PI : C. Codella) and in a spiral galaxy (NGC1566, PI : A. Hughes).

- Participation to observational projects with IRAM instruments (observation of the prestellar core Barnard 1b with Plateau de Bure, PI : M. Gerin; molecular survey of the Orion B molecular cloud in the millimetre range with the 30 m radiotelescope, PI : J. Pety & J. Orkisz).

■ Software developments

- Development of mapping tools (*S³-Tools*) for simulated catalogues of extragalactic sources in the framework of the design of SKA (Wilman *et al.* 2008, Obreschkow *et al.* 2009).

- Development of a joint IDL-Python library for the analysis of polarization data, in collaboration with L. Montier (IRAP Toulouse).

- Participation to the development of the STARFORMAT <http://starformat.obspm.fr> platform (PI : P. Hennebelle) aimed at spreading results of numerical simulations of ISM flows.

- Development of the online access to the ALMA simulator within the "Numerical ISM" platform <http://ism.obspm.fr>, led by Franck Le Petit (LERMA, Meudon).

- Development of fitting methods for radiative transfer models with the RADEX code, to help with the analysis of spectroscopic observations towards massive star-forming regions (Leurini *et al.* 2015, Gusdorf *et al.* 2016).

TEACHING ACTIVITIES

■ Préparation à l'agrégation de sciences physiques [2008 - ..., Master 2 level, 120 h per year]

- Supervision of laboratory work (electronics, optics, mechanics, thermodynamics, ...)
- Course "Experimental uncertainties"
- Correction of both written and oral tests
- Participation to the design and realization of new experiments

■ Formation Interuniversitaire de Physique [2008 - ..., Licence 3 level, 15 h per year]

- Exercise sessions "Introductory astrophysics" complementing the course, taught from 2008 to 2011 by Steve Balbus, and from 2012 by Patrick Hennebelle (topics covered include radiative transfer, formation, structure, and evolution of stars, compact objects and cosmology).

■ Master "Astronomie, Astrophysique et Ingénierie Spatiale" [2013 - ..., Master 2 level, 15 h per year]

- Course "Radiative transfer" (topics covered include photometric quantities, transfer equation, thermodynamic equilibrium, lines and continuum, non-LTE effects, numerical methods).

STUDENT AND POST-DOC SUPERVISION

- **Postdocs** : Jérémy Neveu [ENS Paris, 2014-2015]
- **PhD students** : Manuel Berthet [ENS Paris, 2013-2017]
- **M2 students** : Rémi Paulin [2011, 2 months], Manuel Berthet [2012, 2 months], Bilal Ladjelate [2013, 2 months]
- **M1 students** : Brice Poillot [2011, 1 month]
- **ENS Tutoring** : Rémi Paulin [2010], Sandrine Codis [2010], Pierre Mourier [2013], Félix Driencourt-Mangin [2013], Paul Caucal [2014], Jordan Philidet [2015]
- **PhD juries** : Jean-François Robitaille [Université Laval, Québec, Canada, 3 may 2014].
- **Internship juries** : 46 internship juries since 2012, from L3 to M2 level

COLLECTIVE RESPONSIBILITIES

- **Deputy-director for the “Centre de préparation à l’agrégation de sciences physiques”** [2008 - ...]
 - Recruitment of students, in collaboration with the Director (Jean-Marc Berroir, then Jean-Michel Raimond) and representatives of Universities Paris VI and Paris XI.
 - Establishment of yearly plannings (courses, exercise sessions, laboratory sessions, tests).
 - Organisation of regular academic meetings.
 - Maintenance of the Centre’s web site.
- **ENS representative for the Master “Astronomie, Astrophysique et Ingénierie Spatiale”** [2012 - ...]
 - Recruitment of students, in collaboration with the representatives of Observatoire de Paris and Universities Paris VI, Paris VII, and Paris XI.
 - Participation to academic meetings, yearly planning, and internship jury.
 - Advice to students of ENS wishing to attend the Master’s courses.
- **Member of the jury for admission to ENS** [2012 - ...]
 - Correction of exam papers for the physics test specific to ENS Paris (6h, “PC” competition, ~150 papers to grade per year).
 - Authorship of the subject for the 2014 session, concerning some aspects of the physics involved in the *Planck* mission.
- **Other responsibilities**
 - Member of the *Planck*-HFI Core Team since 2011, and *Planck* Scientist since 2014.
 - Health and Safety representative for the ENS team of LERMA, since September 2009.
 - Member of the committee overseeing the second phase of renovation works for the Physics Department of ENS, since may 2015.
 - LERMA contact for the “Computational grid” initiative (2010-2014).
 - Elected member of LERMA laboratory council (“conseil de laboratoire”), since january 2014.
 - Appointed member of CNU section 34 (“Astronomy, astrophysics”), since november 2015.
 - Member of the Time Allocation Committee of IRAM, since February 2016.

Liste des publications

LIST OF PUBLICATIONS - [92]

Publications as main author - [12]

- **Planck intermediate results. XX. Comparison of polarized thermal emission from Galactic dust with simulations of MHD turbulence.** *Planck* collaboration, *A&A*, 576, 105, 2015
- **Simulated ALMA Observations of Collapsing Low-mass Dense Cores.** F. Levrier *et al.*, *ASP Conference Proceedings*, 476, 313, 2013
- **Synthetic observations of first hydrostatic cores in collapsing low-mass dense cores. II. Simulated ALMA dust emission maps.** B. Commerçon *et al.*, *A&A*, 548, 39, 2012
- **UV-driven chemistry in simulations of the interstellar medium I : Post-processed chemistry with the Meudon PDR code.** F. Levrier *et al.*, *A&A*, 544, 22, 2012
- **Mapping the SKA Simulated Skies with the S³-Tools.** F. Levrier *et al.*, Proceedings of the conference “*Wide Field Science and Technology for the Square Kilometre Array*”, Limelette, Belgium, 3-6 November 2009 (Eds : S. A. Torchinsky, A. van Ardenne, T. van den Brink, A. J. J. van Es, A. J. Faulkner)
- **Simulated [CII] observations for SPICA/SAFARI.** F. Levrier *et al.*, Proceedings of the workshop “*The Space Infrared Telescope for Cosmology & Astrophysics : Revealing the Origins of Planets and Galaxies*”, July 2009, Oxford, United Kingdom
- **ALMA : Fourier phase analysis made possible.** F. Levrier, E. Falgarone & F. Viallefond, *Astrophysics & Space Science*, 313, 2008
- **Fourier phase analysis in radio-interferometry.** F. Levrier, E. Falgarone & F. Viallefond, *A&A*, 456, 205, 2006
- **The HI kinematics and distribution of four Blue Compact Dwarf galaxies.** Trinh Xuan Thuan, J. E. Hibbard & F. Levrier, *Astronomical Journal*, 128, 617, 2004
- **Velocity centroids and the structure of interstellar turbulence I : Analytical study.** F. Levrier, *A&A*, 421, 387, 2004
- **On the use of fractional Brownian motion simulations to determine the three-dimensional statistical properties of interstellar gas.** M.-A. Miville-Deschênes, F. Levrier & E. Falgarone, *ApJ*, 593, 831, 2003
- **HI in four Blue Compact Dwarf galaxies.** Trinh Xuan Thuan, J. E. Hibbard & F. Levrier, *ASP Conference Proceedings*, 240, 865, 2001

Publications with students and post-docs - [3]

- **Magnetic fields and diffuse filaments in the Polaris Flare.** M. Berthet, F. Levrier, P. Hily-Blant, E. Falgarone, P. Bastien, T. Sousbie, *A&A*, submitted.
- **Statistical properties of polarized dust emission : lessons from a model of the turbulent and magnetized interstellar medium.** F. Levrier, J. Neveu, *Highlights of Astronomy*, in press.
- **Intense velocity-shears, magnetic fields and filaments in diffuse gas.** E. Falgarone, P. Hily-Blant, F. Levrier, M. Berthet, P. Bastien, D. Clemens, *Highlights of Astronomy*, 16, 388, 2015

Publications as a major contributor - [11]

- **Magnetic field morphology in nearby molecular clouds as revealed by starlight and submillimetre polarization.** J.D. Soler, F. Alves, F. Boulanger, A. Bracco, E. Falgarone, G.A.P; Franco, V. Guillet, P. Hennebelle, F. Levrier, P.G. Martin, M.-A. Miville-Deschênes, *A&A*, submitted.
- **Planck intermediate results. XXXV. Probing the role of the magnetic field in the formation of structure in molecular clouds.** *Planck* collaboration, *A&A*, 586, 138, 2016.
- **Planck intermediate results. XIX. An overview of the polarized thermal emission from Galactic dust.** *Planck* collaboration, *A&A*, 576, 104, 2015
- **Planck intermediate results. XXI. Comparison of polarized thermal emission from Galactic dust at 353 GHz with optical interstellar polarization.** *Planck* collaboration, *A&A*, 576, 106, 2015
- **Polarisation measurements analysis I. Impact of the full covariance matrix on the polarisation fraction and angle measurements.** L. Montier, S. Plaszczynski, F. Levrier, M. Tristram, D. Alina, I. Ristorcelli & J.-P. Bernard, *A&A*, 574, 135, 2015
- **Polarisation measurements analysis II. Best estimators of the polarization fraction and angle.** L. Montier, S. Plaszczynski, F. Levrier, M. Tristram, D. Alina, I. Ristorcelli & J.-P. Bernard, *A&A*, 574, 136, 2015
- **A novel estimator of the polarization amplitude from normally distributed Stokes parameters.** S. Plaszczynski, L. Montier, F. Levrier, M. Tristram, *MNRAS*, 439, 4048, 2014
- **Hydride spectroscopy of the diffuse interstellar medium : new clues on the fraction of molecular gas and cosmic ray ionization rate in relation to H₃⁺.** M. Gerin, F. Levrier, E. Falgarone, B. Godard, P. Hennebelle, F. Le Petit, M. De Luca, D. Neufeld, P. Sonnentrucker, P. Goldsmith, N. Flagey, D. C. Lis, C. M. Persson, J. H. Black, J. R. Goicoechea, K. M. Menten, *Phil. Trans. R. Soc. A*, 370, 5174, 2012
- **SKA HI end2end simulation.** H.-R. Klöckner, R. Auld, I. Heywood, D. Obreschkow, F. Levrier, S. Rawlings, Proceedings of the conference “*Wide Field Science and Technology for the Square Kilometre Array*”, Limelette, Belgium, 3-6 November 2009 (Eds : S. A. Torchinsky, A. van Ardenne, T. van den Brink, A. J. J. van Es, A. J. Faulkner)

- **A Virtual Sky with Extragalactic HI and CO Lines for the Square Kilometre Array and the Atacama Large Millimeter / Submillimeter Array.** D. Obreschkow, H.-R. Klöckner, I. Heywood, F. Levrier, S. Rawlings, *ApJ*, 703, 1890, 2009
- **A semi-empirical simulation of the extragalactic radio continuum sky for next generation radio telescopes.** R. J. Wilman, L. Miller, M. L. Jarvis, T. Mauch, F. Levrier, F. B Abdalla, S. Rawlings, H.-R. Klöckner, D. Obreschkow, D. Olteanu, S. Young, *MNRAS*, 388, 1335, 2008

Publications as a minor contributor - [15]

- **Polarization measurements analysis III. Analysis of the polarization angle dispersion function with high precision polarization data.** D. Alina, L. Montier, I. Ristorcelli, J.-P. Bernard, F. Levrier, E. Abdikamalov, *A&A*, submitted.
- **Turbulence and star formation efficiency in molecular clouds : solenoidal versus compressive motions in Orion B.** J. Orkisz, J. Pety, M. Gerin, E. Bron, V. V. Guzman, S. Bardeau, J. R. Goicoechea, P. Gratier, F. Le Petit, F. Levrier, H. Liszt, K. Öberg, N. Peretto, E. Roueff, A. Sievers, P. Tremblin, *A&A*, submitted.
- **Planck intermediate results. XLIV. The structure of the Galactic magnetic field from dust polarization maps of the southern Galactic cap.** *Planck* collaboration, *A&A*, submitted.
- **Environmental impacts of irradiated shocks in the G5.89-0.39 massive star-forming region.** A. Gusdorf, M. Gerin, J.R. Goicoechea, A. Marcowith, S. Cabrit, P. Lesaffre, M. Ruaud, F. Levrier, N. Flagey, G. Pineau des Forêts, R. Güsten, *A&A*, submitted.
- **Planck intermediate results. XXXVIII. E- and B-modes of dust polarization from the magnetized filamentary structure of the interstellar medium.** *Planck* collaboration, *A&A*, 586, 141, 2016
- **Planck intermediate results. XXXIV. The magnetic field structure in the Rosette Nebula.** *Planck* collaboration, *A&A*, 586, 137, 2016
- **Planck intermediate results. XXXIII. Signature of the magnetic field geometry of interstellar filaments in dust polarization maps.** *Planck* collaboration, *A&A*, 586, 136, 2016
- **Planck intermediate results. XXXII. The relative orientation between the magnetic field and structures traced by interstellar dust.** *Planck* collaboration, *A&A*, 586, 135, 2016
- **Galactic interstellar filaments as probed by LOFAR and Planck.** S. Zaroubi, V. Jelić, A. G. de Bruyn, F. Boulanger, A. Bracco, R. Kooistra, M. I. R. Alves, M. A. Brentjens, K. Ferrière, T. Ghosh, L. V. E. Koopmans, F. Levrier, M.-A. Miville-Deschênes, L. Montier, V. N. Pandey, J. D. Soler, *MNRAS*, 454, L46, 2015
- **Spectroscopically resolved far-IR observations of the massive star-forming region G5.89-0.39.** S. Leurini, F. Wyrowski, H. Wiesemeyer, A. Gusdorf, R. Güsten, K.M. Menten, M. Gerin, F. Levrier, H.W. Hübers, K. Jacobs, O. Ricken, H. Richter, *A&A*, 584, 70, 2015
- **Planck intermediate results. XXII. Frequency dependence of thermal emission from Galactic dust in intensity and polarization.** *Planck* collaboration, *A&A*, 576, 107, 2015
- **First detection of [NII] 205 μ m absorption in interstellar gas. Herschel-HIFI observations towards W31C, W49N, W51 and G34.3+0.1.** C.M. Persson, M. Gerin, B. Mookerjee, J.H. Black, M. Olberg, J.R. Goicoechea, G.E. Hassel, E. Falgarone, F. Levrier, K.M. Menten, J. Pety, *A&A*, 568, 37, 2014
- **MESMER : MeerKAT Search for Molecules in the Epoch of Reionization.** I. Heywood, R. P. Armstrong, R. Booth, A. J. Bunker, R. P. Deane, M. J. Jarvis, J. L. Jonas, M. E. Jones, H.-R. Klöckner, J.-P. Kneib, K. K. Knudsen, F. Levrier, D. Obreschkow, D. Rigopoulou, S. Rawlings, O. M. Smirnov, A. C. Taylor, A. Verma, J. Dunlop, M. G. Santos, E. R. Stanway, C. Willott, Proceedings of the conference “*Astronomy with megastructures : Joint science with the E-ELT and SKA*”, 10-14 Mai 2010, Crete, Greece (Eds : I. Hook, D. Rigopoulou, S. Rawlings, A. Karastergiou)
- **The structure of the cold diffuse interstellar medium.** E. Falgarone, F. Levrier & P. Hily-Blant, *EAS Publication Series*, 23, 73, 2007
- **Structure of Molecular Clouds.** E. Falgarone, P. Hily-Blant & F. Levrier, *Astrophysics & Space Science*, 292, 89, 2004

Publications within collaborations - [51]

- **Planck 2015 results. XXVIII. The Planck Catalogue of Galactic Cold Clumps.** *Planck* collaboration, *A&A*, submitted.
- **Planck 2015 results. XXVI. The Second Planck Catalogue of Compact Sources.** *Planck* collaboration, *A&A*, submitted.
- **Planck 2015 results. XXV. Diffuse low-frequency Galactic foregrounds.** *Planck* collaboration, *A&A*, submitted.
- **Planck 2015 results. XXIV. Cosmology from Sunyaev-Zeldovich cluster counts.** *Planck* collaboration, *A&A*, submitted.
- **Planck 2015 results. XXIII. The thermal Sunyaev-Zeldovich effect - cosmic microwave background correlation.** *Planck* collaboration, *A&A*, submitted.
- **Planck 2015 results. XXII. A map of the thermal Sunyaev-Zeldovich effect.** *Planck* collaboration, *A&A*, submitted.
- **Planck 2015 results. XXI. The integrated Sachs-Wolfe effect.** *Planck* collaboration, *A&A*, submitted.
- **Planck 2015 results. XX. Constraints on inflation.** *Planck* collaboration, *A&A*, submitted.
- **Planck 2015 results. XIX. Constraints on primordial magnetic fields.** *Planck* collaboration, *A&A*, submitted.
- **Planck 2015 results. XVIII. Background geometry & topology.** *Planck* collaboration, *A&A*, submitted.
- **Planck 2015 results. XVII. Constraints on primordial non-Gaussianity.** *Planck* collaboration, *A&A*, submitted.
- **Planck 2015 results. XVI. Isotropy and statistics of the CMB.** *Planck* collaboration, *A&A*, submitted.
- **Planck 2015 results. XV. Gravitational lensing.** *Planck* collaboration, *A&A*, submitted.
- **Planck 2015 results. XIV. Dark energy and modified gravity.** *Planck* collaboration, *A&A*, submitted.

- **Planck 2015 results. XIII. Cosmological parameters.** *Planck* collaboration, *A&A*, submitted.
- **Planck 2015 results. XII. Full Focal Plane simulations.** *Planck* collaboration, *A&A*, submitted.
- **Planck 2015 results. XI. CMB power spectra, likelihoods, and robustness of parameters.** *Planck* collaboration, *A&A*, submitted.
- **Planck 2015 results. X. Diffuse component separation : Foreground maps.** *Planck* collaboration, *A&A*, submitted.
- **Planck 2015 results. IX. Diffuse component separation : CMB maps.** *Planck* collaboration, *A&A*, submitted.
- **Planck 2015 results. VIII. High Frequency Instrument data processing : Calibration and maps.** *Planck* collaboration, *A&A*, submitted.
- **Planck 2015 results. VII. HFI TOI and beam processing.** *Planck* collaboration, *A&A*, submitted.
- **Planck 2015 results. VI. LFI mapmaking.** *Planck* collaboration, *A&A*, submitted.
- **Planck 2015 results. V. LFI Calibration.** *Planck* collaboration, *A&A*, submitted.
- **Planck 2015 results. IV. Low Frequency Instrument beams and window functions.** *Planck* collaboration, *A&A*, submitted.
- **Planck 2015 results. III. LFI systematic uncertainties.** *Planck* collaboration, *A&A*, submitted.
- **Planck 2015 results. II. Low Frequency Instrument data processing.** *Planck* collaboration, *A&A*, submitted.
- **Planck 2015 results. I. Overview of products and scientific results.** *Planck* collaboration, *A&A*, submitted.
- **Planck intermediate results. L. Evidence for spatial variation of the polarized thermal dust spectral energy distribution and implications for CMB *B*-mode analysis.** *Planck* collaboration, *A&A*, submitted.
- **Planck intermediate results. XLIX. Parity-violation constraints from polarization data.** *Planck* collaboration, *A&A*, submitted.
- **Planck intermediate results. XLVIII. Disentangling Galactic dust emission and cosmic infrared background anisotropies.** *Planck* collaboration, *A&A*, submitted.
- **Planck intermediate results. XLVII. Planck constraints on reionization history.** *Planck* collaboration, *A&A*, submitted.
- **Planck intermediate results. XLVI. Reduction of large-scale systematic effects in HFI polarization maps and estimation of the reionization optical depth.** *Planck* collaboration, *A&A*, submitted.
- **Planck intermediate results. XLV. Radio spectra of northern extragalactic radio sources.** *Planck* collaboration, *A&A*, submitted.
- **Planck intermediate results. XLIII. The spectral energy distribution of dust in clusters of galaxies.** *Planck* collaboration, *A&A*, submitted.
- **Planck intermediate results. XLII. Large-scale Galactic magnetic fields.** *Planck* collaboration, *A&A*, submitted.
- **Planck intermediate results. XLI. A map of lensing-induced *B*-modes.** *Planck* collaboration, *A&A*, submitted.
- **Planck intermediate results. XL. The Sunyaev-Zeldovich signal from the Virgo cluster.** *Planck* collaboration, *A&A*, submitted.
- **Planck intermediate results. XXXIX. The Planck list of high-redshift source candidates.** *Planck* collaboration, *A&A*, submitted.
- **Planck intermediate results. XXXVII. Evidence of unbound gas from the kinetic Sunyaev-Zeldovich effect.** *Planck* collaboration, *A&A*, 586, 140, 2016
- **Planck intermediate results. XXXVI. Optical identification and redshifts of Planck SZ sources with telescopes in the Canary Islands Observatories.** *Planck* collaboration, *A&A*, 586, 139, 2016
- **Planck intermediate results. XXX. The angular power spectrum of polarized dust emission at intermediate and high Galactic latitudes.** *Planck* collaboration, *A&A*, 586, 133, 2016
- **Planck intermediate results. XXIX. All-sky dust modelling with Planck, IRAS, and WISE observations.** *Planck* collaboration, *A&A*, 586, 132, 2016
- **A Joint Analysis of BICEP2/Keck Array and Planck Data.** *BICEP2/Keck* and *Planck* collaborations, *PRL*, 114, 101301, 2015
- **Planck intermediate results. XXVIII. Interstellar gas and dust in the Chamaleon clouds as seen by Fermi LAT and Planck.** *Planck* and *Fermi* collaborations, *A&A*, 582, 31, 2015
- **Planck intermediate results. XXVII. High-redshift infrared galaxy overdensity candidates and lensed sources discovered by Planck and confirmed by Herschel-SPIRE.** *Planck* collaboration, *A&A*, 582, 30, 2015
- **Planck intermediate results. XXVI. Optical identification and redshifts of Planck clusters with the RTT150 telescope.** *Planck* collaboration, *A&A*, 582, 29, 2015
- **Planck intermediate results. XXV. The Andromeda Galaxy as seen by Planck.** *Planck* collaboration, *A&A*, 582, 28, 2015
- **Planck 2013 results. XXXII. The Updated Planck Catalogue of Sunyaev-Zeldovich Sources.** *Planck* collaboration, *A&A*, 581, 14, 2015
- **Planck 2013 results. XI. All-sky model of thermal dust emission.** *Planck* collaboration, *A&A*, 571, 11, 2014
- **Planck intermediate results. XVII. Emission of dust in the diffuse interstellar medium from the far-infrared to microwave frequencies.** *Planck* collaboration, *A&A*, 566, 55, 2014
- **Planck intermediate results. XIV. Dust emission at millimetre wavelengths in the Galactic plane.** *Planck* collaboration, *A&A*, 564, 45, 2014

Dossier de synthèse

Chapitre 1

Introduction

1.1 A lightning-fast overview of the interstellar medium

Mass budget

As the name suggests, when one speaks of the interstellar medium (ISM), one means essentially everything which lies in between the stars within a galaxy. Without any further specification, this refers to the ISM of our own Galaxy, the Milky Way. The term “ISM” is a deceptively simple and mundane one for what is in reality a very complex and fundamentally open physical system, whose role is essential in the “Galactic ecosystem” and the cycle of matter and energy at the heart of the star formation process. The importance of the ISM in the physical machinery that is our Galaxy is all the more fundamental than it represents only a small fraction of its mass : about $7 \times 10^9 M_{\odot}$, which is approximately 7% of the stellar mass content, and less than 1% of the total mass of the Galaxy, which is dominated by the elusive dark matter (Draine 2011).

Elemental composition

The ISM is made up of gas and dust particles, and in truth consists of an ensemble of species forming a continuum, from atomic hydrogen H to simple and more complex molecules, to polycyclic aromatic hydrocarbons (PAHs), to dust aggregates reaching sizes up to approximately $1 \mu\text{m}$ (Kruegel 2003). One could even extend this continuum to larger particles, which are the building blocks of planetesimals and full-fledged planets. The gas and dust of the ISM are generally assumed to be well-mixed. Most of the gas is hydrogen, in ionized (HII), neutral atomic (HI) and molecular (H₂) forms, which altogether amount to approximately 71% of the total mass of the ISM. The second constituent of the ISM in mass is Helium (28%). The remaining percent of the ISM mass is in heavier elements, mostly C, N, O, Ne, Fe, Si, S, Ar, Ni, each amounting to a little more than 0.1% in mass (Draine 2011).

Interstellar chemistry

Despite their very low mass budget, these “heavy” elements play a fundamental role in the physics of the ISM, as they combine to form a large number of molecular species and molecular ions. The first detection of an interstellar molecule dates back to 1937, with the identification of the methylidyne radical CH (Swings & Rosenfeld 1937), and the signatures of these species in absorption or emission have led to a current tally of about two hundred, the largest one being the C₇₀ fullerene (Cami et al.

2010). This underlines the richness of ISM chemistry, even, surprisingly, in its most diffuse regions where the ambient radiation field should prevent the formation of molecules (see, e.g., Liszt et al. 2010, and references therein), or where the gas temperature is not sufficient to activate highly endothermic chemical pathways (Godard et al. 2014). The importance of that interstellar chemistry for understanding the origins of life on Earth needs not be emphasized (Altwegg et al. 2015).

Interstellar dust grains

The second major impact these heavy elements have on ISM physics is that they are essential constitutive elements of dust grains. These reprocess a significant fraction of visible and UV starlight to the far infrared (FIR); they play a vital role in the heating of the gas via the photoelectric effect (see, e.g., Draine 1978; Wolfire et al. 1995); they participate in the chemical networks at play in the ISM by allowing gas phase species to stick to their surfaces (via both chemical and physical adsorption processes) and react with each other to form new molecules which could not be formed directly in the gas phase, given the low temperatures of the ISM. The formation of molecular hydrogen, H_2 , the most abundant molecule in the Universe, is the foremost example of such a grain surface chemical process (see, e.g., Le Bourlot et al. 2012; Bron et al. 2014, and references therein). In cold clouds and prestellar cores, chemical species may freeze-out in ice mantles on the surface of these grains (see, e.g., Jørgensen et al. 2004).

The sizes of dust particles range roughly from 10 \AA to $1 \mu\text{m}$ (Kruegel 2003), with a size distribution that is usually modelled as a power-law¹ (Mathis et al. 1977) such that most of the dust mass is supplied by the biggest grains, and most of the surface area is provided by the smallest ones. Their composition is still a matter of debate, but they can be broadly classified in two types, silicate and carbonaceous grains. As pointed out by Kruegel (2003), these grains are formed in the circumstellar envelopes of AGB stars, and their composition is closely related to the relative elemental abundances of carbon (C) and oxygen (O) in these envelopes.

Cosmic rays

Cosmic rays are ions and electrons which are accelerated to relativistic speeds, sometimes with kinetic energies up to a few 10^{20} eV (Bird et al. 1994). It is believed that they are accelerated at shocks, through a process called diffusive shock acceleration (Drury 1983; Caprioli & Spitkovsky 2014), occurring in supernova remnants (Cristofari et al. 2013), but also in protostellar objects (Padovani et al. 2016). They propagate diffusively throughout the Galaxy (see, e.g., Blasi & Amato 2012), interacting with interstellar structures and thus participating in physical processes in the ISM. In particular, low-energy ($< 1 \text{ GeV}$) cosmic rays provide the main source of ionization in dense gas, thus opening important chemical pathways (Vaupré et al. 2014; Gerin et al. 2012). The importance of cosmic ray processes for ISM physics extends to very small scales, as the proper treatment of the attenuation of their flux in collapsing protostellar objects is necessary to decouple the gas and magnetic field in these objects, allowing to form a centrifugally-supported disk and solving the so-called magnetic-braking catastrophe (Hennebelle & Teyssier 2008; Padovani et al. 2015).

Phases of the ISM gas

As already mentioned, the energetic photons from stars impinging on dust grains strip them from electrons, whose kinetic energy is then redistributed, via collisions, to the other electrons, and then to the rest of the gas (ions and neutral species in turn). This results in gas heating (Bakes & Tielens 1994), with

1. Jura (1994) and Weingartner & Draine (2001) have provided further improvements upon the so-called MRN distribution of Mathis et al. (1977).

timescales usually much shorter than the typical dynamical timescales in the ISM (Spitzer 1978). This is not always the case, as mechanical heating may locally dominate other heating processes, for instance in the wake of shock fronts, and in regions where intermittent turbulence dissipation occurs (Godard et al. 2014). Low-energy cosmic rays provide an additional source of heating via ionization (Goldsmith & Langer 1978; Glassgold et al. 2012), in a process similar to photoionization (Glassgold & Najita 2015). Finally, molecular hydrogen H_2 formed on the surface dust grains is released in the gas phase in a vibrationally excited state, so that collisional de-excitations participate in the heating of the gas (see Le Bourlot et al. 2012, and references therein).

Balancing these heating mechanisms, the ISM may cool radiatively, through optically-thin continuum emission of dust as we will discuss later, through thermal free-free emission, and via different lines depending on the physical state of the gas. These include molecular hydrogen lines (Le Bourlot et al. 1999); lines from other molecular species² such as CO, H_2O , or O_2 (Neufeld et al. 1995); fine-structure atomic lines, mostly [CII] at $158 \mu\text{m}$ (Fixsen et al. 1999; Pineda et al. 2013), [OI] at $63 \mu\text{m}$ and $145 \mu\text{m}$ (Bernard-Salas et al. 2012), [NII] at $122 \mu\text{m}$ and $205 \mu\text{m}$ (Goldsmith et al. 2015); resonance lines from iron and other metals (Gaetz & Salpeter 1983; Lykins et al. 2013); and recombination lines such as Ly- α (Faucher-Giguère et al. 2010).

Heating and cooling mechanisms may be modelled via a net cooling function $\mathcal{L} = n_{\text{H}}^2 \Lambda - n_{\text{H}} \Gamma$, where $n_{\text{H}}^2 \Lambda$ and $n_{\text{H}} \Gamma$ are respectively the cooling and heating rates, emphasizing their dependency on the gas density n_{H} (Wolfire et al. 1995). The computation of thermal equilibrium $\mathcal{L} = 0$ exhibits the possibility for interstellar gas to exist under several different phases³, among which we may note the following (see, e.g., Draine 2011), from the most diffuse to the densest :

- ▶ Hot ionized gas (HIM) : $n_{\text{H}} \sim 4 \times 10^{-3} \text{ cm}^{-3}$, $T_k \sim 5 \times 10^5 \text{ K}$
- ▶ Warm ionized gas (WIM) : $n_{\text{H}} \sim 0.03 \text{ cm}^{-3}$, $T_k \sim 10^4 \text{ K}$
- ▶ Warm neutral atomic HI gas (WNM) : $n_{\text{H}} \sim 0.6 \text{ cm}^{-3}$, $T_k \sim 8000 \text{ K}$
- ▶ Cold neutral atomic HI gas (CNM) : $n_{\text{H}} \sim 30 \text{ cm}^{-3}$, $T_k \sim 100 \text{ K}$
- ▶ Dense molecular H_2 gas : $n_{\text{H}} > 10^3 \text{ cm}^{-3}$, $T_k < 100 \text{ K}$

Spatial distribution

The structures of the ISM cover a large range of scales, from Galactic spiral arms (a few 10^4 pc) to Giant Molecular Clouds (GMC, typically 100 pc), down to scales comparable to those of stellar systems (200 AU or 1 mpc). They lie essentially within thin disks of various scale heights, depending on the phase considered, that are more or less coplanar with the orbits of stars around the Galaxy, although some hot gas is definitely present in the spherical halo (Miller & Bregman 2015). Most of the cold HI gas is located within $100\text{-}200 \text{ pc}$ of the midplane, but another disk of warmer atomic gas extends to about 500 pc (Dickey & Lockman 1990). The molecular gas and dust are distributed with smaller scale heights of about 80 pc for the former⁴ (Clemens et al. 1988; Dame et al. 2001) and 130 pc for the latter (Drimmel & Spergel 2001). One should bear in mind that these are very rough descriptions, since it is recognized that the HI disk is flaring towards the outer Galaxy, that molecular gas is not equally distributed radially⁵, and that both molecular gas and dust are more concentrated along the spiral arms than in the interarm regions.

2. CO is the second most abundant molecule in the ISM, after H_2 , and much more readily observed because of its permanent dipole moment.

3. Of course, the ISM being a dynamic medium, regions exhibiting kinetic temperatures T_k and gas densities n_{H} different from the ones listed below are observed (see references in Hennebelle & Falgarone 2012).

4. Note that a faint, thicker (250 pc scale height) disk of diffuse molecular gas is also suggested by observations (Hennebelle & Falgarone 2012).

5. Roughly speaking, there is a large concentration in the nucleus, a hole near 2 kpc and a molecular ring between 4 and 8 kpc (Scoville & Solomon 1975).

The cycle of interstellar matter

The ISM is a fundamentally open system, constantly exchanging matter and energy with stars and the extragalactic medium⁶. It stands at the crossroads of many chemical and physical processes⁷ over a large range of spatial scales, from Galactic scales and beyond⁸ to stellar system scales. These processes occur on possibly vastly different time scales, and play a central part in the cycle of matter from the ISM to stars and back again, which we briefly describe here, starting with the diffuse WNM.

It is stirred by motions at all scales, due to many different processes : Galactic differential rotation and galaxy-galaxy interactions (Bournaud et al. 2011), the crossing of spiral arms (Falseta-Gonçalves et al. 2015), supernovæ explosions (McKee & Ostriker 1977), and to a lesser extent outflows from young stars (Li et al. 2015). These motions may lead to local compression of the gas, which heats up. If it is able to cool down via radiative processes such as those mentioned earlier, then these local overdensities of now CNM gas may become gravitationally bound (Hennebelle & Audit 2007). They will then form molecular clouds (MC) when their density is sufficient to shield their interior from photodissociation (Valdivia et al. 2016), and these MC will subsequently fragment in a hierarchical structure, down to the scale of dense ($n_{\text{H}} \sim 10^6 \text{ cm}^{-3}$) and cold ($T_k \sim 10 \text{ K}$) prestellar cores (see André et al. 2009, and references therein). These prestellar objects may form young stellar objects (YSO) through gravitational collapse, which requires the evacuation of a large fraction of the prestellar core's angular momentum, leading to the formation of jets and outflows, perpendicularly to the accretion disk around the YSO (Pudritz et al. 2007). Once on the main sequence, stars continue to have an impact on their environment : through radiation, which can ionize the neighbouring gas and clear dust grains via radiation pressure, but also through stellar winds which inject material back into the circumstellar medium (Höfner 2012). Supernovæ⁹ disperse heavy chemical elements and inject large amounts of kinetic energy far out into the ISM, participating in the perpetuation of the matter-energy cycle of the ISM (Iffrig & Hennebelle 2015).

These macroscopic motions dissipate at small scales into gas heating, through various processes such as viscous heating, Ohmic dissipation, and ion-neutral friction (see Momferratos et al. 2014, and references therein). In between the injection and dissipation of energy is the realm of interstellar turbulence (Elmegreen & Scalo 2004; Hennebelle & Falgarone 2012).

1.2 Turbulence in the interstellar medium

A primer in turbulence

Turbulence is characterized by chaotic motions in a fluid which make it impossible to predict, in a deterministic way, its local kinematic description on long timescales. Only statistical tools are appropriate to tackle turbulence (Monin et al. 2007). Mathematically, turbulence arises from the non-linearity and non-locality of the equation describing the time evolution of the velocity field \mathbf{v} in a fluid. Even in the simplest case of a non-magnetized, incompressible fluid, the Navier-Stokes equation presents this

6. Draine (2011) draws the following sketch of the mass exchanges : gas infall from the outskirts of the Galaxy brings in $\sim 0.5 M_{\odot} \text{ yr}^{-1}$. Out of the interstellar gas, stars form at a rate (Star Formation Rate, SFR) $\sim 1.3 M_{\odot} \text{ yr}^{-1}$. In the course of their lives, stars yield back $\sim 0.5 M_{\odot} \text{ yr}^{-1}$ to the ISM in the form of outflows, stellar winds and SNe, and end up forming $\sim 0.2 M_{\odot} \text{ yr}^{-1}$ of stellar remnants (white dwarfs, neutron stars, black holes).

7. The fact that in the ISM, various energy densities (thermal, kinetic, magnetic, cosmic rays, electromagnetic in the far infrared from dust emission, in the UV and visible from direct starlight) are all about $0.2 - 2 \text{ eV cm}^{-3}$ is interpreted as the result of this coupling of processes.

8. Galactic fountains driven by supernovæ (McKee & Ostriker 1977) and cold accretion flows from filamentary structures feeding gas in, for instance.

9. Both core-collapse supernovæ (SNe) marking the end of the life of massive stars (Janka et al. 2012), and thermonuclear SNe associated with a white dwarf's mass tipping over the Chandrasekhar limit by accretion of material from a companion (Mazzali et al. 2007).

particularity¹⁰. The non-linearity of the equation leads to instabilities when the velocity field experiences random fluctuations, leading to the fragmentation of large eddies into ever smaller ones, until the eddies are small enough that the viscous damping time is equal to the eddy turnover time. That picture led to the Kolmogorov description of the turbulent cascade (Kolmogorov 1941, hereafter, K41), which is based on the assumption that the energy transfer rate ϵ from scale to scale is constant, so the solution is statistically time-invariant. Key results from this K41 theory are that the velocity fluctuations δv_l at a scale l are approximately given by $\delta v_l \approx (\epsilon l)^{1/3}$, that the velocity power spectrum scales¹¹ as $P_v(k) \propto \epsilon^{2/3} k^{-5/3}$, where k is the wavenumber, and that the structure functions of the velocity field¹² scale as $S_p(l) = \langle [\mathbf{v}(\mathbf{r} + \mathbf{l}) \cdot \mathbf{u} - \mathbf{v}(\mathbf{r}) \cdot \mathbf{u}]^p \rangle \propto (\epsilon l)^{p/3}$ for any positive integer p . The main flaw of the K41 theory, despite its successes, is that it cannot explain phenomena such as *intermittency*, which is the fact that energy dissipation occurs in intense bursts highly localized in both time and space¹³ (Frisch 1995). In experimental studies, intermittency manifests itself through the presence of non-Gaussian wings in the PDFs of velocity fluctuations δv_l at small scales. She & Leveque (1994) proposed a correction to the scaling exponents of the structure functions that matches quite well the observational data in fully developed turbulence.

The inclusion of compressibility, which is necessary in the case of interstellar turbulence, leads to a modification of the scaling exponents, related to the hierarchical structures in density that arise in the flow. In particular, the velocity power spectrum steepens to k^{-2} while the density power spectrum is flat (Falceta-Gonçalves et al. 2014).

When the fluid is magnetized, which is the case in the ISM, the description becomes even more complex (Biskamp 2003), as the coupling between fluctuations of the velocity field \mathbf{v} and the magnetic field \mathbf{B} depends on whether these fluctuations occur along magnetic field lines or perpendicularly to them, due to magnetic tension and pressure. The Iroshnikov-Kraichnan theory of incompressible MHD turbulence (Iroshnikov 1964; Kraichnan 1965a,b) describes it through the weak interaction of mechanical and magnetic wave packets, and leads to scalings $\delta v_l \approx (\epsilon l v_A)^{1/4}$ and $P_v(k) \propto (\epsilon v_A)^{1/2} k^{-3/2}$, where $v_A = B/\sqrt{4\pi\rho}$ is the Alfvén speed. Note that a combination of the K41 and Iroshnikov-Kraichnan cascades may be possible, as pointed out by Alexakis (2013). A major flaw of this theory is that the eddies are isotropic, which has long been known to be false. The Sridhar-Goldreich theory (Sridhar & Goldreich 1994; Goldreich & Sridhar 1995), describing MHD turbulence through strong coupling of the wave modes, leads on the other hand to an anisotropic ($l_{\parallel} \sim v_A \epsilon^{-1/3} l_{\perp}^{2/3}$) K41-like cascade, with $P_{v_{\perp}}(k) \propto k_{\perp}^{-5/3}$.

Scaling relations for compressible MHD have been studied by Kowal & Lazarian (2007), following the work of Kritsuk et al. (2007). These authors found that the density-weighted velocity $\mathbf{u} = \rho^{1/3} \mathbf{v}$ has a power spectrum following the Kolmogorov $k^{-5/3}$ scaling. The constancy of $\rho \sigma_v^3/l$ observed in the ISM over a wide range of scales l is in remarkable agreement with these theoretical findings (Hennebelle & Falgarone 2012).

Interstellar turbulence

Interstellar turbulence was first suggested 65 years ago by von Weizsäcker (1951) and von Hoerner (1951), and has since then been studied mostly through the statistical analysis of temporal and spatial

10. non-linearity comes from the advection term $(\mathbf{v} \cdot \nabla) \mathbf{v}$, and non-locality from the pressure term $-\nabla p/\rho$.

11. That is integrated over directions. The full 3D power spectrum scales as $k^{-11/3}$.

12. $\mathbf{u} = \mathbf{l}/l$ is the unit vector linking the two points used in the argument.

13. The topology of high-dissipation regions (filaments or sheets) is still a matter of research (see references in Falceta-Gonçalves et al. 2014).

variability of the observed signals¹⁴. In particular, the self-similarity of structures expected from turbulence is illustrated by the observations of power-law power spectra over a large range of scales for a number of tracers, such as the local free electron density (Armstrong et al. 1995) or HI density and velocity fluctuations (Miville-Deschênes et al. 2003a). For instance, that latter analysis showed how the velocity and density power spectra exhibit a K41 scaling over a large range of scales in a Galactic HI cirrus cloud. Although the spectral indices found in other studies reveal a large scatter (Hennebelle & Falgarone 2012), this may be due to projection effects (Miville-Deschênes et al. 2003b; Levrier 2004) and to the large panel of tracers being used.

Line observations also provide the means to study the velocity distribution and exhibit properties suggestive of turbulence, such as the Larson (1981) scaling between the sizes of molecular clouds and the linewidths¹⁵, $\sigma_v \propto l^\alpha$ with $\alpha \sim 0.5$, although the scatter about this relation is quite large (Hennebelle & Falgarone 2012), and a flattening appears at small scales (Falceta-Gonçalves et al. 2010).

Through line observations, hints of the intermittent dissipation of interstellar turbulence are also accessible, at small scales. The non-Gaussian wings of centroid velocity increments in CO observations by Hily-Blant et al. (2008) are linked to the plane-of-the-sky (POS) projection of the vorticity (Lis et al. 1996), and they are shown to arise from coherent, milliparsec-scale filamentary structures exhibiting large velocity shears (Hily-Blant & Falgarone 2009). Similarly, the comparison of linewidths for neutral and ionized species has brought Li & Houde (2008) to estimates of the ambipolar diffusion scale where the magnetic field decouples from the neutral gas¹⁶, and where ion turbulence is damped (Falceta-Gonçalves et al. 2010).

1.3 The interstellar magnetic field and polarization

1.3.1 The Galactic magnetic field

The Milky Way, like other spiral galaxies, is threaded by a magnetic field \mathbf{B} which affects significantly the dynamics of the interstellar medium (see the review by Beck 2016). First, it is directly coupled to the ionized phases of the ISM gas, and indirectly to its neutral phases through ion-neutral friction. The pressure $P_B \propto B^2$ thus provided is a major player in the balance against gravitational collapse. Second, the presence of a magnetic field in protostellar objects is essential to the loss of angular momentum through jets, thus controlling the star formation process. Third, the ISM may be heated through magnetic reconnection (Lazarian & Cho 2004). Finally, magnetic fields also control the propagation of cosmic rays (Strong et al. 2007).

These galactic magnetic fields are thought to be generated in a three-stage process, as described by Beck (2016) : (i) very weak seed fields may be present at very high redshift, either generated in the primordial Universe, or by processes occurring at later times¹⁷, (ii) amplification by turbulent small-scale dynamo, which transfers mechanical energy into magnetic energy (see, e.g., Ferriere 1996), (iii) ordering and sustaining by the $\alpha - \Omega$ effect, a coupling of differential rotation (Ω) and the Coriolis force (α) acting on expanding gas shells driven by SNe explosions (Ferriere 1996; Beck et al. 1996).

The mean-field approximation to the $\alpha - \Omega$ dynamo equation, $\partial_t \mathbf{B}_0 = \nabla \times (\mathbf{v} \times \mathbf{B}_0) + \nabla \times \alpha \mathbf{B}_0 + \eta \nabla^2 \mathbf{B}_0$, where η is the magnetic diffusivity, has solutions that are described in terms of modes m with different

14. One should be cautious, however, when using projected observational results to constrain, e.g., statistical properties of the velocity field, as discussed by, e.g., Lazarian & Pogosyan (2000); Miville-Deschênes et al. (2003b); Levrier (2004).

15. which are significantly supra-thermal

16. This method, based on the compared linewidths of HCN and HCO⁺, has been further employed in Li et al. (2010), Hezareh et al. (2010) and Hezareh et al. (2014).

17. For instance, they may have been ejected by the first stars (Bisnovatyi-Kogan et al. 1973) or by the jets associated with the first black holes (Rees 2005).

azimuthal symmetry in the disk plane¹⁸ and even/odd vertical symmetry (Beck 2016). Thus, the Galactic magnetic field is the sum of this large-scale field \mathbf{B}_0 , which more or less follows the spiral structure of the galaxy (see models by Jaffe et al. 2010; Jansson & Farrar 2012), and a small-scale turbulent field \mathbf{B}_t which is the result of the small-scale dynamo.

The average strength of the magnetic field in the Solar neighbourhood is about $6 \mu\text{G}$, and increases to $20\text{--}40 \mu\text{G}$ near the Galactic center, while larger values still are found in dense regions (Hennebelle & Falgarone 2012). There is an approximate equipartition¹⁹ between the large-scale and turbulent component of the field, both having strengths of a few μG in the local ISM (see, e.g., Haverkorn et al. 2008, and references therein).

The main methods to study the Galactic magnetic field and its fluctuations are :

- (i) the polarization of background starlight by intervening dust clouds in the visible and near-infrared ;
- (ii) the polarization of thermal dust emission ;
- (iii) Zeeman splitting of radio spectral lines ;
- (iv) Faraday rotation and total and polarized synchrotron emission.

The first two, which will be discussed in more detail in the next section, allow to estimate the strength of magnetic fields in the ISM using the Davis-Chandrasekhar-Fermi technique (Davis 1951; Chandrasekhar & Fermi 1953), which is based on the assumption that the variations in polarization angle are related to velocity fluctuations²⁰. Zeeman observations allow the measurement of relatively strong fields in dense clouds : for instance, Crutcher et al. (2010) have compiled an ensemble of such measurements in HI, OH, and CN lines, to show that the maximum strength of the magnetic field scales with density n_{H} as $B_{\text{max}} \propto n_{\text{H}}^{\alpha}$ above $n_{\text{H}} > 300 \text{ cm}^{-3}$, with an exponent $\alpha = 0.65 \pm 0.05$. Finally, synchrotron emission is, among other things, an excellent tracer of the large-scale magnetic fields in the ionized regions of the Milky Way and other Galaxies (Beck 2016). It is usefully complemented by Faraday rotation measurements towards extragalactic sources (Oppermann et al. 2012).

1.3.2 Polarization and interstellar dust

Dust grains, being subject to the UV and visible radiation from the ensemble of stars in the Galaxy, absorb some of it to reach non-zero temperatures of around $15\text{--}20 \text{ K}$. At these temperatures, they emit radiation in the infrared. The dust temperature T_{d} is the result of the balance between absorbed and emitted power²¹. This thermal emission may be modelled as a modified blackbody, such that the emissivity is written

$$\epsilon = \kappa_{\nu} B_{\nu}(T_{\text{d}}) \propto \frac{\nu^{3+\beta}}{\exp\left(\frac{h\nu}{kT_{\text{d}}}\right) - 1}$$

where the absorption coefficient is assumed to follow a power-law in frequency, $\kappa_{\nu} \propto \nu^{\beta}$. The spectral index β is about 2, and depends on the composition of the grains (Kruegel 2003). Of course, this is a crude approximation, as the optical constants of dust grains show variations which are in general not amenable to simple power-laws.

As electrons may be ejected from dust grains via the photoelectric effect, and grains may also collect cosmic-ray electrons and protons (see Ivlev et al. 2015, and references therein), these grains acquire an

18. The observed field reversals may indicate a distortion of the dynamo, or be the remnants from the chaotic seed magnetic field.

19. The same is true in external galaxies, such as M51 (Houde et al. 2013).

20. Major improvements of the method have subsequently been proposed, e.g., Hildebrand et al. (2009) take into account a non-uniform large-scale field, Houde et al. (2009) consider the effect of the telescope beam and line-of-sight (LOS) integration, while Houde et al. (2011) and Houde et al. (2016) extend the analysis to interferometric data.

21. This description fails for small grains, for which a single photon absorption leads to a large increase of the temperature.

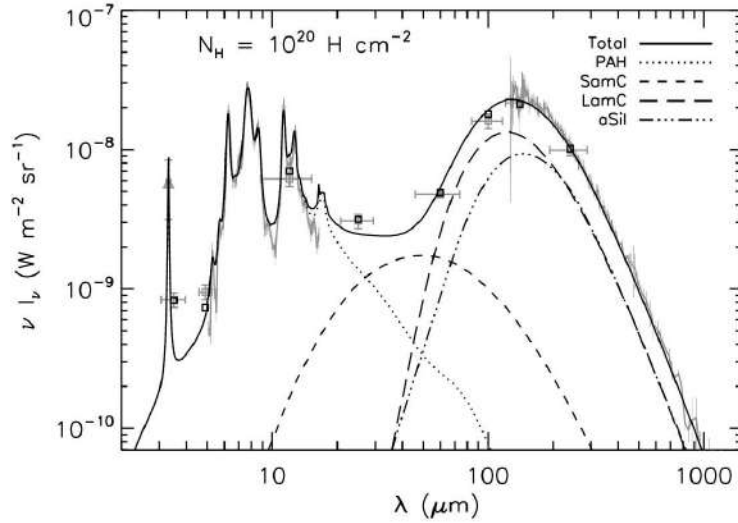


FIGURE 1.1 – Example of dust spectral energy distribution (SED) from the DUSTEM model of Compiègne et al. (2011). The thermal emission of grains dominates the spectrum in the long-wavelength range.

electrical charge. Since they are also spinning, a magnetic dipolar moment appears. Moreover, real dust grains are not spherical, and although the characterization of their shapes is difficult (Jones 2011), it is customary to model them as spheroids (oblate or prolate) of a certain porosity. The absorption and emission cross-sections being related to the geometrical sections, the grains exhibit different emissivities for radiations where the electric vector \mathbf{E} is parallel or perpendicular to a grain's long axis.

The interaction of the magnetic moment with the local magnetic field \mathbf{B} leads to an alignment of the non-spherical grains with \mathbf{B} . Although the details of the process are still unclear, there is evidence that the angular momentum of the grains aligns itself with the magnetic field through a process called *Radiative Torque Alignment* (RAT), by which anisotropic radiation impacting grains with a net helicity causes a difference in the scattering cross section to the left- and right-hand circular polarization components of the radiation field, imparting a torque on the grain. The grain being magnetized, it precesses (Martin 1971) around the magnetic field lines, and the constant torque leads to alignment (see Hoang & Lazarian 2014, for a detailed description of the model and its applications).

The end configuration is that the rotating dust grains will preferentially have their long axes perpendicular to field lines, as shown in Fig. 1.2. Since extinction cross-sections are proportional to the geometrical size, the light from background stars²² experiences a differential cross section when penetrating a cloud of gas and dust where the particles of the latter are preferentially aligned. The light emerging from the cloud is polarized, with the component perpendicular to \mathbf{B} more extinct, so the visible and near-infrared starlight presents a polarization²³ that is parallel to \mathbf{B} (Fig. 1.2, *top*).

Kirchhoff's law states that the thermal emissivity of these dust grains is proportional to the absorption coefficient, which in turn is proportional to the cross-section. Therefore, the dust grains emit light which is

^{22.} which is essentially unpolarized and can therefore be decomposed into a sum of vibrations parallel to the local magnetic field \mathbf{B} and perpendicular to \mathbf{B}

^{23.} Historically, this is how Davis & Greenstein (1951) interpreted the serendipitous discovery of starlight polarization by Hall (1949) and Hiltner (1949).

preferentially polarized along the major axis of the grains, and so perpendicular to \mathbf{B} (Fig. 1.2, *bottom*). Of course, the orientation of the magnetic field varies along the LOS, alignment is not perfect and depends on the composition and size of the grains, and the emission, which depends on the density of the dust grains, needs to be integrated along the LOS... Therefore, one cannot easily derive properties of the magnetic field, or of the dust for that matter, from observations of submillimetre polarized thermal dust emission, but this tracer is still a very valuable one as we will see. In recent years, a number of experiments have dramatically increased the amount of data pertaining to this emission from Galactic dust (e.g. Matthews et al. 2009; Ward-Thompson et al. 2009; Dotson et al. 2010; Bierman et al. 2011; Vaillancourt & Matthews 2012; Poidevin et al. 2013; Hull et al. 2014; Koch et al. 2014). Chief among these is *Planck*, which provided the first full-sky map of this emission, leading to several breakthrough results that we will present in the next chapter.

When observing any line of sight, the total intensity of the thermal dust emission (Stokes I) and the linearly polarized emission (encoded in the Stokes parameters Q and U) are given by

$$I = \int S_\nu e^{-\tau_\nu} \left[1 - p_0 \left(\cos^2 \gamma - \frac{2}{3} \right) \right] d\tau_\nu; \quad (1.1)$$

$$Q = \int p_0 S_\nu e^{-\tau_\nu} \cos(2\phi) \cos^2 \gamma d\tau_\nu; \quad (1.2)$$

$$U = \int p_0 S_\nu e^{-\tau_\nu} \sin(2\phi) \cos^2 \gamma d\tau_\nu. \quad (1.3)$$

where $S_\nu = B_\nu(T_d)$ is the source function of a blackbody at the dust temperature T_d , p_0 is a polarization fraction parameter related to the intrinsic polarization fraction (see Planck Collaboration Int. XX 2015), γ is the angle that the local magnetic field makes with the plane of the sky, and ϕ is the local polarization angle in the HEALPIX convention (Górski et al. 2005). This angle differs by 90° from the angle χ of the plane of the sky (POS) projection of the magnetic field, as defined in Fig. 1.3, and should not be confused with the actual polarization angle ψ . These angles are equal ($\phi = \psi$) only for a uniform magnetic field along the line of sight. We define the magnetic orientation angle as $\bar{\chi} = \psi \pm \pi/2$, which gives the inferred orientation of the POS projection of the magnetic field integrated along the line of sight. Of course, $\bar{\chi} = \chi$ if the magnetic field is uniform on the LOS.

Stokes Q and U encode the linear polarization of the radiation on each line of sight, as shown in Fig. 1.4 (*left*). For instance, a signal whose polarization direction is North-South has positive Stokes Q and null Stokes U . These quantities do not transform as scalars under a rotation of the coordinate frame by an angle θ , as we have rather $(Q, U) \mapsto (Q \cos 2\theta + U \sin 2\theta, -Q \sin 2\theta + U \cos 2\theta)$. Cosmologists have therefore taken the habit of describing polarization in terms not of Q and U , but instead in terms of quantities that do transform as scalars under a rotation, called E and B (Zaldarriaga 2001). This E - B decomposition is a linear transformation of the Q - U field on the sky which is non-local but invertible. E is invariant under a mirror symmetry (parity), while B changes sign (see Fig. 1.4, *right*). This decomposition is of particular interest for CMB studies because density fluctuations associated with the CMB anisotropies in total intensity cannot produce B -mode polarization. This type of pattern arises only from lensing (Lewis & Challinor 2006) or as a signature of primordial gravitational waves in the early Universe (Seljak & Zaldarriaga 1997).

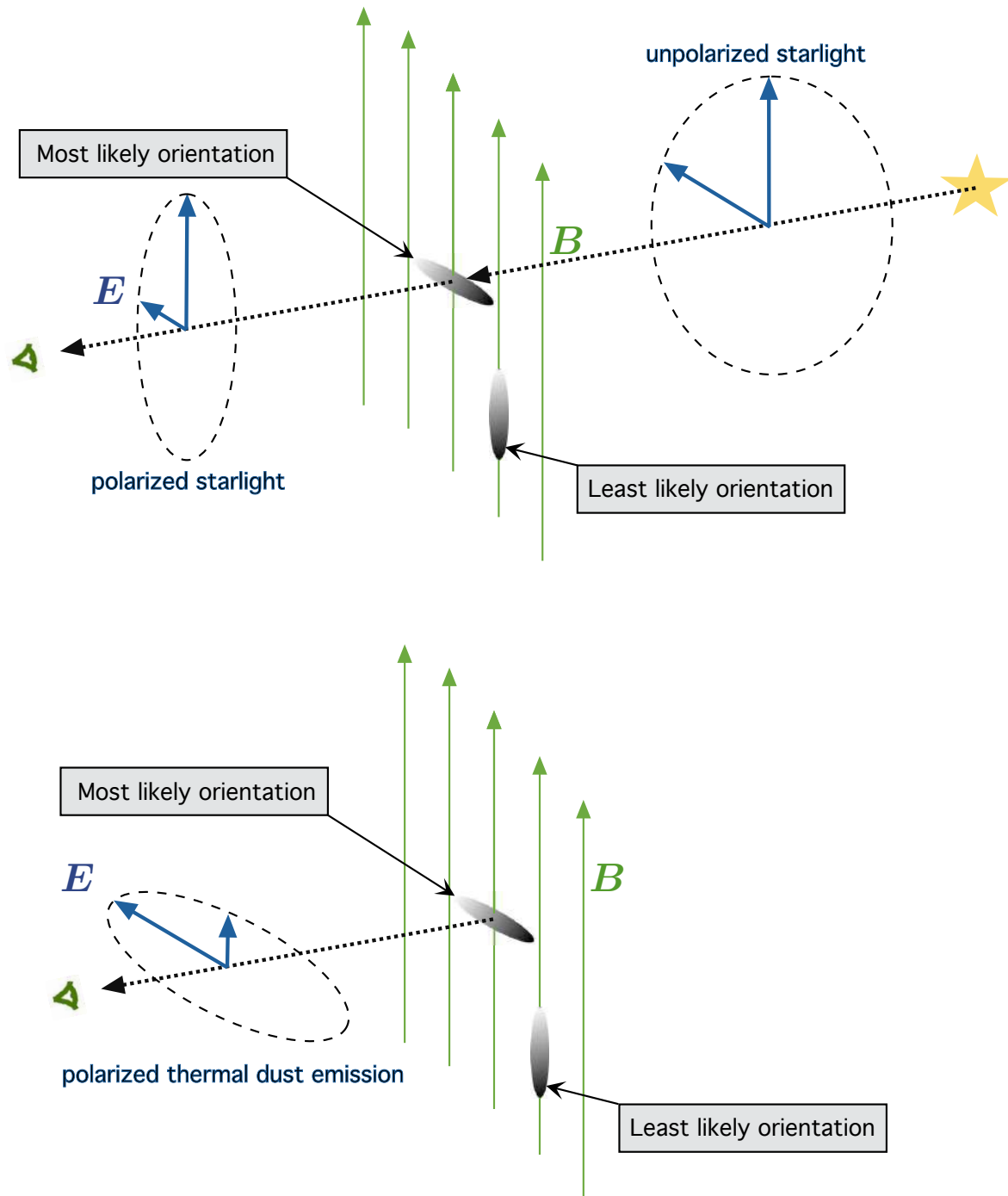


FIGURE 1.2 – Polarization of background starlight by dust grains (*top*) and polarized thermal dust emission by the same grains (*bottom*).

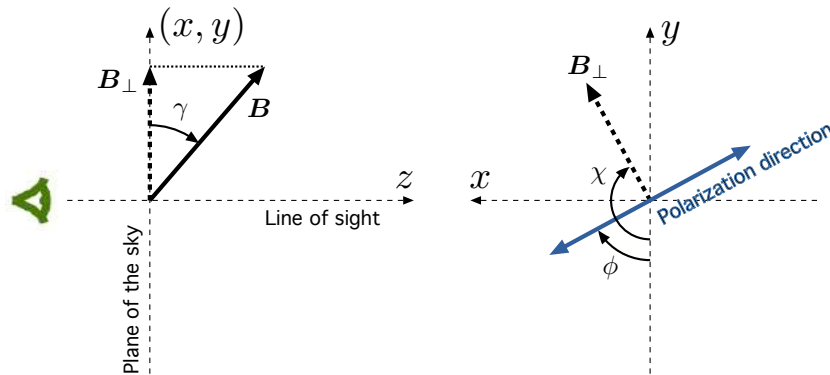


FIGURE 1.3 – Definition of angles. Figure adapted from Planck Collaboration Int. XX (2015).

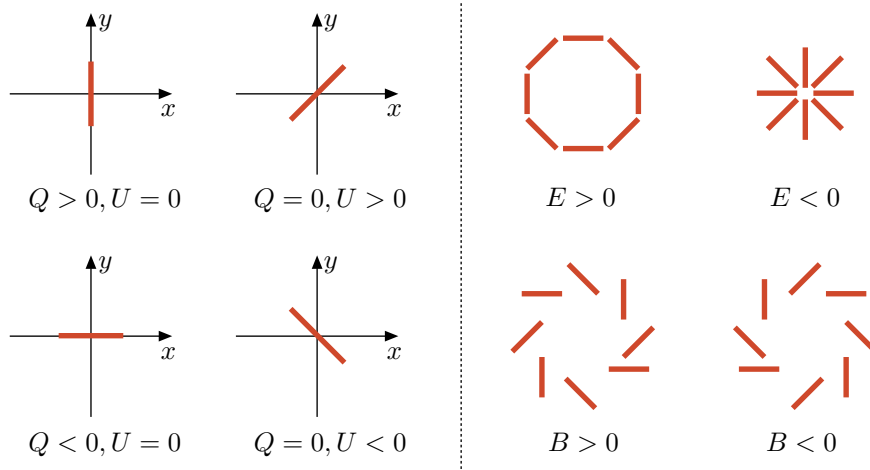


FIGURE 1.4 – *Left* : Stokes Q and U parameters encode the linear polarization of the radiation on each line of sight. The red segment shows the direction of polarization that corresponds to the various Q and U configurations. *Right* : The E - and B -modes encode the morphological structure of the polarization, in a non-local way. Features that are fully mirror-symmetric lead to pure E -modes, while features that are fully mirror-antisymmetric lead to pure B -modes.

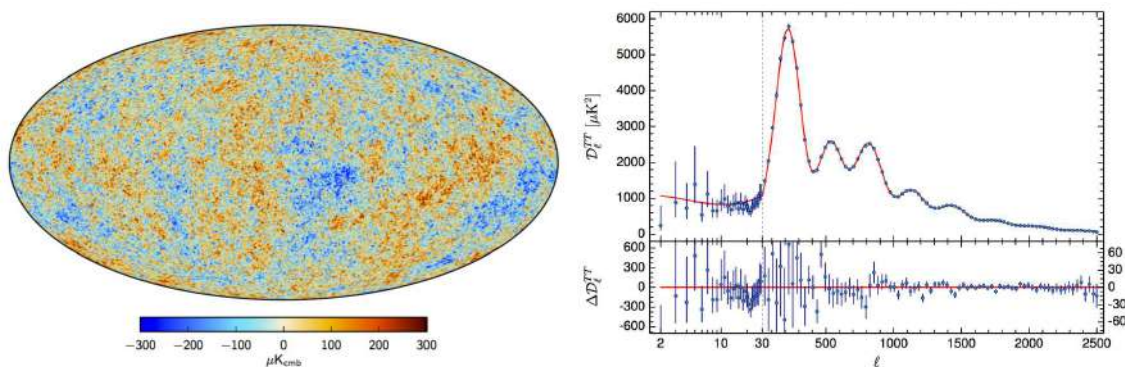


FIGURE 1.5 – *Left* : CMB map produced by *Planck*. *Right* : Temperature (TT) power spectrum with the best-fit Λ CDM model overlaid (the lower plot shows residuals). Figures taken from Planck Collaboration I (2016).

1.4 The *Planck* mission and observations

*Planck*²⁴ (Planck Collaboration I 2016) was the third-generation space mission aimed at mapping the anisotropies of the cosmic microwave background (CMB), after *COBE* (Smoot et al. 1992) and *WMAP* (Bennett et al. 2013). Launched on May 14th, 2009 together with the *Herschel Space Observatory*, and fitted with two instruments, the *High-Frequency Instrument* HFI (Planck HFI Core Team 2011) and the *Low-Frequency Instrument* LFI (Mennella et al. 2011), it surveyed the microwave sky in nine frequency bands²⁵, from August 12th, 2009 to October 23rd, 2013. The scanning strategy of the satellite was such that the entire sky was covered twice each year. The *Planck* mission achieved never before seen performances, through the combination of exquisite sensitivity, complete spatial coverage, extensive frequency coverage, and excellent angular resolution (from 33' to 5').

As already mentioned, the main goal of the *Planck* mission was to map the anisotropies of the CMB in total intensity, which are thought to be the seeds of the large-scale structures that can be observed in the local Universe, without any other limitations but those set by astrophysical signals, and derive from these measurements fundamental constraints on cosmological models of the Universe. The results of this work, presented in Planck Collaboration XIII (2016), show an excellent agreement with the 6-parameter Λ CDM model (Peter & Uzan 2009), with no significant hint of the necessity for an extension of the model (see Fig. 1.5). The mission also provided extremely valuable information regarding extragalactic sources, in particular clusters of galaxies via the Sunyaev-Zeldovich effect (Planck Collaboration XXII 2016; Planck Collaboration XXIII 2016; Planck Collaboration XXIV 2016), and on microwave emission from our own Galaxy's gas and dust contents (Planck Collaboration X 2016; Planck Collaboration XXV 2016; Planck Collaboration XXVIII 2016).

The measurement of CMB anisotropies in polarization was not a primary goal of the mission, but from the initial proposal in 1995 to the final design, technological advances have made it possible for the polarized microwave signal to be measured at unprecedented sensitivity with *Planck*. This is of great importance, since the polarized CMB is a valuable source of cosmological information regarding, e.g., the

24. *Planck* (<http://www.esa.int/Planck>) is a project of the European Space Agency (ESA) with instruments provided by two scientific consortia funded by ESA member states and led by Principal Investigators from France and Italy, telescope reflectors provided through a collaboration between ESA and a scientific consortium led and funded by Denmark, and additional contributions from NASA (USA).

25. Centered on 30, 44, 70, 100, 143, 217, 353, 545, and 857 GHz.

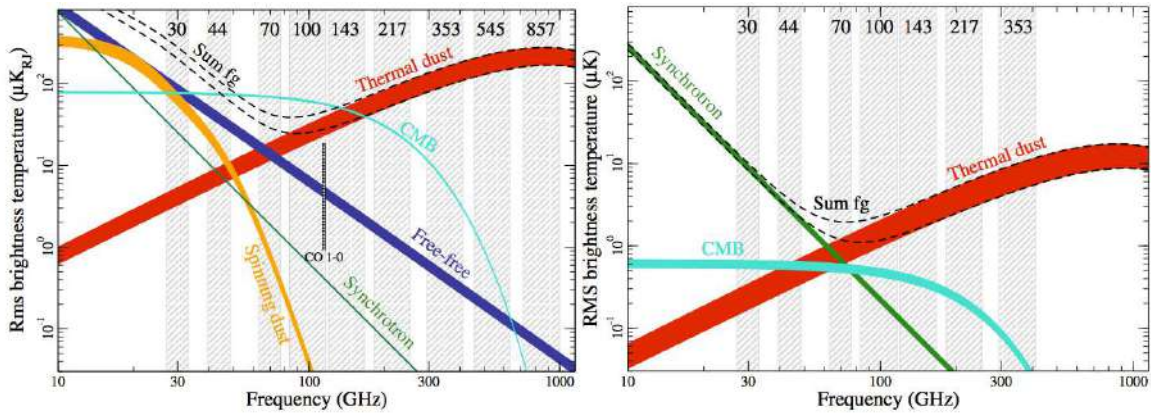


FIGURE 1.6 – Fluctuation levels of various foreground emission components, compared to the CMB, at high Galactic latitude in total intensity (*left*) and polarization (*right*). The *Planck* frequency bands are also indicated. Figure taken from Planck Collaboration I (2016).

generation of primordial magnetic fields (Planck Collaboration XIX 2016), the reionization history of the Universe (Planck Collaboration XLVIII 2016), gravitational lensing due to large-scale structures (Planck Collaboration XV 2016), inflationary models of the early Universe (Planck Collaboration XX 2016), possible non-Gaussian primordial fluctuations (Planck Collaboration XVII 2016), and tests of fundamental physics (Planck Collaboration XLIX 2016).

The three channels of LFI (30, 44, and 70 GHz) and the four lowest frequency channels of HFI (100, 143, 217, and 353 GHz) were fitted with detectors able to measure the linear polarization of the observed radiation²⁶. Fig. 1.6, taken from Planck Collaboration I (2016), shows the spectra of various contributions to the microwave sky in the different *Planck* bands, both in total intensity (*left*) and in linearly polarized intensity (*right*). This figure shows that, at 353 GHz, which is therefore the highest-frequency polarization-sensitive channel of *Planck*, the main polarized signal is dust thermal emission, about two orders of magnitude above the polarized CMB. This means that, to correctly assess the primordial signal, it is necessary to properly remove this foreground. The following chapter details some of the results that *Planck* has provided in the understanding of polarized thermal dust emission and the Galactic magnetic field.

26. The *Planck* detectors were radiometers for LFI, and bolometers for HFI. The latter are of two different kinds : spiderwebs (SWB) and polarization sensitive bolometers (PSB) (Jones et al. 2003; Rosset et al. 2010), which as the name suggests are the only ones able to measure the linear polarization of the incoming radiation. Each PSB is a pair of closely positioned square grids, each of which being metallized in only one direction. The component of the incoming radiation whose electric field is aligned with that metallized direction gets reflected (Houde et al. 2001), and the grid is transparent for the perpendicular component. The two grids of the PSB are placed at 90° from one another, allowing to measure the total intensity $I = |E_x|^2 + |E_y|^2$, but also the Stokes $Q = |E_x|^2 - |E_y|^2$ associated with its local frame (x, y) . Using a second PSB rotated by 45° provides Stokes U .

Chapitre 2

Some *Planck* results on the Galactic magnetic field

2.1 Polarization measurement analysis

2.1.1 From Stokes parameters to polarization fraction and angle

One of the objectives of the *Planck* mission is to put constraints on the polarization of the primordial, cosmological signal. In order to do this, it is necessary to properly understand, if not fully remove, the polarization of foreground signals, in particular that of thermal dust emission. However, the physical quantities used to describe the polarization properties of this signal are not the Stokes parameters. The astrophysical processes linked to dust and the magnetic field are much more readily tackled using the polarization fraction p and angle ψ , which are defined by¹

$$p = \frac{\sqrt{Q^2 + U^2}}{I} \quad \text{and} \quad \psi = \frac{1}{2} \text{atan}(U, Q) \quad (2.1)$$

An essential part of the work involved in the analysis of *Planck* polarization data is therefore to relate the measurement of the (I, Q, U) Stokes parameters to these quantities, which are much more meaningful for astrophysical processes. However, the non-linearity of the transformation $(I, Q, U) \mapsto (I, p, \psi)$ means that, in the presence of noise, the quantities computed via Eq. (2.1) from the measured Stokes parameters are biased estimators of the true polarization fraction and angle, as first discussed by Serkowski (1958).

We therefore need reliable, less biased estimators of p and ψ to understand the physical processes linked to dust and the magnetic field. Moreover, the noise properties of the *Planck* measurements exhibit large-scale variations over the whole sky, in terms of the signal-to-noise ratio (SNR) and the noise covariance matrix². To obtain a uniform survey of the polarization fraction and angle – something that is essential to perform a large-scale modelling of our Galaxy - the impact of the full complexity of the noise has to be taken into account.

1. Note that ψ is here defined in the HEALPIX convention (Górski et al. 2005), which means that angles are counted positively clockwise from the north-south direction. The IAU convention is that polarization angles are counted positively anti-clockwise. The change from one convention to the other is done by the transformation $U \mapsto -U$. Note also that we use the two-argument version of the atan function, in order to avoid the π -ambiguity.

2. The noise covariance matrix is composed of the various covariances σ_{XY} , where X and Y are any of the Stokes parameters. In our study, that matrix is parametrized by the ellipticity ϵ and correlation ρ of the (Q, U) Gaussian noise distribution. See figure 1 of Montier et al. (2015a) for a graphical definition of these parameters.

2.1.2 Characterization of the statistical bias on p and ψ

Within the *Planck* collaboration, we formed a small group dedicated to characterize the bias in p and ψ in the presence of correlated noise in (I, Q, U) , going beyond the strong simplifying assumptions usually made in polarization analysis (Montier et al. 2015a). We derived analytical expressions for the probability density functions (PDF) of p and ψ and we explored, via Monte-Carlo simulations, the impact of the noise properties on the statistical variance and bias of these quantities. We have thus shown that when ellipticities³ do not deviate from the canonical, uncorrelated value of 1 by more than 10%, the bias on p can reach up to 5% of the statistical uncertainty σ_p . In that same regime, the bias on the polarization angle is limited to less than 1° , well below the statistical uncertainty σ_ψ . We have shown that the uncertainty on the total intensity I has to be properly taken into account when analysing polarization data for faint objects, due to I entering the definition of p in the denominator. We have also compared estimates of the uncertainties affecting polarization measurements, addressing limitations of estimates of the SNR, and shown how to build conservative confidence intervals for p and ψ simultaneously.

2.1.3 Comparison of estimators

To go beyond this descriptive analysis, we have compared several estimators of p and ψ (Montier et al. 2015b) including a new frequentist one for p , the modified asymptotic estimator (MAS) introduced in Plaszczyński et al. (2014), and one inspired by a Bayesian analysis. This has allowed us to propose recipes adapted to different use-cases. For instance, we have provided the best estimators to build a mask, to compute large maps of the polarization fraction and angle, and to deal with low SNR data. More generally, we have shown that the traditional estimators suffer from discontinuous⁴ PDFs at low SNR, while the asymptotic and Bayesian methods do not. These two have been shown to present different properties in terms of the shapes of their PDFs, the MAS estimator yielding one that is close to Gaussian, while the Bayesian PDF is strongly asymmetric with a sharp cut at low SNR.

We have also described the statistical bias on a derived quantity, the polarization angle dispersion function, in Alina et al. (2016), which is currently under review.

2.1.4 The PMA library

The tools and methods devised in the course of this work and for this set of papers, commonly referred to as *Polarization Measurement Analysis* (PMA), were extensively used on the *Planck* data to obtain the results which we will discuss next. These tools are currently being organized as an IDL library and a python package, by myself and L. Montier, for a public release. The goal is to spread and facilitate their use in a wider community, as more and more high-precision polarization experiments are being set up, from the ground, on balloons, and in future space missions.

2.2 *Planck* observations of polarized thermal dust emission

As already mentioned (see Fig. 1.6), polarized thermal dust emission is best studied in the highest-frequency *Planck* channel with polarization capabilities, i.e., at 353 GHz⁵. Our first analysis of the *Planck*

3. Actually, *effective* ellipticities (see Montier et al. 2015a).

4. This means that when the *naïve* computation of p using Eq. (2.1) yields a results below some cutoff, these estimators yield a value of zero for the polarization fraction.

5. The full-mission maps of Stokes parameters (I, Q, U) at that frequency, and the associated covariance matrices, are available from the *Planck* Legacy Archive (<http://www.cosmos.esa.int/web/planck/pla>) and are part of the 2015 public release of *Planck* data (Planck Collaboration I 2016). The maps are at a native $4.8'$ resolution in the HEALPIX format (Górski et al. 2005) with $N_{\text{side}} = 2048$.

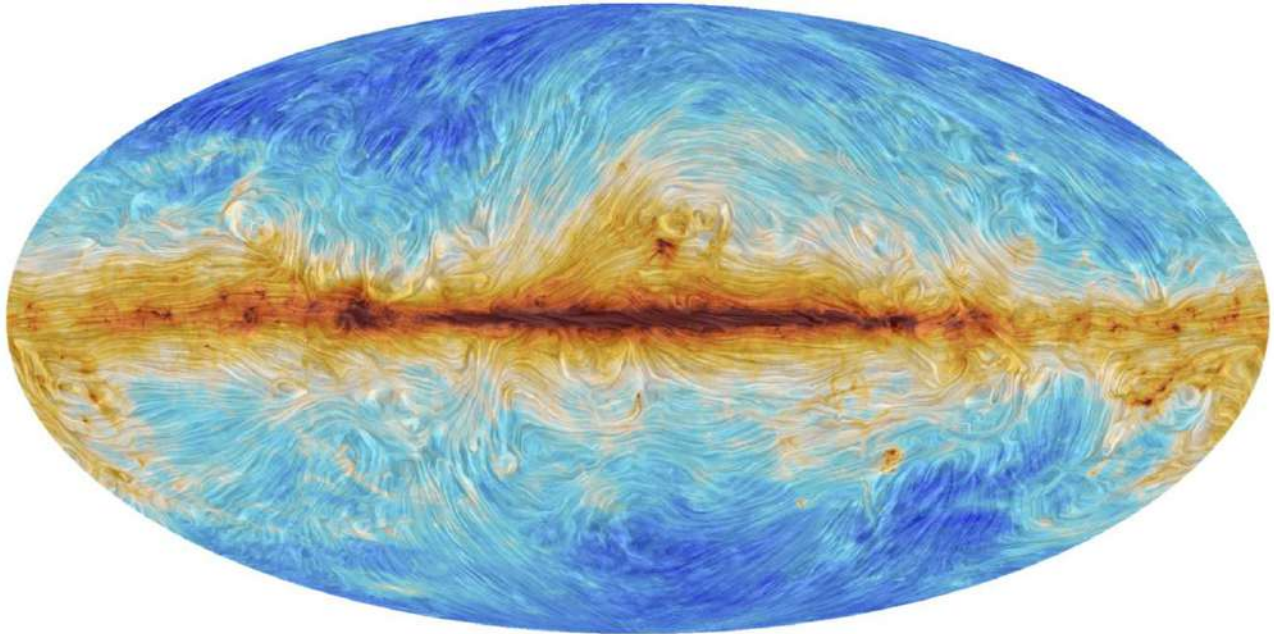


FIGURE 2.1 – All-sky view of the magnetic field and total intensity of dust emission measured by *Planck* at 353 GHz. The colours represent Stokes I , and the “drapery” pattern, produced using the line integral convolution (Cabral & Leedom 1993), indicates the magnetic orientation. Figure taken from Planck Collaboration I (2016)

data focusing on thermal dust polarization therefore made extensive use of that channel (Planck Collaboration Int. XIX 2015; Planck Collaboration Int. XX 2015). Subsequent analyses by our group also made use of lower-frequency channels (e.g., Planck Collaboration Int. XXII 2015; Planck Collaboration Int. L 2016). The following sections present the results of these studies.

2.2.1 The large-scale polarized sky

The large-scale polarized sky as seen by *Planck*-HFI at 353 GHz is presented in Planck Collaboration Int. XIX (2015), including maps of p and ψ and their associated uncertainties. From these, the maximum dust polarization fraction is observed to be quite high ($p_{\max} > 18\%$), in particular in some of the intermediate dust column density regions⁶, confirming results previously obtained by the *Archeops* balloon-borne experiment (Benoit et al. 2004; Ponthieu et al. 2005). The polarization fraction is found to decrease with increasing column density, which is interpreted in terms of magnetic field tangling on the line-of-sight, and of loss of grain alignment with the field in dense regions. The spatial structure of the polarization angle is analyzed in terms of the polarization angle dispersion function, defined as

$$\mathcal{S}(\mathbf{r}, l) = \sqrt{\frac{1}{N(l)} \sum_{i=1}^{N(l)} [\psi(\mathbf{r}) - \psi(\mathbf{r} + \mathbf{l}_i)]^2} \quad (2.2)$$

6. Visual extinction $A_V < 1$.

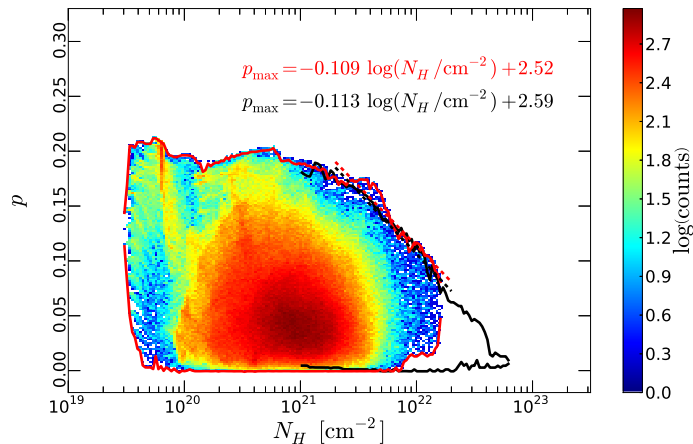


FIGURE 2.2 – Comparison between the distributions of the polarization fractions p and column densities in the simulated observations (colour scale, with upper and lower envelopes in solid red lines) and those of the observations (solid black lines). Dashed lines are linear fits of the form $p_{\max} = m \log(N_{\text{H}}/\text{cm}^{-2}) + c$ on the distributions' upper envelopes. See Planck Collaboration Int. XX (2015) for details.

where the sum extends over the pixels which lie within an annulus of mean radius l centered on \mathbf{r} . This quantity is found to anticorrelate with the polarization fraction, which we interpret as the result of magnetic field tangling on the LOS⁷. The morphological analysis of the \mathcal{S} map shows high-valued filamentary structures which separate regions on the sky where the polarization direction is fairly uniform, but changes abruptly at the filament location. This happens without apparent variations in dust column density.

We also compared the polarized dust emission to the polarized synchrotron emission observed in particular with *Planck*-LFI and *WMAP*. We found a globally similar structure in the Galactic Plane and a few other regions, but a more thorough analysis shows that dust and cosmic rays (associated to the synchrotron emission) sample different media. Much of the structure observed in the 353 GHz polarization map may be attributed to the topology of the magnetic field.

In Planck Collaboration I (2016), we presented a full-sky map showing the magnetic orientation (rotated by 90° with respect to the polarization orientation) as a "drapery" pattern built using the line integral convolution of Cabral & Leedom (1993). This map (Fig. 2.1) shows the large-scale orientation of the field along the Galactic Plane, as well as striking features such as the North Polar Spur, but the orientation pattern is irregular and difficult to interpret in regions where the field varies significantly along the line of sight.

2.2.2 Local statistics and comparison with MHD simulations

Planck Collaboration Int. XX (2015) presents the statistics of p and ψ towards a set of nearby fields, sampling both the diffuse ISM and molecular clouds, and therefore representative of the range of column densities N_{H} from about 10^{20} to a few 10^{22} cm^{-2} . These observations are compared to polarized emission

7. Similar anti-correlations were found by the BLASTPol experiment (Fissel et al. 2015) at the scale of a single Galactic molecular cloud (Vela C).

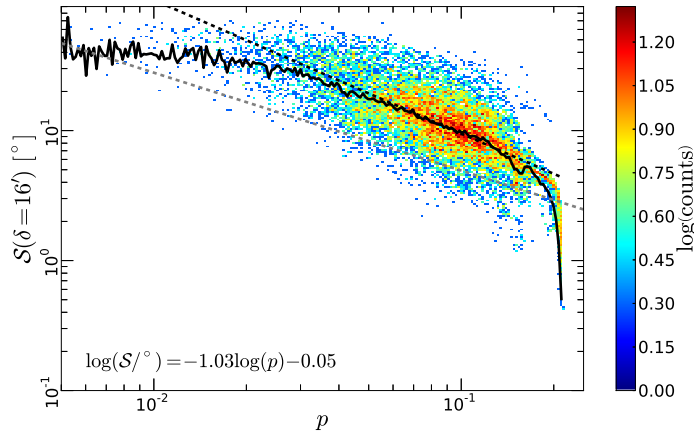


FIGURE 2.3 – Two-dimensional distribution function of $\log(p)$ and $\log(S)$ in simulated observations. The solid black curve represents the evolution of the mean $\log(S)$ per bin of $\log(p)$. A linear fit $\log(S) = m' \log(p) + c'$ is performed, restricted to bins in $\log(p)$ that contain at least 1% of the total number of points. This fit is shown as the dashed black line. The dashed grey line is a large-scale fit to observational data. See Planck Collaboration Int. XX (2015) for details.

maps computed from simulations of anisotropic magnetohydrodynamical (MHD) turbulence, similarly to, e.g. Pelkonen et al. (2007) and Falceta-Gonçalves & Lazarian (2011). In these simulations, however, we assumed a uniform intrinsic polarization fraction of the dust grains. It is shown that the largest polarization fractions are reached in the most diffuse fields and that the maximum polarization fraction p_{\max} decreases with increasing N_{H} . That decrease above $N_{\text{H}} \approx 10^{21} \text{ cm}^{-2}$ is very well reproduced in the simulations, as can be seen in Fig. 2.2, emphasizing the essential role played by the tangling of the magnetic field on the LOS. This underlines the importance of the turbulent structure of the magnetic field on the LOS to account for depolarization, leading to the polarization fraction along a given line of sight being anti-correlated with the local angular dispersion function S , as shown in Fig. 2.3. However, the dispersion of the polarization angle for a given polarization fraction is found to be larger in the simulations than in the observations, suggesting a shortcoming in the physical content of these numerical models. Finally, the dust intrinsic polarization fraction may be recovered if the magnetic field is uniform and perpendicular to the LOS, showing that the large-scale magnetic field orientation with respect to the line of sight plays a major role in the quantitative analysis of polarization data, as already pointed out by Falceta-Gonçalves et al. (2008).

2.2.3 Relative orientation between the magnetic field and dust structures

In nearby molecular clouds

To gain insight on the dynamical role of the magnetic field in the formation of structures within molecular clouds, we performed a statistical assessment of the relative orientation between the magnetic direction in the POS and the structures of matter, in ten nearby ($d < 450 \text{ pc}$) Gould Belt molecular clouds (Planck Collaboration Int. XXXV 2016). The magnetic orientation is inferred from the 353 GHz

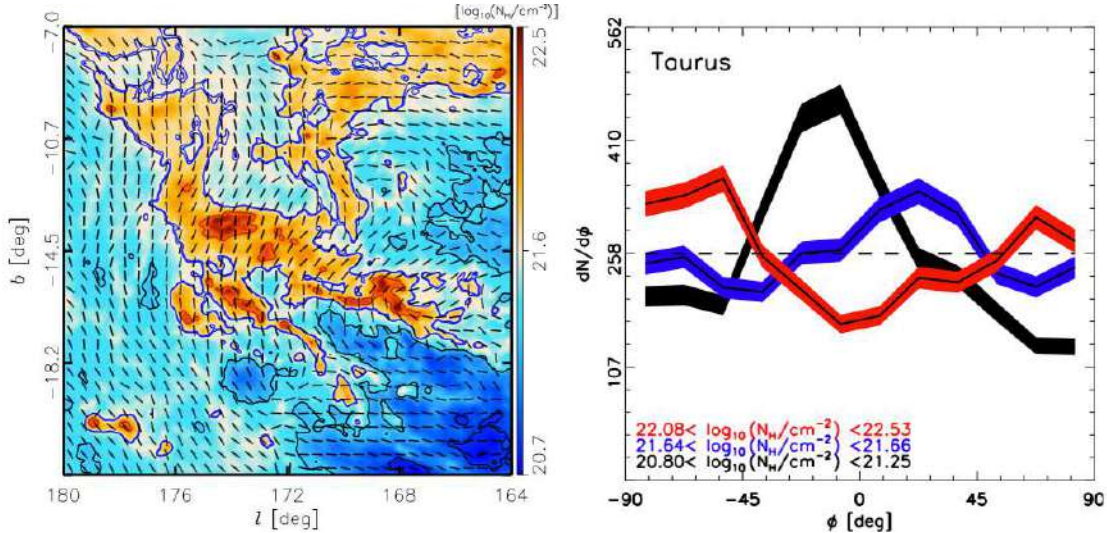


FIGURE 2.4 – *Left* : Column density map of the Taurus Molecular Cloud (TMC), with segments showing the magnetic orientation. *Right* : Histograms of Relative Orientation (HRO) for this field in different N_H bins. An HRO peaking near 0° point to the magnetic field’s projection in the POS being mostly aligned with the dust structures. Figure taken from Planck Collaboration Int. XXXV (2016).

polarized thermal dust emission, and the orientations of dust structures are characterized via the gradient of column density ∇N_H . This analysis is performed on a pixel-by-pixel basis, in bins of N_H , using the *Histogram of Relative Orientations* (Soler et al. 2013). We find that for most clouds the relative orientation changes as column density increases (Fig. 2.4) : in diffuse regions, structures of matter are either preferentially aligned with the magnetic orientation or show no preferred orientation, while the preferred orientation is perpendicular in dense regions. This is found to be consistent with simulated observations obtained from MHD simulations of trans- or sub-Alfvénic turbulence⁸, underlining the dynamical role played by the magnetic field in the formation of structures in molecular clouds at the scales probed by *Planck* (a few parsecs at the distances of the Gould Belt clouds). Using velocity dispersion measurements from CO data by Dame et al. (2001), and applying the Davis-Chandrasekhar-Fermi method (Davis 1951; Chandrasekhar & Fermi 1953) improved upon by Hildebrand et al. (2009), we found the magnetic field in those clouds to be in the range 10-50 μG , although these estimates should be taken with a grain of salt, considering the strong assumptions made when applying this method.

Extension to larger regions

This study of the relative orientation between structures of matter and magnetic field directions inferred from polarization is extended, in Planck Collaboration Int. XXXII (2016), to most of the sky at intermediate and high Galactic latitudes, covering a wide range of column densities, from 10^{20} to 10^{22} cm^{-2} . We found that filamentary structures (ridges) in the intensity map have counterparts in the Stokes Q or U maps. The orientation of the ridges in the I map is estimated using an algorithm based on the analysis of the Hessian matrix : it is found to be preferentially aligned with the magnetic field, all the more so than the lines of sight considered are more diffuse (increasing p and decreasing N_H), in agreement

⁸. $\sigma_v \lesssim B/\sqrt{4\pi\rho}$ where σ_v is the velocity dispersion, B the amplitude of the magnetic field, and ρ the density.

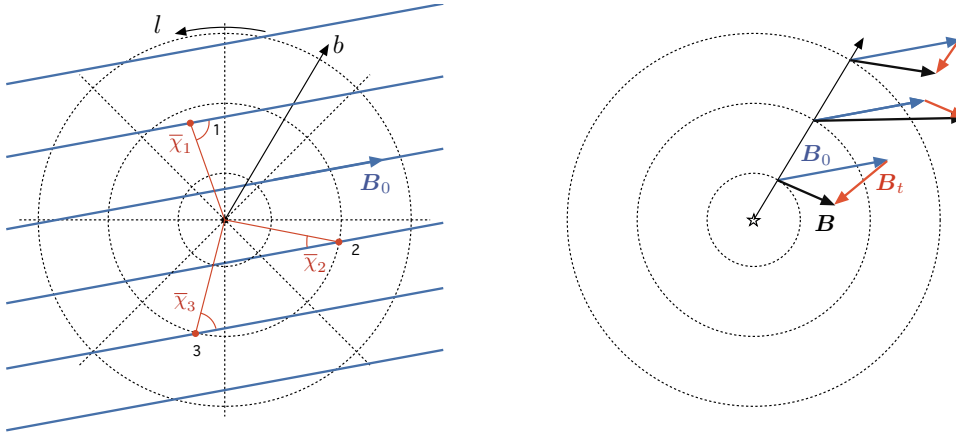


FIGURE 2.5 – *Left* : Uniform magnetic field model of Planck Collaboration Int. XLIV (2016) towards the South Galactic Pole. The dotted lines correspond to constant Galactic latitudes b or longitudes l . At three (red) points we show the magnetic orientation angle $\bar{\chi}$, exhibiting its variation (and therefore those of Q and U apparent in Fig. 2.6). *Right* : Gaussian model used in Planck Collaboration Int. XXXII (2016) and Planck Collaboration Int. XLIV (2016). The Sun is at the center, and each circle represents one of N polarization layer ($N = 1$ in Planck Collaboration Int. XXXII (2016), $N = 7$ in Planck Collaboration Int. XLIV (2016)). The large-scale field \mathbf{B}_0 is the same in each layer, while \mathbf{B}_t is a different, independent Gaussian realization of the turbulent component, as described in the text. Note that in Planck Collaboration Int. XXXII (2016), the uniform field \mathbf{B}_0 is taken to be tangential to the polarization layer.

with the study of Planck Collaboration Int. XXXV (2016). The correlation between an increased p and a statistically preferred alignment of the magnetic field with structures of matter is interpreted in light of projection effects, using an analytical toy model. It consists in assuming that the magnetic field is the sum of a mean component \mathbf{B}_0 aligned with the ridges, and a 3D turbulent component \mathbf{B}_t , whose components are taken to be independent, zero-mean Gaussian random variables with a power-law angular power spectrum⁹ $C_\ell \propto \ell^{\alpha_M}$ (see Fig. 2.5, right). Besides this spectral index, the model introduces a parameter f_M which is the ratio between the standard deviation of \mathbf{B}_t and the modulus of \mathbf{B}_0 . This parameter is estimated to be $f_M = 0.8 \pm 0.2$ from the comparison of polarization angles on and off identified ridges.

Specific analysis of the southern Galactic cap

We analyzed the polarized emission observed by *Planck* at 353 GHz towards high Galactic latitudes, specifically the southern Galactic cap ($b < -60^\circ$), in Planck Collaboration Int. XLIV (2016). The large-scale pattern of this emission (Stokes Q and U maps) shows a particular "butterfly" shape (Fig. 2.6), which we interpret in the framework of an extension to the model of Planck Collaboration Int. XXXII (2016). The mean Galactic field in the Solar neighbourhood, associated with this pattern, is found to be oriented towards Galactic coordinates $(l_0, b_0) = (70 \pm 5^\circ, 24 \pm 5^\circ)$. We study the distributions of p and ψ towards this region, and find that polarization fractions exhibit a mean $\langle p \rangle = 12 \pm 1\%$ with a wide distribution ($\sim 25\%$), while polarization angles are distributed with a standard deviation of about 12° around the pattern expected from a completely uniform field \mathbf{B}_0 (see Fig. 2.5, left). To explain

9. This is for $\ell \geq \ell_0$. For $\ell \leq \ell_0$, the power spectrum is assumed to be constant.

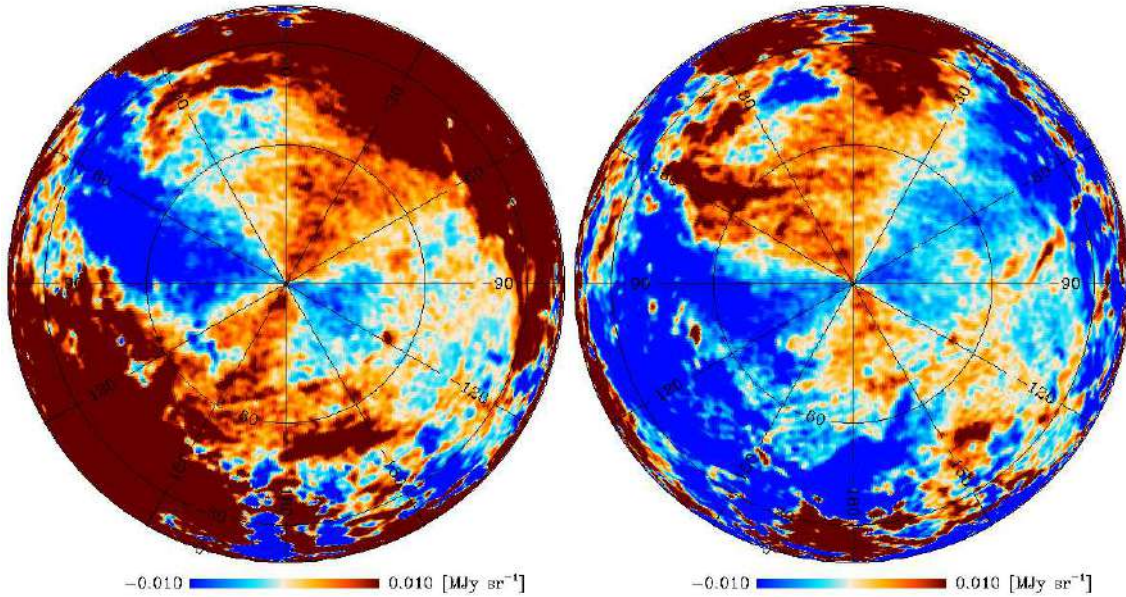


FIGURE 2.6 – Stokes Q (left) and U (right) at 353 GHz towards the southern Galactic cap, showing the "butterfly" pattern below $b < -60^\circ$. Figure adapted from Planck Collaboration Int. XLIV (2016).

these distributions, a phenomenological model is built extending the model of Planck Collaboration Int. XXXII (2016) : the integration along the LOS is replaced by a sum over N independent layers, which may be related to the correlation length of the Galactic magnetic field. Within each layer, the turbulent component \mathbf{B}_t is obtained from Gaussian realizations as in Planck Collaboration Int. XXXII (2016). With $p_0 = 26\%$, $f_M = 0.9$ and $N = 7$, we are able to reproduce the distributions of p and ψ , as shown¹⁰ in Fig. 2.7.

2.2.4 The angular power spectrum of polarized dust emission

In Planck Collaboration Int. XXX (2016), we measured the spatial (angular) power spectrum of the polarized thermal dust emission¹¹ over the multipole range $40 < \ell < 600$, outside of the Galactic plane. We first showed that the statistical spatial properties of dust emission may be characterized over these regions by simple angular power spectra C_ℓ , despite the non-Gaussianity and anisotropy of dust emission. We found that the auto power spectra of E and B modes are well adjusted by power laws $C_\ell^{EE} \propto \ell^{\alpha_{EE}}$ and $C_\ell^{BB} \propto \ell^{\alpha_{BB}}$ with spectral indices $\alpha_{EE, BB} = -2.42 \pm 0.02$. The amplitudes of the power spectra vary with the average brightness, similar to what is observed for the intensity power spectra. The analysis across frequencies from 353 GHz down to 100 GHz shows that the power spectra are consistent with a modified blackbody with $\beta_P = 1.59$ and $T_d = 19.6\text{K}$, in agreement with Planck Collaboration Int.

10. Note that p^2 is used because an unbiased estimator of it can be built from independent subsets of the data.

11. Auto power spectra C_ℓ^{EE} and C_ℓ^{BB} for E and B modes, respectively.

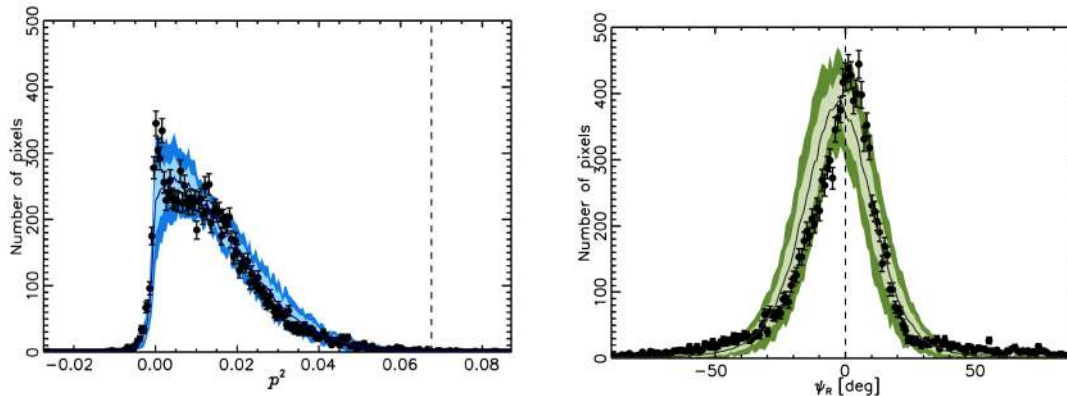


FIGURE 2.7 – Distribution of p^2 (left) and ψ_R (right) towards the Southern Galactic cap, derived from Stokes parameters at 353 GHz. The polarization angle ψ_R is computed relative to the direction expected from a completely uniform magnetic field. Data points are shown in black with error bars, while the solid lines represent the mean distributions over 20 realizations of the Gaussian models discussed in the text, with the shaded areas corresponding to 1σ and 2σ dispersions. The dashed vertical line in the left panel corresponds to $p_0 = 26\%$. Figure adapted from Planck Collaboration Int. XLIV (2016).

XXII (2015). Comparing the two auto power spectra, it is found that there is a systematic difference in amplitude, with $C_\ell^{EE}/C_\ell^{BB} \approx 2$. These properties are preserved at high Galactic latitudes, towards lines of sight with very faint dust emission, and there is therefore no region on the sky where the primordial B -modes could be measured without properly subtracting the foreground polarization. In particular, the level of contamination by dust polarized emission in the BICEP2 field (BICEP2 Collaboration 2014) is estimated to be $\approx 1.32_{-0.24}^{+0.28} \pm 0.29 \times 10^{-2} \mu\text{K}^2$ over the multipole range of the primordial recombination bump ($40 < \ell < 120$), which is comparable to the signal level reported by BICEP2 Collaboration (2014).

The origin of the E/B power asymmetry is traced to the filamentary structures of the ISM in Planck Collaboration Int. XXXVIII (2016). This is done by filtering the 353 GHz Stokes maps at high Galactic latitude to identify filaments¹² in the range of scales where this power asymmetry is observed. We extracted 259 filaments with lengths larger than 2° , and found that their orientation was preferentially aligned with the magnetic orientation inferred from ψ . After rotating the Stokes I , Q , U , as well as the E and B maps of individual filaments, we stacked them together (see Fig. 2.8). From these, and the histogram of relative orientations (Soler et al. 2013; Planck Collaboration Int. XXXV 2016), we derived a mean polarization fraction in the filaments of $\langle p \rangle = 11\%$, in agreement with the results of Planck Collaboration Int. XLIV (2016), and showed that the correlation between the filamentary structures and the magnetic orientation is able to account for the E/B power asymmetry and the C_ℓ^{TE}/C_ℓ^{EE} ratio reported in Planck Collaboration Int. XXX (2016).

2.2.5 Frequency dependence of dust polarized emission

Global analysis at intermediate Galactic latitudes

In Planck Collaboration Int. XXII (2015), we performed a cross-correlation analysis between the 353 GHz I , Q and U maps, taken as dust emission templates, and data from both *Planck* and *WMAP*, to

12. This is done with SMAFF (Bond et al. 2010)

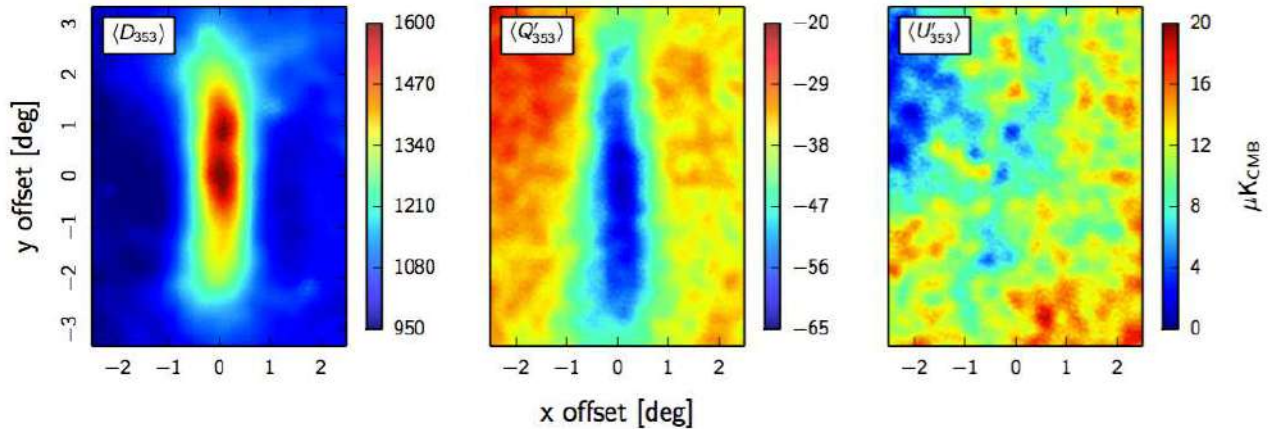


FIGURE 2.8 – Stacked maps of the total intensity (*left*, represented by the D_{353} dust model of Planck Collaboration XI (2014)), Stokes Q (*center*), and Stokes U (*right*) in the extracted filaments at high Galactic latitudes by Planck Collaboration Int. XXXVIII (2016). The maps are rotated to align the filaments along a common North-South direction.

characterize the frequency dependence of dust emission. This analysis is performed over circular patches of 10° radius, at intermediate Galactic latitudes. We have thus determined the spectral indices of dust emission between 100 and 353 GHz in total intensity (β_I) and polarization (β_P) in each patch. These are found to be remarkably uniform over the mask used, with significantly different values : $\beta_I = 1.51 \pm 0.01$ and $\beta_P = 1.59 \pm 0.02$. We derive the mean spectral energy distribution (SED) of the dust microwave emission¹³, and find that it increases below 60 GHz in both total intensity and polarized emission. In the latter case, this may be due to a synchrotron component spatially correlated with dust. The polarization fraction p of dust emission is found to decrease by $21 \pm 6\%$ from 353 to 70 GHz.

Spatial variations of the polarized thermal dust SED

In Planck Collaboration Int. L (2016), the spatial variability of the dust polarized spectral energy distribution (SED) is studied, traced by the correlation ratio of the C_ℓ^{BB} angular power spectra between 217 and 353 GHz. For entirely correlated signals in these two channels, this ratio should be one, and it was found to be smaller. The departure from unity is too large to be ascribed to CMB residuals, instrumental noise or systematics, when combining the results over different high Galactic latitude regions covering 20% to 80% of the sky : the confidence that this is a real decorrelation between dust emission maps at 217 and 353 GHz is over 99%. Also, when comparing the decorrelation in regions with different column densities N_H , it is found to be larger in more diffuse areas of the sky. It is also larger at smaller angular scales. This decorrelation may be ascribed to spatial variations of the dust SED or of the polarization angle, or to a combination of the two. These results are of particular importance for cosmology, in the sense that they pose a fundamental limit to the possibility to extrapolate dust templates at high frequencies down to CMB frequencies (~ 160 GHz) in order to remove this foreground polarized emission. More specifically, ignoring this decorrelation leads to a significant positive bias on the estimation of the tensor-to-scalar ratio r (BICEP2/Keck Array and Planck Collaborations 2015).

13. microwave emission that is correlated with the 353 GHz dust templates.

2.2.6 Comparison with starlight polarization in extinction

Implications for dust models

The dust grains that emit the radiation seen by *Planck* in the submillimetre also extinguish and polarize starlight in the visible and near-infrared (NIR). In Planck Collaboration Int. XXI (2015), we used this property to establish new constraints on the models (see, e.g., Draine & Fraisse 2009) used to describe the properties of these grains (composition, size distribution, shape, ...). Using catalogues of starlight polarization (Heiles 2000), we selected stars for which the reddening $E(B - V)$ yields a column density N_{H} that is comparable to the measure derived from *Planck*'s dust model (Planck Collaboration XI 2014) in the same direction, and the polarization angle in the visible is close to that from *Planck* rotated by 90° . The matter probed by the two methods is thus the same for these lines of sight. Having access to the polarization degree p_V and the optical depth τ_V in the visible V band, and to the 353 GHz polarized intensity P_S and total intensity I_S from *Planck*, we study the ratios $R_{S/V} = (P_S/I_S)/(p_V/\tau_V)$ and $R_{P/p} = P_S/p_V$. Averaged over the 206 lines of sight selected, we find $R_{S/V} = 4.2 \pm 0.2(\text{stat}) \pm 0.3(\text{syst})$ and $R_{P/p} = 5.4 \pm 0.2(\text{stat}) \pm 0.3(\text{syst}) \text{ MJy sr}^{-1}$. The value found for $R_{S/V}$ is compatible with most dust models in the diffuse ISM, so it does not provide strong constraints for these models. On the contrary, $R_{P/p}$ is directly linked to the properties of the polarizing grains and is found not to be compatible with model predictions, which are too low by a factor of about 2.5. This means that changes in the optical properties of aligned grains are required, and we are currently improving the DUSTEM model of Compiègne et al. (2011) to take into account these new constraints (Guillet et al. 2016).

Implications for magnetic field morphology in nearby molecular clouds

In Soler et al. (2016), the magnetic orientation inferred from *Planck* data at 353 GHz is compared, in four nearby ($d < 160 \text{ pc}$) molecular clouds, to that derived from starlight polarization in extinction in the near infrared and visible. The average dispersion of the orientation inferred from starlight polarization within regions of $10'$ diameter¹⁴ is less than 20° , and the mean field orientation within these regions lies on average within 5° from that inferred from the 353 GHz data. Since starlight polarization data probes much smaller scales than *Planck* data, we use the Gaussian model of the Galactic magnetic field introduced in Planck Collaboration Int. XXXII (2016) to establish the robustness of our analysis. We also compare the two sets of data using the second-order structure functions of the magnetic orientation, $S_2^{\text{star}}(l)$ and $S_2^{\text{submm}}(l)$. At scales $l > 10'$, these structure functions exhibit differences up to 14.7° between the starlight and *Planck* data, but our Gaussian model indicates that these are actually small differences, which may be fully accounted for by different angular resolutions. This also means that the estimates of magnetic field strengths reported in Planck Collaboration Int. XXXV (2016) need not be significantly altered at better angular resolution.

14. This is the size of the beam used for *Planck* data in this work.

Chapitre 3

Some perspectives

3.1 Modelling of the turbulent ISM with 3D fBm fields

In Planck Collaboration Int. XXXV (2016), Planck Collaboration Int. XXXII (2016), and Planck Collaboration Int. XLIV (2016), we provided estimates of the ratio f_M between the standard deviation of the turbulent component of the magnetic field, \mathbf{B}_t , and the amplitude of the large-scale component \mathbf{B}_0 . In Planck Collaboration Int. XXXV (2016), we gave an estimate in the range 0.3-0.7 from the statistics of the angle between the magnetic orientation and the direction of structures traced by dust in molecular clouds. Planck Collaboration Int. XXXII (2016) studied that same relative orientation in the diffuse ISM at intermediate and high Galactic latitudes, and the corresponding estimate of f_M lies in the range 0.6-1.0 with a preferred value at 0.8. These estimates are confirmed in Planck Collaboration Int. XLIV (2016), where we find $f_M \simeq 0.9$ towards the Southern Galactic cap. In this last paper, we also roughly estimated the spectral index α_M of \mathbf{B}_t , appearing in the modelling of the angular power spectrum as a power-law $C_\ell \propto \ell^{\alpha_M}$, to be in the range $[-2, -3]$.

In Planck Collaboration Int. XXXII (2016) and Planck Collaboration Int. XLIV (2016), the description of structures, in both dust density and magnetic field, along the LOS is reduced to the bare minimum, while statistical properties in the POS are modelled through f_M and α_M . Orthogonal approaches have also been pursued (e.g. Miville-Deschênes et al. 2008; O’Dea et al. 2012), in which the turbulent component of the magnetic field is modelled along each LOS, independently from the neighbouring ones, as a realization of a Gaussian random field with a power-law power spectrum. In this type of approach there is no correlation from pixel to pixel on the sky, and such studies seek to exploit the depolarization along the LOS, rather than spatial correlations in the POS, to constrain statistical properties of the interstellar magnetic field.

In a forthcoming paper (Levrier et al. 2016), we explore another avenue, using simple, approximate, three-dimensional models for the dust density n_d and the magnetic field \mathbf{B} , on a Cartesian grid, taking into account statistical correlation properties in all three dimensions¹, and building on methods developed in Planck Collaboration Int. XX (2015) to compare *Planck* data with synthetic polarization maps. With this approach, we are able to perform a statistically significant number of simulated polarization maps, exploring a wide range of physical parameters with sufficient sampling. Actual observations may then be compared to these simulated maps, using least-square analysis methods, to extract best-fitting parameters,

1. These models make use of fractional Brownian motions (fBm) (Falconer 1990), which have been used previously as toy models for the fractal structure of molecular clouds, in both density and velocity space (Stutzki et al. 1998; Miville-Deschênes et al. 2003b). The version of these fields used for \mathbf{B}_t ensures the null-divergence property.

in particular the spectral index of the magnetic field², and the ratio of turbulent to regular field³. The other parameters are the depth d of the simulation cubes, the position angle χ of the ordered field (see Fig. 1.3), the spectral index β_n of the density field, and a parameter y_n controlling its fluctuations⁴.

We then build synthetic Stokes I , Q , and U maps following our method in Planck Collaboration Int. XX (2015), add noise according to the *Planck* covariance matrix in the region of the sky we mean to study, and convolve these noisy maps⁵ with a circular 15' FWHM Gaussian beam. The resulting field-of-view is approximately 12°. From the Stokes maps, we build maps of the normalized Stokes $i = I/\langle I \rangle$, $q = Q/I$, and $u = U/I$, polarization fraction p , polarization angle ψ , and polarization angle dispersion function \mathcal{S} . The one-point statistics of the $i, q, u, p, \psi, \mathcal{S}$ maps, the power spectra of the I, Q , and U maps, and the shape of the 2D distribution function⁶ of $\{\mathcal{S}, p\}$ are used as statistical diagnostics for each set of input parameters ($\beta_n, \beta_B, y_n, y_B, \chi, d$)

To analyze a given set of polarization maps, we build the same statistical diagnostics and we explore the input parameter space to find the best-fitting ones, through a simple Metropolis-Hastings algorithm and Monte Carlo Markov Chains (MCMC). These are built to explore the posterior probability distribution of the input parameters, assuming flat priors covering a reasonable range of physical interest⁷. The convergence of the Markov chains is tested using the Gelman-Rubin statistic R (Gelman & Rubin 1992).

The method is first validated on a set of three simulated cases, showing that the input parameters are recovered properly, then applied to *Planck* 353 GHz maps of the Polaris Flare, to constrain the statistical properties of the turbulent magnetic field in this diffuse, highly dynamical, non-starforming molecular cloud. We find in particular that $\beta_B = 2.33_{-0.26}^{+0.26}$ and $y_B^{\text{POS}} = 0.87_{-0.08}^{+0.06}$, in very good agreement with the findings of Planck Collaboration Int. XLIV (2016) in another, larger region of the sky. Fig. 3.1 shows the posterior PDFs of each input parameter and pair of parameters⁸. This method is adapted to the study of small fields, and has the advantage of yielding statistical properties of the density field as well. For instance, in our Polaris Flare study, the best-fit spectral index for the density field is $\beta_n = 2.64_{-0.24}^{+0.25}$. We also constrain the thickness of the molecular cloud to $d = 10.0_{-6.5}^{+2.8}$ pc, which points to a thin "sheet". This is interesting as it is not fully consistent with the findings of Miville-Deschênes et al. (2003a) that the spectral index of the integrated intensity of HI in the nearby Ursa Major cirrus is $\beta_I = -3.6 \pm 0.2$, although the scales probed are somewhat smaller, and it is well-known that the ratio of these scales to the depth of the cloud affects the measurement of the spectral index (Miville-Deschênes et al. 2003b).

It is however not possible, or at least not simple, to introduce non-Gaussian statistics for the density and magnetic field using this method (e.g., filamentary structures), nor the particular correlations observed between the orientations of the structures in the dust and the magnetic field (Planck Collaboration Int. XXXV 2016).

2. which we write β_B in this study, the power spectrum scaling as $P(k) \propto k^{-\beta_B}$ with the wavenumber k . We have the relationship $\alpha_M = -\beta_B$.

3. which we write y_B instead of f_M in this study. Also note that, due to the limited computational power, the field-of-view is necessarily small, so the 3D orientation of \mathbf{B}_0 cannot be constrained as in Planck Collaboration Int. XLIV (2016) and there is a degeneracy between the chosen p_0 parameter and the angle γ . Consequently, the parameter we constrain is not actually y_B , but its equivalent with respect to the POS projection of \mathbf{B}_0 , i.e., $y_B^{\text{POS}} = y_B / \cos \gamma$.

4. The PDF of the density field is log-normal, while those of the components of \mathbf{B}_t (and therefore \mathbf{B} as well) are Gaussian.

5. They are placed at a distance $D = 140$ pc, so that the angular size of each pixel is about 6'.

6. i.e., the linear fit parameters of the observed anti-correlation between the two (See Fig. 2.3).

7. In particular, this analysis was applied to the Polaris Flare whose average column density, $N_H \approx 10^{21} \text{ cm}^{-2}$, is used to set a prior on the depth d of the cube between 0.5 pc and 33 pc, assuming that the total gas density lies between 10 and 500 cm^{-3} .

8. This is an early version, in which we tried to fit y_B and γ independently. The figure underlines how these two parameters are in fact degenerate.

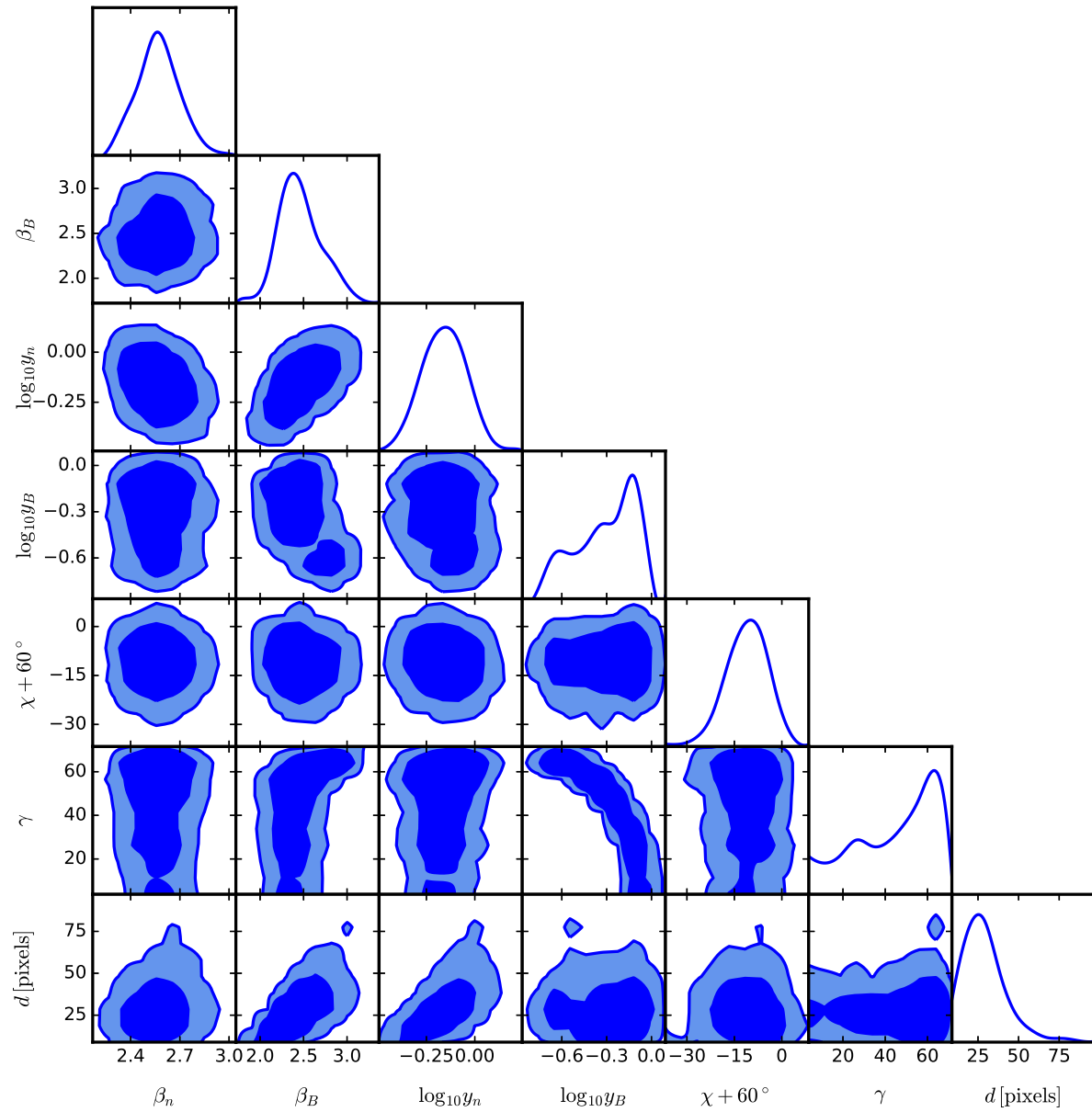


FIGURE 3.1 – Triangle plot showing the 2D PDFs of each pair of input parameters in the analysis of the Polaris Flare *Planck* 353 GHz polarization maps, and on top of each column the marginalized 1D PDF for each parameter separately.

3.2 Simulated polarized emission maps on the sphere

In a forthcoming paper (Vansyngel et al. 2016), we will present a method to build simulated polarized dust emission maps directly on the HEALPIX sphere, with the aim of providing simple ways to generate statistically accurate polarized foreground maps to test component separation methods for the future CMB experiments. This is done in two steps, the first one being identical to the model of Planck Collaboration Int. XLIV (2016) and leading to simulated I , Q , and U maps on the sphere which depend on a set of six parameters : the two angles (l_0, b_0) defining the direction of the large-scale field \mathbf{B}_0 , the parameters f_M and α_M describing the properties of \mathbf{B}_t , the number of polarization layers N , and the intrinsic polarization fraction p_0 .

At this stage, the model does not include the alignment observed between the filamentary structures of the diffuse ISM and the magnetic orientation, so there is no power asymmetry, $C_\ell^{EE}/C_\ell^{BB} = 1$, and no $T - E$ correlation at angular scales $\ell > 30$. To remedy this in a phenomenological way, we propose to alter the maps in spherical harmonics space via the transformation

$$\begin{bmatrix} a_{\ell m}^T \\ a_{\ell m}^E \\ a_{\ell m}^B \end{bmatrix} \mapsto \begin{bmatrix} t a_{\ell m}^T \\ a_{\ell m}^E + p_0 \eta(\ell) a_{\ell m}^T \\ f(\ell) a_{\ell m}^B \end{bmatrix}$$

While t and p_0 are constants, it appears that f and η need to be functions of the angular scale to preserve the statistics of p and ψ which are reproduced by the first-stage maps. Simple functional forms are assumed for these, with limits $f \rightarrow 1$ and $\eta \rightarrow 0$ at low multipoles ℓ . The transition is assumed to be at a large enough angular scale to be consistent with the failure to observe a return to power symmetry in E and B modes at low ℓ in Planck Collaboration Int. XXX (2016).

The parameters are then constrained so that the model power spectra C_ℓ^{EE} , C_ℓ^{BB} , and C_ℓ^{TE} match those measured by *Planck*, in particular the spectral indices of the first two, estimated in Planck Collaboration Int. XXX (2016) to be $\alpha_{EE, BB} = -2.42 \pm 0.02$. These are matched for a spectral index of the turbulent component of the magnetic field in the range $\alpha_M \lesssim -2.5$, consistent with the estimate of Planck Collaboration Int. XLIV (2016) and in fair agreement with the result of Levrier et al. (2016).

The ease with which these models may be computed allows for numerous realizations of Stokes Q and U maps for a given set of parameters, and thus to quantify the variance of dust polarization spectra for any given region of the sky at intermediate and high Galactic latitudes, which is vital to assess the robustness of candidate component separation methods. An extension of the method is also proposed to take into account the observed decorrelation across frequencies (Planck Collaboration Int. L 2016).

3.3 Further perspectives and conclusions

The analyses and modelling approaches presented so far may be extended in several ways :

- The diagnostics used to analyse the *Planck* polarization maps are limited to one- and two-point statistics (distribution functions and power spectra). The next step is to use higher-order tools, such as bispectra, which are already in wide use in a cosmological context to assess non-Gaussianities (Planck Collaboration XVII 2016), and which were already used in simulations of molecular clouds (Burkhart et al. 2009).
- The large-scale magnetic field \mathbf{B}_0 in our modelling is assumed to be uniform, which is probably fine in small fields of view, but definitely a problem in full-sky analyses. A more detailed approach would be to use the models of the large-scale Galactic magnetic field (see, e.g., Planck Collaboration Int. XLII 2016, and references therein). For a Solar-neighbourhood modelling, i.e., of the field in the local bubble, we will

adapt the analytical modelling of the Rosette Nebula (Planck Collaboration Int. XXXIV 2016), which we may combine with the 3D dust density model of Lallement (2015) to build more realistic model maps of polarized dust emission in the diffuse ISM, and constrain the turbulent magnetic field \mathbf{B}_t .

► The modelling of the turbulent magnetic field is currently fully scale-invariant, but we may need to introduce phenomenological cut-offs at low multipoles ℓ to take into account the energy injection scale. At the other end of the scale spectrum, when modelling small-scale fluctuations of the polarized emission, far beyond the capabilities of *Planck* but in the range of scales accessible with *ALMA*, taking into account the various dissipation scales (Momferratos et al. 2014) will become necessary. This also underlines the necessity to take into account velocity data in the analysis, both on the modelling side and on the observational side using line emission.

► These phenomenological, synthetic modelling approaches should be complemented with extended studies using MHD simulations of the ISM, with as much physics as possible (see, e.g., Falceta-Gonçalves & Lazarian 2011; Momferratos et al. 2014; Ntormousi et al. 2016). Only these can justify or refute simplifying assumptions made in synthetic approaches. In particular, it would be interesting to use a modelling of a large part of the Galactic disk such as the one of Hennebelle & Iffrig (2014) and to compute the polarization maps for an observer placed within the disk.

As a conclusion, it seems fit to underline the central part played by cross-fertilization between cosmology and ISM studies within the *Planck* mission, and especially in the results presented here. The Galactic foregrounds may be seen by cosmologists as a nuisance, and the initial misinterpretation of the B -modes detected by the BICEP2 Collaboration (2014) as a cosmological signal may have been the epitome of that, but in truth, the precise understanding of foregrounds helps in constraining cosmological parameters (BICEP2/Keck Array and Planck Collaborations 2015). Conversely, our analysis of the dust emission has largely benefitted from the tools and methods developed in the study of the cosmological signal (e.g., angular power spectra, correlation analyses), and will continue to do so (e.g., non-Gaussianities).

Planck, in this respect as well as in many others, has brought about something of a revolution.

BIBLIOGRAPHIE

- Alexakis, A. 2013, *Physical Review Letters*, 110, 084502
- Alina, D., Montier, L., Ristorcelli, I., et al. 2016, *A&A*
- Altwegg, K., Balsiger, H., Calmonte, U., et al. 2015, in *AAS/Division for Planetary Sciences Meeting Abstracts*, Vol. 47, *AAS/Division for Planetary Sciences Meeting Abstracts*, 503.01
- André, P., Basu, S., & Inutsuka, S. 2009, *The formation and evolution of prestellar cores*, ed. G. Chabrier (Cambridge University Press), 254
- Armstrong, J. W., Rickett, B. J., & Spangler, S. R. 1995, *ApJ*, 443, 209
- Bakes, E. L. O. & Tielens, A. G. G. M. 1994, *ApJ*, 427, 822
- Beck, R. 2016, *ARAA*, 24, 4
- Beck, R., Brandenburg, A., Moss, D., Shukurov, A., & Sokoloff, D. 1996, *ARAA*, 34, 155
- Bennett, C. L., Larson, D., Weiland, J. L., et al. 2013, *ApJS*, 208, 20
- Benoît, A., Ade, P., Amblard, A., et al. 2004, *A&A*, 424, 571
- Bernard-Salas, J., Habart, E., Arab, H., et al. 2012, *A&A*, 538, A37
- BICEP2 Collaboration. 2014, *Phys. Rev. Letters*, 112, 241101
- BICEP2/Keck Array and Planck Collaborations. 2015, *Phys. Rev. Letters*, 114, 101301
- Bierman, E. M., Matsumura, T., Dowell, C. D., et al. 2011, *ApJ*, 741, 81
- Bird, D. J., Corbato, S. C., Dai, H. Y., et al. 1994, *ApJ*, 424, 491
- Biskamp, D. 2003, *Magnetohydrodynamic Turbulence*, 310
- Bisnovatyi-Kogan, G. S., Ruzmaikin, A. A., & Syunyaev, R. A. 1973, *Sov. Ast.*, 17, 137
- Blasi, P. & Amato, E. 2012, *JCAP*, 1, 010
- Bond, N. A., Strauss, M. A., & Cen, R. 2010, *MNRAS*, 409, 156
- Bournaud, F., Powell, L. C., Chapon, D., & Teyssier, R. 2011, in *IAU Symposium*, Vol. 271, *Astrophysical Dynamics : From Stars to Galaxies*, ed. N. H. Brummell, A. S. Brun, M. S. Miesch, & Y. Ponty, 160–169

- Bron, E., Le Bourlot, J., & Le Petit, F. 2014, *A&A*, 569, A100
- Burkhart, B., Falceta-Gonçalves, D., Kowal, G., & Lazarian, A. 2009, *ApJ*, 693, 250
- Cabral, B. & Leedom, L. C. 1993, in *Proceedings of the 20th Annual Conference on Computer Graphics and Interactive Techniques, SIGGRAPH '93* (New York, NY, USA : ACM), 263–270
- Cami, J., Bernard-Salas, J., Peeters, E., & Malek, S. E. 2010, *Science*, 329, 1180
- Caprioli, D. & Spitkovsky, A. 2014, *ApJ*, 783, 91
- Chandrasekhar, S. & Fermi, E. 1953, *ApJ*, 118, 113
- Clemens, D. P., Sanders, D. B., & Scoville, N. Z. 1988, *ApJ*, 327, 139
- Compiègne, M., Verstraete, L., Jones, A., et al. 2011, *A&A*, 525, A103
- Cristofari, P., Gabici, S., Casanova, S., Terrier, R., & Parizot, E. 2013, *MNRAS*, 434, 2748
- Crutcher, R. M., Wandelt, B., Heiles, C., Falgarone, E., & Troland, T. H. 2010, *ApJ*, 725, 466
- Dame, T. M., Hartmann, D., & Thaddeus, P. 2001, *ApJ*, 547, 792
- Davis, L. 1951, *Physical Review*, 81, 890
- Davis, Jr., L. & Greenstein, J. L. 1951, *ApJ*, 114, 206
- Dickey, J. M. & Lockman, F. J. 1990, *ARAA*, 28, 215
- Dotson, J. L., Vaillancourt, J. E., Kirby, L., et al. 2010, *ApJS*, 186, 406
- Draine, B. T. 1978, *ApJS*, 36, 595
- Draine, B. T. 2011, *Physics of the Interstellar and Intergalactic Medium*
- Draine, B. T. & Fraisse, A. A. 2009, *ApJ*, 696, 1
- Drimmel, R. & Spergel, D. N. 2001, *ApJ*, 556, 181
- Drury, L. O. 1983, *Reports on Progress in Physics*, 46, 973
- Elmegreen, B. G. & Scalo, J. 2004, *ARAA*, 42, 211
- Falceta-Gonçalves, D., Bonnell, I., Kowal, G., Lépine, J. R. D., & Braga, C. A. S. 2015, *MNRAS*, 446, 973
- Falceta-Gonçalves, D., Kowal, G., Falgarone, E., & Chian, A. C.-L. 2014, *Nonlinear Processes in Geophysics*, 21, 587
- Falceta-Gonçalves, D. & Lazarian, A. 2011, in *Astronomical Society of the Pacific Conference Series*, Vol. 449, *Astronomical Polarimetry 2008 : Science from Small to Large Telescopes*, ed. P. Bastien, N. Manset, D. P. Clemens, & N. St-Louis, 159
- Falceta-Gonçalves, D., Lazarian, A., & Houde, M. 2010, *ApJ*, 713, 1376
- Falceta-Gonçalves, D., Lazarian, A., & Kowal, G. 2008, *ApJ*, 679, 537

- Falconer, K. J. 1990, *Fractal geometry : mathematical foundations and applications* (Chichester, New York, Weinheim : J. Wiley & sons), réimpr. en 1993, 1995, 1997, 1999, 2000
- Faucher-Giguère, C.-A., Kereš, D., Dijkstra, M., Hernquist, L., & Zaldarriaga, M. 2010, *ApJ*, 725, 633
- Ferriere, K. 1996, *A&A*, 310, 438
- Fissel, L. M., Ade, P. A. R., Angilè, F. E., et al. 2015, *ArXiv e-prints*
- Fixsen, D. J., Bennett, C. L., & Mather, J. C. 1999, *ApJ*, 526, 207
- Frisch, U. 1995, *Turbulence*
- Gaetz, T. J. & Salpeter, E. E. 1983, *ApJS*, 52, 155
- Gelman, A. & Rubin, D. B. 1992, *Statist. Sci.*, 7, 457
- Gerin, M., Levrier, F., Falgarone, E., et al. 2012, *Philosophical Transactions of the Royal Society of London Series A*, 370, 5174
- Glassgold, A. E., Galli, D., & Padovani, M. 2012, *ApJ*, 756, 157
- Glassgold, A. E. & Najita, J. R. 2015, *ApJ*, 810, 125
- Godard, B., Falgarone, E., & Pineau des Forêts, G. 2014, *A&A*, 570, A27
- Goldreich, P. & Sridhar, S. 1995, *ApJ*, 438, 763
- Goldsmith, P. F. & Langer, W. D. 1978, *ApJ*, 222, 881
- Goldsmith, P. F., Yıldız, U. A., Langer, W. D., & Pineda, J. L. 2015, *ApJ*, 814, 133
- Górski, K. M., Hivon, E., Banday, A. J., et al. 2005, *ApJ*, 622, 759
- Guillet, V., Fanciullo, L., Boulanger, F., et al. 2016, *A&A*, in prep.
- Hall, J. S. 1949, *Science*, 109, 166
- Haverkorn, M., Brown, J. C., Gaensler, B. M., & McClure-Griffiths, N. M. 2008, *ApJ*, 680, 362
- Heiles, C. 2000, *AJ*, 119, 923
- Hennebelle, P. & Audit, E. 2007, *A&A*, 465, 431
- Hennebelle, P. & Falgarone, E. 2012, *ARAA*, 20, 55
- Hennebelle, P. & Iffrig, O. 2014, *A&A*, 570, A81
- Hennebelle, P. & Teyssier, R. 2008, *A&A*, 477, 25
- Hezareh, T., Csengeri, T., Houde, M., Herpin, F., & Bontemps, S. 2014, *MNRAS*, 438, 663
- Hezareh, T., Houde, M., McCoey, C., & Li, H.-b. 2010, *ApJ*, 720, 603
- Hildebrand, R. H., Kirby, L., Dotson, J. L., Houde, M., & Vaillancourt, J. E. 2009, *ApJ*, 696, 567
- Hiltner, W. A. 1949, *Nature*, 163, 283

- Hily-Blant, P. & Falgarone, E. 2009, *A&A*, 500, L29
- Hily-Blant, P., Falgarone, E., & Pety, J. 2008, *A&A*, 481, 367
- Hoang, T. & Lazarian, A. 2014, *MNRAS*, 438, 680
- Höfner, S. 2012, *Nature*, 484, 172
- Houde, M., Akeson, R. L., Carlstrom, J. E., et al. 2001, *PASP*, 113, 622
- Houde, M., Fletcher, A., Beck, R., et al. 2013, *ApJ*, 766, 49
- Houde, M., Hull, C. L. H., Plambeck, R. L., Vaillancourt, J. E., & Hildebrand, R. H. 2016, *ApJ*, 820, 38
- Houde, M., Rao, R., Vaillancourt, J. E., & Hildebrand, R. H. 2011, *ApJ*, 733, 109
- Houde, M., Vaillancourt, J. E., Hildebrand, R. H., Chitsazzadeh, S., & Kirby, L. 2009, *ApJ*, 706, 1504
- Hull, C. L. H., Plambeck, R. L., Kwon, W., et al. 2014, *ApJS*, 213, 13
- Iffrig, O. & Hennebelle, P. 2015, *A&A*, 576, A95
- Iroshnikov, P. S. 1964, *Sov. Ast.*, 7, 566
- Ivlev, A. V., Padovani, M., Galli, D., & Caselli, P. 2015, *ApJ*, 812, 135
- Jaffe, T. R., Leahy, J. P., Banday, A. J., et al. 2010, *MNRAS*, 401, 1013
- Janka, H.-T., Hanke, F., Hüdepohl, L., et al. 2012, *Progress of Theoretical and Experimental Physics*, 2012, 01A309
- Jansson, R. & Farrar, G. R. 2012, *ApJL*, 761, L11
- Jones, A. P. 2011, *A&A*, 528, A98
- Jones, W. C., Bhatia, R., Bock, J. J., & Lange, A. E. 2003, in *Proc. SPIE*, Vol. 4855, *Millimeter and Submillimeter Detectors for Astronomy*, ed. T. G. Phillips & J. Zmuidzinas, 227–238
- Jørgensen, J. K., Schöier, F. L., & van Dishoeck, E. F. 2004, *A&A*, 416, 603
- Jura, M. 1994, *ApJ*, 434, 713
- Koch, P. M., Tang, Y.-W., Ho, P. T. P., et al. 2014, *ApJ*, 797, 99
- Kolmogorov, A. 1941, *Akademiia Nauk SSSR Doklady*, 30, 301
- Kowal, G. & Lazarian, A. 2007, *ApJL*, 666, L69
- Kraichnan, R. H. 1965a, *Physics of Fluids*, 8, 1385
- Kraichnan, R. H. 1965b, *Physics of Fluids*, 8, 575
- Kritsuk, A. G., Norman, M. L., Padoan, P., & Wagner, R. 2007, *ApJ*, 665, 416
- Kruegel, E. 2003, *The physics of interstellar dust*
- Lallement, R. 2015, *Journal of Physics Conference Series*, 577, 012016

- Larson, R. B. 1981, *MNRAS*, 194, 809
- Lazarian, A. & Cho, J. 2004, *ApSS*, 289, 307
- Lazarian, A. & Pogosyan, D. 2000, *ApJ*, 537, 720
- Le Bourlot, J., Le Petit, F., Pinto, C., Roueff, E., & Roy, F. 2012, *A&A*, 541, A76
- Le Bourlot, J., Pineau des Forêts, G., & Flower, D. R. 1999, *MNRAS*, 305, 802
- Levrier, F. 2004, *A&A*, 421, 387
- Levrier, F., Neveu, J., Falgarone, E., Boulanger, F., & Bracco, A. 2016, *A&A*, in prep.
- Lewis, A. & Challinor, A. 2006, *Physics Reports*, 429, 1
- Li, H., Li, D., Qian, L., et al. 2015, *ApJS*, 219, 20
- Li, H.-b. & Houde, M. 2008, *ApJ*, 677, 1151
- Li, H.-b., Houde, M., Lai, S.-p., & Sridharan, T. K. 2010, *ApJ*, 718, 905
- Lis, D. C., Pety, J., Phillips, T. G., & Falgarone, E. 1996, *ApJ*, 463, 623
- Liszt, H. S., Pety, J., & Lucas, R. 2010, *A&A*, 518, A45
- Lykins, M. L., Ferland, G. J., Porter, R. L., et al. 2013, *MNRAS*, 429, 3133
- Martin, P. G. 1971, *MNRAS*, 153, 279
- Mathis, J. S., Rumpl, W., & Nordsieck, K. H. 1977, *ApJ*, 217, 425
- Matthews, B. C., McPhee, C. A., Fissel, L. M., & Curran, R. L. 2009, *ApJS*, 182, 143
- Mazzali, P. A., Röpke, F. K., Benetti, S., & Hillebrandt, W. 2007, *Science*, 315, 825
- McKee, C. F. & Ostriker, J. P. 1977, *ApJ*, 218, 148
- Mennella, A., Butler, R. C., Curto, A., et al. 2011, *A&A*, 536, A3
- Miller, M. J. & Bregman, J. N. 2015, *ApJ*, 800, 14
- Miville-Deschênes, M.-A., Joncas, G., Falgarone, E., & Boulanger, F. 2003a, *A&A*, 411, 109
- Miville-Deschênes, M.-A., Levrier, F., & Falgarone, E. 2003b, *ApJ*, 593, 831
- Miville-Deschênes, M.-A., Ysard, N., Lavabre, A., et al. 2008, *A&A*, 490, 1093
- Momferratos, G., Lesaffre, P., Falgarone, E., & Pineau des Forêts, G. 2014, *MNRAS*, 443, 86
- Monin, A., I?A ?glom, A., & Lumley, J. 2007, *Statistical Fluid Mechanics : Mechanics of Turbulence*, Dover books on physics No. vol. 1 (Dover Publications)
- Montier, L., Plaszczyński, S., Levrier, F., et al. 2015a, *A&A*, 574, A135
- Montier, L., Plaszczyński, S., Levrier, F., et al. 2015b, *A&A*, 574, A136

- Neufeld, D. A., Lepp, S., & Melnick, G. J. 1995, *ApJS*, 100, 132
- Ntormousi, E., Hennebelle, P., André, P., & Masson, J. 2016, *A&A*, 589, A24
- O’Dea, D. T., Clark, C. N., Contaldi, C. R., & MacTavish, C. J. 2012, *MNRAS*, 419, 1795
- Oppermann, N., Junklewitz, H., Robbers, G., et al. 2012, *A&A*, 542, A93
- Padovani, M., Galli, D., Hennebelle, P., Commerçon, B., & Joos, M. 2015, *ArXiv e-prints*
- Padovani, M., Marcowith, A., Hennebelle, P., & Ferrière, K. 2016, *A&A*, 590, A8
- Pelkonen, V.-M., Juvela, M., & Padoan, P. 2007, *A&A*, 461, 551
- Peter, P. & Uzan, J. 2009, *Primordial cosmology*, Oxford graduate texts (Oxford University Press)
- Pineda, J. L., Langer, W. D., Velusamy, T., & Goldsmith, P. F. 2013, *A&A*, 554, A103
- Planck HFI Core Team. 2011, *A&A*, 536, A4
- Planck Collaboration XI. 2014, *A&A*, 571, A11
- Planck Collaboration I. 2016, *A&A*, submitted
- Planck Collaboration X. 2016, *A&A*, submitted
- Planck Collaboration XIII. 2016, *A&A*, submitted
- Planck Collaboration XV. 2016, *A&A*, submitted
- Planck Collaboration XVII. 2016, *A&A*, submitted
- Planck Collaboration XIX. 2016, *A&A*, submitted
- Planck Collaboration XX. 2016, *A&A*, submitted
- Planck Collaboration XXII. 2016, *A&A*, submitted
- Planck Collaboration XXIII. 2016, *A&A*, submitted
- Planck Collaboration XXIV. 2016, *A&A*, submitted
- Planck Collaboration XXV. 2016, *A&A*, submitted
- Planck Collaboration XXVIII. 2016, *A&A*, in press
- Planck Collaboration Int. XIX. 2015, *A&A*, 576, A104
- Planck Collaboration Int. XX. 2015, *A&A*, 576, A105
- Planck Collaboration Int. XXI. 2015, *A&A*, 576, A106
- Planck Collaboration Int. XXII. 2015, *A&A*, submitted, 576, A107
- Planck Collaboration Int. XXX. 2016, *A&A*, 586, A133
- Planck Collaboration Int. XXXII. 2016, *A&A*, 586, A135

- Planck Collaboration Int. XXXIV. 2016, *A&A*, 586, A137
- Planck Collaboration Int. XXXV. 2016, *A&A*, 586, A138
- Planck Collaboration Int. XXXVIII. 2016, *A&A*, 586, A141
- Planck Collaboration Int. XLII. 2016, *A&A*, submitted
- Planck Collaboration Int. XLIV. 2016, *A&A*, submitted
- Planck Collaboration Int. L. 2016, accepted
- Planck Collaboration XLVIII. 2016, in preparation
- Planck Collaboration XLIX. 2016, in preparation
- Plaszczynski, S., Montier, L., Levrier, F., & Tristram, M. 2014, *MNRAS*, 439, 4048
- Poidevin, F., Falceta-Gonçalves, D., Kowal, G., de Gouveia Dal Pino, E., & Mário Magalhães, A. 2013, *ApJ*, 777, 112
- Ponthieu, N., Macías-Pérez, J. F., Tristram, M., et al. 2005, *A&A*, 444, 327
- Pudritz, R. E., Ouyed, R., Fendt, C., & Brandenburg, A. 2007, *Protostars and Planets V*, 277
- Rees, M. J. 2005, in *Lecture Notes in Physics*, Berlin Springer Verlag, Vol. 664, *Cosmic Magnetic Fields*, ed. R. Wielebinski & R. Beck, 1
- Rosset, C., Tristram, M., Ponthieu, N., et al. 2010, *A&A*, 520, A13
- Scoville, N. Z. & Solomon, P. M. 1975, *ApJL*, 199, L105
- Seljak, U. & Zaldarriaga, M. 1997, *Physical Review Letters*, 78, 2054
- Serkowski, K. 1958, *Acta Astronomica*, 8, 135
- She, Z.-S. & Leveque, E. 1994, *Physical Review Letters*, 72, 336
- Smoot, G. F., Bennett, C. L., Kogut, A., et al. 1992, *ApJL*, 396, L1
- Soler, J. D., Alves, F. O., Boulanger, F., et al. 2016, *A&A*, submitted
- Soler, J. D., Hennebelle, P., Martin, P. G., et al. 2013, *ApJ*, 774, 128
- Spitzer, L. 1978, *Physical processes in the interstellar medium*
- Sridhar, S. & Goldreich, P. 1994, *ApJ*, 432, 612
- Strong, A. W., Moskalenko, I. V., & Ptuskin, V. S. 2007, *Annual Review of Nuclear and Particle Science*, 57, 285
- Stutzki, J., Bensch, F., Heithausen, A., Ossenkopf, V., & Zielinsky, M. 1998, *A&A*, 336, 697
- Swings, P. & Rosenfeld, L. 1937, *ApJ*, 86, 483
- Vaillancourt, J. E. & Matthews, B. C. 2012, *ApJS*, 201, 13

Valdivia, V., Hennebelle, P., Gérin, M., & Lesaffre, P. 2016, *A&A*, 587, A76

Vansyngel, F., Boulanger, F., Ghosh, T., et al. 2016, *A&A*, in prep.

Vaupré, S., Hily-Blant, P., Ceccarelli, C., et al. 2014, *A&A*, 568, A50

von Hoerner, S. 1951, *Zeit. Ast.*, 30, 17

von Weizsäcker, C. F. 1951, *ApJ*, 114, 165

Ward-Thompson, D., Sen, A. K., Kirk, J. M., & Nutter, D. 2009, *MNRAS*, 398, 394

Weingartner, J. C. & Draine, B. T. 2001, *ApJ*, 548, 296

Wolfire, M. G., Hollenbach, D., McKee, C. F., Tielens, A. G. G. M., & Bakes, E. L. O. 1995, *ApJ*, 443, 152

Zaldarriaga, M. 2001, *Phys. Rev. D*, 64, 103001

Annexes au dossier de synthèse

Polarization measurement analysis

I. Impact of the full covariance matrix on polarization fraction and angle measurements[★]

L. Montier^{1,2}, S. Plaszczynski³, F. Levrier⁴, M. Tristram³, D. Alina^{1,2}, I. Ristorcelli^{1,2}, and J.-P. Bernard^{1,2}

¹ Université de Toulouse, UPS-OMP, IRAP, 31028 Toulouse Cedex 4, France

e-mail: ludovic.montier@irap.omp.eu

² CNRS, IRAP, 9 Av. Colonel Roche, BP 44346, 31028 Toulouse Cedex 4, France

³ Laboratoire de l'Accélérateur Linéaire, Université Paris-Sud 11, CNRS/IN2P3, Orsay, France

⁴ LERMA/LRA – ENS Paris et Observatoire de Paris, 24 rue Lhormond, 75231 Paris Cedex 05, France

Received 12 July 2013 / Accepted 18 November 2014

ABSTRACT

With the forthcoming release of high precision polarization measurements, such as from the *Planck* satellite, the metrology of polarization needs to be improved. In particular, it is important to have full knowledge of the noise properties when estimating polarization fraction and polarization angle, which suffer from well-known biases. While strong simplifying assumptions have usually been made in polarization analysis, we present a method for including the full covariance matrix of the Stokes parameters in estimates of the distributions of the polarization fraction and angle. We thereby quantified the impact of the noise properties on the biases in the observational quantities and derived analytical expressions for the probability density functions of these quantities that take the full complexity of the covariance matrix into account, including the Stokes I intensity components. We performed Monte Carlo simulations to explore the impact of the noise properties on the statistical variance and bias of the polarization fraction and angle. We show that for low variations (<10%) of the effective ellipticity between the Q and U components around the symmetrical case the covariance matrix may be simplified as is usually done, with a negligible impact on the bias. For S/Ns with intensity lower than 10, the uncertainty on the total intensity is shown to drastically increase the uncertainty of the polarization fraction but not the relative bias of the polarization fraction, while a 10% correlation between the intensity and the polarized components does not significantly affect the bias of the polarization fraction. We compare estimates of the uncertainties that affect polarization measurements, addressing limitations of the estimates of the S/N, and we show how to build conservative confidence intervals for polarization fraction and angle simultaneously. This study, which is the first in a set of papers dedicated to analysing polarization measurements, focuses on the basic polarization fraction and angle measurements. It covers the noise regime where the complexity of the covariance matrix may be largely neglected in order to perform further analysis. A companion paper focuses on the best estimators of the polarization fraction and angle and on their associated uncertainties.

Key words. polarization – methods: statistical – methods: data analysis – techniques: polarimetric

1. Introduction

Linear polarization measurements are usually decomposed into their Stokes components (I , Q , and U), from which one can derive polarization fraction (p) and angle (ψ). However, these are known to be potentially biased quantities, as first discussed by Serkowski (1958). At its most fundamental level, this arises because p is constrained to be positive, while ψ is a non-linear function of the ratio of Q and U , so that even if Q and U are Gaussian distributed, p and ψ will not be so simple.

While it is advisable to work with the Stokes parameters as much as possible to avoid such problems, it is sometimes more convenient to use the coordinates p and ψ when connecting polarization data to physical models and interpretations. For instance, we may be interested in the maximum fraction of polarization p observed in our Galaxy or the correlation between the polarization fraction and the structure of the magnetic field, which is not easy to carry out over large regions of the sky when

using the Stokes parameters. Thus, many authors, such as Wardle & Kronberg (1974), Simmons & Stewart (1985), and more recently, Vaillancourt (2006) and Quinn (2012), have suggested ways of dealing with polarization fraction estimates by trying to correct for the biases. Vinokur (1965) was the first to focus on the polarization angle, with later papers by Clarke et al. (1993) and Naghizadeh-Khouei & Clarke (1993). In all such studies there have been strong assumptions about the noise properties of the polarization measurements. The noise on the Q and U components are usually considered to be fully symmetric and to have no correlation between them, and furthermore the intensity is always assumed to be perfectly known. These assumptions, which we call the “canonical simplifications”, can be useful in practice, in that they allow for rapid progress, but on the other hand, they are often simply not the correct assumptions to make.

Our work is motivated by the need to understand polarization emission data at microwave to submillimetre wavelengths, although the analysis is general enough to be applied to any kind of polarization data. Nevertheless, the details of experimental setup design cannot be ignored, since they affect how

[★] Appendices are available in electronic form at <http://www.aanda.org>

correlated the data are. Because computation of the Stokes parameters and their associated uncertainties strongly depends on the instrumental design, technical efforts have been made to limit the impact of the instrumental systematics. For example, single-dish instruments, such as STOKES (Platt et al. 1991), Hertz (Schleunig et al. 1997), SPARO (Renbarger et al. 2004) or SCU-Pol (Greaves et al. 2003), had to face strong systematics due to noise correlation between orthogonal components and atmospheric turbulence, while the SHARP optics (Li et al. 2008) allowed the SHARC-II facility (Dowell et al. 1998) at the Caltech Submillimeter Observatory to be converted into a dual-dish experiment to avoid these noise correlation problems. Nevertheless, polarization measurements obtained until now were limited by systematics and statistical uncertainties. While a full treatment of the polarization covariance matrix has been performed by the WMAP analyses (Page et al. 2007; Jarosik et al. 2011), even in some of the most recent studies, no correction for the bias of the polarization fraction was applied (e.g., Dotson et al. 2010), or only high signal-to-noise ratio (S/N) data were used for analysis ($p/\sigma > 3$) in order to avoid the problem (e.g., Vaillancourt & Matthews 2012). One naturally wonders whether this common choice of S/N greater than 3 is relevant for all experiments and how the noise correlation between orthogonal Stokes components or noise asymmetry between the Stokes parameters could affect this choice.

A major motivation for studying polarized emission in microwaves is extraction of the weak polarization of the cosmic microwave background. It has been demonstrated by the balloon-borne Archeops (Benoît et al. 2004) experiment and via polarization observations by the WMAP satellite (Page et al. 2007) that the polarized cosmological signal is dominated by Galactic foregrounds at large scales and intermediate latitude (with a polarization fraction of 3–10%). Thus the characterization of polarized Galactic dust emission in the submillimetre range has become one of the challenges for the coming decade. The goal is to study the role of magnetic fields for the dynamics of the interstellar medium and star formation, as well as to characterize the foregrounds for the cosmological polarization signal. The limitations of instrumental specifications and data analysis are therefore being continually challenged. Fully mapping the polarization fraction and angle on large scales is going to be a major outcome of these studies for Galactic science in the near future. This makes it increasingly important to address the issues of whether polarization measures are biased.

With new experiments such as the *Planck*¹ satellite (Tauber et al. 2010) and the balloon-borne experiments BLAST-Pol (Fissel et al. 2010) and PILOT (Bernard et al. 2007), or with ground-based facilities with a polarization capability, such as ALMA (Pérez-Sánchez & Vlemmings 2013), SMA (Girart et al. 2006), NOEMA (at Plateau de Bure, Boissier et al. 2009), and XPOL (at the IRAM 30 m telescope, Thum et al. 2008), we are entering a new era in Galactic polarization studies, when much better control of the systematics is being achieved. Comprehensive characterization of the instrumental noise means that it becomes crucial to fully account for knowledge of the noise properties between orthogonal components when analysing these polarization measurements. Because the

Planck data exhibit large-scale variations over the whole sky in terms of S/N and covariance matrix, the impact of the full complexity of the noise will have to be corrected in order to obtain a uniform survey of the polarization fraction and angle – something that is essential to large-scale modelling of our Galaxy.

This paper is the first part in an ensemble of papers dedicated to analysis of polarization measurements and to the methods for handling complex polarized data with a high level of heterogeneity in terms of S/N or covariance matrix configurations. We aim here to present the formalism for discussing polarization fraction and angle, while taking the full covariance matrix into account. We quantify how much the naïve measurements of polarization fraction and angle are affected by the noise covariance and the extent to which the non-diagonal terms of the covariance matrix may be neglected. Another study, focused on the best estimators of the true polarization parameters, will be presented in the second part of this set. Throughout, we will make use of two basic assumptions: (i) the circular polarization (i.e., Stokes V) can be neglected; and (ii) the noise on the other Stokes parameters can be assumed to be Gaussian.

The paper is organized as follows. We first derive in Sect. 2 the full expressions for the probability density functions of polarization fraction and angle measurements, using the full covariance matrix. In Sect. 3 we explore the impact of the complexity of the covariance matrix on polarization measurement estimates and provide conservative domains of the covariance matrix where the canonical simplification remains valid. We finally address the question of the S/N estimate in Sect. 4, where we compare four estimators for the polarization measurement uncertainty.

2. (p, ψ) probability density functions

2.1. Notation

The goal of this paper is to characterize the distribution of naïve polarization measurements, given the true polarization parameters and their associated noise estimates. We denote the true values by (I_0, Q_0, U_0) , representing the true total intensity and Stokes linear polarization parameters, and with $P_0 = \sqrt{Q_0^2 + U_0^2}$. The quantities (I, Q, U) are the same for the measured values. The polarization fraction and polarization angle are defined by

$$p_0 \equiv \frac{\sqrt{Q_0^2 + U_0^2}}{I_0}, \quad \psi_0 \equiv \frac{1}{2} \text{atan} \left(\frac{U_0}{Q_0} \right) \quad (1)$$

for the true values and

$$p \equiv \frac{\sqrt{Q^2 + U^2}}{I}, \quad \psi \equiv \frac{1}{2} \text{atan} \left(\frac{U}{Q} \right) \quad (2)$$

for the measurements. The true Stokes parameters can be expressed by $Q_0 \equiv p_0 I_0 \cos(2\psi_0)$ and $U_0 \equiv p_0 I_0 \sin(2\psi_0)$, while for the measurements $Q \equiv p I \cos(2\psi)$ and $U \equiv p I \sin(2\psi)$. Although the true intensity I_0 is strictly positive, the measured intensity I may be negative due to noise, thus I_0 can take values between 0 and $+\infty$, while I ranges between $-\infty$ and $+\infty$. The measured Stokes parameters Q and U are real, finite quantities, ranging from $-\infty$ to $+\infty$, that with the addition of noise do not necessarily satisfy the relation $Q^2 + U^2 \leq I^2$ obeyed by the underlying quantities, i.e., $Q_0^2 + U_0^2 \leq I_0^2$. The true polarization fraction p_0 can take values in the range 0 to 1, while the measured polarization fraction p ranges between $-\infty$ and $+\infty$. Finally we define ψ_0 and ψ such that they are both defined in the range $[-\pi/2, +\pi/2]$.

¹ *Planck* (<http://www.cosmos.esa.int/web/planck>) is a project of the European Space Agency (ESA) with instruments provided by two scientific consortia funded by ESA member states (in particular the lead countries France and Italy), with contributions from NASA (USA) and with telescope reflectors provided by a collaboration between ESA and a scientific consortium led and funded by Denmark.

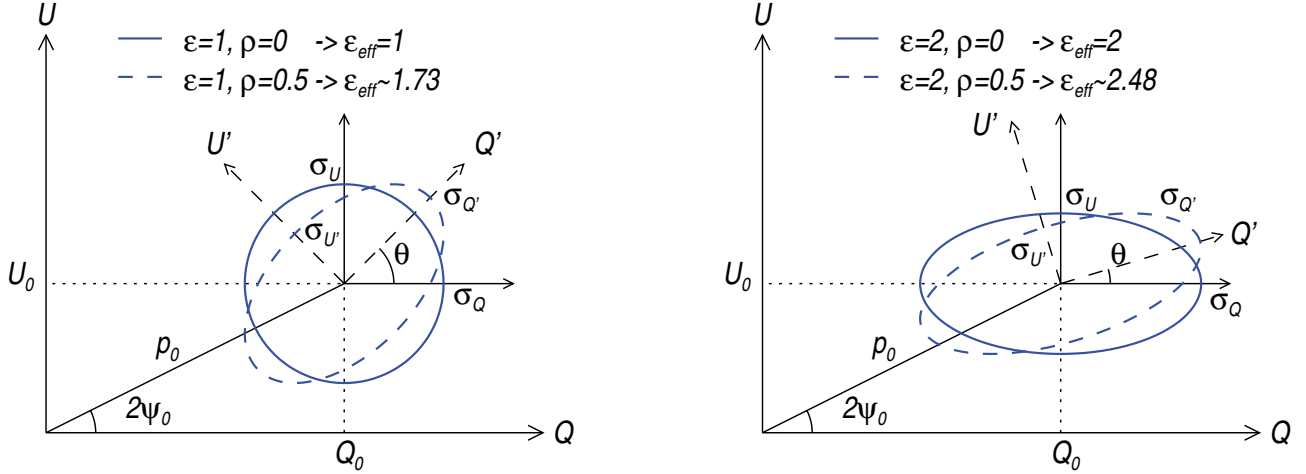


Fig. 1. Illustrations of the noise distribution in the (Q, U) plane. The solid and dashed blue lines represent the 1σ probability contours around the true polarization values (Q_0, U_0) , also parameterized by (p_0, ψ_0) . *Left:* the canonical case ($\varepsilon = 1, \rho = 0$) is shown as a solid line. The dashed line shows the introduction of a correlation $\rho = 0.5$, leading to an effective ellipticity ($\varepsilon_{\text{eff}} > 1$) rotated by an angle θ . *Right:* same transformation, starting from the elliptical case ($\varepsilon = 2, \rho = 0$).

Previous studies of polarization measurements usually made strong assumptions concerning the noise properties, in particular: (i) correlations between the total and polarized intensities were neglected; (ii) correlated noise between Q and U was also neglected; and (iii) equal noise was assumed on Q and U measurements. We propose instead to use the full covariance matrix defined by

$$\Sigma \equiv \begin{pmatrix} \sigma_{II} & \sigma_{IQ} & \sigma_{IU} \\ \sigma_{IQ} & \sigma_{QQ} & \sigma_{QU} \\ \sigma_{IU} & \sigma_{QU} & \sigma_{UU} \end{pmatrix} = \begin{pmatrix} \sigma_I^2 & \rho_Q \sigma_I \sigma_Q & \rho_U \sigma_I \sigma_U \\ \rho_Q \sigma_I \sigma_Q & \sigma_Q^2 & \rho \sigma_Q \sigma_U \\ \rho_U \sigma_I \sigma_U & \rho \sigma_Q \sigma_U & \sigma_U^2 \end{pmatrix}, \quad (3)$$

where σ_{XY} is the covariance of the two random variables X and Y , and the following quantities are usually introduced in the literature to simplify the notation:

$$\varepsilon \equiv \frac{\sigma_Q}{\sigma_U}; \quad \rho \equiv \frac{\sigma_{QU}}{\sigma_Q \sigma_U}; \quad \rho_Q \equiv \frac{\sigma_{IQ}}{\sigma_I \sigma_Q}; \quad \rho_U \equiv \frac{\sigma_{IU}}{\sigma_I \sigma_U}. \quad (4)$$

Here ε is the ellipticity between the Q and U noise components, and ρ (which lies between -1 and $+1$) is the correlation between the Q and U noise components. Similarly, ρ_Q and ρ_U are the correlations between the noise in intensity I and the Q and U components, respectively.

The parameterization just described could be misleading, however, since the ellipticity ε does not represent the effective ellipticity in the (Q, U) plane if the correlation is not zero. This is illustrated in Fig. 1 for two initial values of the ellipticity ε . A new reference frame (Q', U') where the Stokes parameters are now uncorrelated can always be obtained through rotation by an angle

$$\theta = \frac{1}{2} \text{atan} \left(\frac{2\sigma_{QU}}{\sigma_Q^2 - \sigma_U^2} \right). \quad (5)$$

We can calculate the covariance matrix in the rotated frame by taking the usual $\mathbf{R} \Sigma \mathbf{R}^T$. In this new reference frame, the errors on Q' and U' are uncorrelated and defined as

$$\begin{aligned} \sigma_{Q'}^2 &= \sigma_Q^2 \cos^2 \theta + \sigma_U^2 \sin^2 \theta + \sigma_{QU} \sin 2\theta, \\ \sigma_{U'}^2 &= \sigma_Q^2 \sin^2 \theta + \sigma_U^2 \cos^2 \theta - \sigma_{QU} \sin 2\theta, \end{aligned} \quad (6)$$

so that the effective ellipticity ε_{eff} is now given by

$$\varepsilon_{\text{eff}}^2 = \frac{\sigma_{Q'}^2 + \sigma_{U'}^2 + \sigma'^2}{\sigma_{Q'}^2 + \sigma_{U'}^2 - \sigma'^2}, \quad (7)$$

where

$$\sigma'^2 = \sqrt{(\sigma_Q^2 - \sigma_U^2)^2 + 4\sigma_{QU}^2}. \quad (8)$$

When expressed as a function of the (ε, ρ) parameters, we obtain

$$\varepsilon_{\text{eff}}^2 = \frac{1 + \varepsilon^2 + \sqrt{(\varepsilon^2 - 1)^2 + 4\rho^2 \varepsilon^2}}{1 + \varepsilon^2 - \sqrt{(\varepsilon^2 - 1)^2 + 4\rho^2 \varepsilon^2}} \quad (9)$$

and

$$\theta = \frac{1}{2} \text{atan} \left(\frac{2\rho\varepsilon}{\varepsilon^2 - 1} \right). \quad (10)$$

This parameterization of the covariance matrix Σ in terms of ε_{eff} and θ is preferred in our work for two reasons. Firstly, the shape of the noise distribution in the (Q, U) space is now contained in a single parameter, the effective ellipticity ε_{eff} (≥ 1), instead of two parameters, ε and ρ . Secondly, the noise distribution is now independent of the reference frame. This is also related to the fact that the properties of the noise distribution do not depend on three (I_0, p_0, ψ_0) plus six (from Σ) parameters, but only on eight, since it actually only depends on the difference in the angles $2\psi_0 - \theta$, which simplifies the analysis quite a lot. For what follows we also define $\det(\Sigma) = \sigma^6$ as the determinant of the covariance matrix.

2.2. 3D probability density functions

The probability density function (PDF) gives the probability of obtaining a set of values (I, Q, U) , given the true Stokes parameters (I_0, Q_0, U_0) and the covariance matrix Σ . As a short cut, we refer to this as the ‘‘3D PDF’’. When Gaussian noise is assumed for each Stokes component, this distribution in the space (I, Q, U) is given by

$$F(X|X_0, \Sigma) = \sqrt{\frac{\det(\Sigma^{-1})}{(2\pi)^3}} \exp \left(-\frac{(X - X_0)^T \Sigma^{-1} (X - X_0)}{2} \right), \quad (11)$$

where X and X_0 are the vectors of the Stokes parameters $[I, Q, U]$ and $[I_0, Q_0, U_0]$, Σ^{-1} is the inverse of the covariance matrix (also called the ‘‘precision matrix’’), and $\det(\Sigma^{-1}) = \sigma^{-6}$ is the determinant of Σ^{-1} . This definition ensures that the probability density function is normalized to 1. The iso-probability surfaces in the (I, Q, U) space are ellipsoids.

Using normalized polar coordinates, the probability density function $f(I, p, \psi | I_0, p_0, \psi_0, \Sigma)$ can be computed explicitly. However, the expression (see Eq. (A.1)) is a little cumbersome, so we have put it in Appendix A. We point out the presence of a factor $2|p|^2$ in front of the exponential, coming from the Jacobian of the transformation.

2.3. 2D marginal (p, ψ) distribution

We compute the 2D probability density function $f_{2D}(p, \psi)$ by marginalizing the probability density function $f(I, p, \psi)$ (see Eq. (A.1)) over intensity I on the range $-\infty$ to $+\infty$. The computation is quite straightforward (see Appendix B), leading to an expression that depends on the sign of p , given in Eqs. (A.2) and (A.3).

In many cases, two further assumptions can be made: (i) the correlations between I and (Q, U) is negligible, i.e., $\rho_Q = \rho_U = 0$; and (ii) the S/N of the intensity I_0/σ_I is so high that I can be considered to be perfectly known, yielding $I = I_0$, as discussed in Quinn (2012). Making such assumptions allows us to reduce the covariance matrix Σ to a 2×2 matrix, Σ_p , which we define as

$$\Sigma_p = \frac{1}{I_0^2} \begin{pmatrix} \sigma_{QQ} & \sigma_{QU} \\ \sigma_{QU} & \sigma_{UU} \end{pmatrix} = \frac{\sigma_{p,G}^2}{\sqrt{1-\rho^2}} \begin{pmatrix} \varepsilon & \rho \\ \rho & 1/\varepsilon \end{pmatrix}, \quad (12)$$

where $\sigma_{p,G}$ is defined by $\det(\Sigma_p) = \sigma_{p,G}^4$, leading to

$$\sigma_{p,G}^2 = \frac{\sigma_Q^2}{I_0^2} \frac{\sqrt{1-\rho^2}}{\varepsilon} \quad \left(= \frac{\sigma_Q^2}{I_0^2} \frac{1}{\varepsilon_{\text{eff}}} \right). \quad (13)$$

This parameter $\sigma_{p,G}$ is linked to the normalization of the 2D distribution, because it represents the radius of the equivalent spherical Gaussian distribution that has the same integrated area as the elliptical Gaussian distribution. The probability density function f_{2D} can then be simplified, as given in Eq. (A.4). The matching between the two expressions for f_{2D} , Eqs. (A.2)–(A.4), when $I_0/\sigma_I \rightarrow \infty$, is ensured simply by the consistency of the determinants of Σ and Σ_p , when $\rho_Q = \rho_U = 0$:

$$\sigma^6 = \sigma_I^2 \sigma_Q^2 \sigma_U^2 = \sigma_I^4 I_0^4 \sigma_{p,G}^4. \quad (14)$$

We also recall that in the canonical case ($\varepsilon_{\text{eff}} = 1$), the probability density function can be simplified to

$$f_{2D} = \frac{p}{\pi \sigma_p^2} \exp \left\{ -\frac{1}{2\sigma_p^2} \left[p^2 + p_0^2 - 2pp_0 \cos 2(\psi - \psi_0) \right] \right\}, \quad (15)$$

where $\sigma_{p,G}$ also simplifies to $\sigma_p = \sigma_Q/I_0 = \sigma_U/I_0$. We provide illustrations of the 2D PDFs in Appendix C.

2.4. 1D marginal p and ψ distributions

The marginal probability density functions of p and ψ can be obtained by integrating the 2D PDF given by Eq. (A.4) over ψ (between $-\pi/2$ and $+\pi/2$) and p (between 0 and $+\infty$), respectively, when assuming the S/N on the intensity to be infinite. These two probability density functions theoretically depend on

p_0 , ψ_0 , and Σ_p . While the expressions obtained in the general case (Aalo et al. 2007) are provided in Appendix D, the expression for the marginal p distribution reduces to the Rice law (Rice 1945) when $\varepsilon = 1$ and $\rho = 0$:

$$R(p | p_0, \sigma_p) = \frac{p}{\sigma_p^2} \exp \left(-\frac{(p^2 + p_0^2)}{2\sigma_p^2} \right) \mathcal{I}_0 \left(\frac{pp_0}{\sigma_p^2} \right), \quad (16)$$

where $\mathcal{I}_0(x)$ is the zeroth-order modified Bessel function of the first kind (Abramowitz & Stegun 1964). This expression no longer has a dependence on ψ_0 . With the same assumptions, the marginal ψ distribution (extensively studied in Naghizadeh-Khouei & Clarke 1993) is given by

$$G(\psi | p_0, \psi_0, \sigma_p) = \frac{1}{\sqrt{\pi}} \left\{ \frac{1}{\sqrt{\pi}} + \eta_0 e^{\eta_0^2} [1 + \text{erf}(\eta_0)] \right\} e^{-p_0^2 t_0^2 / 2\sigma_p^2}, \quad (17)$$

where $\eta_0 = (p_0 I_0 / \sqrt{2}\sigma_p) \cos 2(\psi - \psi_0)$. This distribution depends on p_0 and is symmetric about ψ_0 .

3. Impact of the covariance matrix on the bias

We now quantify how the effective ellipticity of the covariance matrix affects the bias of the polarization measurements, compared to the canonical case. We would like to determine under what conditions the covariance matrix may be simplified to its canonical expression, in order to minimize computations. The impact of the correlation and the ellipticity of the covariance matrix are first explored in the 2D (p, ψ) plane with infinite intensity S/N. The cases are then investigated of finite S/N on intensity and of the correlation between total and polarized intensity.

3.1. Methodology

Given a collection of measurements of the same underlying polarization parameters (p_0, ψ_0) , we build the statistical bias on p and ψ by averaging the discrepancies $\Delta p = \bar{p} - p_0$ and $\Delta \psi = \bar{\psi} - \psi_0$ (always defining the quantity $\psi - \psi_0$ between $-\pi/2$ and $+\pi/2$). With knowledge of the probability density function $f_{2D}(p, \psi | p_0, \psi_0, \Sigma_p)$, we can obtain the statistical bias directly by computing the mean estimates

$$\Delta p(p_0, \psi_0, \Sigma_p) = \bar{p} - p_0, \quad (18)$$

and

$$\Delta \psi(p_0, \psi_0, \Sigma_p) = \bar{\psi} - \psi_0. \quad (19)$$

Here \bar{p} and $\bar{\psi}$ are the mean estimates from the probability density function, defined as the first moments of f_{2D} :

$$\bar{p} = \int_0^{+\infty} \int_{\psi_0 - \pi/2}^{\psi_0 + \pi/2} p f_{2D}(p, \psi | p_0, \psi_0, \Sigma_p) dp d\psi, \quad (20)$$

and

$$\bar{\psi} = \int_0^{+\infty} \int_{\psi_0 - \pi/2}^{\psi_0 + \pi/2} \psi f_{2D}(p, \psi | p_0, \psi_0, \Sigma_p) dp d\psi. \quad (21)$$

To quantify the importance of this bias, we can compare it to the dispersion of the polarization fraction and angle measurements, $\sigma_{p,0}$ and $\sigma_{\psi,0}$. These are defined as the second moments of the probability density function f_{2D} :

$$\sigma_{p,0}^2 = \int_0^{+\infty} \int_{-\pi/2}^{+\pi/2} (p - \bar{p})^2 f_{2D}(p, \psi | p_0, \psi_0, \Sigma_p) dp d\psi; \quad (22)$$

and

$$\sigma_{\psi,0}^2 = \int_0^{+\infty} \int_{-\pi/2}^{\pi/2} (\psi - \bar{\psi})^2 f_{2D}(p, \psi | p_0, \psi_0, \Sigma_p) dp d\psi. \quad (23)$$

Here subscript 0 signifies that this dispersion has been computed using full knowledge of the true polarization parameters and the associated probability density function.

We chose $\sigma_{p,G}$ introduced in Sect. 2.3 as our characteristic estimate of the polarization fraction noise in its relationship to the covariance matrix Σ_p . This is used to define the S/N of the polarization fraction $p_0/\sigma_{p,G}$, which is kept constant when exploring the ellipticity and correlation of the $Q - U$ components. In Sect. 4 we discuss how robust this estimate is against the true dispersion $\sigma_{p,0}$.

We define three specific setups of the covariance matrix to investigate: (i) the *canonical* case, $\varepsilon_{\text{eff}} = 1$, equivalent to $\varepsilon = 1$, $\rho = 0$; the *low* regime, $1 \leq \varepsilon_{\text{eff}} < 1.1$; and the *extreme* regime, $1 \leq \varepsilon_{\text{eff}} < 2$. These are used in the rest of this paper to quantify departures of the covariance matrix from the canonical case and to characterize the impact of the covariance matrix on polarization measurements in each regime. It is worth recalling that to each value of the effective ellipticity ε_{eff} there corresponds a set of equivalent parameters ε , ρ , and θ . The average level of the effective ellipticity ε_{eff} in the *Planck* data over the full sky on a one-degree scale has been estimated around 1.12 (Planck Collaboration Int. XIX 2014), which lies at the limit of the *low* regime. This does not prevent observing higher effective ellipticities in specific regions of the sky, which could fall in the *extreme* regime.

3.2. $Q-U$ ellipticity

We assume here that the intensity is perfectly known and that there is no correlation between the total intensity I and the polarized intensity, so that $I = I_0$ and $\rho_Q = \rho_U = 0$. In this case we can now refer to Eq. (A.4) for the 2D probability density function.

Unlike the canonical case, where the effective ellipticity differs from $\varepsilon_{\text{eff}} = 1$, the statistical biases on the polarization fraction and angle become dependent on the true polarization angle ψ_0 , as illustrated in Fig. 2 for the special case of $\theta = 0$ (no correlation). For extreme values of the ellipticity (e.g., $\varepsilon_{\text{eff}} = 2$), the relative bias on p oscillates between 0.9 and 1.5 times the canonical bias ($\varepsilon_{\text{eff}} = 1$). These oscillations with ψ_0 quickly vanish when the ellipticity gets closer to 1, as shown for $\varepsilon_{\text{eff}} = 1.1$ in the figure. The presence of correlations (i.e., $\rho \neq 0$) increases the effective ellipticity of the noise distribution associated with a global rotation, as detailed in Sect. 2.1. Thus correlations induce the same oscillation patterns as observed in Fig. 2 for an effective ellipticity larger than 1 and a null correlation, but amplified at the corresponding effective ellipticity ε_{eff} and shifted by an angle $\theta/2$, according to Eqs. (9) and (10), respectively.

The top panel of Fig. 3 shows the dependence of the polarization fraction bias on the effective ellipticity for three levels of S/N, $p_0/\sigma_{p,G} = 1, 2$, and 5, and including the full range of true polarization angle ψ_0 . The figure indicates the variability interval of $\Delta p/\sigma_{p,0}$ for each ellipticity, for changes in ψ_0 over the range $-\pi/2$ to $\pi/2$. We observe that the higher the S/N, the stronger the relative impact of the ellipticity compared to the canonical case. In the *low* regime the relative bias to the dispersion increases from 9% to 12% (compared to 10% in the canonical case) at a S/N of 5, while it spans from 69% and 73% (around the 71% of the canonical case) at a S/N of 1. In the *low* regime, therefore, the impact of the ellipticity on the bias of the polarization fraction represents only about 4% of the dispersion, regardless

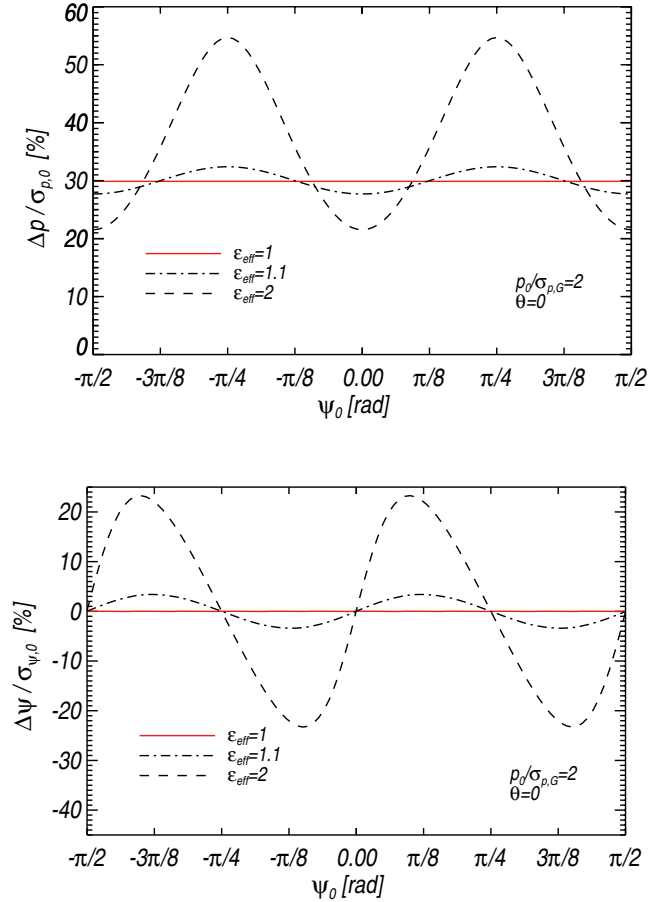


Fig. 2. Impact of the initial true polarization angle ψ_0 and of varying effective ellipticity ε_{eff} on the relative polarization fraction bias $\Delta p/\sigma_{p,0}$ (top) and the relative polarization angle bias $\Delta\psi/\sigma_{\psi,0}$ (bottom). We assume no correlation here, so that $\theta = 0$, and we set the S/N to $p_0/\sigma_{p,G} = 2$. The canonical case ($\varepsilon_{\text{eff}} = 1$) is shown by the red line.

of the S/N, which can therefore be neglected. However, in the *extreme* regime, the impact of the ellipticity can go up to 33% at intermediate S/N (~ 2), which can no longer be neglected.

Concerning the impact on polarization angle – while no bias occurs in the canonical case, some oscillations in the bias $\Delta\psi$ with ψ_0 appear as soon as $\varepsilon_{\text{eff}} > 1$. The amplitude can reach up to 24% of the dispersion in the *extreme* regime and up to 4% in the *low* regime, as illustrated in the bottom panel of Fig. 2. Again, these oscillations are shifted and amplified in the presence of correlations between the Stokes parameters, compared to the case with no correlation. As an overall indicator, in the bottom panel of Fig. 3 we provide the maximum bias $\text{Max}|\Delta\psi|$ normalized by the dispersion $\sigma_{\psi,0}$ over the full range of ψ_0 as a function of the ellipticity. This quantity barely exceeds 24% (i.e., $\sim 9^\circ$) in the worst case, i.e., for $\varepsilon_{\text{eff}} = 2$ and low S/N, and it falls to below 4% (i.e., $\sim 1.5^\circ$) in the *low* regime. Thus the bias on ψ always remains well below the level of the true uncertainty on the polarization angle at the same S/N (see Sect. 4), so that the bias of the polarization angle induced by an ellipticity $\varepsilon_{\text{eff}} > 1$ can be neglected to first order for the *low* regime of the ellipticity, i.e., when there is less than a 10% departure from the canonical case.

3.3. I uncertainty

The uncertainty in the total intensity I has two sources: the measurement uncertainty expressed in the covariance matrix, and an

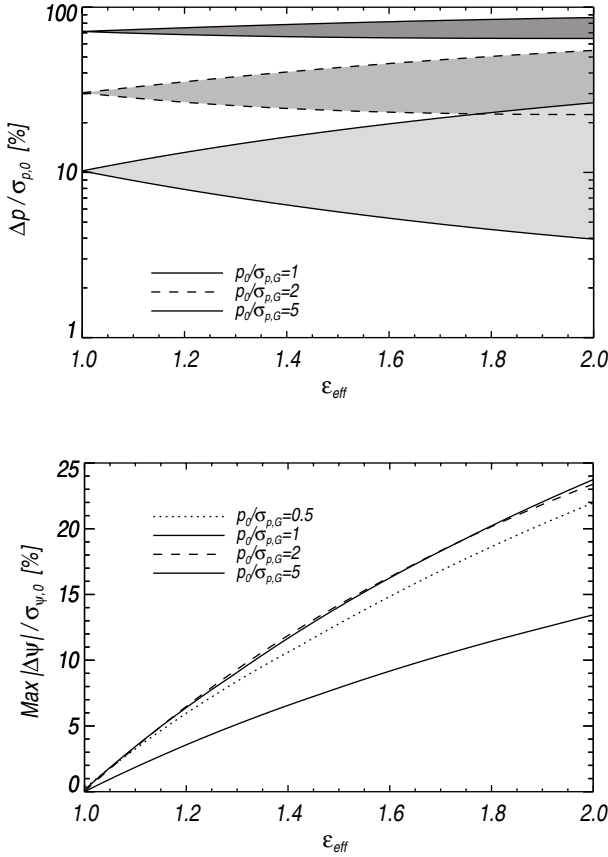


Fig. 3. Impact of the effective ellipticity ϵ_{eff} on the levels of bias. *Top:* $\Delta p / \sigma_{p,0}$ as a function of the effective ellipticity ϵ_{eff} , displayed for three levels of the S/N, $p_0/\sigma_{p,G} = 1, 2$, and 5. The grey shaded regions indicate the whole extent of variability due to ψ_0 and θ spanning the range $-\pi/2$ to $\pi/2$. *Bottom:* maximum $|\Delta\psi|/\sigma_{\psi,0}$ value for ψ_0 and θ spanning the range $-\pi/2$ to $\pi/2$, plotted as a function of the effective ellipticity ϵ_{eff} , displayed for four levels of the S/N, $p_0/\sigma_{p,G} = 0.5, 1, 2$, and 5.

astrophysical component of the uncertainty due to the imperfect characterization of the unpolarized contribution to the total intensity. This second source can be seen, for instance, with the cosmic infrared background in *Planck* data: its unpolarized emission can be viewed as a systematic uncertainty on the total intensity (dominated by the Galactic dust thermal emission), when one is interested in the polarization fraction of the Galactic dust. To retrieve the actual polarization fraction, it is necessary to compute it through

$$p = \frac{\sqrt{Q^2 + U^2}}{(I - \Delta I)}, \quad (24)$$

where ΔI is the unpolarized emission, which is imperfectly known. The uncertainty $\sigma_{\Delta I}$ on this quantity can be viewed as an additional uncertainty σ_I on the total intensity, and therefore the S/N has to be written $I_0/\sigma_I = (I - \Delta I)/\sigma_{\Delta I}$.

To consider the effects on polarization quantities, we first recall that, because of its definition, the measurement of polarization angle ψ is not affected by the uncertainty on intensity (when no correlation exists between I and Q and U), contrary to the polarization fraction p , which is defined as the ratio of the polarized intensity to the total intensity. Thus the uncertainty of the total intensity does not induce any bias on ψ .

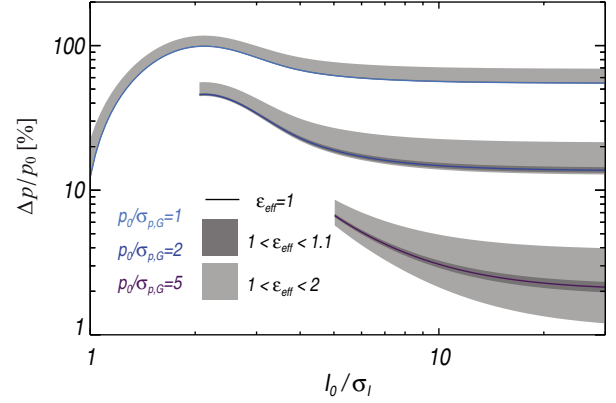


Fig. 4. Polarization fraction bias, normalized to the true value p_0 , as a function of the S/N I_0/σ_I , plotted for three values of the polarization S/N, $p_0/\sigma_{p,G}$, and values of the effective ellipticity ϵ_{eff} covering the *canonical* (full line), *low* (dark grey shaded region), and *extreme* (light grey shaded region) regimes of the covariance matrix. The intensity correlation coefficients are set to $\rho_Q = \rho_U = 0$. We only consider the domain where $(I_0/\sigma_I) > (p_0/\sigma_{p,G})$.

To quantify the influence of a finite S/N I_0/σ_I on the bias of p , we compute the mean polarization fraction over the PDF:

$$\bar{p} = \iiint \frac{\sqrt{Q^2 + U^2}}{I} F(I, Q, U | I_0, Q_0, U_0, \Sigma) dI dQ dU, \quad (25)$$

with F given by Eq. (11). We write it this way, because using f_{2D} given by Eqs. (A.2) and (A.3) would lead to both positive and negative logarithmic divergences for $p \rightarrow \pm\infty$ (related to samples for which $I \rightarrow 0$). These divergences can be shown to be artificial by using the Gaussian PDF of (I, Q, U) instead of f_{2D} .

The presence of noise in total intensity measurements increases the absolute bias $\Delta p = \bar{p} - p_0$, as shown in Fig. 4, where Δp , normalized by the true value p_0 , is plotted as a function of the S/N I_0/σ_I . This is shown for three levels of the polarization S/N $p_0/\sigma_{p,G} = 1, 2$, and 5, and the three regimes of the covariance matrix, assuming that $\rho_Q = \rho_U = 0$.

The bias may be enhanced by a factor of 1.5 to 4 times p_0 when the S/N on I goes from infinite (i.e., perfectly known I) to about 2. It then drops again for lower S/N, which is the result of the increasing number of negative p samples. We only consider the domain where $(I_0/\sigma_I) > (p_0/\sigma_{p,G})$.

Comparison of the bias to the dispersion $\sigma_{p,0}$, as was done in the previous section, is not straightforward when the total intensity is uncertain. This is because the integral defining $\sigma_{p,0}$ (see Eq. (22)) has positive linear divergences for $p \rightarrow \pm\infty$. Unlike the case of \bar{p} , this divergence cannot be alleviated by working in (I, Q, U) space.

To overcome this we therefore used a proxy $\tilde{\sigma}_{p,0}$, which is the dispersion of p computed on a subset of (I, Q, U) space that excludes total intensity values below ωI_0 , with $\omega = 10^{-7}$. This threshold is somewhat arbitrary, as $\tilde{\sigma}_{p,0}$ increases linearly with $1/\omega$. The value 10^{-7} is merely meant to serve as an illustration. Figure 5 shows $\Delta p / \tilde{\sigma}_{p,0}$ as a function of I_0/σ_I for the same values of the polarization S/N $p_0/\sigma_{p,G}$ and the same regimes of the covariance matrix as in Fig. 4. At high S/N for I , we asymptotically recover the values obtained in the top panel of Fig. 3. As long as $I_0/\sigma_I > 5$, the relative bias on p is barely affected by the uncertainty on the intensity, especially for low polarization S/N, $p_0/\sigma_{p,G}$. A minor trend is still seen in the range $5 < I_0/\sigma_I < 10$ for $p_0/\sigma_{p,G} = 5$. The relative bias may be enhanced by a factor

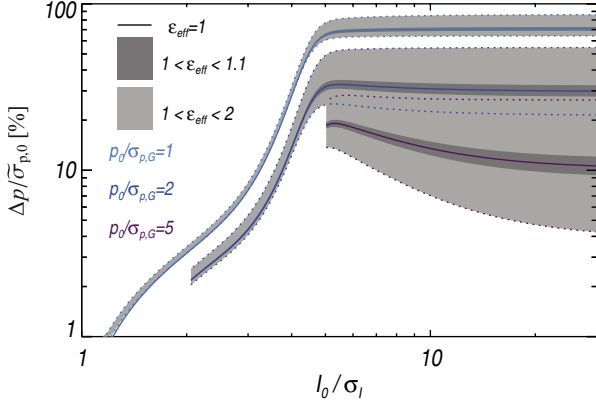


Fig. 5. Same as Fig. 4, but showing the bias on the polarization fraction relative to the dispersion proxy $\bar{\sigma}_{p,0}$. See text for a description of this quantity.

of around 2 in that case, when the S/N on intensity and polarization are ~ 5 . However, this situation is unlikely to be observed in astrophysical data, since the uncertainty on total intensity is usually much less than for polarized intensity.

Contrary to these high S/N ($I_0/\sigma_I > 5$) features, which are quite robust with respect to the choice of threshold ωI_0 , the drop in relative bias at lower intensity S/N, i.e., $I_0/\sigma_I < 5$, is essentially due to the divergence of the dispersion of p . This part of Fig. 4 should thus be taken as nothing more than an illustration of the divergence at low S/N for I . It should be stressed, however, that this increase in the dispersion of p has to be carefully considered when dealing with low S/N intensity data, which can be the case well away from the Galactic plane.

3.4. Correlation between I and $Q-U$

With non-zero noise on total intensity, it becomes possible to explore the effects of the coefficients ρ_Q and ρ_U , corresponding to correlation between the intensity I and the (Q, U) plane. We first note that introducing correlation parameters ρ_Q and ρ_U that are different from zero directly modifies the ellipticity ε and correlation ρ between Stokes Q and U . Simple considerations on the Cholesky decomposition of the covariance matrix Σ (given in Appendix E) show that for a given ellipticity ε and correlation parameter ρ , obtained when $\rho_Q = \rho_U = 0$, the ellipticity ε' and correlation ρ' become

$$\varepsilon' = \varepsilon \sqrt{\frac{1 - \rho_Q^2}{1 - \rho_U^2}} \quad \text{and} \quad \rho' = \rho_Q \rho_U + \rho \sqrt{(1 - \rho_Q^2)(1 - \rho_U^2)} \quad (26)$$

when ρ_Q and ρ_U are no longer zero. Consequently, non-zero ρ_Q and ρ_U lead to similar impacts as found for a non-canonical effective ellipticity ($\varepsilon_{\text{eff}} \neq 1$), discussed in Sect. 3.2. Moreover, to investigate the sole impact of non-zero ρ_Q and ρ_U with a finite S/N on the intensity, we have compared the case $(\varepsilon, \rho, \rho_Q, \rho_U)$ to the reference case $(\varepsilon', \rho', 0, 0)$. We find that the relative change of the polarization fraction bias Δp is at most 10–15% over the whole range of I_0/σ_I explored in this work (i.e., $I_0/\sigma_I \geq 1$).

The difference between the polarization angle bias computed for $(\varepsilon, \rho, \rho_Q, \rho_U)$ and for the reference case $(\varepsilon', \rho', 0, 0)$ is at most $\Delta\psi - \Delta\psi_{\text{ref}} \sim 4^\circ$ and essentially goes to zero above $I_0/\sigma_I \sim 2-3$. The dependence of the change in bias with (ρ_Q, ρ_U) is similar to the one for $\Delta p/\Delta p_{\text{ref}}$, except that it depends solely on ρ_U for $\psi_0 = 0$ and solely on ρ_Q for $\psi_0 = \pi/4$.

4. Polarization uncertainty estimates

If we are given the polarization measurements and the noise covariance matrix of the Stokes parameters, we would like to derive estimates of the uncertainties associated with the polarization fraction and angle. These are required to (i) define the S/N of these polarization measurements and to (ii) quantify how important the bias is compared to the accuracy of the measurements. In the most general case, the uncertainties in the polarization fraction and angle do not follow a Gaussian distribution, so that confidence intervals should be used properly to obtain an estimate of the associated errors, as described in Sect. 4.5. However, it can sometimes be assumed as a first approximation that the distributions are Gaussian, in order to derive quick estimates of the p and ψ uncertainties, defined as the variance of the 2D distribution of the polarization measurements. We explore below the extent to which this approximation can be utilized, when using the most common estimators of these two quantities.

4.1. Standard deviation estimates

To compare the robustness of the uncertainty estimates, we build 10 000 Monte Carlo simulated measurements in each of the three regimes of the covariance matrix (*canonical*, *low*, and *extreme*), by varying the S/N of p and the polarization angle ψ_0 inside the range $-\pi/2$ and $\pi/2$. We use the simulations to compute the posterior fraction of measurements for which the true value p_0 or ψ_0 falls inside the $\pm\sigma$ range around the measurement. This provides the probability \mathcal{P} shown in Figs. 6 and 7 for p and ψ , respectively.

We first focus on the true uncertainty estimates, as defined in Sect. 3.1. We observe that the $\sigma_{p,0}$ true estimates (top left of Fig. 6) fall below the Gaussian value $\text{erf}(\sqrt{2}/2)$ (i.e., 68%) once the S/N goes below 3. The $\sigma_{\psi,0}$ true estimates (left of Fig. 7) provide conservative probabilities ($\mathcal{P} > 68\%$) for $S/N > 0.5$. This is also shown in Fig. 8 as a function of the S/N, for the *canonical*, *low*, and *extreme* regimes of the covariance matrix. It is not strongly dependent on the ellipticity of the covariance matrix. It shows a maximum of $\pi/\sqrt{12} \approx 52^\circ$ at low S/N, and converges slowly to 0 at high S/N (still $\sim 10^\circ$ at $S/N = 3$). Thus we might imagine using such estimates as reasonably good approximations of the uncertainties at high S/N (> 3) for p , and over almost the entire range of S/N for ψ . However, these true p and ψ uncertainties, $\sigma_{p,0}$ and $\sigma_{\psi,0}$, respectively, depend on p_0 and ψ_0 , which remain theoretically unknown. Thus we can only provide specific estimates of those variance quantities, as explained below.

4.2. Geometric and arithmetic estimators

Two estimates of the polarization fraction uncertainty can be obtained independently of the measurements themselves, which makes them easy to compute: (i) the geometric ($\sigma_{p,G}$) estimate; and (ii) the arithmetic ($\sigma_{p,A}$) estimate. The geometric estimator has already been introduced earlier when we derived the expression for the 2D (p, ψ) PDF f_{2D} . It is defined via the determinant of the 2D covariance matrix Σ_p as $\det(\Sigma_p) = \sigma_{p,G}^4$, with its expression given in Eq. (13). We recall that the determinant of the covariance matrix Σ_p is linked to the area inside a probability contour and independent of the reference frame of the Stokes parameters. In the canonical case, this estimate gives back the usual expressions, $\sigma_{p,G} = \sigma_Q/I_0 = \sigma_U/I_0$, used to quantify the noise on the polarization fraction. It can be considered as the geometric

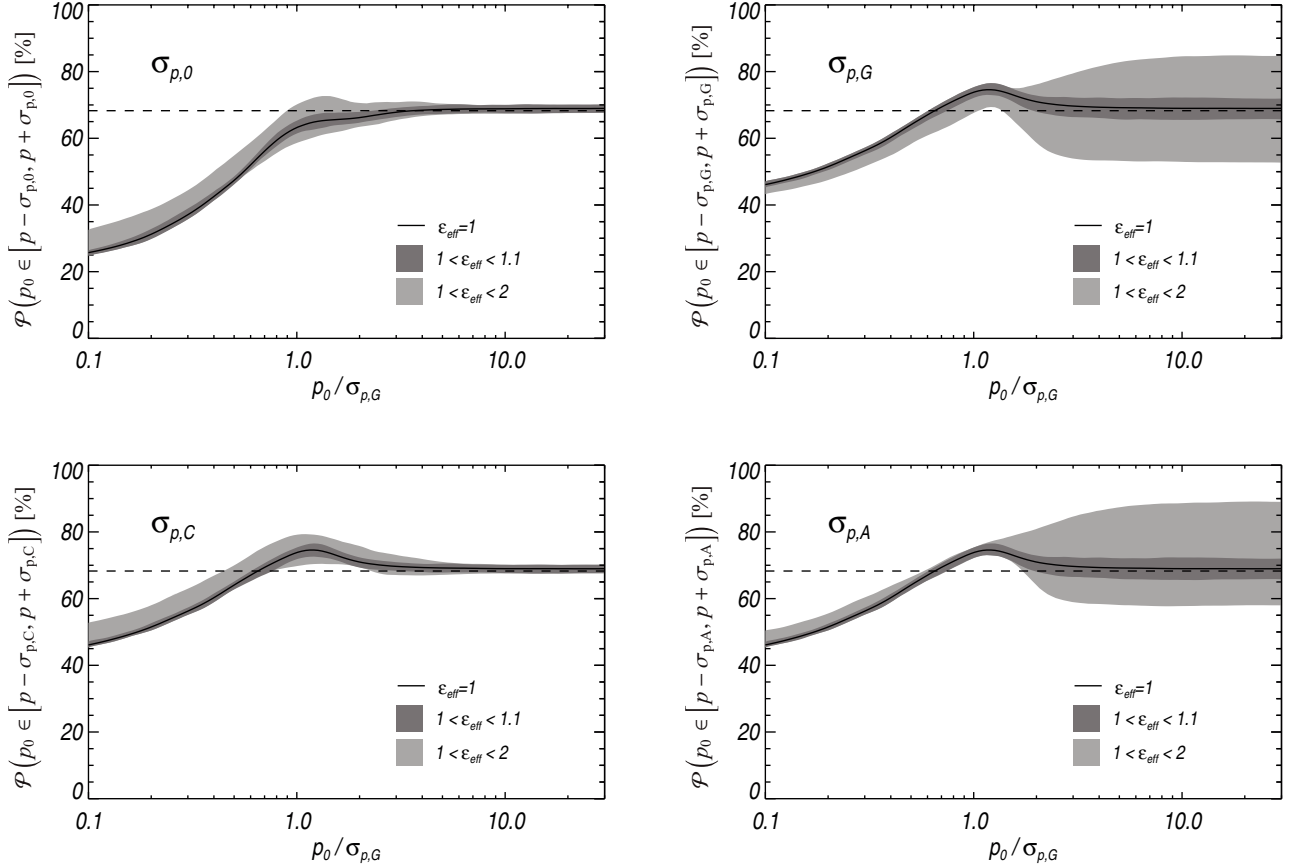


Fig. 6. Probability \mathcal{P} of finding the true polarization fraction p_0 inside the interval $[p - \sigma_p^{\text{low}}, p + \sigma_p^{\text{up}}]$, where σ_p^{low} and σ_p^{up} are the 1σ lower and upper limits, respectively. We plot this for each estimator: true $\sigma_{p,0}$ (top left); conventional $\sigma_{p,C}$ (bottom left); geometric $\sigma_{p,G}$ (top right); and arithmetic $\sigma_{p,A}$ (bottom right). These are plotted as a function of the S/N $p_0/\sigma_{p,G}$. Monte Carlo simulations have been carried out in the *canonical* (solid line), *low* (dark grey), and *extreme* (light grey) regimes of the covariance matrix. The expected 68.27% level is shown as a dashed line.

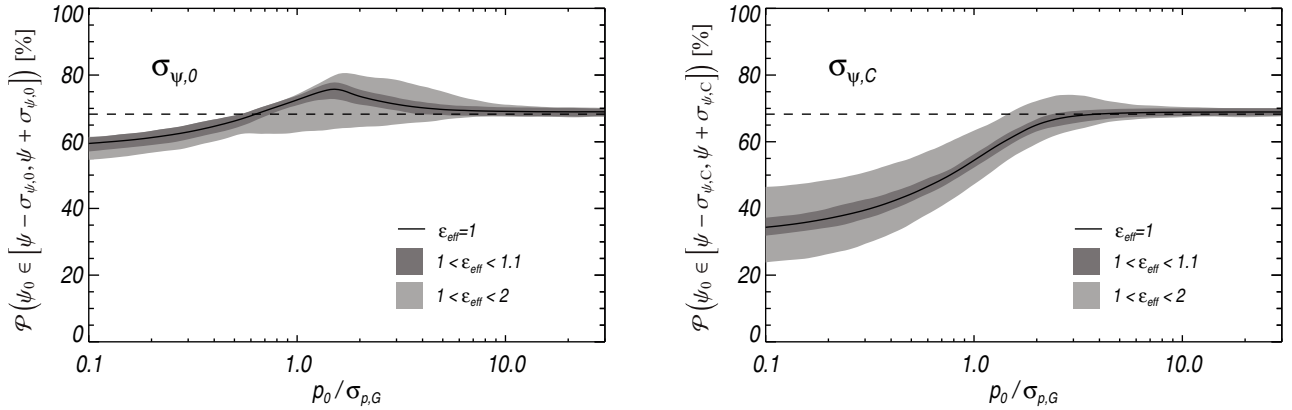


Fig. 7. Same as Fig. 6, but for the polarization angle uncertainty estimators. *Left:* $\sigma_{\psi,0}$. *Right:* conventional $\sigma_{\psi,C}$.

mean of σ_Q and σ_U when there is no correlation between them; i.e., $\sigma_{p,G}^2 = \sigma_Q \sigma_U / I_0^2$.

The arithmetic estimator is defined as a simple quadratic mean of the variance in Q and U :

$$\sigma_{p,A}^2 = \frac{1}{2} \frac{\sigma_Q^2 + \sigma_U^2}{I_0^2} = \frac{\sigma_Q^2 (\varepsilon^2 + 1)}{I_0^2 2\varepsilon^2}. \quad (27)$$

This estimate also gives back $\sigma_{p,A} = \sigma_Q / I_0 = \sigma_U / I_0$ in the canonical case. Furthermore, it is also independent of the reference frame or of the presence of correlations.

The two estimators have very similar behaviour, as can be seen in the top and bottom right-hand panels of Fig. 6. They agree perfectly with a 68% confidence level for S/N $p_0/\sigma_{p,0} > 4$ and for standard simplification of the covariance matrix. Both estimators provide conservative probability ($\mathcal{P} > 68\%$) in the S/N range 0.5–4. The impact of the effective ellipticity of the covariance matrix (grey shaded area) is stronger for higher values of the S/N (> 2) and can yield variations of 30% in the probability \mathcal{P} for the *extreme* regime. These estimators should be used cautiously for high ellipticity, but provide quick and conservative estimates in the other cases.

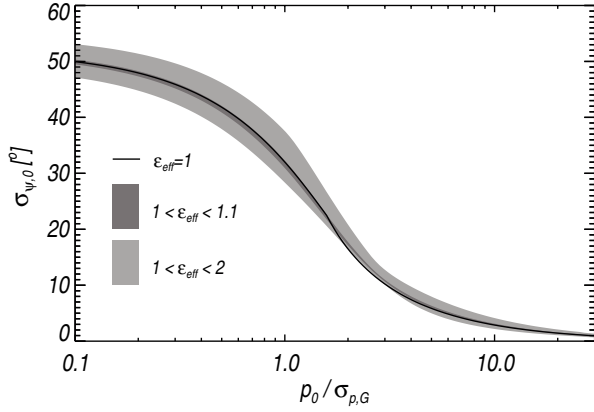


Fig. 8. True polarization angle uncertainty, $\sigma_{\psi,0}$, as a function of the S/N, $p_0/\sigma_{p,G}$. The three regimes (*canonical*, *low*, and *extreme*) of the covariance matrix are explored (solid line, light, and dark grey shaded regions, respectively).

4.3. Conventional estimate

The conventional determination of the uncertainties proposed by [Serkowski \(1958, 1962\)](#) is often used for polarization determinations based on optical extinction data. Although investigated by [Naghizadeh-Khouei & Clarke \(1993\)](#), these conventional uncertainties still do not include asymmetrical terms and correlations in the covariance matrix. Here we extend the method to the general case by using the derivatives of p and ψ around the observed values of the I , Q , and U parameters. It should be noted that, since this approach is based on derivatives around the observed values of (I, Q, U) , it is only valid in the high S/N regime. The detailed derivation, provided in Appendix F, leads to the expressions

$$\sigma_{p,C}^2 = \frac{1}{p^2 I^4} \times (Q^2 \sigma_Q^2 + U^2 \sigma_U^2 + p^4 I^2 \sigma_I^2 + 2QU\sigma_{QU} - 2IQp^2\sigma_{IQ} - 2IU p^2\sigma_{IU}) \quad (28)$$

and

$$\sigma_{\psi,C}^2 = \frac{1}{4} \frac{Q^2 \sigma_U^2 + U^2 \sigma_Q^2 - 2QU\sigma_{QU}}{(Q^2 + U^2)^2} \text{ rad}^2, \quad (29)$$

where I , Q , U , and p are the measured quantities, and σ_{XY} are the elements of the covariance matrix. We recall that the maximum uncertainty on ψ is equal to $\pi/\sqrt{12}$ rad (integral of the variance of the polarization angle over a flat distribution between $-\pi/2$ and $\pi/2$). When σ_I can be neglected, we obtain

$$\sigma_{\psi,C} = \sqrt{\frac{Q^2 \sigma_U^2 + U^2 \sigma_Q^2 - 2QU\sigma_{QU}}{Q^2 \sigma_Q^2 + U^2 \sigma_U^2 + 2QU\sigma_{QU}}} \times \frac{\sigma_{p,C}}{2p} \text{ rad}. \quad (30)$$

Because the uncertainty of ψ is also often expressed in degrees, we provide the associated conversions: $\pi/\sqrt{12}$ rad = 51°96 and $1/2$ rad = 28°65. Moreover, under the canonical assumptions, we recover $\sigma_{p,C} = \sigma_{p,G} = \sigma_Q/I_0 = \sigma_U/I_0$ and $\sigma_{\psi,C} = \sigma_{p,C}/2p$ rad.

Since the conventional estimate of the uncertainty $\sigma_{p,C}$ is equal to $\sigma_{p,G}$ under the standard simplifications of the covariance matrix, it has the same deficiency at low S/N (see bottom left-hand panel of Fig. 6). The impact of the effective ellipticity of the covariance matrix tends to be negligible at high S/N ($p_0/\sigma_{p,G} > 4$) and remains limited at low S/N. Thus this estimator of the polarization fraction uncertainty appears more robust than the geometric and arithmetic estimators, while still being

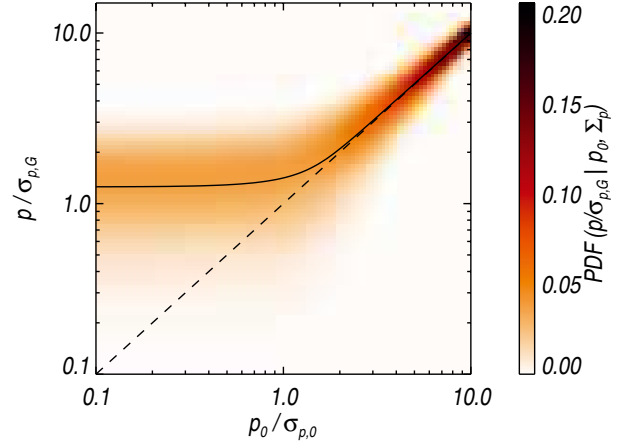


Fig. 9. Probability density function (PDF) of the measured S/N $p/\sigma_{p,G}$ (where $\sigma_{p,G}$ is the geometric estimate) as a function of the true S/N $p_0/\sigma_{p,0}$, with no ellipticity and correlation in the covariance matrix Σ_p . The mean likelihood, $\bar{p}/\sigma_{p,G}$ (full line), tends to $\sqrt{\pi}/2$ at low S/N and to the 1:1 relation (dashed line) at high S/N ($p_0/\sigma_{p,0} > 2$).

easy to compute and valid (even conservative) over a wide range of S/N.

The conventional estimate of the polarization angle uncertainty, $\sigma_{\psi,C}$, is shown in Fig. 7 (right-hand panel) in the *canonical*, *low*, and *extreme* regimes of the covariance matrix. It appears that $\sigma_{\psi,C}$ is strongly under-estimated at low S/N, mainly due to the presence of the term $1/p$ in Eq. (30), where p is strongly biased at low S/N. For $S/N > 4$, the agreement between the probability \mathcal{P} and the expected value is good, while the impact of the ellipticity of the covariance matrix becomes negligible only for $S/N > 10$. This estimator can certainly be used at high S/N.

4.4. S/N estimates

It is important to stress how any measurement of the S/N $p/\sigma_{p,G}$ is strongly affected by the bias on the measured polarization fraction p , as shown in Fig. 9. We observe that at high S/N ($p_0/\sigma_{p,0} > 2$), the measured S/N, here $p/\sigma_{p,G}$, is very close to the true S/N. The mean likelihood of the measured S/N (solid line) flattens for lower true S/N, such that $\bar{p}/\sigma_{p,G}$ tends to $\sqrt{\pi}/2$ for $p_0/\sigma_{p,0} < 1$, which comes from the limit of the [Rice \(1945\)](#) function when $p_0/\sigma_{p,0} \rightarrow 0$. This should be taken into account carefully when dealing with polarization measurements at intermediate S/N. For any measurement with a S/N $p_0/\sigma_{p,0} < 2$, it is in fact impossible to obtain an estimate of the true S/N, because this is fully degenerate owing to the bias of the polarization fraction.

4.5. Confidence intervals

We have seen the limitations of the Gaussian assumption for computing valid estimates of the polarization uncertainties. To obtain a robust estimate of the uncertainty in p and ψ at low S/N, one has to construct the correct confidence regions or intervals. The $\lambda\%$ confidence interval around a measurement p is defined as the interval that has a probability of containing the true value p_0 exactly equal to $\lambda/100$, where $(1 - \lambda)$ is called “critical parameter”. This interval is constructed from the PDF and does not require any estimate of the true polarization parameters. [Mood & Graybill \(1974\)](#), [Simmons & Stewart \(1985\)](#), and [Vaillancourt \(2006\)](#) have provided a simple way to

construct such confidence intervals for the polarization fraction p when the usual simplifications of the covariance matrix are assumed. Naghizadeh-Khouei & Clarke (1993) provide estimates of the confidence intervals for the polarization angle ψ under similar assumptions, and this is even simpler, because in that case $f_\psi(\psi | p_0, \psi_0, \Sigma_p)$ only depends on the S/N $p_0/\sigma_{p,0}$.

Once the covariance matrix is allowed to include ellipticity and correlations, we see in Sect. 2.4 and Appendix D how the marginalized PDFs $f_p(p | p_0, \psi_0, \Sigma_p)$ and $f_\psi(\psi | p_0, \psi_0, \Sigma_p)$ depend on the true polarization fraction p_0 and the true polarization angle ψ_0 . This leads us to consider ψ_0 as a ‘‘nuisance parameter’’ when building confidence intervals of p_0 , and vice-versa. We propose below an extension of the Simmons & Stewart (1985) technique, using an iterative method to build the confidence intervals of p_0 and ψ_0 simultaneously.

For each possible value of p_0 and ψ_0 (spanning the range 0 to 1, and $-\pi/2$ to $\pi/2$, respectively), we compute the quantities $p_-, p^-, \psi_-,$ and ψ^- , which provide the lower and upper limits in p and ψ of the region $\Omega(\lambda, p_0, \psi_0)$ defined by

$$\iint_{\Omega(\lambda, p_0, \psi_0)} f_{2D}(p, \psi | p_0, \psi_0, \Sigma_p) dpd\psi = \frac{\lambda}{100} \quad (31)$$

such that the contour of the region Ω is an iso-probability contour of the PDF f_{2D} . We stress that the choice of a confidence interval is still subjective and may be shifted by any arbitrary value of p or ψ , provided that the integral over the newly defined region is also $\lambda/100$. The definition we have chosen ensures that the region $\Omega(\lambda, p_0, \psi_0)$ is the smallest possible. We also note that

$$\int_{p_-}^{p^+} \int_{\psi_-}^{\psi^+} f_{2D} dpd\psi > \iint_{\Omega(\lambda, p_0, \psi_0)} f_{2D} dpd\psi, \quad (32)$$

which implies that the rectangular region bounded by $p_-, p^+, \psi_-,$ and ψ^+ is a conservative choice. For a given λ and covariance matrix Σ_p , we can finally obtain a set of four upper and lower limits on p and ψ : $p_-(p_0, \psi_0)$; $p^+(p_0, \psi_0)$; $\psi_-(p_0, \psi_0)$; and $\psi^+(p_0, \psi_0)$. We illustrate this with the example of (p, ψ) set to $(0.1, \pi/8)$ in Fig. 10. For given polarization measurements (p, ψ) , we trace the loci $p_-(p_0, \psi_0) = p$ (dashed line), $p^+(p_0, \psi_0) = p$ (dot-dash line), $\psi_-(p_0, \psi_0) = \psi$ (long dashed line), and $\psi^+(p_0, \psi_0) = \psi$ (dash-dot-dot-dot line). Finally, the 68% confidence intervals $[p_0^{\text{low}}, p_0^{\text{up}}]$ of p_0 and $[\psi_0^{\text{low}}, \psi_0^{\text{up}}]$ of ψ_0 are defined by building the smallest rectangular region (solid line in Fig. 10) that simultaneously covers the domain in p_0 and ψ_0 between the upper and lower limits defined above and which satisfies the conditions:

$$\begin{aligned} p_0^{\text{low}} &= \min_{p_0} \left(p = p^- \left\{ p_0, \psi_0 \in [\psi_0^{\text{low}}, \psi_0^{\text{up}}] \right\} \right); \\ p_0^{\text{up}} &= \max_{p_0} \left(p = p^+ \left\{ p_0, \psi_0 \in [\psi_0^{\text{low}}, \psi_0^{\text{up}}] \right\} \right); \\ \psi_0^{\text{low}} &= \min_{\psi_0} \left(\psi = \psi^- \left\{ p_0 \in [p_0^{\text{low}}, p_0^{\text{up}}], \psi_0 \right\} \right); \\ \psi_0^{\text{up}} &= \max_{\psi_0} \left(\psi = \psi^+ \left\{ p_0 \in [p_0^{\text{low}}, p_0^{\text{up}}], \psi_0 \right\} \right). \end{aligned} \quad (33)$$

Using these conditions, the confidence interval of p_0 takes the nuisance parameter ψ_0 over its own confidence interval into account, and vice-versa. This has to be constructed iteratively, starting with $\psi_0^{\text{low}} = -\pi/2$ and $\psi_0^{\text{up}} = \pi/2$, to build first guesses for p_0^{low} and p_0^{up} , which are then used to build a new estimate of the confidence intervals of ψ_0 , and so on until convergence. In practice, it converges very quickly. We emphasize that these confidence intervals are conservative, because they include the

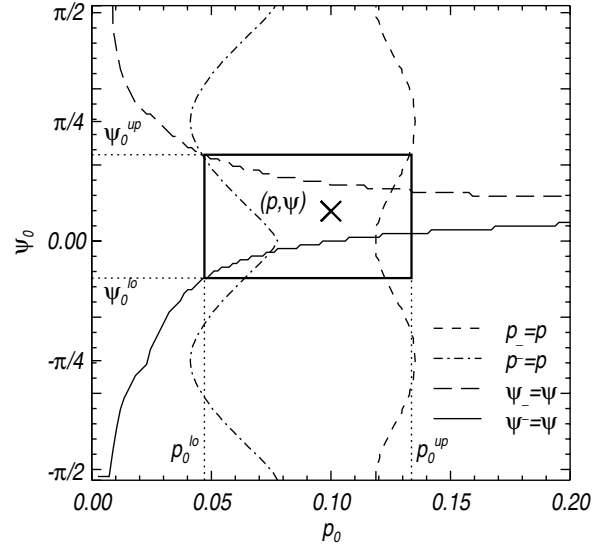


Fig. 10. Construction of 68% confidence intervals $[p_0^{\text{low}}, p_0^{\text{up}}]$ and $[\psi_0^{\text{low}}, \psi_0^{\text{up}}]$ (full line box) of p_0 and ψ_0 , based on the upper and lower loci $p = p_-, p = p^+, \psi = \psi_-,$ and $\psi = \psi^+$, built from PDFs f_{2D} and a given measurement (p, ψ) (indicated by the cross).

impact of the nuisance parameters, implying that

$$\Pr \left(p_0^{\text{low}} \leq p_0 \leq p_0^{\text{up}}; \psi_0^{\text{low}} \leq \psi_0 \leq \psi_0^{\text{up}} \right) \Big|_{p, \psi, \Sigma_p} \geq \frac{\lambda}{100} \quad (34)$$

regardless of the true values p_0, ψ_0 .

5. Summary

This paper represents the first step in an extensive study of polarization analysis methods. We focused here on the impact of the full covariance matrix on naïve polarization measurements and especially the impact on the bias. We derived analytical expressions for the PDF of the polarization parameters (I, p, ψ) in the 3D and 2D cases, taking the full covariance matrix Σ of the Stokes parameters $I, Q,$ and U into account.

The asymmetries of the covariance matrix can be characterized by the effective ellipticity ε_{eff} , expressed as a function of the ellipticity ε and the correlation ρ between Q and U in a given reference frame, and by the correlation parameters ρ_Q and ρ_U between the intensity I and the Q and U parameters. We quantified departures from the canonical case ($\varepsilon_{\text{eff}} = 1$), which are usually assumed in earlier works on polarization. We explored this effect for three regimes of the covariance matrix: the *canonical* case ($\varepsilon_{\text{eff}} = 1$); the *low* regime, $1 < \varepsilon_{\text{eff}} < 1.1$; and the *extreme* regime $1 < \varepsilon_{\text{eff}} < 2$. We first emphasized the impact of the true polarization angle ψ_0 , which can produce variations in the polarization fraction bias of up to 30% of the dispersion of p , in the *extreme* regime, and up to 5% in the *low* regime. We then estimated the statistical bias on the polarization angle measurement ψ . This can reach up to 9° when the ellipticity or the correlation between the Q and U Stokes components becomes important ($\varepsilon_{\text{eff}} \sim 2$) and the S/N is low. However, when values of the effective ellipticity are in the *low* regime (i.e., less than 10% greater than the canonical values) the bias on ψ remains limited (i.e., $< 1^\circ$), and well below the level of the measurement uncertainty (by a factor of 5–25). Thus the bias on ψ can be neglected, to first order, for small departures of the covariance matrix from the canonical case.

On the other hand, we quantified the impact of the uncertainty of the intensity on the relative and absolute statistical bias of the polarization fraction and angle. We provided the modified PDF in (p, ψ) arising from a finite S/N of the intensity, I_0/σ_I . We showed that, above an intensity S/N of 5, the relative bias on the polarization fraction p generally remains unchanged at polarization S/N $p_0/\sigma_{p,G} < 2$, while it is slightly enhanced when the intensity and the polarization S/N lie in the intermediate range, $p_0/\sigma_{p,G} > 2$. For S/N of the intensity I_0/σ_I below 5, the relative bias on p suddenly drops to 0, because of the increasing dispersion. Indeed, the absolute bias can be higher by a factor as large as 5 when the S/N on I drops below 2 to 3; this is associated with a dramatic increase in the dispersion of the polarization fraction, which diverges and strongly overwhelms the increase of the bias at low S/N. The uncertainty of the intensity thus has to be taken into account properly when analysing polarization data for faint objects, in order to derive the correct polarization fraction bias and uncertainty. Similarly, the case of faint polarized objects on top of a varying but unpolarized background can lead to a question about the correct intensity offset to subtract, yielding an effective additional uncertainty on the intensity.

The impact of correlations between the intensity and the Q and U components has also been quantified in the case of a finite S/N on the intensity. It has been shown that the bias on p is only slightly affected (below 10% difference compared with the canonical case) even at low S/N on I , when the correlations ρ_Q and ρ_U span the range -0.2 to 0.2 .

We have additionally addressed the question of how to obtain a robust estimate of the uncertainties on polarization measurements (p, ψ) . We extended the often-used procedure of [Simmons & Stewart \(1985\)](#) by building confidence intervals for polarization fraction and angle simultaneously, taking the full properties of the covariance matrix into account. This method makes it possible to build conservative confidence intervals around polarization measurements.

We have explored the domain of validity for the commonly used polarization uncertainty estimators based on the variance of the PDF (assuming a Gaussian distribution). The true dispersion of the polarization fraction has been shown to provide robust estimates only at high S/N (above 3), while the true dispersion of the polarization angle yields conservative estimates for $S/N > 0.5$. Simple estimators, such as the geometric and arithmetic polarization fraction uncertainties, appear sensitive to the effective ellipticity of the covariance matrix at high S/N, while they provide conservative estimates over a wide range of S/N (above 0.5) in the canonical case. The conventional method, usually adopted to analyse optical extinction polarization data, provides the most robust estimates of σ_p for S/N above 0.5, with respect to the ellipticity of the covariance matrix, but poor estimates of σ_ψ , which are valid only at very high S/N (above 5).

We have seen how much the naïve polarization estimates provide poor determinations of the true polarization parameters and how it can be difficult to recover the true S/N of a measurement. In a companion paper ([Montier et al. 2015](#)), we review different estimators of the true polarization from experimental measurements that partially correct this bias

in p and ψ , using full knowledge of the polarization covariance matrix.

Acknowledgements. This paper was developed to support the analysis of data from the *Planck* satellite. The development of *Planck* has been supported by: ESA; CNES and CNRS/INSU-IN2P3-INP (France); ASI, CNR, and INAF (Italy); NASA and DoE (USA); STFC and UKSA (UK); CSIC, MICINN, JA, and RES (Spain); Tekes, AoF, and CSC (Finland); DLR and MPG (Germany); CSA (Canada); DTU Space (Denmark); SER/SSO (Switzerland); RCN (Norway); SFI (Ireland); FCT/MCTES (Portugal); and PRACE (EU). A description of the Planck Collaboration and a list of its members, including the technical or scientific activities in which they have been involved, can be found at <http://www.cosmos.esa.int/web/planck/planck-collaboration>. We would also like to thank P. Leahy, S. Prunet, and D. Scott for their very useful comments.

References

- Aalo, V. A., Efthymoglou, G. P., & Chayawan, C. 2007, *IEEE Comm. Lett.*, 11, 985
- Abramowitz, M., & Stegun, I. 1964, *Handbook of Mathematical Functions* (National Bureau of Standards)
- Benoît, A., Ade, P., Amblard, A., et al. 2004, *A&A*, 424, 571
- Bernard, J.-P., Ade, P., De Bernardis, P., et al. 2007, in *EAS Pub. Ser.* 23, eds. M.-A. Miville-Deschênes, & F. Boulanger, 189
- Boissier, J., Bockelée-Morvan, D., Biver, N., et al. 2009, *Earth Moon Planets*, 105, 89
- Clarke, D., Naghizadeh-Khouei, J., Simmons, J. F. L., & Stewart, B. G. 1993, *A&A*, 269, 617
- Dotson, J. L., Vaillancourt, J. E., Kirby, L., et al. 2010, *ApJS*, 186, 406
- Dowell, C. D., Hildebrand, R. H., Schleuning, D. A., et al. 1998, *ApJ*, 504, 588
- Fissel, L. M., Ade, P. A. R., Angilè, F. E., et al. 2010, in *SPIE Conf. Ser.*, 7741
- Girart, J. M., Rao, R., & Marrone, D. P. 2006, *Science*, 313, 812
- Gradshteyn, I. S., & Ryzhik, I. M. 2007, *Table of Integrals, Series, and Products* (Elsevier)
- Greaves, J. S., Holland, W. S., Jenness, T., et al. 2003, *MNRAS*, 340, 353
- Jarosik, N., Bennett, C. L., Dunkley, J., et al. 2011, *ApJS*, 192, 14
- Li, H., Dowell, C. D., Kirby, L., Novak, G., & Vaillancourt, J. E. 2008, *Appl. Opt.*, 47, 422
- Montier, L. A., Plaszczyński, S., Levrier, F., et al. 2015, *A&A*, 574, A136
- Mood, A. M., & Graybill, A. F. 1974, *Introduction to the Theory of Statistics*, 3rd edn. (New-York: McGraw-Hill)
- Naghizadeh-Khouei, J., & Clarke, D. 1993, *A&A*, 274, 968
- Page, L., Hinshaw, G., Komatsu, E., et al. 2007, *ApJS*, 170, 335
- Pérez-Sánchez, A. F., & Vlemmings, W. H. T. 2013, *A&A*, 551, A15
- Planck Collaboration Int. XIX. 2014, *A&A*, submitted [[arXiv:1405.0871](https://arxiv.org/abs/1405.0871)]
- Platt, S. R., Hildebrand, R. H., Pernic, R. J., Davidson, J. A., & Novak, G. 1991, *PASP*, 103, 1193
- Quinn, J. L. 2012, *A&A*, 538, A65
- Renbarger, T., Chuss, D. T., Dotson, J. L., et al. 2004, *PASP*, 116, 415
- Rice, S. O. 1945, *Bell Systems Tech. J.*, 24, 46
- Schleuning, D. A., Dowell, C. D., Hildebrand, R. H., Platt, S. R., & Novak, G. 1997, *PASP*, 109, 307
- Serkowski, K. 1958, *Acta Astron.*, 8, 135
- Serkowski, K. 1962, *Adv. Astron. Astrophys.*, 1, 290
- Simmons, J. F. L., & Stewart, B. G. 1985, *A&A*, 142, 100
- Tauber, J. A., Mandolesi, N., Puget, J., et al. 2010, *A&A*, 520, A1
- Thum, C., Wiesemeyer, H., Paubert, G., Navarro, S., & Morris, D. 2008, *PASP*, 120, 777
- Vaillancourt, J. E. 2006, *PASP*, 118, 1340
- Vaillancourt, J. E., & Matthews, B. C. 2012, *ApJS*, 201, 13
- Vinokur, M. 1965, *Ann. Astrophys.*, 28, 412
- Wardle, J. F. C., & Kronberg, P. P. 1974, *ApJ*, 194, 249

Appendix A: Expressions for PDFs

Here we present expressions for the 2D PDFs that are discussed in Sect. 2:

$$f(I, p, \psi | I_0, p_0, \psi_0, \Sigma) = \frac{2|p|I^2}{\sqrt{(2\pi)^3}\sigma^3} \exp \left[-\frac{1}{2} \begin{bmatrix} I - I_0 \\ pI \cos(2\psi) - p_0 I_0 \cos(2\psi_0) \\ pI \sin(2\psi) - p_0 I_0 \sin(2\psi_0) \end{bmatrix}^T \Sigma^{-1} \begin{bmatrix} I - I_0 \\ pI \cos(2\psi) - p_0 I_0 \cos(2\psi_0) \\ pI \sin(2\psi) - p_0 I_0 \sin(2\psi_0) \end{bmatrix} \right]; \quad (\text{A.1})$$

$$f_{2D}(p, \psi | I_0, p_0, \psi_0, \Sigma) = \frac{|p|}{2\pi\sigma^3} \exp \left(-\frac{I_0^2}{2}\gamma \right) \left\{ \sqrt{\frac{2\beta I_0}{\pi \alpha^2}} + \frac{1}{\alpha^{3/2}} \left[1 + \frac{\beta^2 I_0^2}{\alpha} \right] \exp \left(\frac{\beta^2 I_0^2}{2\alpha} \right) \left[1 + \operatorname{erf} \left(\frac{\beta I_0}{\sqrt{2\alpha}} \right) \right] \right\} \quad \text{for } p \geq 0; \quad (\text{A.2})$$

$$f_{2D}(p, \psi | I_0, p_0, \psi_0, \Sigma) = \frac{|p|}{2\pi\sigma^3} \exp \left(-\frac{I_0^2}{2}\gamma \right) \left\{ -\sqrt{\frac{2\beta I_0}{\pi \alpha^2}} + \frac{1}{\alpha^{3/2}} \left[1 + \frac{\beta^2 I_0^2}{\alpha} \right] \exp \left(\frac{\beta^2 I_0^2}{2\alpha} \right) \left[1 - \operatorname{erf} \left(\frac{\beta I_0}{\sqrt{2\alpha}} \right) \right] \right\} \quad \text{for } p \leq 0; \quad (\text{A.3})$$

$$f_{2D}(p, \psi | p_0, \psi_0, \Sigma_p) = \frac{p}{\pi\sigma_{p,G}^2} \exp \left[-\frac{1}{2} \begin{bmatrix} p \cos(2\psi) - p_0 \cos(2\psi_0) \\ p \sin(2\psi) - p_0 \sin(2\psi_0) \end{bmatrix}^T \Sigma_p^{-1} \begin{bmatrix} p \cos(2\psi) - p_0 \cos(2\psi_0) \\ p \sin(2\psi) - p_0 \sin(2\psi_0) \end{bmatrix} \right] \quad \text{for } \sigma_I = 0. \quad (\text{A.4})$$

where we have defined the functions

$$\begin{aligned} \alpha &= \begin{pmatrix} 1 \\ p \cos 2\psi \\ p \sin 2\psi \end{pmatrix}^T \Sigma^{-1} \begin{pmatrix} 1 \\ p \cos 2\psi \\ p \sin 2\psi \end{pmatrix}, \\ \beta &= \begin{pmatrix} 1 \\ p \cos 2\psi \\ p \sin 2\psi \end{pmatrix}^T \Sigma^{-1} \begin{pmatrix} 1 \\ p_0 \cos 2\psi_0 \\ p_0 \sin 2\psi_0 \end{pmatrix}, \\ \gamma &= \begin{pmatrix} 1 \\ p_0 \cos 2\psi_0 \\ p_0 \sin 2\psi_0 \end{pmatrix}^T \Sigma^{-1} \begin{pmatrix} 1 \\ p_0 \cos 2\psi_0 \\ p_0 \sin 2\psi_0 \end{pmatrix}. \end{aligned} \quad (\text{A.5})$$

Appendix B: Computation of f_{2D}

The 3D PDF of (I, p, ψ) is given by

$$f(I, p, \psi) = 2|p|I^2 F(I, pI \cos 2\psi, pI \sin 2\psi). \quad (\text{B.1})$$

To compute the 2D PDF of (p, ψ) , we marginalize over total intensity. However, some care is required here, because the above expression for $f(I, p, \psi)$ is only valid for $pI \geq 0$ (i.e., we cannot measure negative p unless I happens to be negative owing to noise) and f must be taken to be zero otherwise. This means that the marginalization is performed over $I \geq 0$ for positive p and over $I \leq 0$ for negative p :

$$f_{2D} = \int_0^{+\infty} 2|p|I^2 F(I, pI \cos 2\psi, pI \sin 2\psi) dI, \quad \text{for } p \geq 0; \quad (\text{B.2})$$

$$f_{2D} = \int_{-\infty}^0 2|p|I^2 F(I, pI \cos 2\psi, pI \sin 2\psi) dI, \quad \text{for } p \leq 0. \quad (\text{B.3})$$

The integrand may be written so as to exhibit the dependence on total intensity,

$$f = \frac{2|p|I^2}{(2\pi)^{3/2}\sigma^3} \exp \left[-\frac{1}{2} (I^2\alpha - 2II_0\beta + I_0^2\gamma) \right], \quad (\text{B.4})$$

and then we make use of the functions (Gradshteyn & Ryzhik 2007):

$$G_-(x, y) = \int_{-\infty}^0 I^2 e^{-xI^2 + 2yI} dI = -\frac{y}{2x^2} + \sqrt{\frac{\pi}{x^5}} \frac{2y^2 + x}{4} \exp \left(\frac{y^2}{x} \right) \left[1 - \operatorname{erf} \left(\frac{y}{\sqrt{x}} \right) \right]; \quad (\text{B.5})$$

$$G_+(x, y) = \int_0^{+\infty} I^2 e^{-xI^2 + 2yI} dI = \frac{y}{2x^2} + \sqrt{\frac{\pi}{x^5}} \frac{2y^2 + x}{4} \exp \left(\frac{y^2}{x} \right) \left[1 + \operatorname{erf} \left(\frac{y}{\sqrt{x}} \right) \right]. \quad (\text{B.6})$$

Elementary replacement of (x, y) by $(\alpha/2, I_0\beta/2)$ yields the PDF of Eqs. (A.2) and (A.3).

Appendix C: Illustrations of f_{2D}

We illustrate the shape of the 2D PDF $f_{2D}(p, \psi | I_0, p_0, \psi_0, \Sigma)$ in Fig. C.1, for the case of a perfectly known intensity having no correlation with the polarization. Starting from a given couple of true polarization parameters, $\psi_0 = 0^\circ$ and $p_0 = 0.1$, the PDF is computed for various S/Ns, $p_0/\sigma_{p,G}$, and settings of the covariance matrix. The S/N $p_0/\sigma_{p,G}$ is varied from 0.01 to 0.5, 1, and 5 (top to bottom). The dashed crossing lines show the location of the initial true polarization values. The leftmost column shows the results obtained when the covariance matrix is assumed to be diagonal and symmetric, (i.e., $\varepsilon = 1$ and $\rho = 0$), as was usually done in previous works on polarization data. The distribution along the ψ axis is fully symmetric around 0, implying the absence of bias on the polarization angle. When varying the ellipticity ε from 1/2 to 2 (Cols. 2 and 3), we still observe symmetrical PDFs in this configuration, but multiple peaks appear at low S/N. In the presence of correlation, i.e., $\rho = -1/2$ and $1/2$ (Cols. 4 and 5), the maximum peak is now slightly shifted in p and ψ , with an asymmetric PDF around the initial ψ_0 value.

In the usual canonical case, $\varepsilon = 1$ and $\rho = 0$, the PDF remains strictly symmetric regardless of the value of the initial true polarization angle ψ_0 . However, when changing the true polarization angle ψ_0 , as shown in Fig. C.2, the PDF may become asymmetrical once the ellipticity $\varepsilon \neq 1$ or the correlation $\rho \neq 0$. This will induce a statistical bias in the measurement of the polarization angle ψ , which could be positive or negative depending on the covariance matrix and the true value ψ_0 , as discussed in Sect. 3.

Examples of 2D PDFs $f_{2D}(p, \psi | I_0, p_0, \psi_0, \Sigma)$ for finite values of I_0/σ_I (1, 2, and 5), and various ε and ρ situations, are shown in Fig. C.3 for the case $\rho_Q = \rho_U = 0$. The true polarization parameters are $p_0 = 0.1$ and $\psi_0 = 0^\circ$, and the polarization S/N is set to $p_0/\sigma_{p,G} = 1$, so these plots may be directly compared to the third row of Fig. C.1. The effect of varying I_0/σ_I on the overall shape of the PDF seems rather small, but the position of the maximum likelihood in (p, ψ) is noticeably changed to lower values of p when $I_0/\sigma_I \lesssim 2$, while the mean likelihood appears to be increased.

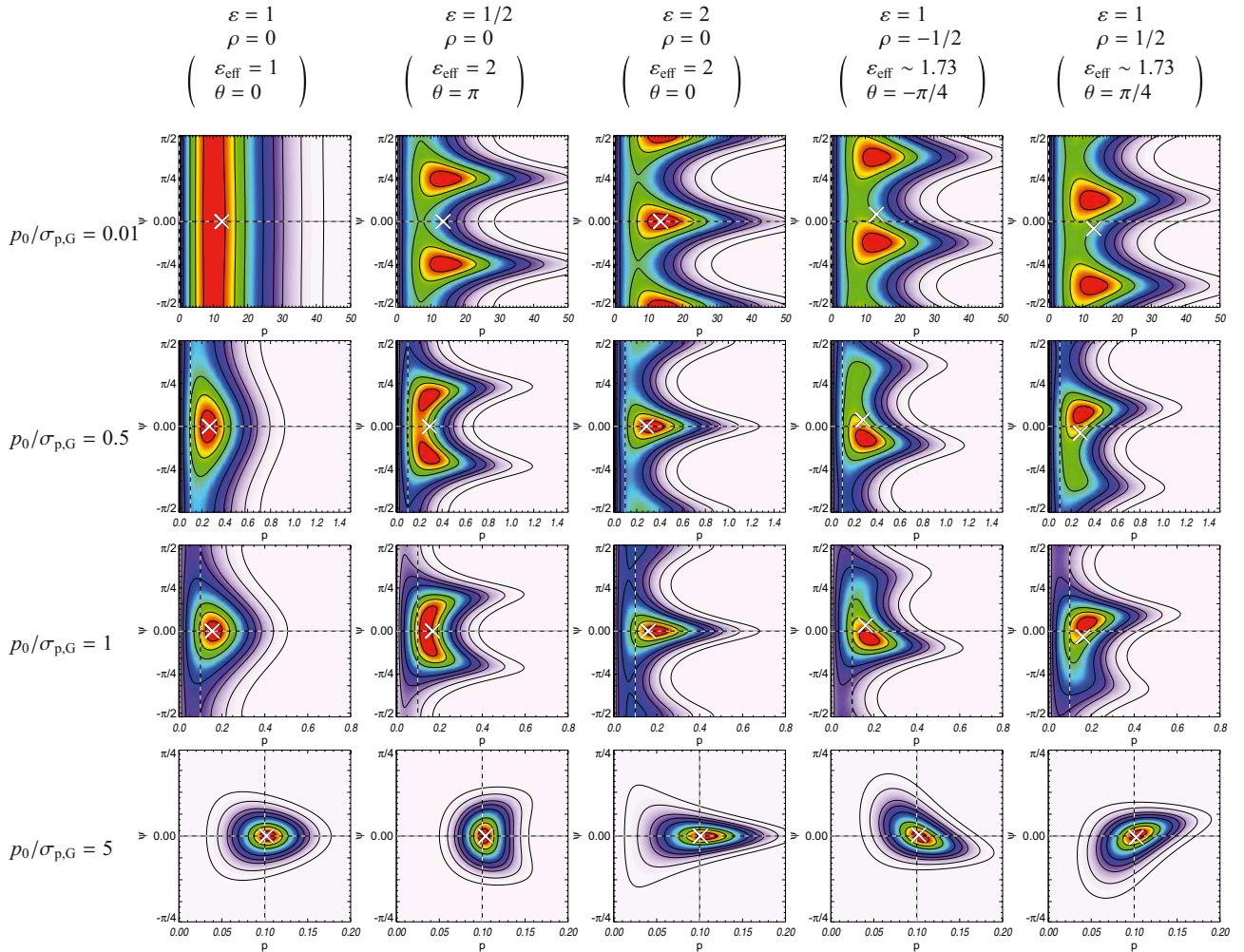


Fig. C.1. Probability density functions, $f_{2D}(p, \psi | p_0, \psi_0, \Sigma_p)$, with infinite S/N on intensity, computed for a given set of polarization parameters, namely $\psi_0 = 0^\circ$ and $p_0 = 0.1$ (dashed lines). Each row corresponds to a specific level of the S/N $p_0/\sigma_{p,G} = 0.01, 0.5, 1$, and 5 , from top to bottom. Various configurations of the covariance matrix are shown (in the different columns). Furthest left is the standard case: no ellipticity and no correlation. The next two columns show the impact of ellipticities $\varepsilon = 1/2$ and 2 . The last two columns deal with correlations $\rho = -1/2$ and $+1/2$. White crosses indicate the mean likelihood estimates of the PDF $(\bar{p}, \bar{\psi})$. The contour levels are shown at 0.1, 1, 5, 10, 20, 50, 70, and 90% of the maximum of the distribution.

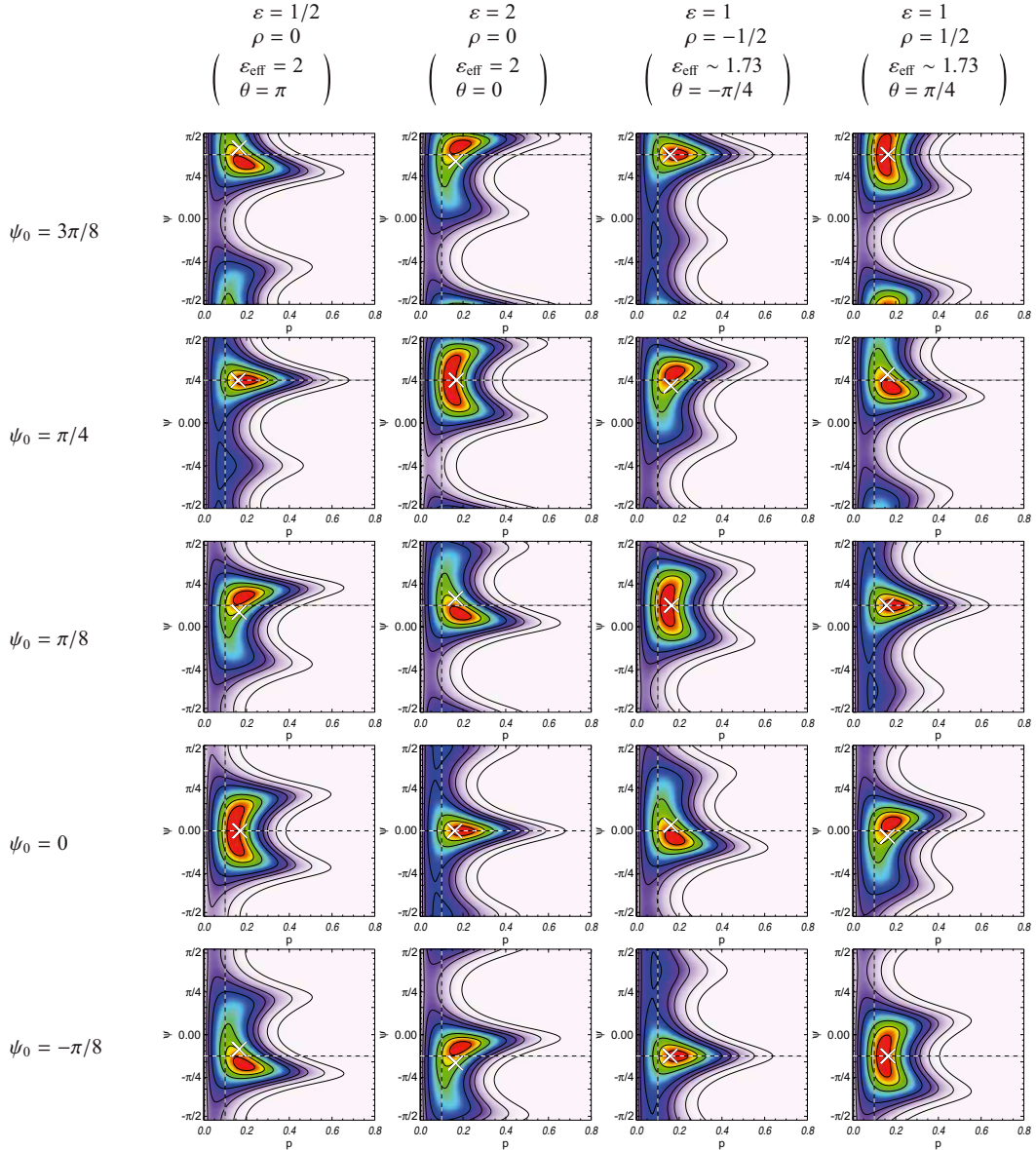


Fig. C.2. Probability density functions, $f_{2D}(p, \psi | p_0, \psi_0, \Sigma_p)$, plotted for various values of ψ_0 (rows), spanning from $-\pi/8$ to $3\pi/8$, and computed for four configurations of the covariance matrix (columns), parameterized by ϵ and ρ . The S/N on the intensity I is assumed to be infinite here. A true value of polarization $p_0 = 0.1$ has been chosen, and with S/N $p_0/\sigma_{p,G} = 1$. White crosses indicate the mean likelihood estimates of the PDF $(\bar{p}, \bar{\psi})$. The contour levels are provided at 0.1, 1, 5, 10, 20, 50, 70, and 90% of the maximum of the distribution.

Appendix D: General PDF of p and ψ

In the context of communication network science, [Aalo et al. \(2007\)](#) derived full expressions for the PDFs of envelope and phase quantities in the general case. These expressions can be directly translated to express the PDF of the polarization fraction and angle, p and ψ .

We can apply the rotation of the covariance introduced in Sect. 2.1 by an angle θ , given by Eq. (5), to remove the correlation term between the Stokes parameters. We define the mean and the variance of the normalized Stokes parameters in this new frame by

$$\mu_1 = p_0 \cos(2\psi_0 - \theta), \quad \mu_2 = p_0 \sin(2\psi_0 - \theta) \quad (\text{D.1})$$

and

$$\sigma_1^2 = (\sigma_Q^2 \cos^2 \theta + \sigma_U^2 \sin^2 \theta + \rho \sigma_Q \sigma_U \sin 2\theta) / I_0^2, \quad \sigma_2^2 = (\sigma_Q^2 \sin^2 \theta + \sigma_U^2 \cos^2 \theta - \rho \sigma_Q \sigma_U \sin 2\theta) / I_0^2. \quad (\text{D.2})$$

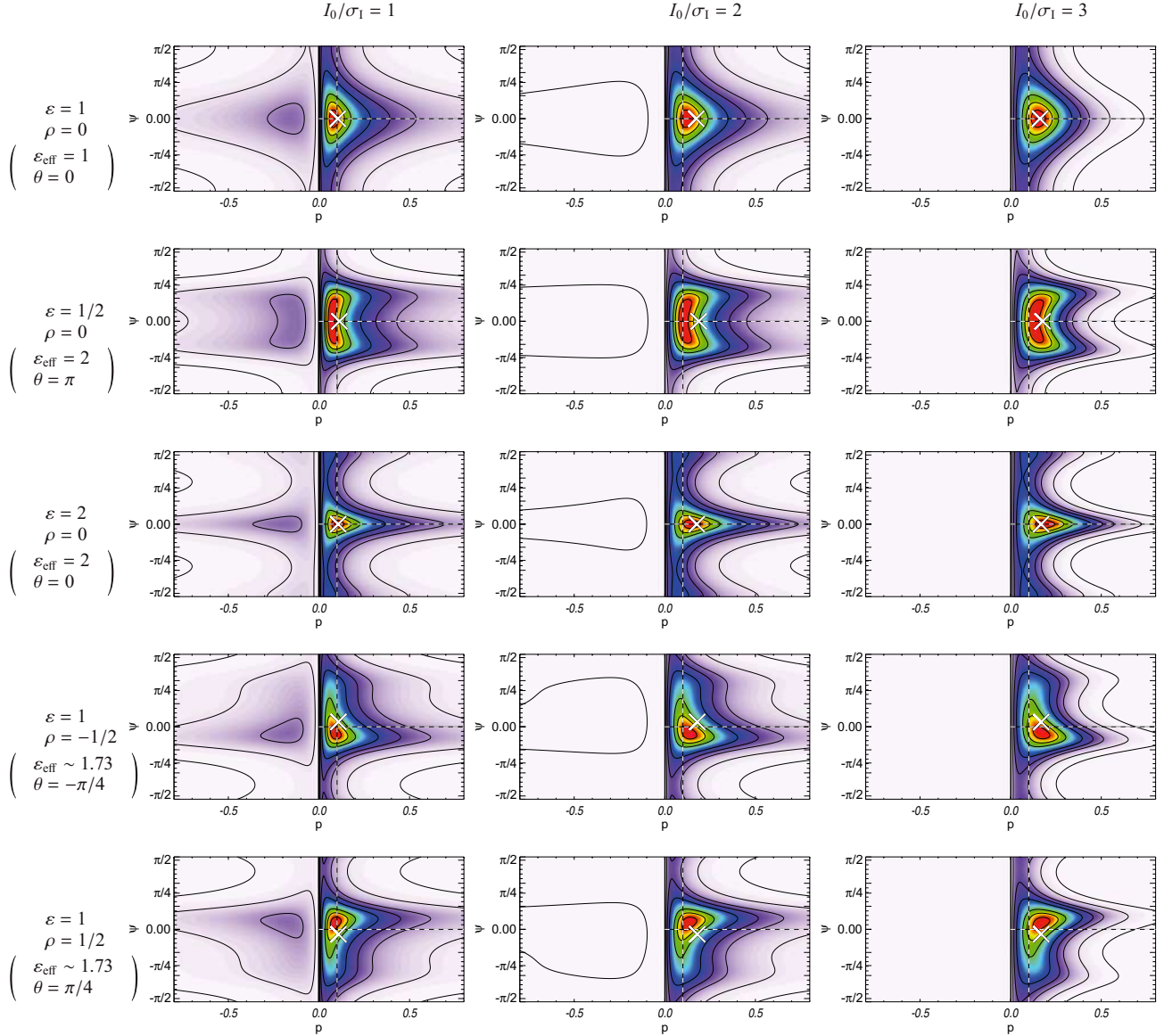


Fig. C.3. Probability density functions, $f_{2D}(p, \psi | I_0, p_0, \psi_0, \Sigma)$, with finite S/N on intensity, $I_0/\sigma_I = 1, 2$, and 5 (columns from left to right), computed for a given set of polarization parameters, $\psi_0 = 0^\circ$ and $p_0 = 0.1$ (dashed lines), and a S/N on the polarized intensity set to $p_0/\sigma_{p,G} = 1$. Correlation coefficients ρ_Q and ρ_U are set to zero. Various configurations of the covariance matrix are shown (rows). White crosses indicate the mean likelihood estimates of the PDF $(\bar{p}, \bar{\psi})$. The contour levels are provided at 0.1, 1, 5, 10, 20, 50, 70, and 90% of the maximum of the distribution. The polarization fraction is here defined over both the negative and positive ranges, due to the noise of the intensity.

The PDF of p is now written as

$$f_p(p | p_0, \psi_0, \Sigma_p) = \frac{p}{2\sigma_1\sigma_2} \exp \left\{ -\frac{1}{2} \left[\frac{\mu_1^2}{\sigma_1^2} + \frac{\mu_2^2}{\sigma_2^2} + \frac{p^2}{2} \left(\frac{1}{\sigma_1^2} + \frac{1}{\sigma_2^2} \right) \right] \right\} \times \sum_{n=0}^{\infty} \frac{\zeta_n \mathcal{I}_n \left(\frac{p^2}{4} \left(\frac{1}{\sigma_2^2} - \frac{1}{\sigma_1^2} \right) \right)}{\left[\left(\frac{\mu_1}{\sigma_1} \right)^2 + \left(\frac{\mu_2}{\sigma_2} \right)^2 \right]^n} \left\{ \mathcal{I}_{2n} \left(p \sqrt{\left(\frac{\mu_1}{\sigma_1} \right)^2 + \left(\frac{\mu_2}{\sigma_2} \right)^2} \right) \sum_{k=0}^n \delta_k C_k^n \left[\left(\frac{\mu_1}{\sigma_1} \right)^2 - \left(\frac{\mu_2}{\sigma_2} \right)^2 \right]^{n-k} \left(2 \frac{\mu_1 \mu_2}{\sigma_1^2 \sigma_2^2} \right)^k \right\}, \quad (\text{D.3})$$

with \mathcal{I}_n the n th-order modified Bessel function of the first kind. Here $\zeta_0 = 1$ and $\zeta_n = 2$ for $n \neq 0$, $C_k^n \equiv n!/k!(n-k)!$ are binomial coefficients, and δ_k is defined by

$$\delta_k = \begin{cases} 0 & \text{for } k \text{ odd,} \\ 2(-1)^{k/2} & \text{for } k \text{ even.} \end{cases} \quad (\text{D.4})$$

It should be noted that the above expression converges so fast that only a few terms of the infinite sum are required to obtain sufficient accuracy. On the other hand, the PDF of the polarization angle is given by

$$f_{\psi}(\psi | p_0, \psi_0, \Sigma_p) = \exp \left[-\frac{1}{1-\rho^2} \left(\frac{Q_0^2}{2\sigma_Q^2} + \frac{U_0^2}{2\sigma_U^2} - \frac{\rho Q_0 U_0}{\sigma_Q \sigma_U} \right) \right] \times \frac{\sqrt{1-\rho^2}}{\pi \sigma_Q \sigma_U \mathcal{A}(\psi)} \left\{ 1 + \frac{\sqrt{\pi} \mathcal{B}(\psi)}{\sqrt{\mathcal{A}(\psi)}} \exp \left[\frac{\mathcal{B}^2(\psi)}{\mathcal{A}(\psi)} \right] \operatorname{erfc} \left[-\frac{\mathcal{B}(\psi)}{\sqrt{\mathcal{A}(\psi)}} \right] \right\}, \quad (\text{D.5})$$

where

$$\mathcal{A}(\psi) = \frac{2 \cos^2 2\psi}{\sigma_Q^2} + \frac{2 \sin^2 2\psi}{\sigma_U^2} - 4 \frac{\rho \sin 2\psi \cos 2\psi}{\sigma_Q \sigma_U}, \quad (\text{D.6})$$

$$\mathcal{B}(\psi) = \frac{1}{\sqrt{1-\rho^2}} \left[\frac{\cos 2\psi}{\sigma_Q} \left(\frac{Q_0}{\sigma_Q} - \frac{\rho U_0}{\sigma_U} \right) + \frac{\sin 2\psi}{\sigma_U} \left(\frac{U_0}{\sigma_U} - \frac{\rho Q_0}{\sigma_Q} \right) \right], \quad (\text{D.7})$$

and

$$\operatorname{erfc}(z) = \frac{2}{\sqrt{\pi}} \int_z^{\infty} \exp[-x^2] dx \quad (\text{D.8})$$

is the complementary error function.

Appendix E: Impact of ρ_Q and ρ_U on ε and ρ

The covariance matrix Σ is positive definite, so may be written as a Cholesky product $\Sigma = \mathbf{L}^T \mathbf{L}$, with

$$\mathbf{L} = \begin{pmatrix} L_{11} & 0 & 0 \\ L_{12} & L_{22} & 0 \\ L_{13} & L_{23} & L_{33} \end{pmatrix}. \quad (\text{E.1})$$

The six L_{ij} are independent, unlike the six parameters of the covariance matrix, $(\sigma_I, \sigma_Q, \sigma_U, \rho, \rho_Q, \rho_U)$, or the parameters that we use in this paper, $(\sigma_I, \sigma_Q, \varepsilon, \rho, \rho_Q, \rho_U)$. In the general case, these are given in terms of the L_{ij} as (assuming $I_0 = 1$)

$$\rho = \frac{L_{12}L_{13} + L_{22}L_{23}}{\sqrt{(L_{12}^2 + L_{22}^2)(L_{13}^2 + L_{23}^2 + L_{33}^2)}}, \quad \varepsilon = \sqrt{\frac{L_{13}^2 + L_{23}^2 + L_{33}^2}{L_{12}^2 + L_{22}^2}},$$

$$\rho_Q = \frac{L_{12}}{\sqrt{L_{12}^2 + L_{22}^2}}, \quad \text{and} \quad \rho_U = \frac{L_{13}}{\sqrt{L_{13}^2 + L_{23}^2 + L_{33}^2}}. \quad (\text{E.2})$$

When there is no correlation between I and the Q or U components, then $L_{12} = L_{13} = 0$, which leads to the following system:

$$\rho = \rho_0 = \frac{L_{22}L_{23}}{|L_{22}| \sqrt{L_{23}^2 + L_{33}^2}}; \quad \varepsilon = \varepsilon_0 = \frac{\sqrt{L_{23}^2 + L_{33}^2}}{|L_{22}|}. \quad (\text{E.3})$$

The ellipticity and the correlation coefficient are therefore modified by the presence of the correlation between I and (Q, U) . A little algebra leads to expressions for ε and ρ as functions of $\varepsilon_0, \rho_0, \rho_Q$, and ρ_U , namely

$$\varepsilon = \varepsilon_0 \sqrt{\frac{1-\rho_Q^2}{1-\rho_U^2}} \quad \text{and} \quad \rho = \rho_Q \rho_U + \rho_0 \sqrt{(1-\rho_Q^2)(1-\rho_U^2)}, \quad (\text{E.4})$$

which are Eqs. (26).

Appendix F: Derivation of conventional uncertainties

We describe here how the expressions for the conventional uncertainties of p and ψ , which were introduced in Sect. 4.3, are obtained from the derivatives of p and ψ . We first note that we generally have

$$\sigma_X^2 = E[(X - E[X])^2] = E[(dX)^2], \quad (\text{F.1})$$

where $dX = X - E[X]$ is an infinitesimal element.

The conventional uncertainty of p can therefore be given by the expression $\sigma_{p,C}^2 = E[(dp)^2]$. Using the expression for p we obtain

$$\begin{aligned} (dp)^2 &= \left(\frac{\partial p}{\partial Q} dQ + \frac{\partial p}{\partial U} dU + \frac{\partial p}{\partial I} dI \right)^2 \\ &= \left(\frac{\partial p}{\partial Q} \right)^2 (dQ)^2 + \left(\frac{\partial p}{\partial U} \right)^2 (dU)^2 + \left(\frac{\partial p}{\partial I} \right)^2 (dI)^2 + 2 \frac{\partial p}{\partial Q} \frac{\partial p}{\partial U} dQ dU + 2 \frac{\partial p}{\partial Q} \frac{\partial p}{\partial I} dQ dI + 2 \frac{\partial p}{\partial U} \frac{\partial p}{\partial I} dU dI, \end{aligned} \quad (\text{F.2})$$

where the partial derivatives are

$$\frac{\partial p}{\partial Q} = \frac{1}{2} \frac{2Q}{I\sqrt{Q^2+U^2}} = \frac{Q}{pI^2}, \quad \frac{\partial p}{\partial U} = \frac{1}{2} \frac{2U}{I\sqrt{Q^2+U^2}} = \frac{U}{pI^2}, \quad \text{and} \quad \frac{\partial p}{\partial I} = -\frac{\sqrt{Q^2+U^2}}{I^2} = -\frac{p}{I}. \quad (\text{F.3})$$

This leads to the following expression for the conventional uncertainty:

$$\begin{aligned} \sigma_{p,C}^2 &= \frac{1}{p^2 I^4} E \left[Q^2 (dQ)^2 + U^2 (dU)^2 + p^4 I^2 (dI)^2 + 2QU dQ dU - 2QI p^2 dQ dI - 2UI p^2 dU dI \right] \\ &= \frac{1}{p^2 I^4} \left(Q^2 E[(Q - E[Q])^2] + U^2 E[(U - E[U])^2] + p^4 I^2 E[(I - E[I])^2] \right. \\ &\quad \left. + 2QUE[(Q - E[Q])(U - E[U])] - 2QI p^2 E[(Q - E[Q])(I - E[I])] - 2UI p^2 E[(U - E[U])(I - E[I])] \right). \end{aligned} \quad (\text{F.4})$$

This finally leads to

$$\sigma_{p,C}^2 = \frac{1}{p^2 I^4} \left(Q^2 \sigma_Q^2 + U^2 \sigma_U^2 + p^4 I^2 \sigma_I^2 + 2QU \sigma_{QU} - 2IQ p^2 \sigma_{IQ} - 2IU p^2 \sigma_{IU} \right). \quad (\text{F.5})$$

Similarly we can derive an expression for the non-conventional uncertainty of the polarization angle, ψ , given by $\sigma_{\psi,C}^2 = E[(d\psi)^2]$. Using the expression of ψ , we obtain the partial derivatives

$$\frac{\partial \psi}{\partial U} = \frac{1}{2} \frac{Q}{Q^2 + U^2} \quad \text{and} \quad \frac{\partial \psi}{\partial Q} = -\frac{1}{2} \frac{U}{Q^2 + U^2}, \quad (\text{F.6})$$

as well as an expression for the conventional ψ uncertainty:

$$\begin{aligned} \sigma_{\psi,C}^2 &= E \left[\left(\frac{\partial \psi}{\partial U} dU + \frac{\partial \psi}{\partial Q} dQ \right)^2 \right] = E \left[\left(\frac{QdU - UdQ}{2p^2 I^2} \right)^2 \right] = E \left[\frac{Q^2 dU^2 + U^2 dQ^2 - 2QU dQ dU}{4p^4 I^4} \right] \\ &= \frac{Q^2 \sigma_{UU} + U^2 \sigma_{QQ} - 2QU \sigma_{QU}}{4p^4 I^4}. \end{aligned} \quad (\text{F.7})$$

Using Eq. (F.5) and assuming $\sigma_{II} = \sigma_{IQ} = \sigma_{IU} = 0$, we find

$$p^2 I^4 = \frac{Q^2 \sigma_Q^2 + U^2 \sigma_U^2 + 2QU \sigma_{QU}}{\sigma_{p,C}^2}, \quad (\text{F.8})$$

and replacing this expression in Eq. (F.7) finally leads to

$$\sigma_{\psi,C} = \sqrt{\frac{Q^2 \sigma_U^2 + U^2 \sigma_Q^2 - 2QU \sigma_{QU}}{Q^2 \sigma_Q^2 + U^2 \sigma_U^2 + 2QU \sigma_{QU}}} \times \frac{\sigma_{p,C}}{2p}. \quad (\text{F.9})$$

The above two expressions for the conventional estimates have been obtained in the small-error limit, and therefore they are formally inapplicable to the large uncertainty regime. In Sect. 4 we discuss the extent to which they can provide reasonable proxies for the errors, even at low S/N.

Polarization measurement analysis

II. Best estimators of polarization fraction and angle[★]

L. Montier^{1,2}, S. Plaszczyński³, F. Levrier⁴, M. Tristram³, D. Alina^{1,2}, I. Ristorcelli^{1,2}, J.-P. Bernard^{1,2}, and V. Guillet⁵

¹ Université de Toulouse, UPS-OMP, IRAP, 31028 Toulouse Cedex 4, France
e-mail: ludovic.montier@irap.omp.eu

² CNRS, IRAP, 9 Av. Colonel Roche, BP 44346, 31028 Toulouse Cedex 4, France

³ Laboratoire de l'Accélérateur Linéaire, Université Paris-Sud 11, CNRS/IN2P3, Orsay, France

⁴ LERMA/LRA-ENS Paris et Observatoire de Paris, 24 rue Lhormond, 75231 Paris Cedex 05, France

⁵ Institut d'Astrophysique Spatiale, CNRS (UMR8617), Université Paris-Sud 11, Bâtiment 121, Orsay, France

Received 23 June 2014 / Accepted 25 November 2014

ABSTRACT

With the forthcoming release of high precision polarization measurements, such as from the *Planck* satellite, it becomes critical to evaluate the performance of estimators for the polarization fraction and angle. These two physical quantities suffer from a well-known bias in the presence of measurement noise, as described in Part I of this series. In this paper, Part II of the series, we explore the extent to which various estimators may correct the bias. Traditional frequentist estimators of the polarization fraction are compared with two recent estimators: one inspired by a Bayesian analysis and a second following an asymptotic method. We investigate the sensitivity of these estimators to the asymmetry of the covariance matrix, which may vary over large datasets. We present for the first time a comparison among polarization angle estimators, and evaluate the statistical bias on the angle that appears when the covariance matrix exhibits effective ellipticity. We also address the question of the accuracy of the polarization fraction and angle uncertainty estimators. The methods linked to the credible intervals and to the variance estimates are tested against the robust confidence interval method. From this pool of polarization fraction and angle estimators, we build recipes adapted to different uses: the best estimators to build a mask, to compute large maps of the polarization fraction and angle, and to deal with low signal-to-noise data. More generally, we show that the traditional estimators suffer from discontinuous distributions at a low signal-to-noise ratio, while the asymptotic and Bayesian methods do not. Attention is given to the shape of the output distribution of the estimators, which is compared with a Gaussian distribution. In this regard, the new asymptotic method presents the best performance, while the Bayesian output distribution is shown to be strongly asymmetric with a sharp cut at a low signal-to-noise ratio. Finally, we present an optimization of the estimator derived from the Bayesian analysis using adapted priors.

Key words. polarization – methods: data analysis – methods: statistical

1. Introduction

The complexity of polarization measurement analysis has been described by [Serkowski \(1958\)](#) when discussing the presence of a systematic bias in optical measurements of linear polarization from stars, and then by [Wardle & Kronberg \(1974\)](#) when addressing the same issue in the field of radio astronomy. The bias of polarization measurements happens when one is interested in the polarization intensity $P \equiv \sqrt{Q^2 + U^2}$ or in the polarization fraction $p \equiv P/I$ and the polarization angle $\psi = \frac{1}{2} \text{atan}(U/Q)$ where I , Q , and U are the Stokes parameters, quantities that become systematically biased in the presence of noise. Working with the Stokes parameters Q and U as far as possible avoids this kind of bias.

Once a physical modelling of p and ψ is available and can be translated into Q and U , a likelihood analysis can be performed directly on the Stokes parameters. For the other cases, where no modelling is available, [Simmons & Stewart \(1985\)](#) proposed the first compilation and comparison of methods to deal with the problem of getting unbiased polarization estimates of the polarization fraction and angle, with their associated uncertainties. Then [Naghizadeh-Khouei & Clarke \(1993\)](#) extended the work of [Simmons & Stewart \(1985\)](#) to the characterization

of the polarization angle uncertainties, and [Vaillancourt \(2006\)](#) have proposed a method for building confidence limits on polarization fraction measurements.

More recently, [Quinn \(2012\)](#) has suggested using a Bayesian approach to get better polarization estimates. In all these studies, the authors have made strong assumptions: negligible or no noise on the intensity I and no correlation between the Q and U components, which were also assumed to have equal noise properties. [Montier et al. \(2015, hereafter PMA I\)](#) have quantified the impact of the asymmetry and the correlation between the Q and U noise components on the bias of the polarization fraction and angle measurements. They have shown that the asymmetry of the noise properties cannot be systematically neglected as is usually done and that the uncertainty of the intensity may significantly affect the polarization measurements in the low signal-to-noise (S/N) regime.

In the context of the new generation of polarization data, such as *Planck*¹ ([Planck Collaboration I 2011](#)), Blast-Pol (The Balloon-borne Large Aperture Submillimeter Telescope for

¹ *Planck* (<http://www.cosmos.esa.int/web/planck>) is a project of the European Space Agency (ESA) with instruments provided by two scientific consortia funded by ESA member states (in particular the lead countries France and Italy), with contributions from NASA (USA) and telescope reflectors provided by a collaboration between ESA and a scientific consortium led and funded by Denmark.

[★] Appendices are available in electronic form at <http://www.aanda.org>

$$f(I, p, \psi | I_0, p_0, \psi_0, \Sigma) = \frac{2|p|I^2}{\sqrt{(2\pi)^3}\sigma^3} \exp \left(-\frac{1}{2} \begin{bmatrix} I - I_0 \\ pI \cos 2\psi - p_0 I_0 \cos 2\psi_0 \\ pI \sin 2\psi - p_0 I_0 \sin 2\psi_0 \end{bmatrix}^T \Sigma^{-1} \begin{bmatrix} I - I_0 \\ pI \cos 2\psi - p_0 I_0 \cos 2\psi_0 \\ pI \sin 2\psi - p_0 I_0 \sin 2\psi_0 \end{bmatrix} \right), \quad (1)$$

$$f_{2D}(p, \psi | I_0, p_0, \psi_0, \Sigma_p) = \frac{p}{\pi\sigma_p^2} \exp \left(-\frac{1}{2} \left(p^2 \begin{bmatrix} \cos 2\psi \\ \sin 2\psi \end{bmatrix}^T \Sigma_p^{-1} \begin{bmatrix} \cos 2\psi \\ \sin 2\psi \end{bmatrix} - 2pp_0 \begin{bmatrix} \cos 2\psi \\ \sin 2\psi \end{bmatrix}^T \Sigma_p^{-1} \begin{bmatrix} \cos 2\psi_0 \\ \sin 2\psi_0 \end{bmatrix} + p_0^2 \begin{bmatrix} \cos 2\psi_0 \\ \sin 2\psi_0 \end{bmatrix}^T \Sigma_p^{-1} \begin{bmatrix} \cos 2\psi_0 \\ \sin 2\psi_0 \end{bmatrix} \right) \right). \quad (2)$$

Polarimetry, Fissel et al. 2010), PILOT (Bernard et al. 2007), or ALMA (Pérez-Sánchez & Vlemmings 2013), which benefit from much better control of the noise properties, it is essential to take the full covariance matrix into account when deriving the polarization measurement estimates. In recent works no correction for the bias of the polarization fraction has been applied (e.g., Dotson et al. 2010), or only high S/N data were used for analysis (>3) to avoid these issues (e.g., Vaillancourt & Matthews 2012). Two issues are immediately apparent. First, this choice of the S/N threshold may not be relevant for all measurements, and the asymmetry between the orthogonal Stokes noise components could affect the threshold choice. Second, the question remains of how to deal with low S/N data. Using simply the measurements of the polarization parameters (we call them the “naïve” ones) as estimators of the true values leads to very poor performance, because they lack any information on the noise power. Instead, we would like to perform some transformation on the polarization parameters, in order to remove bias and improve the variance.

This work is the second in a series on “Polarization measurement analysis”. Its aim is to describe how to recover the true polarization fraction p_0 and polarization angle ψ_0 with their associated uncertainties from a measurement (p, ψ) , taking the full covariance matrix Σ into account. We compare the performance of the various estimators that are available and study the impact of the correlation and ellipticity of the covariance matrix on these estimates. We stress that we adopt a frequentist approach to investigate the properties of these estimators, even when dealing with the method inspired by the Bayesian analysis. This means that the estimators are defined as single-value estimates, instead of considering the probability density function (PDF) as the proper estimate, as is usually done in Bayesian methods. The performance of these estimators will be evaluated using three main criteria: the minimum bias, the smallest risk function, and the shape of the distribution of the output estimates. The choice of the most appropriate estimator may vary with the application at hand, and a compromise among them may be chosen to achieve good overall performance. Throughout this work we make the following two assumptions: i) circular polarization is assumed to be negligible; and ii) the noise on Stokes parameters is assumed to be Gaussian. We also define four regimes of the covariance matrix to quantify its asymmetry in terms of effective ellipticity (ε_{eff}) as described in PMA I: the *extreme* ($1 < \varepsilon_{\text{eff}} < 2$), the *low* ($1 < \varepsilon_{\text{eff}} < 1.1$), the *tiny* ($1 < \varepsilon_{\text{eff}} < 1.01$), and the *canonical* ($\varepsilon_{\text{eff}} = 1$) regimes.

The paper is organized as follows. We first review in Sect. 2 the expression and the limitations of the polarization estimators, which are extended to take the full covariance matrix into account. In Sect. 3, we discuss the meaning of the polarization uncertainties and present the different uncertainty estimators. We then compare the performance of the estimators of the polarization fraction in Sect. 4 and of the polarization angle in Sect. 5. In Sect. 6, we discuss some aspects of the problem when the total intensity I is not perfectly known. We conclude with general recipes in Sect. 7.

2. Polarization estimators

Early work on polarization estimators was based on the Rice (1945) distribution, which provides the probability of finding a measurement p for a given true value p_0 and the noise estimate σ_p of the Q and U Stokes parameters. The noise values of the Stokes parameters were assumed to be equal ($\sigma_p = \sigma_Q/I_0 = \sigma_U/I_0$), and the total intensity was assumed to be perfectly known, $I = I_0$. Since we would like to include the full covariance matrix, we used the generalized expression of the PDF from PMA I, which provides the probability of getting the measurements (I, p, ψ) , given the true values (I_0, p_0, ψ_0) and the covariance matrix Σ . Following the notations of PMA I, the expression of the PDF in 3D, including the intensity terms, denoted $f(I, p, \psi | I_0, p_0, \psi_0, \Sigma)$, is given by Eq. (1), where $\text{Det}(\Sigma) = \sigma^6$, and the PDF in 2D, $f_{2D}(p, \psi | I_0, p_0, \psi_0, \Sigma_p)$, by Eq. (2) when the intensity I_0 is assumed to be perfectly known. We introduced the covariance matrix reduced in 2D,

$$\Sigma_p = \frac{1}{I_0^2} \begin{pmatrix} \sigma_Q^2 & \sigma_{QU} \\ \sigma_{QU} & \sigma_U^2 \end{pmatrix} = \frac{\sigma_{p,G}^2}{\sqrt{1-\rho^2}} \begin{pmatrix} \varepsilon & \rho \\ \rho & 1/\varepsilon \end{pmatrix}, \quad (3)$$

where $\varepsilon = \sigma_Q/\sigma_U$ is the ellipticity and $\rho = \sigma_{QU}/\sigma_Q\sigma_U$ is the correlation between the Q and U noise components, leading to an effective ellipticity given by

$$\varepsilon_{\text{eff}} = \sqrt{\frac{1 + \varepsilon^2 + \sqrt{(\varepsilon^2 - 1)^2 + 4\rho^2\varepsilon^2}}{1 + \varepsilon^2 - \sqrt{(\varepsilon^2 - 1)^2 + 4\rho^2\varepsilon^2}}}. \quad (4)$$

With these notations, we have $\text{Det}(\Sigma_p) = \sigma_{p,G}^4$ and

$$\sigma_{p,G}^2 = \frac{\sigma_Q^2}{I_0^2} \frac{\sqrt{1-\rho^2}}{\varepsilon}, \quad (5)$$

which represents the equivalent radius of a circular Gaussian distribution with the same integrated area as the elliptical one. We also define $\sigma_p = \sigma_Q/I_0 = \sigma_U/I_0$ when $\varepsilon_{\text{eff}} = 1$. Finally the PDFs of p and ψ , f_p , and f_ψ are obtained by marginalization of f_{2D} over ψ and p , respectively. The expressions for the 1D PDFs f_p and f_ψ depend on the full set of initial parameters (I_0, p_0, ψ_0) in the general case, unlike the case under the canonical simplifications (see Appendix C of PMA I for fully developed analytical expressions).

We describe below the various estimators of the polarization fraction and angle listed in Table 1. We stress that most of the expressions derived in this work have been obtained when restricting the analysis in the 2D case, assuming furthermore that the true intensity I_0 is perfectly known, except for the Bayesian estimator where we present a 3D development (see Sect. 6).

2.1. Maximum likelihood estimators

The maximum likelihood (ML) estimators are defined as the values of p_0 and ψ_0 that maximize the PDF calculated at the polarization measurements p and ψ . When computed using the 2D PDF f_{2D} to fit p_0 and ψ_0 simultaneously, this estimator gives

Table 1. List of the acronyms of the estimators used in this work.

Acronym	Description	Parameters
ML	Maximum likelihood	p/ψ
MP	Most probable in 1D	p/ψ
MP2	Most probable in 2D	p & ψ
AS	Asymptotic	p
MAS	Modified asymptotic	p
MAP	Maximum a posteriori	p/ψ
MAP2	Maximum a posteriori in 2D	p & ψ
MB	Mean posterior Bayesian	I & p & ψ

Notes. The parameters to which each estimator applies, independently (/) or simultaneously (&), are given in the last column.

back the measurements, regardless of the bias and the covariance matrix, and is inefficient at correcting the bias of the data.

After marginalization of the PDF f_{2D} over ψ , the 1D ML estimator of p_0 , \hat{p}_{ML} , is now defined by

$$0 = \frac{\partial f_p}{\partial p_0} (p | p_0, \psi_0, \Sigma_p) \Big|_{p_0 = \hat{p}_{ML}}. \quad (6)$$

The expression of f_p is independent of the measurement ψ , but it still theoretically depends on the true value ψ_0 , which is unknown. In the canonical case ($\epsilon_{\text{eff}} = 1$), ψ_0 disappears from the expression, but it must be considered as a nuisance parameter in the general case. One way to proceed in such a case is to compute the mean of the solutions \hat{p}_{ML} for ψ_0 varying in the range $-\pi/2$ to $\pi/2$. As already stressed by [Simmons & Stewart \(1985\)](#), this estimator yields a zero estimate below a certain threshold of the measurement p , which implies a strong discontinuity in the resulting distribution of this p_0 estimator. Nevertheless, unlike the 2D ML estimators, the p ML estimator does not give back the initial measurements, and is often used to build polarization estimates.

Similarly, the 1D ML estimator of ψ_0 , $\hat{\psi}_{ML}$, is given after marginalization of f_{2D} over p by

$$0 = \frac{\partial f_\psi}{\partial \psi_0} (\psi | p_0, \psi_0, \Sigma_p) \Big|_{\psi_0 = \hat{\psi}_{ML}}. \quad (7)$$

As mentioned for the ML estimator \hat{p}_{ML} , the unknown parameter p_0 in the above expression has to be considered as a nuisance parameter when solving Eq. (7). We stress that because the canonical simplifications have always been assumed in the literature, bias on the ψ measurements has not been previously considered, and the $\hat{\psi}_{ML}$ estimator has not yet been used and qualified to correct this kind of bias. This analysis is done in Sect. 5.

2.2. Most probable estimators

The most probable (MP) estimators of p_0 and ψ_0 are the values for which the PDF f_{2D} reaches its maximum at the measurement values (p, ψ) . The MP estimators ensure that the measurement values (p, ψ) are the most probable values of the PDF computed for this choice of p_0 and ψ_0 ; i.e., they take the maximum probability among all possible measurements with this set of p_0 and ψ_0 . As a comparison, the ML estimators ensure that the measurement values (p, ψ) take the maximum probability for this choice of p_0 and ψ_0 compared to the probability of the same measurement values (p, ψ) for all other possible sets of p_0 and ψ_0 .

The 2D MP estimators (MP2), \hat{p}_{MP2} and $\hat{\psi}_{MP2}$, are defined as the values of p_0 and ψ_0 simultaneously satisfying the two following relations:

$$0 = \frac{\partial f_{2D}}{\partial p} (p, \psi | p_0, \psi_0, \Sigma_p) \Big|_{\substack{p_0 = \hat{p}_{MP2} \\ \psi_0 = \hat{\psi}_{MP2}}} \quad (8)$$

and

$$0 = \frac{\partial f_{2D}}{\partial \psi} (p, \psi | p_0, \psi_0, \Sigma_p) \Big|_{\substack{p_0 = \hat{p}_{MP2} \\ \psi_0 = \hat{\psi}_{MP2}}}. \quad (9)$$

These relations can be solved using the fully developed expression of f_{2D} , including the terms of the inverse matrix Σ_p^{-1} , as provided in Appendix A. When canonical simplifications are assumed, this yields

$$\begin{aligned} \hat{\psi}_{MP2} &= \psi, \\ \hat{p}_{MP2} &= \begin{cases} p - \sigma_p^2/p & \text{for } p > \sigma_p \\ 0 & \text{for } p \leq \sigma_p, \end{cases} \end{aligned} \quad (10)$$

as found in [Wang et al. \(1997\)](#) and [Quinn \(2012\)](#). We observe that the MP2 estimate of the polarization fraction is systematically lower than the measurements, so that this estimator tends to over-correct p , as shown in Sect. 4.

After marginalization over p or ψ , the 1D MP estimators, \hat{p}_{MP} and $\hat{\psi}_{MP}$, are defined independently by

$$0 = \frac{\partial f_p}{\partial p} (p | p_0, \psi_0, \Sigma_p) \Big|_{p_0 = \hat{p}_{MP}} \quad (11)$$

and

$$0 = \frac{\partial f_\psi}{\partial \psi} (\psi | p_0, \psi_0, \Sigma_p) \Big|_{\psi_0 = \hat{\psi}_{MP}}. \quad (12)$$

The 1D and 2D estimators are not expected to provide the same estimates. Under the canonical assumptions, the MP estimator of p is commonly known as the [Wardle & Kronberg \(1974\)](#) estimator.

As mentioned earlier, the MP estimator yields a zero estimate below a certain threshold of p ([Simmons & Stewart 1985](#)), which implies a strong discontinuity in the resulting distribution of these estimators for low S/N measurements.

2.3. Asymptotic estimator

The asymptotic estimator (AS) of the polarization fraction p is usually defined in the canonical case by

$$\hat{p}_{AS} = \begin{cases} \sqrt{p^2 - \sigma_p^2} & \text{for } p > \sigma_p \\ 0 & \text{for } p \leq \sigma_p. \end{cases} \quad (13)$$

The output distribution of the AS estimator appears as the asymptotic limit of the [Rice \(1945\)](#) distribution when p/σ_p tends to ∞ , just as for the ML and MP estimators, and given by

$$\text{PDF} \left(\frac{p}{\sigma_p} \right) \rightarrow \mathcal{N} \left(\sqrt{\left(\frac{p_0}{\sigma_p} \right)^2 + 1}, 1 \right), \quad (14)$$

where $\mathcal{N}(\mu, \sigma)$ denotes the Gaussian distribution of mean μ and variance σ^2 . As with the previously presented estimators, this one suffers from a strong discontinuity at $\hat{p}_{AS} = 0$.

In the general case, when the canonical simplification is not assumed, it has been shown by [Płaszczynski et al. \(2014, hereafter P14\)](#) that the expression of the asymptotic estimator can be extended to a general expression by changing the term σ_p^2 in Eq. (13) into a “noise-bias” parameter b^2 defined by

$$b^2 = \frac{\sigma_U^2 \cos^2(2\psi_0 - \theta) + \sigma_Q^2 \sin^2(2\psi_0 - \theta)}{I_0^2}, \quad (15)$$

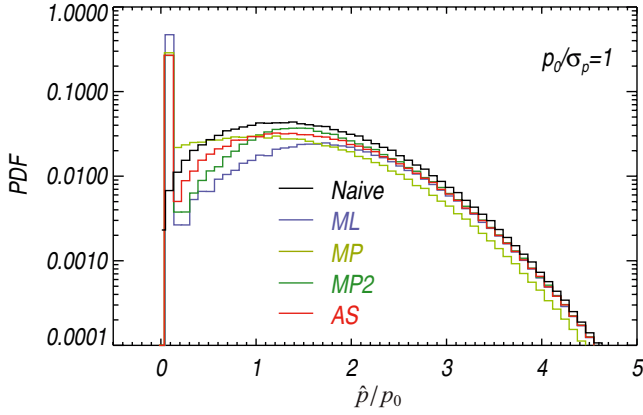


Fig. 1. Distributions of \hat{p} estimates obtained with the standard estimators: naïve (black), ML (blue), MP (light green), MP2 (green), and AS (red). We assume the covariance matrix to be canonical, and a S/N of $p_0/\sigma_p = 1$. Based on 100 000 Monte-Carlo simulations with an initial value of $p_0 = 1\%$.

where θ represents the position angle of the iso-probability bivariate distribution, and σ_Q^2, σ_U^2 the rotated variances

$$\theta = \frac{1}{2} \operatorname{atan} \left(\frac{2\rho\sigma_Q\sigma_U}{\sigma_Q^2 - \sigma_U^2} \right), \quad (16)$$

$$\sigma_Q^2 = \sigma_Q^2 \cos^2 \theta + \sigma_U^2 \sin^2 \theta + \rho\sigma_Q\sigma_U \sin 2\theta, \quad (17)$$

$$\sigma_U^2 = \sigma_Q^2 \sin^2 \theta + \sigma_U^2 \cos^2 \theta - \rho\sigma_Q\sigma_U \sin 2\theta, \quad (18)$$

and ψ_0 is the true polarization angle, which can be approximated asymptotically by the naïve measurement ψ or, even better, by the estimate ψ_{ML} of Sect. 2.1. It has been shown that b^2 ensures the minimal bias of \hat{p}_{AS} .

2.4. Discontinuous estimators

The estimators of \hat{p} introduced above (ML, MP, and AS) exhibit a common feature: below some cutoff value the estimator yields exactly zero. This means that the estimator distribution is discontinuous and is a mixture of a discrete one (at $\hat{p} = 0$) and a continuous one (for $\hat{p} > 0$). This type of distribution is illustrated in Fig. 1 for a S/N of $p_0/\sigma_p = 1$ and a canonical covariance matrix. The distribution of the naïve measurements is built using 100 000 Monte-Carlo simulations, starting from true polarization parameters p_0 and ψ_0 . The other three distributions of \hat{p} are obtained after applying the ML, MP and AS estimators. A non-negligible fraction of the measurements provide null estimates of \hat{p} . As shown in Fig. 2, this fraction of null estimates reaches 40% at low S/N with the MP and AS estimators, and more than 50% with the ML estimator for $S/N < 1$. It converges to 0% for $S/N > 4$.

If taken into account as a reliable estimate of \hat{p} , null estimates will somewhat artificially lower the statistical bias of the \hat{p} estimates compared to the true value p_0 , as explained in Sect. 4. A null value of these estimators should be understood as an indicator of the low S/N of this measurement, which actually has to be included in any further analysis as an upper limit value. In practice, the user seldom has various realizations at hand. Using these estimators then leads to a result with upper limits mixed with non-zero estimates in the analysis. Such complications may be especially hard to handle when studying polarized maps of the interstellar medium. On the other hand, it would be disastrous to omit those estimates in any statistical analysis, since weakly polarized points would be systematically rejected. To avoid such

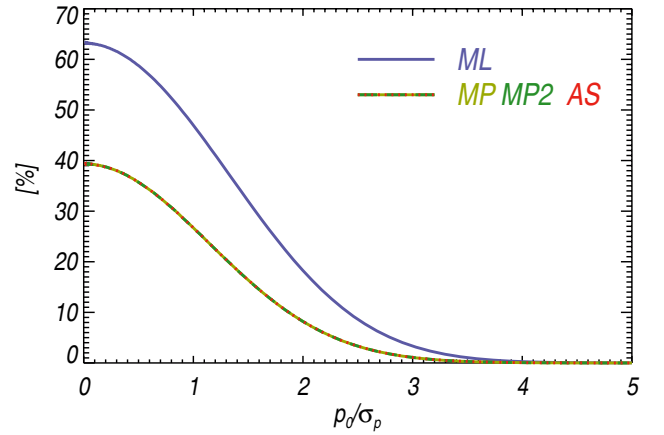


Fig. 2. Statistical fraction of null estimates of \hat{p} provided by the ML, MP, MP2, and AS estimators applied to 100 000 Monte-Carlo measurements, as a function of the S/N in the canonical case.

complications, we explore below other estimators that avoid this issue and lead to continuous distributions. This is especially important in the range of S/N between 2 and 3, where the discontinuous estimators still yield up to 20% of null estimates.

2.5. Modified asymptotic estimator

A novel asymptotic estimator has been introduced by P14 to eliminate the discontinuous distribution of the standard estimators while still keeping the asymptotic properties. It has been derived from the first-order development of the asymptotic estimator, which has been modified to ensure positivity, smoothness, and asymptotical convergence at high S/N. The modified asymptotic (MAS) estimator is defined as

$$\hat{p}_{\text{MAS}} = p - b^2 \cdot \frac{1 - e^{-p^2/b^2}}{2p}, \quad (19)$$

where the “noise-bias” b^2 is given by Eq. (15) and computed using a polarization angle assessed from each sample using the asymptotic estimator ψ .

P14 also provides a sample estimate of the variance of the estimator that is shown to represent asymptotically the absolute risk function (defined in Sect. 3.1) of the estimator:

$$\sigma_{\hat{p}, \text{MAS}}^2 = \frac{\sigma_Q^2 \cos^2(2\psi - \theta) + \sigma_U^2 \sin^2(2\psi - \theta)}{I_0^2}. \quad (20)$$

This estimator focuses on getting a “good” distribution, which transforms smoothly from a Rayleigh-like to a Gaussian one, the latter being reached in the canonical case for a S/N of about 2.

2.6. Bayesian estimators

The PDFs introduced in Sect. 2 provide the probability of observing a set of polarization measurements (I, p, ψ) given the true polarization parameters (I_0, p_0, ψ_0) and the covariance matrix Σ . Because we are interested in the opposite, i.e., getting an estimate of the true polarization parameters given a measurement and knowledge of the noise properties, we use the Bayes theorem to build the posterior distribution. The posterior PDF B is given in the 3D case by

$$B(I_0, p_0, \psi_0 | I, p, \psi, \Sigma) = \frac{f(I, p, \psi | I_0, p_0, \psi_0, \Sigma) \cdot \kappa(I_0, p_0, \psi_0)}{\int_0^{+\infty} \int_0^1 \int_{-\pi/2}^{\pi/2} f(I, p, \psi | I'_0, p'_0, \psi'_0, \Sigma) \kappa(I'_0, p'_0, \psi'_0) d\psi'_0 dp'_0 dI'_0}, \quad (21)$$

$$B(I_0, p_0, \psi_0 | I, p, \psi, \Sigma) \propto \sqrt{\frac{\text{Det}(\Sigma^{-1})}{2\pi^3}} \exp \left\{ -\frac{1}{2} \begin{bmatrix} p I \cos(2\psi) - p_0 I_0 \cos(2\psi_0) \\ p I \sin(2\psi) - p_0 I_0 \sin(2\psi_0) \end{bmatrix}^T \Sigma^{-1} \begin{bmatrix} p I \cos(2\psi) - p_0 I_0 \cos(2\psi_0) \\ p I \sin(2\psi) - p_0 I_0 \sin(2\psi_0) \end{bmatrix} \right\}, \quad (22)$$

$$B_{2D}(p_0, \psi_0 | p, \psi, \Sigma_p) \propto \frac{1}{\pi \sigma_{p,G}^2} \exp \left\{ -\frac{1}{2} \begin{bmatrix} p \cos(2\psi) - p_0 \cos(2\psi_0) \\ p \sin(2\psi) - p_0 \sin(2\psi_0) \end{bmatrix}^T \Sigma_p^{-1} \begin{bmatrix} p \cos(2\psi) - p_0 \cos(2\psi_0) \\ p \sin(2\psi) - p_0 \sin(2\psi_0) \end{bmatrix} \right\}. \quad (24)$$

where $\kappa(I_0, p_0, \psi_0)$ is the prior distribution, which represents the a priori knowledge of the true polarization parameters and has to be non-negative everywhere. When no a priori knowledge is provided, we have to properly define a non-informative prior, which encodes the ignorance of the prior. A class of non-informative priors is given by the Jeffreys' prior (Jeffrey 1939) where the ignorance is defined under symmetry transformations that leave the prior invariant. As discussed by Quinn (2012) for the 2D case, this kind of prior can be built as a uniform prior in cartesian space (Q_0, U_0) , but it will lead to an under-sampling of the low values of p in polar space (p_0, ψ_0) . However, for the last reason, we prefer a uniform prior in polar space, which ensures uniform sampling even for low values of p_0 , but which can no longer be considered as a non-informative prior. While p_0 and ψ_0 are only defined on a finite range $([0, 1]$ and $[-\pi/2, \pi/2])$, respectively, the intensity I_0 may be infinite in theory, which leads to a problem when defining the ignorance prior. In practice, an approximation of the ignorance prior for I_0 will be chosen as a top hat centred on the measurement I and chosen to be wide enough to cover the wings of the distribution until it becomes negligible. Such uniform priors lead to the expression of B given in Eq. (22), where the normalization factor has been omitted. We emphasize that the definition of the ignorance prior introduced above becomes data-dependent, which does not strictly follow the Bayesian approach. Furthermore, the question of the definition range of the prior and the introduction of non-flat priors are discussed in Sect. 4.3 in the context of comparing the performance of the estimators inspired by the Bayesian approach.

Similarly, the posterior PDF in 2D (i.e., when the total intensity is perfectly known, $I = I_0$) is defined by

$$B_{2D}(p_0, \psi_0 | p, \psi, \Sigma_p) = \frac{f_{2D}(p, \psi | p_0, \psi_0, \Sigma_p) \cdot \kappa(p_0, \psi_0)}{\int_0^1 \int_{-\pi/2}^{+\pi/2} f_{2D}(p, \psi | p'_0, \psi'_0, \Sigma_p) \kappa(p'_0, \psi'_0) d\psi'_0 dp'_0}. \quad (23)$$

The analytical expressions of the posterior PDF B_{2D} with a flat prior is given in Eq. (24), where the normalization factors have been omitted, and the intensity has been assumed to be perfectly known. Illustrations of this posterior PDF are presented in Appendix B. We also introduce B_p and B_ψ , the Bayesian posterior PDFs of p and ψ in 1D, respectively, and defined as the marginalization of B_{2D} over ψ and p , respectively. We use the Bayesian posterior PDFs to build two frequentist estimators: the MAP and the MB.

The MAP2 and MAP estimators in 2D and 1D, respectively, are simply defined as the (p_0, ψ_0) values corresponding to the maximum of the posterior PDF, B_{2D} , and B_p and B_ψ , respectively. We recall that these estimators match the ML estimators of Sect. 2 in one and two dimensions exactly, respectively, when a uniform prior is assumed. As a result, the MAP2 estimators yield back the polarization measurements, whereas the MAP estimators provide a simple way to compute the ML estimates.

The mean Bayesian posterior (MB) estimators are defined as the first-order moments of the posterior PDF:

$$\hat{p}_{\text{MB}} \equiv \int_{-\pi/2}^{+\pi/2} \int_0^1 p_0 B_{2D}(p_0, \psi_0 | p, \psi, \Sigma_p) dp_0 d\psi_0 \quad (25)$$

and

$$\hat{\psi}_{\text{MB}} \equiv \int_{-\pi/2}^{+\pi/2} \int_0^1 \psi_0 B_{2D}(p_0, \psi_0 | p, \psi, \Sigma_p) dp_0 d\psi_0. \quad (26)$$

In the definition of $\hat{\psi}_{\text{MB}}$, the integral over ψ_0 is performed over a range centred on the measurement ψ . This has to be done to take the circularity of the posterior PDF over the ψ_0 dimension into account (see also Quinn 2012, when dealing with the circularity of the polarization angle). We note that $B_{2D}(p_0, \psi_0 | p, \psi, \Sigma_p) = B_{2D}(p_0, \psi_0 + \pi | p, \psi, \Sigma_p)$.

The frequentist estimators inspired by a Bayesian approach, \hat{p}_{MB} and $\hat{\psi}_{\text{MB}}$, introduced above in the 2D case can be easily extended to the 3D case by integrating the PDF $B(I_0, p_0, \psi_0 | I, p, \psi, \Sigma)$ of Eq. (21) over the I , p , and ψ dimensions. This is extremely powerful when the uncertainty of the intensity I has to be taken into account in the estimate of the polarization parameters, which is highly recommended in some circumstances, such as a low S/N on I (<5) or the presence of an unpolarized component on the line of sight (see Sect. 6 and PMA I for more details).

3. Uncertainties

We introduce here the various estimates of the uncertainty associated with a polarization measurement, making a clear distinction between the notions of variance and risk function. We emphasize the difference between two approaches: one based on the posterior uncertainties and the second based on confidence intervals.

3.1. Variance and risk function

It is important not to confuse the variance (noted V) of an estimator with its absolute risk function (noted R). For any distribution of the random variable X the definitions are

$$V \equiv E[(X - E[X])^2] \quad \text{and} \quad (27)$$

$$R \equiv E[(X - X_0)^2], \quad (28)$$

where $E[X]$ is the expectation of the random variable X and X_0 is the true value. Introducing the absolute bias, B , in $E[X] = X_0 + B$ and expanding both relations, the link between the variance and the absolute risk function is simply

$$V = R - B^2. \quad (29)$$

Therefore, for a constant absolute risk function, the variance decreases with the absolute bias, and both are equal when the estimator is unbiased. The variance does not require knowing

the true value of the random variable, which makes it useful to provide an uncertainty estimate, but it has to be used extremely carefully in the presence of bias. In such cases, the variance will always underestimate the uncertainty.

Furthermore, it is known that the variance is not appropriate for providing uncertainties with non-Gaussian distributions, which is the case for the polarization fraction and angle. In such circumstances, confidence intervals (see Sect. 3.3) are the preferred method for obtaining robust uncertainties. The variance, however, is often used as a proxy of the uncertainty in the high regime of the S/N. In Sects. 4.5 and 5.3, we detail the conditions under which this can still be applied.

3.2. Posterior uncertainties

One of the main benefits of the Bayesian approach is to provide simple estimates of the uncertainties associated with the polarization estimates. One option is to build credible intervals around the MAP estimates as it has been discussed by Vaillancourt (2006) or also Quinn (2012), and the other option is to use the variance of the PDF.

Given a polarization measurement (p, ψ) and the posterior PDF $B_{2D}(p_0, \psi_0 | p, \psi, \Sigma_p)$, the lower and upper limits of the $\lambda\%$ credible intervals are defined as the lower and upper limits of p_0 and ψ_0 for the iso-probability region $\Omega(\lambda, p, \psi)$ over which the integral of B equals $\lambda\%$, so that

$$\iint_{\Omega(\lambda, p, \psi)} B_{2D}(p_0, \psi_0 | p, \psi, \Sigma_p) dp_0 d\psi_0 = \frac{\lambda}{100}. \quad (30)$$

These intervals, $[p_{\text{MAP2}}^{\text{low}}, p_{\text{MAP2}}^{\text{up}}]$ and $[\psi_{\text{MAP2}}^{\text{low}}, \psi_{\text{MAP2}}^{\text{up}}]$, estimated from the 2D expression of B_{2D} , are defined around the MAP2 estimates \hat{p}_{MAP2} and $\hat{\psi}_{\text{MAP2}}$, which are equal to the measurements (p, ψ) . It has to be noticed that, in general, 2D intervals are not uniquely defined (see Eq. (32) of PMA I).

A similar definition can be given in the 1D case, which leads to different results. The lower and upper limits, $p_{\text{MAP}}^{\text{low}}$ and $p_{\text{MAP}}^{\text{up}}$, around \hat{p}_{MAP} are defined as

$$\int_{p_{\text{MAP}}^{\text{low}}}^{p_{\text{MAP}}^{\text{up}}} B_p(p_0 | p, \Sigma_p) dp_0 = \frac{\lambda}{100}, \quad (31)$$

with the constraint that the posterior probability function is identical for $p_{\text{MAP}}^{\text{low}}$ and $p_{\text{MAP}}^{\text{up}}$. Similarly, the lower and upper limits, $\psi_{\text{MAP}}^{\text{low}}$ and $\psi_{\text{MAP}}^{\text{up}}$, around $\hat{\psi}_{\text{MAP}}$ are given by

$$\int_{\psi_{\text{MAP}}^{\text{low}}}^{\psi_{\text{MAP}}^{\text{up}}} B_\psi(\psi_0 | \psi, \Sigma_p) d\psi_0 = \frac{\lambda}{100}. \quad (32)$$

We recall that this integral has to be computed around the measurement value $\hat{\psi}_{\text{MAP}}$ to take the circularity of the posterior PDF with the polarization angle into account. The credible intervals built in 1D or 2D are not supposed to be identical, because $(\hat{p}_{\text{MAP2}}, \hat{\psi}_{\text{MAP2}})$ and $(\hat{p}_{\text{MAP}}, \hat{\psi}_{\text{MAP}})$ are not equal in the general case.

The second definition of the uncertainty comes from the second moment of the 1D posterior probability density functions B_p and B_ψ , as follows:

$$\sigma_{p, \text{MB}}^2 \equiv \int_0^1 (p_0 - \hat{p}_{\text{MB}})^2 B_p(p_0 | p, \Sigma_p) dp_0 \quad (33)$$

and

$$\sigma_{\psi, \text{MB}}^2 \equiv \int_{\psi - \pi/2}^{\psi + \pi/2} (\psi_0 - \hat{\psi}_{\text{MB}})^2 B_\psi(\psi_0 | \psi, \Sigma_p) d\psi_0. \quad (34)$$

The operation of subtraction between the two polarization angles must be done with care, restricting the maximum distance to $\pi/2$. At very low S/N, i.e., an almost flat uniform PDF, the uncertainty reaches the upper limit $\sigma_{\psi, \text{MB}} \leq \pi/\sqrt{12}$ rad = 51.96° . We stress that these 1σ estimates may not be associated with the usual 68% confidence intervals of the normal distribution, because of the asymmetric shape of the posterior distribution and because of the circularity of the angular variable.

3.3. Confidence intervals

So far we have considered point estimation of the true p_0 value which is somewhat tricky in the low S/N regime because of the non-Gaussian nature of the estimator distribution. A different approach that takes the entire shape of the distribution into account is to build confidence regions (or intervals), which allows bounds on the true value to be obtained at some significance level given an estimator value.

Simmons & Stewart (1985) have built the so-called Neyman “confidence belt” for the naïve estimator in the canonical case. PMA I proposed the construction of 2D (p_0, ψ_0) intervals, for the general covariance matrix case. The classical construction suffers from a standard problem: at very low S/N the confidence interval lies entirely in the unphysical $p < 0$ region, and both previous studies provide over-conservative regions.

P14 has implemented the Feldman-Cousins prescription (Feldman & Cousins 1998), which is based on using a likelihood ratio criterium in the Neyman construction. This allows building intervals that always lie in the physical region without ever being conservative. They provided these intervals for the MAS estimator, including analytical approximations to the upper and lower limits for 68%, 95%, and 99.5% significance levels.

4. \hat{p} estimator performance

We investigate in this section the capability of providing polarization fraction estimates with low bias using the seven \hat{p} estimators introduced in the previous sections: the naïve measurement p , the ML, the MP and MP2, the AS, the MAS, and the MB estimators. Their performance is first quantified in terms of relative bias and the risk function of the resulting estimates.

4.1. Methodology

Given true polarization parameters (p_0, ψ_0) and a covariance matrix Σ_p , we build a sample of one million simulated measurements (p, ψ) by adding noise on the true Stokes parameters using the covariance matrix. We define the relative bias and risk function on p as

$$\text{Bias}_p \equiv \frac{\langle \hat{p} \rangle - p_0}{\sigma_{p,G}} \quad \text{and} \quad \text{Risk}_p \equiv \frac{\langle (\hat{p} - p_0)^2 \rangle}{\sigma_{p,G}^2}, \quad (35)$$

where \hat{p} is the polarization fraction estimate computed on the simulated measurements p , p_0 is the true polarization fraction, $\langle \rangle$ denotes the average computed over the simulated sample, and $\sigma_{p,G}$ is the estimate of the noise of the polarization fraction. The choice of $\sigma_{p,G}$ to scale the absolute bias and risk function, as a proxy of the \hat{p} uncertainty, is motivated by the fact that it only depends on the effective ellipticity and not on ψ_0 . This choice can lead to a relative risk function falling below 1 at low S/N, because $\sigma_{p,G}^2 > V$ (variance, see Eq. (27)) in this regime. The accuracy of the p estimators is also quantified regarding the shape

of their output distributions. We use the Jarque-Bera estimator (Jarque & Bera 1980) as a test of normality of the output distribution, and defined by

$$JB = \frac{n}{6} \left(\frac{\mu_3^2}{\mu_2^3} + \left(\frac{\mu_4}{\mu_2^2} - 3 \right) / 4 \right), \quad (36)$$

where n is the number of samples and μ_i is the naïve estimate of the i th central moment of the distribution. This test is based on the joint hypothesis of the skewness and the excess kurtosis being zero simultaneously. A value $JB = 0$ means a perfect agreement with normality to fourth order, but does not prevent departure from normality at higher orders. This JB estimator tends to a χ^2 test with two degrees of freedom when n becomes large enough. The JB therefore has to satisfy the condition $JB < \chi_{\alpha}^2$ once a significance level α is chosen. For a significance level $\alpha = 5\%$ and 1% , we get the conditions $JB < 5.99$ and $JB < 9.21$, respectively.

4.2. Canonical case

We first assume the canonical simplification of the covariance matrix ($\varepsilon_{\text{eff}} = 1$). The relative Bias _{p} and Risk _{p} quantities are shown in Fig. 3 for the seven \hat{p} estimators and estimated using 100 000 Monte-Carlo simulations. We recall that the discontinuous estimators have an output distribution presenting a strong peak at zero, which artificially lowers the statistical relative Bias _{p} when simply including null values instead of using upper limits, as discussed in Sect. 2.4. Actually, these estimators show the lowest relative biases (top panel of Fig. 3) compared to the MAS and MB estimators. The ML and MP2 estimators thus seem to statistically over-correct the data, below $S/N = 3$. Consequently, the ML, MP, and AS \hat{p} estimators have to be used with extreme care to deal with null estimates. We suggest focusing on the two continuous estimators, MAS and MB.

MAS provides the better performances in terms of relative bias over the whole range of S/N, while MB appears less and less efficient at correcting the bias when the S/N tends to zero. At higher S/N (>2), MB tends to slightly over-correct with a small negative relative bias (2% of σ_p) up to $S/N \sim 5$, while MAS converges quickly to a null relative bias for $S/N > 3$.

The MB estimator clearly minimizes the risk function in the range $0.7 < S/N < 3.2$ (see middle panel of Fig. 3), as expected for this kind of posterior estimator. At higher S/N (>3.2), both MAS and MB have roughly the same behaviour, even if the risk function associated to MAS appears slightly lower.

The resulting \hat{p}_{MB} distribution is highly asymmetric at low S/N (see top panel of Fig. 4), with a sharp cutoff at $0.8\sigma_p$. Moreover, we note that the output \hat{p}_{MB} distribution depends not only on the S/N p_0/σ_p , but also on the value of the true polarization fraction p_0 . We report two cases, $p_0 = 1\%$ and 50% in Fig. 4. This comes from the prior of the Bayesian method, which bounds the estimate \hat{p}_{MB} between 0 and 1. As a consequence, the normality of the Bayesian distribution is extremely poor, as pointed out in the bottom panel of Fig. 3, where we show that the JB test of the MB estimator is larger than 9.21 (consistent with a $\chi_{0.01}^2$ test) over the whole range of S/N explored here (up to $S/N \sim 5$). In contrast, the resulting \hat{p}_{MAS} distribution of Fig. 4 looks much better, mimicking the Rayleigh distribution for low S/N and going neatly to the Gaussian regime, as pointed out by P14. The JB of the MAS estimator is the lowest for $S/N > 3$ (see bottom panel of Fig. 3), illustrating the consistency between the MAS distribution and the normal distribution.

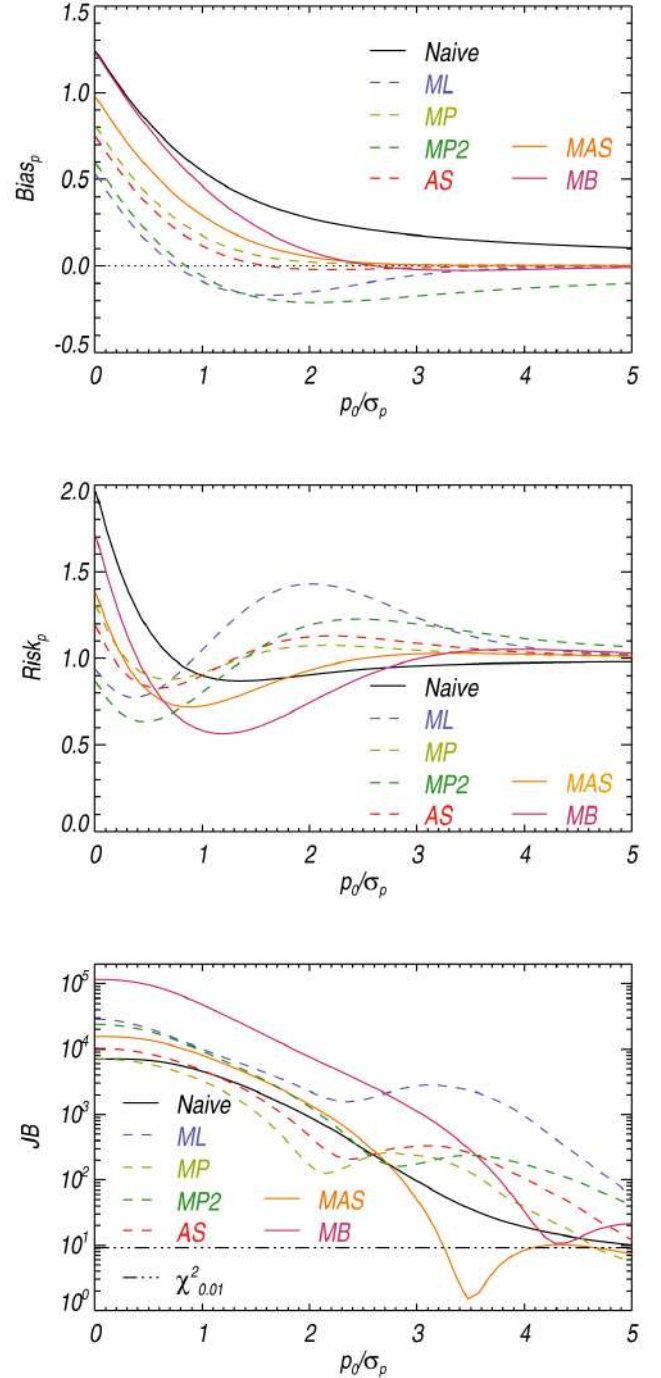


Fig. 3. Comparison of the average relative bias (*top*), risk function (*middle*) and Jarque-Bera test (*bottom*) of the pure measurements (naïve, black), ML (dashed blue), MP (dashed light green), MP2 (dashed green), AS (dashed red), MAS (orange) and MB (pink) \hat{p} estimators in the canonical case, as a function of the S/N p_0/σ_p . The dashed lines stand for the discontinuous estimators presenting a peak of their output distribution at $\hat{p} = 0$. Based on 100 000 Monte Carlo simulations. The limit $JB = \chi_{\alpha}^2$ for $\alpha = 1\%$ is shown in dot-dot-dashed line.

All distributions, naïve, MAS, and MB, converge to a Gaussian distribution at higher S/N.

4.3. Impact of the Bayesian prior

The choice of the prior is crucial in the Bayesian approach, and we have seen how it is hard to define a non-informative prior

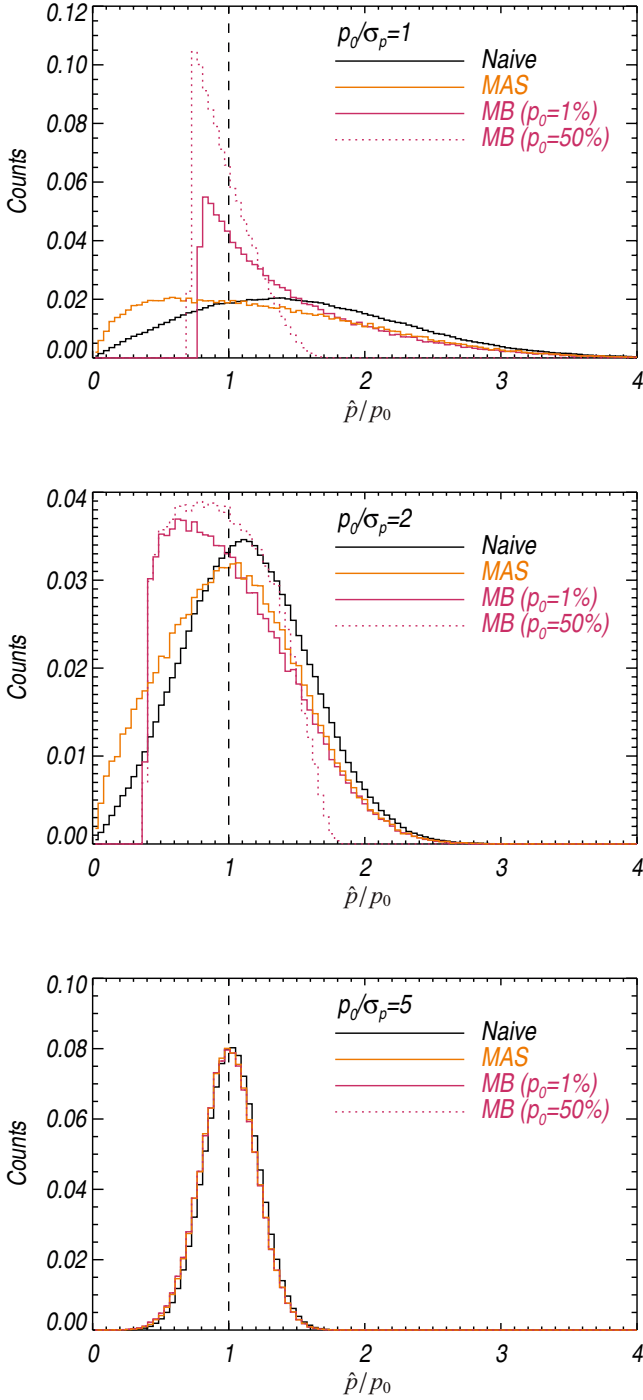


Fig. 4. Output distributions of the naïve (black), MAS (orange) and the MB (pink) \hat{p} estimators applied to 100 000 Monte-Carlo simulations using a covariance matrix in the canonical case ($\varepsilon_{\text{eff}} = 1$), for three levels of the S/N $p_0/\sigma_p = 1, 2$, and 5 (from top to bottom). In the case of the MB estimator, we show two setups of $p_0 = 1\%$ and 50% to illustrate the dependence of the output distribution on the p_0 value, due to the prior used in the Bayesian approach ($\hat{p}_{\text{MB}} \in [0, 1]$ so that $\hat{p}_{\text{MB}}/p_0 \in [0, 1/p_0]$). The other estimators are not sensitive to the true value p_0 . The MB and MAS curves overlap in the bottom panel.

in Sect. 2.6. The MB estimator studied up to now assumes a flat prior in p_0 between 0 and 1, which is already an informative prior (see Quinn 2012). In practice when dealing with astrophysical data, we can bound the expected true values of the polarization fraction between much tighter limits. We know, for

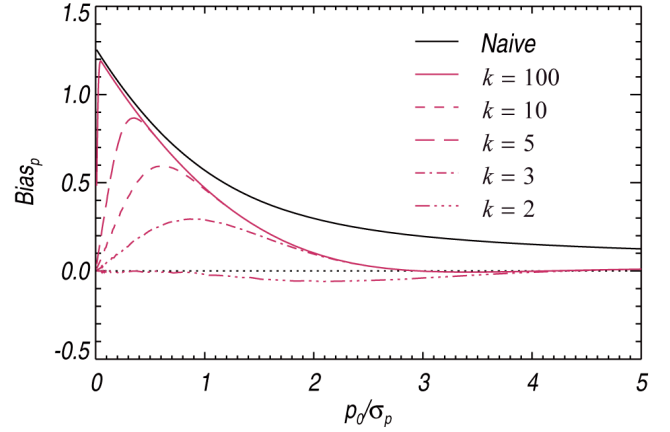


Fig. 5. Impact of the flat prior interval upper limit (see Eq. (37)) on the relative Bias_p performance of the MB estimator.

example, that the polarization fraction of the synchrotron signal peaks at $\sim 75\%$, but never reaches this maximum due to line of sight averaging. The maximum polarization fraction of the dust thermal emission is still a debated issue, but is unlikely to be greater than 20% to 30% (Benoît et al. 2004). Appropriate priors can then be introduced to take this a priori physical knowledge into account in the MB estimator.

We have already observed in Sect. 4.2 how the output distribution of the \hat{p}_{MB} estimates is affected by the value of the true p_0 (1% or 50%) due to the upper limit ($p_0 < 1$) of the prior, see Fig. 4. We explore here a family of simple priors defined by

$$\kappa(p'_0) = \begin{cases} 1/(kp_0) & \text{for } p'_0 \in [0, kp_0] \\ 0 & \text{otherwise,} \end{cases} \quad (37)$$

where we adjust the upper limit of the prior as a function of the expected true value. We performed Monte Carlo simulations in the canonical case by setting the true value at $p_0 = 1\%$ and varying the upper limit of the prior ($k = 2, 3, 5, 10$, and 100). The statistical relative Bias_p of the MB estimators associated with each version of the priors is shown in Fig. 5. The lower the upper limit, the lower the relative Bias_p , as expected. However, the upper limit of the prior has to be very constraining ($k \leq 3$) to observe a decrease in the relative bias in the range of S/N between 1.5 and 3. This requires very good a priori knowledge. Using more relaxed priors ($k \geq 5$) will significantly not improve the performances of the MB estimator at $S/N > 1$.

When dealing with maps of polarized data, an interesting approach would be to start by estimating the histogram of p values in the map and use it as a prior in our MB estimators, even if this moves away from a strictly Bayesian approach again by introducing a data-dependent prior. As a first guess, the prior can be set to the histogram of the naïve estimates of \hat{p} , but a more sophisticated prior would be an histogram of p deconvolved from the errors, using a maximum entropy method, for example.

We illustrate the performance of the MB estimator with this kind of prior in Figs. 6 and 7. We start with a sample of 10 000 independent true values ($p_{0,i}$) ranging between 0% and 20% polarization fractions, with a distribution shown in Fig. 7 on which a random realization of the noise is added with the same noise level over the whole sample, leading to varying S/Ns through the sample. We explore two extreme cases of the Bayesian prior, corresponding to i) an idealistic perfect knowledge of the input distribution and ii) its first guess provided by the naïve estimates. The prior is therefore chosen as the input distribution of the true

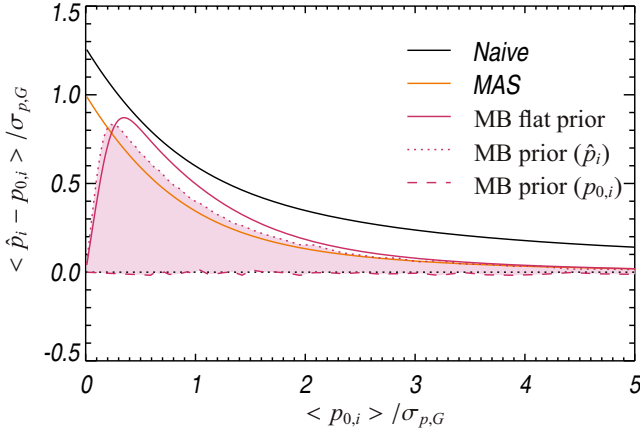


Fig. 6. Illustration of the improvement in the MB estimator performances when using evolved priors. Starting from an input distribution of 10 000 simulated true values ($p_{0,i}$), shown in Fig. 7, and the statistical relative bias is shown for four estimators: naïve, MAS, and MB with three different priors.

$p_{0,i}$ values and the output distribution of the naïve estimates. We compare the performance of these two new versions of the MB estimators with the naïve, MAS, and flat prior MB estimators, in terms of relative bias in Fig. 6.

We stress that the relative bias values are not defined as previously done in Sect. 4.1, but refer now to the mean of the difference between each sample of true value $p_{0,i}$ and its associated estimate \hat{p}_i . The pink shaded region provides the domain of the possible improvement of the MB estimators, by setting an appropriate prior as close as possible to the true distribution. The improvements may seem spectacular, leading to a statistical relative bias close to zero at all S/Ns in the best configuration (dashed line). Caution is warranted, however, when looking at the output distributions associated with these new MB estimators in Fig. 7, shown for three levels of the noise chosen so that the mean S/N is $\overline{p_0}/\sigma_{p,G} = 1, 2$ and 3. At low S/N (≈ 1), the output distribution of the MB estimator with a *perfect* prior (dashed line) is extremely peaked around the mean value of the sample $\overline{p_0}$, but does not match the input distribution at all. Even at higher S/N (2–3), the three MB output distributions suffer from the same feature already mentioned in Sect. 4.2, a sharp cutoff at low values of p . Using a prior that is too constraining will yield dramatic cuts of the extremes values of the input distribution. By contrast, the naïve prior is quite effective in that it allows the MB estimator to recover the upper limit of the input distribution reasonably well at a $S/N \gtrsim 2$, while the other estimators fail to do so at such low S/N.

The performance of the MB estimator with an evolved prior will also strongly depend on the initial true distribution of the polarization fraction. For example we duplicated the analysis made above with a different initial distribution ($p_{0,i}$) centred on 20% of polarization fraction instead of 10% (see Fig. 8). In this configuration, the output distributions of the Bayesian estimators are not as much affected by the cut-off at low p as observed in Fig. 7. The MB estimator with the naïve prior appears extremely effective, even at low S/N (~ 2).

4.4. Robustness to the covariance matrix

In PMA I we have extensively discussed the impact of the asymmetry of the covariance matrix on the measurements of the polarization fraction. In particular, we stressed that once the effective

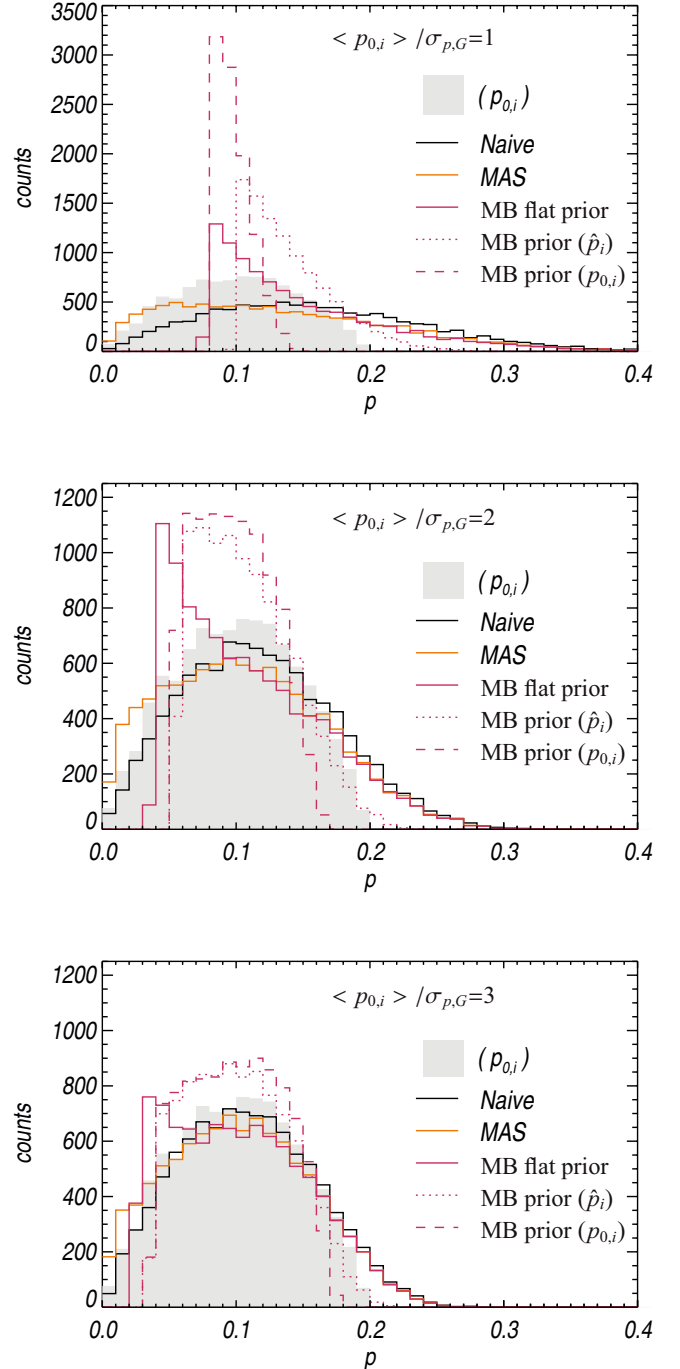


Fig. 7. Output distributions of the \hat{p} estimates starting from a distribution of 10 000 simulated independent true values ($p_{0,i}$) centred on 10% of polarization fraction (grey shaded region) shown at three levels of noise characterized by the mean S/N $\langle p_{0,i} \rangle / \sigma_{p,G} = 1, 2$, and 3 (top, middle, and bottom, respectively). The naïve (black) and MAS (orange) output distributions are compared to the MB output distributions obtained with three different priors: flat prior between 0 and 1 (solid pink), to the naïve output distribution (dotted pink), and to the true input distribution (dashed pink).

ellipticity departs from the canonical case, the bias on the polarization fraction depends on the true polarization angle ψ_0 , which remains unknown. We would like to explore in this section how the performance of the various \hat{p} estimators are sensitive to the effective ellipticity of the covariance matrix.

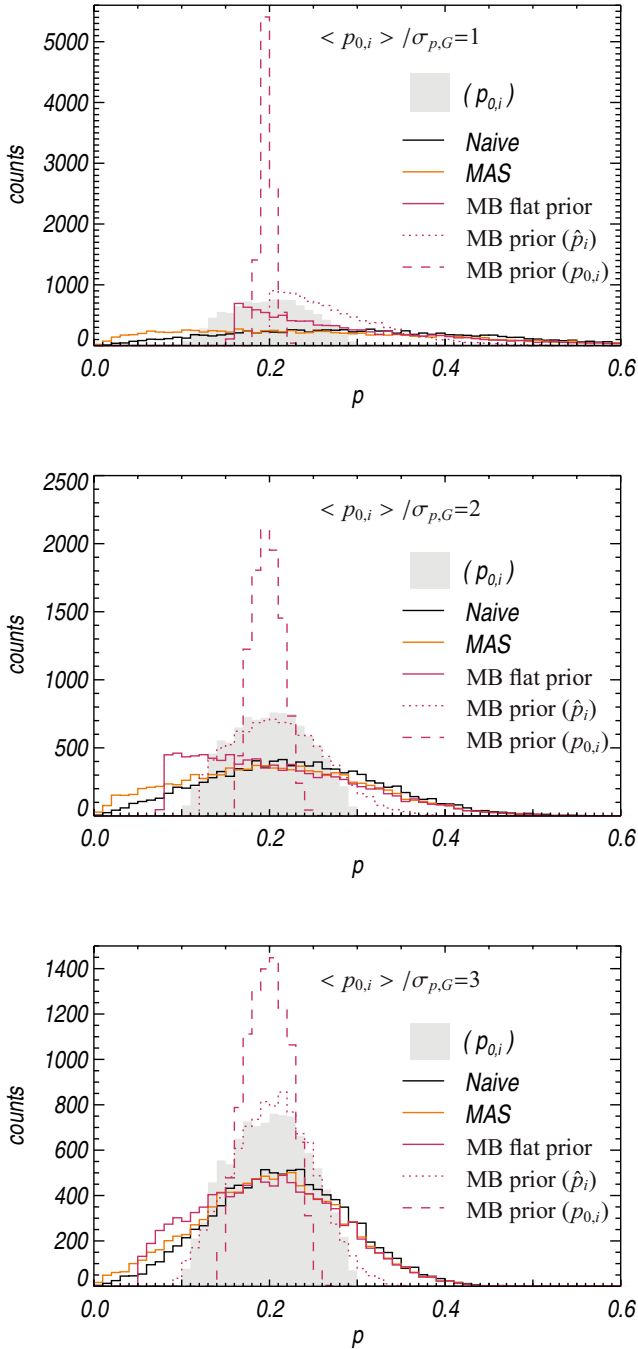


Fig. 8. Same as Fig. 7 with a different initial distribution ($p_{0,i}$) centred on a 20% polarization fraction.

We illustrate the dependence of the \hat{p} estimators on the true polarization angle ψ_0 in Fig. 9. Given true polarization parameters ($p_0 = 0.1$ and ψ_0 ranging between $-\pi/2$ and $\pi/2$), a covariance matrix characterized by $\varepsilon_{\text{eff}} = 2$ and $\theta = 0$ (left-hand panel), and a S/N $p_0/\sigma_{p,G} = 1$, we first set the polarization measurements (p, ψ) to the maximum of the PDF f_{2D} (left-hand panel). We apply then the six estimators on these measurements to get the \hat{p} estimates for each ψ_0 between $-\pi/2$ and $\pi/2$. With this particular setting, the MP2 (green) estimator gives back the true polarization fraction p_0 whatever the polarization angle ψ_0 , by definition of this estimator and the choice of the measurement in this example. On the contrary, the MP (light green) and the ML (blue) estimators are extremely sensitive to the true polarization angle ψ_0 , yielding estimates spanning a large range

between 0 and $2.2p_0$, while the AS (red) and MAS (orange) estimators yield results ranging between 1 to $1.8p_0$ when ψ_0 varies. The MB (pink) estimator provides stable estimates in the range 1.4 to $1.5p_0$, which is consistent with the fact that the posterior estimators minimize the risk function. This of course has a cost, and the MB estimator provides the largest averaged relative bias here compared to the other methods, with the exception of the naïve (black) one.

More generally, for each value of the true polarization angle ψ_0 between $-\pi/2$ and $\pi/2$, we build a sample of 10 000 simulated measurements using the same setup of the covariance matrix as above. Then we compute the statistical average of the naïve, MAS, and MB estimates (black, orange, and pink lines, respectively) obtained on this simulated sample, with their associated 1σ dispersion (black, orange, and pink dot-dashed lines, respectively), as shown in the right-hand panel of Fig. 9. The averaged MB estimates present the same characteristic as shown in the left-hand panel. By contrast, the averaged MAS estimates are independent of the unknown ψ_0 true polarization angle. The MAS 1σ dispersion is, however, slightly larger than the MB 1σ dispersion.

The impact of the effective ellipticity of the covariance matrix is then analysed statistically for the MAS and MB estimators only in Fig. 10. Instead of looking at the accuracy of the \hat{p} estimators around one particular measurement (the most probable one) as done in Fig. 9, for each set of true polarization parameters ($p_0 = 0.1, \psi_0$), with ψ_0 ranging between $-\pi/2$ and $\pi/2$, we perform Monte Carlo simulations. For each set of true polarization parameters, we build a sample of 100 000 simulated measurements on which we apply the MAS and MB estimators to finally compute the statistical relative Bias $_p$ and Risk $_p$, as defined in Sect. 4.1. This is done for various setups of the covariance matrix chosen to cover the whole range of the *extreme* and *low* regimes. The minimum and maximum relative Bias $_p$ and Risk $_p$ are then computed over the whole range of ψ_0 and effective ellipticity ε_{eff} in each regime of the covariance matrix to build the shaded regions of Fig. 10 for the MAS (top panels) and MB (bottom panels) \hat{p} estimators. It appears that the relative Bias $_p$ of the MAS estimator is less affected by a change in ellipticity for $S/N > 2$ than the MB estimator, even in the *extreme* regime of the covariance matrix. The dependence of the risk function on the ellipticity is almost identical for the two estimators around their respective canonical curve. The thickness of the risk function region is slightly smaller for the MB estimator than for the MAS estimator at low S/N (<3), while it is the opposite for higher S/N (>3), as already observed in the canonical case.

4.5. Polarization fraction uncertainty estimates

The questions of estimating the polarization uncertainties and how uncertainties are propagated are essential in reliable polarization analysis. The best approach consists of building the confidence intervals to retrieve robust estimates of the lower and upper limits of the 68%, 95%, or 99.5% intervals, which is valid even when the distribution is not Gaussian. As already mentioned in Sect. 3.3, building optimized confidence intervals including the full knowledge of the covariance matrix may represent a challenge for large samples of data. As a result, P14 provides analytic approximations of such confidence intervals for the MAS estimator, which can be extremely useful.

A commonly used approach, however, is to provide the 1σ dispersion, assuming the Gaussian distribution of the \hat{p} estimates as a first approximation. We have already stressed the difference

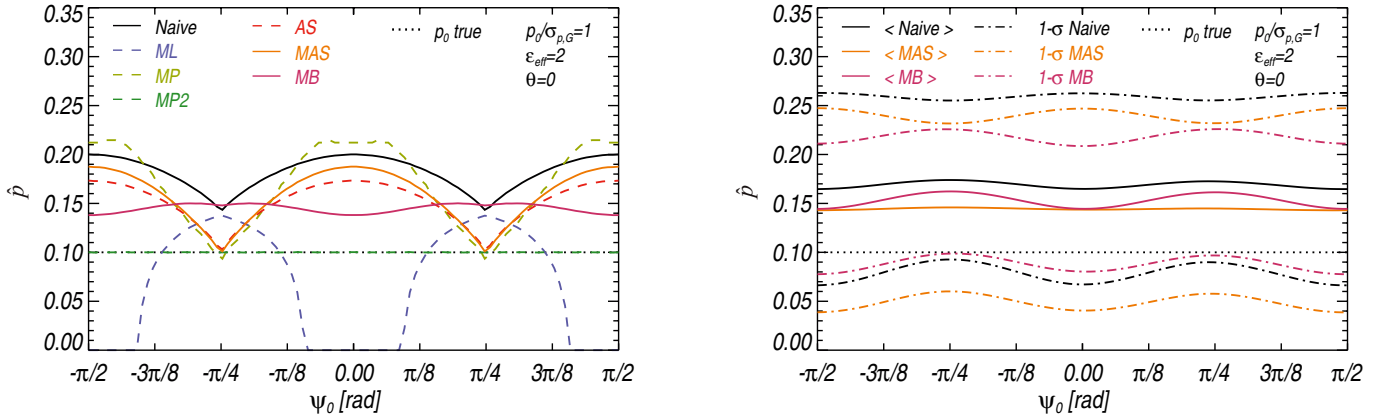


Fig. 9. Illustration of the robustness of the \hat{p} estimators against the unknown ψ_0 parameter when the covariance matrix departs from the canonical value. The covariance matrix is set up with $\varepsilon_{\text{eff}} = 2$ and a S/N $p_0/\sigma_{p,G} = 1$, and a true polarization fraction $p_0 = 0.1$. For each value of ψ_0 , we first illustrate (in the *left-hand panel*) the performance of the seven estimators on one particular measurement set to the maximum of the PDF. We focus then on the statistical average estimates \hat{p} computed over 10 000 Monte-Carlo realizations for each value of the polarization angle for the naive, MAS, and MB estimators (*right-hand panel*), where the full lines stand for the mean, and the dot-dashed lines for the 1σ dispersion.

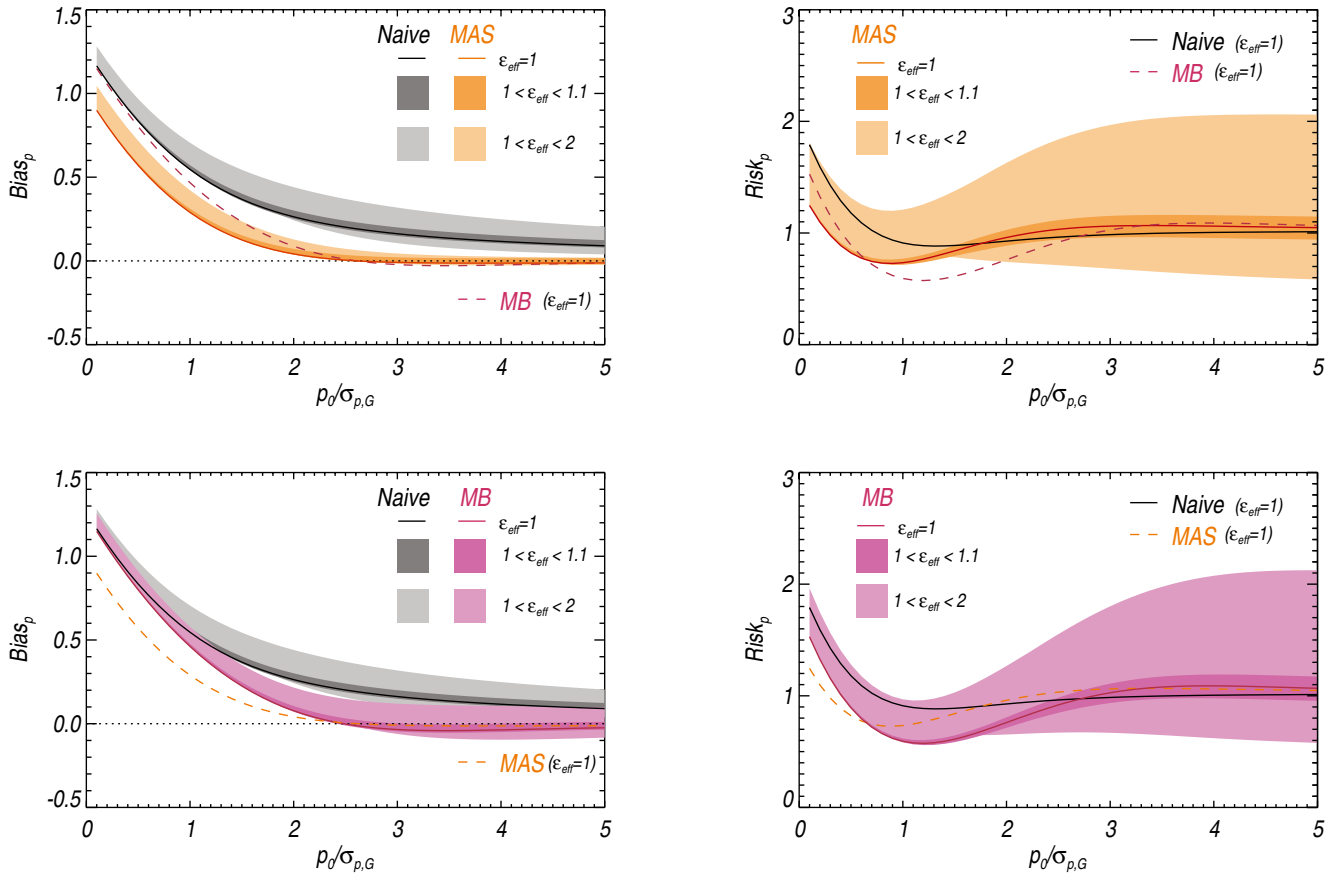


Fig. 10. Impact of the effective ellipticity of the covariance matrix on the statistical relative Bias_p (*left column*) and Risk_p (*right column*) quantities in the *extreme* (light shaded region) and *low* (dark shaded regions) regimes, for both MAS (orange, *top*) and MB (pink, *bottom*) \hat{p} estimators. The domain of the naive measurements is repeated in grey shaded regions on both plots. The canonical case of the MAS (and MB) is also repeated on each panel in dashed orange (and pink) lines. This is based on 100 000 Monte-Carlo simulations for each set-up of the covariance matrix, the S/N, and the true polarization parameters.

between the risk function and the variance, and the limitations of the latter to derive robust uncertainties in the presence of bias. We compare below the performance of the usual uncertainty estimates introduced in Sect. 3 to provide robust 68% tolerance intervals: MAS variance, credible intervals MAP, and 1σ a posteriori dispersion MB.

Starting with a true p_0 value, we performed Monte-Carlo simulations in the *low* regime of the covariance matrix, by exploring the whole range of the true polarization angle ψ_0 , with a S/N ranging from 0 to 30. For each simulated measurement (p, ψ) , we compute the \hat{p} estimates with their uncertainty estimators $\sigma_{\hat{p}}$. We then compute the a posteriori probability to find

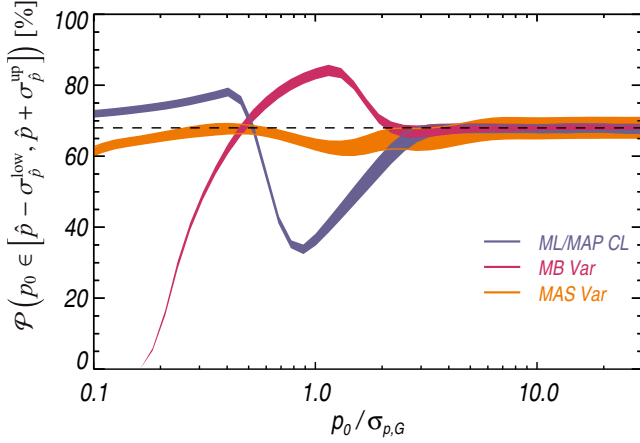


Fig. 11. Probability of finding the true polarization fraction p_0 inside the interval $[\hat{p} - \sigma_{\hat{p}}^{\text{low}}, \hat{p} + \sigma_{\hat{p}}^{\text{up}}]$, where $\sigma_{\hat{p}}^{\text{low}}$ and $\sigma_{\hat{p}}^{\text{up}}$ are the lower and upper limits of each estimator: credible intervals ML/MAP (blue), a posteriori variance MB (pink), and MAS variance (orange). It is plotted as a function of the S/N $p_0/\sigma_{p,G}$. 10 000 Monte-Carlo simulations for each setup of the S/N have been performed assuming a covariance matrix in the *low* regime. The Gaussian level at 68% is shown as a dashed line.

the true p_0 inside the interval $[\hat{p} - \sigma_{\hat{p}}^{\text{low}}, \hat{p} + \sigma_{\hat{p}}^{\text{up}}]$. In the case of the MAP estimator, the lower and upper limits of the interval, $\hat{p}_{\text{MAP}} - \sigma_{\hat{p}_{\text{MAP}}}^{\text{low}}$ and $\hat{p}_{\text{MAP}} + \sigma_{\hat{p}_{\text{MAP}}}^{\text{up}}$, are set to $p_{\text{MAP}}^{\text{low}}$ and $p_{\text{MAP}}^{\text{up}}$, respectively, (with $\lambda = 68$ as defined in Sect. 3.2), which can be asymmetric. We report the results compared to the expected 68% level in Fig. 11. We recall that this comparison approach is frequentist, while anything derived from the Bayesian PDF is used to build single estimates and to be compared with the confidence intervals.

As pointed out in Sect. 3.1, the theoretical variance associated with the MAS estimator still tends to provide slightly lower probabilities than the expected 68% at low S/N, mainly due to the asymmetry of the distribution. The variance associated with the MB estimator, which is more biased at low S/N, gives extremely low probability of recovering the true p_0 value at low S/N (<0.5). By contrast, it provides probabilities greater than 68% (as high as 90%) for S/N between 0.5 and 2. This comes from the fact that the MB variance statistically over-estimates, by a factor of 2, the exact variance of the a posteriori \hat{p}_{MB} distribution at low S/N (<2). Thus the MB uncertainty estimator yields conservative estimates of the uncertainty for $S/N > 0.5$. At high S/N (>3), all these uncertainty estimators provide compatible estimates of the probability close to 68%.

Because the true S/N is always unknown (see Sect. 4.6), the probability of finding the true p_0 value in the confidence interval is also shown as a function of the measured S/N in Fig. 12. This much more realistic picture shows that the variance estimates provide reliable probability for measured S/N greater than ~ 6 .

4.6. Polarization signal-to-noise ratio

In any real measurement, the true S/N $p_0/\sigma_{p,G}$ remains unknown. From observations, we only have access to the measured S/N, which can be obtained by the ratio $\hat{p}/\sigma_{\hat{p}}$ associated with each estimator or by a confidence interval approach (see P14), which is much more robust at a low true S/N. We show in Fig. 13 the accuracy of the measured S/N compared to the true S/N for the four following methods: the naive estimate plus conventional estimate of the uncertainty, the MAS estimate with the associated variance, the MB estimate and its variance, and the

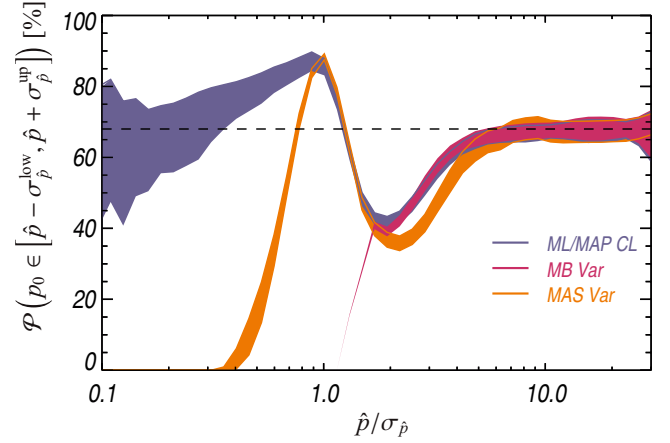


Fig. 12. Same as Fig. 11 but plotted as a function of the measured S/N $\hat{p}/\sigma_{\hat{p}}$.

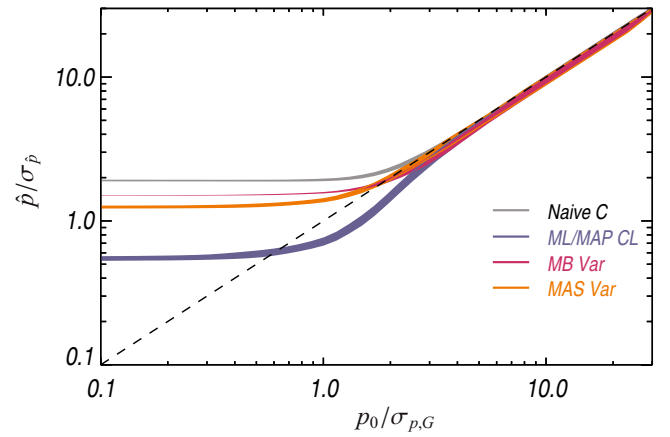


Fig. 13. Average measured S/N computed over 10 000 Monte-Carlo simulations as a function of the true S/N for four methods: naive $\hat{p}/\sigma_{p,C}$ (dark), MAP confidence intervals $\hat{p}_{\text{ML}}/\sigma_{\hat{p}_{\text{MAP}}}$ (blue), MB $\hat{p}_{\text{MB}}/\sigma_{\hat{p}_{\text{MB}}}$ (pink), and MAS variance $\hat{p}_{\text{MAS}}/\sigma_{\hat{p}_{\text{MAS}}}$ (orange). The covariance matrix is taken in its *low* regime.

ML estimate with the MAP credible intervals. We observe that all methods agree only for a true S/N over 3, giving back the true S/N in this regime. Below this true S/N, the measured S/N becomes extremely biased regardless of the method used, due to the bias of the measurement \hat{p} itself, but also due to the bias introduced by the variance as an estimate of the uncertainty when the output distribution departs from the Gaussian regime.

5. $\hat{\psi}$ estimator performance

As pointed out by PMA I, once the covariance matrix is not canonical ($\varepsilon_{\text{eff}} > 1$), a bias of the polarization angle measurements ψ appears with respect to the true polarization angle ψ_0 . This bias may be positive or negative. We propose to compare the accuracy at correcting the bias of the polarization angle of the four following $\hat{\psi}$ estimators: naive measurements ψ , the ML $\hat{\psi}_{\text{ML}}$ (which is equivalent to the MAP $\hat{\psi}_{\text{MAP}}$), the MP2 $\hat{\psi}_{\text{MP2}}$, and the MB $\hat{\psi}_{\text{MB}}$.

5.1. Methodology

Similarly to the \hat{p} estimators, we define the relative bias and risk function on $\hat{\psi}$ as

$$\text{Bias}_{\psi} \equiv \frac{\langle \hat{\psi} - \psi_0 \rangle}{\sigma_{\psi,0}} \quad \text{and} \quad \text{Risk}_{\psi} \equiv \frac{\langle (\hat{\psi} - \psi_0)^2 \rangle}{\sigma_{\psi,0}^2}, \quad (38)$$

where $\hat{\psi}$ is the polarization angle estimate computed on the simulated measurements ψ , ψ_0 is the true polarization angle, $\langle \rangle$ denotes the average computed over the simulated sample, and $\sigma_{\psi,0}$ is the standard deviation of the simulated measurements.

5.2. Performance comparison

We explore the performance of the four $\hat{\psi}$ estimators at four $S/N = 0.5, 1, 2,$ and 5 (from top to bottom) and a covariance matrix with an effective ellipticity $\varepsilon_{\text{eff}} = 2$, in Fig. 14. The relative Bias $_{\psi}$ (left-hand panels) and Risk $_{\psi}$ (right-hand panels) are plotted as a function of the true polarization angle ψ_0 . While the MB estimator seems to provide the least biased estimates with the lowest risk function at low $S/N (<1)$, it becomes the least efficient at higher S/N . In contrast, the ML (or MAP too) presents poor performances at low S/N , but provides impressive results at high S/N , reducing the relative bias close to zero at a S/N of 5. The MP2 estimator does not present any satisfactory properties: strong relative bias and risk function in almost all cases. This $\hat{\psi}_{\text{MP2}}$ estimator can therefore be ruled out.

An overview of the performance of the four $\hat{\psi}$ estimators as a function of the S/N is shown in Fig. 15 after marginalization over all the possible values of the ψ_0 parameter. Since the relative Bias $_{\psi}$ can be positive or negative depending on ψ_0 , we compute the average of the absolute value of the relative bias, $\langle |\text{Bias}_{\psi}| \rangle$ as an indicator of the statistical performance of the estimators regardless of the true polarization angle. We observe again in the left-hand panel of Fig. 15 that the MB estimator provides the lowest relative bias for $S/N < 1.2$, while the ML is especially powerful for $S/N > 2$. All estimators provide almost the same results for the average Risk $_{\psi}$ (left-hand panel), even if MB appears slightly better than the others, including the naïve measurements.

The examples provided above were computed with an *extreme* effective ellipticity ($\varepsilon_{\text{eff}} = 2$) to emphasize the observations, but the same conclusions can be reached for lower values of the ellipticity. See, for example, the case with $\varepsilon_{\text{eff}} = 1.1$ shown in Fig. 15. In the *low* regime of the covariance matrix, however, the statistical relative bias on ψ is very small, typically smaller than 5% of the dispersion, so that the need to correct the bias on ψ remains extremely limited.

5.3. Polarization angle uncertainty estimates

Once a reliable estimate of $\hat{\psi}$ based on the MB and ML (MAP) estimators has been obtained, we would like to build a robust estimate of the associated uncertainties $\sigma_{\hat{\psi}}$, which should be done by building confidence intervals. Because building confidence intervals may represent a hard task in some cases, for example when dealing with the full covariance matrix, we explain other methods below.

One option is to use the uncertainty associated with the MB estimator, $\sigma_{\hat{\psi},\text{MB}}$ (see Eq. (34)). Another is to use the credible intervals built around the MAP estimates on the posterior PDF. We can keep the lower and upper limits, $\psi_{\text{MAP}}^{\text{low}}$ and $\psi_{\text{MAP}}^{\text{up}}$ computed for a 68% credible interval or build a symmetrized uncertainty:

$$\sigma_{\hat{\psi},\text{MAP}} = \frac{1}{2} \left(\psi_{\text{MAP}}^{\text{up}} - \psi_{\text{MAP}}^{\text{low}} \right). \quad (39)$$

A third option consists in taking the conventional uncertainty given in PMA I, derived from the derivatives of the polarization parameters. PMA I has already shown that this $\hat{\psi}$ uncertainty estimator, associated with the naïve measurements,

tends to systematically underestimate the true dispersion of the ψ distribution.

We first assume the canonical simplification of the covariance matrix, which implies that the ψ measurements are not statistically biased. We also recall that under such assumptions, the ML (MAP) and MB $\hat{\psi}$ estimators will give back the measurements ψ . We study, however, how the uncertainties associated with these two estimators can be used to get a reliable estimate of the uncertainty $\sigma_{\hat{\psi}}$. Starting from a true point (p_0, ψ_0) , we simulate a sample of 1000 simulated measurements p, ψ at a given S/N p_0/σ_p , on which we apply the two ML (MAP) and MB $\hat{\psi}$ estimators and their associated uncertainty $\sigma_{\hat{\psi},\text{MAP}}$ and $\sigma_{\hat{\psi},\text{MB}}$, respectively. From this simulated set, we can derive the averaged $\sigma_{\hat{\psi}}$ for both methods. Because all estimators give back the measurements in the canonical case, we compare the MAP and MB polarization angle uncertainties estimators directly to the true dispersion of the ψ measurements in Fig. 16. We also repeat the average of the conventional estimates of the polarization uncertainty estimate, which has been shown by PMA I (see their Fig. 7) to underestimate by a factor of two the true uncertainty at low $S/N (<2)$. We observe that the MAP estimator $\sigma_{\hat{\psi},\text{MAP}}$ provides an extremely good estimate of the polarization angle uncertainty compared to the true one over the whole range of S/N , even if slightly conservative up to a S/N of 5. The MB estimator $\sigma_{\hat{\psi},\text{MB}}$ provides consistent estimates of the uncertainty from intermediate $S/N \sim 1$, but still underestimates at lower $S/N (<1)$.

In the non-canonical case a statistical bias on ψ appears, which can be partially corrected using the appropriate $\hat{\psi}$ estimators (see Sect. 5.2), leading to an output distribution of the $\hat{\psi}$ estimates. We quantify the performance of the ψ uncertainty estimators via Monte-Carlo simulations, as done for the \hat{p} uncertainties. Starting from a set of polarization parameters ($p_0 = 0.1$, $-\pi/2 < \psi_0 < \pi/2$), we build a sample of simulated measurements (p, ψ) using various setups of the covariance matrix in the *low* regime, and various S/N s ranging from 0 to 30. We then compute the a posteriori probability to find the true polarization angle ψ_0 in the interval $[\hat{\psi} - \sigma_{\hat{\psi}}^{\text{low}}, \hat{\psi} + \sigma_{\hat{\psi}}^{\text{up}}]$, where $\sigma_{\hat{\psi}}^{\text{low}}$ and $\sigma_{\hat{\psi}}^{\text{up}}$ are symmetrized. The results are shown as a function of the true S/N $p_0/\sigma_{p,G}$ in Fig. 17 and of the measured S/N $\hat{p}/\sigma_{\hat{p}}$ in Fig. 18. We observe that the MAP estimator provides slightly conservative probabilities over the whole range of S/N . The MB estimator gives low probabilities to recover the true polarization angle ψ_0 for a true $S/N < 1$ and a measured $S/N < 2$.

6. Three-dimensional case

In all of the preceding sections, the total intensity I was assumed to be perfectly known, $I = I_0$. In some cases, however, this assumption is not valid as discussed by PMA I. For instance, one needs to subtract any unpolarized component from the observed intensity signal, leading to three main problems: i) the derived polarization fraction may be grossly underestimated if this is not done properly; ii) this subtraction may be subject to a relatively large uncertainty, larger than the noise on the total intensity, and could lead to diverging estimates of the polarization fraction when intensity crosses null values; iii) this uncertainty on this unpolarized component intensity level should be included in the 3D noise covariance matrix and propagated to the uncertainty estimates of the polarization fraction. This happens, for instance, when dealing with the polarization fraction of the Galactic dust component at high latitude, where the total intensity of the signal is strongly contaminated by the unpolarized signal of the cosmic infrared background (CIB).

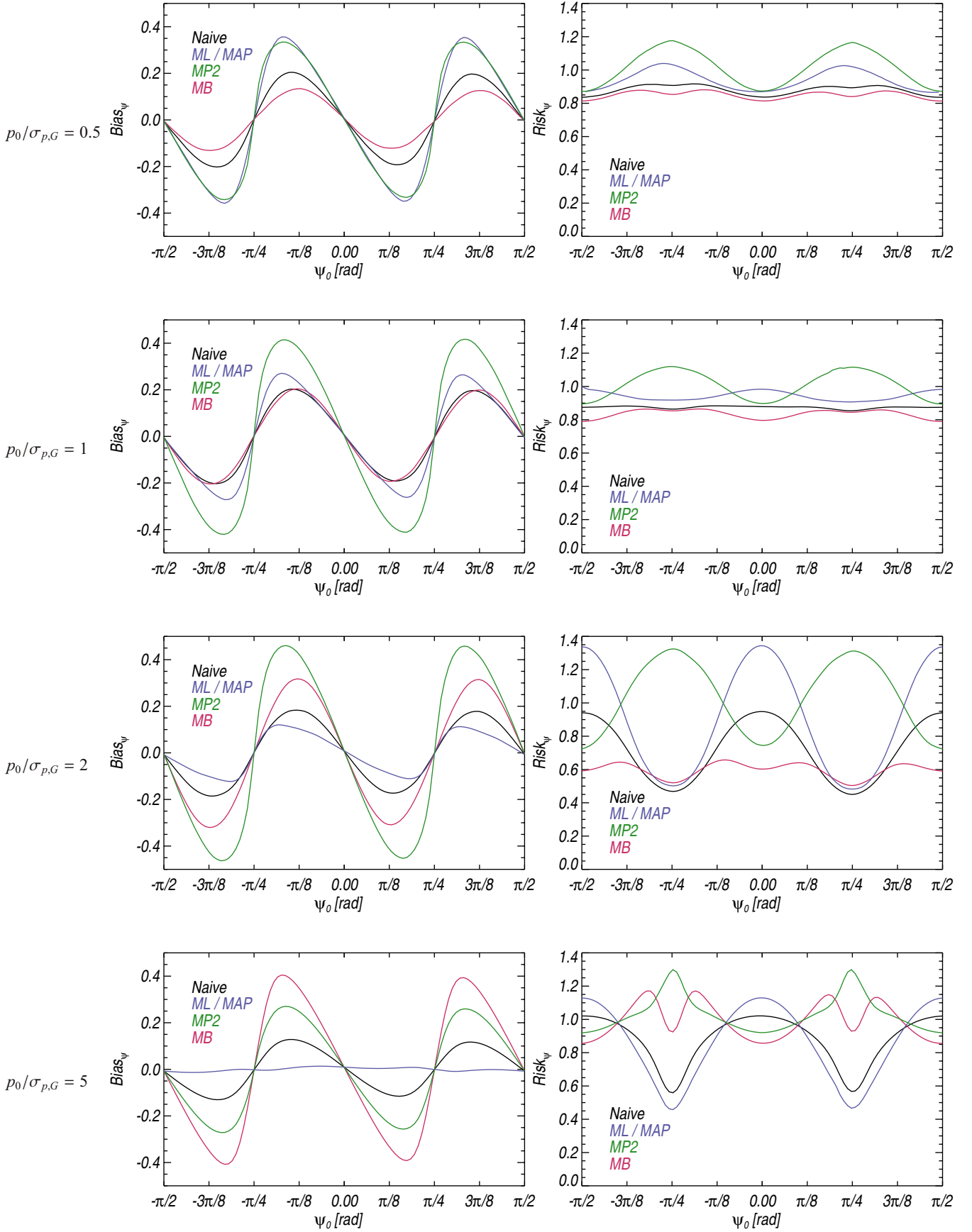


Fig. 14. Comparison of the relative Bias_ψ (left) and Risk_ψ (right) quantities of the four $\hat{\psi}$ estimators: naïve (black), ML (blue), MP2 (green), and MB (pink) plotted as a function of the true polarization angle ψ_0 and computed at four S/Ns of $p_0/\sigma_{p,G} = 0.5, 1, 2,$ and 5 . The covariance matrix is set to $\varepsilon = 2$ and $\rho = 0$ ($\varepsilon_{\text{eff}} = 2$). 1000 Monte Carlo realizations are performed for each set of the polarization angle and the S/N.

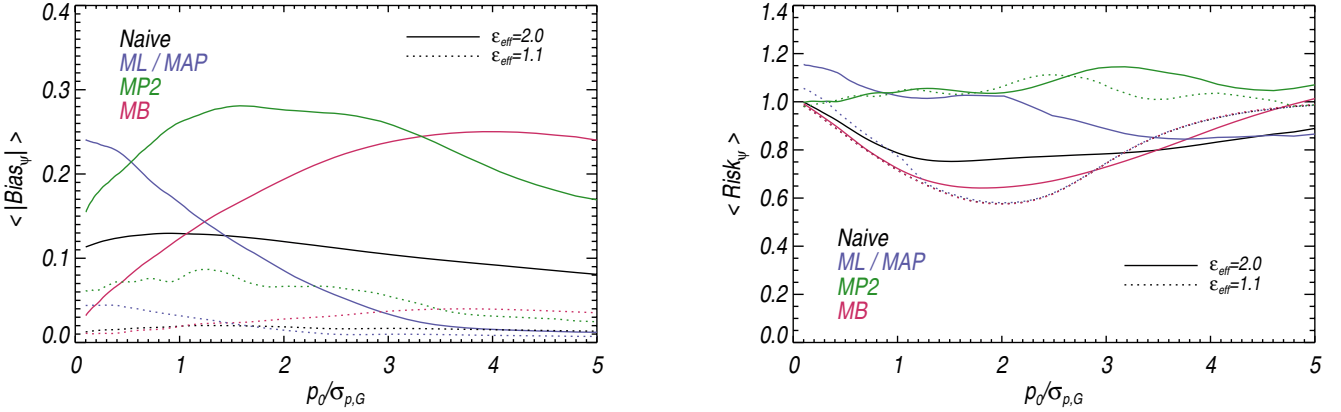


Fig. 15. Statistical relative $|\text{Bias}_\psi|$ (left-hand panel) and Risk_ψ (right-hand panel) averaged over ψ_0 between $-\pi/2$ and $\pi/2$, as a function of the S/N on $p_0/\sigma_{p,G}$, for the four $\hat{\psi}$ estimators: naïve (black), ML / MAP (blue), MP2 (green), and MB (pink). We consider two set-ups of the covariance matrix here: $\varepsilon_{\text{eff}} = 2$ (solid line) and $\varepsilon_{\text{eff}} = 1.1$ (dotted line). 1000 Monte Carlo realizations are performed for each S/N, and for each one of the 100 values of the polarization angle used in the average.

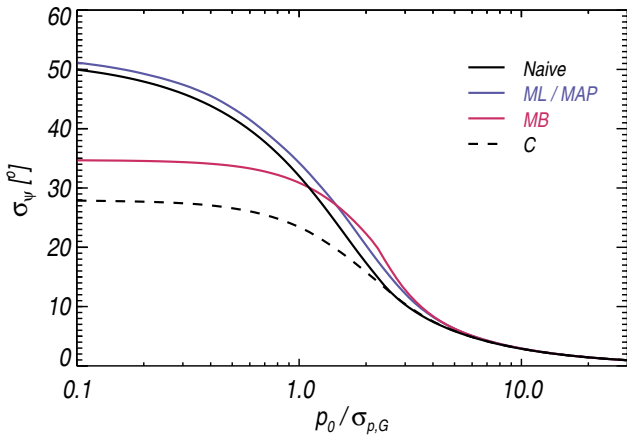


Fig. 16. Average polarization angle uncertainty as a function of the S/N in the canonical case and computed over 1000 Monte-Carlo simulations for each value of the S/N: true uncertainty $\sigma_{\psi,0}$ (black), conventional estimate $\sigma_{\psi,C}$ (C, dashed dark), ML $\sigma_{\psi,\text{MAP}}$ (blue), and MB $\sigma_{\psi,\text{MB}}$ (pink) estimators. The covariance matrix is assumed to be canonical.

The Bayesian approach has the definite advantage over other estimators discussed here in that it can deal fairly easily with 3D (I, Q, U) noise. However, an uncertain total intensity still poses problems, which are most acute in low brightness regions, since the noisy I may become zero or negative, leading to infinite or negative polarization fractions. With this in mind, it is possible that the choice of the prior in p_0 and I_0 may have a strong impact on the \hat{p}_{MB} estimate. One may, for instance, choose to allow for negative I_0 in low-brightness regions, which implies extending the definition range of the polarization fraction to the negative part, leading to a prior defined on $[-1, 1]$. Another possibility in this case, and a possible development of the present paper, is to extend the dimensionality of the problem to include the unpolarized intensity component I_{offset} , e.g., with a flat prior between $I_{\text{offset,min}}$ and $I_{\text{offset,max}}$, while still imposing $I_0 > 0$.

We stress that the Bayesian approach is also currently the only one that can deal with correlation between total intensity I to Stokes parameters Q and U . We note, however, (i) new and forthcoming polarization data sets have a much more control over these systematics; and (ii) the impact of these correlations between noise components on the polarization fraction and angle bias is quite limited, as shown by PMA I.

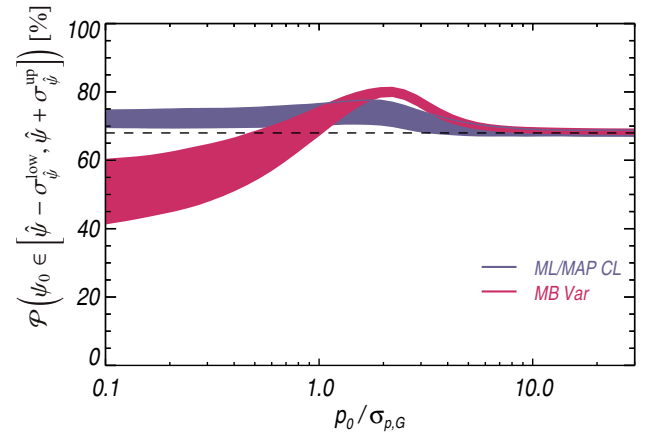


Fig. 17. Probability of finding the true polarization angle ψ_0 inside the interval $[\hat{\psi} - \sigma_{\hat{\psi}}^{\text{low}}, \hat{\psi} + \sigma_{\hat{\psi}}^{\text{up}}]$, where $\sigma_{\hat{\psi}}^{\text{low}}$ and $\sigma_{\hat{\psi}}^{\text{up}}$ are the lower and upper uncertainties for each estimator, ML/MAP (blue) and MB (pink), and plotted as a function of the S/N $p_0/\sigma_{p,G}$. For each value of the S/N 1000 Monte-Carlo simulations have been carried out in the *low* regime of the covariance matrix. The expected level at 68% is shown as a dashed line.

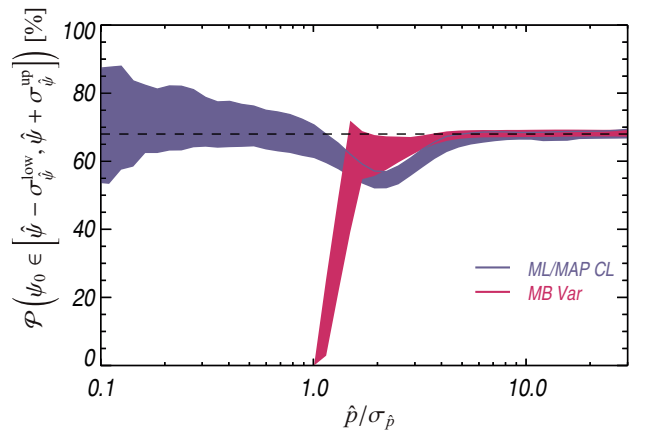


Fig. 18. Same as Fig. 17, but plotted as a function of the measured S/N $\hat{p}/\sigma_{\hat{p}}$.

7. Conclusion

We have presented in this work an extensive comparison of the performance of polarization fraction and angle estimators. While

Simmons & Stewart (1985) focused on the common estimators of the polarization fraction, such as the maximum likelihood (ML), the most probable (MP), and the asymptotic (AS), and Quinn (2012) suggested using a Bayesian approach to estimate the polarization fraction, we have generalized all these methods to consider the full covariance matrix of the Stokes parameters. We also included in this comparison a novel estimator of the polarization fraction, the modified asymptotic (MAS, Plaszczyński et al. 2014). In addition, we performed the first comparison of the performance of the polarization angle estimators, since a statistical bias of ψ is expected when the covariance matrix departs from its canonical form. We followed a frequentist methodology to investigate the properties of the polarization estimators, even when dealing with the frequentist estimators inspired by the Bayesian approach.

The question of the performance of a \hat{p} or $\hat{\psi}$ estimator depends intrinsically on the analysis we would like to carry out with these quantities. Whether one includes the full covariance matrix or not is one of the first questions that must be handled, but the more important aspect relies on the properties of the output distribution of each estimator. In practice, a compromise between three frequentist criteria has to be found: a minimum bias, a minimum risk function, and the shape of the output distribution, in terms of non-Gaussianity. We present below a few recipes associated to typical use cases:

- *Build a mask.* It is usually recommended to build a mask on the intensity map, instead of using the S/N of the polarization fraction, so that no values of the polarization fraction (especially low values of p) are discarded in the further analysis. It can be useful, however, to build a mask based on the S/N of a polarization fraction map when we are interested in strong values of the polarization fraction only, and we try to reject p estimates artificially boosted by the noise. This is the case when we look for the maximum value of p , for example. In this context we suggest following the prescription of P14, using a combination of the MAS estimator with confidence intervals. This method allows building conservative domains where the S/N is ensured to be greater than a given threshold. P14 provide numerical approximations in the canonical case. If one wants to take the specificity of the noise properties in each pixel into account, confidence intervals can be built for any covariance matrix (including ellipticity and correlation), but it could require intensive computing. Another alternative in that case is to build credible intervals using the posterior distribution (MAP).
- *Large maps of the polarization fraction with high S/N on the intensity.* Another typical use is to provide large maps of the polarization fraction with the associated uncertainty, when the intensity is assumed to be perfectly known. Because of their discontinuous distributions presenting a peak at $\hat{p} = 0$ and their strong dependence on the unknown true polarization angle ψ_0 , the common estimators of p (ML, MP, and AS) are not designed well for this purpose. These estimators could produce highly discontinuous patterns with zero values over the output \hat{p} map when the S/N goes below 4, which may imply complicated analysis that include upper limit values. To avoid these issues, we first suggest using the MAS estimator, which has been shown to produce the lowest relative bias, with a continuous output distribution that becomes close to a Gaussian for S/N greater than 2. Moreover, the relative risk function associated with the MAS estimator becomes competitive for $S/N > 3$, while the MB estimator minimizes the relative risk function for an intermediate S/N between 1 and 3. The uncertainties can then be derived again from the confidence or credible intervals, depending on the ellipticity of the covariance matrix. A second option, especially suited to intermediate S/N (2–3), consists in performing a preliminary analysis on the data to build a prior from the \hat{p} distribution, which can then be injected into the MB estimator. The performance of this method strongly relies on the properties of the initial true distribution. It is particularly efficient for true polarization fractions largely greater than zero, to avoid the major drawback of the MB estimator presenting a lower limit that is proportional to the noise level. The MB (with flat prior) estimator therefore presents a cut-off at $0.8\sigma_p$, so that it can never provide null estimates of \hat{p} . We stress that above a S/N of 4, all methods (except MP2) fall into agreement.
- *Combined polarization fraction and angle analysis.* The Bayesian estimators of \hat{p}_{MB} and $\hat{\psi}_{\text{MB}}$ may be used to build estimates of the polarization fraction and angle simultaneously, by taking the full covariance matrix into account, including the ellipticity and correlation between Q and U , and the correlation between total and polarized intensity. This could be useful when performing an analysis over large areas with inhomogeneous noise properties, when the S/N on the intensity becomes problematic or when an important correlation between I and (Q, U) exists. Nevertheless, we stress that the output distributions of the MB estimates are strongly asymmetric at low S/N (<3) and that the Bayesian uncertainty estimates cannot be used as typical Gaussian 68% tolerance intervals.
- *Low S/N on the intensity.* We recommend in this case to use the Bayesian estimators that allow simultaneous estimates of the intensity and the polarization parameters, taking the full covariance matrix into account, and to include the impact of the uncertainty of the intensity on the polarization fraction estimate.
- *Very low S/N studies.* Very low S/N studies may require different approaches. We have seen that at low S/N, all estimators provide biased estimates of the polarization fraction, with highly asymmetric distributions. The more conservative option in this case is to use the confidence or credible intervals. Similarly the question of assessing the unpolarized level of a set of data (i.e., $S/N \sim 0$) has been first raised by Clarke et al. (1993). They suggested using a Kolmogorov test to compare the measurement distributions with the expectation derived from the Rice distribution with $p_0 = 0$. Another option is to build the likelihood in two dimensions (Q, U) to perform a χ^2 test with $Q_0 = U_0 = 0$. A last method could be to use the Bayesian posterior probability $B(p_0|p, \sigma_p)$ to assess the probability of having p_0 within a specified interval of zero (or exactly $p_0 = 0$ if delta functions are allowed in the prior) for a given measurement or a series of measurements by convolving all individual PDFs (see Quinn 2012, for details about the complications that can arise in such an analysis).
- *Polarization angle.* Concerning the polarization angle estimates $\hat{\psi}$, we have shown that the ML provides the best performance in terms of relative bias and risk function for $S/N > 1$. It corrects a potential bias of ψ when the covariance matrix is not in its canonical form. Because the ML and MAP estimators give equivalent results, the MAP can be used to efficiently build credible intervals and symmetric uncertainties, which have been shown to be in a very good agreement with the output distributions. Nevertheless, we stress that the level of the absolute bias of ψ remains extremely limited

compared to the dispersion of the polarization angle in most cases (i.e., in the *low* and *tiny* regimes of the covariance matrix), so that it can usually be neglected.

Acknowledgements. This paper was developed to support the analysis of data from the *Planck* satellite. The development of *Planck* has been supported by: ESA; CNES, and CNRS/INSU-IN2P3-INP (France); ASI, CNR, and INAF (Italy); NASA and DoE (USA); STFC and UKSA (UK); CSIC, MICINN, JA, and RES (Spain); Tekes, AoF, and CSC (Finland); DLR and MPG (Germany); CSA (Canada); DTU Space (Denmark); SER/SSO (Switzerland); RCN (Norway); SFI (Ireland); FCT/MCTES (Portugal); and PRACE (EU). A description of the Planck Collaboration and a list of its members, including the technical or scientific activities in which they have been involved, can be found at <http://www.cosmos.esa.int/web/planck/planck-collaboration>. We would also like to thank P. Leahy, S. Prunet, and M. Seiffert for their very useful comments, and J. Quinn for his efficient refereeing of this manuscript.

References

- Benoît, A., Ade, P., Amblard, A., et al. 2004, *A&A*, 424, 571
- Bernard, J.-P., Ade, P., De Bernardis, P., et al. 2007, *EAS Pub. Ser.* 23, eds. M.-A. Miville-Deschênes, & F. Boulanger, 189
- Clarke, D., Naghizadeh-Khouei, J., Simmons, J. F. L., & Stewart, B. G. 1993, *A&A*, 269, 617
- Dotson, J. L., Vaillancourt, J. E., Kirby, L., et al. 2010, *ApJS*, 186, 406
- Feldman, G. J., & Cousins, R. D. 1998, *Phys. Rev. D*, 57, 3873
- Fissel, L. M., Ade, P. A. R., Angilè, F. E., et al. 2010, in *SPIE Conf. Ser.*, 7741
- Gradshteyn, I. S., & Ryzhik, I. M. 2007, *Table of Integrals, Series, and Products* (Elsevier)
- Jarque, C., & Bera, A. 1980, *Economic Lett.*, 6, 255
- Jeffrey, H. 1939, *Theory of probability* (Oxford University Press)
- Montier, L. A., Plaszczynski, S., Levrier, F., et al. 2015, *A&A*, 574, A135
- Naghizadeh-Khouei, J., & Clarke, D. 1993, *A&A*, 274, 968
- Pérez-Sánchez, A. F., & Vlemmings, W. H. T. 2013, *A&A*, 551, A15
- Planck Collaboration I. 2011, *A&A*, 536, A1
- Plaszczynski, S., Montier, L., Levrier, F., & Tristram, M. 2014, *MNRAS*, 439, 4048
- Prudnikov, A. P., Brychkov, Yu. A., & Marichev, O. I. 1986, *Integrals and Series: Elementary Functions*, Vol. 1 (New York: Gordon & Breach Science Publishers), 798
- Quinn, J. L. 2012, *A&A*, 538, A65
- Rice, S. O. 1945, *Bell Systems Tech. J.*, 24, 46
- Serkowski, K. 1958, *Acta Astron.*, 8, 135
- Simmons, J. F. L., & Stewart, B. G. 1985, *A&A*, 142, 100
- Vaillancourt, J. E. 2006, *PASP*, 118, 1340
- Vaillancourt, J. E., & Matthews, B. C. 2012, *ApJS*, 201, 13
- Wang, L., Wheeler, J. C., & Höflich, P. 1997, *ApJ*, 476, L27
- Wardle, J. F. C., & Kronberg, P. P. 1974, *ApJ*, 194, 249

Appendix A: Most probable in general case

The MP2 estimators, \hat{p}_{MP2} and $\hat{\psi}_{\text{MP2}}$, have to satisfy Eqs. (8) and (9) simultaneously. These relations can be solved using the fully developed expression of $f_{2\text{D}}$, including the terms of the inverse matrix Σ_p^{-1} :

$$\Sigma_p^{-1} = \begin{pmatrix} v_{11} & v_{12} \\ v_{12} & v_{22} \end{pmatrix} \quad (\text{A.1})$$

leading to

$$\hat{\psi}_{\text{MP2}} = \frac{1}{2} \arctan \left(\frac{\left((v_{11}v_{22} - v_{12}^2)p^2 - v_{11} \right) \sin 2\psi + v_{12} \cos 2\psi}{\left((v_{11}v_{22} - v_{12}^2)p^2 - v_{22} \right) \cos 2\psi + v_{12} \sin 2\psi} \right),$$

$$\hat{p}_{\text{MP2}} = \frac{A_1}{A_2 \cos 2\hat{\psi}_{\text{MP2}} + A_3 \sin 2\hat{\psi}_{\text{MP2}}}, \quad (\text{A.2})$$

with

$$\begin{aligned} A_1 &\equiv p \left(v_{11} \cos^2 2\psi + v_{22} \sin^2 2\psi + 2v_{12} \cos 2\psi \sin 2\psi \right) - 1/p, \\ A_2 &\equiv v_{11} \cos 2\psi + v_{12} \sin 2\psi, \\ A_3 &\equiv v_{22} \sin 2\psi + v_{12} \cos 2\psi. \end{aligned} \quad (\text{A.3})$$

This analytical solution only depends on the input measurements (p, ψ) and the covariance matrix Σ_p . Because the polarization fraction must be positive, there is a lower limit of the S/N so that $\hat{p}_{\text{MP2}} = 0$. In that case, $\hat{\psi}_{\text{MP2}}$ is not constrained anymore and can be chosen to be any possible value. We set it equal to

the measurement ψ . Moreover, this expression can be simplified when $\rho = 0$, which implies that $v_{12} = 0$, leading to

$$\hat{\psi}_{\text{MP2}} = \frac{1}{2} \arctan \left(\frac{p^2 - 1/v_{22}}{p^2 - 1/v_{11}} \tan 2\psi \right), \quad (\text{A.4})$$

$$\hat{p}_{\text{MP2}} = \frac{p \left(v_{11} \cos^2 2\psi + v_{22} \sin^2 2\psi \right) - 1/p}{v_{11} \cos 2\psi \cos 2\hat{\psi}_{\text{MP2}} + v_{22} \sin 2\psi \sin 2\hat{\psi}_{\text{MP2}}}.$$

In the canonical case ($v_{12} = 0, v_{11} = v_{22} = 1/\sigma_p^2$), we recover the expression derived by Quinn (2012):

$$\begin{aligned} \hat{\psi}_{\text{MP2}} &= \psi, \\ \hat{p}_{\text{MP2}} &= \begin{cases} p - \sigma_p^2/p & \text{for } p > \sigma_p \\ 0 & \text{for } p \leq \sigma_p. \end{cases} \end{aligned} \quad (\text{A.5})$$

Appendix B: Bayesian posterior PDF

We illustrate the shape of the posterior PDF in Fig. B.1, where $B_{2\text{D}}(p_0, \psi_0 | p, \psi, \Sigma_p)$ is shown at four levels of the S/N and five couples of (ε, ρ) . It is interesting to notice that the posterior PDF allows the polarization fraction to be zero at low S/N, when these values were rejected by the PDF (see Appendix B of PMA I). Moreover, the posterior PDF peaks at the location of the measurements used to compute it. As largely emphasized in PMA I, we also recall that once the effective ellipticity of the covariance matrix departs from the canonical simplification, the PDFs are sensitive to the initial true polarization angle ψ_0 .

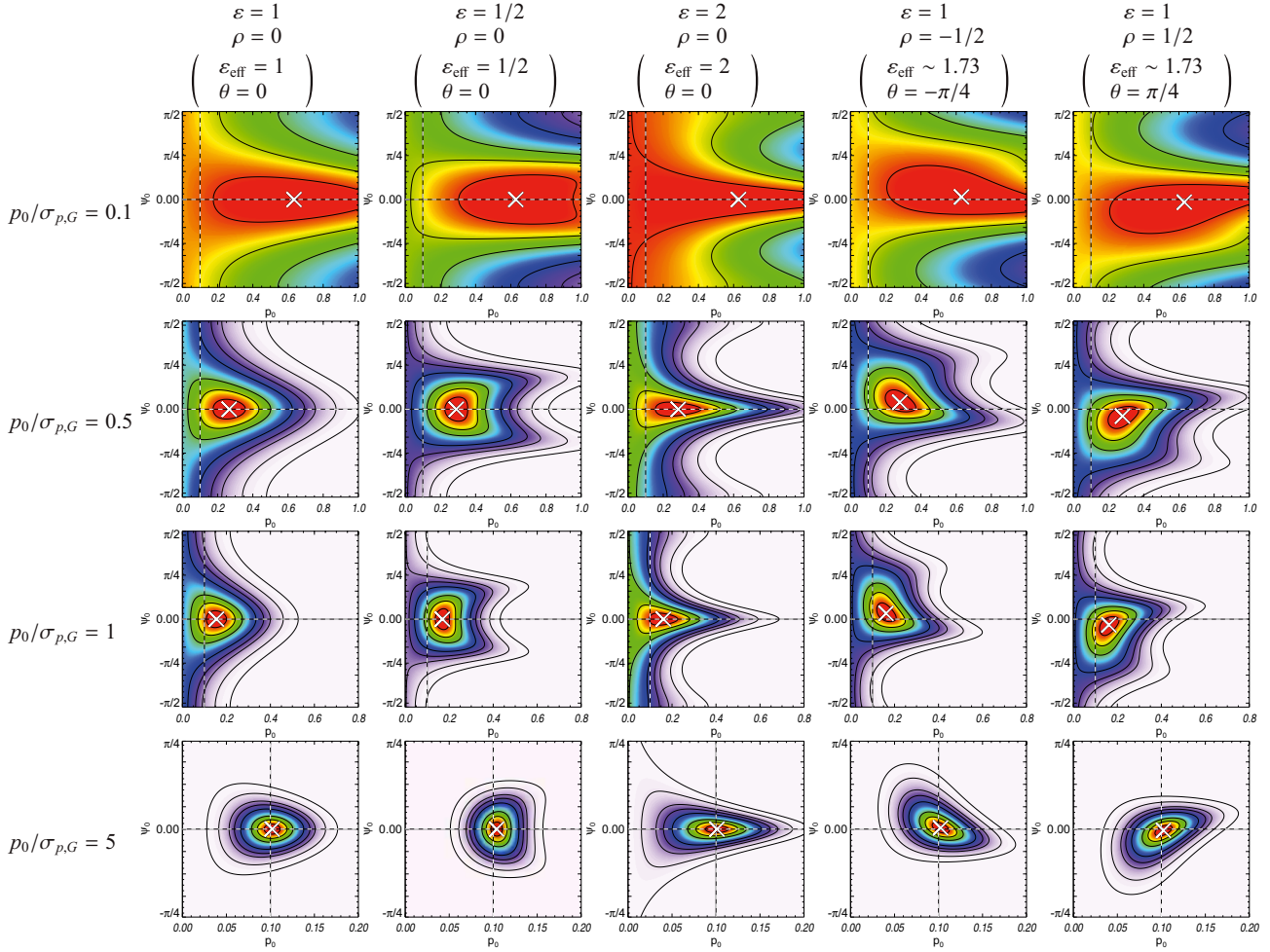


Fig. B.1. Posterior probability density functions $B_{2D}(p_0, \psi_0 | p, \psi, \Sigma_p)$ computed for the most probable measurements (p, ψ) of the f_{2D} distribution (crosses), which were obtained for a given set of true polarization parameters $\psi_0 = 0^\circ$ and $p_0 = 0.10$ (dashed lines) and various configurations of the covariance matrix, at four levels of S/N $p_0/\sigma_{p,G} = 0.1, 0.5, 1,$ and 5 (top to bottom). The scales of the p_0 and ψ_0 axes may vary from one row to the next in order to focus on the interesting part of the PDF. The black contours provide the 90, 70, 50, 20, 10, 5, 1, and 0.1% levels.

Appendix C: Mean Bayesian posterior analytical expression

In the canonical case, the MB estimator of the polarization fraction p takes a simple analytical expression. The Bayesian posterior on p is given in this case by

$$B_p(p_0 | p, \Sigma_p) = \frac{R(p | p_0, \Sigma_p) \cdot \kappa(p_0)}{\int_0^1 R(p | p'_0, \Sigma_p) \kappa(p'_0) dp'_0}, \quad (\text{C.1})$$

where κ is the prior chosen equal to one over the definition range ($[0, 1]$), and R denotes the Rice (1945) function which is defined by

$$R(p | p_0, \Sigma_p) = \frac{p}{\sigma_p^2} \exp\left(-\frac{p^2 + p_0^2}{2\sigma_p^2}\right) I_0\left(\frac{pp_0}{\sigma_p^2}\right), \quad (\text{C.2})$$

where $I_0(x)$ is the zeroth-order modified Bessel function of the first kind (Gradshteyn & Ryzhik 2007), and $\sigma_p = \sigma_Q/I_0 = \sigma_U/I_0$ is the characteristic noise level of the polarization fraction.

The MB estimator and the posterior variance take the following forms

$$\hat{p}_{\text{MB}} = \frac{\int_0^1 p_0 e^{(-p_0^2/2\sigma_p^2)} I_0\left(\frac{pp_0}{\sigma_p^2}\right) dp_0}{\int_0^1 e^{(-p_0^2/2\sigma_p^2)} I_0\left(\frac{pp_0}{\sigma_p^2}\right) dp_0} \quad (\text{C.3})$$

and

$$\hat{\sigma}_{p,\text{MB}}^2 = \frac{\int_0^1 (p_0 - \hat{p}_{\text{MB}})^2 e^{(-p_0^2/2\sigma_p^2)} I_0\left(\frac{pp_0}{\sigma_p^2}\right) dp_0}{\int_0^1 e^{(-p_0^2/2\sigma_p^2)} I_0\left(\frac{pp_0}{\sigma_p^2}\right) dp_0}. \quad (\text{C.4})$$

If we assume in a first approximation that the integral of p_0 over $[0, 1]$ can be taken over $[0, +\infty)$ (which is fine at high S/N), and we use the formula of Prudnikov et al. (1986),

$$\int_0^\infty x^{a-1} e^{-bx^2} I_0(cx) dx = \frac{1}{2} b^{-a/2} \Gamma(a/2) {}_1F_1\left(\frac{a}{2}, 1, \frac{c^2}{4b}\right), \quad (\text{C.5})$$

where Γ is the Gamma function, ${}_1F_1$ the confluent hypergeometric function of the first kind, and $a, b,$ and c all positive reals, we can derive

$$\begin{aligned} \int_0^\infty e^{(-p_0^2/2\sigma_p^2)} I_0\left(\frac{pp_0}{\sigma_p^2}\right) dp_0 &= \frac{1}{2} \left(\frac{1}{2\sigma_p^2}\right)^{-\frac{1}{2}} \Gamma\left(\frac{1}{2}\right) {}_1F_1\left(\frac{1}{2}, 1, \frac{p^2}{2\sigma_p^2}\right) \\ &= \sqrt{\pi/2} \sigma_p e^{p^2/4\sigma_p^2} I_0\left(p^2/4\sigma_p^2\right) \end{aligned} \quad (\text{C.6})$$

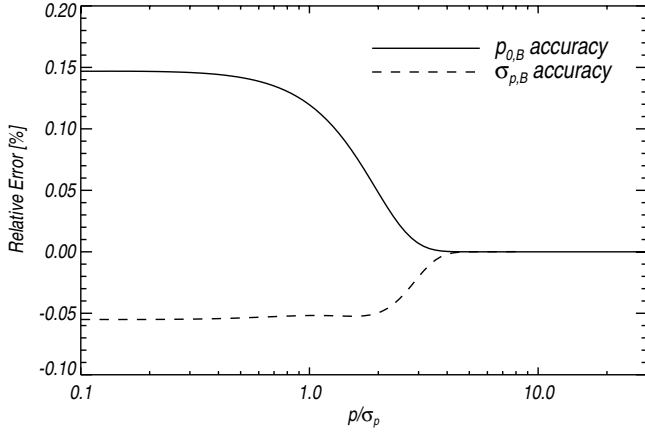


Fig. C.1. Accuracy of the approximate analytical expression of the Bayesian estimates of the polarization fraction \hat{p}_{MB} (solid line) and its associated uncertainty $\hat{\sigma}_{p,\text{MB}}$ (dashed line), as a function of the S/N of the measurement p/σ_p , where $\sigma_p = \sigma_Q/I_0 = \sigma_U/I_0$.

and

$$\int_0^\infty p_0 e^{(-p_0^2/2\sigma_p^2)} \mathcal{I}_0\left(\frac{pp_0}{\sigma_p^2}\right) dp_0 = \sigma_p^2 {}_1F_1\left(1, 1, \frac{p^2}{2\sigma_p^2}\right) = \sigma_p^2 e^{p^2/2\sigma_p^2}, \quad (\text{C.7})$$

and finally

$$\int_0^\infty p_0^2 e^{(-p_0^2/2\sigma_p^2)} \mathcal{I}_0\left(\frac{pp_0}{\sigma_p^2}\right) dp_0 = \frac{1}{2} \left(\frac{1}{2\sigma_p^2}\right)^{-\frac{3}{2}} \Gamma\left(\frac{3}{2}\right) {}_1F_1\left(\frac{3}{2}, 1, \frac{p^2}{2\sigma_p^2}\right) = \sqrt{\pi/2} \sigma_p^3 {}_1F_1\left(\frac{3}{2}, 1, \frac{p^2}{2\sigma_p^2}\right). \quad (\text{C.8})$$

We finally obtain the simple expression of the MB estimator and the associated Bayesian variance:

$$\hat{p}_{\text{MB}} = \frac{\sigma_p \sqrt{\frac{2}{\pi}} \exp\left(\frac{p^2}{4\sigma_p^2}\right)}{\mathcal{I}_0\left(\frac{p^2}{4\sigma_p^2}\right)} \quad (\text{C.9})$$

and

$$\hat{\sigma}_{p,\text{MB}} = \hat{p}_{\text{MB}} \sqrt{\frac{\pi}{2} \exp\left(\frac{-3p^2}{4\sigma_p^2}\right) \mathcal{I}_0\left(\frac{p^2}{4\sigma_p^2}\right) {}_1F_1\left(\frac{3}{2}, 1, \frac{p^2}{2\sigma_p^2}\right) - 1}. \quad (\text{C.10})$$

As shown in Fig. C.1, this analytical approximation gives less than 0.15% of relative error at low S/N compared to the exact \hat{p}_{MB} estimate and less than 0.05% for the associated uncertainty. This small departure quickly tends to 0 for a $S/N > 4$. Thus these expressions may be used to speed up the computing time when the canonical simplification may be assumed.

We explore in Fig. C.2 to the extent at which the canonical simplification may be done in the presence of an effective ellipticity of the covariance matrix. In this more general case, we suggest changing σ_p into $\sigma_{p,G}$ in the Eqs. (C.9) and (C.10). The relative error between the approximate estimate and the exact Bayesian estimate has been explored in two regimes of the covariance matrix, the *low* ($1 < \varepsilon_{\text{eff}} < 1.1$) and *tiny*

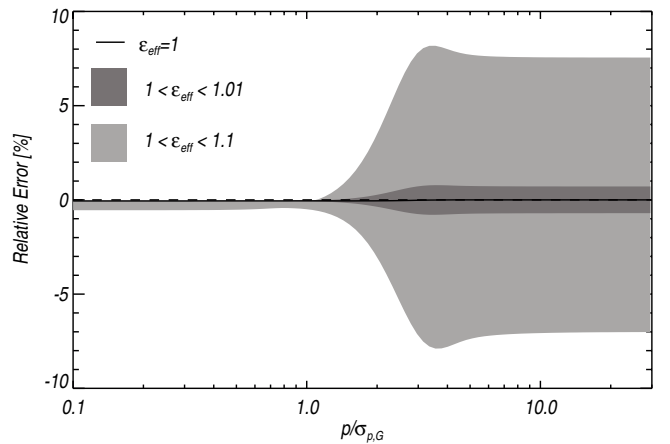
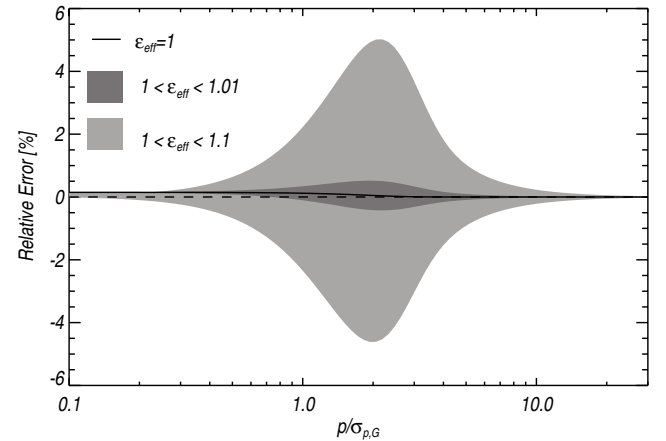


Fig. C.2. Accuracy of the generalized approximate analytical expression of the Bayesian estimates \hat{p}_{MB} (top) and $\hat{\sigma}_{p,\text{MB}}$ (bottom), taking the full covariance matrix components into account, in the *low* (light grey) and *tiny* (dark grey) regimes.

($1 < \varepsilon_{\text{eff}} < 1.01$) regimes. Three domains are observed in the top panel of Fig. C.2 dealing with the accuracy of the \hat{p}_{MB} estimate: i) at low S/N (< 1), the bias on p is so large that the presence of an effective ellipticity does not significantly affect the estimate in comparison; ii) for an intermediate range of the S/N ($1 < S/N < 4$), the effective ellipticity of the Σ_p significantly affects the Bayesian estimate so that the departure of the analytical approximation from the exact estimate becomes important; iii) at high S/N (> 4), the noise is so low that the Bayesian estimate is not sensitive to the asymmetry of the covariance matrix anymore. Consequently, the approximate analytical expression provides very good estimates of \hat{p}_{MB} for $S/N < 1$ and $S/N > 4$, and 5% to 0.5% of relative error for intermediate $1 < S/N < 4$ in the *low* and *tiny* regimes of the covariance matrix, respectively. In the *extreme* regime of the covariance matrix, the relative error increases up to 20%.

Concerning the accuracy of the Bayesian approximate estimate $\hat{\sigma}_{p,\text{MB}}$ of the polarization fraction uncertainty (bottom panel), the agreement is better than 0.1% for $S/N < 1$, and about 8% $S/N > 1$ in the *low* regime, and 1% in the *tiny* regime. Because the uncertainty becomes small compared to the polarization fraction at high S/N, up to 8% of error in $\hat{\sigma}_{p,\text{MB}}$ is still acceptable for this approximation.

Planck intermediate results. XIX. An overview of the polarized thermal emission from Galactic dust[★]

Planck Collaboration: P. A. R. Ade⁷⁸, N. Aghanim⁵⁴, D. Alina^{83,10}, M. I. R. Alves⁵⁴, C. Armitage-Caplan⁸¹, M. Arnaud⁶⁷, D. Arzoumanian⁵⁴, M. Ashdown^{64,6}, F. Atrio-Barandela¹⁸, J. Aumont⁵⁴, C. Baccigalupi⁷⁷, A. J. Banday^{83,10}, R. B. Barreiro⁶¹, E. Battaner^{85,86}, K. Benabed^{55,82}, A. Benoit-Lévy^{24,55,82}, J.-P. Bernard^{83,10,★★}, M. Bersanelli^{33,47}, P. Bielewicz^{83,10,77}, J. J. Bock^{62,11}, J. R. Bond⁹, J. Borrill^{13,79}, F. R. Bouchet^{55,82}, F. Boulanger⁵⁴, A. Bracco⁵⁴, C. Burigana^{46,31}, R. C. Butler⁴⁶, J.-F. Cardoso^{68,1,55}, A. Catalano^{69,66}, A. Chamballu^{67,15,54}, R.-R. Chary⁵³, H. C. Chiang^{27,7}, P. R. Christensen^{74,36}, S. Colombi^{55,82}, L. P. L. Colombo^{23,62}, C. Combet⁶⁹, F. Couchot⁶⁵, A. Coulais⁶⁶, B. P. Crill^{62,75}, A. Curto^{6,61}, F. Cuttaia⁴⁶, L. Danese⁷⁷, R. D. Davies⁶³, R. J. Davis⁶³, P. de Bernardis³², E. M. de Gouveia Dal Pino⁶⁰, A. de Rosa⁴⁶, G. de Zotti^{43,77}, J. Delabrouille¹, F.-X. Désert⁵¹, C. Dickinson⁶³, J. M. Diego⁶¹, S. Donzelli⁴⁷, O. Doré^{62,11}, M. Douspis⁵⁴, J. Dunkley⁸¹, X. Dupac³⁹, G. Efstathiou⁵⁷, T. A. Enßlin⁷², H. K. Eriksen⁵⁸, E. Falgarone⁶⁶, K. Ferrière^{83,10}, F. Finelli^{46,48}, O. Forni^{83,10}, M. Frailis⁴⁵, A. A. Fraisse²⁷, E. Franceschi⁴⁶, S. Galeotta⁴⁵, K. Gangui¹, T. Ghosh⁵⁴, M. Giard^{85,10}, Y. Giraud-Héraud¹, J. González-Nuevo^{61,77}, K. M. Górski^{62,87}, A. Gregorio^{34,45,50}, A. Gruppuso⁴⁶, V. Guillet⁵⁴, F. K. Hansen⁵⁸, D. L. Harrison^{57,64}, G. Helou¹¹, C. Hernández-Monteagudo^{12,72}, S. R. Hildebrandt¹¹, E. Hivon^{55,82}, M. Hobson⁶, W. A. Holmes⁶², A. Hornstrup¹⁶, K. M. Huffenberger²⁵, A. H. Jaffe⁵², T. R. Jaffe^{83,10}, W. C. Jones²⁷, M. Juvela²⁶, E. Keihänen²⁶, R. Keskitalo¹³, T. S. Kisner⁷¹, R. Kneissl^{38,8}, J. Knoche⁷², M. Kunz^{17,54,3}, H. Kurki-Suonio^{26,41}, G. Lagache⁵⁴, A. Lähteenmäki^{2,41}, J.-M. Lamarre⁶⁶, A. Lasenby^{6,64}, C. R. Lawrence⁶², J. P. Leahy⁶³, R. Leonardi³⁹, F. Levrier⁶⁶, M. Liguori³⁰, P. B. Lilje⁵⁸, M. Linden-Vørnle¹⁶, M. López-Cañiego⁶¹, P. M. Lubin²⁸, J. F. Macías-Pérez⁶⁹, B. Maffei⁶³, A. M. Magalhães⁶⁰, D. Maino^{33,47}, N. Mandolesi^{46,5,31}, M. Maris⁴⁵, D. J. Marshall⁶⁷, P. G. Martin⁹, E. Martínez-González⁶¹, S. Masi³², S. Matarrese³⁰, P. Mazzotta³⁵, A. Melchiorri^{32,49}, L. Mendes³⁹, A. Mennella^{33,47}, M. Migliaccio^{57,64}, M.-A. Miville-Deschênes^{54,9}, A. Moneti⁵⁵, L. Montier^{83,10}, G. Morgante⁴⁶, D. Mortlock⁵², D. Munshi⁷⁸, J. A. Murphy⁷³, P. Naselsky^{74,36}, F. Nati³², P. Natoli^{31,4,46}, C. B. Netterfield²⁰, F. Novello⁶³, D. Novikov⁵², I. Novikov⁷⁴, C. A. Oxborrow¹⁶, L. Pagano^{32,49}, F. Pajot⁵⁴, R. Paladini⁵³, D. Paoletti^{46,48}, F. Pasian⁴⁵, T. J. Pearson^{11,53}, O. Perdereau⁶⁵, L. Perotto⁶⁹, F. Perrotta⁷⁷, F. Piacentini³², M. Piat¹, D. Pietrobon⁶², S. Plaszczynski⁶⁵, F. Poidevin^{24,59,37}, E. Pointecouteau^{83,10}, G. Polenta^{4,44}, L. Popa⁵⁶, G. W. Pratt⁶⁷, S. Prunet^{55,82}, J.-L. Puget⁵⁴, J. P. Rachen^{21,72}, W. T. Reach⁸⁴, R. Rebolo^{59,14,37}, M. Reinecke⁷², M. Remazeilles^{63,54,1}, C. Renault⁶⁹, S. Ricciardi⁴⁶, T. Riller⁷², I. Ristorcelli^{83,10}, G. Rocha^{62,11}, C. Rosset¹, G. Roudier^{1,66,62}, J. A. Rubiño-Martín^{59,37}, B. Rusholme⁵³, M. Sandri⁴⁶, G. Savini⁷⁶, D. Scott²², L. D. Spencer⁷⁸, V. Stolyarov^{6,64,80}, R. Stompor¹, R. Sudiwala⁷⁸, D. Sutton^{57,64}, A.-S. Suur-Uski^{26,41}, J.-F. Sygnet⁵⁵, J. A. Tauber⁴⁰, L. Terenzi⁴⁶, L. Toffolati^{19,61}, M. Tomasi^{33,47}, M. Tristram⁶⁵, M. Tucci^{17,65}, G. Umata⁴², L. Valenziano⁴⁶, J. Valiviita^{26,41}, B. Van Tent⁷⁰, P. Vielva⁶¹, F. Villa⁴⁶, L. A. Wade⁶², B. D. Wandelt^{55,82,29}, A. Zacchei⁴⁵, and A. Zonca²⁸

(Affiliations can be found after the references)

Received 28 April 2014 / Accepted 30 January 2015

ABSTRACT

This paper presents an overview of the polarized sky as seen by *Planck* HFI at 353 GHz, which is the most sensitive *Planck* channel for dust polarization. We construct and analyse maps of dust polarization fraction and polarization angle at 1° resolution, taking into account noise bias and possible systematic effects. The sensitivity of the *Planck* HFI polarization measurements allows for the first time a mapping of Galactic dust polarized emission on large scales, including low column density regions. We find that the maximum observed dust polarization fraction is high ($p_{\max} = 19.8\%$), in particular in some regions of moderate hydrogen column density ($N_{\text{H}} < 2 \times 10^{21} \text{ cm}^{-2}$). The polarization fraction displays a large scatter at N_{H} below a few 10^{21} cm^{-2} . There is a general decrease in the dust polarization fraction with increasing column density above $N_{\text{H}} \approx 1 \times 10^{21} \text{ cm}^{-2}$ and in particular a sharp drop above $N_{\text{H}} \approx 1.5 \times 10^{22} \text{ cm}^{-2}$. We characterize the spatial structure of the polarization angle using the angle dispersion function. We find that the polarization angle is ordered over extended areas of several square degrees, separated by filamentary structures of high angle dispersion function. These appear as interfaces where the sky projection of the magnetic field changes abruptly without variations in the column density. The polarization fraction is found to be anti-correlated with the dispersion of polarization angles. These results suggest that, at the resolution of 1°, depolarization is due mainly to fluctuations in the magnetic field orientation along the line of sight, rather than to the loss of grain alignment in shielded regions. We also compare the polarization of thermal dust emission with that of synchrotron measured with *Planck*, low-frequency radio data, and Faraday rotation measurements toward extragalactic sources. These components bear resemblance along the Galactic plane and in some regions such as the Fan and North Polar Spur regions. The poor match observed in other regions shows, however, that dust, cosmic-ray electrons, and thermal electrons generally sample different parts of the line of sight.

Key words. ISM: general – dust, extinction – ISM: magnetic fields – ISM: clouds – submillimeter: ISM

1. Introduction

Our Galaxy is pervaded by an interstellar magnetic field of a few microgauss, which fills the entire disk and halo. This magnetic field manifests itself in a variety of ways, including Zeeman splitting of atomic and molecular spectral lines, Faraday rotation of polarized radio signals, synchrotron emission from relativistic

* Appendices are available in electronic form at <http://www.aanda.org>

** Corresponding author: J.-P. Bernard,
e-mail: Jean-Philippe.Bernard@irap.omp.eu

electrons, and polarization of starlight and thermal dust emission. With a pressure larger than the thermal pressure of all phases and comparable to that of the cosmic rays (Cox 2005), the Galactic magnetic field (GMF) plays a crucial role in the ecosystem of our Galaxy. In conjunction with gravity, it governs the structure and the dynamics of the interstellar medium (ISM), regulates the process of star formation, accelerates cosmic rays, and channels their trajectories to confine them to the Galaxy. In addition to a large-scale regular, or coherent, component and a fluctuating component produced by interstellar turbulence (with scales up to 100 pc; e.g., Gaensler & Johnston 1995; Haverkorn et al. 2008), the GMF also possesses an ordered random (e.g., Beck 2009; Jaffe et al. 2010), or striated random (Jansson & Farrar 2012a), component, whose orientation remains nearly constant over large scales, but whose strength and sign vary on small scales. Such fields are probably produced through compression or shearing of isotropic random fields by the Galactic differential rotation, or at large-scale spiral arm shocks, or else by rising hot plasma bubbles.

Our knowledge and understanding of the GMF has improved considerably over the past few years, as a result of both progress in the quality (sensitivity and resolution) of radio observations and extensive modelling efforts (e.g., Sun et al. 2008; Sun & Reich 2010; Ruiz-Granados et al. 2010; Jaffe et al. 2010, 2011; Pshirkov et al. 2011; Fauvet et al. 2012, 2013; Jansson & Farrar 2012a,b). However, the existing radio observations have inherent limitations, as both Faraday rotation measures (RMs) and synchrotron (total and polarized) intensities are quantities integrated over the line of sight (LOS), which depend on the poorly constrained density distributions of thermal and relativistic electrons, respectively. A promising avenue to obtain a more complete and more robust picture of the GMF structure is to complement the radio data with *Planck*¹ measurements of the polarized thermal emission from interstellar dust, which is independent of the electron densities.

A glance at the *Planck* all-sky intensity maps (Planck Collaboration I 2014) reveals that, in addition to the mottled structure of the cosmic microwave background (CMB) at high Galactic latitudes, the dominant pattern is that of the emission from our Galaxy. At the lowest frequencies, from the 30 GHz to 70 GHz bands of the *Planck* Low Frequency Instrument (LFI, Bersanelli et al. 2010), synchrotron emission dominates; at the highest frequencies, from the 217 GHz to 857 GHz bands of the High Frequency Instrument (HFI, Lamarre et al. 2010), thermal emission from interstellar dust is the dominant emission. These foregrounds have to be understood and taken into account for detailed CMB studies, but they also provide a unique opportunity to study the Galaxy's ISM.

In particular, the thermal dust emission is linearly polarized (e.g., Benoît et al. 2004; Vaillancourt 2007). This polarized emission overpowers any other polarized signal at the higher *Planck* frequencies (e.g., Tucci et al. 2005; Dunkley et al. 2009; Fraise et al. 2009). In addition to hindering the detection of the sought-after, odd-parity, *B*-mode polarization of the CMB (Planck Collaboration Int. XXX 2015), the polarized dust emission provides, in combination with the emission spectrum itself,

a powerful constraint on the physical properties of the dust and on the structure of the magnetic field in the Galaxy.

The linear polarization of the thermal dust emission arises from a combination of two main factors. Firstly, a fraction of the dust grain population is non-spherical, and this gives rise to different emissivities for radiation with the electric vector parallel or orthogonal to a grain's longest axis. Secondly, the grains are aligned by the interstellar magnetic field because they are rotating, probably with differing efficiencies depending on grain size and composition (Draine & Fraise 2009). While the details of this process remain unclear (Lazarian 2003, 2007), there is a consensus that the angular momentum of a grain spun up by photon-grain interactions (Dolginov & Mitrofanov 1976; Draine & Weingartner 1996, 1997; Lazarian & Hoang 2007; Hoang & Lazarian 2008) becomes aligned with the grain's shortest axis, and then with the magnetic field via precession (e.g., Martin 1971). The end result is that, if we look across magnetic field lines, the rotating grain has its long axis orthogonal to the field lines, and accordingly dust emission is linearly polarized with its electric vector normal to the sky-projected magnetic field².

A related phenomenon occurs at near-UV/optical/NIR wavelengths (e.g., Martin 2007), where the light from background sources becomes linearly polarized as a result of dichroic extinction by the aligned dust grains (Davis & Greenstein 1951). Because extinction is higher for light vibrating parallel to the grain's longest axis, i.e., perpendicular to the field lines, the transmitted light is linearly polarized with its electric vector parallel to the sky-projected magnetic field. In fact, historically, the optical polarization caused by dust extinction led to the prediction that thermal dust emission would be polarized in the millimetre and submillimetre domains (Stein 1966). The predicted orthogonality of the electric vectors in the optical and submillimetre on the same line of sight has been demonstrated (Planck Collaboration Int. XXI 2015).

Thus, polarized thermal dust emission carries important information on the interstellar magnetic field structure, on the grain alignment mechanisms, and on the grain geometrical and physical properties. For example, polarization observations between 300 μm and 3 mm, essentially the domain of the *Planck* HFI instrument, can potentially discriminate between the polarizing grain materials, e.g., silicate and graphite dust versus silicate-only grains (Martin 2007; Draine & Fraise 2009; Planck Collaboration Int. XXI 2015; Planck Collaboration Int. XXII 2015).

The far-IR dust thermal emission being a tracer of the dust mass along the LOS, sensitivity limits explain why detailed dust polarized emission was observed mostly in fairly dense, massive regions of the ISM (Dotson et al. 2000; Curran & Chrysostomou 2007; Matthews et al. 2009; Dotson et al. 2010), in general close to the Galactic plane. Measurements of the more diffuse medium were obtained at relatively low ($\geq 2^\circ$) angular resolution. At these large scales, the Archeops balloon experiment (Benoît et al. 2004; Ponthieu et al. 2005) detected the thermal dust emission polarization at 353 GHz. The highest frequency channel of WMAP (Page et al. 2007; Bennett et al. 2013), 94 GHz, picked up the long-wavelength Rayleigh-Jeans tail of the diffuse dust emission and its polarization (in addition to synchrotron emission).

¹ *Planck* (<http://www.esa.int/Planck>) is a project of the European Space Agency (ESA) with instruments provided by two scientific consortia funded by ESA member states (in particular the lead countries France and Italy), with contributions from NASA (USA) and telescope reflectors provided by a collaboration between ESA and a scientific consortium led and funded by Denmark.

² Note that Faraday rotation is unimportant at the frequency considered here (353 GHz). Even an RM of up to ~ 1000 [rad/m²] through the Galactic plane (see, e.g., Van Eck et al. 2011) results in a rotation of the polarization direction less than a tenth of a degree.

The *Planck* satellite’s HFI instrument has led to the first all-sky survey of the polarized submillimetre and millimetre sky, where thermal dust emission dominates. At 353 GHz, the *Planck* data have an angular resolution of $5'$. The polarization sensitivity was expected to be such that, at a resolution of $15'$, ISM structures with $A_V = 1$ mag would be detected with a relative uncertainty on the polarization fraction of about 40% and an uncertainty on the polarization angle of about 30° (Pelkonen et al. 2009). These figures improve significantly at higher A_V and/or lower resolution. The polarized *Planck* data bring the first all-sky fully sampled map of the polarized emission from dust. As such, they provide unprecedented information on the magnetic field geometry and the dust polarization properties relevant to the disk of the Milky Way (MW) and star forming regions, for which they provide statistical information that is missing in stellar polarization extinction data. It should be emphasized, however, that the dust polarized emission provides information mostly on the orientation of the sky-projected magnetic field and only very indirect indication about the angle of that field with respect to the plane of the sky, and it is expected to be insensitive to the field strength.

This paper presents a subset of the *Planck* polarization data and their large-scale statistical properties. A companion paper (Planck Collaboration Int. XX 2015) analyses the variations of the polarization fraction and angle described here, in the framework of simulations of anisotropic magneto-hydrodynamic (MHD) turbulence. Two other papers provide a detailed analysis of the wavelength dependence of the dust polarization, as seen by the HFI instrument (Planck Collaboration Int. XXII 2015) and a comparison between the dust polarization at visible and submillimetre wavelengths (Planck Collaboration Int. XXI 2015).

In Sect. 2 we describe the data, including discussion of systematic effects and the effects of the CMB intensity and polarization. Maps are presented in Sect. 3, as well as the statistics of the data. Sect. 4 discusses the implications of the 353 GHz polarimetry for our understanding of the GMF structure, and the conclusions are drawn in Sect. 5. Three appendices discuss the smoothing of the noise covariance matrices, which is needed when the original data are averaged, the debiasing methods for obtaining polarization estimates, and tests for the effects of systematic noise bias on the structures that we observe in maps of the polarization angle dispersion function.

2. Data

The *Planck* mission results are presented in Planck Collaboration I (2014) and the in-flight performance of the two focal plane instruments, the High Frequency Instrument (HFI) and the Low Frequency Instrument (LFI), are given in Planck HFI Core Team (2011) and Mennella et al. (2011), respectively. The data processing and calibration of the HFI data used here are described in Planck Collaboration VI (2014), Planck Collaboration VII (2014), Planck Collaboration VIII (2014), Planck Collaboration IX (2014) and Planck Collaboration X (2014). The data processing and calibration of the LFI data are described in Planck Collaboration II (2014), Planck Collaboration III (2014), Planck Collaboration IV (2014), and Planck Collaboration V (2014).

The *Planck* polarization and total intensity data that we use in this analysis have been generated in exactly the same manner as the data publicly released in March 2013 and described in Planck Collaboration I (2014) and associated papers. Note however that the publicly available data include only temperature

maps based on the first two surveys. Planck Collaboration XVI (2014) shows the very good consistency of cosmological models derived solely from total intensity with polarization data at small scale (high CMB multipoles). However, as detailed in Planck Collaboration VI (2014; see their Fig. 27), the 2013 polarization data are known to be affected by systematic effects at low multipoles which were not yet fully corrected, and thus, not used for cosmology. We have been careful to check that the Galactic science results in this paper are robust with respect to these systematics. The error-bars we quote include uncertainties associated with residual systematics as estimated by repeating the analysis on different subsets of the data. We have also checked our data analysis on the latest version of the maps available to the collaboration, to check that the results we find are consistent within the error-bars quoted in this paper.

The maps used include data from five independent consecutive sky surveys (called Survey1-Survey5) for HFI, taken six months apart. Due to the scanning strategy of the *Planck* mission, surveys taken one year apart (i.e., odd surveys 1 and 3 and even surveys 2 and 4) share the same observing pattern, which is different for even and odd surveys. Survey5 had a different scan pattern from the other odd-numbered surveys, owing to a change in the precession phase. The products also include data binned into the first and second halves of the *Planck* stable pointing periods, or “half-rings” (called HR1 and HR2). Both single-survey and half-ring data are used for consistency checks and to assess the level of systematic effects. Here, we only analyse the polarization data at 353 GHz, which is the highest frequency *Planck* channel with polarization capabilities and the one with the best S/N for dust polarization. We use the 30 GHz LFI data in our comparison of the dust emission at 353 GHz with the microwave and radio synchrotron emission presented in Sect. 4.4.

In the *Planck* map-making process (Planck Collaboration VIII 2014), measurements from various detectors at the same frequency are combined to obtain the Stokes parameters (I , Q , and U) at each position on the sky. The reconstructed polarization is a linear combination of the weighted differences between the signal from pairs of polarization sensitive bolometers (PSBs) with different orientations on the sky. The resulting maps of the *Planck* Stokes parameters Q and U used in this paper are shown in Fig. 1. The corresponding map of the observed polarization intensity $P = (Q^2 + U^2)^{1/2}$ is shown in Fig. 2. The total intensity map used in this work is shown in Fig. 5.

2.1. Conventions and notations

The relations between the observed Stokes parameters (I , Q , and U) and the polarization fraction (p) and polarization angle (ψ) are given by

$$p = \frac{\sqrt{Q^2 + U^2}}{I} \quad (1)$$

and

$$\psi = 0.5 \times \arctan(U, Q), \quad (2)$$

where the two arguments function $\arctan(Y, X)$ is used to compute $\text{atan}(Y/X)$ avoiding the π ambiguity, such that

$$\begin{aligned} Q &= p \times I \times \cos(2\psi), \\ U &= p \times I \times \sin(2\psi). \end{aligned} \quad (3)$$

For the Stokes parameters provided in the *Planck* data, the angle convention above is with respect to Galactic coordinates

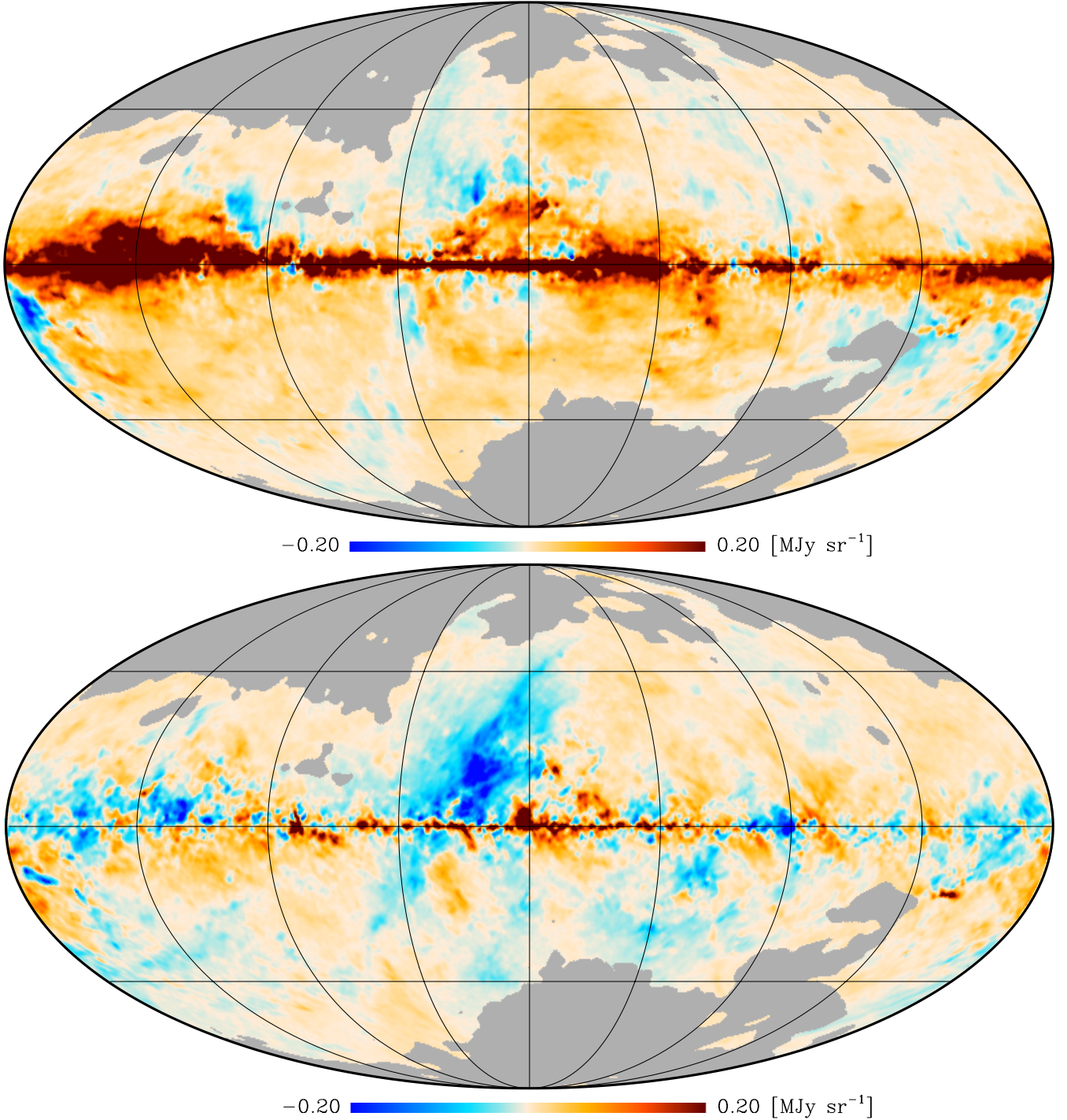


Fig. 1. *Planck* 353 GHz polarization maps at 1° resolution. *Upper:* Q Stokes parameter map. *Lower:* U Stokes parameter map. The maps are shown with the same colour scale. High values are saturated to enhance mid-latitude structures. The values shown have been bias corrected as described in Sect. 2.3. These maps, as well as those in following figures, are shown in Galactic coordinates with the Galactic centre in the middle and longitude increasing to the left. The data are masked as described in Sect. 2.4.

with $-90^\circ < \psi < +90^\circ$, $\psi = 0^\circ$ toward Galactic north, and ψ becoming positive toward Galactic west, the direction of decreasing Galactic longitude (i.e., ψ increases clockwise). Note that this convention is the one used in the HEALPix³ software (Górski et al. 2005), but is different from the IAU convention (Hamaker & Bregman 1996), which is $\psi = 0^\circ$ toward Galactic north but with ψ becoming positive toward Galactic east, the direction

of increasing Galactic longitude (i.e., ψ increases counterclockwise). The conversion between *Planck* Stokes parameters and the IAU convention is given by:

$$\psi_{\text{IAU}} = 0.5 \times \arctan(-U, Q). \quad (4)$$

In this paper, all quoted values of the polarization angle are given in the IAU convention.

³ <http://healpix.jpl.nasa.gov>

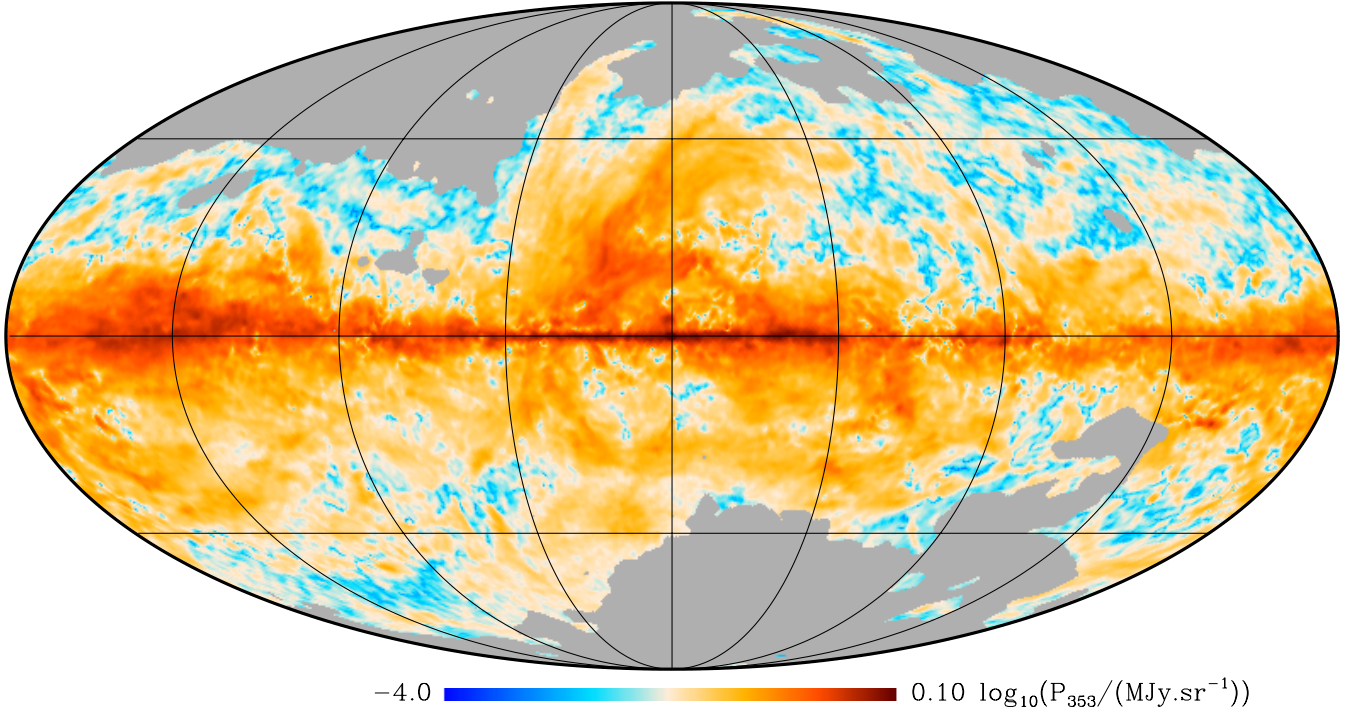


Fig. 2. *Planck* 353 GHz polarized intensity (P) map at 1° resolution in \log_{10} scale. The values shown have been bias corrected as described in Sect. 2.3. The same mask as in Fig. 1 is applied.

2.2. Bandpass mismatch leakage correction

Owing to the way the polarization maps are constructed, any instrumental difference between detectors of the same channel may produce a fake polarization signal, even for unpolarized sky signal inputs. This is the case for the bandpass mismatch (BPM) between detectors that affects *Planck* polarization maps. In practice, the effect corresponds to a leakage term from total intensity I into polarization Q and U . The BPM polarization leakage effect is therefore strongest in regions of high intensity, i.e., along the Galactic plane, and affects both p and ψ . Because the 353 GHz intensity data used here are calibrated on the CMB signal, no BPM leakage is produced by the CMB anisotropies. Other astrophysical emission sources, however, produce BPM polarization leakage.

Knowing the actual *Planck* sky scanning strategy and the orientations of the polarization sensitive bolometers in the focal plane, the BPM polarization leakage corrections can be estimated from the relative responses of each detector to a given sky astrophysical emission. The Planck Collaboration is exploring different methods to compute the relative responses of detectors, as well as to produce total intensity maps for each sky emission source. Two methods have been used to determine the relative responses (Planck Collaboration IX 2014). The first one (method A) involves computing the BPM leakage between bolometers using the ground-measured bandpasses (Planck Collaboration IX 2014). The second one (method B) deduces the relative detector response on regions of the sky where we can obtain I , Q , and U maps for each detector individually. Note that this can only be performed in limited regions of the sky, outside the Galactic plane, which have been scanned in a large number of configurations, allowing for the full reconstruction of I , Q , and U per detector. A comparison between the two methods is presented in Planck Collaboration IX (2014).

When folding the above coefficients into the *Planck* scanning strategy, we have chosen to produce template maps $T_{b(\nu)}^X$ of the

BPM leakage contribution for each frequency (ν) channel, for each bolometer ($b(\nu)$) and for each Stokes parameter (X being Q or U). The BPM polarization leakage correction is

$$L_\nu^X = \sum_{b(\nu)} R_{b(\nu)} I_\nu T_{b(\nu)}^X, \quad (5)$$

where $R_{b(\nu)}$ represents the detector relative responses and I_ν is the sky total intensity. For the purpose of the study presented here we only take into account BPM leakage from dust thermal emission, because this is the dominant term at 353 GHz. The template maps in Eq. (5) were computed using the *Planck* thermal dust model described in Planck Collaboration XI (2014). We used the standard *Planck* map-making procedure presented in Planck Collaboration VIII (2014). Note that the *Planck* 353 GHz channel also includes emission from the CO ($J = 3 \rightarrow 2$) line (see Planck Collaboration VI 2014), which should also in principle be included in the BPM leakage correction. This, however, is relatively weak with respect to dust thermal emission and the corresponding BPM effect is expected to be small compared to that from dust. Because we do not concentrate on regions with strong molecular emission in this paper, no correction was applied for the CO emission BPM leakage.

Figure 3 shows the effect of the correction for BPM on the observed distribution of polarization angles toward the plane of the Milky Way ($|b_{\text{II}}| < 5^\circ$) in the four Galactic quadrants (Q1, Q2, Q3 and Q4, defined by $0^\circ < \ell_{\text{II}} < 90^\circ$, $90^\circ < \ell_{\text{II}} < 180^\circ$, $180^\circ < \ell_{\text{II}} < 270^\circ$, and $270^\circ < \ell_{\text{II}} < 360^\circ$, respectively). When no BPM leakage correction is applied, angles are observed to be distributed around $+20^\circ$ and -5° for the inner (Q1 and Q4) and outer (Q2 and Q3) MW regions, respectively. The difference in sign is due to the difference in average detector orientation during Galaxy crossings, resulting from the relative orientation of the scanning strategy and the Galactic plane. Using the two methods discussed above for the determination of the coupling coefficients leads to similar BPM leakage estimates. Note

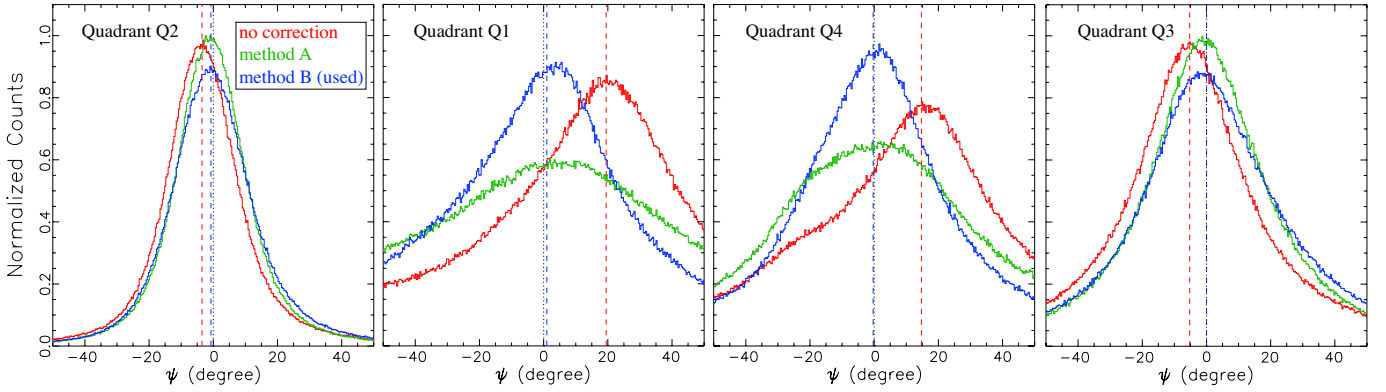


Fig. 3. Histograms of the observed polarized angle at the full data resolution toward the Galactic plane ($|b_{\text{II}}| < 5^\circ$) for the four Galactic quadrants. The various curves show data uncorrected for bandpass mismatch (red), and corrected using sky coupling coefficients derived either from ground (method A: green) or sky measurements (method B: dark blue). The vertical dashed lines show the peak value obtained from fitting the histograms with a Gaussian.

also that because the magnetic field is expected to be statistically aligned with the Galactic plane (see, e.g., [Ferrière 2011](#)) we expect the polarization direction toward the plane to be on average around $\psi = 0^\circ$. The fact that both correction methods bring the peak of the histograms toward this value confirms the validity of the BPM correction method used here. In the following, we adopted the coefficients from method B. We note, however, that although the situation is clearly improved by the BPM leakage correction, the average observed angle distributions still peak a few degrees away from $\psi = 0^\circ$, with the same sign pattern as for the uncorrected data. This could in principle be due to incomplete correction. However, preliminary tests have shown that the remaining correction could be due to non-linearity in the analogue-to-digital conversion (ADC) of the signal, which produces an additional correction with the same sign as observed here and roughly the right amplitude.

We do not attempt here to fully assess the quality of the different corrections, but simply use them to estimate where on the sky the uncertainties in the corrections are small enough to be unimportant for this study. A plot of the BPM-leakage-corrected polarization angle versus the uncorrected polarization angle shows the magnitude of the correction, while the correlation coefficient gives a quantitative measure. For the different corrections considered above, the correlation coefficient is over 0.95 for most regions of the sky at $|b_{\text{II}}| > 5^\circ$. Above $|b_{\text{II}}| = 10^\circ$, the correlation coefficients are above 0.98, implying that the correction becomes very small. This is a natural result of the fact that the intensity that is leaking into polarization is brightest toward the Galactic plane. As measured from the difference between method A and B, the corresponding uncertainties on the polarization angle ψ and fraction p are $|\Delta\psi| < 10^\circ$ and $\Delta p < 1\%$, respectively, toward the inner Galactic plane. These uncertainties become less than the random errors away from the plane. However, BPM leakage corrections are probably not the dominant uncertainty at high Galactic latitudes and very low signal levels, where other systematic effects remaining in the data become more important (see Sect. 2.4). For this reason, we do not discuss specifically the polarization properties in the lowest brightness sky area in this paper and defer this discussion to future papers.

The above discussion applies to the HFI data, but we will also compare the thermal dust emission at 353 GHz to the 30 GHz emission from LFI, which has a similar bandpass leakage issue. The LFI BPM correction is discussed in [Planck Collaboration II \(2014\)](#), where the principle difference is the

presence of multiple astrophysical foregrounds, with different spatial and spectral distributions. The component separation products are therefore used in the LFI BPM correction. From a comparison of the different surveys, we estimate that the uncertainties are of the order $10 \mu\text{K}$ in the polarized intensity and dominated by the noise rather than the leakage except in the innermost plane ($|l_{\text{II}}| < 30^\circ$ and $|b_{\text{II}}| < 3^\circ$), where the effect is only slightly above the noise level. For the polarization angle, we estimate the uncertainties as roughly 15° in the plane ($|b_{\text{II}}| < 5^\circ$) and 35° away. Again the uncertainty appears dominated by noise, with no obvious structure related to the bandpass leakage or scan pattern. We have also cross-checked with WMAP 23 GHz data and verified that the results in Sect. 4.4 are very similar.

2.3. Deriving polarization parameters

The polarization parameters I , p , and ψ are derived from the observed Stokes parameters I , Q , and U using the Bayesian method described in [Montier et al. \(2015a\)](#). This method extends that described in [Quinn \(2012\)](#) by using the full 3×3 noise covariance matrix of each pixel. The effective ellipticity, as defined in [Montier et al. \(2015a\)](#), characterizes the shape of the noise covariance matrix and couples all the terms in Q and U . $\epsilon_{\text{eff}} = 1$ corresponds to the case described in [Quinn \(2012\)](#), whereas $\epsilon_{\text{eff}} > 1$ means that the relation between C_{QQ} , C_{QU} , C_{UU} is not trivial, and there are asymmetries in the noise covariance matrix. We calculated ϵ_{eff} for the *Planck* data used here. At 1° resolution it is normally distributed with a mean value of 1.12 and a standard deviation of 0.04. At the full *Planck* resolution, the distribution of ϵ_{eff} is a bit wider (standard deviation of 0.05), but the mean value does not change. Thus, although they are not very strong, the asymmetries of the noise covariance matrix cannot be neglected, and the Bayesian method is well suited for the analysis of the data.

We use a flat prior on all three parameters p , ψ , and I over a range centred on the conventional value given by Eqs. (1) and (2) for p and ψ and the observed value for I , and a width corresponding to 20σ , where σ is the conventional estimate for the uncertainties (see Appendix B.1). The range on p and ψ is further limited to $-1 < p < 1$ and $-90^\circ < \psi < 90^\circ$, respectively, allowing negative values of p in order to reduce bias in the posterior probability. We compute the 3D posterior probability distribution function (PDF) using 2^7 values on each axis over the parameter range. The values of the polarization parameters are obtained using the mean posterior (MP) estimator on the posterior

3D PDF. A comparison between the polarization parameters and uncertainties obtained with this method and using the conventional approach described in Appendix B.1 is shown in Fig. B.1 for the *Planck* data at 1° resolution.

When spatial smoothing is applied to the polarization data, Stokes parameter maps are convolved with a Gaussian kernel of the appropriate width using the dedicated smoothing software part of the HEALPix library, which guarantees proper transport of Q and U . The maps are then resampled to larger pixel size (as specified by the HEALPix N_{side} parameter) so as to preserve full sampling of the data (pixel size smaller than $1/2.4$ times the data FWHM resolution). The corresponding smoothing of data covariances was performed using the method described in Appendix A. The corresponding smoothed maps of p and ψ are then computed as described above. The statistical uncertainties in p and ψ (σ_p^{stat} and $\sigma_\psi^{\text{stat}}$, respectively) have been estimated as described in Appendix B.3.

2.4. Impact of systematic effects, CIB, ZL, and CMB

We assessed the level of contamination by systematic effects by comparing the maps of p and ψ obtained at 1° resolution for the full *Planck* data with those obtained for the various individual *Planck* surveys (see introduction to Sect. 2). We constructed maps of systematic uncertainties on p and ψ (σ_p^{sys} and σ_ψ^{sys} , respectively) by averaging these differences over the *Planck* individual surveys. These were added to the statistical uncertainty maps σ_p^{stat} and $\sigma_\psi^{\text{stat}}$, to obtain the total uncertainty maps used in the rest of the analysis.

In this paper we only show the *Planck* polarization data and derived quantities where the systematic uncertainties are small and where the dust signal dominates total emission. For this purpose we defined a mask such that $\sigma_p^{\text{sys}} < 3\%$ and $I_{353} > 0.1 \text{ MJy sr}^{-1}$. We defined the mask at a resolution of 1° and smoothed it to 3° resolution to avoid complex edges. As a result, the maps shown exclude 21% of the sky. Note that a different mask is used for the polarization angle dispersion function, as defined in Sect. 3.3.

The cosmic infrared background (CIB) is due to emission from a large number of distant galaxies with random orientations and is expected to be, on average, unpolarized. However, it can contribute non-negligible emission at 353 GHz in low brightness regions of the sky and hence reduces the apparent degree of dust polarization. The zero level of the 353 GHz total intensity map has been established by correlation with Galactic HI, using the method described in Planck Collaboration XI (2014), as was done for the publicly released 2013 maps. This offset is $0.0887 \text{ MJy sr}^{-1}$ (uncertainty $0.0068 \text{ MJy sr}^{-1}$) and was subtracted from the total intensity map we use, which therefore does not contain the CIB monopole. We added the corresponding uncertainty in quadrature with the uncertainty of the total intensity, so that the statistical uncertainties on p include the uncertainty on the CIB subtraction.

The zodiacal light (ZL) has a smooth distribution on the sky. From the model constrained by its detection in the *Planck* bands (Planck Collaboration XIV 2014), its median total intensity at 353 GHz is $1.9 \times 10^{-2} \text{ MJy sr}^{-1}$ over the sky area studied here, and reaches $\approx 4.3 \times 10^{-2} \text{ MJy sr}^{-1}$ in dust lanes near the ecliptic plane. Its polarization in the submillimetre is currently unconstrained observationally. Because this intensity is subdominant over most of the sky fraction and the polarization level of ZL is currently unknown, we apply no correction for the possible contribution of ZL. We note that, if ZL was assumed

unpolarized, subtracting its intensity would raise the observed polarization levels by about 0.5% of the observed polarization fraction, on average over the sky region studied here, and would not change the observed polarization angles. We have checked that no noticeable systematic variation of the polarization fraction is detected in our maps along zodiacal dust lanes.

CMB fluctuations are polarized at a level of 0.56 mK (Kovac et al. 2002) at a resolution of about 1° , which corresponds to $1.6 \times 10^{-4} \text{ MJy sr}^{-1}$ at 353 GHz. In the mask we use here, the effect of CMB polarized fluctuations is therefore negligible and we did not attempt to correct for those fluctuations.

No additional correction was applied to the data.

2.5. External data

In Sect. 4.4, we compare the *Planck* HFI polarization maps with low-frequency radio and microwave observations that are dominated by synchrotron emission over most of the sky. These include:

- the 408 MHz total intensity map of Haslam et al. (1982) from the LAMBDA⁴ site;
- the 1.4 GHz total intensity map of the northern (Reich 1982; Reich & Reich 1986) and southern (Reich et al. 2001) sky;
- the 1.4 GHz polarized intensity maps of the northern (Wolleben et al. 2006) and southern (Testori et al. 2008) sky.

For the analysis in Sect. 4.4, the *Planck* HFI and LFI maps are smoothed to 1° FWHM resolution to match these radio data and downgraded to $N_{\text{side}} = 256$. Most of the 1.4 GHz maps are available on the Bonn survey site⁵ as FITS images in Cartesian coordinates. They are converted into HEALPix using the procedure described in Paradis et al. (2012) and are made available in this form on the CADE site⁶. The resolution of the observations is roughly 1° , and so no additional smoothing is applied to the radio data. The total intensity map at 1.4 GHz is estimated to have an offset of 2.8 K (Reich et al. 2004) due to the combination of zero-level calibration uncertainty, unresolved extragalactic sources, and the CMB, and so this was subtracted from the data.

The total intensity data include thermal bremsstrahlung (free-free) emission, particularly in the plane. This is not negligible at 408 MHz or 1.4 GHz. We use the WMAP MEM free-free solution (Gold et al. 2011) to subtract it. We note that this free-free template likely includes anomalous dust emission, and there are indications that it is an overestimate by roughly 20 to 30% (Alves et al. 2010; Jaffe et al. 2011). Because synchrotron dominates over free-free emission at low radio frequencies, even on the Galactic plane, the uncertainties on the free-free correction are not expected to affect the qualitative comparison with dust emission in this paper. But the MEM template is not sufficiently accurate to correct for free-free when the synchrotron is subdominant at 30 GHz. Furthermore, the 30 GHz total intensity also includes anomalous dust emission for which we have no correction. We therefore do not use 30 GHz in total intensity, but only in polarization.

⁴ <http://lambda.gsfc.nasa.gov>

⁵ <http://www.mpifr-bonn.mpg.de/survey.html>. The southern part of the 1.4 GHz total intensity data was provided by Reich (priv. comm.).

⁶ Analysis Center for Extended Data, <http://cade.irap.omp.eu>

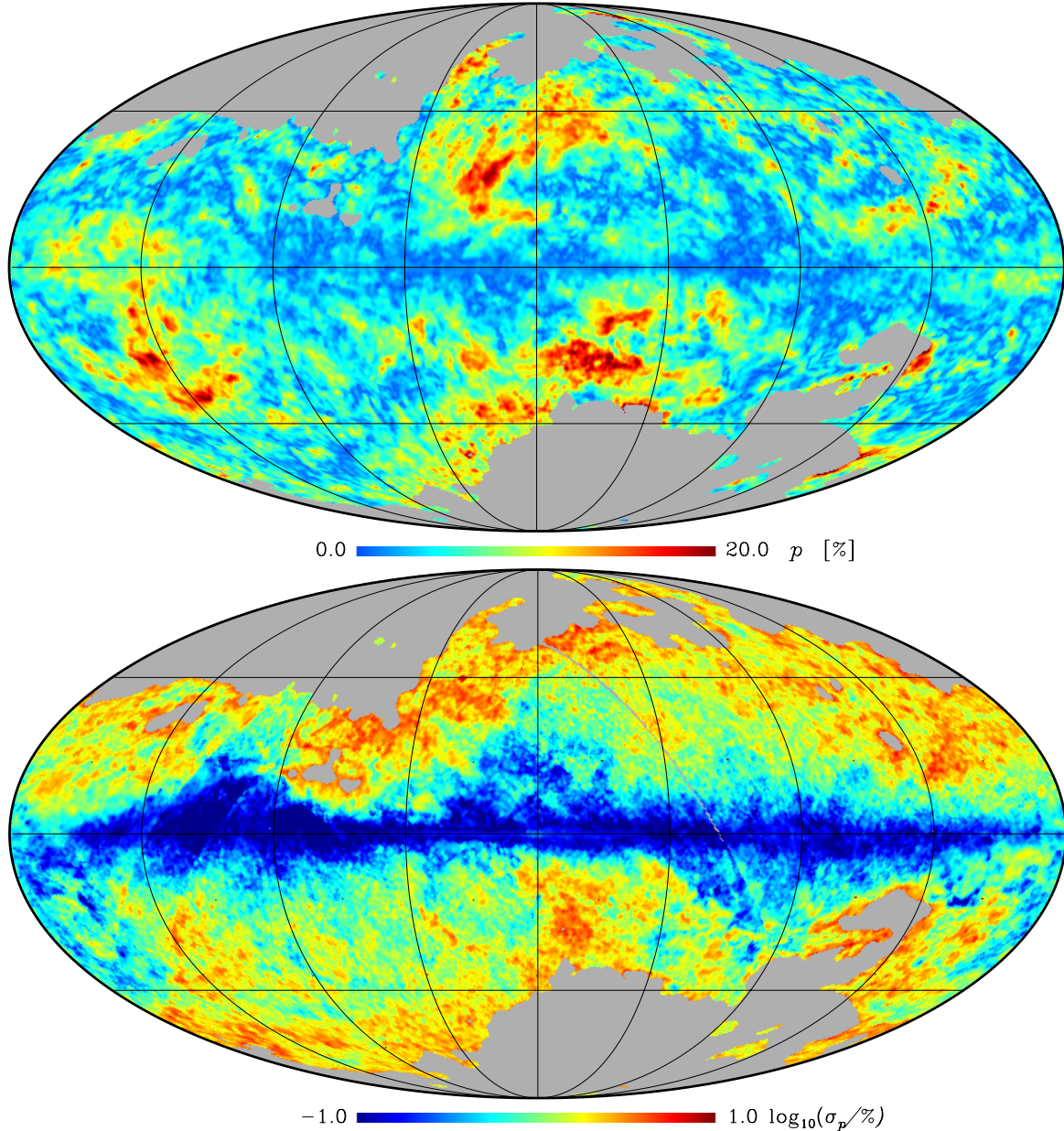


Fig. 4. *Upper:* map of the 353 GHz polarization fraction p at 1° resolution. The colour scale is linear and ranges from 0% to 20%. *Lower:* map of the 353 GHz polarization fraction uncertainty, σ_p , at 1° resolution in \log_{10} scale. The colour scale is from $\sigma_p = 0.1\%$ to $\sigma_p = 10\%$. The data are not shown in the grey areas where the dust emission is not dominant or where residuals were identified comparing individual surveys (see Sect. 2.4). The polarization fraction is obtained using the Bayesian method with a mean posterior estimator (see Sect. 2.3). The uncertainty map includes statistical and systematic contributions. The same mask as in Fig. 1 is applied.

3. Description of the *Planck* polarization maps

Figure 4 shows the maps of the polarization fraction (p) at a resolution of 1° . The map in Fig. 5 is based on the polarization direction, also at a resolution of 1° . Both figures also show the corresponding map of the total uncertainty, which includes the contribution from statistical and systematic uncertainty estimates, as described in Sect. 2.4. The maps were masked as described in Sect. 2.4 in regions where large residual systematic uncertainties were evident or where the total intensity at 353 GHz is not dominated by dust emission. Figures 4 and 5 were constructed using the Bayesian method described in Sect. 2.3, Montier et al. (2015a), and Appendix B.3, in particular the Mean Posterior Bayesian estimator defined in Montier et al. (2015b). These figures are discussed in Sects. 3.1 and 3.2.

In Fig. 6 we highlight several regions of interest that we will discuss below; parameters of these regions are given in Table 1.

3.1. Polarization fraction

As seen from Fig. 4, the measured polarization fraction shows significant variations on the sky. One of the aims of this paper is to characterize those variations as a step toward understanding their origin. These characteristics are compared to those of polarized emission maps computed in simulations of anisotropic MHD turbulence in a companion paper (Planck Collaboration Int. XX 2015).

Figure 4 shows that the polarization fraction of the thermal dust emission can reach up to about 20% in several large-scale

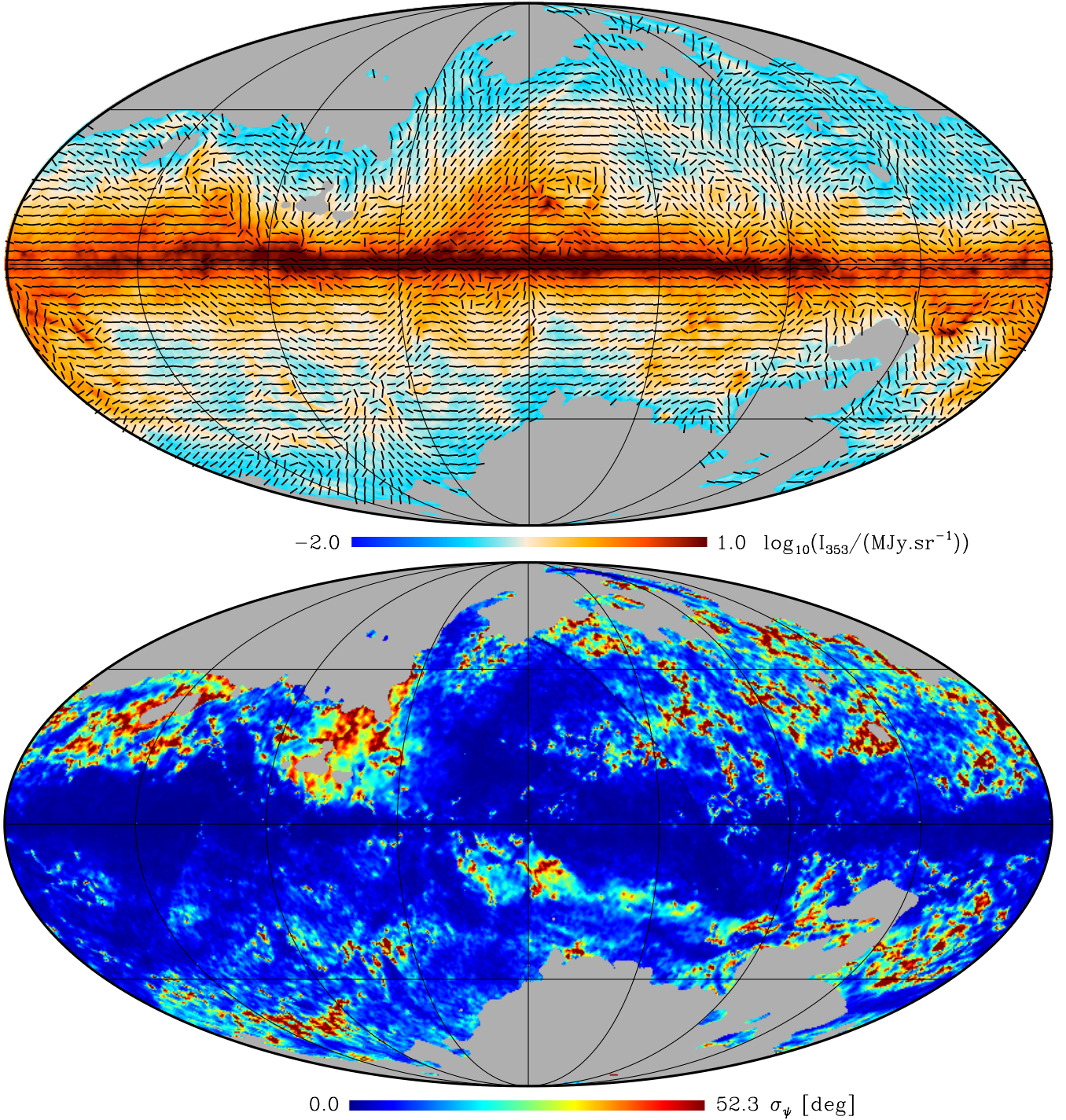


Fig. 5. *Upper:* map of the apparent magnetic field ($\langle \mathbf{B}_\perp \rangle$) orientation. The polarization segments from the measured 353 GHz polarization, having been rotated by 90° , show the orientation of the apparent magnetic field, but their length is constant, not reflecting the changing polarization fraction. The colour map shows the 353 GHz emission in \log_{10} scale and ranges from 10^{-2} to 10 MJy sr $^{-1}$. *Lower:* map of the 353 GHz polarization angle uncertainty (σ_ψ) at 1° resolution. The scale is linear from $\sigma_\psi = 0^\circ$ to $\sigma_\psi = 52.3^\circ$. The polarization angle is obtained using the Bayesian method with a mean posterior estimator (see Sect. 2.3). The uncertainty map includes statistical and systematic contributions. The same mask as in Fig. 1 is applied.

regions of the sky. This is particularly the case in the second Galactic quadrant ($\ell_{\text{II}} \approx 145^\circ$, $b_{\text{II}} \approx 0^\circ$, including a region at low latitude known as “the Fan”⁷), the Perseus area

($\ell_{\text{II}} \approx 143^\circ$, $b_{\text{II}} \approx -25^\circ$), the Loop I area ($\ell_{\text{II}} \approx 40^\circ$, $b_{\text{II}} \approx +45^\circ$) and a region in Microscopium ($\ell_{\text{II}} \approx 15^\circ$, $b_{\text{II}} \approx -40^\circ$). The

⁷ The term “the Fan” generally refers to an area extending over roughly $120^\circ \lesssim \ell_{\text{II}} \lesssim 160^\circ$ and $0^\circ \lesssim b_{\text{II}} \lesssim 20^\circ$ seen in the earliest maps of Galactic polarized radio emission in the 1960s. The region is one of the brightest features of the polarized radio sky and has a distinctive

fan-like appearance of the polarization vectors at low radio frequencies. The “fanning” of these vectors disappears at higher frequencies where Faraday rotation is weak, leaving a large region with coherent polarization that as yet has no definitive explanation. See, e.g., van de Hulst (1967) and Wolleben et al. (2006).

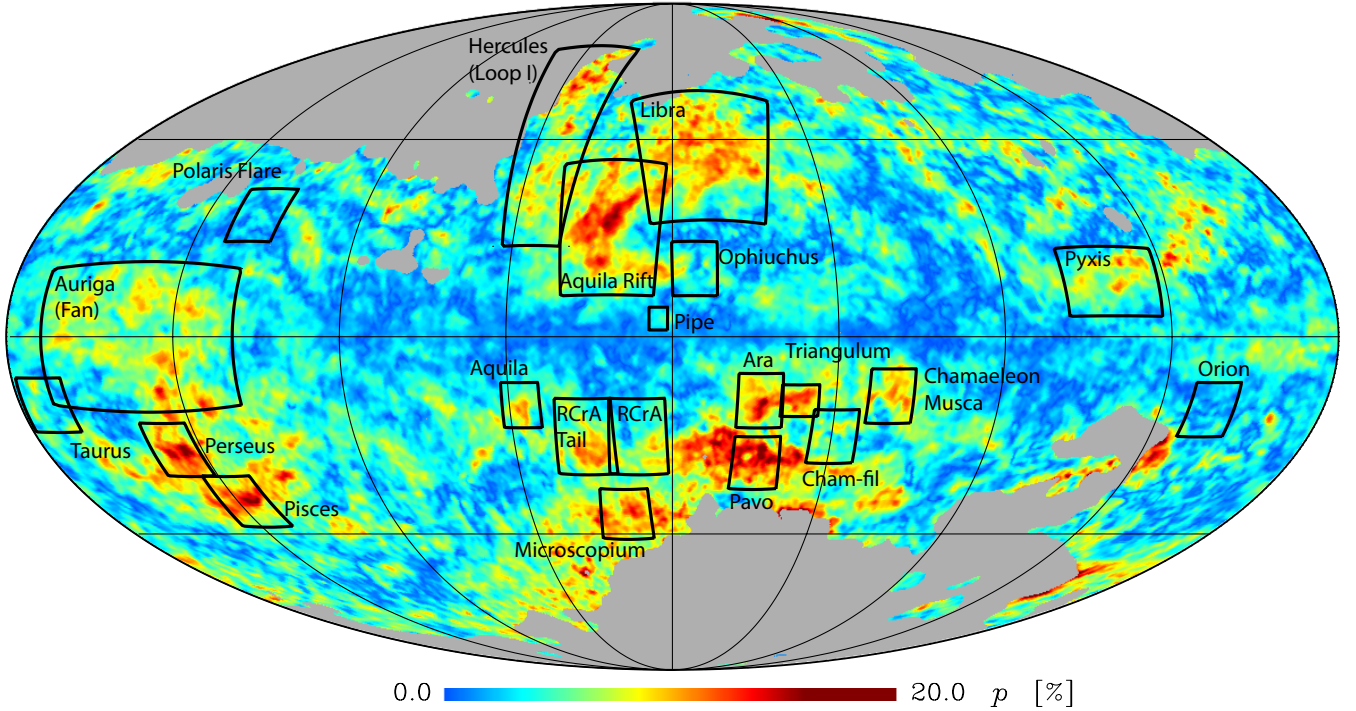


Fig. 6. Map of polarization fraction p from Fig. 4 with selected regions marked; statistics of these regions are given in Table 1.

large-scale distribution of these regions is consistent with predictions from the Galactic magnetic field model used in the Planck Sky Model (PSM) (Delabrouille et al. 2013). This model, based on a simple description of the spiral magnetic field structure of the Milky Way, was optimized to match the WMAP and Archeops data (e.g., Fauvet et al. 2011, 2012). The model computes a dust polarization geometrical efficiency factor g_d , which results from the LOS integration of the magnetic field direction, weighted by the assumed dust density distribution. This factor has a maximum toward the Galactic anticentre at a position corresponding roughly to that of the Fan region and shows two strong maxima at mid-latitude toward the inner Galaxy $\ell_{\text{II}} \simeq 0^\circ$ and $|b_{\text{II}}| \simeq 45^\circ$ which match fairly well with the highly polarized regions detected with *Planck* around Aquila Rift, Libra, and Pavo, above and below the Galactic plane, respectively.

Figure 7 shows the distribution of p as a function of the polarization geometrical efficiency factor g_d , in particular the polarization fraction computed for the bi-symmetrical spiral model of the magnetic field on large scales from Miville-Deschênes et al. (2008). It can be seen that the upper envelope of the distribution roughly matches that allowed by the model, indicating that it is only when g_d is close to unity, i.e., toward regions where the large-scale Galactic magnetic field is preferentially orthogonal to the LOS, that high p values are observed. The dispersion of the points below this line is explained by small scale variations of p of a different origin, described later in this paper.

Figure 8 displays the histogram of the polarized fraction p over the sky fraction shown in Fig. 4, the whole Galactic plane ($|b_{\text{II}}| < 5^\circ$) and the inner Galactic plane ($|b_{\text{II}}| < 5^\circ$, $|\ell_{\text{II}}| < 90^\circ$) at a resolution of 1° . In the plane, the most likely value of p is a few percent while the rest of the mid-latitude sky has a wider distribution, with a peak of the histogram near 4%. The maximum p values can reach about 20%. A more accurate determination of the maximum p value p_{max} , taking into account the effects of data resolution and noise, is given in Sect. 4.1 and leads to a similarly high value. We note that this maximum value is much

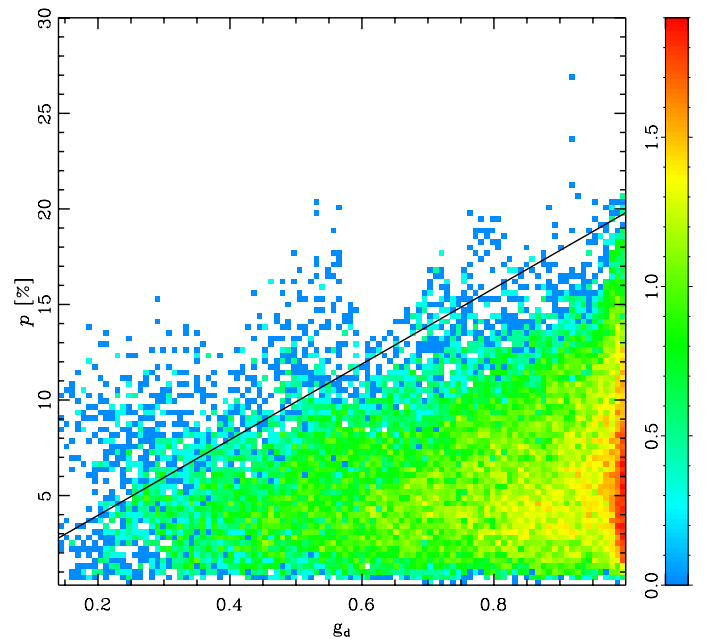


Fig. 7. Distribution (logarithmic scale) of the values of the polarization fraction p as a function of the polarization geometrical efficiency factor g_d . The line shows $p = g_d \times p_{\text{max}}$ where p_{max} is the maximum value discussed in Sect. 4.1.

higher than values reported previously from ground-based observations in the submillimetre. This is mainly because such low brightness regions are too faint to be observed from the ground, and because higher column density and brighter regions, which can be observed from the ground, have a tendency to be less polarized than faint regions (see Sect. 4.2). However, we show in Sect. 4.2 that the high maximum p values in low brightness regions is not a trivial consequence of the decrease of the emission intensity. We also note that the high polarization fractions

Table 1. Polarization characteristics of individual regions shown in Fig. 6, computed at 1° resolution.

Region	ℓ_{II} [°]	b_{II} [°]	$\Delta\ell_{\text{II}}$ [°]	Δb_{II} [°]	min(p) [%]	Mean(p) [%]	Med(p) [%]	Max(p) [%]	σ_p [%]	Med(ψ) [°]	$\hat{\sigma}_\psi$ [°]
Polaris Flare.....	120.0	27.0	12.0	12.0	0.10	3.11	2.94	7.40	1.50	176.72	44.92
Orion.....	211.0	-16.0	12.0	12.0	0.08	3.22	2.97	10.23	1.73	177.17	41.64
Pipe.....	0.0	4.5	5.5	5.5	0.31	3.85	3.53	8.45	1.90	143.13	15.69
Ophiuchus.....	354.0	15.0	12.0	12.0	0.11	5.11	4.59	12.22	2.60	0.84	19.56
Taurus.....	173.0	-15.0	12.0	12.0	0.16	5.08	4.83	11.62	2.19	129.00	58.77
RCrA.....	10.0	-22.0	15.0	17.0	0.30	6.80	6.71	13.97	2.94	11.62	14.36
Chamaeleon-South.....	315.0	-22.0	12.0	12.0	1.40	6.95	6.78	15.29	2.22	14.32	7.41
Pyxis.....	240.0	12.0	25.0	15.0	0.34	7.09	6.96	16.71	3.03	171.04	14.32
Aquila.....	42.0	-15.0	10.0	10.0	0.88	7.71	7.10	14.63	3.00	58.61	11.83
Auriga.....	145.0	0.0	50.0	30.0	0.12	7.55	7.58	18.64	2.76	1.69	11.16
RCrA-Tail.....	25.0	-22.0	15.0	17.0	1.66	8.63	8.40	15.53	3.16	170.71	13.42
Hercules.....	40.0	45.0	15.0	50.0	0.37	8.67	8.59	37.49	3.69	65.26	57.43
Libra.....	350.0	40.0	30.0	30.0	0.34	9.35	9.90	21.39	3.42	20.03	22.47
Chamaeleon-Musca.....	300.0	-13.0	12.0	12.0	0.89	9.29	9.98	15.08	3.15	15.06	9.74
Aquila Rift.....	18.0	24.0	25.0	30.0	0.12	10.25	10.21	20.15	3.55	50.91	11.94
Ara.....	336.0	-14.0	12.0	12.0	3.15	11.18	10.85	21.09	2.99	177.49	7.75
Pisces.....	133.0	-37.0	12.0	12.0	4.32	12.10	11.72	20.81	3.22	15.60	3.97
Microscopium.....	15.0	-40.0	12.0	12.0	6.20	11.78	11.76	18.63	2.27	24.66	9.72
Triangulum.....	325.0	-14.0	10.0	7.0	5.21	12.12	12.12	17.14	2.82	6.66	3.95
Perseus.....	143.0	-25.0	12.0	12.0	5.66	12.68	12.68	21.10	3.20	9.68	4.84
Pavo.....	336.0	-28.0	12.0	12.0	3.60	14.13	14.33	21.77	3.61	14.29	6.78

Notes. The table gives the region name (Col. 1), the Galactic coordinates and extent of the region (Cols. 2–5), the minimum, mean, median, maximum, and standard deviation of p over the region (Cols. 6–10), and the median and standard deviation of ψ (Cols. 11, 12). Note that the values of ψ are given in the IAU convention and the standard deviation of ψ , $\hat{\sigma}_\psi$, is computed after resolving polarization angle ambiguities. Regions are ordered by increasing median p .

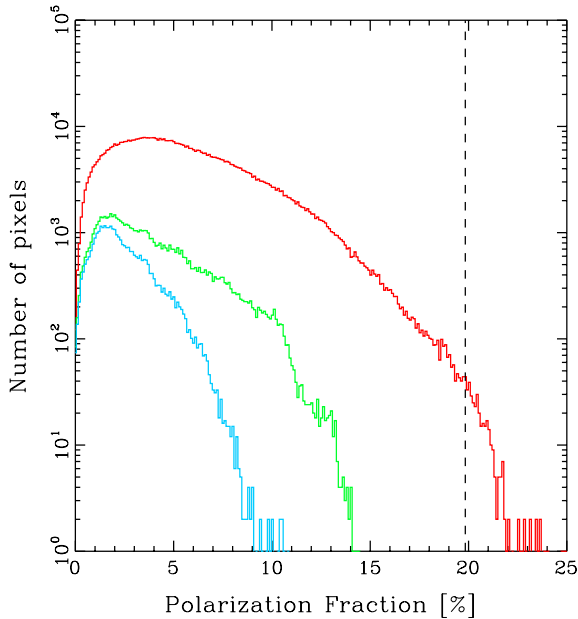


Fig. 8. Histograms of the observed polarization fraction at 1° resolution for the whole sky shown in Fig. 1 (red), the Galactic plane within $|b_{\text{II}}| < 5^\circ$ (green) and the inner Galactic plane within $|b_{\text{II}}| < 5^\circ$ and $|\ell_{\text{II}}| < 90^\circ$ (blue). The vertical dashed line shows the maximum value p_{max} discussed in Sect. 4.1.

observed here are consistent with the value inferred from the Archeops measurements at 353 GHz, which was derived to be as high as 10–20% (Benoît et al. 2004) along the outer Galactic plane, a region which includes the Fan region.

Figures 9–11 display maps around some of the regions outlined in Fig. 6 and listed in Table 1. Figure 9 shows the Aquila

Rift and Fan regions, which show high polarization fraction. These highly polarized regions are generally located in low intensity parts of the sky (e.g., Microscopium, Libra, Pavo or Ara), or at the edge of bright regions (e.g., the Aquila Rift). They are also located in regions of the sky where the polarization direction is uniform over very large areas. For instance, in the Fan region, the magnetic field is oriented almost completely parallel to the Galactic plane (i.e., polarization is orthogonal to the plane) with high accuracy over a region spanning more than 30°, where the polarization fraction consistently has $p > 8\%$ and reaches $p \approx 15\%$ in some areas. Similarly, the highly polarized Aquila Rift region has a \mathbf{B} -field sky projection aligned with the elongated structure of the ridge and the nearby Loop I over most of the extent of the source, and the polarization fraction there reaches up to 20%. The highly polarized region is in fact located on the gradient of the dust emission of the Aquila Rift, and mid-way between the Aquila Rift itself and the radio emission of Loop I. In the Perseus region, the large polarization also appears in fairly low brightness regions, where the orientation of the field is coherent over regions of the sky with typical sizes of a few degrees. Some of these structures were detected in polarized light at other wavelengths. For instance, the Fan, Perseus, and Loop I regions seem to have counterparts detected in polarized thermal dust and synchrotron emission, as well as in the WMAP foreground emission (Gold et al. 2011; Ruiz-Granados et al. 2010; Jansson & Farrar 2012a, and references therein) and in Faraday depth surveys of polarized emission at radio frequencies, such as the Global Magneto-Ionic Medium Survey (GMIMS; Wolleben et al. 2010b). In particular, from the Faraday depth data of GMIMS, a significant portion (about 5%) of the sky was found to be dominated by the magnetic field around a nearby HI bubble (at a distance of ≈ 100 pc) in the general direction of the Loop I region described above (Wolleben et al. 2010a). In general, such regions are identified with nearby Galactic structures

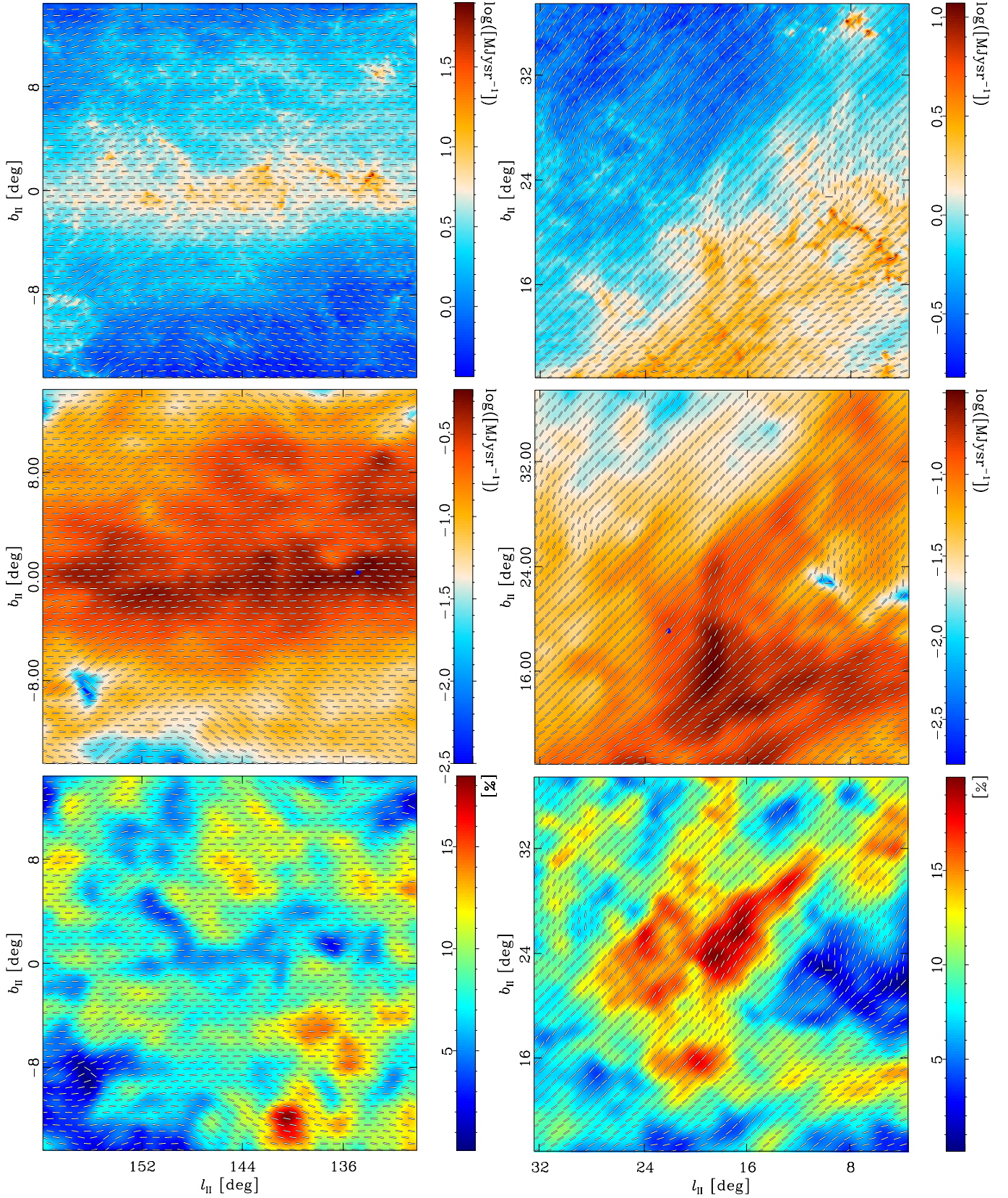


Fig. 9. Maps of the total intensity (*upper*), polarized intensity (*middle*), and polarization fraction (*lower*) at 353 GHz for two of the most polarized regions: the Fan (*left column*), and the Aquila Rift (*right column*). The total intensity map is shown at the full *Planck* resolution, while the polarization information is shown at a resolution of 1° . The polarization segments show the orientation of the apparent magnetic field, but their length is constant, not reflecting the changing polarization fraction. Note that the boundaries of the regions shown here do not match exactly those in Table 1 and Fig. 6.

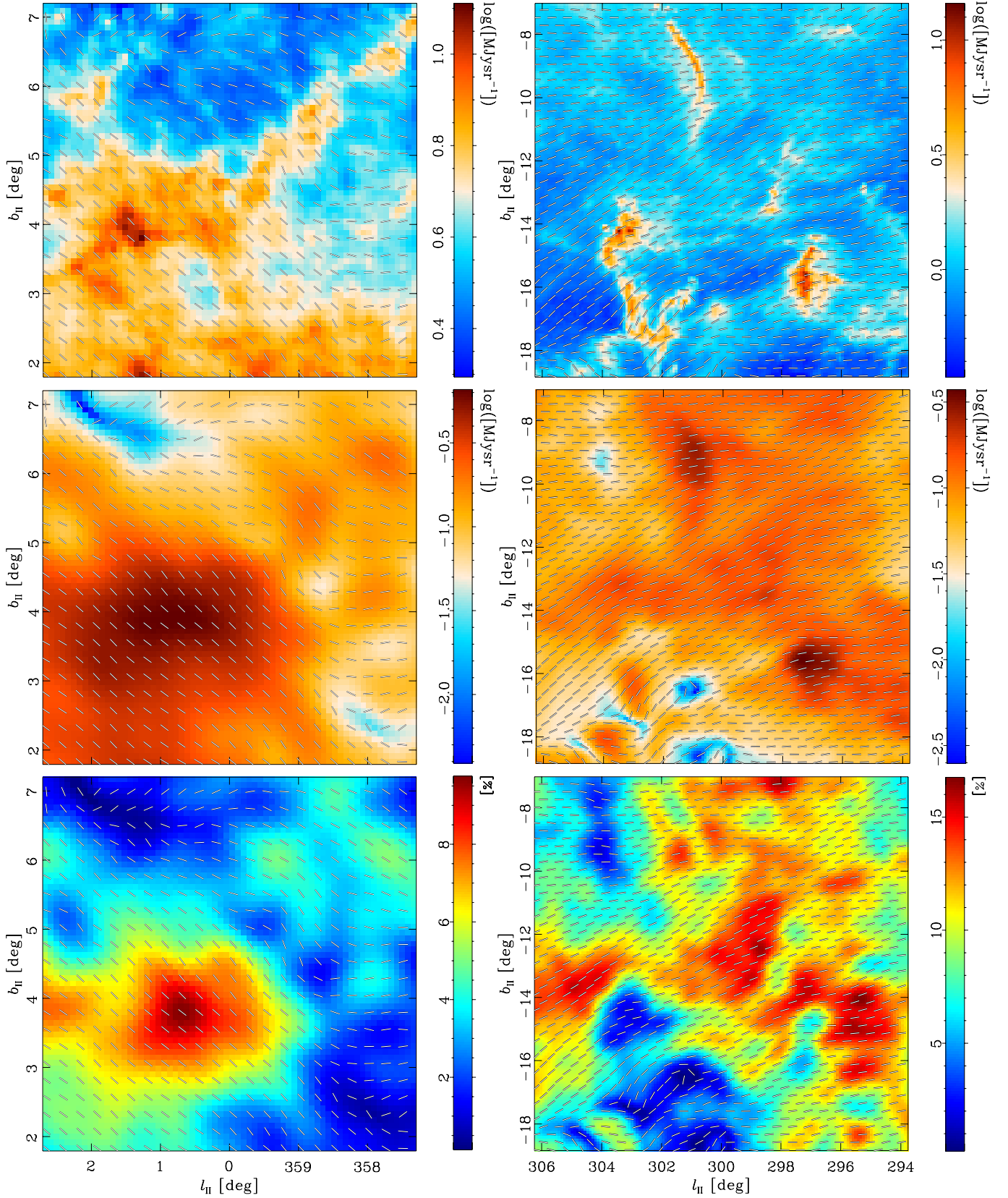


Fig. 10. Maps of the total intensity (*upper*), polarized intensity (*middle*) and polarization fraction (*lower*) at 353 GHz for the Pipe Nebula (*left column*), and Chamaeleon-Musca (*right column*) regions. The total intensity map is shown at the full *Planck* resolution, while the polarization information is shown at a resolution of 30'. The polarization segments show the orientation of the apparent magnetic field, but their length is constant, not reflecting the changing polarization fraction. Note that the boundaries of the regions shown here do not match exactly those in Table 1 and Fig. 6.

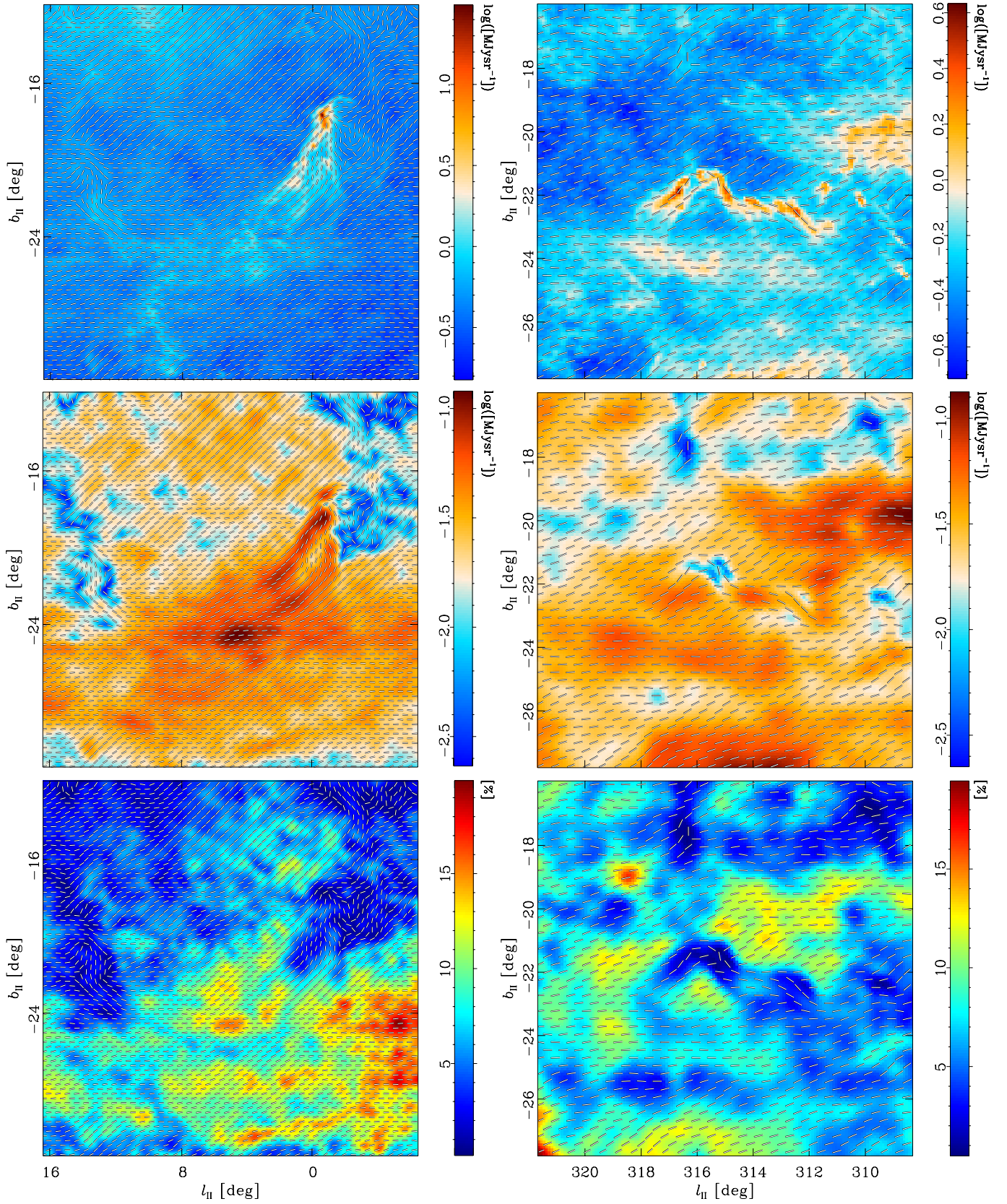


Fig. 11. Maps of the total intensity (*upper*), polarized intensity (*middle*) and polarization fraction (*lower*) at 353 GHz for the RCrA and RCrA-Tail (*left column*), and Chamaeleon-South (*right column*) regions. The total intensity map is shown at the full *Planck* resolution, while the polarization information is shown at a resolution of 30'. The polarization segments show the orientation of the apparent magnetic field, but their length is constant, not reflecting the changing polarization fraction. Note that the boundaries of the regions shown here do not match exactly those in Table 1 and Fig. 6.

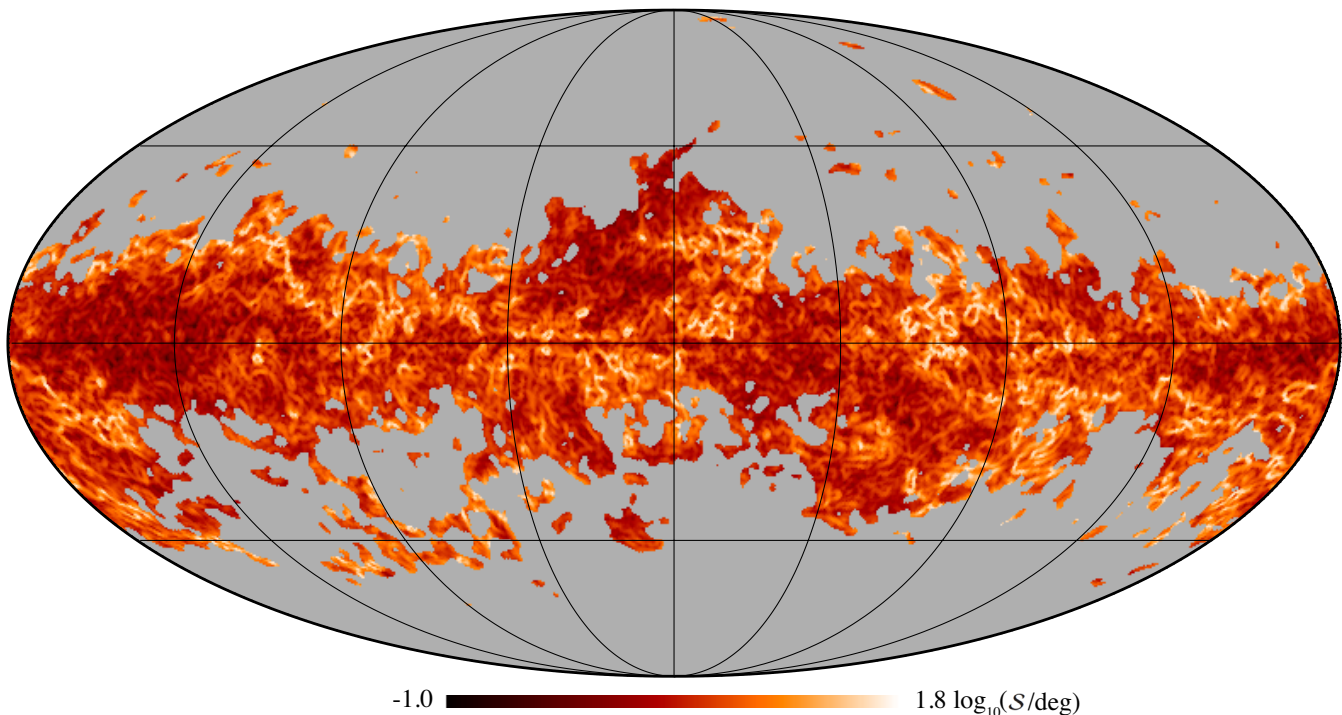


Fig. 12. Map of the polarization angle dispersion function S at 353 GHz with 1° resolution and for lag $\delta = 30'$. The map is shown in \log_{10} scale over the range $0.1^\circ < S < 70^\circ$. Only sky regions where the S/N on S is larger than 3 are shown (see text).

(e.g., supernova remnants and bubbles), which can distort the underlying more regular large-scale pattern of the Galactic magnetic field. Finally, other regions, such as Microscopium, have almost no known counterpart structure at other wavelengths. The area around Ara and Triangulum has been identified only as a region with warmer dust in [Planck Collaboration XIX \(2011\)](#). Here too, the polarization fraction is typically $p > 10\%$ (see also Sect. 4).

As seen in Figs. 4 and 8, the inner Galactic plane shows much lower polarization fractions than the highly polarized regions described above. Because the polarized emission also increases in that region, the decrease of p is a real depolarization effect. It results from a combination of depolarization due to LOS integration and the presence of dense clouds, which tend to have lower polarization fractions (see Sect. 4.2).

Note that the map of polarized intensity itself, Fig. 2, exhibits narrow features where the polarized intensity drops. These regions are also seen as narrow features where the polarization fraction drops (Fig. 6). For instance, one can be followed over several tens of degrees, rising from the Galactic plane at $\ell_{\text{II}} = 90^\circ$ and crossing the Polaris Flare region in Figs. 6 and 17. Inspection of Figs. 9–11 shows that these regions are not trivially peaks of the total intensity with no polarized intensity counterpart. They are sometimes regions with higher gas column density N_{H} (see Sect. 4.2), but not always. They can also be regions where the orientation of the field changes more abruptly (see Sect. 3.2 for a full discussion).

3.2. Polarization angle

Figure 5 shows the large-scale distribution of the polarization direction. In the figure, the direction shown by the normalized segments is that of the observed polarization direction (ψ) rotated by 90° . The figure therefore shows the orientation of the apparent

magnetic field ($\langle \mathbf{B}_\perp \rangle$). In the simplified case that the direction of \mathbf{B} remains homogenous along the LOS, $\langle \mathbf{B}_\perp \rangle$ measures the projection of \mathbf{B} onto the plane of the sky, i.e., perpendicular to the LOS. However, in the more realistic case of a disordered \mathbf{B} structure and inhomogeneous dust distribution along the LOS, it is important to remember that $\langle \mathbf{B}_\perp \rangle$ is a LOS-averaged quantity, weighted by dust emission.

Figure 5 shows that, toward the Galactic plane, $\langle \mathbf{B}_\perp \rangle$ is mostly oriented along the plane, corresponding to a polarization angle close to 0° . This is especially the case toward the outer MW regions. There are a few exceptions, in particular toward lines of sight that are tangent to spiral arms (Cygnus X, $\ell_{\text{II}} \approx 81^\circ$, $b_{\text{II}} \approx 0^\circ$; Carina, $\ell_{\text{II}} \approx 277^\circ$, $b_{\text{II}} \approx -9^\circ$), where the polarization signal is actually the smallest in the plane because in those regions the large-scale magnetic field is parallel to the LOS. This was already noted by [Heiles \(1996\)](#) (and references therein) and [Benoît et al. \(2004\)](#). We also note that the homogeneity of the field orientation being parallel to the plane extends away from the plane and up to $|b_{\text{II}}| \approx 10^\circ$ in many regions (in particular the Fan). At intermediate latitudes, the field orientation follows a few of the well known filamentary intensity structures of the local ISM. In particular, this is the case for the Aquila Rift and most of Loop I (outside the latitude range $b_{\text{II}} \approx 50^\circ - 60^\circ$), where the structure of $\langle \mathbf{B}_\perp \rangle$ follows the intensity flare and loop elongation. As addressed earlier, this orientation of $\langle \mathbf{B}_\perp \rangle$ in those regions was already noted in the synchrotron polarized maps of WMAP ([Gold et al. 2011](#)). Other regions, however, show a variety of relative orientations between the field projection and intensity structures, which can also be orthogonal in some instances. Thus studies with *Planck* submillimetre polarization ([Planck Collaboration Int. XXXII 2015](#); [Planck Collaboration Int. XXXIII 2015](#)) hold promise as a valuable complement to optical and near infrared polarization studies of

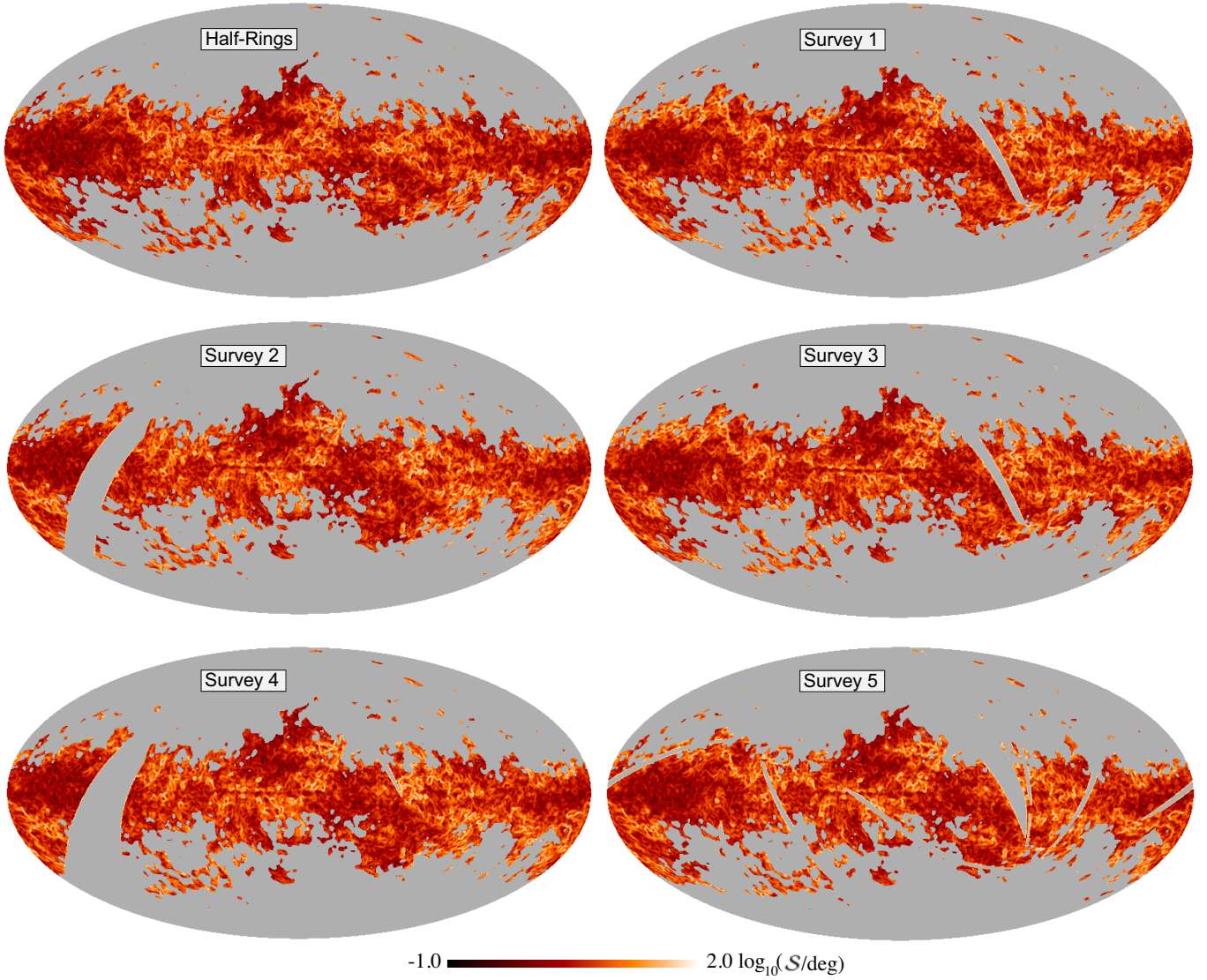


Fig. 13. Maps of the polarization angle dispersion function \mathcal{S} computed from half-ring correlations (\mathcal{S}_H) and for individual *Planck* surveys. The maps are shown with a common \log_{10} scale.

the relative orientation of the magnetic field and structure (e.g., Goodman et al. 1990; Chapman et al. 2011).

3.3. Polarization angle dispersion function

In order to quantify the regularity of the \mathbf{B} field revealed by the polarization measurements, we use the polarization “angle dispersion function” given by

$$\mathcal{S}(\mathbf{x}, \delta) = \left(\frac{1}{N} \sum_{i=1}^N (\Delta\psi_{xi})^2 \right)^{1/2}, \quad (6)$$

where $\Delta\psi_{xi} = \psi(\mathbf{x}) - \psi(\mathbf{x} + \delta_i)$ is the angle difference between $\psi(\mathbf{x})$, the polarization angle at a given sky position \mathbf{x} (the central pixel), and $\psi(\mathbf{x} + \delta_i)$ the polarization angle at a sky position displaced from the centre by the displacement vector δ_i . The average in Eq. (6) is taken over an annulus around the central pixel of radius $\delta = |\delta|$ (the “lag”) and width $\Delta\delta$ and containing N pixels. Note that the angle dispersion function as defined in Eq. (6) is a two-point function, but depends both on position and lag. In that sense, it is distinct from structure functions often used to

describe polarization direction (see Serkowski 1958; Kobulnicky et al. 1994; Hildebrand et al. 2009) which do not depend on position. Note also that different ways of characterizing the field geometry have been used in the literature, such as the normalized spatial gradient of the polarized intensity ($|\nabla P|/P$) discussed in Burkhart et al. (2012) and used in Iacobelli et al. (2014). We have also estimated this quantity using the *Planck* data and the map obtained exhibited the same structure as the map of \mathcal{S} .

In practice, $\Delta\psi_{xi}$ is computed from the Stokes parameters as

$$\Delta\psi_{xi} = \frac{1}{2} \arctan(Q_i U_x - Q_x U_i, Q_i Q_x + U_i U_x), \quad (7)$$

where indices x and i stand for the central and displaced values, respectively. We use $\Delta\delta = \delta$ so that individual pixels are not counted twice when estimating \mathcal{S} at different lags.

The polarization angle dispersion function orientation, irrespective of absolute direction. It provides important information on the magnetic field distribution and orientation (see, e.g., Falceta-Gonçalves et al. 2008; Poidevin et al. 2013). Regions where the sky projection of the magnetic field is well ordered have $\mathcal{S} \simeq 0^\circ$, while regions with a twisted or disordered \mathbf{B} field

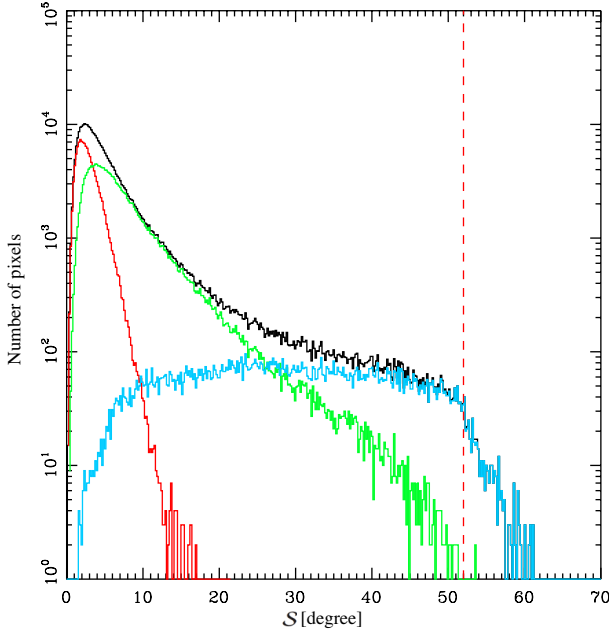


Fig. 14. Histogram of \mathcal{S} at 353 GHz at 1° resolution and a lag $\delta = 30'$. The black curve shows the full distribution over the sky area covered in Fig. 12. The red, green, and blue curves show the histograms for regions covered in Fig. 12 with $p > 5\%$, $1\% < p < 5\%$, and $p < 1\%$, respectively. The vertical dashed line shows $\mathcal{S} = 52^\circ$, which is the limit for pure random noise on \mathcal{S} .

can in principle have up to $\mathcal{S} = 90^\circ$. In addition, because the *Planck* convention for Q and U is defined with respect to the Galactic coordinate system, even a homogeneous field would produce $\mathcal{S} \neq 0^\circ$, due to the coordinate singularity at the poles. In order to avoid this, we have rotated Q and U locally to a different coordinate system so that the current point is at the equator of the new system, before applying Eq. (7). When the signal is dominated by noise, \mathcal{S} converges to $\mathcal{S} = \pi / \sqrt{12} (\approx 52^\circ)$. The angle dispersion function \mathcal{S} is observed to increase with δ , as the coherence is gradually lost when going further away from a given point of the sky. It is expected to increase linearly with lag in the presence of an ordered magnetic field and to steepen at small lags due to either the turbulent component of the magnetic field or the angular resolution of the data used (see, e.g., Hildebrand et al. 2009). The dependence of \mathcal{S} on lag δ can be better probed from the analysis of individual regions at higher resolution, either in emission or in absorption toward stellar clusters (Magalhães et al. 2005; Falceta-Gonçalves et al. 2008; Franco et al. 2010).

Like other quadratic functions, \mathcal{S} is biased positively when noise is present. As described in Hildebrand et al. (2009), \mathcal{S} can be debiased using

$$\mathcal{S}_{\text{db}}^2(\delta) = \mathcal{S}^2(\delta) - \sigma_{\mathcal{S}}^2, \quad (8)$$

where $\sigma_{\mathcal{S}}^2$ is the variance on \mathcal{S} . In the conventional approach, $\sigma_{\mathcal{S}}^2$ can be expressed as a function of σ_{ψ} through partial derivatives as

$$\sigma_{\mathcal{S}}^2 = \frac{1}{N^2 \mathcal{S}^2} \left(\left(\sum_{i=1}^N \Delta\psi_{xi} \right)^2 \sigma_{\psi}^2 + \sum_{i=1}^N (\Delta\psi_{xi})^2 \sigma_{\psi}(\delta_i)^2 \right), \quad (9)$$

where σ_{ψ} is the straightforward standard deviation of ψ , i.e., computed without resolving polarization angle ambiguities. However, this approximation is valid only close to the solution

and leads to a poor estimate of the bias at low S/N. Nonetheless, it is clear from Eqs. (9) and (B.7) that regions with low polarization having higher values of σ_p/p have higher σ_{ψ} and therefore more biased \mathcal{S} .

In order to assess the importance of the bias, we use the two independent half-ring maps H_1 and H_2 of the *Planck* data to compute an unbiased estimate of \mathcal{S}^2 as

$$\mathcal{S}_H^2(\mathbf{x}, \delta) = \frac{1}{N} \sum_{i=1}^N \Delta\psi_{xi}^{H_1} \Delta\psi_{xi}^{H_2}, \quad (10)$$

where $\Delta\psi_{xi}^{H_j}$ is the angle difference for half-ring map H_j , i.e., $\Delta\psi_{xi}^{H_j} = \psi^{H_j}(\mathbf{x}) - \psi^{H_j}(\mathbf{x} + \delta_i)$. In practice, $\Delta\psi_{xi}^{H_j}$ is computed as

$$\Delta\psi_{xi}^{H_j} = \frac{1}{2} \arctan \left(Q_i^{H_j} U_x^{H_j} - Q_x^{H_j} U_i^{H_j}, Q_i^{H_j} Q_x^{H_j} + U_i^{H_j} U_x^{H_j} \right). \quad (11)$$

Although \mathcal{S}_H^2 is unbiased, it suffers from higher noise because only half of the *Planck* data are used. Note also that, unlike \mathcal{S}^2 , \mathcal{S}_H^2 can be negative.

We evaluate \mathcal{S} from the full *Planck* survey (we call this estimate simply \mathcal{S} by default) and \mathcal{S}_H at each pixel of the map using Eqs. (7) and (11), respectively. We also perform a Monte Carlo noise simulation on I , Q , and U for each pixel using the full covariance matrix (using Eq. (A.23)), and assuming that different pixels have independent noise and that the half-ring maps have independent noise. This simulation is used to construct the PDF of \mathcal{S} , \mathcal{S}^2 and \mathcal{S}_H^2 using 1000 noise samples. We then compute the mean posterior estimates and uncertainties of \mathcal{S} , \mathcal{S}^2 and \mathcal{S}_H^2 by integrating over the PDF.

Figure 12 shows the sky distribution of \mathcal{S} computed from the full survey at 353 GHz at 1° resolution for a lag of $\delta = 30'$. Figure 13 shows the same maps obtained from the half-ring survey correlation (\mathcal{S}_H), as well as for individual *Planck* surveys. The mask used in these figures was obtained from the uncertainty on \mathcal{S} , $\sigma_{\mathcal{S}}$, derived from the Monte Carlo analysis described above. The mask is such that the S/N on \mathcal{S} is larger than 3 ($\mathcal{S}/\sigma_{\mathcal{S}} > 3$) and retains 52% of the sky at the adopted analysis resolution of 1° . The differences between individual panels of Fig. 13 are smaller than the 33% statistical uncertainty in the determination of \mathcal{S} within the mask. Figure 14 shows the histogram of \mathcal{S} within the above mask, as well as in subsets of the data with various cuts in p . It shows that most sky pixels with reliable \mathcal{S} have low \mathcal{S} values, and that most of these pixels have large polarization fractions, above $p = 5\%$.

As can be seen in Figs. 12 and 13, a similar structure for \mathcal{S} appears in all estimates in the selection mask, clearly showing that these structures are not caused by a single subsection of the data. We note that, outside the mask, \mathcal{S} shows structures similar to those observed in the mask. However, significant differences appear in some regions, in particular between odd and even *Planck* surveys. We attribute those to an imperfect band-pass mismatch correction or to the fact that no ADC correction has been applied here. We have also conducted tests in order to quantify the possible noise-induced bias on \mathcal{S} . Those are described in Appendix C. Figure 15 shows the map of \mathcal{S} when the resulting estimate of the bias has been subtracted. Comparison with Fig. 12 shows that the effect of bias essentially reduces low \mathcal{S} values, but does not explain the patterns observed in the map. We therefore conclude that the structures seen in the map of the polarization angle dispersion function \mathcal{S} are real, rather than being induced by noise and/or bias. In the rest of the analysis carried out here, we use the map of \mathcal{S} derived from the full survey and only consider pixels where the S/N on \mathcal{S} as derived from

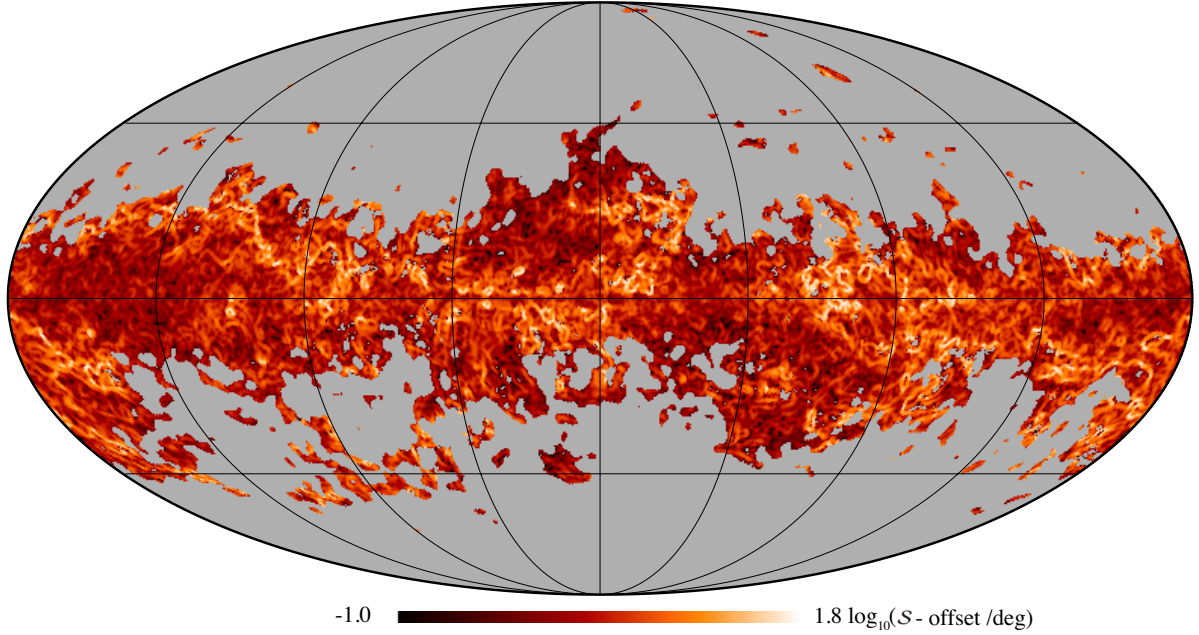


Fig. 15. Same as Fig. 12 but with the noise-induced offset subtracted, as derived from a test with $S = 0^\circ$ (see Appendix C for details).

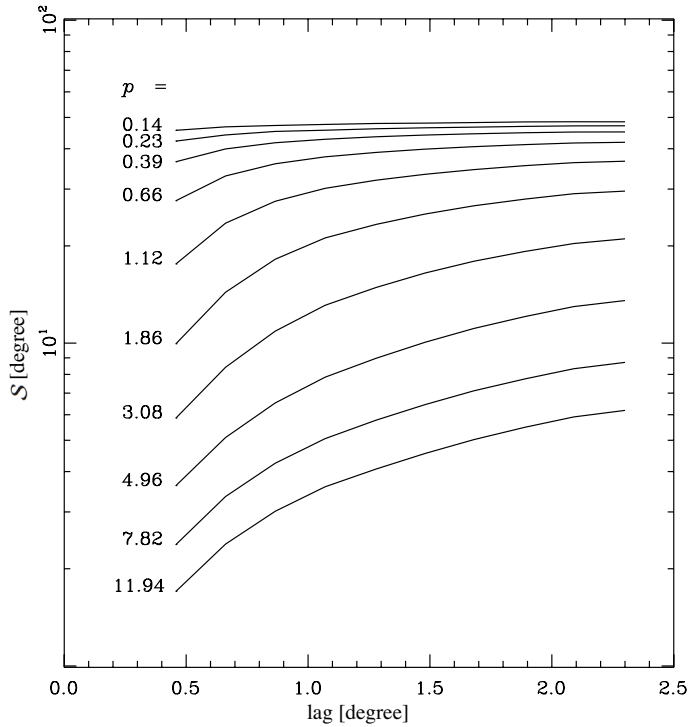


Fig. 16. Evolution of the polarization angle dispersion function (S) at 353 GHz as a function of lag δ , binned in intervals of the polarization fraction p . The curves are labelled with the median polarization fraction in the bin as a percentage.

our Monte Carlo analysis is larger than 3. The resulting map is shown in Fig. 12.

The maps of S reveal that regions with large variations of the polarization direction are organized in an intricate network of elongated and filamentary structures, some spanning several tens of degrees in the sky. The filamentary aspects of the maps generally persist in regions of low S . These structures seem to have little to no correlation with structures in the total intensity

map, except for the few degrees along the inner Galactic plane that systematically show low values of S . Further analysis of the angular distribution function and the comparison with the polarization fraction are presented in Sect. 4.3.

Figure 16 shows the values of the observed S averaged in bins of p as a function of the lag value. As expected, the angle dispersion function increases steadily with increasing lag. Lower values of S systematically correspond to higher p values, as discussed in Sect. 4.3. Figure 17 shows details of S for a few selected regions.

4. Discussion

In this section we analyse the observed variations of the polarization fraction and angle at 353 GHz and discuss the possible implications in terms of dust physics and magnetic field structure.

4.1. Maximum polarization fraction

The maximum dust polarization fraction (p_{\max}) is a parameter of importance for the physics of dust and its alignment with respect to the magnetic field, because it directly provides an upper limit to the intrinsic polarization fraction, p_0 , for the optimal orientation of the magnetic field, i.e., in the plane of the sky. It is also important for the CMB component separation in polarization, as it sets the maximum amplitude of dust polarization. The observed p values are, however, affected by averaging in the beam and along any given LOS. Variations of the \mathbf{B} direction within the beam or along the LOS necessarily result in a decrease of the observed p . Similarly, dilution by an additional unpolarized source of emission, such as free-free or spinning dust emission, can only decrease p . Therefore, derived values of p_{\max} can only be lower limits to the intrinsic polarization fraction p_0 .

Here, we use the *Planck* maps at 353 GHz to evaluate p_{\max} . Because p is a biased quantity and noise depends upon the data resolution, the observed maximum polarization fraction depends upon resolution. It is therefore crucial to take uncertainties into account. Figure 18 shows the sky fraction, $f_{\text{sky}}(p > p_v)$,

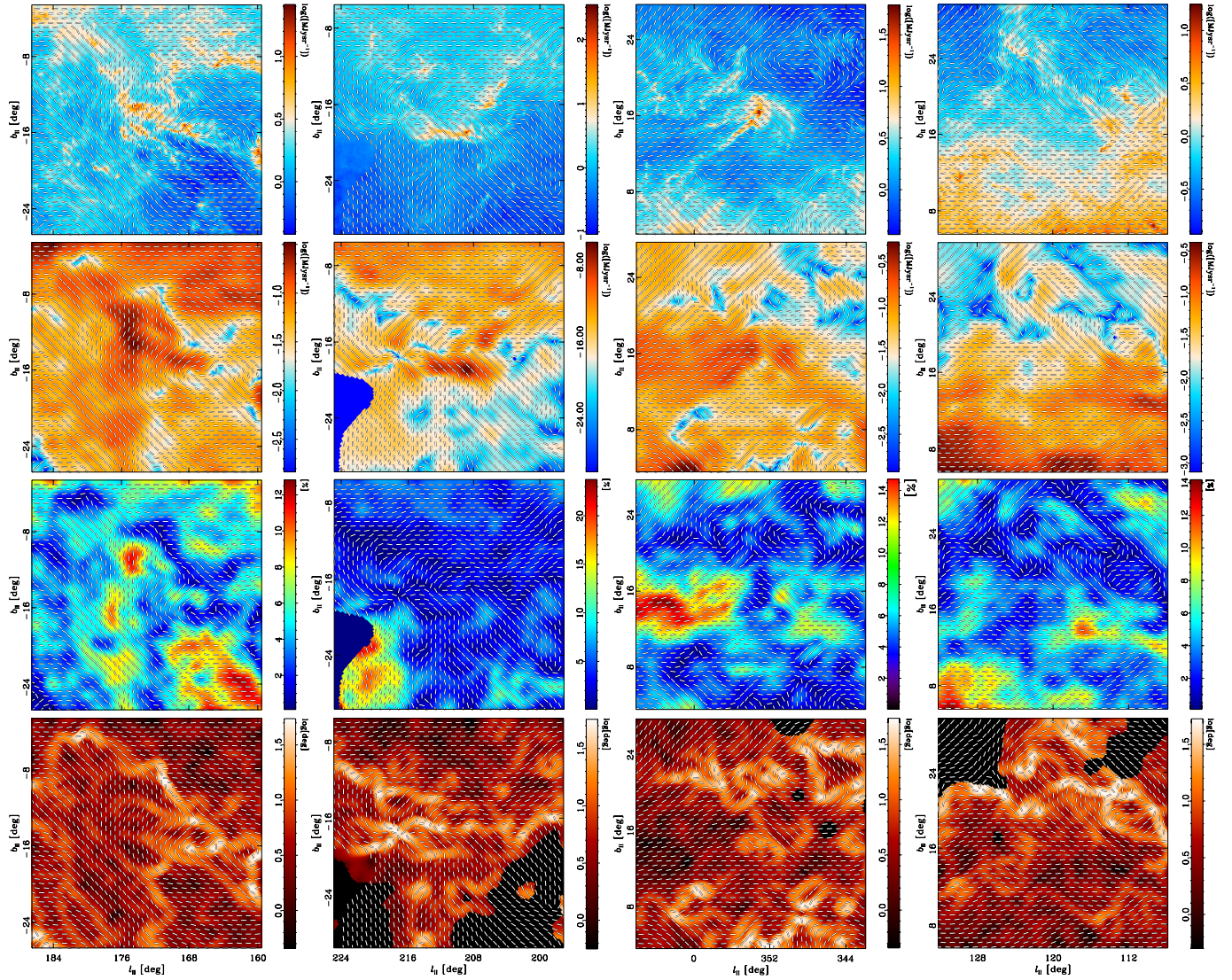


Fig. 17. Maps of a few selected regions illustrating the relation between polarization fraction and polarization angle dispersion function. Rows *from top to bottom* show total intensity at 353 GHz, polarized intensity, polarization fraction, and polarization angle dispersion function, S . Columns *from left to right* are for Taurus, Orion, Ophiuchus, and Polaris. The polarization segments show the orientation of the apparent magnetic field, but their length is constant, not reflecting the changing polarization fraction. Note that the boundaries of the regions shown here do not match exactly those in Table 1 and Fig. 6.

Table 2. Statistics of the percentage polarization fraction p at various data resolutions, θ .

θ	Med(p)	Max(p)	Max($p - 4\sigma_p$)
15'	5.5	81.8	20.3
30'	5.3	48.7	20.0
1°0	5.1	25.6	19.0
Average			19.8 ± 0.7%

Notes. The table gives the data resolution (Col. 1) and the median and maximum values of p (Cols. 2 and 3). The last Col. 4 shows the maximum values for $p - 4\sigma_p$. The average value is computed in the last line and used as the value for p_{\max} .

where the observed polarization fraction is higher than a given value p_v as a function of that p_v . The various curves are for data resolutions of 1°, 30', and 15'. The coloured area shown correspond to $f_{\text{sky}}(p \pm 4\sigma_p > p_v)$ for the various resolutions.

At low f_{sky} values and high resolutions, high values of p are observed. Inspection of the maps indicates that these are point-like objects, either isolated pixels or actual point sources. Because we are interested in diffuse emission only, these isolated values are ignored in evaluating p_{\max} . Table 2 lists the maximum and median values of p at different resolutions. It also shows the maximum value of $p - 4\sigma_p$ observed at each resolution. We use the average of these values as a conservative estimate of p_{\max} and find $p_{\max} > 19.8\%$. This indicates that, in the most favourable conditions for dust alignment, the intrinsic polarization fraction p_0 is larger than 19.8%.

The value for p_{\max} derived here is significantly larger than generally found in polarization measurements in emission. Apart from the large 10–20% values observed with the Archeops experiment (Benoit et al. 2004), most previous observations have reported polarization fractions of less than 10%. Physical interpretation of this high value in terms of the physics of dust alignment and optical properties is beyond the scope of this paper. Note that a detailed comparison between the polarization

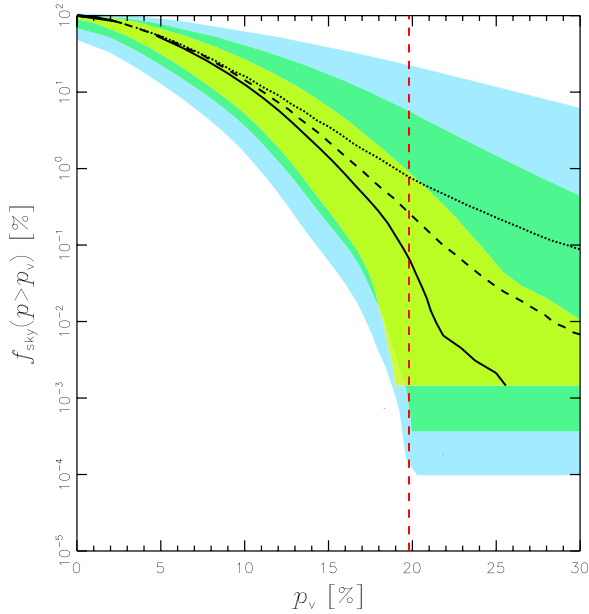


Fig. 18. Fraction of the sky $f_{\text{sky}}(p > p_v)$ above a given polarization fraction value p_v , as a function of p_v at the resolution of 1° (solid line, yellow), $30'$ (dashed line, green), and $15'$ (dotted line, blue). The range shown is the sky fraction corresponding to $p \pm 4\sigma_p > p_v$. The vertical dashed line shows the adopted common value of $p_{\text{max}} = 19.8\%$.

fraction seen in emission in the *Planck* data and that seen in extinction in the visible is presented in [Planck Collaboration Int. XXI \(2015\)](#).

4.2. Polarization fraction vs. column density

We now analyse the variations of the polarization fraction p with dust column density. We use the Bayesian mean posterior estimate of p described in Sect. 2.3 and shown in Fig. 4, computed at 1° resolution. For the dust optical depth map, we use the map of τ_{353} derived in [Planck Collaboration XI \(2014\)](#) computed at 1° resolution and we adopt their conversion factor from τ_{353} to gas column density, derived from the correlation with HI data:

$$N_{\text{H}} = (1.6 \times 10^{26} \text{ cm}^{-2}) \tau_{353}. \quad (12)$$

Figure 19 shows the distribution of the observed polarization fraction p as a function of N_{H} , as derived from dust optical depth, both for the sky fraction shown in Fig. 4 and for the same region but excluding the inner Galactic plane (i.e., excluding $\ell_{\text{II}} < 90^\circ$ or $\ell_{\text{II}} > 270^\circ$, $|b_{\text{II}}| < 2^\circ$). As can be seen in the figure, the plot shows both considerable scatter at a given N_{H} , and also systematic trends with N_{H} . The scatter is remarkable: for all column densities below $N_{\text{H}} = 10^{22} \text{ cm}^{-2}$ ($A_{\text{V}} \simeq 5 \text{ mag}$ ⁸), the polarization fraction spans all the values between the noise limit and maximum values up to 15–20%. At higher column densities, there is a sharp decrease of the values but the scatter, down to the noise limit is still present. The sensitivity of the *Planck* polarization measurements allows for the first time to detect a behaviour which is more complex than a power-law dependence of p with N_{H} . The scatter in p may be due to depolarization caused by fluctuations of the magnetic field orientation along the LOS or in the beam, and/or by intrinsic variations in p . Possible origins of this scatter are analysed in [Planck Collaboration Int. XX \(2015\)](#).

⁸ Adopting the conversion $N_{\text{H}}/A_{\text{V}} = 1.9 \times 10^{21} \text{ cm}^{-2}$ from [Bohlin et al. \(1978\)](#).

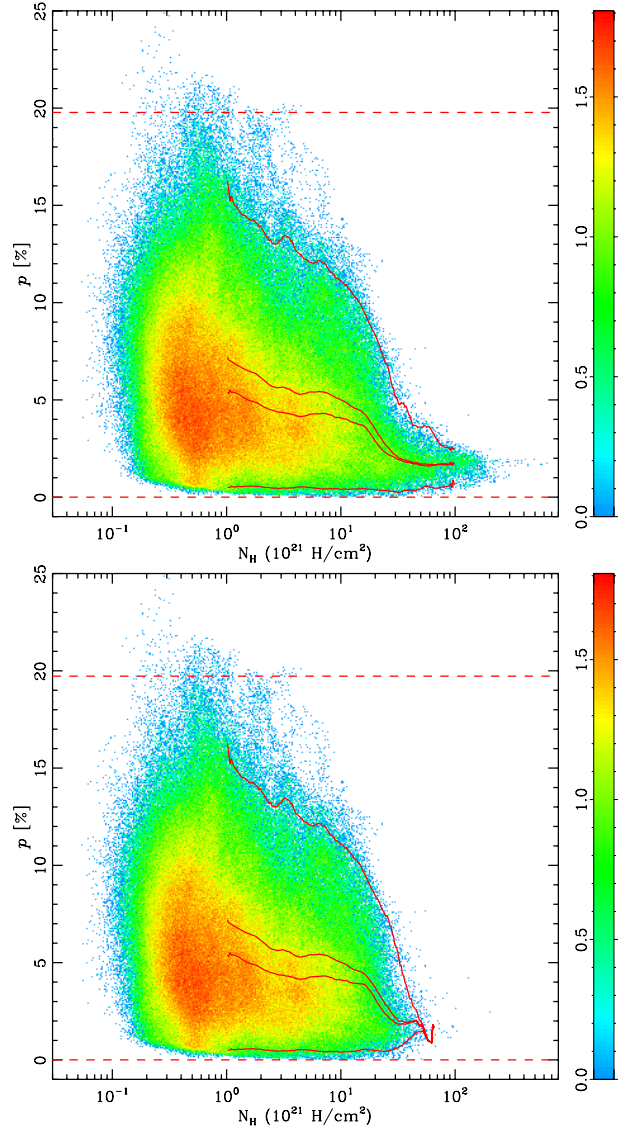


Fig. 19. Distribution of the polarization fraction (p) as a function of gas column density over the whole sky shown in Fig. 1 (*upper panel*) and in regions of the sky excluding the inner Galactic plane (excluding $\ell_{\text{II}} < 90^\circ$ or $\ell_{\text{II}} > 270^\circ$, $|b_{\text{II}}| < 2^\circ$) (*lower panel*). The values of p were computed at 1° resolution. The gas column density is derived from the dust optical depth at 353 GHz (see text). The colour scale shows the pixel density in \log_{10} scale. The curves show, *from top to bottom*, the evolution of the upper 1% percentile, mean, median and lower 1% percentile of p for pixels with $N_{\text{H}} > 10^{21} \text{ cm}^{-2}$. Horizontal dashed lines show the location of $p = 0$ and $p_{\text{max}} = 19.8\%$.

The largest polarization fractions are reached in the range of column densities $2 \times 10^{20} \text{ cm}^{-2} < N_{\text{H}} < 10^{21} \text{ cm}^{-2}$ ($0.1 < A_{\text{V}} < 0.5 \text{ mag}$). We observe an ensemble average polarization fraction, $\langle p \rangle$ of 7% at $N_{\text{H}} = 10^{21} \text{ cm}^{-2}$ ($A_{\text{V}} = 0.5 \text{ mag}$). The average values of p at lower column densities are not discussed in this paper, because a proper treatment would require a careful analysis of the residual bias in the method used to derive p . This will be the subject of an upcoming paper. At larger N_{H} ($10^{21} \text{ cm}^{-2} < N_{\text{H}} < 1.5 \times 10^{22} \text{ cm}^{-2}$, $0.5 < A_{\text{V}} < 8 \text{ mag}$), the bulk of the p values are below $p \simeq 10\%$ and the maximum values show a steady decline. Over that range of column densities, the average polarization fraction $\langle p \rangle$ decreases down to $\simeq 4\%$. We observe a sharp drop in $\langle p \rangle$ starting at about $N_{\text{H}} \simeq 1.5 \times 10^{22} \text{ cm}^{-2}$ ($A_{\text{V}} \simeq 8 \text{ mag}$).

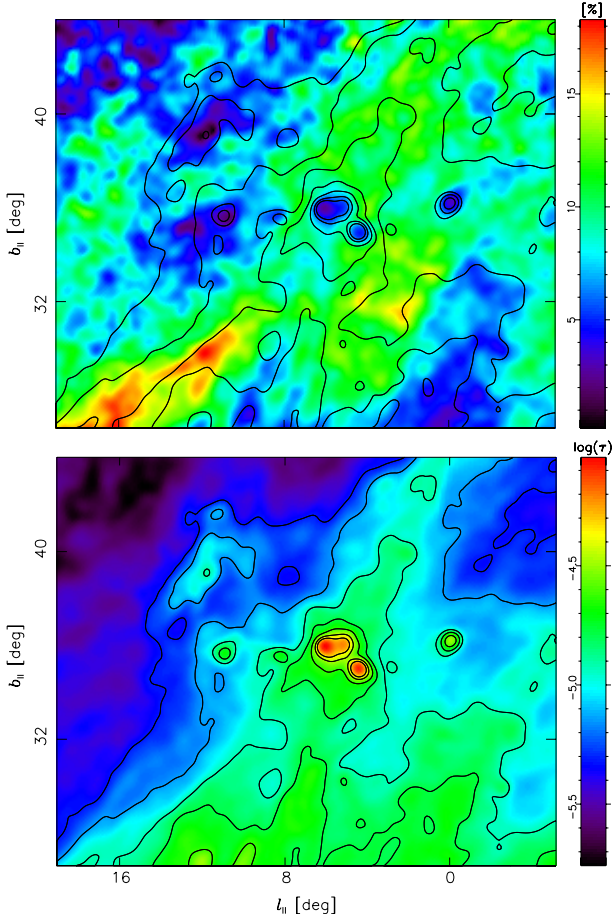


Fig. 20. *Top:* map of the polarization fraction toward the dark molecular cloud L134, overlaid with contours of the dust optical depth at 353 GHz. The levels are $\tau_{353} = 1.4, 2.9, \text{ and } 5.8 \times 10^{-5}$, corresponding to $A_V = 1.2, 2.4, \text{ and } 4.8$ mag. *Bottom:* same for the dust optical depth. The maps are shown at a common resolution of $30'$.

Above $N_H \approx 4 \times 10^{22} \text{ cm}^{-2}$ ($A_V \approx 20$ mag) values of p are systematically below 4% with an average value of $\langle p \rangle \approx 1\text{--}2\%$.

Toward nearby dense cores ($n_H > 3 \times 10^4 \text{ cm}^{-3}$, size ~ 0.1 pc, $N_H > 10^{22} \text{ cm}^{-2}$) the polarization fraction is observed to decrease systematically with N_H . This effect contributes to the sharp drop observed at $2 \times 10^{22} \text{ cm}^{-2}$ (Fig. 19, bottom panel). Inspection of the *Planck* polarization map at 353 GHz shows many examples of such dips in p associated with nearby dense clouds. A systematic statistical study in the vicinity of *Planck* cold clumps will be presented in a forthcoming paper. Figure 20 shows the example of the dark cloud L134 (Tucker et al. 1976; Mattila et al. 1979) which is located at high Galactic latitude in the otherwise highly polarized Aquila Rift. L134 is one of the coldest Cold Clumps in the *Planck* catalogue (Planck Collaboration XXIII 2011). It is clearly seen that p can be as large as 10% in the external regions and decreases to values as low as 1% at the column density peak. This behaviour appears to be common in the high-latitude sky and confirms previous studies. Such a decrease of the polarization fraction toward large column densities on small (\sim a few 0.1 pc) scales was reported previously in ground-based measurements of polarization both in emission (Ward-Thompson et al. 2000; Matthews & Wilson 2000) and extinction (e.g., Gerakines & Whittet 1995; Whittet et al. 2008). This is usually interpreted as being due to a gradual loss of alignment of dust grains in dense shielded regions. In the likely hypothesis that dust alignment processes involve radiative

torques responsible for the rotation of dust grains (Draine & Weingartner 1996; Hoang & Lazarian 2008), polarization in externally heated clouds is expected to drop off in the most shielded regions. The sharp decrease of p observed for $N_H > 10^{22} \text{ cm}^{-2}$ in Fig. 19 is roughly consistent with such a scenario.

However, an increase of column density in the Galaxy is not necessarily associated with an increase of shielding, and the decrease of the polarization fraction with increasing column density could also be due to fluctuations in the orientation of the magnetic field along a long LOS, causing depolarization. In order to shed light on this depolarization effect, the companion paper Planck Collaboration Int. XX (2015) compares the polarization properties of the *Planck* dust emission with maps of polarized emission computed in simulations of MHD turbulence. The simulations are anisotropic to allow for an analysis of the influence of a large-scale magnetic field combined with a turbulent field. The polarized dust emission is computed using a uniform dust intrinsic polarization fraction $p_0 = 20\%$. A large scatter in the polarization fraction p per bin of column density and a decrease of the maximum (and mean) values of p with N_H are found in the simulated maps, similar to those observed. The analysis reported in Planck Collaboration Int. XX (2015) however does not encompass the specific case of dense cores, but we cannot rule out that fluctuations of the magnetic field direction also contribute to depolarization within dense cores.

As shown in Fig. 19, which displays the dependence of p on N_H over the intermediate Galactic latitude sky and in regions excluding the inner Galactic plane, most lines of sight with very low p values are within the inner Galactic plane. The large gas column densities in the inner Galaxy ($A_V > 20$ mag) arise both in massive star forming regions (i.e., dense gas with $n_H > 3 \times 10^4 \text{ cm}^{-3}$ for regions around 0.3 to 1 pc), but also along long lines of sight (say a few kpc) sampling mostly low density gas in the Molecular Ring. We argue that the contribution from such star forming regions in the inner Galaxy is small in the *Planck* maps at a resolution of $1'$, because such regions have angular sizes smaller than $1'$ if they are located further than 2 kpc from the Sun. The tail of high column densities in the inner Galaxy is therefore mostly due to long lines of sight sampling low density gas.

For lines of sight toward the inner Galactic plane, a related question is whether they are probing a dense cold medium, shielded from the ambient UV field, or if they result from the accumulation of low density material distributed over large distances. The apparent dust temperature can in principle be used to discriminate between these two situations. Figure 21 shows the distribution of the apparent dust temperature (T_{obs}), as derived from the dust SED fitting in Planck Collaboration XI (2014) using a modified grey-body fit, as a function of column density. As discussed in Planck Collaboration XI (2014) the apparent dust temperature steadily decreases with increasing column density, up to $N_H \approx 10^{22} \text{ cm}^{-2}$. The figure shows that, at higher column densities, T_{obs} increases again with N_H . The bulk of the large column densities above about $3 \times 10^{22} \text{ cm}^{-2}$ therefore probes material in which dust is warmer than in the cold shielded cores, because it resides either in the low density medium, weakly shielded from the UV field of the inner Galaxy, or close to star-forming regions. In this case, the observed decrease of p is unlikely to be due to radiative transfer effects alone. This is taken as additional evidence that the fluctuations of the magnetic field direction could be the main origin of the decrease of p with column density.

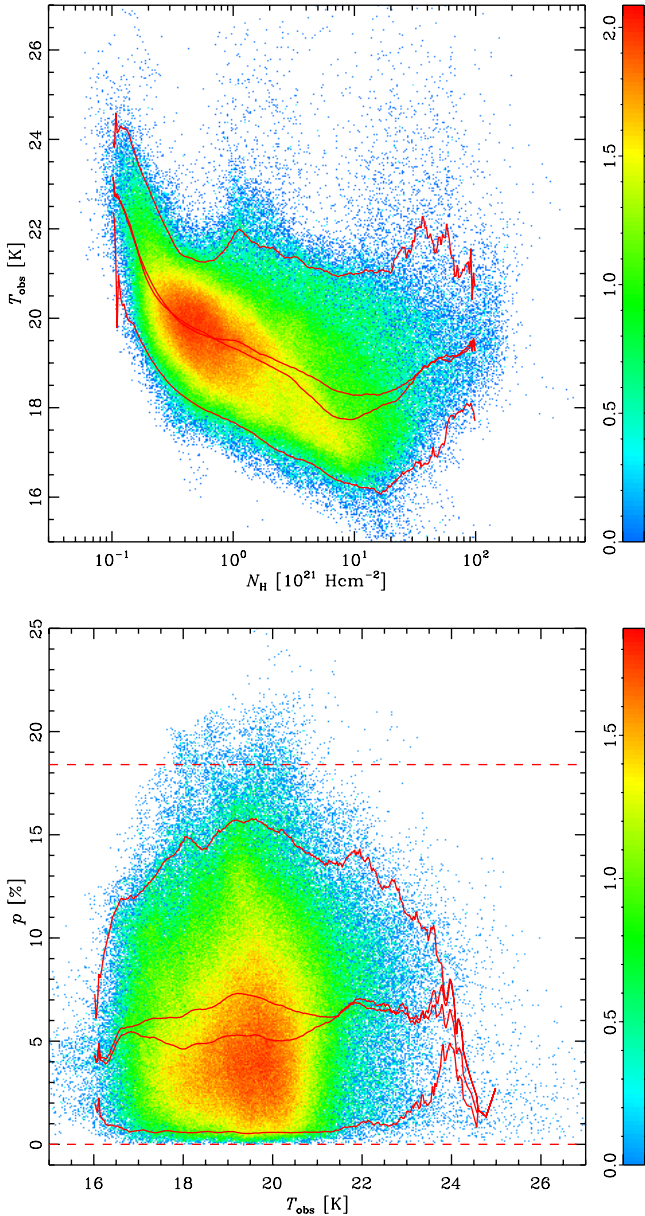


Fig. 21. *Top:* distribution of the apparent dust temperature (T_{obs}) and column density, as derived in Planck Collaboration XI (2014). *Bottom:* distribution of the polarization fraction (p) as a function of T_{obs} in regions of the sky excluding the inner Galactic plane (excluding $\ell_{\text{II}} < 90^\circ$ or $\ell_{\text{II}} > 270^\circ$, $|b_{\text{II}}| < 2^\circ$). Both plots are for pixels not masked in Fig. 1. The colour scale shows the pixel density on a \log_{10} scale. The curves show, from top to bottom, the evolution of the upper 1% percentile, mean, median and lower 1% percentile of p . Horizontal dashed lines show the location of $p = 0$ and $p_{\text{max}} = 19.8\%$.

4.3. Polarization fraction vs. angle dispersion function

Figure 12 shows the distribution of S computed as described in Sect. 3.3 from the full survey at 353 GHz for 1° resolution and with a $\delta = 30'$ lag used in the analysis.

The map of S exhibits a wide range of values. A striking feature of the map is the existence of confined regions of high S values, often reaching 50° to 70° , which are organized in an intricate network of filamentary structures, some of which span more than 30° in length. Figure 17 shows maps of selected regions around some of these high S regions. Inspection of the polarization maps shows that these filamentary features generally

lie at the boundary between regions with uniform, but different, magnetic field orientations on the sky. In order to quantify this statement, we decompose the S map using the watershed morphological operator (e.g., Beucher & Meyer 1993). This allows us to segment the maps into a set of connected cells, equivalent to adjacent catchment basins, separated by the larger S filamentary structures. The cells defined in this way are shown in Fig. 22 (top) for the first Galactic quadrant.

In the decomposition the cells are separated by one map pixel, an amount chosen to match the resolution of the S map so that the S values in cell areas do not include the high values present in the filamentary structures. Cells defined in this way have an average surface area of a few square degrees. For each cell i we compute the average polarization angle $\bar{\psi}_i$ and its dispersion $\sigma_{\psi,i}$. We then consider each pair of adjacent cells, computing the difference between their average polarization angles $\Delta\bar{\psi}_{ij} = \bar{\psi}_i - \bar{\psi}_j$ and its associated uncertainty from $\sigma_{\Delta\bar{\psi},ij}^2 = \sigma_{\psi,i}^2 + \sigma_{\psi,j}^2$. We also compute the average \bar{S}_{ij} of S over the boundary between the two cells in the pair. Figure 22 shows the fraction f of cell pairs with $\Delta\bar{\psi}_{ij} > \sigma_{\Delta\bar{\psi},ij}$ plotted as a function of \bar{S}_{ij} . It can be seen that about 70% of cell pairs are separated in average angle by more than the uncertainty. The calculation was repeated for the four Galactic quadrants and led to the same conclusion.

Maps computed at larger lags look similar to those shown in Fig. 12, although with wider filamentary features, due to the larger scale of the analysis. Maps computed at smaller lags show filamentary features at the same locations as in Fig. 12, which indicates that the structures are in general unresolved. We also derived maps of S at higher resolution. However, the noise and bias on S increase quickly at higher resolution, which makes it impossible to follow the structure of the filamentary features down to the full *Planck* resolution of $5'$ in most regions of the sky.

Comparison of S in Fig. 12 and the observed polarization fraction map of Fig. 4 on large scales shows that, overall, the filamentary features of high S correspond to low values of p . A similar trend was observed previously in the OMC-2/3 molecular clouds regions by Poidevin et al. (2010), using $14''$ resolution polarimetry data at 353 GHz. The *Planck* maps show that this is a general trend, as confirmed by the plot in Fig. 23, which shows that p and S are anti-correlated. The best-fit correlation shown is given by

$$\log_{10}(S) = \alpha \times \log_{10}(p) + \beta, \quad (13)$$

with $\alpha = -0.834$ and $\beta = -0.504$, where p is unitless and S is in degrees. Low p regions often correspond to regions where the observed polarization direction ψ changes. This result is in line with the findings of the previous section and further supports the view that variations in the magnetic field orientation play an important role in lowering the observed polarization fraction, as a result of integration along the LOS and/or within the beam.

The above results are compared with those inferred from MHD simulations in Planck Collaboration Int. XX (2015). The simulations clearly show an anti-correlation between S and p , with a slope similar to that observed in the data. It is worth noting that in the noiseless simulations, the observed trend cannot be produced by the bias on S resulting from higher uncertainties in polarization angles in regions of low signal and/or polarization fraction. It results from averaging effects of the polarization angle along the LOS. In brief, fluctuations of the magnetic field direction weaken the apparent polarization fraction, especially when the large-scale field tends to be aligned with the LOS.

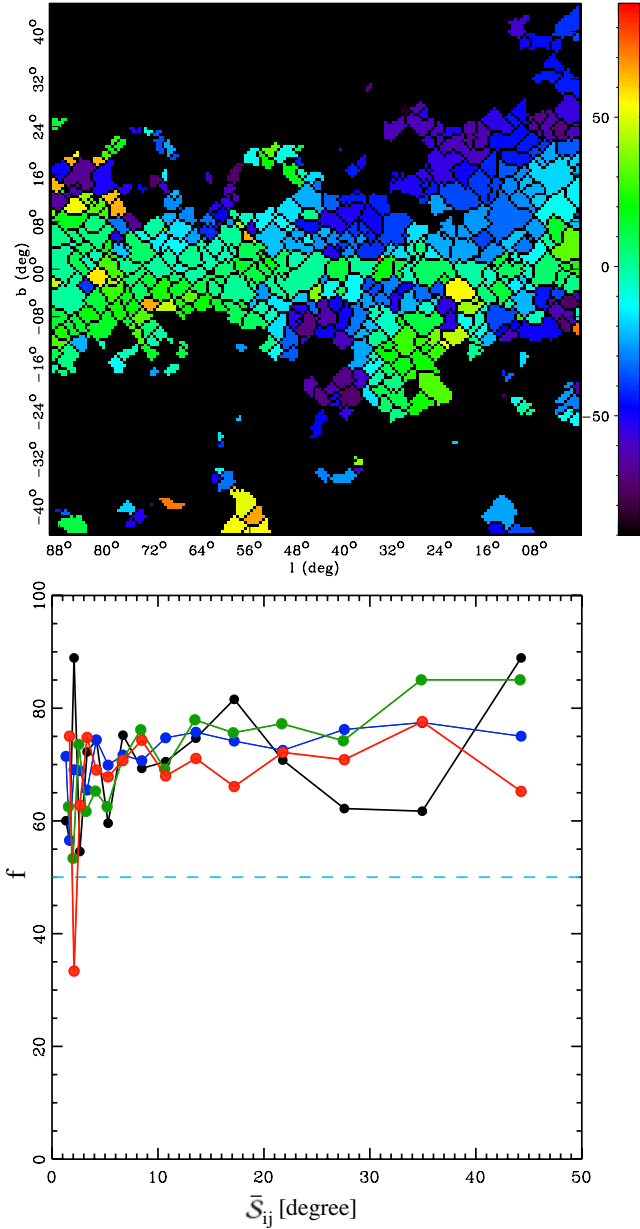


Fig. 22. *Top:* first Galactic quadrant map of the average value of ψ in individual cells defined using the watershed segmentation on the map of S . Black pixels show the boundaries between cells, corresponding to local maxima of S . *Bottom:* variation of the fraction f of pairs of adjacent cells with angle departure $\Delta\psi_{ij}$ larger than the combined uncertainty $\sigma_{\Delta\psi_{ij}}$ of the pair, as a function of the average value of S in the contact region between cells. The black, blue, green, and red curves are for Galactic quadrants 1 to 4, respectively. The horizontal line shows 50%.

The regions of large S bear a morphological resemblance to features detected in maps of radio polarized emission, so-called “depolarization canals” (e.g., [Haverkorn et al. 2000](#)) and regions of high polarization gradient ([Gaensler et al. 2011](#)). The radio depolarization canals arise from Faraday rotation effects: they are thought to be due to either differential Faraday rotation (and hence depolarization) within synchrotron emission regions or discontinuities in foreground Faraday rotation screens (e.g., [Fletcher & Shukurov 2007](#)). The observed positions of depolarization canals vary with radio frequency and do not correspond to true physical structures. On the other hand, regions of high radio polarization gradient are somewhat similar

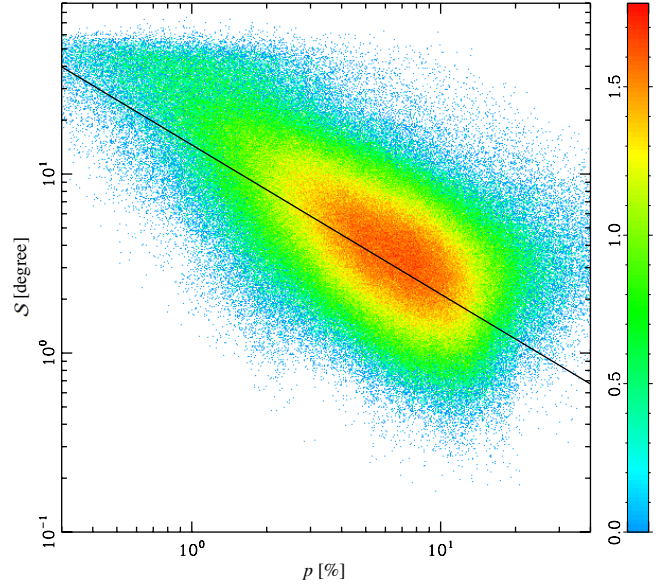


Fig. 23. Scatter plot of the polarization angle dispersion function S as a function of polarization fraction p at 353 GHz. The colour scale shows the pixel density on a \log_{10} scale. The line indicates the best fit (see text).

to our filamentary features of large S , insofar as each can be traced back to physical discontinuities. However, both the physical quantities that undergo a discontinuity to produce the phenomenon (free-electron density and LOS field component for the former versus sky-projected field orientation for the latter) and the places where the discontinuities occur (foreground Faraday rotation screens for the former versus dust-emitting regions for the latter) are unrelated. Therefore, one does not expect any one-to-one correspondence in morphology. Indeed, this is what we observe when comparing the distribution of the *Planck* filamentary features with maps of S constructed using the 1.4 GHz synchrotron maps of [Wolleben et al. \(2006\)](#) and [Testori et al. \(2008\)](#).

Nevertheless, their morphological resemblance is rooted in a fundamental property of magnetized turbulence that goes beyond the detailed nature of the flows and of the specific ISM phase. Sub- or trans-sonic, super-Alfvénic turbulence in the warm ionized medium (WIM) is found to create filaments with high polarization gradients similar to those observed in the radio. They are shown to result from vorticity or shock compression ([Gaensler et al. 2011](#)). In the neutral ISM, both compressible and incompressible non-ideal magnetized turbulence generate filamentary structures with high S at small scales similar to those observed ([Planck Collaboration Int. XX 2015](#); [Falgarone et al. 2015](#); [Momferratos 2014](#)). In the incompressible case, these filamentary structures are shown to follow current sheets of high intensity.

Finally, [Fig. 24](#) shows the distribution of S with column density. Several results are visible in these plots: (1) there is a large scatter of S at all column densities, in particular below $N_{\text{H}} \approx 2 \times 10^{22} \text{ cm}^{-2}$; (2) the largest values of S are reached at low column densities, a fact that is well illustrated in the maps of [Fig. 17](#); and (3) there is no more dependence of S with N_{H} than found in that of p with N_{H} : the mean value of S barely decreases with N_{H} over the narrow range $5 \times 10^{21} < N_{\text{H}} < 2 \times 10^{22} \text{ cm}^{-2}$, then it increases sharply up to $N_{\text{H}} \approx 4 \times 10^{22} \text{ cm}^{-2}$ and decreases again at larger column densities in the plot that includes sightlines across the Galactic plane. The small range of column

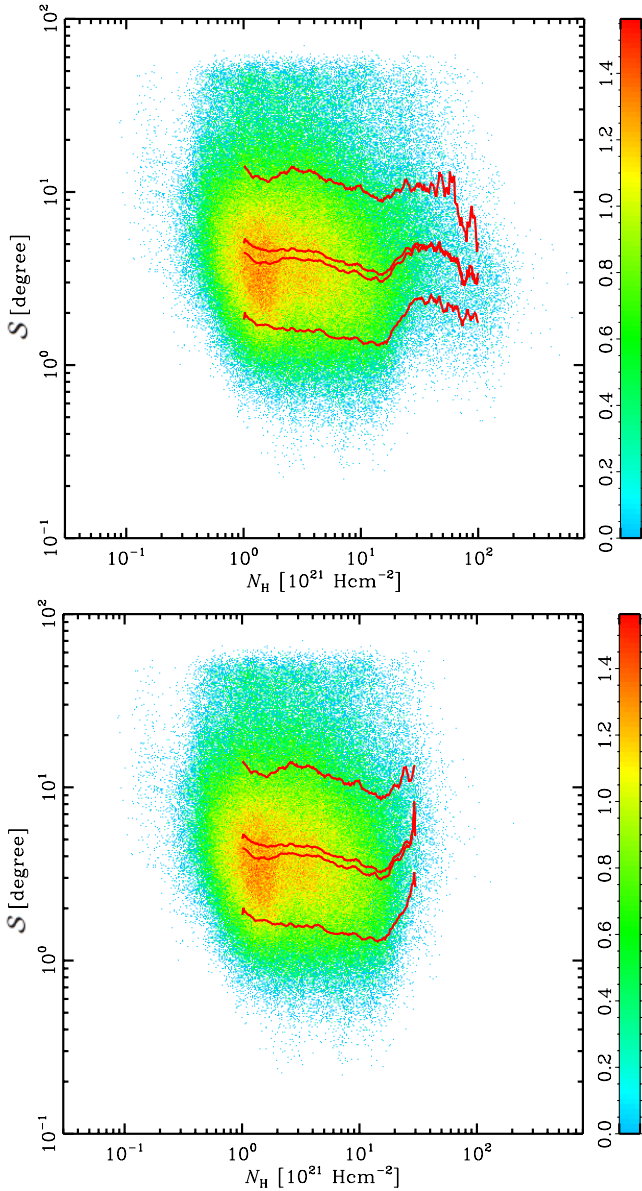


Fig. 24. Distribution of the polarization angle dispersion function (S) as a function of gas column density over the whole sky shown in Fig. 1 (*upper panel*) and in regions of the sky excluding the inner Galactic plane (excluding $\ell_{\text{II}} < 90^\circ$ or $\ell_{\text{II}} > 270^\circ$, $|b_{\text{II}}| < 2^\circ$) (*lower panel*). The gas column density is derived from the dust optical depth at 353 GHz (see text). The colour scale shows the pixel density in \log_{10} scale. The curves show, from top to bottom, the evolution of the upper 1% percentile, mean, median and lower 1% percentile of S .

densities over which S increases with N_{H} is the same as that over which the polarization fraction (p) drops sharply (Fig. 19). This range corresponds to long lines of sight across the Galactic disk at Galactic latitudes $> 2^\circ$. We take this result as an additional indication that, in that range of column densities, the drop of p is due to the fluctuations of the magnetic field orientation along the LOS and/or within the beam. This does not preclude other explanations, such as reduced dust alignment, for the low polarization fractions observed toward more opaque lines of sight. The dust polarization in dense *Planck* cold clumps, such as those described in [Planck Collaboration XXII \(2011\)](#), will be analysed in a forthcoming publication.

4.4. Dust vs. synchrotron polarization

In this section we compare the dust polarization as seen at 353 GHz with the synchrotron polarization that dominates at much lower frequencies. Our aim is to test how much the complementary observables trace the same magnetic fields and how their polarization properties are affected by the irregular component of the field. These comparisons tell us not only about the fields but also about the relative distributions of dust grains and relativistic electrons.

When Faraday rotation is negligible, the synchrotron and dust emission are both linearly polarized perpendicular to the local sky-projected magnetic field. The emissivities, however, have different dependencies on the magnetic field strength: the dust emission does not depend on the field strength, whereas the synchrotron emissivity is given by $\mathcal{E}_{\text{syn}} \propto n_e B_{\perp}^{(\gamma+1)/2}$, where n_e is the density of relativistic electrons and γ is the power-law index of the relativistic-electron energy spectrum (typically $\gamma \simeq 3$, so that $\mathcal{E}_{\text{syn}} \propto n_e B_{\perp}^2$). Synchrotron and dust polarization are also affected by different depolarization mechanisms. Some differences arise when the magnetic field in dust clouds differs from that in the diffuse synchrotron-emitting medium. Other differences arise because of the emissivity dependence on the field strength that weights the emission differently along the LOS. Any single direction may have a combination of these effects. We would therefore expect to see similar polarization structures where the particles sample the same average field, but not identical structures. A correlation analysis between dust and synchrotron polarization is also reported by [Planck Collaboration Int. XXII \(2015\)](#). Their cross-correlation between the Q and U maps at WMAP and LFI frequencies with the corresponding maps at 353 GHz shows that some of the polarized synchrotron emission at intermediate Galactic latitudes is correlated with dust polarization in both polarized intensity and angle. We might further expect to see statistical correlations even where the irregular component perturbs the large-scale magnetic field, but the degree of the correlation is complicated to predict.

The data sets are described in Sect. 2.5. Figure 25 compares both the polarization fraction and the polarization angle of the dust emission at 353 GHz (the Bayesian estimates where the S/N of p is greater than 3) with polarized synchrotron emission at 30 GHz. The comparison between the polarization angles is straightforward, because synchrotron is dominant and there is little Faraday rotation at that frequency. The comparison between the polarization fractions is more complex, however, because in the microwave and radio data there are additional total intensity components, such as free-free and anomalous microwave emission. To avoid contamination from anomalous microwave emission at 30 GHz, we begin with the 408 MHz map of [Haslam et al. \(1982\)](#) for total intensity. We correct for free-free emission as described in Sect. 2.5. This correction is approximate, but the synchrotron component dominates at low frequencies. Then we extrapolate the corrected 408 MHz synchrotron total intensity to 30 GHz in order to construct the polarization fraction, assuming a spectral index of -2.88 (see, e.g., [Jaffe et al. 2011](#)). Note that a change in the constant value adopted for this index simply shifts the synchrotron polarization fraction systematically up or down and does not affect whether there would be an observed correlation. However, any spatial variations in the index that are not accounted for remain a limitation of this simple approach; they constitute an effective noise term that may blur the correlations we look for below but would not produce a spurious correlation.

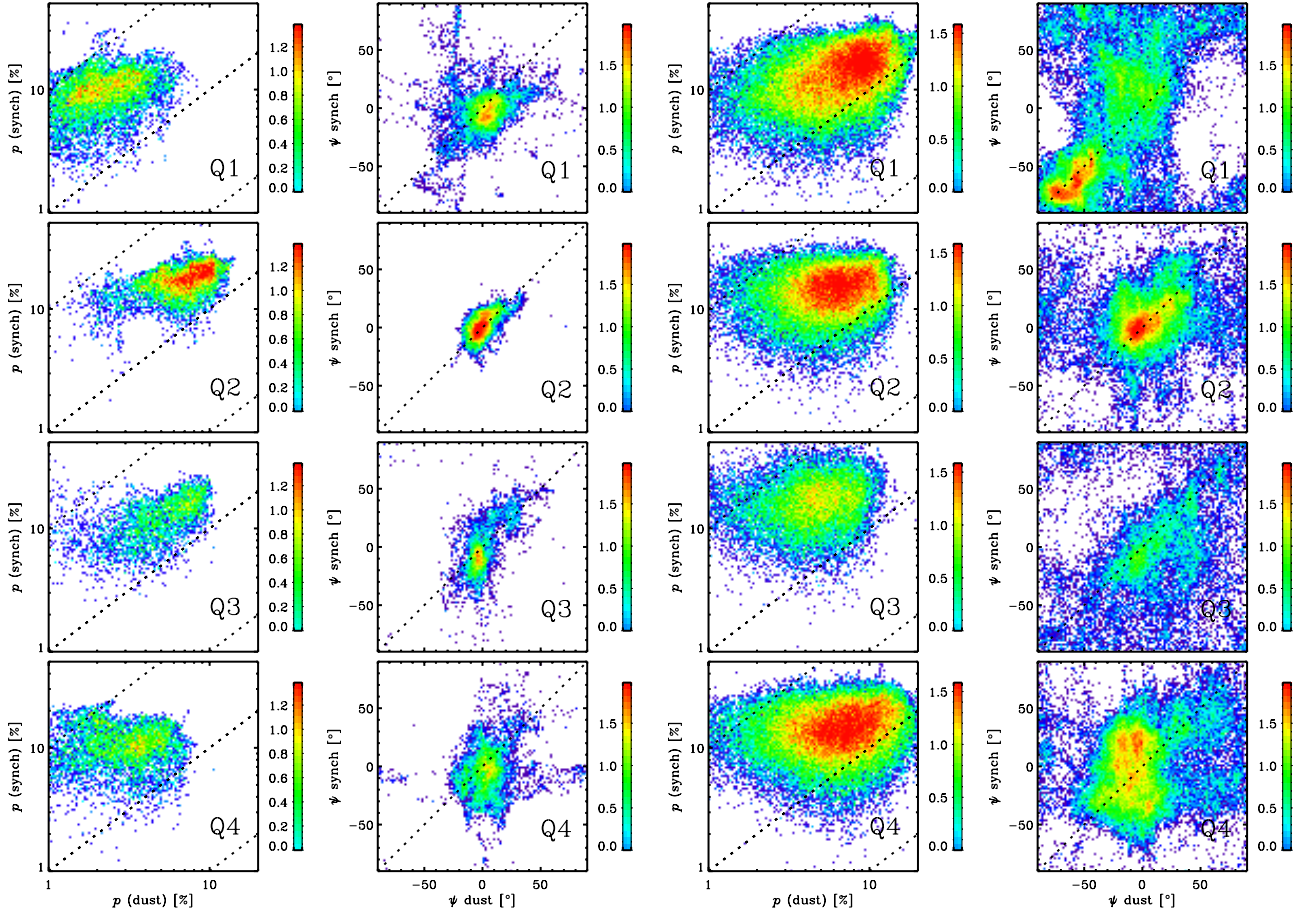


Fig. 25. Comparison of dust and synchrotron polarization fraction and polarization angle for $|b_{||}| < 5^\circ$ (left panels) and off the plane for $|b_{||}| > 5^\circ$ (right panels), separated in the four Galactic quadrants (top to bottom). The colour scale shows the pixel density on a \log_{10} scale.

Table 3. Slope, intercept, and Pearson correlation coefficient of the correlation between dust and synchrotron polarization fraction, computed over Galactic quadrants in the Galactic plane and off the plane.

Quadrant	$ b_{ } < 5^\circ$			$ b_{ } > 5^\circ$		
	Slope	Intercept	Pearson	Slope	Intercept	Pearson
Q1	0.310	-0.551	0.341	0.280	-0.548	0.288
Q2	0.355	-0.379	0.470	0.144	-0.687	0.155
Q3	0.229	-0.646	0.300	0.101	-0.679	0.091
Q4	0.135	-0.835	0.170	0.053	-0.818	0.058
All	0.346	-0.462	0.469	0.137	-0.704	0.144

The left two columns of Fig. 25 show the Galactic plane ($|b_{||}| < 5^\circ$), while the right two show the results for the rest of the sky. The correlations are quantified by linear fits and Pearson correlation coefficients (r) listed in Table 3. In all but the fourth quadrant, there is weak but visible correlation ($r > 0.3$) in the polarization fraction in the plane, where the polarized intensity is strong. In the plane, we also see that the polarization angles remain near zero, i.e., the LOS integrated “apparent” magnetic field remains largely parallel to the plane. This confirms that at the largest scales probed through the full disk, the synchrotron and dust average over roughly the same structured magnetic fields. With a few notable exceptions, however, there is little correlation away from the plane, where isolated local structures and the irregular field component become more important.

A most interesting region for comparison is the second quadrant containing the Fan. In the Galactic plane this shows a relatively strong correlation ($r = 0.47$) in polarization fraction (as does the third quadrant to a lesser degree). Out of the plane, the correlation in p disappears. But we still see a correlation in the polarization angles off the plane, where they both remain concentrated around zero, indicating that the apparent magnetic field is parallel to the plane even at latitudes above 5° .

A second interesting region for the comparison is the first quadrant, where the sky is dominated by the radio loop I, i.e., the North Polar Spur (NPS). Here the high-latitude polarization angles show correlation where the two observables clearly trace the same magnetic fields.

We also compared the dust polarization angle dispersion with the polarized synchrotron emission at 1.4 GHz where it is subject to significant Faraday rotation effects. In Fig. 1 of Burigana et al. (2006) (based on data described in Sect. 2.5), the polarization fraction shows strong depolarization of the synchrotron emission within 30° of the plane, with the exception of the Fan region in the second quadrant. Much of the depolarization is so-called “beam depolarization”. A diffuse background source viewed through the roughly 1° beam results in emission co-added along slightly different lines of sight that pass through different turbulent cells; polarized emission even with initially uniform polarization angles gets Faraday-rotated differently and cancels out. One might then expect that the resulting synchrotron polarization fraction would anti-correlate with the dust polarization angle dispersion. Lines of sight toward highly turbulent

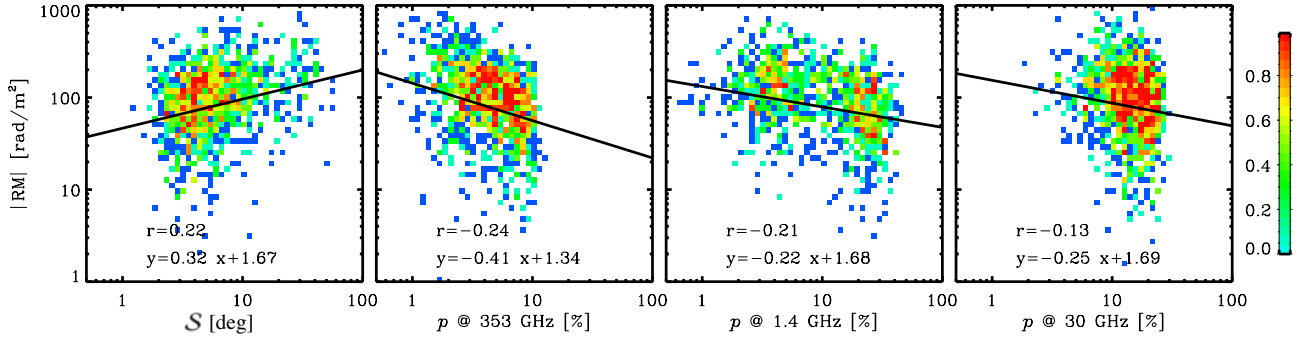


Fig. 26. Faraday RMs in the Galactic plane ($|b_{\text{II}}| < 5^\circ$) compared to (left to right): dust angle dispersion; dust polarization fraction at 353 GHz; synchrotron polarization fraction at 1.4 GHz; and synchrotron polarization fraction at 30 GHz. The overplotted lines show the result of a simple linear fit between the two data sets, with the Pearson correlation coefficient r quantifying the degree of correlation. The colour scale shows the pixel density on a \log_{10} scale.

regions should have low synchrotron polarization due to Faraday effects and high dust polarization angular dispersion. Such correlations are not generally apparent; however, in some regions such as the second quadrant dominated by the Fan we see this effect, implying that the dust and synchrotron emission in the Fan are tracing some of the same turbulent magnetic fields.

Finally, it is instructive to compare the dust polarization fraction with Faraday RMs of extragalactic radio sources. Recall that RMs are proportional to the LOS field component (which is positive/negative if the field points toward/away from the observer) times the free-electron density and integrated along the LOS, whereas the dust polarization fraction is an increasing function of the inclination angle of the magnetic field to the LOS. Therefore, if the large-scale field is coherent along the LOS through the Galaxy, then a field orientation close to the LOS tends to make RMs of extragalactic sources large (in absolute value) and the dust or synchrotron polarization fraction small, whereas a field orientation close to the plane of the sky does the opposite. As a result, one might expect a rough anti-correlation between RMs of extragalactic sources and dust polarization fraction. However, only a very loose anti-correlation may be expected at best because: (1) Faraday rotation and dust emission take place in different environments, with possibly different magnetic field directions; (2) RMs depend not only on the field inclination to the LOS, but also on the total field strength and on the free-electron column density; and (3) the LOS field component could undergo reversals, which would decrease RMs without correspondingly increasing the dust polarization fraction. Similarly, one might expect a rough positive correlation between RMs of extragalactic sources (again in absolute value) and dust polarization angle dispersion, because if the large-scale field is globally oriented closer to the LOS, the dust polarization angle is more sensitive to the fluctuating field.

Using the catalogues of Brown et al. (2003), Brown et al. (2007), Taylor et al. (2009), and Van Eck et al. (2011), in Fig. 26 we compare the RM of each source with the properties S and p of the polarized emission in the corresponding map pixel. This figure confirms the expected trends for the large-scale field in the Galactic plane, using both synchrotron and dust emission. Away from the plane (not shown) where more local structures dominate, we find no correlations. Because of the considerations outlined above, further work modeling the magnetized ISM on large scales and studying individual regions in detail will be necessary to understand the nature of the relationships among these observables.

We compared the dust observables with the standard deviation σ_{RM} of the extragalactic RM measures binned into low-resolution ($N_{\text{side}} = 16$ or $\sim 4^\circ$) pixels. Again, in the plane, we found the expected loose anti-correlation ($r = -0.3$), where regions of high RM variation have low dust polarization fraction. In this case, the anti-correlation is likely due to changes in the field orientation, where lines of sight toward more turbulent regions measure both increased RM variation and decreased dust polarization due to depolarization effects. In the framework of this interpretation, we expect a weak positive correlation between the σ_{RM} and the dust angle dispersion function, an effect that we barely see as a hint of a correlation, with $r = 0.2$.

Lastly, we compared the degree of polarization of the extragalactic sources themselves with that of the diffuse Galactic dust emission in the same direction. Because a source's degree of polarization anti-correlates with the standard deviation of the RM due to turbulent depolarization (Haverkorn et al. 2008), we might expect a positive correlation in the degree of polarization of the sources compared to the Galactic dust emission if the two observables are affected by the same turbulence. We find a hint of this correlation ($r = 0.2$) in the plane, but not at higher latitude.

The *Planck* polarization data at 353 GHz provide a new tracer of magnetic fields and an important complement to radio observations due to the different origins of the photons. This first look at the comparison of these observables confirms the expected large-scale correspondence as well as interesting correlations in the Fan and NPS regions. We find only weak correlations over much of the sky where the effects of local structures and the irregular field component dominate. This is not surprising but is nonetheless worth noting as it highlights the importance of, as well as the challenges inherent to, combining these data to build a coherent picture of the Galactic magnetic fields.

5. Conclusions

We have presented the *Planck* large-scale maps of polarized thermal dust emission at 353 GHz. This emission arises from non-spherical grains aligned with respect to the magnetic field. These data allow us for the first time to study dust polarization over large angular scales and open the field for many detailed studies to come.

The dust polarization fraction p displays a large scatter at all column densities below $N_{\text{H}} \sim 10^{22} \text{ cm}^{-2}$. The maximum p is high, and we derive a lower limit to its maximal value of $p_{\text{max}} = 19.8\%$. The highest polarization fractions are observed in

a handful of individual regions, usually located in intermediate to low column density parts of the sky.

The large-scale spatial distribution of p shows a modulation of its upper values that is in general agreement with predictions of the general magnetic field structure of the MW, as constrained previously from synchrotron and RM data.

In addition to the large scatter of p , from the noise limit to more than 15%, there is a tendency for both its ensemble average and maximum value at a given N_{H} to steadily decrease with total column density. However, the decrease is shallow below $N_{\text{H}} = 10^{22} \text{ cm}^{-2}$, becoming steeper between $N_{\text{H}} = 10^{22} \text{ cm}^{-2}$ and $N_{\text{H}} = 4 \times 10^{22} \text{ cm}^{-2}$, and reaches a somewhat constant value of 2% above $N_{\text{H}} = 4 \times 10^{22} \text{ cm}^{-2}$.

The *Planck* polarization data at 353 GHz also allow precise measurements of the polarization direction ψ over most of the sky. Rotated by 90° , this direction shows the orientation of the apparent magnetic field projected on the plane of the sky, weighted by the dust emission and integrated on the LOS. The polarization angles in the Galactic plane are observed to be consistent with \mathbf{B} lying mostly in the plane, as strongly suggested by previous synchrotron measurements. This is particularly true in the inner MW and in the highly polarized Fan region.

In order to characterize the structure of this apparent field, we compute a local measure of the dispersion of polarization angles at a given lag, the polarization angle dispersion function \mathcal{S} . It increases with lag, as previous observations have shown at smaller scales in specific regions. The sky distribution of \mathcal{S} reveals a spectacular network of unresolved filamentary structures with large \mathcal{S} values. This is the first time such structures have been observed for dust polarization. When they can be followed down to the *Planck* resolution, their widths are smaller than the beam, and some of them span large angular distances (several tens of degrees). These filamentary structures anti-correlate with p , in the sense that regions with maximal angle dispersions correspond to the lowest polarization fractions. We show that, in the large fraction of the sky we study, this is not due to any noise-induced bias on \mathcal{S} and is therefore a real effect. The filamentary structures appear to be separating regions that have different but homogeneous field orientations.

The anti-correlation between \mathcal{S} and p suggests that fluctuations of the magnetic field orientation have a major contribution to depolarization. This is also found in simulations of anisotropic MHD turbulence, without variations of the alignment properties of dust grains (see details in [Planck Collaboration Int. XX 2015](#)).

The filamentary structures of high \mathcal{S} bear some resemblance to the depolarization canals that are observed at radio frequencies and attributed to Faraday rotation effects, although there is no correspondence at small scales, which comes as no surprise because they have a different origin.

We compared the dust polarization fraction and angle with polarized synchrotron data. There are indications that the two tracers see the same magnetic field orientation, particularly interesting to see in the Fan region and the North Polar Spur, but that the detailed distributions of dust and high-energy electrons must be different in order to explain the observed maps. We infer a loose statistical correlation between extragalactic-source RMs and both the dust polarization fraction p and the angle dispersion function \mathcal{S} (negative and positive, respectively).

Acknowledgements. The development of *Planck* has been supported by: ESA; CNES and CNRS/INSU-IN2P3-INP (France); ASI, CNR, and INAF (Italy); NASA and DoE (USA); STFC and UKSA (UK); CSIC, MICINN, J.A., and RES (Spain); Tekes, AoF, and CSC (Finland); DLR and MPG (Germany); CSA (Canada); DTU Space (Denmark); SER/SSO (Switzerland); RCN (Norway); SFI (Ireland); FCT/M CTES (Portugal); and PRACE (EU).

A description of the Planck Collaboration and a list of its members, including the technical or scientific activities in which they have been involved, can be found at http://www.sciops.esa.int/index.php?project=planck&page=Planck_Collaboration. The research leading to these results has received funding from the European Research Council under the European Union's Seventh Framework Programme (FP7/2007-2013)/ ERC grant agreement no 267934 and from a joint agreement between University of São Paulo, Brazil, and COFECUB, France (grant nos. USP 2007.1.433.14.2 and COFECUB Uc Te 114/08). We acknowledge the use of the Legacy Archive for Microwave Background Data Analysis (LAMBDA), part of the High Energy Astrophysics Science Archive Center (HEASARC). HEASARC/LAMBDA is a service of the Astrophysics Science Division at the NASA Goddard Space Flight Center. Some of the results in this paper have been derived using the HEALPix package.

References

- Alves, M. I. R., Davies, R. D., Dickinson, C., et al. 2010, *MNRAS*, **405**, 1654
 Beck, R. 2009, in IAU Symp. 259, eds. K. G. Strassmeier, A. G. Kosovichev, & J. E. Beckman, 3
 Bennett, C. L., Larson, D., Weiland, J. L., et al. 2013, *ApJS*, **208**, 20
 Benoît, A., Ade, P., Amblard, A., et al. 2004, *A&A*, **424**, 571
 Bersanelli, M., Mandolesi, N., Butler, R. C., et al. 2010, *A&A*, **520**, A4
 Beucher, S., & Meyer, F. 1993, in *Mathematical Morphology in Image Processing*, ed. E. R. Dougherty, 433
 Bohlin, R. C., Savage, B. D., & Drake, J. F. 1978, *ApJ*, **224**, 132
 Brown, J. C., Taylor, A. R., & Jackel, B. J. 2003, *ApJS*, **145**, 213
 Brown, J. C., Haverkorn, M., Gaensler, B. M., et al. 2007, *ApJ*, **663**, 258
 Burigana, C., La Porta, L., Reich, P., & Reich, W. 2006, *Astron. Nachr.*, **327**, 491
 Burkhart, B., Lazarian, A., & Gaensler, B. M. 2012, *ApJ*, **749**, 145
 Chapman, N. L., Goldsmith, P. F., Pineda, J. L., et al. 2011, *ApJ*, **741**, 21
 Cox, D. P. 2005, *ARA&A*, **43**, 337
 Curran, R. L., & Chrysostomou, A. 2007, *MNRAS*, **382**, 699
 Davis, Jr., L., & Greenstein, J. L. 1951, *ApJ*, **114**, 206
 Delabrouille, J., Betoule, M., Melin, J.-B., et al. 2013, *A&A*, **553**, A96
 Dolginov, A. Z., & Mitrofanov, I. G. 1976, *Ap&SS*, **43**, 291
 Dotson, J. L., Davidson, J., Dowell, C. D., Schleunig, D. A., & Hildebrand, R. H. 2000, *ApJS*, **128**, 335
 Dotson, J. L., Vaillancourt, J. E., Kirby, L., et al. 2010, *ApJS*, **186**, 406
 Draine, B. T., & Fraise, A. A. 2009, *ApJ*, **696**, 1
 Draine, B. T., & Weingartner, J. C. 1996, *ApJ*, **470**, 551
 Draine, B. T., & Weingartner, J. C. 1997, *ApJ*, **480**, 633
 Dunkley, J., Komatsu, E., Nolta, M. R., et al. 2009, *ApJS*, **180**, 306
 Falcata-Gonçalves, D., Lazarian, A., & Kowal, G. 2008, *ApJ*, **679**, 537
 Falgarone, E., Momferratos, G., & Lesaffre, P. 2015, in *Astrophys. Space Sci. Lib.* 407, eds. A. Lazarian, E. M. de Gouveia Dal Pino, & C. Melioli, 227
 Fauvet, L., Macías-Pérez, J. F., Aumont, J., et al. 2011, *A&A*, **526**, A145
 Fauvet, L., Macías-Pérez, J. F., & Désert, F. X. 2012, *Astrophys. Phys.*, **36**, 57
 Fauvet, L., Macías-Pérez, J. F., Hildebrandt, S. R., & Désert, F.-X. 2013, *Adv. Astron.*, 2013, 746020
 Ferrière, K. 2011, *Mem. Soc. Astron. It.*, **82**, 824
 Fletcher, A., & Shukurov, A. 2007, in *EAS Pub. Ser.* 23, eds. M.-A. Miville-Deschênes, & F. Boulanger, 109
 Fraise, A. A., Brown, J.-A. C., Dobler, G., et al. 2009, in *AIP Conf. Ser.*, 1141, eds. S. Dodelson, D. Baumann, A. Cooray, et al., 265
 Franco, G. A. P., Alves, F. O., & Girart, J. 2010, *ApJ*, **723**, 146
 Gaensler, B. M., & Johnston, S. 1995, *MNRAS*, **277**, 1243
 Gaensler, B. M., Haverkorn, M., Burkhart, B., et al. 2011, *Nature*, **478**, 214
 Gerakines, P. A., & Whittet, D. C. B. 1995, *Planet. Space Sci.*, **43**, 1325
 Gold, B., Odegard, N., Weiland, J. L., et al. 2011, *ApJS*, **192**, 15
 Goodman, A. A., Bastien, P., Menard, F., & Myers, P. C. 1990, *ApJ*, **359**, 363
 Górski, K. M., Hivon, E., Banday, A. J., et al. 2005, *ApJ*, **622**, 759
 Hamaker, J. P., & Bregman, J. D. 1996, *A&AS*, **117**, 161
 Haslam, C. G. T., Stoffel, H., Salter, C. J., & Wilson, W. E. 1982, *A&AS*, **47**, 1
 Haverkorn, M., Katgert, P., & de Bruyn, A. G. 2000, *A&A*, **356**, L13
 Haverkorn, M., Brown, J. C., Gaensler, B. M., & McClure-Griffiths, N. M. 2008, *ApJ*, **680**, 362
 Heiles, C. 1996, *ApJ*, **462**, 316
 Hildebrand, R. H., Kirby, L., Dotson, J. L., Houde, M., & Vaillancourt, J. E. 2009, *ApJ*, **696**, 567
 Hoang, T., & Lazarian, A. 2008, *MNRAS*, **388**, 117
 Iacobelli, M., Burkhart, B., Haverkorn, M., et al. 2014, *A&A*, **566**, A5
 Jaffe, T. R., Leahy, J. P., Banday, A. J., et al. 2010, *MNRAS*, **401**, 1013
 Jaffe, T. R., Banday, A. J., Leahy, J. P., Leach, S., & Strong, A. W. 2011, *MNRAS*, **416**, 1152
 Jansson, R., & Farrar, G. R. 2012a, *ApJ*, **757**, 14
 Jansson, R., & Farrar, G. R. 2012b, *ApJ*, **761**, L11

- Keegstra, P. B., Smoot, G. F., Gorski, K. M., Hinshaw, G., & Tenorio, L. 1997, *Astronomical Data Analysis Software and Systems VI*, 125, 198
- Kobulnicky, H. A., Molnar, L. A., & Jones, T. J. 1994, *AJ*, 107, 1433
- Kovac, J., Leitch, E., Pryke, C., et al. 2002, *Nature*, 420, 772
- Lamarre, J., Puget, J., Ade, P. A. R., et al. 2010, *A&A*, 520, A9
- Lazarian, A. 2003, *J. Quant. Spectr. Rad. Transf.*, 79, 881
- Lazarian, A. 2007, *J. Quant. Spectr. Rad. Transf.*, 106, 225
- Lazarian, A., & Hoang, T. 2007, *MNRAS*, 378, 910
- Magalhães, A. M., Pereyra, A., Melgarejo, R., et al. 2005, in *Astronomical Polarimetry: Current Status and Future Directions*, eds. A. Adamson, C. Aspin, C. Davis, & T. Fujiyoshi, *ASP Conf. Ser.*, 343, 305
- Martin, P. G. 1971, *MNRAS*, 153, 279
- Martin, P. G. 2007, in *EAS Pub. Ser. 23*, eds. M.-A. Miville-Deschênes, & F. Boulanger, 165
- Matthews, B. C., & Wilson, C. D. 2000, *ApJ*, 531, 868
- Matthews, B. C., McPhee, C. A., Fissel, L. M., & Curran, R. L. 2009, *ApJS*, 182, 143
- Mattila, K., Winnberg, A., & Grasshoff, M. 1979, *A&A*, 78, 275
- Mennella, A., Butler, R. C., Curto, A., et al. 2011, *A&A*, 536, A3
- Miville-Deschênes, M.-A., Ysard, N., Lavabre, A., et al. 2008, *A&A*, 490, 1093
- Momferratos, G. 2014, Ph.D. Thesis, Université Paris Sud
- Montier, L., Plaszczynski, S., Levrier, F., et al. 2015a, *A&A*, 574, A135
- Montier, L., Plaszczynski, S., Levrier, F., et al. 2015b, *A&A*, 574, A136
- Page, L., Hinshaw, G., Komatsu, E., et al. 2007, *ApJS*, 170, 335
- Paradis, D., Dobashi, K., Shimoikura, T., et al. 2012, *A&A*, 543, A103
- Pelkonen, V.-M., Juvela, M., & Padoan, P. 2009, *A&A*, 502, 833
- Planck Collaboration XIX. 2011, *A&A*, 536, A19
- Planck Collaboration XXII. 2011, *A&A*, 536, A22
- Planck Collaboration XXIII. 2011, *A&A*, 536, A23
- Planck Collaboration I. 2014, *A&A*, 571, A1
- Planck Collaboration II. 2014, *A&A*, 571, A2
- Planck Collaboration III. 2014, *A&A*, 571, A3
- Planck Collaboration IV. 2014, *A&A*, 571, A4
- Planck Collaboration V. 2014, *A&A*, 571, A5
- Planck Collaboration VI. 2014, *A&A*, 571, A6
- Planck Collaboration VII. 2014, *A&A*, 571, A7
- Planck Collaboration VIII. 2014, *A&A*, 571, A8
- Planck Collaboration IX. 2014, *A&A*, 571, A9
- Planck Collaboration X. 2014, *A&A*, 571, A10
- Planck Collaboration XI. 2014, *A&A*, 571, A11
- Planck Collaboration XIV. 2014, *A&A*, 571, A14
- Planck Collaboration XVI. 2014, *A&A*, 571, A16
- Planck Collaboration Int. XX. 2015, *A&A*, 576, A105
- Planck Collaboration Int. XXI. 2015, *A&A*, 576, A106
- Planck Collaboration Int. XXII. 2015, *A&A*, 576, A107
- Planck Collaboration Int. XXX. 2015, *A&A*, in press, DOI: [10.1051/0004-6361/201425034](https://doi.org/10.1051/0004-6361/201425034)
- Planck Collaboration Int. XXXII. 2015, *A&A*, submitted [[arXiv:1409.6728](https://arxiv.org/abs/1409.6728)]
- Planck Collaboration Int. XXXIII. 2015, *A&A*, submitted [[arXiv:1411.2271](https://arxiv.org/abs/1411.2271)]
- Planck HFI Core Team 2011, *A&A*, 536, A4
- Poidevin, F., Bastien, P., & Matthews, B. C. 2010, *ApJ*, 716, 893
- Poidevin, F., Falceta-Gonçalves, D., Kowal, G., de Gouveia Dal Pino, E., & Mário Magalhães, A. 2013, *ApJ*, 777, 112
- Ponthieu, N., Macías-Pérez, J. F., Tristram, M., et al. 2005, *A&A*, 444, 327
- Pshirkov, M. S., Tinyakov, P. G., Kronberg, P. P., & Newton-McGee, K. J. 2011, *ApJ*, 738, 192
- Quinn, J. L. 2012, *A&A*, 538, A65
- Reich, W. 1982, *A&AS*, 48, 219
- Reich, P., & Reich, W. 1986, *A&AS*, 63, 205
- Reich, P., Testori, J. C., & Reich, W. 2001, *A&A*, 376, 861
- Reich, P., Reich, W., & Testori, J. C. 2004, in *The Magnetized Interstellar Medium*, eds. B. Uyaniker, W. Reich, & R. Wielebinski, 63
- Ruiz-Granados, B., Rubiño-Martín, J. A., & Battaner, E. 2010, *A&A*, 522, A73
- Serkowski, K. 1958, *Acta Astron.*, 8, 135
- Stein, W. 1966, *ApJ*, 144, 318
- Sun, X.-H., & Reich, W. 2010, *RA&A*, 10, 1287
- Sun, X. H., Reich, W., Waelkens, A., & Enßlin, T. A. 2008, *A&A*, 477, 573
- Taylor, A. R., Stil, J. M., & Sunstrum, C. 2009, *ApJ*, 702, 1230
- Tegmark, M., & de Oliveira-Costa, A. 2001, *Phys. Rev. D*, 64, 63001
- Testori, J. C., Reich, P., & Reich, W. 2008, *A&A*, 484, 733
- Tucci, M., Martínez-González, E., Vielva, P., & Delabrouille, J. 2005, *MNRAS*, 360, 935
- Tucker, K. D., Dickman, R., & Encenaz, P. 1976, *ApJ*, 210, 679
- Vaillancourt, J. E. 2007, in *EAS Pub. Ser. 23*, eds. M.-A. Miville-Deschênes, & F. Boulanger, 147
- van de Hulst, H. C. 1967, *ARA&A*, 5, 167
- Van Eck, C. L., Brown, J. C., Stil, J. M., et al. 2011, *ApJ*, 728, 97
- Ward-Thompson, D., Kirk, J. M., Crutcher, R. M., et al. 2000, *ApJ*, 537, L135
- Whittet, D. C. B., Hough, J. H., Lazarian, A., & Hoang, T. 2008, *ApJ*, 674, 304
- Wolleben, M., Landecker, T. L., Reich, W., & Wielebinski, R. 2006, *A&A*, 448, 411
- Wolleben, M., Fletcher, A., Landecker, T. L., et al. 2010a, *ApJ*, 724, L48
- Wolleben, M., Landecker, T. L., Hovey, G. J., et al. 2010b, *AJ*, 139, 1681

- ³¹ Dipartimento di Fisica e Scienze della Terra, Università di Ferrara, via Saragat 1, 44122 Ferrara, Italy
- ³² Dipartimento di Fisica, Università La Sapienza, P. le A. Moro 2, 00185 Roma, Italy
- ³³ Dipartimento di Fisica, Università degli Studi di Milano, via Celoria 16, 20133 Milano, Italy
- ³⁴ Dipartimento di Fisica, Università degli Studi di Trieste, via A. Valerio 2, 34127 Trieste, Italy
- ³⁵ Dipartimento di Fisica, Università di Roma Tor Vergata, via della Ricerca Scientifica 1, 00133 Roma, Italy
- ³⁶ Discovery Center, Niels Bohr Institute, Blegdamsvej 17, 2100 Copenhagen, Denmark
- ³⁷ Dpto. Astrofísica, Universidad de La Laguna (ULL), 38206 La Laguna, Tenerife, Spain
- ³⁸ European Southern Observatory, ESO Vitacura, Alonso de Cordova 3107, Vitacura, Casilla 19001, Santiago, Chile
- ³⁹ European Space Agency, ESAC, Planck Science Office, Camino bajo del Castillo, s/n, Urbanización Villafranca del Castillo, Villanueva de la Cañada, 28692 Madrid, Spain
- ⁴⁰ European Space Agency, ESTEC, Keplerlaan 1, 2201 AZ Noordwijk, The Netherlands
- ⁴¹ Helsinki Institute of Physics, Gustaf Hällströmin katu 2, University of Helsinki, 00100 Helsinki, Finland
- ⁴² INAF-Osservatorio Astrofisico di Catania, via S. Sofia 78, 95123 Catania, Italy
- ⁴³ INAF-Osservatorio Astronomico di Padova, Vicolo dell'Osservatorio 5, 35122 Padova, Italy
- ⁴⁴ INAF-Osservatorio Astronomico di Roma, via di Frascati 33, 00040 Monte Porzio Catone, Italy
- ⁴⁵ INAF-Osservatorio Astronomico di Trieste, via G.B. Tiepolo 11, 34131 Trieste, Italy
- ⁴⁶ INAF/IASF Bologna, via Gobetti 101, 40129 Bologna, Italy
- ⁴⁷ INAF/IASF Milano, via E. Bassini 15, 20133 Milano, Italy
- ⁴⁸ INFN, Sezione di Bologna, via Irnerio 46, 40126 Bologna, Italy
- ⁴⁹ INFN, Sezione di Roma 1, Università di Roma Sapienza, Piazzale Aldo Moro 2, 00185 Roma, Italy
- ⁵⁰ INFN/National Institute for Nuclear Physics, via Valerio 2, 34127 Trieste, Italy
- ⁵¹ IPAG: Institut de Planétologie et d'Astrophysique de Grenoble, Université Grenoble Alpes, IPAG, CNRS, 38000 Grenoble, France
- ⁵² Imperial College London, Astrophysics group, Blackett Laboratory, Prince Consort Road, London, SW7 2AZ, UK
- ⁵³ Infrared Processing and Analysis Center, California Institute of Technology, Pasadena, CA 91125, USA
- ⁵⁴ Institut d'Astrophysique Spatiale, CNRS (UMR8617), Université Paris-Sud 11, Bâtiment 121, 91405 Orsay, France
- ⁵⁵ Institut d'Astrophysique de Paris, CNRS (UMR7095), 98 bis Boulevard Arago, 75014 Paris, France
- ⁵⁶ Institute for Space Sciences, 077125 Bucharest-Magurale, Romania
- ⁵⁷ Institute of Astronomy, University of Cambridge, Madingley Road, Cambridge CB3 0HA, UK
- ⁵⁸ Institute of Theoretical Astrophysics, University of Oslo, Blindern, 0371 Oslo, Norway
- ⁵⁹ Instituto de Astrofísica de Canarias, C/vía Láctea s/n, La Laguna, 38205 Tenerife, Spain
- ⁶⁰ Instituto de Astronomia, Geofísica e Ciências Atmosféricas, Universidade de São Paulo, 05508-090 São Paulo, Brazil
- ⁶¹ Instituto de Física de Cantabria (CSIC-Universidad de Cantabria), Avda. de los Castros s/n, 39005 Santander, Spain
- ⁶² Jet Propulsion Laboratory, California Institute of Technology, 4800 Oak Grove Drive, CA 91109 Pasadena, California, USA
- ⁶³ Jodrell Bank Centre for Astrophysics, Alan Turing Building, School of Physics and Astronomy, The University of Manchester, Oxford Road, Manchester, M13 9PL, UK
- ⁶⁴ Kavli Institute for Cosmology Cambridge, Madingley Road, Cambridge, CB3 0HA, UK
- ⁶⁵ LAL, Université Paris-Sud, CNRS/IN2P3, 91400 Orsay, France
- ⁶⁶ LERMA, CNRS, Observatoire de Paris, 61 Avenue de l'Observatoire, 75014 Paris, France
- ⁶⁷ Laboratoire AIM, IRFU/Service d'Astrophysique – CEA/DSM – CNRS – Université Paris Diderot, Bât. 709, CEA-Saclay, 91191 Gif-sur-Yvette Cedex, France
- ⁶⁸ Laboratoire Traitement et Communication de l'Information, CNRS (UMR 5141) and Télécom ParisTech, 46 rue Barrault 75634 Paris Cedex 13, France
- ⁶⁹ Laboratoire de Physique Subatomique et de Cosmologie, Université Joseph Fourier Grenoble I, CNRS/IN2P3, Institut National Polytechnique de Grenoble, 53 rue des Martyrs, 38026 Grenoble Cedex, France
- ⁷⁰ Laboratoire de Physique Théorique, Université Paris-Sud 11 & CNRS, Bâtiment 210, 91405 Orsay, France
- ⁷¹ Lawrence Berkeley National Laboratory, Berkeley, CA 94720 California, USA
- ⁷² Max-Planck-Institut für Astrophysik, Karl-Schwarzschild-Str. 1, 85741 Garching, Germany
- ⁷³ National University of Ireland, Department of Experimental Physics, Maynooth, Co. Kildare, Ireland
- ⁷⁴ Niels Bohr Institute, Blegdamsvej 17, 2100 Copenhagen, Denmark
- ⁷⁵ Observational Cosmology, Mail Stop 367-17, California Institute of Technology, Pasadena, CA 91125, USA
- ⁷⁶ Optical Science Laboratory, University College London, Gower Street, WC1E 6BT London, UK
- ⁷⁷ SISSA, Astrophysics Sector, via Bonomea 265, 34136 Trieste, Italy
- ⁷⁸ School of Physics and Astronomy, Cardiff University, Queens Buildings, The Parade, Cardiff, CF24 3AA, UK
- ⁷⁹ Space Sciences Laboratory, University of California, Berkeley, CA 94720 California, USA
- ⁸⁰ Special Astrophysical Observatory, Russian Academy of Sciences, Nizhny Arkhyz, Zelenchukskiy region, 369167 Karachai-Cherkessian Republic, Russia
- ⁸¹ Sub-Department of Astrophysics, University of Oxford, Keble Road, Oxford OX1 3RH, UK
- ⁸² UPMC Univ Paris 06, UMR7095, 98 bis Boulevard Arago, 75014 Paris, France
- ⁸³ Université de Toulouse, UPS-OMP, IRAP, 31028 Toulouse Cedex 4, France
- ⁸⁴ Universities Space Research Association, Stratospheric Observatory for Infrared Astronomy, MS 232-11, Moffett Field, CA 94035, USA
- ⁸⁵ University of Granada, Departamento de Física Teórica y del Cosmos, Facultad de Ciencias, 18071 Granada, Spain
- ⁸⁶ University of Granada, Instituto Carlos I de Física Teórica y Computacional, 18071 Granada, Spain
- ⁸⁷ Warsaw University Observatory, Aleje Ujazdowskie 4, 00-478 Warszawa, Poland

Appendix A: Noise estimates for *Planck* smoothed maps

Here, we show how to smooth polarization maps and derive the covariance matrix associated to the smoothed maps.

A.1. Analytical expressions for smoothing maps of the Stokes parameters and noise covariance matrices

Smoothing total intensity maps is straightforward, but this is not the case for polarization maps. Because the polarization frame follows the sky coordinates and rotates from one centre pixel to a neighbouring pixel whose polarization will be included in the smoothing, in principle the (Q, U) doublet must be also rotated at the same time (e.g., [Keegstra et al. 1997](#)). The issue is similar for evaluating the effects of smoothing on the 3×3 noise covariance matrix, though with mathematically distinct results. In this Appendix, we present an exact analytical solution to the local smoothing of maps of the Stokes I , Q , and U , as well as the effects of smoothing on their corresponding noise covariance matrix.

A.1.1. Smoothing of Stokes parameters

Figure [A.1](#) presents the geometry of the problem. Let us consider a HEALPix pixel j at point J on the celestial sphere, with spherical coordinates (φ_*, θ_*) . To perform smoothing around this position with a Gaussian beam with standard deviation $\sigma_{1/2} = FWHM/2.35$ centred at the position of this pixel we select all HEALPix pixels that fall within 5 times the FWHM of the smoothing beam (this footprint is sufficient for all practical purposes). Let k be one such pixel, centred at the point K with

coordinates (φ_k, θ_k) , at angular distance β from J defined by

$$\cos \beta = \cos \theta_* \cos \theta_k + \sin \theta_* \sin \theta_k \cos (\varphi_k - \varphi_*). \quad (\text{A.1})$$

The normalized Gaussian weight is then

$$w_k = \frac{e^{-(\beta/\sigma_{1/2})^2/2}}{\sum_i e^{-(\beta/\sigma_{1/2})^2/2}} \quad (\text{A.2})$$

and $\sum_k w_k = 1$. Before averaging in the Gaussian beam, we need to rotate the polarization reference frame in K so as align it with that in J. For that the reference frame is first rotated by ψ_k into the great circle running through K and J, then translated to J, and finally rotated through $-\psi_*$. The net rotation angle of the reference frame from point K to point J is then

$$\psi_k^* = \psi_k - \psi_*. \quad (\text{A.3})$$

Due to the cylindrical symmetry around axis z , evaluating ψ_k^* does not depend on the longitudes φ_* and φ_k taken separately, but only on their difference

$$\varphi_k^* = \varphi_k - \varphi_*. \quad (\text{A.4})$$

Using spherical trigonometry in [Fig. A.1](#) with the HEALPix convention for angles ψ_* and ψ_k , we find:

$$\sin \psi_* = \sin \theta_k \sin \varphi_k^* / \sin \beta \quad (\text{A.5})$$

$$\sin \psi_k = \sin \theta_* \sin \varphi_k^* / \sin \beta \quad (\text{A.6})$$

$$\cos \psi_* = -(\cos \theta_k \sin \theta_* - \cos \theta_* \sin \theta_k \cos \varphi_k^*) / \sin \beta \quad (\text{A.7})$$

$$\cos \psi_k = (\cos \theta_* \sin \theta_k - \cos \theta_k \sin \theta_* \cos \varphi_k^*) / \sin \beta. \quad (\text{A.8})$$

To derive ψ_k and ψ_* we use the two-parameter arctan function that resolves the π ambiguity in angles:

$$\psi_k^* = \arctan(\sin \psi_k, \cos \psi_k) - \arctan(\sin \psi_*, \cos \psi_*). \quad (\text{A.9})$$

Because of the tan implicitly used, $\sin \beta$ (a positive quantity) is eliminated in the evaluation of ψ_* , ψ_k , and ψ_k^* .

We can now proceed to the rotation. It is equivalent to rotate the polarization frame at point K by the angle ψ_k^* , or to rotate the data triplet (I_k, Q_k, U_k) at point K by an angle $-2\psi_k^*$ around the axis I . The latter is done with the rotation matrix (e.g., [Tegmark & de Oliveira-Costa 2001](#))

$$[\mathbf{R}]_k = \begin{bmatrix} 1 & 0 & 0 \\ 0 & \cos 2\psi_k^* & \sin 2\psi_k^* \\ 0 & -\sin 2\psi_k^* & \cos 2\psi_k^* \end{bmatrix}. \quad (\text{A.10})$$

Finally, the smoothed I , Q , and U maps are calculated by:

$$\begin{pmatrix} I \\ Q \\ U \end{pmatrix}_j = \sum_k w_k [\mathbf{R}]_k \begin{pmatrix} I \\ Q \\ U \end{pmatrix}_k. \quad (\text{A.11})$$

A.1.2. Computing the noise covariance matrix for smoothed polarization maps

We want to compute the noise covariance matrix $[\mathbf{C}]_*$ at the position of a HEALPix pixel j for the smoothed polarization maps, given the noise covariance matrix $[\mathbf{C}]$ at the higher resolution of the original data. We will assume that the noise in different pixels is uncorrelated. From the given covariance matrix $[\mathbf{C}]_k$ at any pixel k we can produce random realizations of Gaussian noise through the Cholesky decomposition of the covariance matrix:

$$[\mathbf{C}]_k = [\mathbf{L}]_k \times [\mathbf{L}]_k^T, \quad (\text{A.12})$$

$$(\mathbf{N})_k = [\mathbf{L}]_k \times (\mathbf{G})_k, \quad (\text{A.13})$$

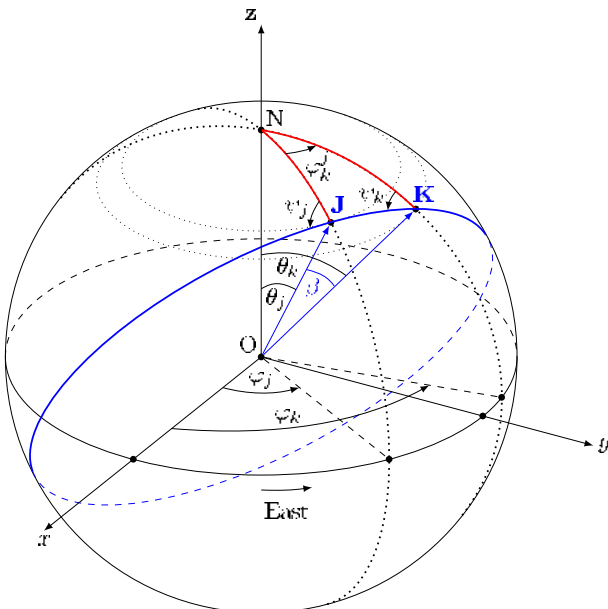


Fig. A.1. Definition of points and angles on the sphere involved in the geometry of the smoothing of polarization maps (adapted from [Keegstra et al. 1997](#)). J is the position of the centre of the smoothing beam, and K a neighbouring pixel, with spherical coordinates (φ_*, θ_*) and (φ_k, θ_k) , respectively. The great circle passing through J and K is shown in blue. The position angles ψ_* and ψ_k here are in the HEALPix convention, increasing from Galactic north toward decreasing Galactic longitude (west) on the celestial sphere as seen by the observer at O.

where in the decomposition $[\mathbf{L}]_k^T$ is the transpose of the matrix $[\mathbf{L}]_k$ and $(\mathbf{G})_k = (G_I, G_Q, G_U)_k$ is a vector of normal Gaussian variables for I , Q , and U .

Applying Eq. (A.11) to the Gaussian noise realization, we obtain

$$(\mathbf{N})_j = \sum_k w_k [\mathbf{R}]_k \begin{pmatrix} N_I \\ N_Q \\ N_U \end{pmatrix} = \sum_k w_k [\mathbf{R}]_k (\mathbf{N})_k. \quad (\text{A.14})$$

The covariance matrix of the smoothed at the position J is given by

$$\begin{aligned} [\mathcal{C}]_\star &= \langle (\mathbf{N})_j (\mathbf{N})_j^T \rangle \\ &= \left\langle \sum_k w_k [\mathbf{R}]_k [\mathbf{L}]_k (\mathbf{G})_k \sum_i w_i (\mathbf{G})_i^T [\mathbf{L}]_i^T [\mathbf{R}]_i^T \right\rangle \\ &= \sum_{k,i} w_k [\mathbf{R}]_k [\mathbf{L}]_k \langle (\mathbf{G})_k (\mathbf{G})_i^T \rangle w_i [\mathbf{L}]_i^T [\mathbf{R}]_i^T. \end{aligned} \quad (\text{A.15})$$

If the noise in distinct pixels is independent, as assumed, then $\langle (\mathbf{G})_k (\mathbf{G})_i \rangle = \delta_{ki}$, the Kronecker symbol, and so

$$[\mathcal{C}]_\star = \sum_k w_k^2 [\mathbf{R}]_k [\mathbf{C}]_k [\mathbf{R}]_k^T, \quad (\text{A.16})$$

which can be computed easily with Eq. (A.10).

Developing each term of the matrix, we can see more explicitly how the smoothing mixes the different elements⁹ of the noise covariance matrix:

$$\mathcal{C}_{II}^\star = \sum_k w_k^2 \mathbf{C}_{IIk} \quad (\text{A.17})$$

$$\mathcal{C}_{IQ}^\star = \sum_k w_k^2 (a \mathbf{C}_{IQk} + b \mathbf{C}_{IUk}) \quad (\text{A.18})$$

$$\mathcal{C}_{IU}^\star = \sum_k w_k^2 (-b \mathbf{C}_{IQk} + a \mathbf{C}_{IUk}) \quad (\text{A.19})$$

$$\mathcal{C}_{QQ}^\star = \sum_k w_k^2 (a^2 \mathbf{C}_{QQk} + 2ab \mathbf{C}_{QUk} + b^2 \mathbf{C}_{UUk}) \quad (\text{A.20})$$

$$\mathcal{C}_{QU}^\star = \sum_k w_k^2 ((a^2 - b^2) \mathbf{C}_{QUk} + ab (\mathbf{C}_{UUk} - \mathbf{C}_{QQk})) \quad (\text{A.21})$$

$$\mathcal{C}_{UU}^\star = \sum_k w_k^2 (b^2 \mathbf{C}_{QQk} - 2ab \mathbf{C}_{QUk} + a^2 \mathbf{C}_{UUk}), \quad (\text{A.22})$$

where we note that $a = \cos 2\psi_k^\star$ and $b = \sin 2\psi_k^\star$ depend on j and k . The mixing of the different elements of the covariance matrix during the smoothing is due not to the smoothing itself, but to the rotation of the polarization frame within the smoothing beam.

A.1.3. Smoothing of the noise covariance matrix with a Monte Carlo approach

For the purpose of this paper, we obtained smoothed covariance matrices using a Monte Carlo approach.

We first generate correlated noise maps (n_I, n_Q, n_U) on I , Q , and U at the resolution of the data using

$$\begin{pmatrix} n_I \\ n_Q \\ n_U \end{pmatrix} = \begin{pmatrix} L_{11} & 0 & 0 \\ L_{12} & L_{22} & 0 \\ L_{13} & L_{23} & L_{33} \end{pmatrix} \times \begin{pmatrix} G_I \\ G_Q \\ G_U \end{pmatrix}, \quad (\text{A.23})$$

⁹ For example, \mathcal{C}_{II}^\star is the first element of matrix $[\mathcal{C}]_\star$ which is being evaluated at the pixel centred on J .

where G_I, G_Q , and G_U are Gaussian normalized random vectors and L is the Cholesky decomposition of the covariance matrix $[\mathbf{C}]$ defined in Eq. (A.12).

The above noise I, Q , an U maps are then smoothed to the requested resolution using the smoothing procedure of the HEALPix package. The noise maps are further resampled using the udgrade procedure of the HEALPix package, so that pixellization respects the Shannon theorem for the desired resolution. The smoothed covariance matrices for each sky pixel are then derived from the statistics of the smoothed noise maps. The Monte Carlo simulations have been performed using 1000 realizations.

Both the analytical and the Monte Carlo approaches have been estimated on the *Planck* data and shown to give equivalent results.

Appendix B: Debiasing methods

Because p is a quadratic function of the observed Stokes parameters (see Eq. (1)) it is affected by a positive bias in the presence of noise. The bias becomes dominant at low S/N. Below we describe briefly a few of the techniques that have been investigated in order to correct for this bias. For a full discussion of the various debiasing methods, see the introductions in Montier et al. (2015a,b) and references therein.

B.1. Conventional method (method 1)

This method is the conventional determination often used on extinction polarization data. It uses the internal variances provided with the *Planck* data, which includes the white noise estimate on the total intensity (\mathbf{C}_{II}) as well as on the Q and U Stokes parameters (\mathbf{C}_{QQ} and \mathbf{C}_{UU}) and the off-diagonal terms of the noise covariance matrix ($\mathbf{C}_{IQ}, \mathbf{C}_{IU}, \mathbf{C}_{QU}$).

The debiased p^2 values are computed using

$$p_{\text{db}}^2 = p_{\text{obs}}^2 - \sigma_p^2, \quad (\text{B.1})$$

where σ_p^2 is the variance of p computed from the observed Stokes parameters and the associated variances as follows:

$$\begin{aligned} \sigma_p^2 &= \frac{1}{p^2 I_{\text{obs}}^4} \times \left\{ Q^2 \mathbf{C}_{QQ} + U^2 \mathbf{C}_{UU} + \frac{\mathbf{C}_{II}}{I^2} \times (Q^2 + U^2)^2 \right. \\ &\quad \left. + 2QU \mathbf{C}_{QU} \right. \\ &\quad \left. - 2Q \frac{(Q^2 + U^2)}{I} \mathbf{C}_{IQ} - 2U \frac{(Q^2 + U^2)}{I} \mathbf{C}_{IU} \right\}. \end{aligned} \quad (\text{B.2})$$

The uncertainty on ψ is given by

$$\sigma_\psi = 28.65^\circ \times \sqrt{\frac{Q^2 \mathbf{C}_{UU} + U^2 \mathbf{C}_{QQ} - 2QU \mathbf{C}_{QU}}{Q^2 \mathbf{C}_{QQ} + U^2 \mathbf{C}_{UU} + 2QU \mathbf{C}_{QU}}} \times \sigma_p, \quad (\text{B.3})$$

where σ_p is the uncertainty on the polarized intensity:

$$\sigma_p^2 = \frac{1}{p^2} (Q^2 \mathbf{C}_{QQ} + U^2 \mathbf{C}_{UU} + 2QU \mathbf{C}_{QU}). \quad (\text{B.4})$$

In the case where I is supposed to be perfectly known, $\mathbf{C}_{II} = \mathbf{C}_{IQ} = \mathbf{C}_{IU} = 0$,

$$\sigma_\psi = 28.65^\circ \times \sqrt{\frac{Q^2 \mathbf{C}_{UU} + U^2 \mathbf{C}_{QQ} - 2QU \mathbf{C}_{QU}}{Q^2 \mathbf{C}_{QQ} + U^2 \mathbf{C}_{UU} + 2QU \mathbf{C}_{QU}}} \times \frac{\sigma_p}{p}. \quad (\text{B.5})$$

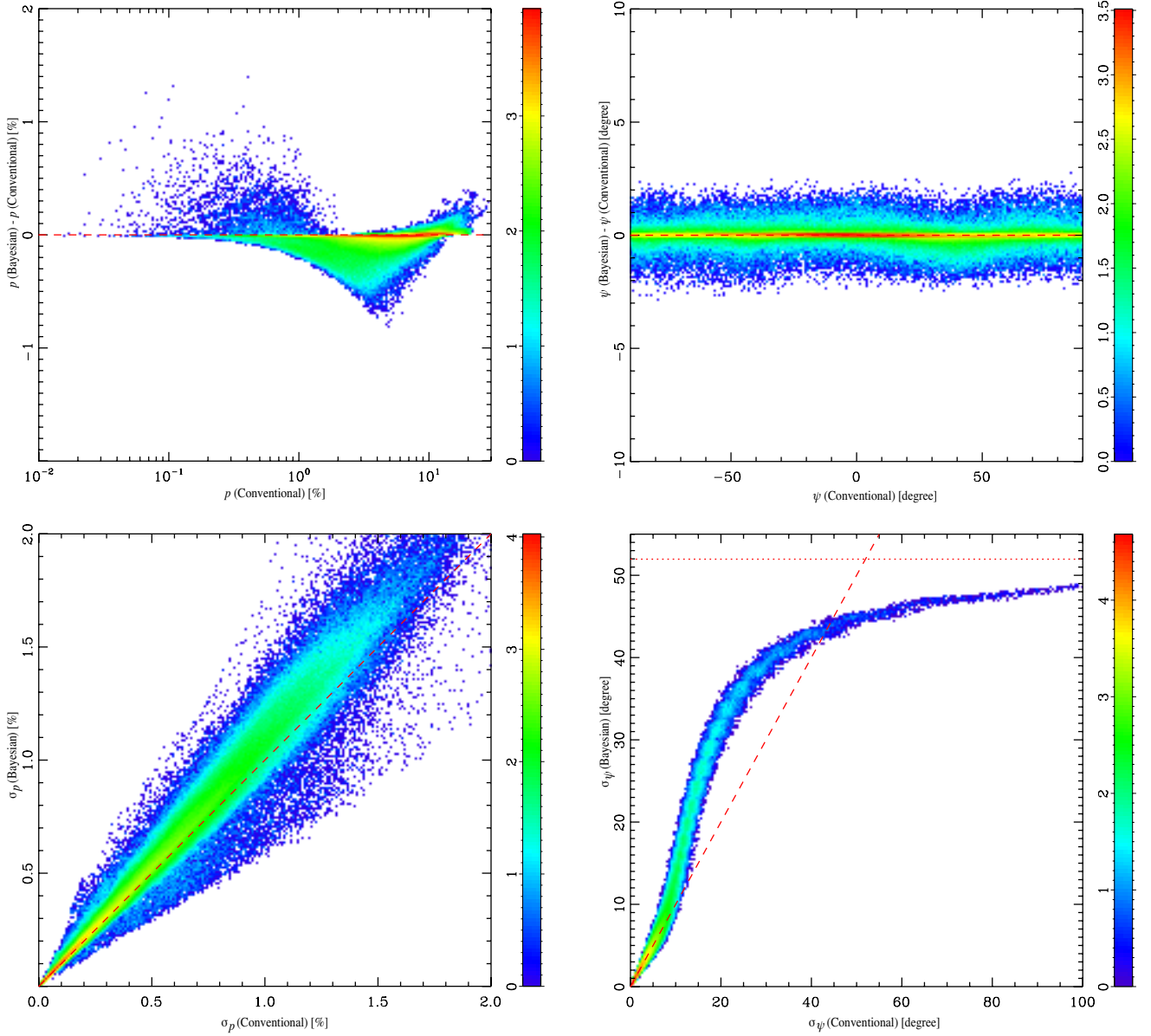


Fig. B.1. *Upper panels:* difference between the conventional and the Bayesian mean posterior estimates of p and ψ as a function of the conventional estimate. *Lower panels:* Bayesian mean posterior estimates of σ_p and σ_ψ as a function of the conventional estimate. The dashed red lines show where the two methods give the same result. Each plot shows the density of points in log-scale for the *Planck* data at 1° resolution. The dotted line in the *lower right plot* shows the value for pure noise. The colour scale shows the pixel density on a \log_{10} scale.

Because it is based on derivatives around the true value of the I , Q , and U parameters, this is only valid in the high S/N regime. The conventional values of uncertainties derived above are compared to the ones obtained using the Bayesian approach in Fig. B.1.

B.2. Time cross-product method (method 2)

This method consists in computing cross products between estimates of Q and U with independent noise properties. In the case of *Planck* HFI, each sky pixel has been observed at least four times and the four independent surveys can be used for this purpose. Another option is to use half-ring maps which have been produced from the first and second halves of each ring. These methods have the disadvantage of using only part of the data, but the advantage of efficiently debiasing the data if the noise

is effectively independent, without assumptions about the Q and U uncertainties.

In that case, p_{db}^2 can be computed as

$$p_{\text{db}}^2 = \frac{\sum_{i>j} Q_i Q_j + U_i U_j}{\sum_{i>j} I_i I_j}, \quad (\text{B.6})$$

where the sum is carried out either over independent survey maps or half-ring maps.

The uncertainty of p^2 can in turn be evaluated from the dispersion between pairs

$$\sigma^2(p_{\text{db}}^2) = \frac{\sigma^2(Q^2) + \sigma^2(U^2) + (Q^2 + U^2)/I^2 \sigma^2(I^2)}{I^4}. \quad (\text{B.7})$$

B.3. Bayesian methods (method3)

We use a method based on the one proposed by Quinn (2012) and extended to the more general case of an arbitrary covariance matrix by Montier et al. (2015a). We use the Mean Posterior Bayesian (MB) estimator described in Montier et al. (2015b). Unlike the conventional method presented in Sect. B.1, this method is in principle accurate at any signal-to-noise ratio. Figure B.1 compares the Bayesian predictions for p and ψ and their uncertainties σ_p and σ_ψ with those obtained from the conventional method (Eqs. (1), (2), and (B.1)–(B.4)) as predicted from the *Planck* data at 1° resolution. As can be seen in the figure, the bias on p is generally important even at this low resolution. The conventional uncertainties are accurate only at low uncertainties, as expected because Eqs. (B.4) and (B.5) are obtained from Taylor expansion around the true values of the parameters. The difference in the uncertainties is the greatest for σ_ψ as the true value can only reach 52° for purely random orientations.

Appendix C: Tests on the bias of S

We have performed tests in which we used the *Planck* noise covariance matrices in order to check that the structures we observe in the maps of the polarization angle dispersion function S are not caused by systematic noise bias. One of the tests (called $S = 52^\circ$) consisted of assigning each pixel a random polarization angle ψ . The second one (called $S = 0^\circ$) consisted of setting ψ to a constant value over the whole sky map, which leads to $S = 0^\circ$ (except near the poles). In that case, changing ψ in the data was done while preserving the value of p and σ_p computed as in Eq. (B.2), through the appropriate modification of I , Q , and U . The tests also use the noise covariance of the data, so that the tests are performed with the same sky distribution of the polarization S/N as in the data. This is critical for investigating the spatial distribution of the noise-induced bias on S . In both tests, we added correlated noise on I , Q , and U using the actual noise covariance matrix at each pixel, and computed the map of S using Eq. (6) and the same lag value as for the *Planck* data.

Figure C.1 (upper) shows the histograms of the S values obtained for these two tests, both for the whole sky and in the mask used in the analysis of the real data. histograms peak at the value of S for Gaussian noise only (no signal, $S = 52^\circ$). The corresponding map of S does not exhibit the filamentary structure of the actual data shown in Fig. 12. Similarly, the test histograms of S do not resemble that of the real data shown in Fig. 14.

The $S = 0^\circ$ test is important for assessing the amplitude of the noise-induced bias, as Monte Carlo simulations show that assuming a true value of $S_0 = 0^\circ$ maximizes the bias. We therefore use this test as a determination of the upper limit for the bias given the polarization fraction and noise properties of the data. Figure C.1 (upper) shows that the histograms of the recovered values peak at $S = 0^\circ$. The histogram is also narrower in the high S S/N region than over larger sky regions at lower S/N. In the high S S/N mask, 60% of the data points have a noise-induced bias smaller than 1.6° , and 97% have a bias smaller than 9.6° . The maps of the bias computed for this test show a correlation with the map of S . However, as shown in Fig. C.1 (lower panel), the effect of the bias (the size of the offset) is small at high values of S for most pixels and can reach up to 50% for a larger fraction of points at lower S values (say below $S = 10^\circ$). This

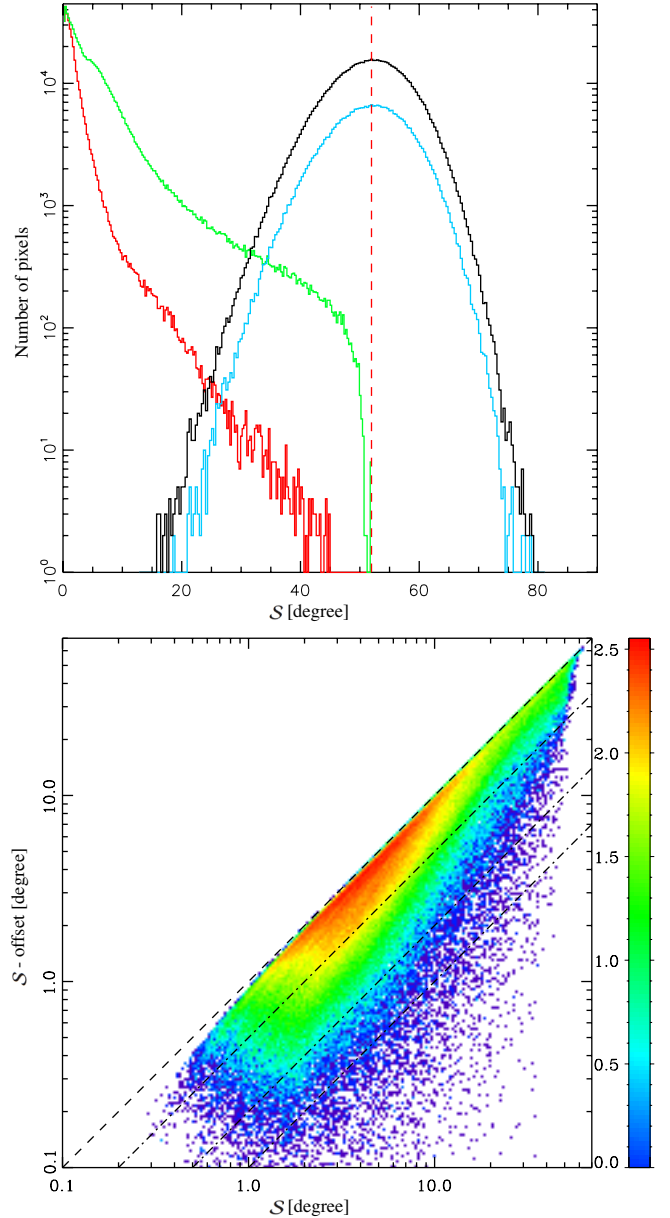


Fig. C.1. Upper: histogram of S obtained on simulated data assuming either $S = 0^\circ$ (curves peaking at $S = 0^\circ$) or a random value for S (curves peaking at $S = 52^\circ$) and noise simulated using the actual *Planck* noise covariance matrices. The green and black curves show the histograms over the sky fraction shown in Fig. 4 and the blue and red curves show histograms where the S/N on S is larger than 3. The vertical dashed line shows $S = 52^\circ$, which is the value for pure random noise on Q and U . Lower: distribution of the bias-corrected S (S minus the offset derived from a simulation with $S = 0^\circ$), with respect to S , in the region where the S/N on S is larger than 3. Dashed lines show $S = n \times (S - \text{offset})$, with $n = 1, 2, 5, 10$. The colour scale shows the pixel density on a \log_{10} scale.

bias correction does not significantly change the structure of the map shown in Fig. 12 and so, in particular, bias does not cause the filamentary structures observed. We note, however, that the noise-induced bias can change the slope of the correlation between S and p .

Planck intermediate results. XX. Comparison of polarized thermal emission from Galactic dust with simulations of MHD turbulence[★]

Planck Collaboration: P. A. R. Ade⁷¹, N. Aghanim⁵⁰, D. Alina^{76,9}, M. I. R. Alves⁵⁰, G. Aniano⁵⁰, C. Armitage-Caplan⁷⁴, M. Arnaud⁶¹, D. Arzoumanian⁵⁰, M. Ashdown^{58,5}, F. Atrio-Barandela¹⁶, J. Aumont⁵⁰, C. Baccigalupi⁷⁰, A. J. Banday^{76,9}, R. B. Barreiro⁵⁵, E. Battaner^{77,78}, K. Benabed^{51,75}, A. Benoit-Lévy^{22,51,75}, J.-P. Bernard^{76,9}, M. Bersanelli^{31,44}, P. Bielewicz^{76,9,70}, J. R. Bond⁸, J. Borrill^{12,72}, F. R. Bouchet^{51,75}, F. Boulanger⁵⁰, A. Bracco⁵⁰, C. Burigana^{43,29}, J.-F. Cardoso^{62,1,51}, A. Catalano^{63,60}, A. Chamballu^{61,113,50}, H. C. Chiang^{25,6}, P. R. Christensen^{68,34}, S. Colombi^{51,75}, L. P. L. Colombo^{21,56}, C. Combet⁶³, F. Couchot⁵⁹, A. Coulais⁶⁰, B. P. Crill^{56,69}, A. Curto^{5,55}, F. Cuttaia⁴³, L. Danese⁷⁰, R. D. Davies⁵⁷, R. J. Davis⁵⁷, P. de Bernardis³⁰, A. de Rosa⁴³, G. de Zotti^{40,70}, J. Delabrouille¹, C. Dickinson⁵⁷, J. M. Diego⁵⁵, S. Donzelli⁴⁴, O. Doré^{56,10}, M. Douspis⁵⁰, X. Dupac³⁶, G. Efstathiou⁵³, T. A. Enßlin⁶⁶, H. K. Eriksen⁵⁴, E. Falgarone⁶⁰, L. Fanciullo⁵⁰, K. Ferrière^{76,9}, F. Finelli^{43,45}, O. Forni^{76,9}, M. Frailis⁴², A. A. Fraisse²⁵, E. Franceschi⁴³, S. Galeotta⁴², K. Ganga¹, T. Ghosh⁵⁰, M. Giard^{76,9}, Y. Giraud-Héraud¹, J. González-Nuevo^{55,70}, K. M. Górski^{56,79}, A. Gregorio^{32,42,47}, A. Gruppuso⁴³, V. Guillet⁵⁰, F. K. Hansen⁵⁴, D. L. Harrison^{53,58}, G. Helou¹⁰, C. Hernández-Monteagudo^{11,66}, S. R. Hildebrand¹⁰, E. Hivon^{51,75}, M. Hobson⁵, W. A. Holmes⁵⁶, A. Hornstrup¹⁴, K. M. Huffenberger²³, A. H. Jaffe⁴⁸, T. R. Jaffe^{76,9}, W. C. Jones²⁵, M. Juvela²⁴, E. Keihänen²⁴, R. Kesitalo¹², T. S. Kisner⁶⁵, R. Kneissl^{35,7}, J. Knoche⁶⁶, M. Kunz^{15,50,2}, H. Kurki-Suonio^{24,38}, G. Lagache⁵⁰, J.-M. Lamarre⁶⁰, A. Lasenby^{5,58}, C. R. Lawrence⁵⁶, R. Leonardi³⁶, F. Levrier^{60,★★}, M. Liguori²⁸, P. B. Lilje⁵⁴, M. Linden-Vørnle¹⁴, M. López-Cañiego⁵⁵, P. M. Lubin²⁶, J. F. Macías-Pérez⁶³, D. Maino^{31,44}, N. Mandolesi^{43,4,29}, M. Maris⁴², D. J. Marshall⁶¹, P. G. Martin⁸, E. Martínez-González⁵⁵, S. Masi³⁰, S. Matarrese²⁸, P. Mazzotta³³, A. Melchiorri^{30,46}, L. Mendes³⁶, A. Mennella^{31,44}, M. Migliaccio^{53,58}, M.-A. Miville-Deschênes^{50,8}, A. Moneti⁵¹, L. Montier^{76,9}, G. Morgante⁴³, D. Mortlock⁴⁸, D. Munshi⁷¹, J. A. Murphy⁶⁷, P. Naselsky^{68,34}, F. Nati³⁰, P. Natoli^{29,3,43}, C. B. Netterfield¹⁸, F. Noviello⁵⁷, D. Novikov⁴⁸, I. Novikov⁶⁸, C. A. Oxborrow¹⁴, L. Pagano^{30,46}, F. Pajot⁵⁰, D. Paoletti^{43,45}, F. Pasian⁴², V.-M. Pelkonen⁴⁹, O. Perdereau⁵⁹, L. Perotto⁶³, F. Perrotta⁷⁰, F. Piacentini³⁰, M. Piat¹, D. Pietrobon⁵⁶, S. Plaszczynski⁵⁹, E. Pointecouteau^{76,9}, G. Polenta^{3,41}, L. Popa⁵², G. W. Pratt⁶¹, S. Prunet^{51,75}, J.-L. Puget⁵⁰, J. P. Rachen^{19,66}, M. Reinecke⁶⁶, M. Remazeilles^{57,50,1}, C. Renault⁶³, S. Ricciardi⁴³, T. Riller⁶⁶, I. Ristorcelli^{76,9}, G. Rocha^{56,10}, C. Rosset¹, G. Roudier^{1,60,56}, B. Rusholme⁴⁹, M. Sandri⁴³, D. Scott²⁰, J. D. Soler⁵⁰, L. D. Spencer⁷¹, V. Stolyarov^{5,58,73}, R. Stompor¹, R. Sudiwala⁷¹, D. Sutton^{53,58}, A.-S. Suur-Uski^{24,38}, J.-F. Sygnet⁵¹, J. A. Tauber³⁷, L. Terenzi⁴³, L. Toffolatti^{17,55}, M. Tomasi^{31,44}, M. Tristram⁵⁹, M. Tucci^{15,59}, G. Umata³⁹, L. Valenziano⁴³, J. Valiviita^{24,38}, B. Van Tent⁶⁴, P. Vielva⁵⁵, F. Villa⁴³, L. A. Wade⁵⁶, B. D. Wandelt^{51,75,27}, and A. Zonca²⁶

(Affiliations can be found after the references)

Received 28 April 2014 / Accepted 4 September 2014

ABSTRACT

Polarized emission observed by *Planck* HFI at 353 GHz towards a sample of nearby fields is presented, focusing on the statistics of polarization fractions p and angles ψ . The polarization fractions and column densities in these nearby fields are representative of the range of values obtained over the whole sky. We find that: (i) the largest polarization fractions are reached in the most diffuse fields; (ii) the maximum polarization fraction p_{\max} decreases with column density N_{H} in the more opaque fields with $N_{\text{H}} > 10^{21} \text{ cm}^{-2}$; and (iii) the polarization fraction along a given line of sight is correlated with the local spatial coherence of the polarization angle. These observations are compared to polarized emission maps computed in simulations of anisotropic magnetohydrodynamical turbulence in which we assume a uniform intrinsic polarization fraction of the dust grains. We find that an estimate of this parameter may be recovered from the maximum polarization fraction p_{\max} in diffuse regions where the magnetic field is ordered on large scales and perpendicular to the line of sight. This emphasizes the impact of anisotropies of the magnetic field on the emerging polarization signal. The decrease of the maximum polarization fraction with column density in nearby molecular clouds is well reproduced in the simulations, indicating that it is essentially due to the turbulent structure of the magnetic field: an accumulation of variously polarized structures along the line of sight leads to such an anti-correlation. In the simulations, polarization fractions are also found to anti-correlate with the angle dispersion function \mathcal{S} . However, the dispersion of the polarization angle for a given polarization fraction is found to be larger in the simulations than in the observations, suggesting a shortcoming in the physical content of these numerical models. In summary, we find that the turbulent structure of the magnetic field is able to reproduce the main statistical properties of the dust polarization as observed in a variety of nearby clouds, dense cores excluded, and that the large-scale field orientation with respect to the line of sight plays a major role in the quantitative analysis of these statistical properties.

Key words. ISM: general – dust, extinction – ISM: magnetic fields – ISM: clouds – infrared: ISM – submillimeter: ISM

1. Introduction

*Planck*¹ (Tauber et al. 2010; Planck Collaboration I 2011) is the third generation space-mission aimed at mapping the

[★] Appendices are available in electronic form at <http://www.aanda.org>

^{★★} Corresponding author: F. Levrier,
e-mail: francois.levrier@ens.fr

¹ *Planck* (<http://www.esa.int/Planck>) is a project of the European Space Agency (ESA) with instruments provided by two scientific consortia funded by ESA member states (in particular the lead countries France and Italy), with contributions from NASA (USA) and

anisotropies of the cosmic microwave background (CMB). With its unprecedented sensitivity and large spectral coverage (nine channels from 30 GHz to 857 GHz) it has provided exquisite maps of that relic radiation (Planck Collaboration I 2014). With its polarimetric capabilities up to 353 GHz, *Planck* will also provide clues on the physics of the early Universe, by measuring the CMB polarization. However, dominant foreground emission is also partially polarized, masking the primordial signal. In the

telescope reflectors provided by a collaboration between ESA and a scientific consortium led and funded by Denmark.

range of the High Frequency Instrument (HFI, [Lamarre et al. 2010](#)), from 100 GHz to 857 GHz, the main contribution to the observed radiation, besides point sources, is thermal emission from dust grains.

The angular momenta of aspherical and spinning grains tend to align with the local magnetic field, although the details of how this alignment proceeds are still the subject of study: see for instance [Andersson \(2012\)](#) for a review on observational constraints regarding grain alignment with respect to current dust models. Submillimetre thermal dust emission is therefore polarized and represents a powerful tool to study interstellar magnetic fields and dust properties. Ideally, we would like to know where in interstellar clouds, and with what efficiency the dust emission and extinction is polarized. This would allow us to use polarization data to infer the spatial structure of the magnetic field. There is an extensive literature on this topic based on observations of starlight polarization, which have been interpreted from two different viewpoints, i.e., grain alignment and magnetic field structure, without achieving a clear understanding of the respective roles of these processes in accounting for variations of polarization across the sky. A number of papers (e.g., [Pereyra & Magalhães 2007](#); [Alves et al. 2008](#); [Marchwinski et al. 2012](#)) use the data to infer the magnetic field strength using the Chandrasekhar-Fermi method ([Chandrasekhar & Fermi 1953](#)). Other papers focus on the observed decrease of polarization fraction p with N_{H} to interpret the data as a decrease of the dust alignment efficiency in dense clouds ([Lazarian et al. 1997](#); [Whittet et al. 2008](#); [Chapman et al. 2011](#)).

Magnetohydrodynamical (MHD) simulations provide a theoretical framework to consider both aspects in the interpretation of polarization datasets. [Ostriker et al. \(2001\)](#) were among the first to present simulated polarization maps from MHD simulations, for comparison with data and to study the field structure beyond the simple Chandrasekhar-Fermi method. [Falceta-Gonçalves et al. \(2008\)](#) used a similar technique to study the effect of the Alfvénic Mach number, while [Pelkonen et al. \(2009\)](#) added to this approach the modelling of the alignment process by radiative torques ([Hoang & Lazarian 2008](#)).

Planck has mapped the polarized dust emission with great sensitivity and resolution ([Planck Collaboration Int. XIX 2014](#)), allowing us to characterize spatial variations of dust polarization and compare data with MHD simulations with unprecedented statistics. This paper is the second in a series of four dealing with a first presentation of the *Planck* polarized thermal emission from Galactic dust. The other three are the following: [Planck Collaboration Int. XIX \(2014\)](#) describes the polarized dust emission at 353 GHz as seen by *Planck* over the whole sky and shows in particular that the maximum polarization fraction p_{max} at a given total gas column density N_{H} decreases as N_{H} increases, and that there is an anti-correlation between polarization fractions p and angle dispersion functions \mathcal{S} , an effect which has also been seen with starlight polarization data ([Hatano et al. 2013](#)). [Planck Collaboration Int. XXI \(2014\)](#) compares polarized thermal emission from dust at 353 GHz to polarization in extinction in the visible towards a sample of stars. Finally, [Planck Collaboration Int. XXII \(2014\)](#) discusses the variation of polarized thermal emission from dust with frequency, from 70 to 353 GHz. Both [Planck Collaboration Int. XXI \(2014\)](#) and [Planck Collaboration Int. XXII \(2014\)](#) aim at providing constraints for models of interstellar dust.

In this paper, we use *Planck* polarization data at 353 GHz to present statistics of polarization fractions and angles in nearby interstellar clouds seen outside the Galactic plane. We then compare the *Planck* results with simulated observations of polarized

thermal dust emission at 353 GHz built from a three-dimensional MHD simulation of the formation of a molecular cloud within colliding flows ([Hennebelle et al. 2008](#)).

In these simulated observations, we work under the assumption that the optical properties and the intrinsic polarization fraction of dust grains are constant. At this stage we do not aim at testing models of grain alignment. In this picture, it is expected that the polarization fraction should be maximal when the magnetic field is in the plane of the sky and should, in this case, yield valuable information on the intrinsic polarization fraction. That is why we first focus on the decrease of the maximum value of p , rather than its mean or median values, with increasing column density. We then consider the correlation between polarization fractions and local measures of the dispersion in polarization angles, as it is expected that larger angular dispersions should lower the observed polarization fraction.

The paper is organized as follows. Section 2 describes the *Planck* data used and the statistics drawn from them in the selected regions. Section 3 presents simulated polarized emission observations based on an MHD simulation of interstellar turbulence and compares their statistical properties with those found towards similar fields in the *Planck* data. Conclusions are given in Sect. 4. Appendix A presents supplementary figures, and Appendix B details the derivation of the equations yielding the Stokes parameters for dust emission.

2. *Planck* observations of polarized dust emission

2.1. *Planck* all-sky data post-processing

The data processing of *Planck* HFI is presented in [Planck Collaboration VI \(2014\)](#), [Planck Collaboration VII \(2014\)](#), [Planck Collaboration VIII \(2014\)](#), [Planck Collaboration IX \(2014\)](#), and [Planck Collaboration X \(2014\)](#). The specifics of the data processing in terms of polarization are given in [Planck Collaboration Int. XIX \(2014\)](#). We use the same *Planck* data set as that presented in [Planck Collaboration Int. XIX \(2014\)](#), i.e., full 5-survey HFI mission data for Stokes I , Q , and U at 353 GHz (which is the *Planck* channel offering the best signal-to-noise ratio for dust polarization) from the “DR3” internal data release. Bandpass mismatch between individual elements of a pair of polarization sensitive bolometers (PSBs) is corrected using in-flight measurements for the dust emission but not for the negligible CO $J = 3 \rightarrow 2$ emission ([Planck Collaboration IX 2014](#)). From the total intensity map we subtract the offset $I_{\text{offset}} = 0.0887 \text{ MJy sr}^{-1}$ to set the Galactic zero level at 353 GHz ([Planck Collaboration XI 2014](#)). Note that this value includes the cosmic infrared background (CIB) monopole and is slightly different from the one given in [Planck Collaboration XI \(2014\)](#), as the maps are not the same (full mission vs. nominal mission). We do not correct for zodiacal light emission, nor for the residual dipole identified by [Planck Collaboration XI \(2014\)](#) at 353 GHz. CMB and CIB fluctuations are ignored, since the regions selected in this study are outside the CMB-CIB mask described in [Planck Collaboration Int. XIX \(2014\)](#), so the polarized emission there is dominated by the dust.

The *Planck* polarization and intensity data that we use in this analysis have been generated in exactly the same manner as the data publicly released in March 2013 and described in [Planck Collaboration I \(2014\)](#) and associated papers. Note, however, that the publicly available data include only temperature maps based on the first two surveys. [Planck Collaboration XVI \(2014\)](#) shows the very good consistency of cosmological models

derived from intensity only with polarization data at small scales (high CMB multipoles). However, as detailed in [Planck Collaboration VI \(2014\)](#); see their Fig. 27), the 2013 polarization data are known to be affected by systematic effects at low multipoles which were not yet fully corrected, and thus these data were not used for cosmology². We have been careful to check that the Galactic science results in this paper are robust with respect to these systematics³.

We focus in this paper on the polarization fractions p and the polarization angles ψ derived from the Stokes I , Q , and U maps obtained by *Planck* at 353 GHz and at an angular resolution of $15'$. In the absence of noise, p and ψ are defined by

$$p = \frac{\sqrt{Q^2 + U^2}}{I}, \quad (1)$$

and

$$\psi = \frac{1}{2} \text{atan}(U, Q). \quad (2)$$

Note that ψ is here defined in the HEALPix⁴ convention ([Górski et al. 2005](#)), which means that angles are counted positively clockwise from the north-south direction. Working in that convention instead of the IAU one, which is anti-clockwise ([Planck Collaboration Int. XXI 2014](#)), has however no impact on the results presented here. Additionally, since we work on ratios of Stokes parameters, no colour correction is necessary.

When (possibly correlated) noise affects the Stokes parameters, the polarization fraction computed directly using Eq. (1) is biased. We call this one the “naïve” estimator of p , but various methods have been devised to correct for the bias ([Montier et al. 2014a](#)), and their respective efficiencies are compared in [Montier et al. \(2014b\)](#). Among them is the modified asymptotic (MAS) estimator introduced by [Plaszczynski et al. \(2014\)](#), which is computed from the naive estimator and the noise covariance matrix pertaining to Q and U . Another estimator of the polarization fraction and angle is the Bayesian estimator described in [Montier et al. \(2014a\)](#) and [Planck Collaboration Int. XIX \(2014\)](#), which has the advantage of taking into account the full noise covariance matrix in I , Q and U , and also taking into account the uncertainty on the zero-level offset for I . In the rest of this paper, except where noted, the maps of polarization fraction p and polarization angle ψ at 353 GHz refer to these Bayesian estimators. The Bayesian method also provides maps of the polarization fraction and angle uncertainties, σ_p and σ_ψ .

For the total hydrogen column density map N_{H} , we use a conversion from the optical depth at 353 GHz, τ_{353} , derived from [Planck Collaboration XI \(2014\)](#): for $N_{\text{H}} \gtrsim 2 \times 10^{21} \text{ cm}^{-2}$, the dust opacity is approximately constant, with $\sigma_{353} = \tau_{353}/N_{\text{H}} \simeq 1.2 \times 10^{-26} \text{ cm}^2$. We are aware that this conversion is crude, with possible variations in dust opacity of the order of 20% to 25%, but our findings do not critically depend on that calibration.

All of the maps used in this study have a HEALPix resolution $N_{\text{side}} = 1024$.

² The full mission maps for intensity as well as for polarization will be made publicly available in the end of 2014.

³ The error-bars we quote include uncertainties associated with residual systematics as estimated by repeating the analysis on different subsets of the data. We have also checked our data analysis on the latest version of the maps available to the consortium to check that the results we find are consistent within the error-bars quoted in this paper.

⁴ <http://healpix.jpl.nasa.gov>. See in particular the latest version of the HEALPix primer, available at <http://healpix.jpl.nasa.gov/pdf/intro.pdf>

2.2. Overview of the statistics of polarized emission in various fields

We have selected ten regions, each $12^\circ \times 12^\circ$ in size, that are highlighted in Fig. 1 and whose locations are given in Table 1. These are the same as some of the individual regions mentioned in [Planck Collaboration Int. XIX \(2014\)](#). All of these fields are outside the Galactic plane and probe nearby interstellar material, but they exhibit very different physical conditions, from the diffuse, turbulent ISM with little to no star-forming activity (Polaris Flare), to self-gravitating, star-forming clouds (Orion). They also differ in terms of polarized emission. Some diffuse regions have high polarization fractions (e.g., Pavo), while some have low polarization fractions (e.g., Polaris Flare). This variety of conditions in terms of polarization fraction and gas content is emphasized in Fig. 2, which shows the distribution of p and N_{H} in these regions, compared with the large-scale distribution shown in [Planck Collaboration Int. XIX \(2014\)](#). The latter is represented by its upper and lower envelopes, computed from the 0.01% and 99.99% percentiles of the p distribution within each bin in column density. All the envelopes of two-dimensional distribution functions shown in this paper are computed in this fashion. Note that to facilitate the comparison with [Planck Collaboration Int. XIX \(2014\)](#), Fig. 2 uses maps at 1° resolution. In the rest of the paper, as already stated, we use $15'$ resolution maps.

It appears that for column densities between a few times 10^{20} cm^{-2} and a few times 10^{22} cm^{-2} , the selected fields probe most of the range of polarization fractions observed over the whole sky in this range of column densities. The diffuse Polaris Flare field shows low polarization, while high polarization fractions are reached at similar column densities in the Chamaeleon-Musca complex, which, being closer to the Galactic plane, is threaded by the large-scale Galactic magnetic field. Another notable feature of Fig. 2 is the fact that in regions with the largest column densities (Taurus, Orion, and Ophiuchus) the maximum polarization fraction decreases with increasing N_{H} , and that the slopes are comparable to the large-scale trend.

In the following, we perform statistical analyses of the polarization data in these nearby fields by simply selecting HEALPix pixels whose centres fall within the region of interest, directly from the large-scale maps. Only pixels for which $p/\sigma_p > 3$ are retained. This threshold is a reasonable value above which the polarization signal-to-noise ratio is properly estimated ([Montier et al. 2014b](#)). Note that some of the fields in Table 1 are quite diffuse (e.g., Pavo), so that the dynamic range in column densities is too small to exhibit a significant relationship between p_{max} and N_{H} . These diffuse fields are therefore discarded in the later analysis.

We also build local maps of polarized emission using gnomonic projections of the HEALPix maps. These are shown in the middle row panels of Fig. 3 for the Ophiuchus and Chamaeleon-Musca fields. Similar figures for all other fields are given in Appendix A. On all these maps, which share the same scale, we show the polarization fractions p at 353 GHz (colour scale) overlaid with contours of the total gas column density and bars of constant length giving the orientation of the apparent projection of the magnetic field on the plane of the sky. These are built by rotating the 353 GHz polarization bars by 90° so as to recover the average magnetic field orientation in the plane of the sky. In the rest of the paper, we will refer to the rotated polarization bars as the magnetic orientation bars. Note that although they are plotted once every few pixels only, to improve visibility, each of these bars represents the orientation at the given pixel. In other

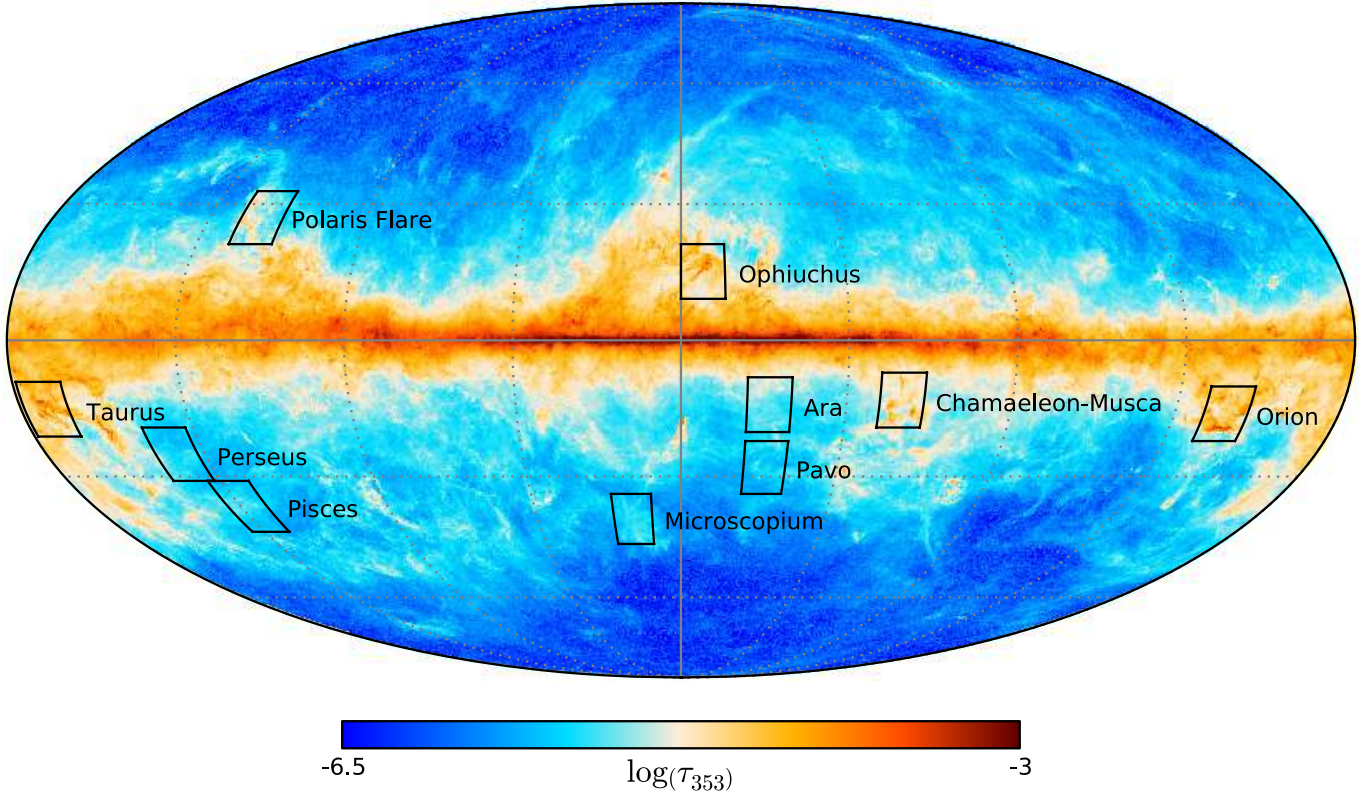


Fig. 1. Locations of the selected nearby fields. The background map represents optical depth τ_{353} at 353 GHz on a logarithmic scale, at 5' resolution (Planck Collaboration XI 2014). The map uses a Mollweide projection in Galactic coordinates, with $(l, b) = (0^\circ, 0^\circ)$ at the centre.

Table 1. Locations and properties of the selected fields.

Field	l [°]	b [°]	Distance ^a [pc]	Mass ^b [M_\odot]	Age ^c [Myr]	$\langle N_H \rangle$ [10^{21} cm^{-2}]	Max(N_H) [10^{21} cm^{-2}]	f_{22} [%]	f_{21} [%]
Polaris Flare	120	27	130–140	–	–	1.1	5.0	0	58
Taurus	173	–15	140	2×10^4	20	4.1	26	4.2	0.8
Orion	211	–16	414	3×10^5	>12	4.0	40	5.4	7.3
Chamaeleon-Musca	300	–13	160–180	5×10^3	>2	2.0	21	0.5	7.5
Ophiuchus	354	15	120–140	3×10^4	>2–5	3.1	62	2.2	3.8
Microscopium	15	–40	–	–	–	0.4	1.1	0	99
Pisces	133	–37	–	–	–	0.4	1.9	0	99
Perseus	143	–25	–	–	–	0.4	1.5	0	99
Ara	336	–14	–	–	–	0.8	2.1	0	75
Pavo	336	–28	–	–	–	0.4	1.4	0	99

Notes. The table includes: Galactic longitudes l and latitudes b of the centre of the $12^\circ \times 12^\circ$ fields; estimates of distances, masses and ages, where available; average and maximum column densities at $15'$ resolution; fraction f_{22} of the pixels with $N_H > 10^{22} \text{ cm}^{-2}$; and fraction f_{21} of the pixels with $N_H < 10^{21} \text{ cm}^{-2}$. These fields are the same as several of those listed in Table 1 of Planck Collaboration Int. XIX (2014). ^(a) Estimates of distances are from Elias (1978) for Taurus, Zagury et al. (1999) for Polaris Flare, de Zeeuw et al. (1999) for Ophiuchus, Whittet et al. (1997) for Chamaeleon-Musca, and Draine (2011) for Orion. ^(b) Estimates of masses are from Ungerechts & Thaddeus (1987) for Taurus, Loren (1989) for Ophiuchus, Luhman (2008) for Chamaeleon-Musca, and Draine (2011) for Orion. ^(c) Estimates of ages are from Palla & Stahler (2002) for Taurus, Wilking et al. (2008) for Ophiuchus, Luhman (2008) for Chamaeleon-Musca, and Bally (2008) for Orion.

words, beyond the $15'$ smoothing performed on the Stokes maps, no further averaging is done to plot the orientation bars on Fig. 3 and similar plots.

The large-scale structure of the Galactic magnetic field appears clearly (see e.g., the top part of the Chamaeleon-Musca field, Fig. 3). There is also a strong correlation between the coherence of the polarization orientation and the level of polarization fraction, in the sense that more ordered regions have

higher polarization fractions. This feature, which is already seen at $1'$ resolution in Planck Collaboration Int. XIX (2014), is discussed later on in Sect. 2.5.

A final qualitative aspect of these maps is that regions with higher column densities tend to be less polarized than their surroundings. An example of this effect can be seen in the Chamaeleon-Musca field (Fig. 3, center right panel) near $(l, b) = (301^\circ, -9^\circ)$, where $p \simeq 10\%$, while it is surrounded

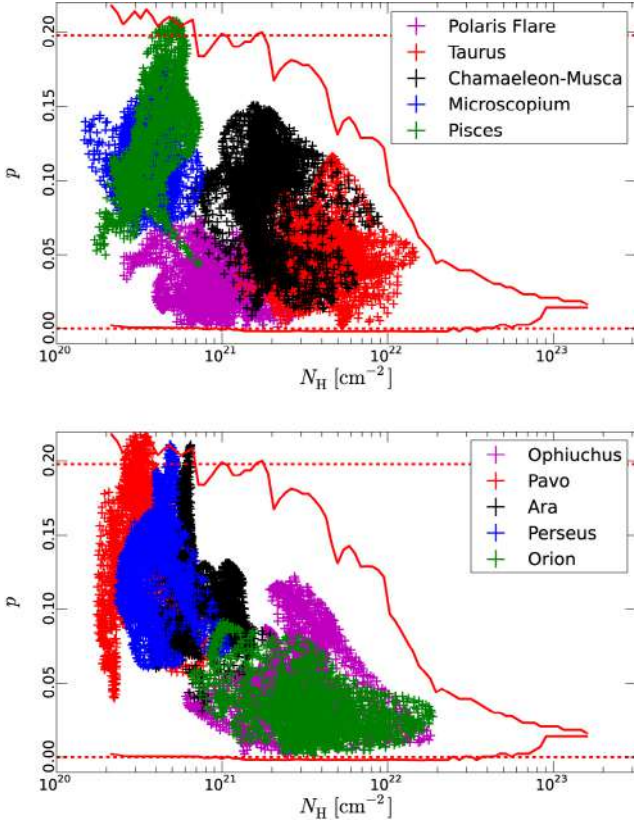


Fig. 2. Two-dimensional distribution functions of polarization fraction p and column density N_{H} in the fields highlighted in Fig. 1. *Top:* Polaris Flare (magenta), Taurus (red), Chamaeleon-Musca (black), Microscopium (blue), and Pisces (green). *Bottom:* Ophiuchus (magenta), Pavo (red), Ara (black), Perseus (blue), and Orion (green). On both panels, the solid red lines show the upper and lower envelopes (see text) of the large-scale distribution of p and N_{H} , clipped below $N_{\text{H}} = 2 \times 10^{20} \text{ cm}^{-2}$, while the dashed red lines correspond to $p = 0$ and the maximum value $p = 0.198$ (i.e., 19.8%) quoted in Planck Collaboration Int. XIX (2014).

by more diffuse material with $p \approx 15\%$. A future paper (Planck Collaboration Int. XIII 2014) will discuss in more detail the structure of the polarized thermal emission with respect to the morphology of the clouds themselves.

2.3. Maximum polarization fraction

We give in Table 2 the maximum polarization fractions p_{max} in all the selected fields. Note that for the most diffuse fields Microscopium, Pisces, Perseus, Ara, and Pavo, the quoted values should be taken with caution, since most pixels in these regions have $N_{\text{H}} \leq 10^{21} \text{ cm}^{-2}$, which corresponds roughly to $I_{353} \leq 0.5 \text{ MJy sr}^{-1}$, and therefore the effect of the (uncertain) zero-level offset on the polarization fraction p may not be negligible.

In the less diffuse fields, the values of p_{max} are noticeably larger than those found in the same fields at 1° resolution in Planck Collaboration Int. XIX (2014)⁵, which shows the strong effect of spatial resolution on polarization measurements. The uncertainties $\sigma_{p_{\text{max}}}$ on the maximum polarization fractions, listed

⁵ See their Table 1, which also lists extrema, mean and median values for p , as well as median values for ψ .

in Table 2, are derived from the various sources of uncertainty involved.

First, the noise properties on the Stokes parameters I , Q , and U in each pixel are described in the data by the noise covariance matrices, which are input in the Bayesian method of Montier et al. (2014a) and Planck Collaboration Int. XIX (2014), and lead to a map of the uncertainty σ_p on the polarization fraction. This includes the $0.0068 \text{ MJy sr}^{-1}$ uncertainty on the zero-level offset. We then compute the difference $\sigma_{p_{\text{max}},p}$ between the maximum polarization fractions found in the maps of $p - \sigma_p$ and $p + \sigma_p$.

Second, there is a part of the uncertainty related to the method used to debias the data (Montier et al. 2014a). We have computed the standard deviation $\sigma_{p_{\text{max},d}}$ of the maximum polarization fractions obtained in each field when using the “naïve” $\sqrt{Q^2 + U^2}/I$, modified asymptotic (MAS, Plaszczyński et al. 2014) and Bayesian estimators of p .

Third, we have computed the standard deviation $\sigma_{p_{\text{max},s}}$ of the maximum polarization fractions obtained in each field when considering subsets of the data, namely half-ring maps (one half of each stable pointing period) and detector set maps (one half of the detectors).

The final uncertainty quoted in Table 2 is then given by the quadratic sum

$$\sigma_{p_{\text{max}}}^2 = \sigma_{p_{\text{max},p}}^2 + \sigma_{p_{\text{max},d}}^2 + \sigma_{p_{\text{max},s}}^2/2. \quad (3)$$

It should be noted that the last contribution is usually the dominant one in the selected fields, and that the uncertainty related to the debiasing method is much smaller than the other two.

2.4. Polarization fraction vs. column density

We show the distributions of p and N_{H} for the Ophiuchus and Chamaeleon-Musca fields in Fig. 4 and for all other fields in Appendix A. The decrease in maximum polarization fraction p_{max} at higher column densities is apparent for all fields, above a given threshold in N_{H} that depends on the field and is of the order of 10^{21} to $3 \times 10^{21} \text{ cm}^{-2}$, corresponding to visual extinctions $A_V \approx 0.6$ to 1.7 , for the fields that are not too diffuse (Polaris Flare, Taurus, Orion, Chamaeleon-Musca, and Ophiuchus). Below this threshold, the polarization fraction may be related to the background more than to the clouds themselves. To quantify the decrease in maximum polarization fraction p_{max} with increasing N_{H} , we consider the upper envelope of the distribution of p and N_{H} , computed as described in Sect. 2.2, and fit this curve with a function $p_{\text{max}} = m \log(N_{\text{H}}/\text{cm}^{-2}) + c$, restricted to a range of column densities that depends on the field considered (see Table 2). Note that we perform this fit for the above five fields only, for which there is a large enough dynamic range in column density.

Results of these fits are shown as solid black lines on each panel of Fig. 4, and values of the slopes m and intercepts c are listed in Table 2. Uncertainties on these parameters are derived in the same way as for the maximum polarization fractions p_{max} in the previous section. The slopes m range between -0.068 for Orion and -0.140 for Taurus, and regions exhibiting stronger column density peaks (e.g., Orion) tend to have shallower slopes than more diffuse molecular clouds (e.g., Polaris Flare).

As mentioned before, the pixels selected for plotting Fig. 4 and performing the fits are those for which the polarization signal-to-noise ratio is $p/\sigma_p > 3$. We have checked that modifying this threshold does not change our results, as can be seen in Fig. 5, which shows the same as the top panel of

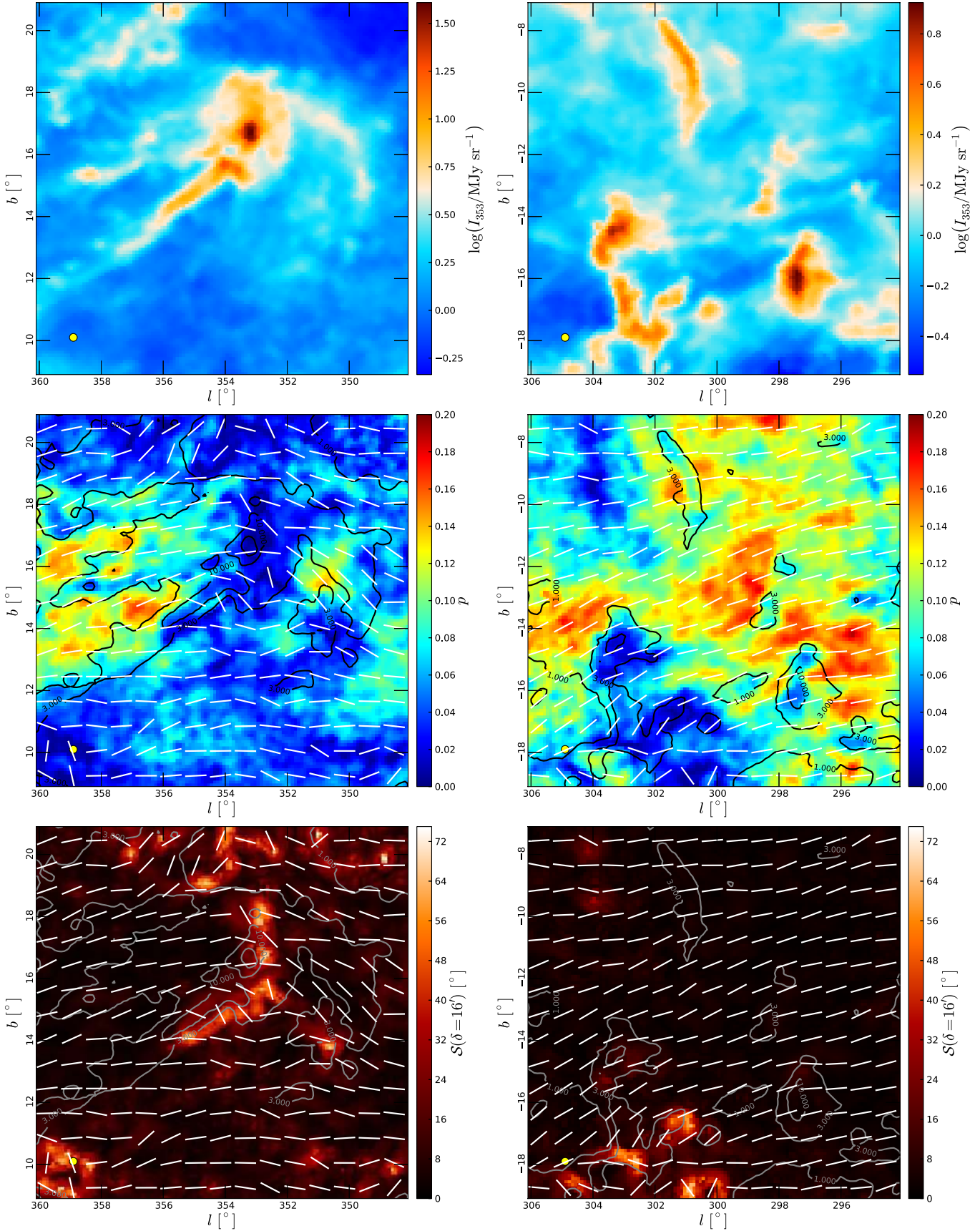


Fig. 3. Maps of the Ophiuchus and Chamaeleon-Musca fields. *Left:* Ophiuchus field. *Right:* Chamaeleon-Musca field. *Top:* total intensity at 353 GHz. *Middle:* polarization fraction p , column density N_{H} (contours in units of 10^{21} cm^{-2}), and magnetic orientation (bars, see text). *Bottom:* angle dispersion function S with lag $\delta = 16'$ (see Sect. 2.5) with contours and bars identical to the middle row. In all maps, the $15'$ beam is shown in the lower-left corner.

Table 2. Polarization statistics in the selected fields.

Field	p_{\max}	$p_{\max} = m \log(N_{\text{H}}/\text{cm}^{-2}) + c$	N_{H} range	$\log(S) = m' \log(p) + c'$
		m c	$[10^{21} \text{ cm}^{-2}]$	m' c'
Polaris Flare	0.134 ± 0.015	-0.114 ± 0.014 2.5 ± 0.3	1–4	-0.56 ± 0.08 0.25 ± 0.17
Taurus	0.149 ± 0.011	-0.140 ± 0.004 3.2 ± 0.1	5–25	-0.87 ± 0.09 -0.31 ± 0.11
Orion	0.129 ± 0.014	-0.068 ± 0.003 1.6 ± 0.1	3–40	-0.87 ± 0.11 -0.25 ± 0.13
Chamaeleon-Musca	0.190 ± 0.008	-0.134 ± 0.003 3.0 ± 0.1	3–20	-0.94 ± 0.03 -0.39 ± 0.02
Ophiuchus	0.166 ± 0.006	-0.129 ± 0.004 2.9 ± 0.1	3–40	-0.92 ± 0.05 -0.30 ± 0.04
Microscopium	0.24 ± 0.05	– –	–	-0.41 ± 0.07 0.38 ± 0.07
Pisces	0.30 ± 0.11	– –	–	-0.67 ± 0.13 0.21 ± 0.12
Perseus	0.33 ± 0.09	– –	–	-0.46 ± 0.09 0.37 ± 0.06
Ara	0.27 ± 0.03	– –	–	-0.48 ± 0.07 0.15 ± 0.06
Pavo	0.48 ± 0.18	– –	–	-0.27 ± 0.05 0.57 ± 0.03

Notes. The table includes: absolute maximum polarization fraction at 15' resolution; linear fit parameters m and c to the decrease of p_{\max} with $\log(N_{\text{H}}/\text{cm}^{-2})$, with fitting range indicated; and linear fit parameters of the $\log(S)$ vs. $\log(p)$ correlation. See text for the derivation of the listed uncertainties. The figures given here are for a signal-to-noise threshold $p/\sigma_p > 3$.

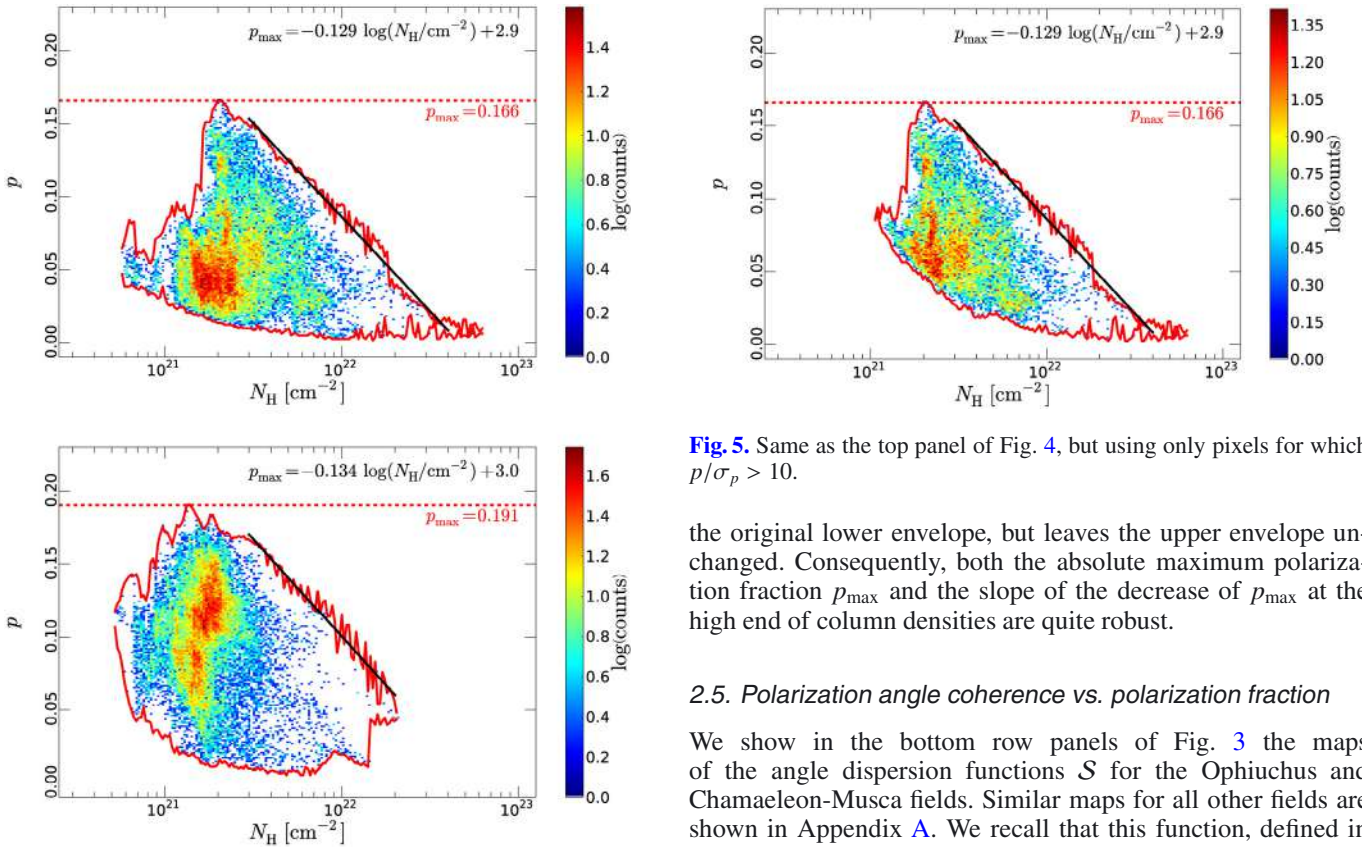


Fig. 4. Two-dimensional distribution function of polarization fraction p and column density N_{H} . *Top:* Ophiuchus field. *Bottom:* Chamaeleon-Musca field. The distribution functions are presented in logarithmic colour scale and include only points for which $p/\sigma_p > 3$. The dashed red lines correspond to the absolute maximum polarization fractions p_{\max} and the solid red curves show the upper and lower envelopes of p as functions of N_{H} . The solid black line is a linear fit $p_{\max} = m \log(N_{\text{H}}/\text{cm}^{-2}) + c$ to the decrease of the maximum polarization fraction with column density at the high end of N_{H} (see Table 2 for the fitting ranges and fit parameters).

Fig. 4 but with a signal-to-noise ratio threshold $p/\sigma_p > 10$. The effect of that stricter selection is to remove points below

Fig. 5. Same as the top panel of Fig. 4, but using only pixels for which $p/\sigma_p > 10$.

the original lower envelope, but leaves the upper envelope unchanged. Consequently, both the absolute maximum polarization fraction p_{\max} and the slope of the decrease of p_{\max} at the high end of column densities are quite robust.

2.5. Polarization angle coherence vs. polarization fraction

We show in the bottom row panels of Fig. 3 the maps of the angle dispersion functions \mathcal{S} for the Ophiuchus and Chamaeleon-Musca fields. Similar maps for all other fields are shown in Appendix A. We recall that this function, defined in Planck Collaboration Int. XIX (2014), is

$$\mathcal{S}(\mathbf{r}, \delta) = \sqrt{\frac{1}{N} \sum_{i=1}^N [\psi(\mathbf{r}) - \psi(\mathbf{r} + \delta_i)]^2}, \quad (4)$$

where the sum extends over pixels whose distances from the central pixel \mathbf{r} are between $\delta/2$ and $3\delta/2$. Here they are computed at a lag $\delta = 16'$, comparable to the size of the beam's FWHM. One can readily see filamentary structures that correspond to regions where the polarization angle is less ordered or where it changes abruptly. These filaments are already noted at 1° resolution in Planck Collaboration Int. XIX (2014) over several degrees. These regions of large angular dispersions correspond to

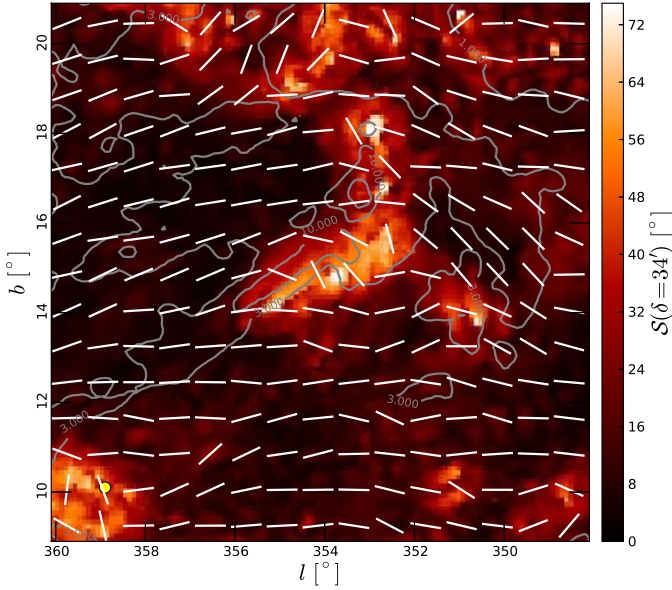


Fig. 6. Map of S for the Ophiuchus field computed at $\delta = 34'$. Contours are the same as in the map at $\delta = 16'$ (bottom left panel of Fig. 3).

regions of low polarization fraction, as can be seen for instance by comparing the middle and bottom row panels of Fig. 3.

When increasing the value of the lag δ , we obtain maps of S such as that presented in Fig. 6 for the Ophiuchus field at $\delta = 34'$ (approximately twice the FWHM). It appears that the overall value of S increases with lag, as already noted in Hildebrand et al. (2009) and Planck Collaboration Int. XIX (2014). However, since S has an upper limit of 90° , this means that the anti-correlation with p (see below) will flatten out at large lags. Note however that a completely random sample yields $S = \pi/\sqrt{12} \simeq 52^\circ$ (Planck Collaboration Int. XIX 2014). Values larger than this are few, but they do exist, as can be seen on the maps of S in Figs. 3 and 6. They may be linked to sharp boundaries between two well-ordered regions: for instance, the angle dispersion function at the interface between two half-planes with orthogonal magnetic orientations is $S = \pi/\sqrt{8} \simeq 64^\circ$.

To confirm the visual impression that the spatial coherence of the polarization angle is anti-correlated with the polarization fraction, we show the distribution function of these two quantities for the Ophiuchus and Chamaeleon-Musca fields in Figs. 7 and 8, respectively, and for all other fields in Appendix A.

The large-scale anti-correlation seen in Planck Collaboration Int. XIX (2014) at 1° resolution and $\delta = 30'$ is also present when using a lag close to the beam size. With $\delta = 1^\circ 07'$, we find it to be $\log(S) = -0.75 \log p - 0.06$, where S is measured in degrees. Since in this case the ratio δ/FWHM is the same as for our higher resolution maps ($\text{FWHM} = 15'$ and $\delta = 16'$), we compare the anti-correlations found in the selected fields to this law. Note that the slope -0.75 is similar to the value -0.834 quoted in Planck Collaboration Int. XIX (2014), but the intercept is larger (-0.06 vs. -0.504). This points to a global increase of S at larger δ/FWHM values, which we interpret as a decorrelation of polarization angles at larger lags.

The distributions of p and S in the various fields considered show an anti-correlation very similar to the large-scale trend, with slopes and intercepts of the fits through the data points that are very close to the large-scale fit values. When increasing the lag at the same resolution, however, S increases and the anti-correlation with p flattens out, as can be seen in Fig. 9. The linear

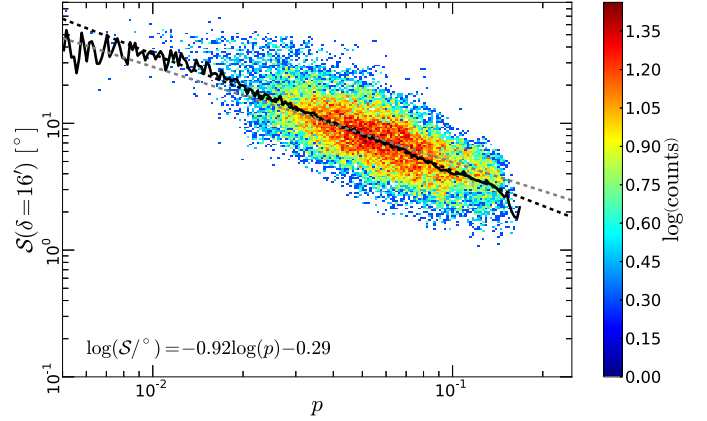


Fig. 7. Two-dimensional distribution function of S and polarization fraction p for the Ophiuchus field. The angle dispersion function S is computed at a lag $\delta = 16'$. Only pixels for which $p/\sigma_p > 3$ are retained. The dashed grey line is the large-scale fit (with $\text{FWHM} = 1^\circ$ and $\delta = 1^\circ 07'$) $\log(S) = -0.75 \log(p) - 0.06$, the solid black line shows the mean S for each bin in p (the bin size is $\Delta \log(p) = 0.008$) and the dashed black line is a linear fit of that curve in log-log space, restricted to bins in p which contain at least 1% of the total number of points (so about 150 points per bin).

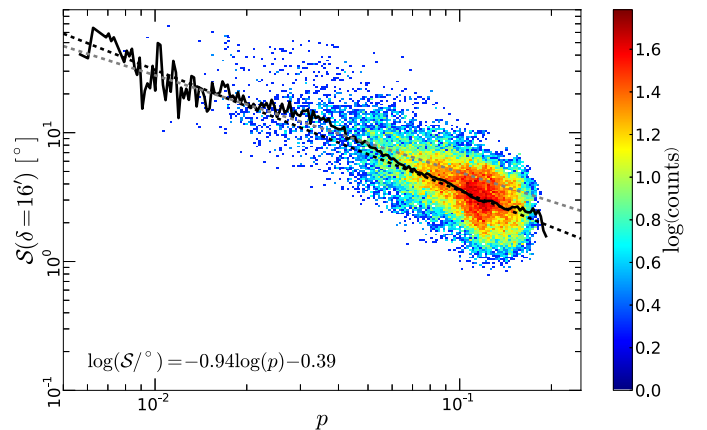


Fig. 8. Same as Fig. 7, but for the Chamaeleon-Musca field.

fits $\log(S) = m' \log p + c'$ for the individual fields are listed in Table 2. The uncertainties on the parameters m' and c' are the quadratic sums of uncertainties obtained in three ways: (i) by performing the linear regression using the three estimators of p , i.e., the “naïve”, MAS and Bayesian ones; (ii) by using half-ring maps and detector set maps; (iii) via a Monte-Carlo simulation using the maps of polarization fraction uncertainty σ_p and angle dispersion function uncertainty σ_S (Planck Collaboration Int. XIX 2014).

3. Simulations of polarized emission

3.1. Simulations of MHD turbulence

We aim to compare the observed polarization statistics in the selected fields to predictions built on the results of a numerical simulation of MHD turbulence. This simulation is described in

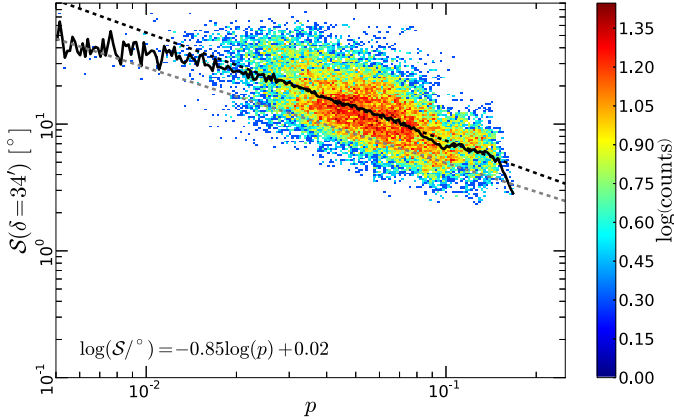


Fig. 9. Same as Fig. 7, but for a lag $\delta = 34'$.

detail in Hennebelle et al. (2008)⁶. It follows the formation of clumps of dense and cold gas (cold neutral medium, CNM) out of magnetized warm neutral atomic gas (warm neutral medium, WNM) in an open box of 50 pc on each side, without reaching the stage when cold cores of column density larger than $2 \times 10^{22} \text{ cm}^{-2}$ form.

The simulation cube initially contains a uniform distribution of WNM with density $n_{\text{H}} = 1 \text{ cm}^{-3}$ and temperature $T = 8000 \text{ K}$, and two converging flows of that same gas are injected from opposing faces along the x axis with a velocity $\Delta V_x \simeq 40 \text{ km s}^{-1}$ relative to each other. Spatial modulations of the velocity are imposed on the incoming flows, with amplitudes relative to the mean flow of about unity and a periodicity of about 10 pc. Periodic boundary conditions are applied on the remaining four faces. The total mass contained in the cube continuously increases with time. The magnetic field's initial direction is along that of the incoming flows, and its intensity is about $5 \mu\text{G}$, consistent with observational values at these densities (Crutcher et al. 2010). There is therefore a large-scale anisotropic component of the magnetic field throughout the simulation, as well as a turbulent component linked to the velocity perturbations imposed on the converging flows.

These flows collide near the midplane, where the combined effects of cooling and self-gravity eventually lead to the formation of dense ($n_{\text{H}} > 100 \text{ cm}^{-3}$) clumps of cold gas (T of the order of 10–50 K; Hennebelle & Audit 2007). To follow that condensation, the grid is adaptively refined, with an effective (maximum) resolution of 0.05 pc.

In this paper, we select a cubic subset (18 pc \times 18 pc \times 18 pc) of the density and magnetic field in the simulation snapshot timed at $t = 10.9 \text{ Myr}$, which corresponds to an evolved state of the simulation, given the crossing time $t_c \simeq 2.4 \text{ Myr}$. The structures present in the simulation are due to the collision of the incoming flows and not to a pure gravitational collapse, since the initial free-fall time is $t_{\text{ff}} \simeq 44 \text{ Myr}$. However, some of the densest structures ($n_{\text{H}} > 10^4 \text{ cm}^{-3}$) may have had time to collapse.

The chosen subset is located near the midplane, so that the influence of boundary conditions is minimal. It contains approximately $3200 M_{\odot}$ of gas; its physical properties are listed in Table 3, and the distribution functions of total gas density n_{H} and magnetic field components B_x , B_y , B_z are shown in Figs. 10

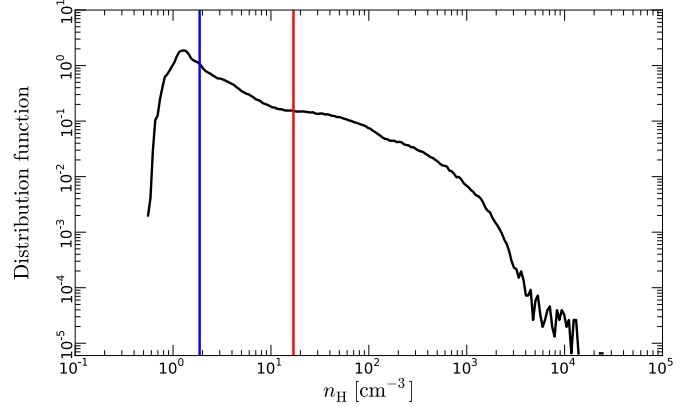


Fig. 10. Distribution function of the total gas density n_{H} in the selected subset of the simulation, with cell sizes $0.1 \text{ pc} \times 0.1 \text{ pc} \times 0.1 \text{ pc}$. The solid red line shows the mean value $\langle n_{\text{H}} \rangle = 17 \text{ cm}^{-3}$ and the solid blue line the median value $n_{\text{H}}^{\text{med}} = 2 \text{ cm}^{-3}$.

Table 3. Physical properties of the subset of the simulation.

F	$\langle F \rangle$	Min(F)	Max(F)	$\sigma(F)$
$N_{\text{H}} [10^{21} \text{ cm}^{-2}] \dots$	1.0	0.05	13.4	1.0
$n_{\text{H}} [\text{cm}^{-3}] \dots$	16.4	0.5	4.1×10^4	92
$B_x [\mu\text{G}] \dots$	5.8	-32.5	25.8	3.2
$B_y [\mu\text{G}] \dots$	-0.1	-26.1	26.5	3.0
$B_z [\mu\text{G}] \dots$	0.3	-22.3	30.6	3.3

Notes. These values correspond to $\alpha = 0^\circ$ (see text and Fig. 13).

and 11, respectively. The standard deviations are very similar for all three magnetic field components, but only the x component has a significant mean value, which shows that the mean magnetic field within the cube is approximately aligned with the x axis, that is with the incoming flows.

We would like to stress here that the MHD simulations we use for comparison with the *Planck* polarization data do not faithfully reproduce the whole range of densities and column densities spanned by the cloud sample of Table 1, i.e., from diffuse molecular clouds (Polaris Flare) to massive star-forming clouds (Orion). However, as shown in Table 1, only a few percent of the pixels (at most 5.4% in Orion) have column densities larger than 10^{22} cm^{-2} in these fields, the regions of star formation filling only a small fraction of the area in each field. The MHD simulations with their broad range of densities (Fig. 10) and column densities reaching⁷ $N_{\text{H}} = 1.6 \times 10^{22} \text{ cm}^{-2}$ are therefore representative of the dynamics of the bulk of the gas. Together with their anisotropy, due to the large-scale magnetic field pervading the cube, these simulations are particularly well suited to analyse the polarization properties of nearby molecular clouds immersed in their low density and large-scale environment.

To compute simulated polarization fractions p , the local gas density n_{H} and magnetic field components B_x , B_y , B_z are extracted from the simulation and interpolated on a regular grid at the next-to-highest spatial resolution available, so that pixel sizes are approximately $\Delta x = 0.1 \text{ pc}$. These cubes are used in the following section to build simulated polarized emission maps. However, they are first rotated around the y axis, as sketched out

⁶ It was performed with the RAMSES code (Teysier 2002; Fromang et al. 2006), whose adaptive mesh refinement capabilities allow for a locally high spatial sampling. It is freely available via the STARFORMAT project, <http://starformat.obspm.fr/>. To be precise, it is the *Fiducial* run under the tab *Colliding flow simulation*.

⁷ This value is computed over the whole range of viewing angles α .

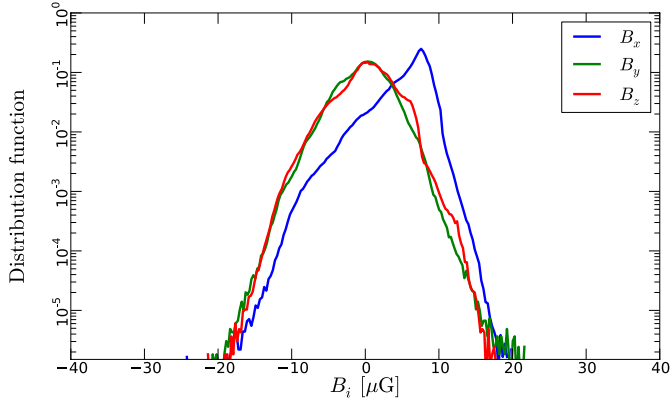


Fig. 11. Distribution functions of the components of the magnetic field, B_x (blue), B_y (green), and B_z (red), in the selected subset of the simulation, with cell sizes $0.1 \text{ pc} \times 0.1 \text{ pc} \times 0.1 \text{ pc}$.

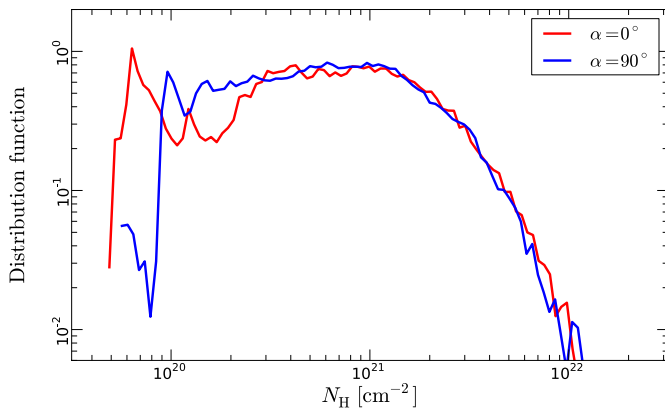


Fig. 12. Distribution functions of the total gas column density N_{H} in the selected subset of the simulation, using viewing angles $\alpha = 0^\circ$ (red) and $\alpha = 90^\circ$ (blue). These distribution functions are computed after convolution with the $15'$ beam.

in Fig. 13, to explore the full range of possible angles between the mean magnetic field and the line of sight, and therefore to test the effects of the large-scale magnetic field's anisotropy. The viewing angle α introduced in Fig. 13 is such that the mean magnetic field is approximately in the plane of the sky for $\alpha = 0^\circ$, and along the line of sight for $\alpha = 90^\circ$.

3.2. Simulated Planck observations

We build simulated Stokes I , Q , and U maps by integrating along the line of sight (z' in Fig. 13) through the rotated simulation cube, following the method in Wardle & Königl (1990), Fiege & Pudritz (2000), Pelkonen et al. (2009), and Padovani et al. (2012). Because of a number of inconsistencies in the literature, we give the correct derivation in Appendix B, drawing on the works of Lee & Draine (1985) and Wardle & Königl (1990). This results in:

$$I = \int S_\nu e^{-\tau_\nu} \left[1 - p_0 \left(\cos^2 \gamma - \frac{2}{3} \right) \right] d\tau_\nu; \quad (5)$$

$$Q = \int p_0 S_\nu e^{-\tau_\nu} \cos(2\phi) \cos^2 \gamma d\tau_\nu; \quad (6)$$

$$U = \int p_0 S_\nu e^{-\tau_\nu} \sin(2\phi) \cos^2 \gamma d\tau_\nu. \quad (7)$$

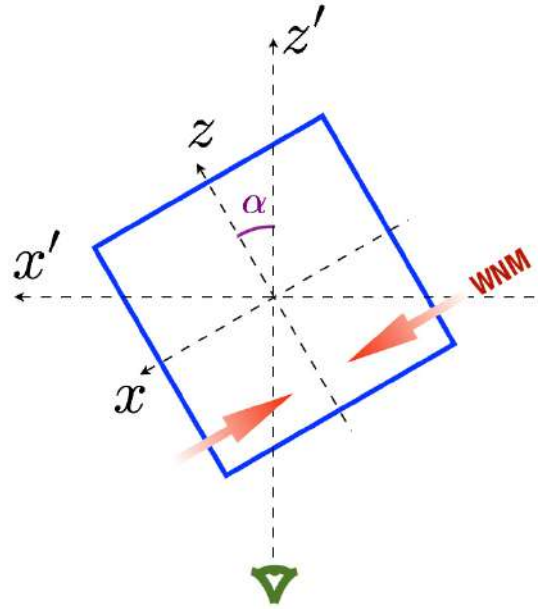


Fig. 13. Sketch of the rotation of the simulation subset.

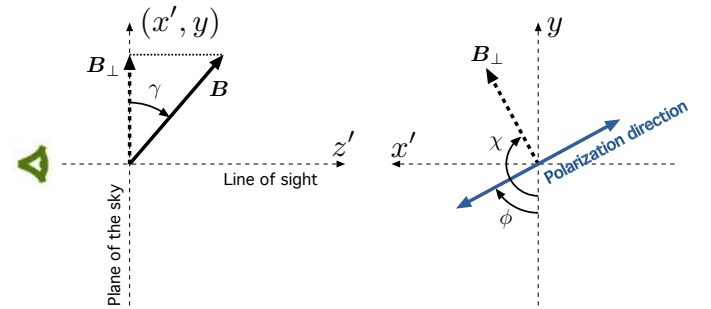


Fig. 14. Definition of angles. Here the line of sight is along the z' axis (see Fig. 13), γ is the angle the magnetic field \mathbf{B} makes with the plane of the sky, ϕ is the local polarization angle, and χ is the position angle of the plane of the sky projection \mathbf{B}_\perp , both in the HEALPix convention, so counted positively clockwise from the north-south direction, while the IAU convention is anti-clockwise (Planck Collaboration Int. XIX 2014).

Here p_0 is a polarization fraction parameter related to the intrinsic polarization fraction (see Eq. (8) and Appendix B), γ is the angle that the local magnetic field makes with the plane of the sky, and ϕ is the local polarization angle in the HEALPix convention. This angle differs by 90° from the angle χ of the plane of the sky projection of the magnetic field, as defined in Fig. 14, and should not be confused with the actual polarization angle ψ . These angles are equal ($\phi = \psi$) only for a uniform magnetic field along the line of sight.

Note that the corrective term in Eq. (5) is incorrectly written in Fiege & Pudritz (2000), Gonçalves et al. (2005), Pelkonen et al. (2009), and Padovani et al. (2012), with $p_0/2$ instead of p_0 .

The hypotheses made here, besides the absence of background radiation, are that $p_0 = 0.2$ is uniform, that the source function $S_\nu = B_\nu(T_d)$ is that of a blackbody with an assumed uniform dust temperature $T_d = 18 \text{ K}$, and that since we are working at 353 GHz the optical depth is simply given by $d\tau_\nu = \sigma_{353} n_{\text{H}} dz'$. We use the value $\sigma_{353} = 1.2 \times 10^{-26} \text{ cm}^2$ (see Sect. 2.1), and n_{H} is the total gas density in the simulation. Given the maximum gas column density in the simulation

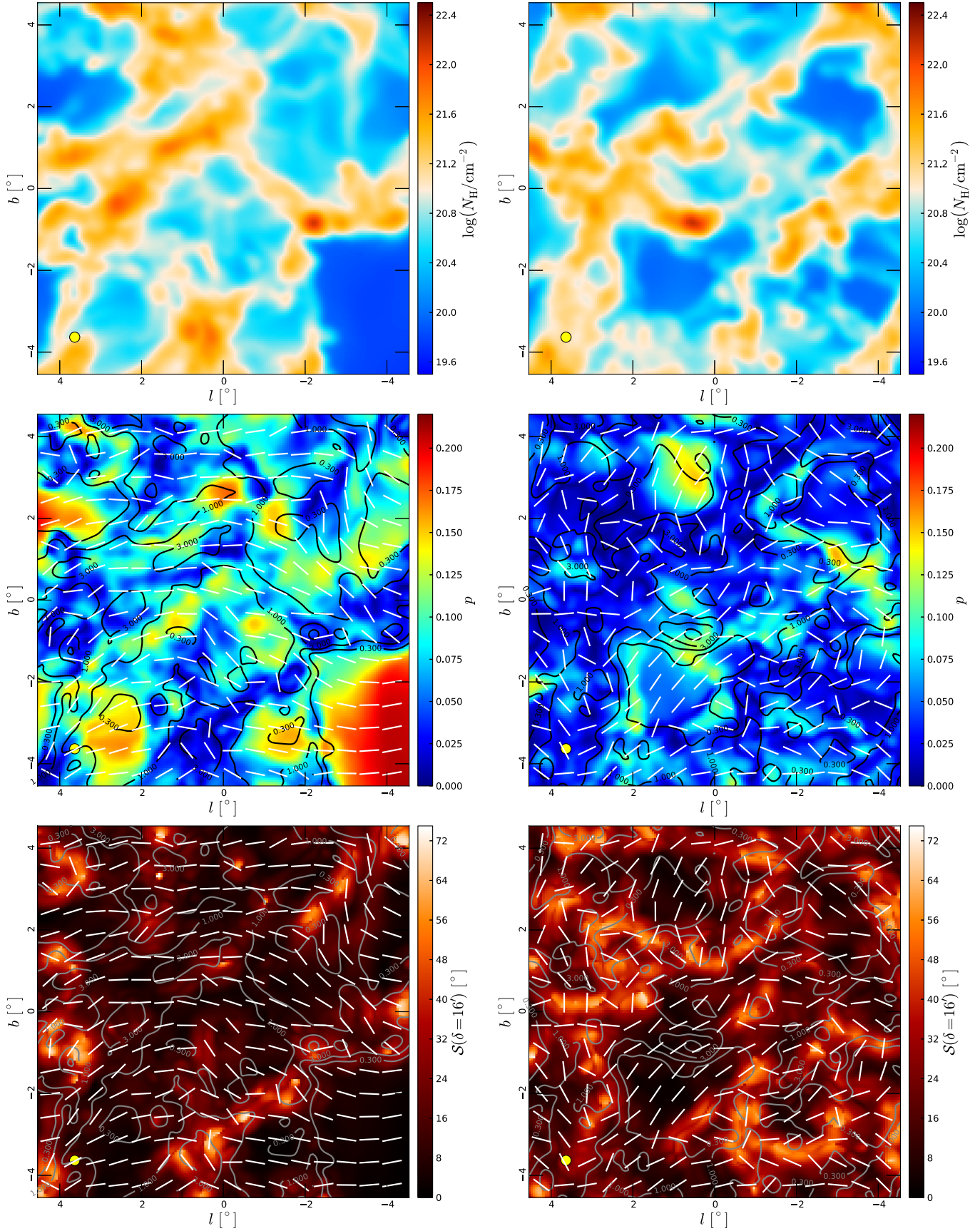


Fig. 15. Simulated *Planck* maps. *Top:* total gas column density. *Middle:* polarization fraction and angle, with contours being the column density at values indicated in units of 10^{21} cm^{-2} , and the bars indicate magnetic orientation. *Bottom:* angle dispersion function at lag $\delta = 16'$, with the same contours and bars as in the middle row. *Left:* viewing angle $\alpha = 0^\circ$. *Right:* viewing angle $\alpha = 90^\circ$. In each row, the same colour scale is used. In the lower left corner of each plot (yellow circle) is the 15' FWHM beam.

subset computed over all possible viewing angles α , $N_{\text{H,max}} = 1.6 \times 10^{22} \text{ cm}^{-2}$, the maximum optical depth at 353 GHz using this conversion factor is $\tau_{\text{max}} = 1.9 \times 10^{-4}$, so we may safely neglect optical depth effects and take $e^{-\tau_\nu} = 1$ in the I , Q , and U integrals. We are aware (Planck Collaboration XI 2014) that the opacity actually varies with N_{H} , but the variation is at most a factor of 3 from the value assumed here, so the optical depth is in any case much lower than unity. Moreover, the choice of the conversion factor has no impact on the simulated maps of polarization fractions and angles, provided that a constant value is assumed along each line of sight.

We note that the dense cores that exist in our simulated cube are only weakly shielded from the ambient UV radiation field. Indeed, the mean column density through the cube is about 10^{21} cm^{-2} (corresponding to $A_V \simeq 0.6$), which is comparable to the values in the simulation of Pelkonen et al. (2009), but over a much larger volume (18 pc box compared to less than 1 pc); the bulk of the gas is therefore more fragmented and radiation penetrates more easily (Levrier et al. 2012). That is why we take a uniform parameter p_0 .

The maps of Stokes parameters are placed at a distance of $D = 100$ pc and convolved with a circular $15'$ FWHM Gaussian beam (corresponding to a physical size 0.44 pc). The resulting field of view is a little less than 10° across, which is comparable to the selected *Planck* fields, and small enough that separate smoothing of Stokes I , Q , and U is not an issue (see Appendix A of Planck Collaboration Int. XIX 2014). Maps of polarization fractions and angles are then built from these convolved Stokes parameter maps using Eqs. (1), (2) for consistency with the *Planck* data. Let us stress that ψ is defined in the HEALPix convention, which means that it is counted positively clockwise from the north-south direction, and not in the IAU convention (anti-clockwise).

Figure 15 (middle row) shows the maps of polarization fraction p and magnetic orientation in these simulated observations, when integrating along the mean magnetic field ($\alpha = 90^\circ$), and perpendicular to it ($\alpha = 0^\circ$). The large-scale component of the magnetic field is clearly visible in several regions, for instance in the lower right corner of the $\alpha = 0^\circ$ case: it leads to long-range coherence in the polarization angle, which correlates with the highest polarization fractions and lowest column densities. Conversely, when integrating along the direction of the large-scale field ($\alpha = 90^\circ$, right column), p is on average much lower, and no such long-range ordering of χ is visible, although some local correlations are present. These effects are expected from the vectorial nature of the polarization: with the magnetic field more or less aligned with the line of sight, only its transverse fluctuations lead to a signal in polarization, and these fluctuations are isotropic in the plane of the sky, so they cancel out in the integration (along the line of sight and also through beam dilution). This correlation between p and spatial coherence of the polarization angle is discussed later on (Sect. 3.4).

Statistics of simulated maps of the polarization fraction (maximum, mean and standard deviation) are shown as a function of the viewing angle α in Fig. 16. We find the maximum polarization fraction to be $p_{\text{max}} \simeq 0.14\text{--}0.21$ (depending on the viewing angle α). On some lines of sight, in the most tenuous parts of the map integrated perpendicularly to the large-scale \mathbf{B} (e.g., in the lower right corner of the map in the $\alpha = 0^\circ$ case), p_{max} almost reaches the theoretical maximum value possible, which is the intrinsic polarization fraction,

$$p_i = \frac{p_0}{1 - \frac{p_0}{3}}, \quad (8)$$

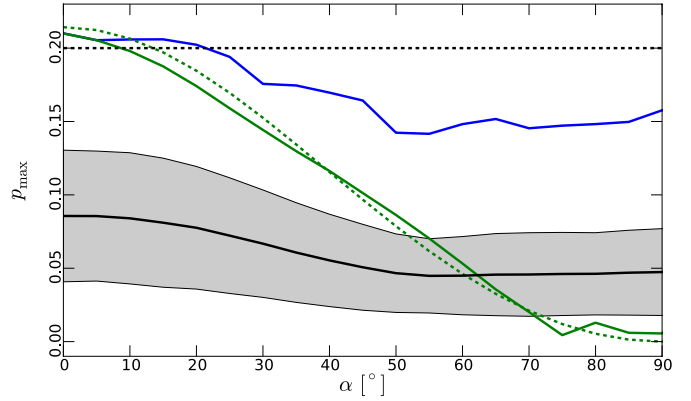


Fig. 16. Statistics of polarization fractions in the simulated *Planck* observations as a function of viewing angle α (see Fig. 13). The solid blue line shows p_{max} , the solid black line shows the mean p , and the solid green line shows the value of p for the most diffuse lines of sight in the map. The dashed black line marks the polarization fraction parameter p_0 and the dashed green line gives the theoretical polarization fraction in the case where the density and magnetic field are homogeneous and the latter makes an angle α with the plane of the sky (see text). The grey region shows the $\pm 1\sigma$ spread around the mean p .

obtained when the medium is homogeneous and the magnetic field is uniform and parallel to the plane of the sky ($\gamma = 0^\circ$). Figure 16 emphasizes the importance of the magnetic field geometry on the measured p_{max} , as that value varies by about 40% over the range of viewing angles.

3.3. Polarization fraction vs. column density

We show in Fig. 17 the joint distribution function of polarization fractions p and total gas column densities N_{H} in the simulated observations when integrating along both directions used in Fig. 15, and in the intermediate case $\alpha = 45^\circ$. The most striking feature of the plots in Fig. 17 is the different behaviour at low column densities $N_{\text{H}} < 10^{20} \text{ cm}^{-2}$. Along these lines of sight, the density is essentially uniform, with n_{H} of about 2 cm^{-3} , so the computed polarization is entirely due to magnetic field geometry; when we integrate with $\alpha = 0^\circ$ the mean magnetic field is almost in the plane of the sky, $\gamma \simeq 0^\circ$, and polarized emission is at its highest, while when we integrate with $\alpha = 90^\circ$, then the ordered field is almost along the line of sight, so $\gamma \simeq 90^\circ$ and no polarized emission appears. In fact, for each value of α , polarization fractions observed towards the most diffuse lines of sight are well reproduced by the formula for a homogeneous medium, easily derived from Eqs. (5)–(7),

$$p = \frac{p_0 \cos^2 \alpha}{1 - p_0 \left(\cos^2 \alpha - \frac{2}{3} \right)} \quad (9)$$

as can be seen in Fig. 16. We may therefore only derive the polarization fraction parameter p_0 from the maximum observed value p_{max} if the angle between the magnetic field and the plane of the sky is known, which is a strong assumption.

The second striking feature of Fig. 17 is the decrease of the maximum polarization fraction with increasing column density, as observed in the data. The same linear fit yields slopes $\Delta p_{\text{max}} / \Delta \log(N_{\text{H}} / \text{cm}^{-2})$ that span values from -0.025 (for $\alpha = 80^\circ$) to -0.15 (for $\alpha = -15^\circ$), the latter being comparable to those found in the data for the selected fields.

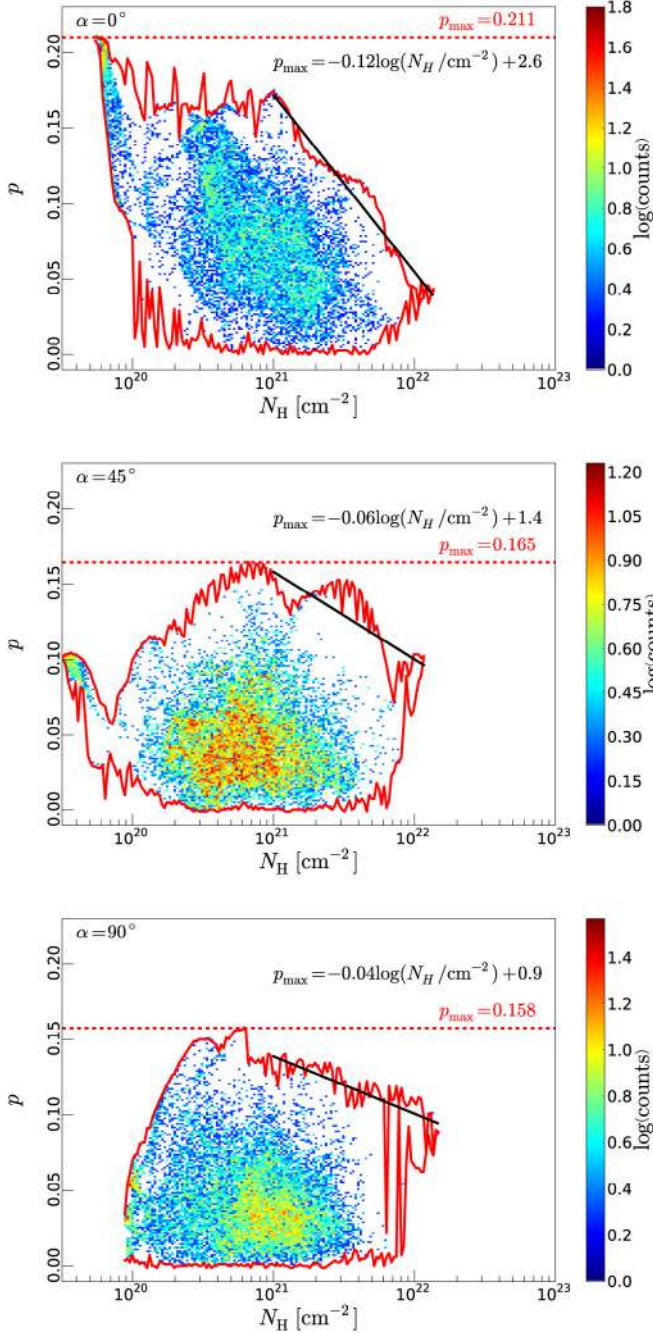


Fig. 17. Two-dimensional distribution functions of polarization fractions and logarithmic column densities in the simulated *Planck* observations. *Top*: viewing angle $\alpha = 0^\circ$. *Middle*: viewing angle $\alpha = 45^\circ$. *Bottom*: viewing angle $\alpha = 90^\circ$. The dashed red horizontal lines and the solid red and black lines are the same as in Fig. 4. The fits to the upper envelopes are performed for $N_H > 10^{21} \text{ cm}^{-2}$.

For a global comparison between simulations and observations, we show in Fig. 18 the distribution of p and N_H for all the simulated fields, with their upper and lower envelopes, together with the envelope for the selected sky fields. Linear fits to the distributions' upper envelopes are performed, restricted to a common range of column densities $2 \times 10^{21} \text{ cm}^{-2} < N_H < 2 \times 10^{22} \text{ cm}^{-2}$. They yield similar values in terms of both slopes ($m = -0.109$ for simulations, compared to $m = -0.113$ for the selected fields) and intercepts ($c = 2.52$ for simulations, compared to $c = 2.59$ for the selected fields). Note that the “ripple”

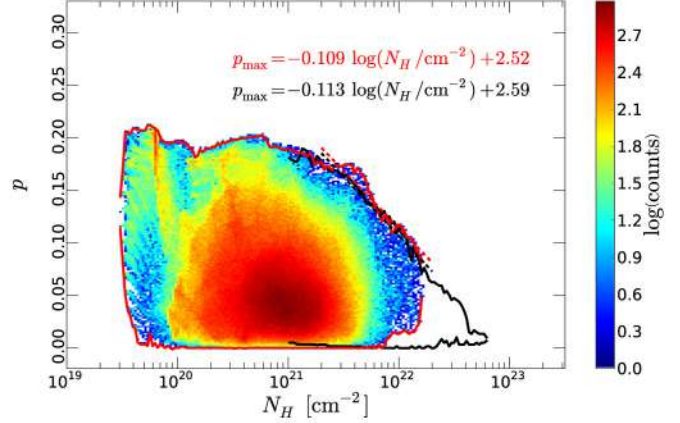


Fig. 18. Comparison between the distributions of the polarization fractions p and logarithmic column densities in the simulations (colour scale, all viewing angles combined, with upper and lower envelopes in solid red lines) and those of the observations in the selected fields (solid black lines). Note that the latter are restricted to $N_H > 10^{21} \text{ cm}^{-2}$. Dashed lines are linear fits of the form $p_{\max} = m \log(N_H / \text{cm}^{-2}) + c$ on the distributions' upper envelopes, restricted to a common range of column densities $2 \times 10^{21} \text{ cm}^{-2} < N_H < 2 \times 10^{22} \text{ cm}^{-2}$.

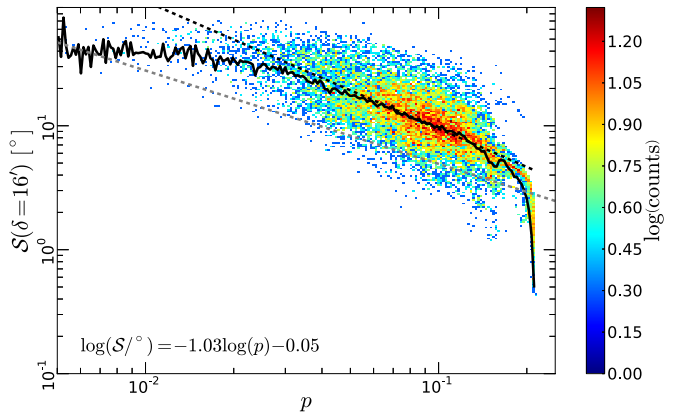


Fig. 19. Two-dimensional distribution function of $\log(p)$ and $\log(S)$ in the simulated observations for $\delta = 16'$ and $\alpha = 0^\circ$. The solid black curve represents the evolution of the mean $\log(S)$ per bin of $\log(p)$. A linear fit $\log(S) = m' \log(p) + c'$ is performed, restricted to bins in $\log(p)$ that contain at least 1% of the total number of points. This fit is shown as the dashed black line. The dashed grey line is the large-scale fit presented in Sect. 2.5.

pattern in the density plot at low N_H is due to the sampling in viewing angles α , and is a signature of the decrease of p with viewing angle for the most diffuse lines of sight, as already noted in Fig. 16.

3.4. Polarization angle coherence vs. polarization fraction

The angle dispersion function S is computed from the simulated ψ maps, using a lag $\delta = 16'$, as we did for the data. We first note that the mean angle dispersion function is larger when the large-scale magnetic field is oriented along the line of sight, with $\langle S \rangle \simeq 12^\circ$ for $\alpha = 0^\circ$ and $\langle S \rangle \simeq 20^\circ$ for $\alpha = 90^\circ$, a result that is consistent with the findings of Falceta-Gonçalves et al. (2008). Maps of S (for the $\alpha = 0^\circ$ and $\alpha = 90^\circ$ cases) can be

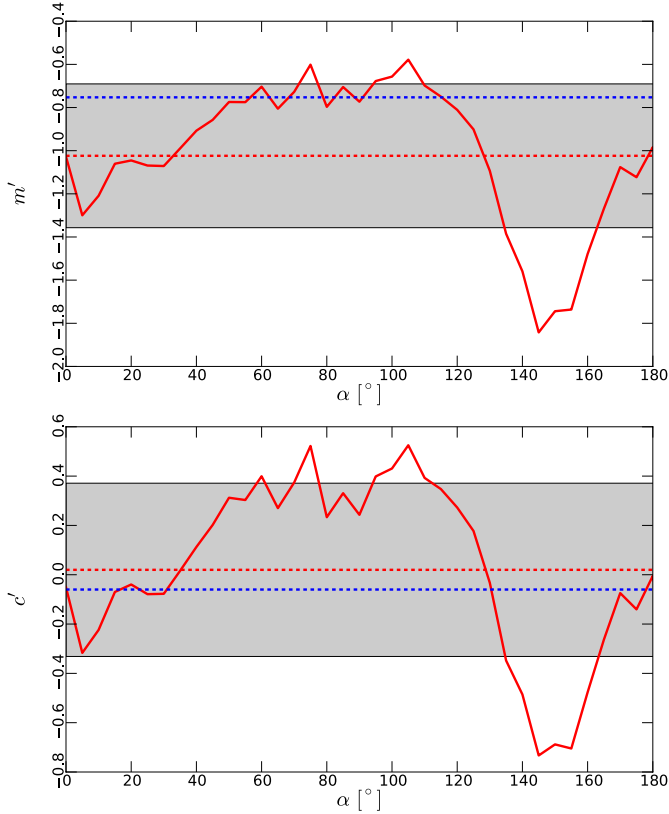


Fig. 20. Slopes m' (top) and intercepts c' (bottom) of the linear fits $\log(S) = m' \log(p) + c'$ to the distribution of $\log(p)$ and $\log(S)$ in the simulated observations, as a function of viewing angle α . The lag is $\delta = 16'$. The dashed blue lines indicate the values for the large-scale fit presented in Sect. 2.5, the dashed red lines represent the average slope and intercept over the range of α , and the grey areas indicate $\pm 1\sigma$ around the mean, with the standard deviation σ computed statistically over all angles.

seen in the lower row panels of Fig. 15, exhibiting filamentary patterns similar to those found in observations. These filaments of high S also correspond to regions where the polarization angle rotates on small scales, and are correlated with regions of low polarization fraction p (compare with the middle row panels of Fig. 15). This anti-correlation is clearly seen in distribution functions of $\log(p)$ and $\log(S)$, as shown in Fig. 19 for the $\alpha = 0^\circ$ case. A linear fit $\log(S) = m' \log(p) + c'$ to the mean $\log(S)$ per bin of $\log(p)$ is performed, restricted to bins which contain at least 1% of the total number of points and limited to $p < p_0$ to avoid the most diffuse lines of sight. The slope and intercept of the anti-correlation observed in the data are fairly well reproduced ($m' = -1.0 \pm 0.3$ and $c' = 0.02 \pm 0.34$ over the range of α , compared to $m' = -0.75$ and $c' = -0.06$ in observations) with steeper slopes for viewing angles $\alpha \approx 0^\circ$ and shallower slopes for viewing angles $\alpha \approx 90^\circ$ (see Fig. 20). However, since the slopes in simulations are generally steeper than what is observed, but with very similar intercepts at $p = 1$, the angle dispersion function S in simulations is globally higher than in observations for a given polarization fraction.

This result suggests that, in the simulations, the angle dispersion function is too large for a given polarization fraction, i.e., that the magnetic field is too tangled. Since the physical processes one can think of to reduce the field's tangling (e.g., larger field intensity with respect to turbulence or partial ion-neutral decoupling) would also affect p , we propose that this difference

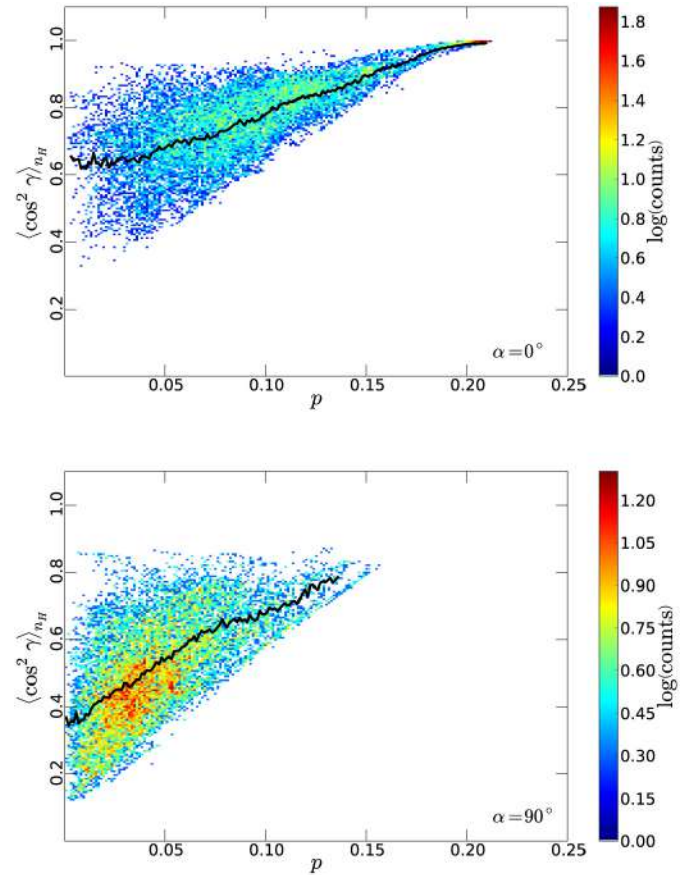


Fig. 21. Distribution functions of polarization fraction p and density-weighted mean of $\cos^2 \gamma$ (γ is the angle of the magnetic field with respect to the plane of the sky, see Fig. 14) along the line of sight z' in the simulation cube. *Top:* viewing angle $\alpha = 0^\circ$. *Bottom:* viewing angle $\alpha = 90^\circ$. The solid black lines show the mean values per bin of p .

comes from the lack of power in the low frequency modes of the simulated turbulence, as illustrated by the fact that the power spectra of the velocity and magnetic field components flatten out at small wavenumber k . In reality, molecular clouds are organized in a self-similar structure over a broad range of scales and that is therefore not properly reproduced in the simulations we used. In short, the large-scale fluctuations of the magnetic field are closer to random in simulations than in reality.

3.5. Statistics on the magnetic field fluctuations in the simulations

We investigate here the possible causes of the variations in the polarization fraction p and the dispersion of the polarization angle S in the simulations, i.e., what are the respective roles of the field tangling and the orientation of the large-scale field in the variations of p and S . To quantify these roles, we compute the average and dispersion along the line of sight of both $\cos^2 \gamma$ and $\sin \chi$ (see Fig. 14 for the definition of angles). These quantities are computed for different viewing angles. In the following, we write the magnetic field as $\mathbf{B} = \mathbf{B}_0 + \Delta\mathbf{B}$, where \mathbf{B}_0 is the large-scale ordered field and $\Delta\mathbf{B}$ is the fluctuating part of \mathbf{B} .

The role of the average values of the angles γ and χ along the line of sight is illustrated in Figs. 21 and 22. First, the role of the large-scale field \mathbf{B}_0 is clear: the largest values of p are obtained

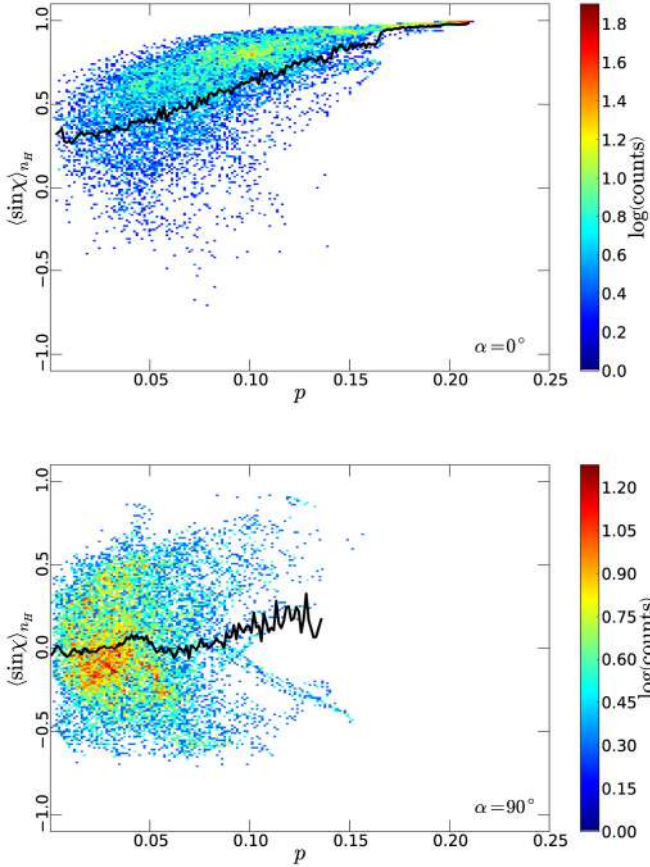


Fig. 22. Distribution functions of polarization fraction p and density-weighted mean of $\sin \chi$ (χ is the position angle of the projection of the magnetic field in the plane of the sky, see Fig. 14) along the line of sight z' in the simulation cube. *Top*: viewing angle $\alpha = 0^\circ$. *Bottom*: viewing angle $\alpha = 90^\circ$. The solid black lines show the mean values per bin of p .

when \mathbf{B}_0 is viewed in the plane of the sky ($\alpha \simeq 0^\circ$). The largest p values are obtained when the average of $\cos^2 \gamma$ along the line of sight stays close to unity. In that case, the field perturbations are such that they keep the field close to the plane of the sky, on average, hence the large p . The same effect is visible in the top panel of Fig. 22 where the largest polarization fractions are obtained for average values of χ close to 90° .

However, even in this configuration ($\alpha = 0^\circ$), small values of p are obtained. The fraction of low p values is clearly larger when the large-scale field is viewed along the line of sight ($\alpha = 90^\circ$). The remarkable feature visible in Fig. 21 (bottom panel) is the proportionality of p_{\max} with the average of $\cos^2 \gamma$: the smaller this average, the closer γ is to 90° , therefore the closer the field is aligned with the line of sight, and the smaller the resulting value of p_{\max} . One also sees in Fig. 21 that $\langle \cos^2 \gamma \rangle$ reaches much smaller values when \mathbf{B}_0 is along the line of sight (bottom panel), producing lower values of p than in the case where \mathbf{B}_0 is in the plane of the sky (top panel).

We note, interestingly, that the same effect is not visible in Fig. 22, which displays the line of sight average of $\sin \chi$ versus p : there is no such upper value of p that would scale with the average of $\sin \chi$ because this fluctuation of the field direction is measured in the plane of the sky and does not affect the maximal polarization fraction that can be obtained. Instead, when \mathbf{B}_0 is along the line of sight for instance, the scatter of $\langle \sin \chi \rangle$ along

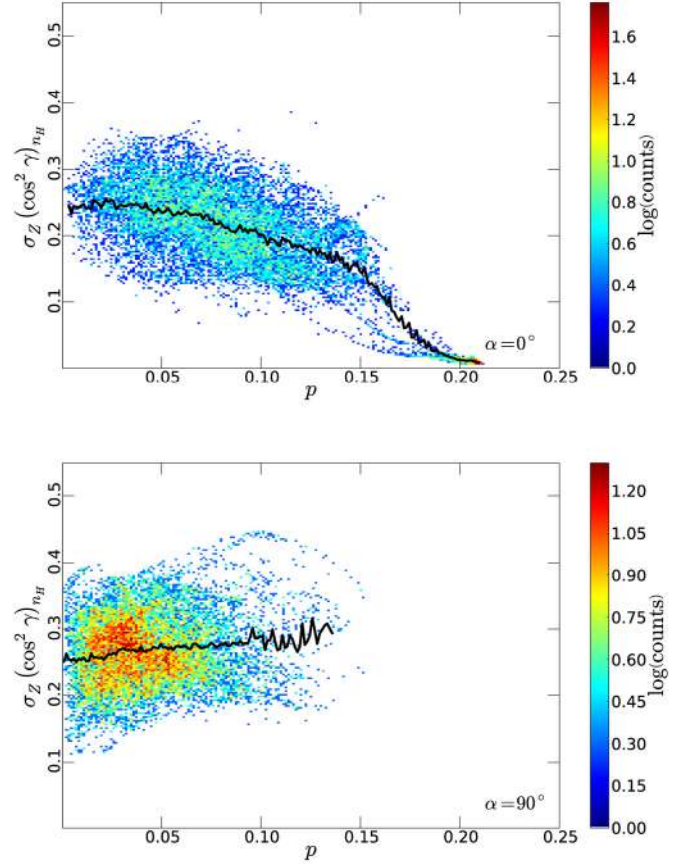


Fig. 23. Distribution functions of polarization fraction p and density-weighted standard deviation of $\cos^2 \gamma$ along the line of sight z' in the simulation cube. *Top*: viewing angle $\alpha = 0^\circ$. *Bottom*: viewing angle $\alpha = 90^\circ$. The solid black lines show the mean values per bin of p .

the line of sight is the largest and the resulting values of p are low.

Figure 23 also illustrates the effect of the field tangling: the larger the dispersion of $\cos^2 \gamma$ along the line of sight (and the larger the scatter of this dispersion), the smaller p is. Obviously, when the line of sight is dominated by the large-scale field, the scatter is the lowest.

Figure 24 shows the joint distribution of the average of $\cos^2 \gamma$ and \mathcal{S} , where one recognizes the role of the large-scale field when $\alpha = 0^\circ$: the lowest values of \mathcal{S} are obtained when γ stays close to 0° , meaning that the field is more or less in the plane of the sky. Clearly, the largest values of \mathcal{S} are obtained when the influence of the large-scale field is minimized ($\alpha = 90^\circ$, bottom panel).

4. Conclusions

To summarize, the maximum polarization fraction p_{\max} observed towards the sample of nearby fields selected in this study is reached in the most diffuse fields. The large-scale decrease of p_{\max} with increasing N_{H} is seen in the individual fields considered here, as soon as $N_{\text{H}} > 10^{21} \text{ cm}^{-2}$. This trend is fairly well reproduced by numerical simulations of anisotropic MHD turbulence, even assuming uniform dust temperatures and grain alignment efficiencies in the gas weakly shielded from the UV radiation. The polarization of thermal dust emission observed by *Planck* towards these regions is essentially related to

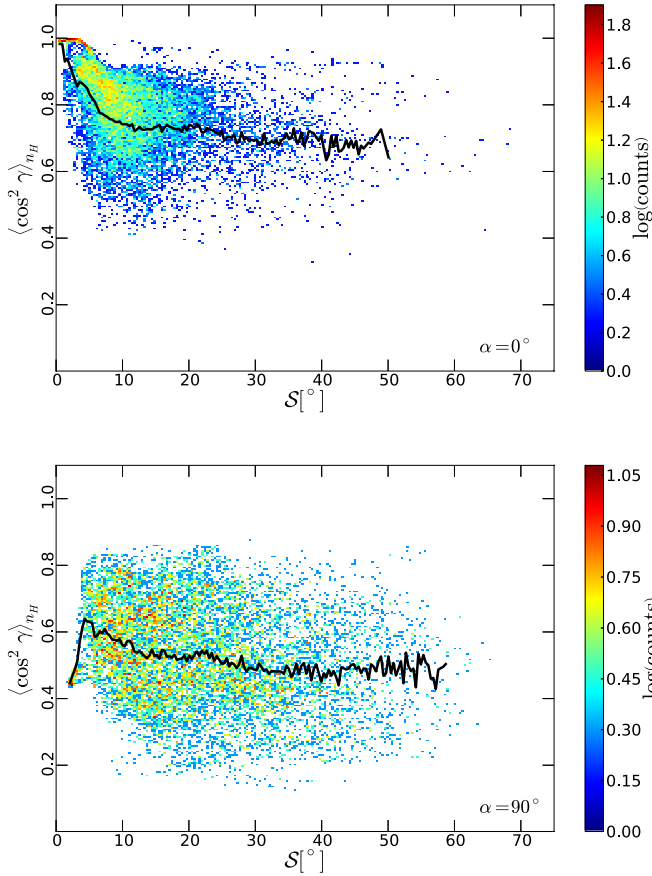


Fig. 24. Distribution functions of angle dispersion function S ($\delta = 16^\circ$) and density-weighted mean of $\cos^2 \gamma$ in the simulation cube. *Top:* viewing angle $\alpha = 0^\circ$. *Bottom:* viewing angle $\alpha = 90^\circ$. The solid black lines show the mean values per bin of S .

the geometry of the magnetic field and in particular to its orientation at large scales with respect to the line of sight. We do not discuss the evolution of polarization fractions at large column densities $N_H > 3 \times 10^{22} \text{ cm}^{-2}$, for which the MHD simulation considered is not suitable. It is clear, however, that additional processes must be at work to achieve the change of slope in the p_{max} vs. $\log(N_H/\text{cm}^{-2})$ relation observed towards the most opaque lines of sight. This change is probably related to variations in the properties of dust alignment, as pointed out by Soler et al. (2013). We also find that polarization fractions observed by *Planck* towards these nearby regions correlate well with the local coherence of the polarization angle, which is measured using the angle dispersion function S . This correlation is also found in simulations, with slopes that are very close to observational values. In simulations, however, values of S for a given polarization fraction are globally too high compared to observations, which points to a possible limitation of the specific MHD simulation used.

Acknowledgements. The development of *Planck* has been supported by: ESA; CNES and CNRS/INSU-IN2P3-INP (France); ASI, CNR, and INAF (Italy); NASA and DoE (USA); STFC and UKSA (UK); CSIC, MICINN, JA and RES (Spain); Tekes, AoF and CSC (Finland); DLR and MPG (Germany); CSA (Canada); DTU Space (Denmark); SER/SSO (Switzerland); RCN (Norway); SFI (Ireland); FCT/MCTES (Portugal); and PRACE (EU). A description of the *Planck* Collaboration and a list of its members, including

the technical or scientific activities in which they have been involved, can be found at http://www.sciops.esa.int/index.php?project=planck&page=Planck_Collaboration. Some of the results in this paper have been derived using the HEALPix package. The authors would like to thank Charles Beichman for his careful reading of the manuscript and useful comments. The research leading to these results has received funding from the European Research Council under the European Union's Seventh Framework Programme (FP7/2007-2013) / ERC grant agreement No. 267934.

References

- Alves, F. O., Franco, G. A. P., & Girart, J. M. 2008, *A&A*, 486, L13
 Andersson, B.-G. 2012, *Magnetic Fields in Diffuse Media*, submitted [[arXiv:1208.4393](https://arxiv.org/abs/1208.4393)]
 Bally, J. 2008, *Overview of the Orion Complex*, ed. B. Reipurth (ASP), 459
 Chandrasekhar, S., & Fermi, E. 1953, *ApJ*, 118, 113
 Chapman, N. L., Goldsmith, P. F., Pineda, J. L., et al. 2011, *ApJ*, 741, 21
 Crutcher, R. M., Wandelt, B., Heiles, C., Falgarone, E., & Troland, T. H. 2010, *ApJ*, 725, 466
 de Zeeuw, P. T., Hoogerwerf, R., de Bruijne, J. H. J., Brown, A. G. A., & Blaauw, A. 1999, *AJ*, 117, 354
 Draine, B. T. 2011, *Physics of the Interstellar and Intergalactic Medium* (Princeton University Press)
 Draine, B. T., & Fraisse, A. A. 2009, *ApJ*, 696, 1
 Elias, J. H. 1978, *ApJ*, 224, 857
 Falceta-Gonçalves, D., Lazarian, A., & Kowal, G. 2008, *ApJ*, 679, 537
 Fiege, J. D., & Pudritz, R. E. 2000, *ApJ*, 544, 830
 Fromang, S., Hennebelle, P., & Teyssier, R. 2006, *A&A*, 457, 371
 Gonçalves, J., Galli, D., & Walmsley, M. 2005, *A&A*, 430, 979
 Górski, K. M., Hivon, E., Banday, A. J., et al. 2005, *ApJ*, 622, 759
 Hatano, H., Nishiyama, S., Kurita, M., et al. 2013, *AJ*, 145, 105
 Hennebelle, P., & Audit, E. 2007, *A&A*, 465, 431
 Hennebelle, P., Banerjee, R., Vázquez-Semadeni, E., Klessen, R. S., & Audit, E. 2008, *A&A*, 486, L43
 Hildebrand, R. H., Kirby, L., Dotson, J. L., Houde, M., & Vaillancourt, J. E. 2009, *ApJ*, 696, 567
 Hoang, T., & Lazarian, A. 2008, *MNRAS*, 388, 117
 Lamarre, J., Puget, J., Ade, P. A. R., et al. 2010, *A&A*, 520, A9
 Lazarian, A., Goodman, A. A., & Myers, P. C. 1997, *ApJ*, 490, 273
 Lee, H. M., & Draine, B. T. 1985, *ApJ*, 290, 211
 Levrier, F., Le Petit, F., Hennebelle, P., et al. 2012, *A&A*, 544, A22
 Loren, R. B. 1989, *ApJ*, 338, 902
 Luhman, K. L. 2008, *Chamaeleon*, ed. B. Reipurth (ASP), 169
 Marchwinski, R. C., Pavel, M. D., & Clemens, D. P. 2012, *ApJ*, 755, 130
 Martin, P. G. 1972, *MNRAS*, 159, 179
 Martin, P. G. 1974, *ApJ*, 187, 461
 Martin, P. G. 1975, *ApJ*, 202, 393
 Montier, L., Plaszczynski, S., Levrier, F., et al. 2014a, *A&A*, submitted
 Montier, L., Plaszczynski, S., Levrier, F., et al. 2014b, *A&A*, submitted
 Ostriker, E. C., Stone, J. M., & Gammie, C. F. 2001, *ApJ*, 546, 980
 Padovani, M., Brinch, C., Girart, J. M., et al. 2012, *A&A*, 543, A16
 Palla, F., & Stahler, S. W. 2002, *ApJ*, 581, 1194
 Pelkonen, V.-M., Juvela, M., & Padoan, P. 2009, *A&A*, 502, 833
 Pereyra, A., & Magalhães, A. M. 2007, *ApJ*, 662, 1014
 Planck Collaboration I. 2011, *A&A*, 536, A1
 Planck Collaboration I. 2014, *A&A*, 571, A1
 Planck Collaboration VI. 2014, *A&A*, 571, A6
 Planck Collaboration VII. 2014, *A&A*, 571, A7
 Planck Collaboration VIII. 2014, *A&A*, 571, A8
 Planck Collaboration IX. 2014, *A&A*, 571, A9
 Planck Collaboration X. 2014, *A&A*, 571, A10
 Planck Collaboration XI. 2014, *A&A*, 571, A11
 Planck Collaboration XVI. 2014, *A&A*, 571, A16
 Planck Collaboration Int. XIII. 2014, 561, A97
 Planck Collaboration Int. XIX. 2014, *A&A*, submitted [[arXiv:1405.0871](https://arxiv.org/abs/1405.0871)]
 Planck Collaboration Int. XXI. 2014, *A&A*, submitted [[arXiv:1405.0873](https://arxiv.org/abs/1405.0873)]
 Planck Collaboration Int. XXII. 2014, *A&A*, submitted [[arXiv:1405.0874](https://arxiv.org/abs/1405.0874)]
 Plaszczynski, S., Montier, L., Levrier, F., & Tristram, M. 2014, *MNRAS*, 439, 4048
 Soler, J. D., Hennebelle, P., Martin, P. G., et al. 2013, *ApJ*, 774, 128
 Tauber, J. A., Mandolesi, N., Puget, J., et al. 2010, *A&A*, 520, A1
 Teyssier, R. 2002, *A&A*, 385, 337
 Ungerechts, H., & Thaddeus, P. 1987, *ApJS*, 63, 645
 Wardle, M., & König, A. 1990, *ApJ*, 362, 120
 Whittet, D. C. B., Prusti, T., Franco, G. A. P., et al. 1997, *A&A*, 327, 1194
 Whittet, D. C. B., Hough, J. H., Lazarian, A., & Hoang, T. 2008, *ApJ*, 674, 304

- Wilking, B. A., Gagné, M., & Allen, L. E. 2008, *Star Formation in the ρ Ophiuchi Molecular Cloud*, ed. B. Reipurth (ASP), 351
- Zagury, F., Boulanger, F., & Banchet, V. 1999, *A&A*, 352, 645
-
- ¹ APC, AstroParticule et Cosmologie, Université Paris Diderot, CNRS/IN2P3, CEA/Irfu, Observatoire de Paris, Sorbonne Paris Cité, 10 rue Alice Domon et Léonie Duquet, 75205 Paris Cedex 13, France
 - ² African Institute for Mathematical Sciences, 6-8 Melrose Road, 7945 Muizenberg, Cape Town, South Africa
 - ³ Agenzia Spaziale Italiana Science Data Center, via del Politecnico snc, 00133 Roma, Italy
 - ⁴ Agenzia Spaziale Italiana, Viale Liegi 26, 00198 Roma, Italy
 - ⁵ Astrophysics Group, Cavendish Laboratory, University of Cambridge, J J Thomson Avenue, Cambridge CB3 0HE, UK
 - ⁶ Astrophysics & Cosmology Research Unit, School of Mathematics, Statistics & Computer Science, University of KwaZulu-Natal, Westville Campus, Private Bag X54001, 4000 Durban, South Africa
 - ⁷ Atacama Large Millimeter/submillimeter Array, ALMA Santiago Central Offices, Alonso de Cordova 3107, Vitacura, Casilla 763 0355 Santiago, Chile
 - ⁸ CITA, University of Toronto, 60 St. George St., Toronto, ON M5S 3H8, Canada
 - ⁹ CNRS, IRAP, 9 Av. colonel Roche, BP 44346, 31028 Toulouse Cedex 4, France
 - ¹⁰ California Institute of Technology, Pasadena, California, USA
 - ¹¹ Centro de Estudios de Física del Cosmos de Aragón (CEFCA), Plaza San Juan, 1, planta 2, 44001 Teruel, Spain
 - ¹² Computational Cosmology Center, Lawrence Berkeley National Laboratory, Berkeley, California, USA
 - ¹³ DSM/Irfu/SPP, CEA-Saclay, 91191 Gif-sur-Yvette Cedex, France
 - ¹⁴ DTU Space, National Space Institute, Technical University of Denmark, Elektrovej 327, 2800 Kgs. Lyngby, Denmark
 - ¹⁵ Département de Physique Théorique, Université de Genève, 24 quai E. Ansermet, 1211 Genève 4, Switzerland
 - ¹⁶ Departamento de Física Fundamental, Facultad de Ciencias, Universidad de Salamanca, 37008 Salamanca, Spain
 - ¹⁷ Departamento de Física, Universidad de Oviedo, Avda. Calvo Sotelo s/n, 33007 Oviedo, Spain
 - ¹⁸ Department of Astronomy and Astrophysics, University of Toronto, 50 Saint George Street, Toronto, Ontario, Canada
 - ¹⁹ Department of Astrophysics/IMAPP, Radboud University Nijmegen, PO Box 9010, 6500 GL Nijmegen, The Netherlands
 - ²⁰ Department of Physics & Astronomy, University of British Columbia, 6224 Agricultural Road, Vancouver, British Columbia, Canada
 - ²¹ Department of Physics and Astronomy, Dana and David Dornsife College of Letter, Arts and Sciences, University of Southern California, Los Angeles, CA 90089, USA
 - ²² Department of Physics and Astronomy, University College London, London WC1E 6BT, UK
 - ²³ Department of Physics, Florida State University, Keen Physics Building, 77 Chieftan Way, Tallahassee, Florida, USA
 - ²⁴ Department of Physics, Gustaf Hällströmin katu 2a, University of Helsinki, 00014 Helsinki, Finland
 - ²⁵ Department of Physics, Princeton University, Princeton, New Jersey, USA
 - ²⁶ Department of Physics, University of California, Santa Barbara, California, USA
 - ²⁷ Department of Physics, University of Illinois at Urbana-Champaign, 1110 West Green Street, Urbana, Illinois, USA
 - ²⁸ Dipartimento di Fisica e Astronomia G. Galilei, Università degli Studi di Padova, via Marzolo 8, 35131 Padova, Italy
 - ²⁹ Dipartimento di Fisica e Scienze della Terra, Università di Ferrara, via Saragat 1, 44122 Ferrara, Italy
 - ³⁰ Dipartimento di Fisica, Università La Sapienza, P.le A. Moro 2, 00185 Roma, Italy
 - ³¹ Dipartimento di Fisica, Università degli Studi di Milano, via Celoria, 16, 20133 Milano, Italy
 - ³² Dipartimento di Fisica, Università degli Studi di Trieste, via A. Valerio 2, 34 127 Trieste, Italy
 - ³³ Dipartimento di Fisica, Università di Roma Tor Vergata, via della Ricerca Scientifica, 1, 00133 Roma, Italy
 - ³⁴ Discovery Center, Niels Bohr Institute, Blegdamsvej 17, 2100 Copenhagen, Denmark
 - ³⁵ European Southern Observatory, ESO Vitacura, Alonso de Cordova 3107, Vitacura, Casilla 19001 Santiago, Chile
 - ³⁶ European Space Agency, ESAC, Planck Science Office, Camino bajo del Castillo, s/n, Urbanización Villafranca del Castillo, 28691 Villanueva de la Cañada, Madrid, Spain
 - ³⁷ European Space Agency, ESTEC, Keplerlaan 1, 2201 AZ Noordwijk, The Netherlands
 - ³⁸ Helsinki Institute of Physics, Gustaf Hällströmin katu 2, University of Helsinki, 00014 Helsinki, Finland
 - ³⁹ INAF – Osservatorio Astrofisico di Catania, via S. Sofia 78, 95123 Catania, Italy
 - ⁴⁰ INAF – Osservatorio Astronomico di Padova, Vicolo dell’Osservatorio 5, 35122 Padova, Italy
 - ⁴¹ INAF – Osservatorio Astronomico di Roma, via di Frascati 33, 00040 Monte Porzio Catone, Italy
 - ⁴² INAF – Osservatorio Astronomico di Trieste, via G.B. Tiepolo 11, 34143 Trieste, Italy
 - ⁴³ INAF/IASF Bologna, via Gobetti 101, 40129 Bologna, Italy
 - ⁴⁴ INAF/IASF Milano, via E. Bassini 15, 20133 Milano, Italy
 - ⁴⁵ INFN, Sezione di Bologna, via Irnerio 46, 40126 Bologna, Italy
 - ⁴⁶ INFN, Sezione di Roma 1, Università di Roma Sapienza, P.le Aldo Moro 2, 00185, Roma, Italy
 - ⁴⁷ INFN/National Institute for Nuclear Physics, via Valerio 2, 34127 Trieste, Italy
 - ⁴⁸ Imperial College London, Astrophysics group, Blackett Laboratory, Prince Consort Road, London, SW7 2AZ, UK
 - ⁴⁹ Infrared Processing and Analysis Center, California Institute of Technology, Pasadena, CA 91125, USA
 - ⁵⁰ Institut d’Astrophysique Spatiale, CNRS (UMR 8617), Université Paris-Sud 11, Bâtiment 121, 91405 Orsay, France
 - ⁵¹ Institut d’Astrophysique de Paris, CNRS (UMR 7095), 98bis boulevard Arago, 75014 Paris, France
 - ⁵² Institute for Space Sciences, 077125 Bucharest-Magurale, Romania
 - ⁵³ Institute of Astronomy, University of Cambridge, Madingley Road, Cambridge CB3 0HA, UK
 - ⁵⁴ Institute of Theoretical Astrophysics, University of Oslo, Blindern, 0315 Oslo, Norway
 - ⁵⁵ Instituto de Física de Cantabria (CSIC-Universidad de Cantabria), Avda. de los Castros s/n, Santander, Spain
 - ⁵⁶ Jet Propulsion Laboratory, California Institute of Technology, 4800 Oak Grove Drive, Pasadena, California, USA
 - ⁵⁷ Jodrell Bank Centre for Astrophysics, Alan Turing Building, School of Physics and Astronomy, The University of Manchester, Oxford Road, Manchester, M13 9PL, UK
 - ⁵⁸ Kavli Institute for Cosmology Cambridge, Madingley Road, Cambridge, CB3 0HA, UK
 - ⁵⁹ LAL, Université Paris-Sud, CNRS/IN2P3, 91898 Orsay, France
 - ⁶⁰ LERMA, CNRS, Observatoire de Paris, 61 avenue de l’Observatoire, 75014 Paris, France
 - ⁶¹ Laboratoire AIM, IRFU/Service d’Astrophysique – CEA/DSM – CNRS – Université Paris Diderot, Bât. 709, CEA-Saclay, 91191 Gif-sur-Yvette Cedex, France
 - ⁶² Laboratoire Traitement et Communication de l’Information, CNRS (UMR 5141) and Télécom ParisTech, 46 rue Barrault, 75634 Paris Cedex 13, France
 - ⁶³ Laboratoire de Physique Subatomique et de Cosmologie, Université Joseph Fourier Grenoble I, CNRS/IN2P3, Institut National Polytechnique de Grenoble, 53 rue des Martyrs, 38026 Grenoble Cedex, France

- ⁶⁴ Laboratoire de Physique Théorique, Université Paris-Sud 11 & CNRS, Bâtiment 210, 91405 Orsay, France
- ⁶⁵ Lawrence Berkeley National Laboratory, Berkeley, California, USA
- ⁶⁶ Max-Planck-Institut für Astrophysik, Karl-Schwarzschild-Str. 1, 85741 Garching, Germany
- ⁶⁷ National University of Ireland, Department of Experimental Physics, Maynooth, Co. Kildare, Ireland
- ⁶⁸ Niels Bohr Institute, Blegdamsvej 17, 2100 Copenhagen, Denmark
- ⁶⁹ Observational Cosmology, Mail Stop 367-17, California Institute of Technology, Pasadena, CA 91125, USA
- ⁷⁰ SISSA, Astrophysics Sector, via Bonomea 265, 34136 Trieste, Italy
- ⁷¹ School of Physics and Astronomy, Cardiff University, Queens Buildings, The Parade, Cardiff, CF24 3AA, UK
- ⁷² Space Sciences Laboratory, University of California, Berkeley, California, USA
- ⁷³ Special Astrophysical Observatory, Russian Academy of Sciences, Nizhnij Arkhyz, Zelenchukskiy region, Karachai-Cherkessian Republic, 369167, Russia
- ⁷⁴ Sub-Department of Astrophysics, University of Oxford, Keble Road, Oxford OX1 3RH, UK
- ⁷⁵ UPMC Univ Paris 06, UMR 7095, 98bis boulevard Arago, 75014, Paris, France
- ⁷⁶ Université de Toulouse, UPS-OMP, IRAP, 31028 Toulouse Cedex 4, France
- ⁷⁷ University of Granada, Departamento de Física Teórica y del Cosmos, Facultad de Ciencias, 18071 Granada, Spain
- ⁷⁸ University of Granada, Instituto Carlos I de Física Teórica y Computacional, 18071 Granada, Spain
- ⁷⁹ Warsaw University Observatory, Aleje Ujazdowskie 4, 00-478 Warszawa, Poland

Appendix A: Additional figures

In the main body of the paper, we showed maps and plots for the Chamaeleon-Musca and Ophiuchus fields. In this appendix we show similar figures for the remaining eight fields, in the same order as in Tables 1 and 2. We first show maps similar to Fig. 3 (Figs. A.1 to A.8), then distribution functions of p and N_H similar to Fig. 4 (Figs. A.9 to A.16), and finally distribution functions of S ($\delta = 16'$) and p similar to Fig. 7 (Figs. A.17 to A.24).

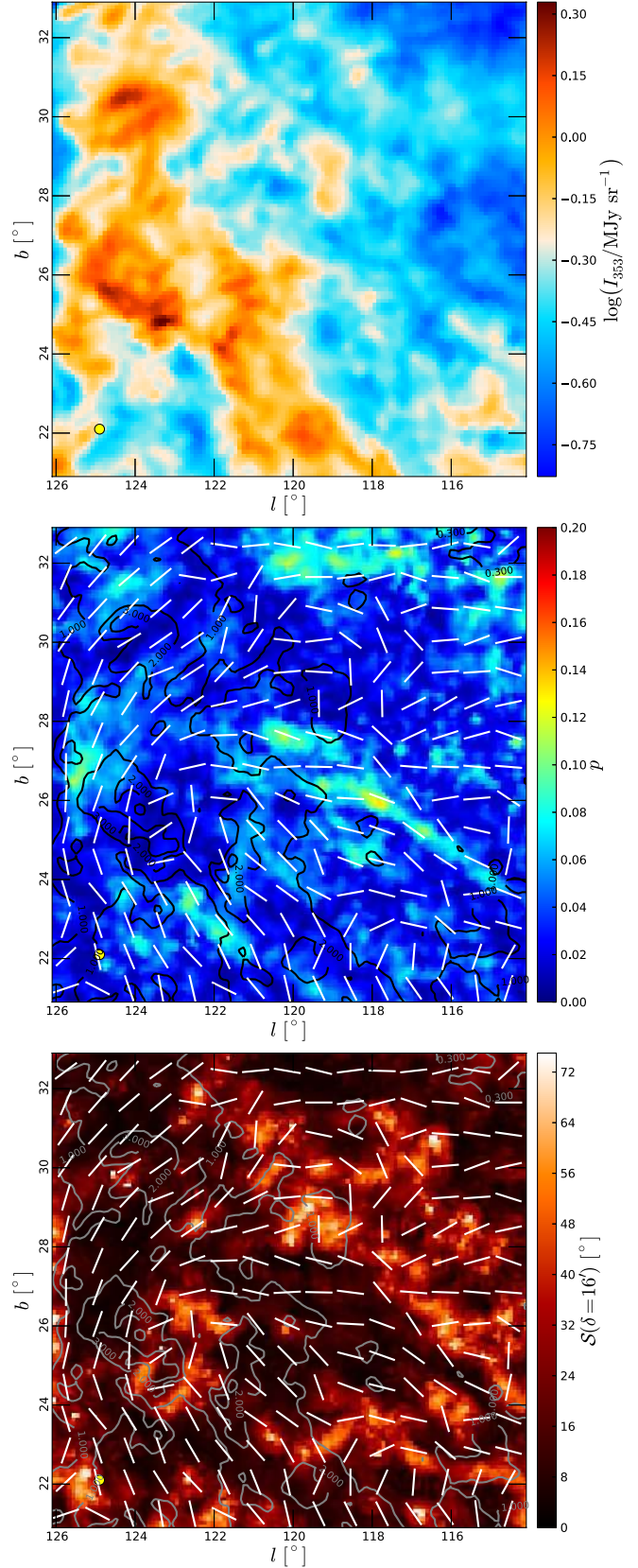


Fig. A.1. Same as Fig. 3, but for the Polaris Flare field. *Top*: total intensity at 353 GHz. *Middle*: polarization fraction p , column density N_H (contours in units of 10^{21} cm^{-2}), and magnetic orientation (bars). *Bottom*: angle dispersion function S with lag $\delta = 16'$ (see Sect. 2.5) with contours and bars identical to the middle row. Note that contours levels are different from those of Fig. 3.

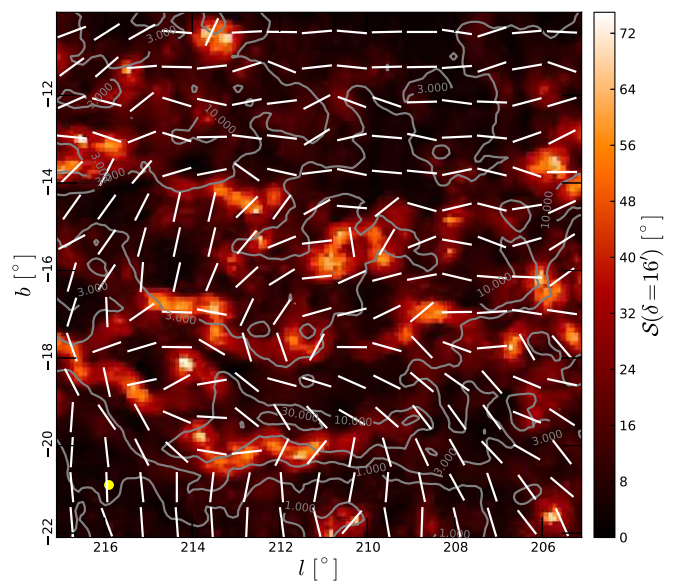
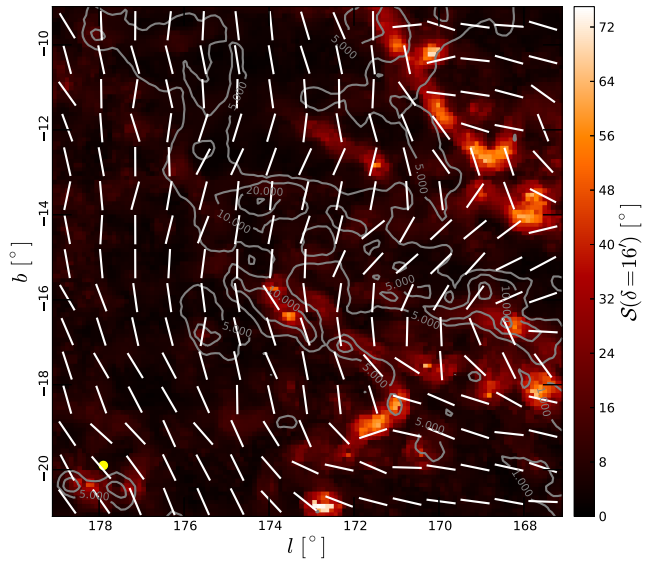
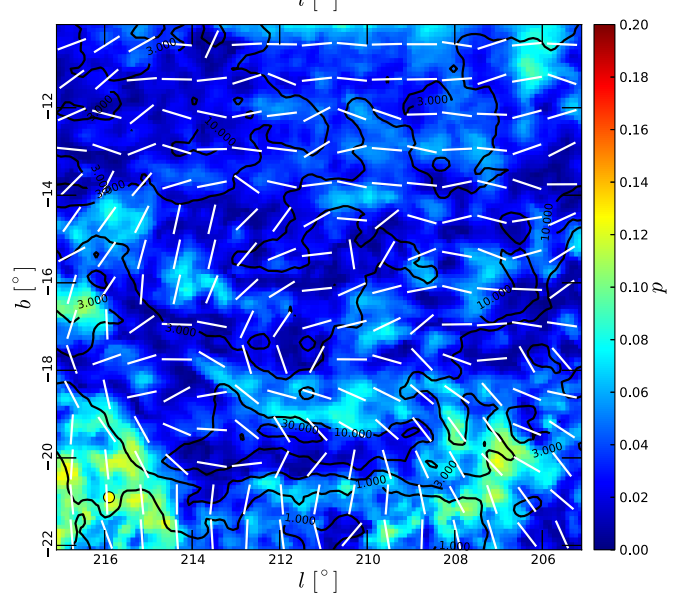
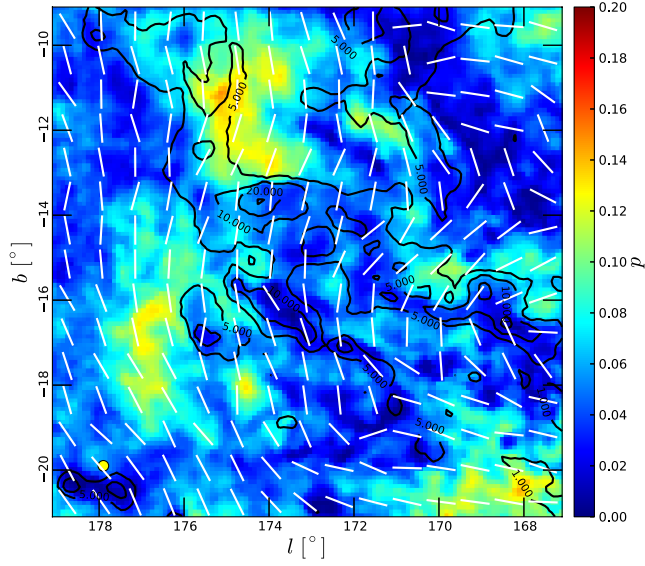
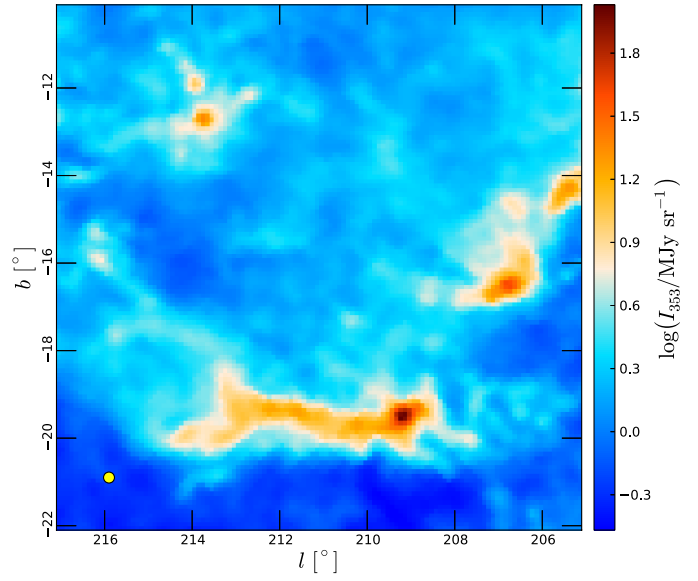
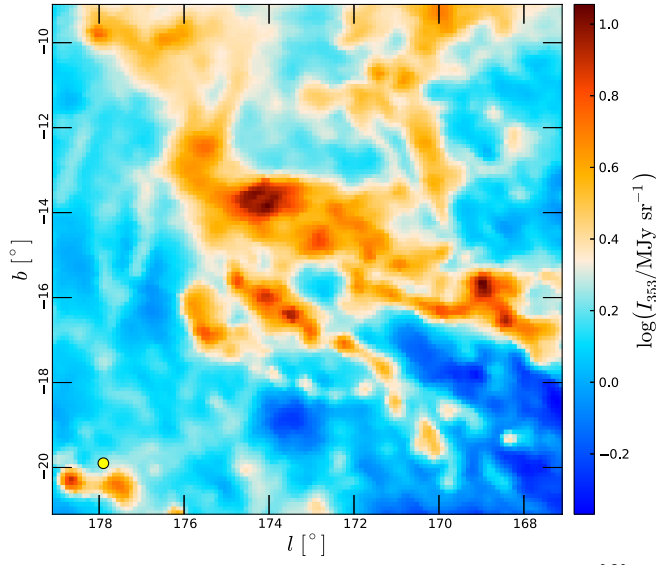


Fig. A.2. Same as Fig. 3, but for the Taurus field.

Fig. A.3. Same as Fig. 3, but for the Orion field.

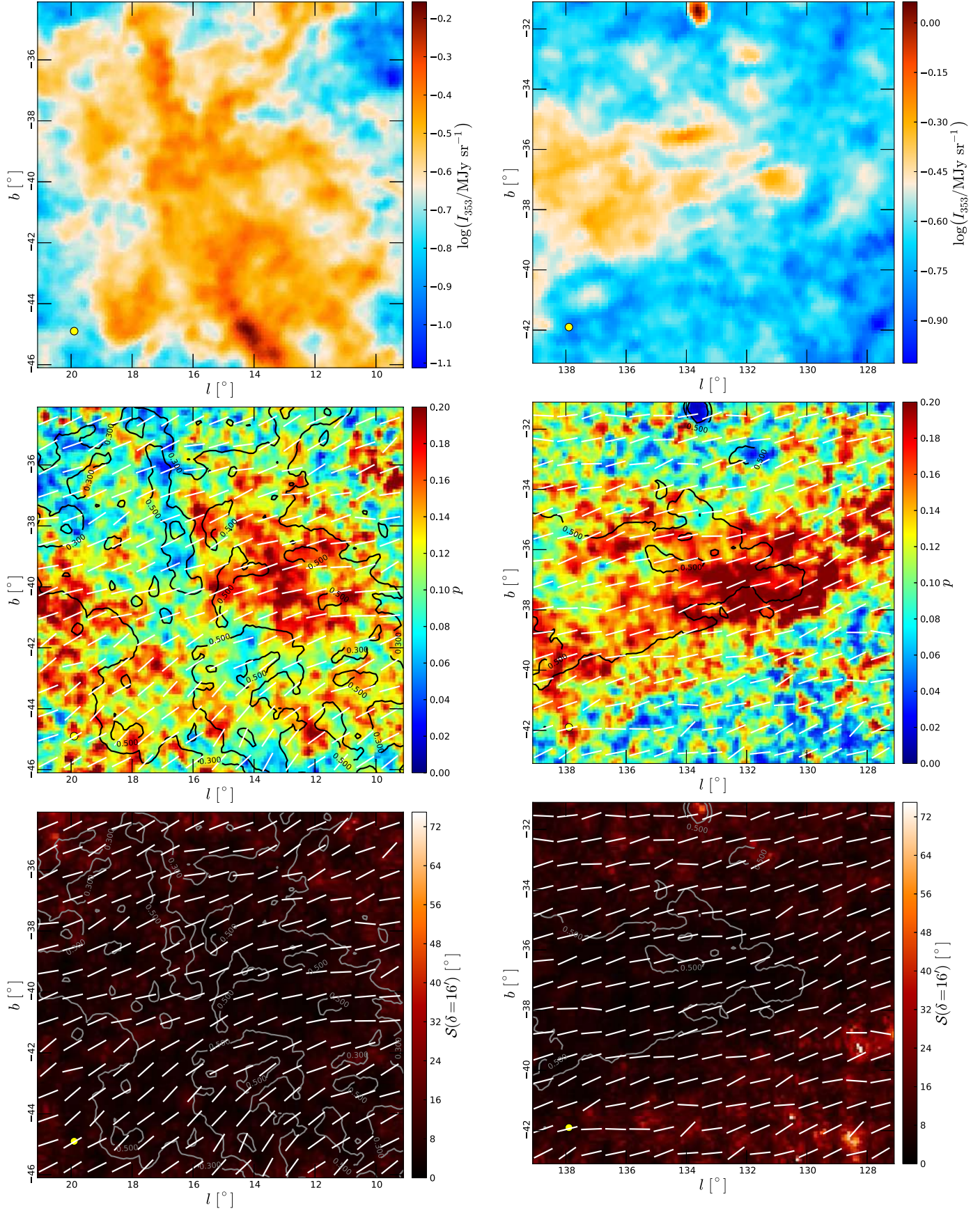


Fig. A.4. Same as Fig. 3, but for the Microscopium field.

Fig. A.5. Same as Fig. 3, but for the Pisces field.

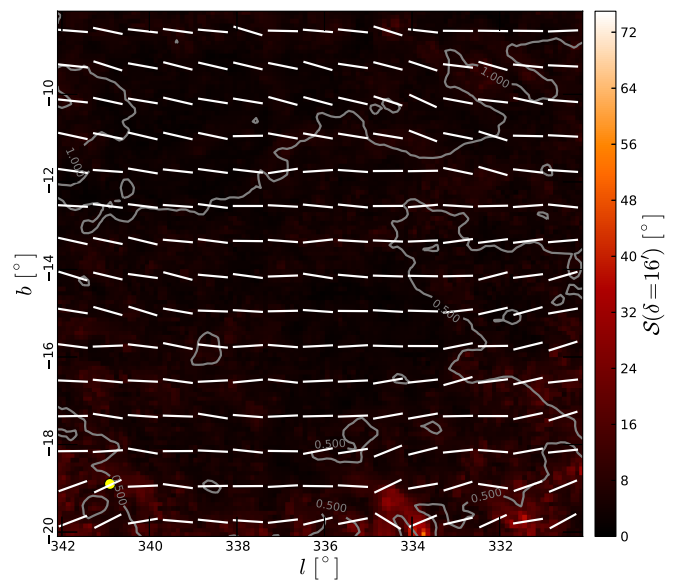
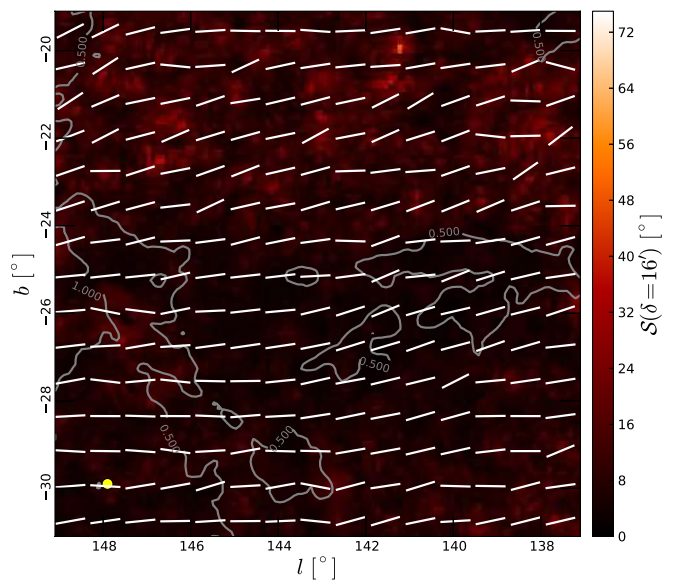
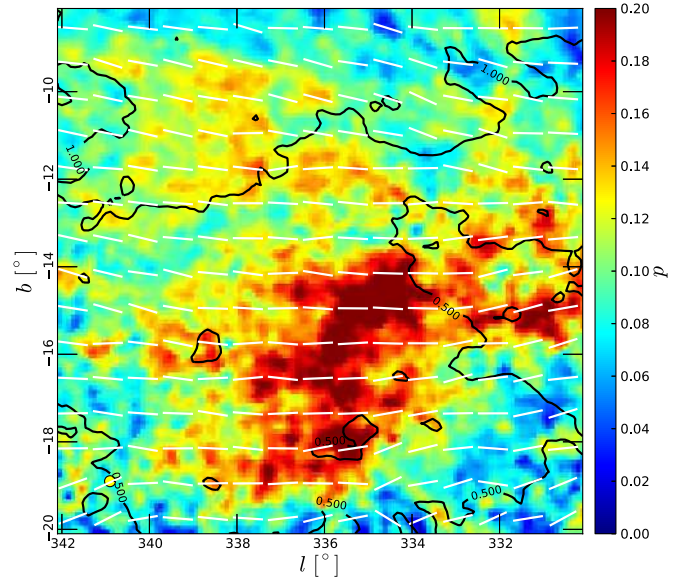
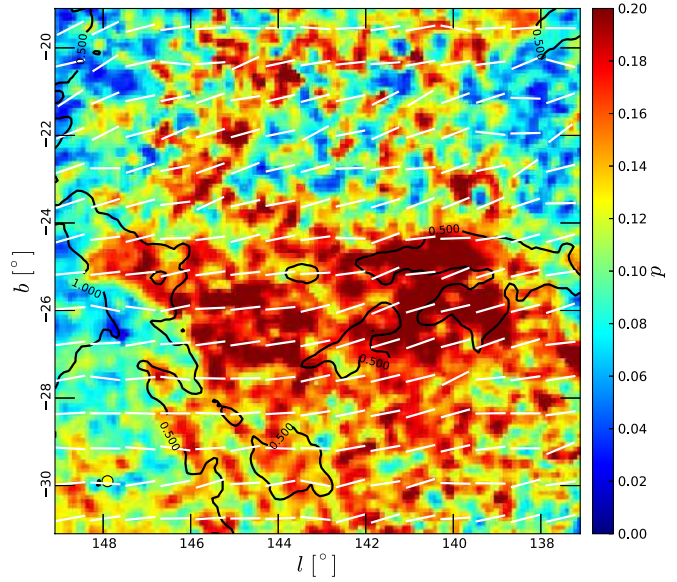
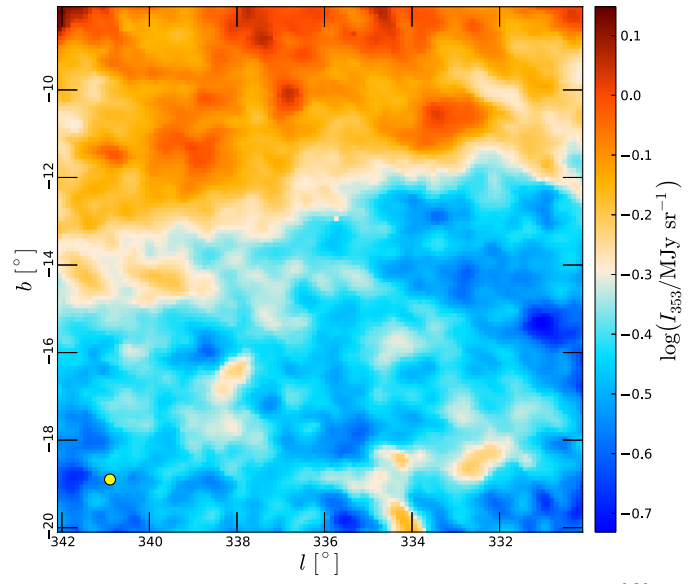
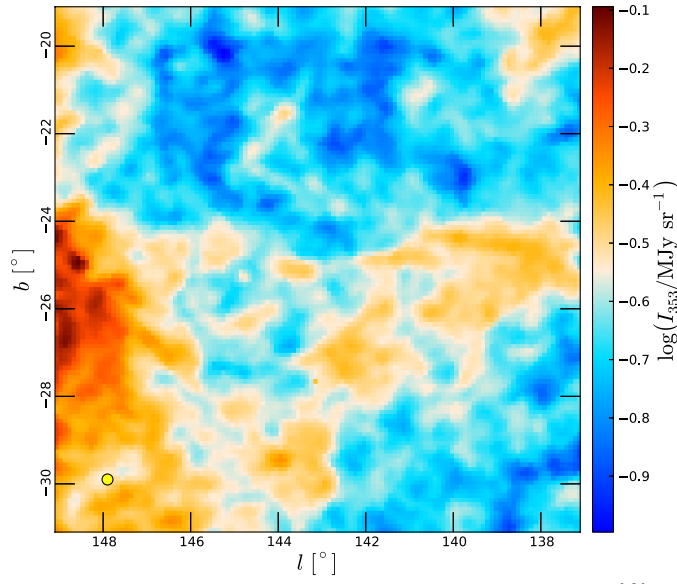


Fig. A.6. Same as Fig. 3, but for the Perseus field.

Fig. A.7. Same as Fig. 3, but for the Ara field.

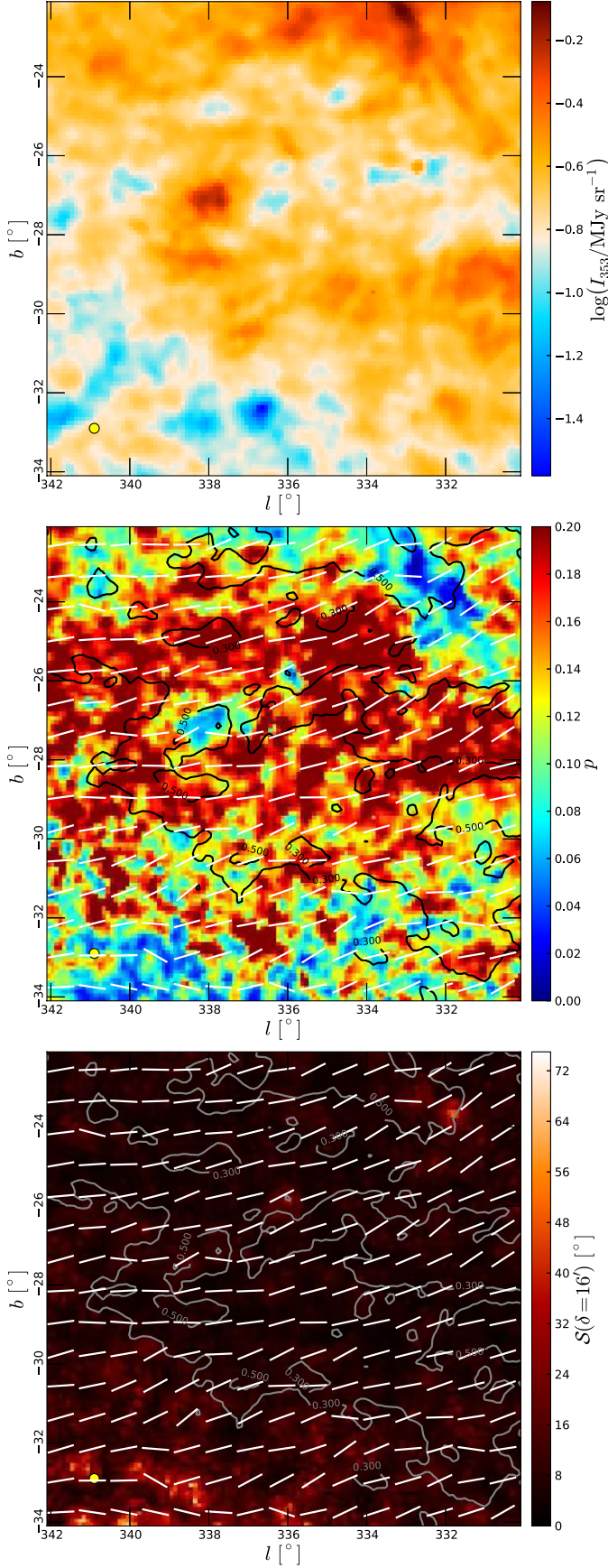


Fig. A.8. Same as Fig. 3, but for the Pavo field.

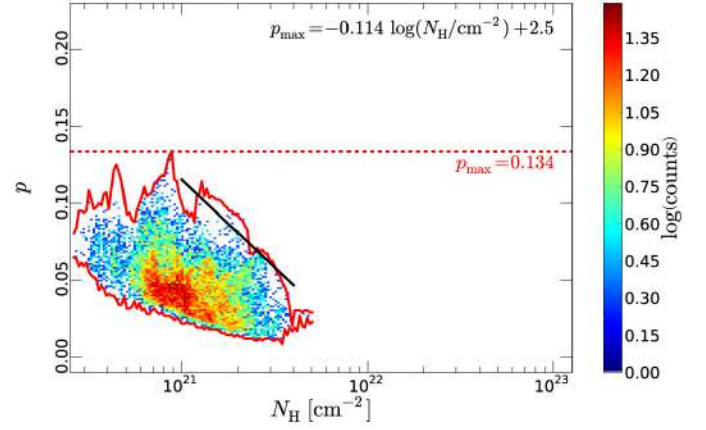


Fig. A.9. Same as Fig. 4, but for the Polaris Flare field. Two-dimensional distribution function of polarization fraction p and column density N_{H} . The distribution function is presented in logarithmic colour scale and includes only points for which $p/\sigma_p > 3$. The dashed red line corresponds to the absolute maximum polarization fraction p_{max} and the solid red curves show the upper and lower envelopes of p as functions of N_{H} . The solid black line is a linear fit $p_{\text{max}} = m \log(N_{\text{H}}/\text{cm}^{-2}) + c$ to the decrease of the maximum polarization fraction with column density at the high end of N_{H} (see Table 2 for the fitting parameters and fit parameters).

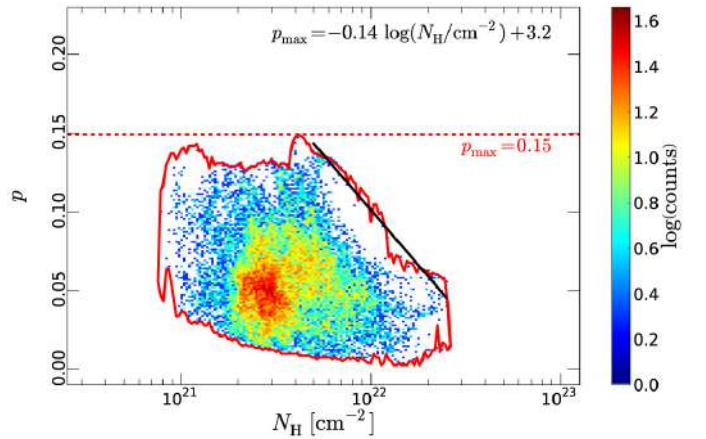


Fig. A.10. Same as Fig. 4, but for the Taurus field.

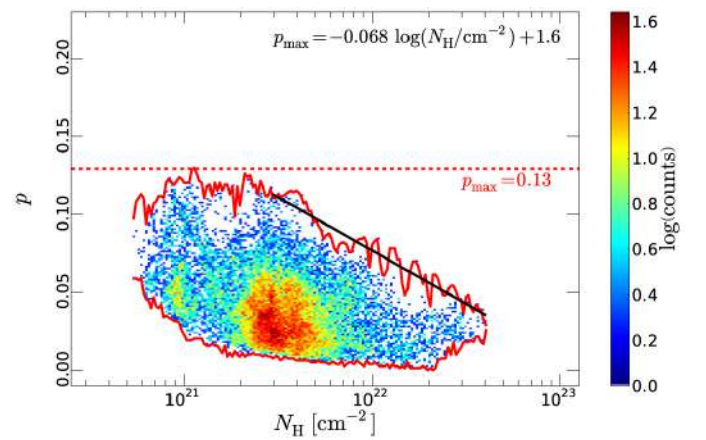


Fig. A.11. Same as Fig. 4, but for the Orion field.

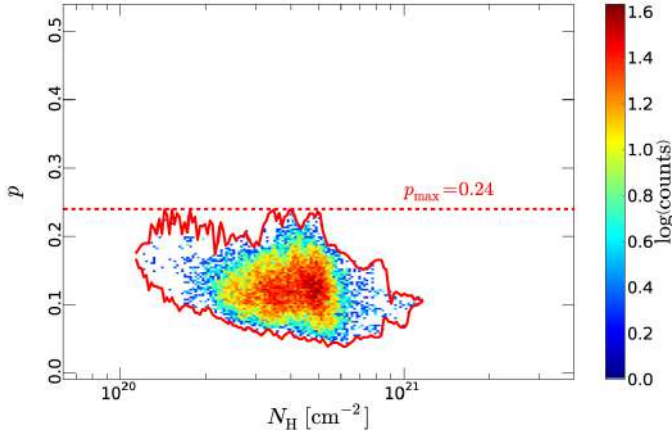


Fig. A.12. Same as Fig. 4, but for the Microscopium field. Note that the ranges in N_{H} and p are different from Fig. 4, and that no fit is performed.

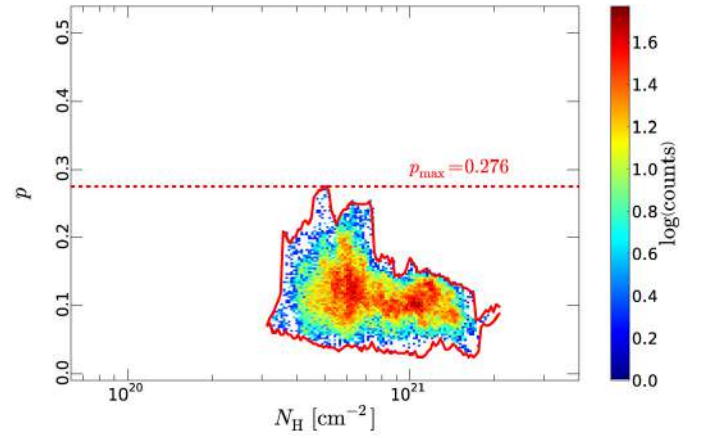


Fig. A.15. Same as Fig. 4, but for the Ara field. Note that the ranges in N_{H} and p are different from Fig. 4, and that no fit is performed.

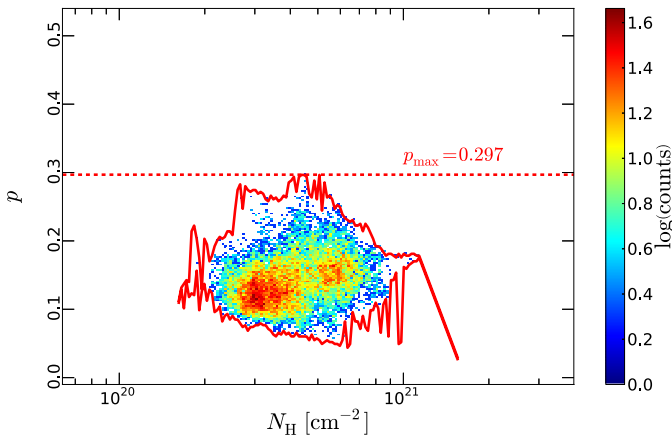


Fig. A.13. Same as Fig. 4, but for the Pisces field. Note that the ranges in N_{H} and p are different from Fig. 4, and that no fit is performed.

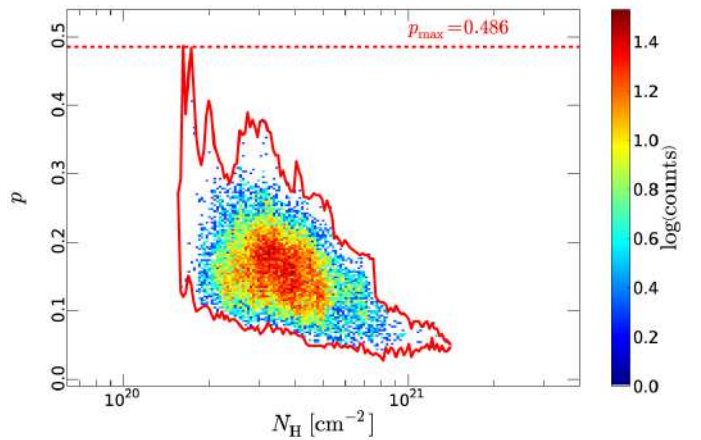


Fig. A.16. Same as Fig. 4, but for the Pavo field. Note that the ranges in N_{H} and p are different from Fig. 4, and that no fit is performed.

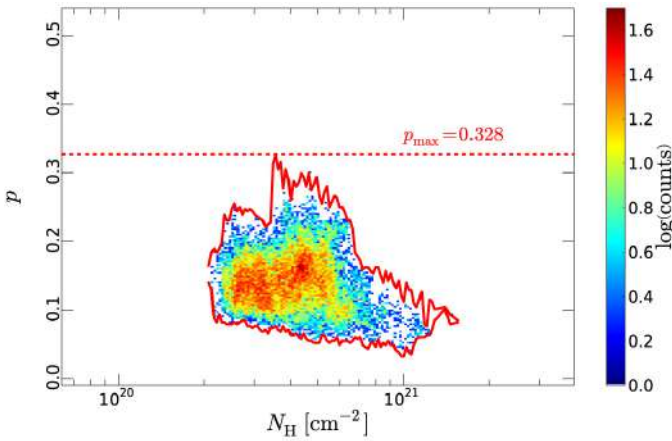


Fig. A.14. Same as Fig. 4, but for the Perseus field. Note that the ranges in N_{H} and p are different from Fig. 4, and that no fit is performed.

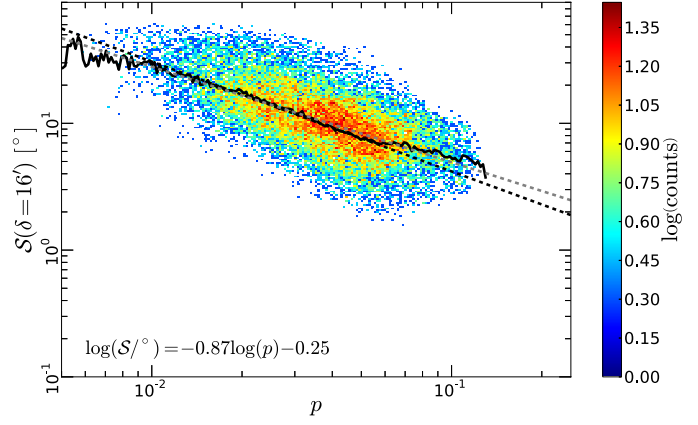
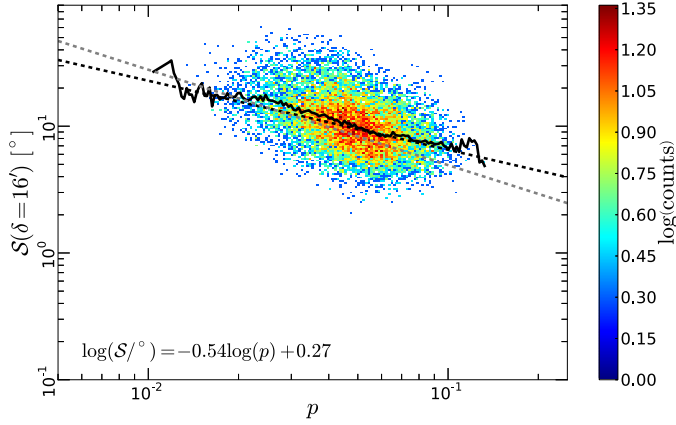


Fig. A.17. Same as Fig. 7, but for the Polaris Flare field. Two-dimensional distribution function of S and polarization fraction p . The angle dispersion function S is computed at a lag $\delta = 16'$. Only pixels for which $p/\sigma_p > 3$ are retained. The dashed grey line is the large-scale fit (with $FWHM = 1^\circ$ and $\delta = 1:07$) $\log(S) = -0.75 \log(p) - 0.06$, the solid black line shows the mean S for each bin in p (the bin size is $\Delta \log(p) = 0.008$) and the dashed black line is a linear fit of that curve in log-log space, restricted to bins in p which contain at least 1% of the total number of points (so about 150 points per bin).

Fig. A.19. Same as Fig. 7, but for the Orion field.

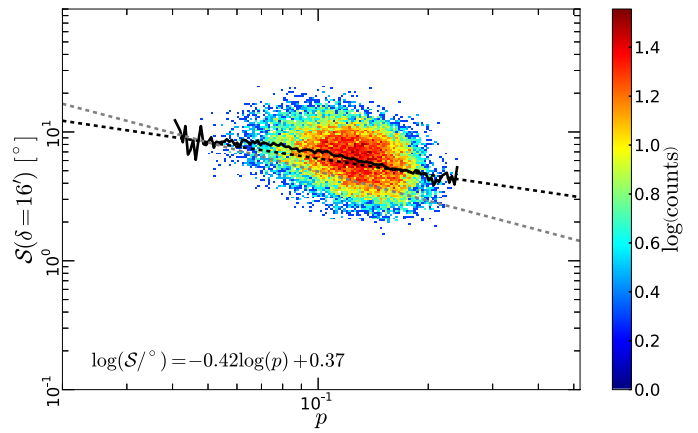
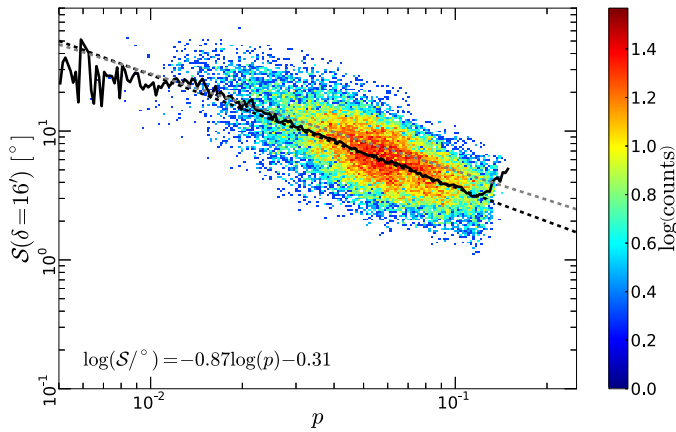


Fig. A.18. Same as Fig. 7, but for the Taurus field.

Fig. A.20. Same as Fig. 7, but for the Microscopium field. Note that the range in p is different from Fig. 7.

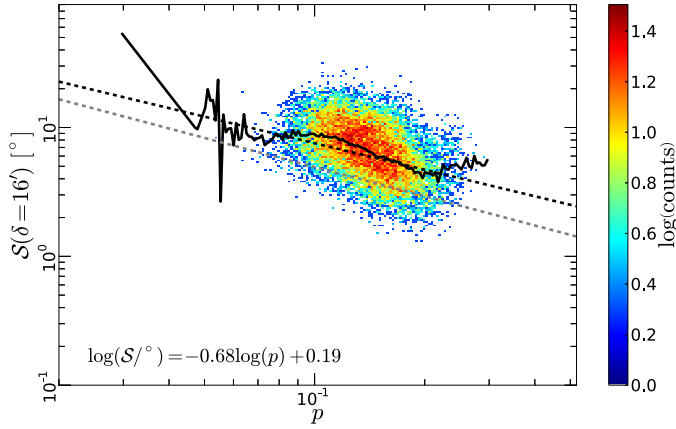


Fig. A.21. Same as Fig. 7, but for the Pisces field. Note that the range in p is different from Fig. 7.

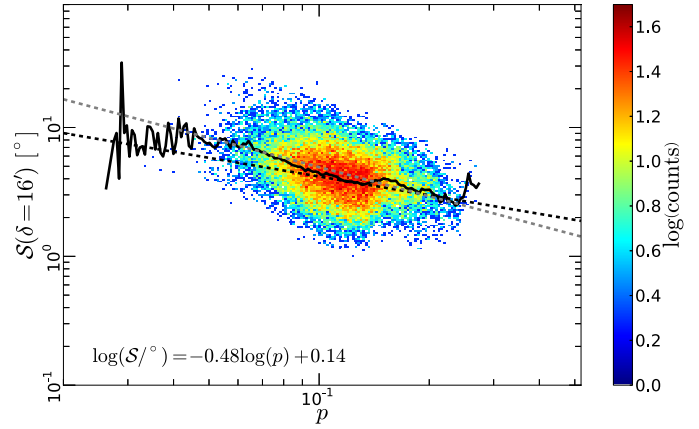


Fig. A.23. Same as Fig. 7, but for the Ara field. Note that the range in p is different from Fig. 7.

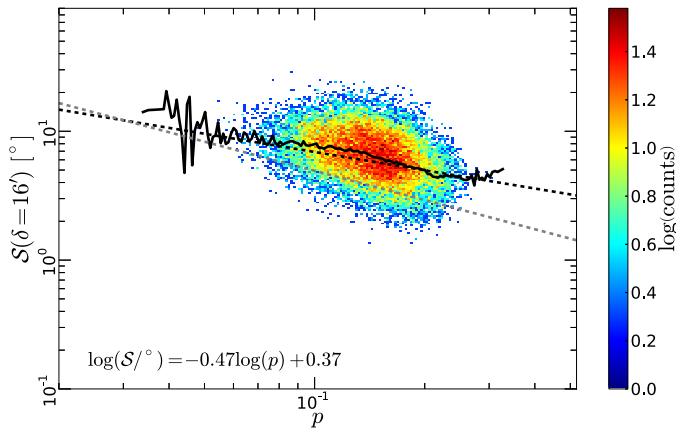


Fig. A.22. Same as Fig. 7, but for the Perseus field. Note that the range in p is different from Fig. 7.

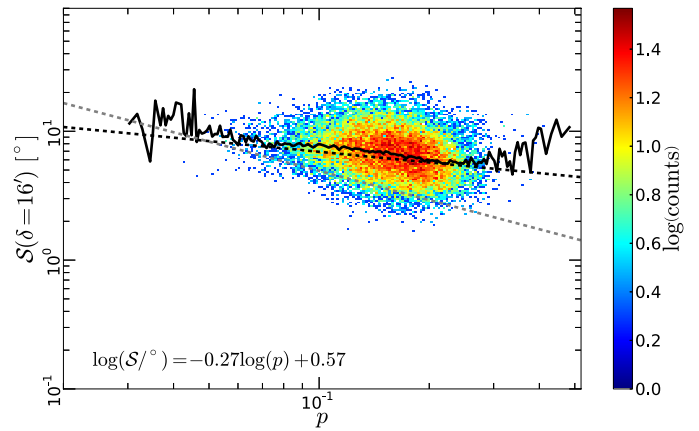


Fig. A.24. Same as Fig. 7, but for the Pavo field. Note that the range in p is different from Fig. 7.

Appendix B: Derivation of the Stokes parameters for emission

The derivation of the Stokes equations Eqs. (5)–(7), as presented by [Wardle & Königl \(1990\)](#) based upon [Lee & Draine \(1985\)](#), considers the extinction cross sections C_{\parallel} and C_{\perp} for light that is polarized parallel or perpendicular to the grain symmetry axis, and distinguishes oblate and prolate grains. Say that at each point M on the line of sight we define a reference frame $(Mx_0y_0z_0)$ such that z_0 points to the observer, and the local magnetic field \mathbf{B} is in the (My_0z_0) plane. With β the angle between \mathbf{B} and the angular momentum \mathbf{J} of a rotating grain at M , and γ the angle between \mathbf{B} and the plane of the sky, as defined in Fig. 14, [Lee & Draine \(1985\)](#) give, for oblate grains

$$C_{x_0} = C_{\perp} - \frac{C_{\perp} - C_{\parallel}}{2} \sin^2 \beta \quad (\text{B.1})$$

$$C_{y_0} = C_{\perp} - \frac{C_{\perp} - C_{\parallel}}{2} \left[\sin^2 \beta + \cos^2 \gamma (3 \cos^2 \beta - 1) \right] \quad (\text{B.2})$$

and for prolate grains

$$C_{x_0} = C_{\perp} + \frac{C_{\parallel} - C_{\perp}}{4} (1 + \cos^2 \beta) \quad (\text{B.3})$$

$$C_{y_0} = C_{\perp} + \frac{C_{\parallel} - C_{\perp}}{4} \left[1 + \cos^2 \beta - \cos^2 \gamma (3 \cos^2 \beta - 1) \right]. \quad (\text{B.4})$$

For spherical grains, all these cross-sections are of course equal, $C_{x_0} = C_{y_0} = C_{\perp} = C_{\parallel}$. The expressions for the Stokes parameters in terms of the cross-sections are

$$I = \int n_d B_{\nu}(T_d) \frac{\langle C_{x_0} + C_{y_0} \rangle}{2} ds \quad (\text{B.5})$$

$$Q = \int n_d B_{\nu}(T_d) \frac{\langle C_{x_0} - C_{y_0} \rangle}{2} \cos(2\phi) ds \quad (\text{B.6})$$

$$U = \int n_d B_{\nu}(T_d) \frac{\langle C_{x_0} - C_{y_0} \rangle}{2} \sin(2\phi) ds \quad (\text{B.7})$$

where the average $\langle \dots \rangle$ is performed on the possible angles β . The equivalent expressions given by [Wardle & Königl \(1990\)](#) are incorrect in omitting the factor 1/2 (it is easily checked that our expressions match the expected form of I in the case of spherical grains, and of P/I in the case of fully polarizing grains: 100% polarization when $C_{y_0} = 0$).

Computation of the sums and differences of C_{x_0} and C_{y_0} for both grain geometries leads to the same expressions for the Stokes parameters

$$I = \int n_d B_{\nu}(T_d) C_{\text{avg}} \left[1 - p_0 \left(\cos^2 \gamma - \frac{2}{3} \right) \right] ds \quad (\text{B.8})$$

$$Q = \int n_d B_{\nu}(T_d) C_{\text{avg}} p_0 \cos(2\phi) \cos^2 \gamma ds \quad (\text{B.9})$$

$$U = \int n_d B_{\nu}(T_d) C_{\text{avg}} p_0 \sin(2\phi) \cos^2 \gamma ds \quad (\text{B.10})$$

where we have introduced the average cross-section

$$C_{\text{avg}} = \frac{1}{3} (2C_{\perp} + C_{\parallel}), \quad (\text{B.11})$$

and the polarization cross section

$$C_{\text{pol}} = \frac{C_{\perp} - C_{\parallel}}{2} \quad (\text{for oblate grains}) \quad (\text{B.12})$$

$$C_{\text{pol}} = \frac{C_{\parallel} - C_{\perp}}{4} \quad (\text{for prolate grains}). \quad (\text{B.13})$$

These expressions match those in [Martin \(1972\)](#), [Martin \(1974\)](#), [Martin \(1975\)](#), and [Draine & Fraisse \(2009\)](#); those adopted by [Lee & Draine \(1985\)](#) are a factor 2 larger. The parameter p_0 is then given by

$$p_0 = \frac{C_{\text{pol}}}{C_{\text{avg}}} \frac{3}{2} \left(\langle \cos^2 \beta \rangle - \frac{1}{3} \right) = \frac{C_{\text{pol}}}{C_{\text{avg}}} R \quad (\text{B.14})$$

with R a Rayleigh reduction factor accounting for the chosen form of imperfect alignment ([Lee & Draine 1985](#)). Writing the equations for I , Q and U using the optical depth τ_{ν} (which is small in the submillimetre) in place of the physical position s on the line of sight, one is led to Eqs. (5)–(7).

The intrinsic polarization fraction is easily computed for both grain geometries:

$$p_i = \frac{C_{\perp} - C_{\parallel}}{C_{\perp} + C_{\parallel}} \quad (\text{for oblate grains}) \quad (\text{B.15})$$

$$p_i = \frac{C_{\parallel} - C_{\perp}}{3C_{\perp} + C_{\parallel}} \quad (\text{for prolate grains}). \quad (\text{B.16})$$

Planck intermediate results. XXXV. Probing the role of the magnetic field in the formation of structure in molecular clouds

Planck Collaboration: P. A. R. Ade⁸³, N. Aghanim⁵⁶, M. I. R. Alves⁵⁶, M. Arnaud⁷⁰, D. Arzoumanian⁵⁶, M. Ashdown^{66,5}, J. Aumont⁵⁶, C. Baccigalupi⁸¹, A. J. Banday^{89,8}, R. B. Barreiro⁶¹, N. Bartolo^{27,62}, E. Battaner^{90,91}, K. Benabed^{57,88}, A. Benoît⁵⁴, A. Benoit-Lévy^{21,57,88}, J.-P. Bernard^{89,8}, M. Bersanelli^{30,46}, P. Bielewicz^{78,8,81}, J. J. Bock^{63,9}, L. Bonavera⁶¹, J. R. Bond⁷, J. Borrill^{11,85}, F. R. Bouchet^{57,84}, F. Boulanger⁵⁶, A. Bracco⁵⁶, C. Burigana^{45,28,47}, E. Calabrese⁸⁷, J.-F. Cardoso^{71,1,57}, A. Catalano^{72,69}, H. C. Chiang^{24,6}, P. R. Christensen^{79,33}, L. P. L. Colombo^{20,63}, C. Combet⁷², F. Couchot⁶⁸, B. P. Crill^{63,9}, A. Curto^{61,5,66}, F. Cuttaia⁴⁵, L. Danese⁸¹, R. D. Davies⁶⁴, R. J. Davis⁶⁴, P. de Bernardis²⁹, A. de Rosa⁴⁵, G. de Zotti^{42,81}, J. Delabrouille¹, C. Dickinson⁶⁴, J. M. Diego⁶¹, H. Dole^{56,55}, S. Donzelli⁴⁶, O. Doré^{63,9}, M. Douspis⁵⁶, A. Ducout^{57,52}, X. Dupac³⁵, G. Efstathiou⁵⁸, F. Elsner^{21,57,88}, T. A. Enßlin⁷⁶, H. K. Eriksen⁵⁹, D. Falceta-Gonçalves^{82,34}, E. Falgarone⁶⁹, K. Ferrière^{89,8}, F. Finelli^{45,47}, O. Forni^{89,8}, M. Frailis⁴⁴, A. A. Fraisse²⁴, E. Franceschi⁴⁵, A. Frejsel⁷⁹, S. Galeotta⁴⁴, S. Galli⁶⁵, K. Gangal¹, T. Ghosh⁵⁶, M. Giard^{89,8}, E. Gjerløw⁵⁹, J. González-Nuevo^{16,61}, K. M. Górski^{63,92}, A. Gregorio^{31,44,50}, A. Gruppuso⁴⁵, J. E. Gudmundsson²⁴, V. Guillet⁵⁶, D. L. Harrison^{58,66}, G. Helou⁹, P. Hennebelle⁷⁰, S. Henrot-Versillé⁶⁸, C. Hernández-Monteagudo^{10,76}, D. Herranz⁶¹, S. R. Hildebrandt^{63,9}, E. Hivon^{57,88}, W. A. Holmes⁶³, A. Hornstrup¹³, K. M. Huffenberger²², G. Hurier⁵⁶, A. H. Jaffe⁵², T. R. Jaffe^{89,8}, W. C. Jones²⁴, M. Juvela²³, E. Keihänen²³, R. Keskitalo¹¹, T. S. Kisner⁷⁴, J. Knoche⁷⁶, M. Kunz^{14,56,2}, H. Kurki-Suonio^{23,40}, G. Lagache^{4,56}, J.-M. Lamarre⁶⁹, A. Lasenby^{5,66}, M. Lattanzi²⁸, C. R. Lawrence⁶³, R. Leonardi³⁵, F. Levrier⁶⁹, M. Liguori^{27,62}, P. B. Lilje⁵⁹, M. Linden-Vørnle¹³, M. López-Caniego^{35,61}, P. M. Lubin²⁵, J. F. Macías-Pérez⁷², D. Maino^{30,46}, N. Mandolesi^{45,28}, A. Mangilli^{56,68}, M. Maris⁴⁴, P. G. Martin⁷, E. Martínez-González⁶¹, S. Masi²⁹, S. Matarrese^{27,62,38}, A. Melchiorri^{29,48}, L. Mendes³⁵, A. Mennella^{30,46}, M. Migliaccio^{58,66}, M.-A. Miville-Deschênes^{56,7}, A. Moneti⁵⁷, L. Montier^{89,8}, G. Morgante⁵², D. Mortlock⁵², D. Munshi⁸³, J. A. Murphy⁷⁷, P. Naselsky^{79,33}, F. Nati²⁴, C. B. Netterfield¹⁷, F. Noviello⁶⁴, D. Novikov⁷⁵, I. Novikov^{79,75}, N. Oppermann⁷, C. A. Oxborrow¹³, L. Pagano^{29,48}, F. Pajot⁵⁶, R. Paladini⁵³, D. Paoletti^{45,47}, F. Pasian⁴⁴, L. Perotto⁷², V. Pettorino³⁹, F. Piacentini²⁹, M. Piat¹, E. Pierpaoli²⁰, D. Pietrobon⁶³, S. Plaszczynski⁶⁸, E. Pointecouteau^{89,8}, G. Polenta^{3,43}, N. Ponthieu^{56,51}, G. W. Pratt⁷⁰, S. Prunet^{57,88}, J.-L. Puget⁵⁶, J. P. Rachen^{18,76}, M. Reinecke⁷⁶, M. Remazeilles^{64,56,1}, C. Renault⁷², A. Renzi^{32,49}, I. Ristorcelli^{89,8}, G. Rocha^{63,9}, M. Rossetti^{30,46}, G. Roudier^{1,69,63}, J. A. Rubiño-Martín^{60,15}, B. Rusholme⁵³, M. Sandri⁴⁵, D. Santos⁷², M. Savelainen^{23,40}, G. Savini⁸⁰, D. Scott¹⁹, J. D. Soler^{56*}, V. Stolyarov^{5,86,67}, R. Sudiwala⁸³, D. Sutton^{58,66}, A.-S. Suur-Uski^{23,40}, J.-F. Sygnet⁵⁷, J. A. Tauber³⁶, L. Terenzi^{37,45}, L. Toffolatti^{16,61,45}, M. Tomasi^{30,46}, M. Tristram⁶⁸, M. Tucci¹⁴, G. Umata⁴¹, L. Valenziano⁴⁵, J. Valiviita^{23,40}, B. Van Tent⁷³, P. Vielva⁶¹, F. Villa⁴⁵, L. A. Wade⁶³, B. D. Wandelt^{57,88,26}, I. K. Wehus⁶³, N. Ysard²³, D. Yvon¹², and A. Zonca²⁵

(Affiliations can be found after the references)

Received 13 February 2015 / Accepted 25 May 2015

ABSTRACT

Within ten nearby ($d < 450$ pc) Gould Belt molecular clouds we evaluate statistically the relative orientation between the magnetic field projected on the plane of sky, inferred from the polarized thermal emission of Galactic dust observed by *Planck* at 353 GHz, and the gas column density structures, quantified by the gradient of the column density, N_{H} . The selected regions, covering several degrees in size, are analysed at an effective angular resolution of $10'$ FWHM, thus sampling physical scales from 0.4 to 40 pc in the nearest cloud. The column densities in the selected regions range from $N_{\text{H}} \approx 10^{21}$ to 10^{23} cm⁻², and hence they correspond to the bulk of the molecular clouds. The relative orientation is evaluated pixel by pixel and analysed in bins of column density using the novel statistical tool called “Histogram of Relative Orientations”. Throughout this study, we assume that the polarized emission observed by *Planck* at 353 GHz is representative of the projected morphology of the magnetic field in each region, i.e., we assume a constant dust grain alignment efficiency, independent of the local environment. Within most clouds we find that the relative orientation changes progressively with increasing N_{H} , from mostly parallel or having no preferred orientation to mostly perpendicular. In simulations of magnetohydrodynamic turbulence in molecular clouds this trend in relative orientation is a signature of Alfvénic or sub-Alfvénic turbulence, implying that the magnetic field is significant for the gas dynamics at the scales probed by *Planck*. We compare the deduced magnetic field strength with estimates we obtain from other methods and discuss the implications of the *Planck* observations for the general picture of molecular cloud formation and evolution.

Key words. ISM: general, dust, magnetic fields, clouds – Infrared: ISM – Submillimetre: ISM

* Corresponding author: Juan D. Soler (jsolerpu@ias.u-psud.fr)

1. Introduction

The formation and evolution of molecular clouds (MCs) and their substructures, from filaments to cores and eventually to stars, is the product of the interaction between turbulence, magnetic fields, and gravity (Bergin & Tafalla 2007; McKee & Ostriker 2007). The study of the relative importance of these dynamical processes is limited by the observational techniques used to evaluate them. These limitations have been particularly critical when integrating magnetic fields into the general picture of MC dynamics (Elmegreen & Scalo 2004; Crutcher 2012; Heiles & Haverkorn 2012; Hennebelle & Falgarone 2012).

There are two primary methods of measuring magnetic fields in the dense interstellar medium (ISM). First, observation of the Zeeman effect in molecular lines provides the line-of-sight component of the field B_{\parallel} (Crutcher 2005). Second, polarization maps – in extinction from background stars and emission from dust – reveal the orientation of the field averaged along the line of sight and projected on the plane of the sky (Hiltner 1949; Davis & Greenstein 1951; Hildebrand 1988; Planck Collaboration Int. XXI 2014).

Analysis of the Zeeman effect observations presented by Crutcher et al. (2010) shows that in the diffuse ISM sampled by H I lines ($n_{\text{H}} < 300 \text{ cm}^{-3}$), the maximum magnetic field strength B_{max} does not scale with density. This is interpreted as the effect of diffuse clouds assembled by flows along magnetic field lines, which would increase the density but not the magnetic field strength. In the denser regions ($n_{\text{H}} > 300 \text{ cm}^{-3}$), probed by OH and CN spectral lines, the same study reports a scaling of the maximum magnetic field strength $B_{\text{max}} \propto n_{\text{H}}^{0.65}$. The latter observation can be interpreted as the effect of isotropic contraction of gas too weakly magnetized for the magnetic field to affect the morphology of the collapse. However, given that the observations are restricted to pencil-like lines of sight and the molecular tracers are not homogeneously distributed, the Zeeman effect measurements alone are not sufficient to determine the relative importance of the magnetic field at the multiple scales within MCs.

The observation of starlight polarization provides an estimate of the projected magnetic field orientation in particular lines of sight. Starlight polarization observations show coherent magnetic fields around density structures in MCs (Pereyra & Magalhães 2004; Franco et al. 2010; Sugitani et al. 2011; Chapman et al. 2011; Santos et al. 2014). The coherent polarization morphology can be interpreted as the result of dynamically important magnetic fields. However, these observations alone are not sufficient to map even the projected magnetic field morphology fully and in particular do not tightly constrain the role of magnetic fields in the formation of structure inside MCs.

The study of magnetic field orientation within the MCs is possible through the observation of polarized thermal emission from dust. Far-infrared and submillimetre polarimetric observations have been limited to small regions up to hundreds of square arcminutes within clouds (Li et al. 2006; Matthews et al. 2014) or to large sections of the Galactic plane at a resolution of several degrees (Benoît et al. 2004; Bierman et al. 2011). On the scale of prestellar cores and cloud segments, these observations reveal both significant levels of polarized emission and coherent field morphologies (Ward-Thompson et al. 2000; Dotson et al. 2000; Matthews et al. 2009).

The strength of the magnetic field projected on the plane of the sky (B_{\perp}) can be estimated from polarization maps using the Davis-Chandrasekhar-Fermi (DCF) method (Davis 1951; Chandrasekhar & Fermi 1953). As discussed in Appendix D, it is

assumed that the dispersion in polarization angle ζ_{ψ} ¹ is entirely due to incompressible and isotropic turbulence. Turbulence also affects the motion of the gas and so broadens profiles of emission and absorption lines, as quantified by dispersion $\sigma_{v_{\parallel}}$. In the DCF interpretation B_{\perp} is proportional to the ratio $\sigma_{v_{\parallel}}/\zeta_{\psi}$. Application of the DCF method to subregions of the Taurus MC gives estimates of $B_{\perp} \approx 10 \mu\text{G}$ in low-density regions and ≈ 25 to $\approx 42 \mu\text{G}$ inside filamentary structures (Chapman et al. 2011). Values of $B_{\perp} \approx 760 \mu\text{G}$ have been found in dense parts of the Orion MC region (Houde et al. 2009). Because of the experimental difficulties involved in producing large polarization maps, a complete statistical study of the magnetic field variation across multiple scales is not yet available.

Additional information on the effects of the magnetic field on the cloud structure is found by studying the magnetic field orientation inferred from polarization observations relative to the orientation of the column density structures. Patterns of relative orientation have been described qualitatively in simulations of magnetohydrodynamic (MHD) turbulence with different degrees of magnetization. This is quantified as half the ratio of the gas pressure to the mean-field magnetic pressure (Ostriker et al. 2001; Heitsch et al. 2001), with the resulting turbulence ranging from sub-Alfvénic to super-Alfvénic. Quantitative analysis of simulation cubes, where the orientation of \mathbf{B} is available directly, reveals a preferred orientation relative to density structures that depends on the initial magnetization of the cloud (Hennebelle 2013; Soler et al. 2013). Using simple models of dust grain alignment and polarization efficiency to produce synthetic observations of the simulations, Soler et al. (2013) showed that the preferred relative orientation and its systematic dependence on the degree of magnetization are preserved.

Observational studies of relative orientation have mostly relied on visual inspection of polarization maps (e.g., Myers & Goodman 1991; Dotson 1996). This is adequate for evaluating general trends in the orientation of the field. However, it is limited ultimately by the need to represent the field orientation with pseudo-vectors, because when a large polarization map is to be overlaid on a scalar-field map, such as intensity or column density, only a selection of pseudo-vectors can be plotted. On the one hand, if the plotted pseudo-vectors are the result of averaging the Stokes parameters over a region, then the combined visualization illustrates different scales in the polarization and in the scalar field. On the other hand, if the plotted pseudo-vectors correspond to the polarization in a particular pixel, then the illustrated pattern is influenced by small-scale fluctuations that might not be significant in evaluating any trend in relative orientation.

Tassis et al. (2009) present a statistical study of relative orientation between structures in the intensity and the inferred magnetic field from polarization measured at $350 \mu\text{m}$ towards 32 Galactic clouds in maps of a few arcminutes in size. Comparing the mean direction of the field to the semi-major axis of each cloud, they find that the field is mostly perpendicular to that axis. Similarly, Li et al. (2013) compared the relative orientation in 13 clouds in the Gould Belt, calculating the main cloud orientation from the extinction map and the mean orientation of the intercloud magnetic field from starlight polarization. That study reported a bimodal distribution of relative cloud and field orientations; that is, some MCs are oriented perpendicular and some parallel to the mean orientation of the intercloud field. In both studies each cloud constitutes one independent observation

¹ We use ζ_{ψ} to avoid confusion with σ_{ψ} , which was introduced in Planck Collaboration Int. XIX (2014) as the uncertainty in the polarization angle ψ .

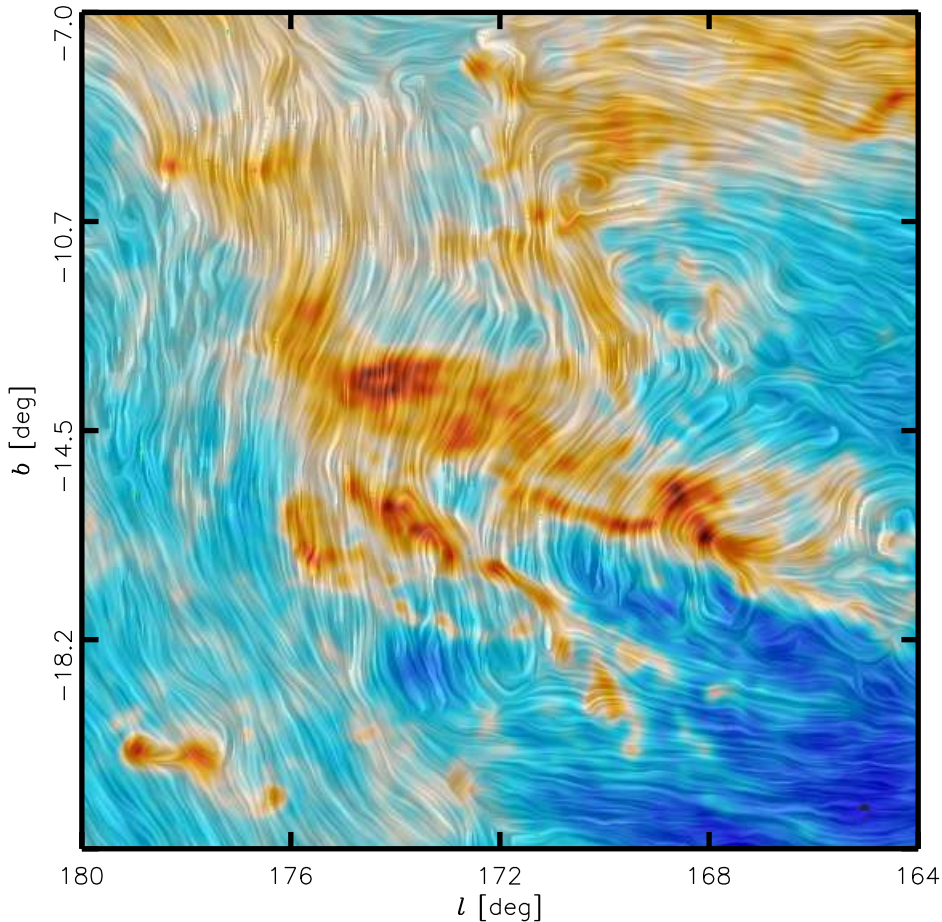


Fig. 1. Magnetic field and column density measured by *Planck* towards the Taurus MC. The colours represent column density. The “drapery” pattern, produced using the line integral convolution method (LIC, Cabral & Leedom 1993), indicates the orientation of magnetic field lines, orthogonal to the orientation of the submillimetre polarization.

of relative orientation, so that the statistical significance of each study depends on the total number of clouds observed. In a few regions of smaller scales, roughly a few tenths of a parsec, Koch et al. (2013) report a preferred orientation of the magnetic field, inferred from polarized dust emission, parallel to the gradient of the emission intensity.

By measuring the intensity and polarization of thermal emission from Galactic dust over the whole sky and down to scales that probe the interiors of nearby MCs, *Planck*² provides an unprecedented data set from a single instrument and with a common calibration scheme, for studying the morphology of the magnetic field in MCs and the surrounding ISM, as illustrated for the Taurus region in Fig. 1. We present a quantitative analysis of the relative orientation in a set of nearby ($d < 450$ pc) well-known MCs to quantify the role of the magnetic field in the formation of density structures on physical scales ranging from tens of parsecs to approximately one parsec in the nearest clouds.

The present work is an extension of previous findings, as reported by the *Planck* collaboration, on their study of the polarized thermal emission from Galactic dust. Previous studies in-

clude an overview of this emission (Planck Collaboration Int. XIX 2014), which reported dust polarization percentages up to 20% at low N_{H} , decreasing systematically with increasing N_{H} to a low plateau for regions with $N_{\text{H}} > 10^{22} \text{ cm}^{-2}$. Planck Collaboration Int. XX (2014) presented a comparison of the polarized thermal emission from Galactic dust with results from simulations of MHD turbulence, focusing on the statistics of the polarization fractions and angles. Synthetic observations were made of the simulations under the simple assumption of homogeneous dust grain alignment efficiency. Both studies reported that the largest polarization fractions are reached in the most diffuse regions. Additionally, there is an anti-correlation between the polarization percentage and the dispersion of the polarization angle. This anti-correlation is reproduced well by the synthetic observations, indicating that it is essentially caused by the turbulent structure of the magnetic field.

Over most of the sky Planck Collaboration Int. XXXII (2014) analysed the relative orientation between density structures, which is characterized by the Hessian matrix, and polarization, revealing that most of the elongated structures (filaments or ridges) have counterparts in the Stokes Q and U maps. This implies that in these structures, the magnetic field has a well-defined mean direction on the scales probed by *Planck*. Furthermore, the ridges are predominantly aligned with the magnetic field measured on the structures. This statistical trend becomes more striking for decreasing column density and, as ex-

² *Planck* (<http://www.esa.int/Planck>) is a project of the European Space Agency (ESA) with instruments provided by two scientific consortia funded by ESA member states (in particular the lead countries France and Italy), with contributions from NASA (USA) and telescope reflectors provided by a collaboration between ESA and a scientific consortium led and funded by Denmark.

pected from the potential effects of projection, for increasing polarization fraction. There is no alignment for the highest column density ridges in the $N_{\text{H}} \gtrsim 10^{22} \text{ cm}^{-2}$ sample. Planck Collaboration Int. XXXIII (2014) studied the polarization properties of three nearby filaments, showing by geometrical modelling that the magnetic field in those representative regions has a well-defined mean direction that is different from the field orientation in the surroundings.

In the present work, we quantitatively evaluate the relative orientation of the magnetic field inferred from the Planck polarization observations with respect to the gas column density structures, using the histogram of relative orientations (HRO, Soler et al. 2013). The HRO is a novel statistical tool that quantifies the relative orientation of each polarization measurement with respect to the column density gradient, making use of the unprecedented statistics provided by the Planck polarization observations. The HRO can also be evaluated in both 3D simulation data cubes and synthetic observations, thereby providing a direct comparison between observations and the physical conditions included in MHD simulations. We compare the results of the HRO applied to the Planck observations with the results of the same analysis applied to synthetic observations of MHD simulations of super-Alfvénic, Alfvénic, and sub-Alfvénic turbulence.

Thus by comparison with numerical simulations of MHD turbulence, the HRO provides estimates of the magnetic field strength without any of the assumptions involved in the DCF method. For comparison, we estimate B_{\perp} using the DCF method and the related method described by Hildebrand et al. (2009) (DCF+SF, for DCF plus structure function) and provide a critical assessment of their applicability.

This paper is organized as follows. Section 2 introduces the Planck 353 GHz polarization observations, the gas column density maps, and the CO line observations used to derive the velocity information. The particular regions where we evaluate the relative orientation between the magnetic field and the column density structures are presented in Sect. 3. Section 4 describes the statistical tools used for the study of these relative orientations. In Sect. 5 we discuss our results and their implications in the general picture of cloud formation. Finally, Sect. 6 summarizes the main results. Additional information on the selection of the polarization data, the estimation of uncertainties affecting the statistical method, and the statistical significance of the relative orientation studies can be found in Appendices A, B, and C, respectively. Appendix D presents alternative estimates of the magnetic field strength in each region.

2. Data

2.1. Thermal dust polarization

Over the whole sky Planck observed the linear polarization (Stokes Q and U) in seven frequency bands from 30 to 353 GHz (Planck Collaboration I 2014). In this study, we used data from the High Frequency Instrument (HFI, Lamarre et al. 2010) at 353 GHz, the highest frequency band that is sensitive to polarization. Towards MCs the contribution of the cosmic microwave background (CMB) polarized emission is negligible at 353 GHz, making this the Planck map that is best suited to studying the spatial structure of the dust polarization (Planck Collaboration Int. XIX 2014; Planck Collaboration Int. XX 2014).

We used the Stokes Q and U maps and the associated noise maps made from five independent consecutive sky surveys of the Planck cryogenic mission, which together correspond to the

DR3 (delta-DX11d) internal data release. We refer to previous Planck publications for the data processing, map making, photometric calibration, and photometric uncertainties (Planck Collaboration II 2014; Planck Collaboration V 2014; Planck Collaboration VI 2014; Planck Collaboration VIII 2014). As in the first Planck polarization papers, we used the International Astronomical Union (IAU) conventions for the polarization angle, measured from the local direction to the north Galactic pole with positive values increasing towards the east.

The maps of Q , U , their respective variances σ_Q^2 , σ_U^2 , and their covariance σ_{QU} are initially at 4.8 resolution in HEALPix format³ with a pixelization at $N_{\text{side}} = 2048$, which corresponds to an effective pixel size of 1.7. To increase the signal-to-noise ratio (S/N) of extended emission, we smoothed all the maps to 10' resolution using a Gaussian approximation to the Planck beam and the covariance smoothing procedures described in Planck Collaboration Int. XIX (2014).

The maps of the individual regions are projected and resampled onto a Cartesian grid by using the gnomonic projection procedure described in Paradis et al. (2012). The HRO analysis is performed on these projected maps.

2.2. Column density

We used the dust optical depth at 353 GHz (τ_{353}) as a proxy for the gas column density (N_{H}). The τ_{353} map (Planck Collaboration XI 2014) was derived from the all-sky Planck intensity observations at 353, 545, and 857 GHz, and the IRAS observations at 100 μm , which were fitted using a modified black body spectrum. Other parameters obtained from this fit are the temperature and the spectral index of the dust opacity. The τ_{353} map, computed initially at 5' resolution, was smoothed to 10' to match the polarization maps. The errors resulting from smoothing the product τ_{353} map, rather than the underlying data, are negligible compared to the uncertainties in the dust opacity and do not significantly affect the results of this study.

To scale from τ_{353} to N_{H} , following Planck Collaboration XI (2014), we adopted the dust opacity found using Galactic extinction measurements of quasars,

$$\tau_{353}/N_{\text{H}} = 1.2 \times 10^{-26} \text{ cm}^2. \quad (1)$$

Variations in dust opacity are present even in the diffuse ISM and the opacity increases systematically by a factor of 2 from the diffuse to the denser ISM (Planck Collaboration XXIV 2011; Martin et al. 2012; Planck Collaboration XI 2014), but our results do not critically depend on this calibration.

3. Analysed regions

The selected regions, shown in Fig. 2, correspond to nearby ($d < 450 \text{ pc}$) MCs, whose characteristics are well studied and can be used for cloud-to-cloud comparison (Poppel 1997; Reipurth 2008). Their properties are summarized in Table 1, which includes: Galactic longitude l and latitude b at the centre of the field; field size $\Delta l \times \Delta b$; estimate of distance; mean and maximum total column densities from dust, $\langle N_{\text{H}} \rangle$ and $\text{max}(N_{\text{H}})$, respectively; and mean H_2 column density from CO.

In the table the regions are organized from the nearest to the farthest in three groups: (a) regions located at $d \approx 150 \text{ pc}$, namely Taurus, Ophiuchus, Lupus, Chamaeleon-Musca, and Corona Australis (CrA); (b) regions located at $d \approx 300 \text{ pc}$,

³ Górski et al. (2005), <http://healpix.sf.net>

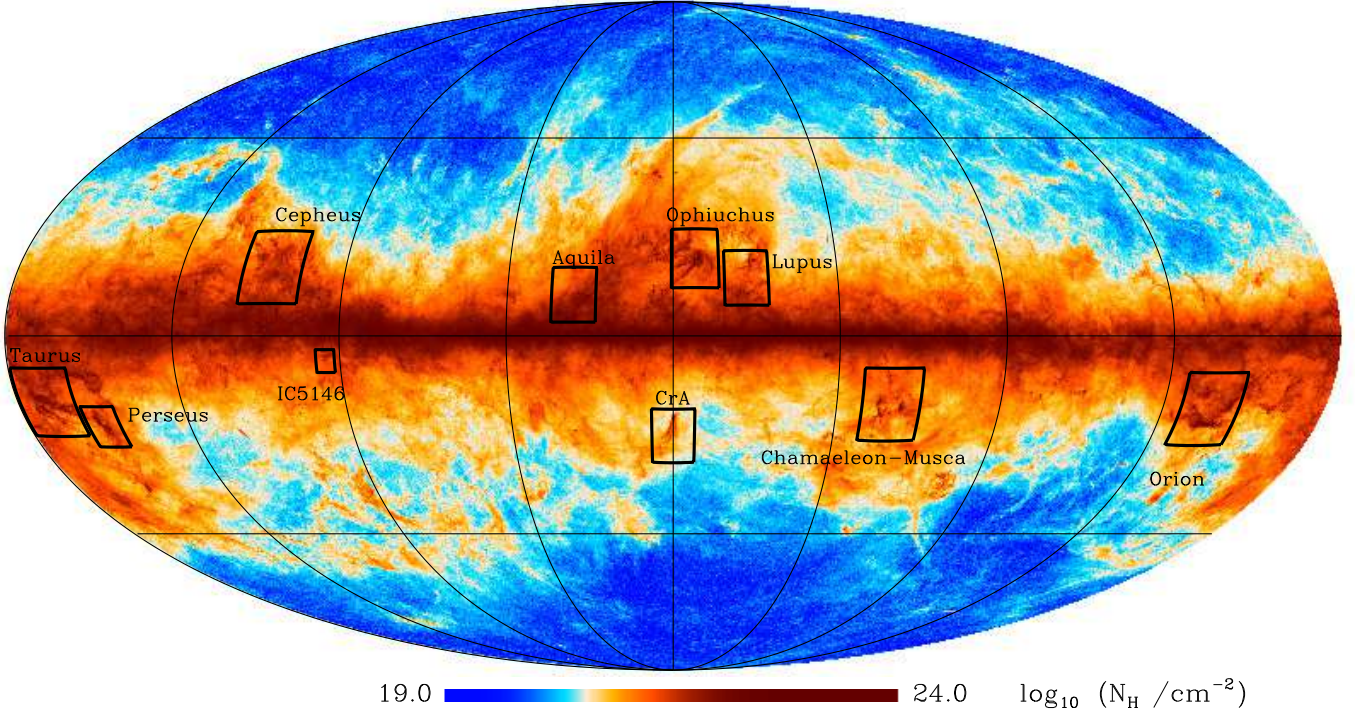


Fig. 2. Locations and sizes of the regions selected for analysis. The background map is the gas column density, N_H , derived from the dust optical depth at 353 GHz (Planck Collaboration XI 2014).

Table 1. Locations and properties of the selected regions

Region	l [°]	b [°]	Δl [°]	Δb [°]	Distance ^a [pc]	$\langle N_H \rangle^b$ [10^{21} cm^{-2}]	Max (N_H) ^b [10^{21} cm^{-2}]	$\langle N_{H_2} \rangle^c$ [10^{21} cm^{-2}]
Taurus	172.5	-14.5	15.0	15.0	140	5.4	51.9	1.6
Ophiuchus	354.0	17.0	13.0	13.0	140	4.4	103.3	1.1
Lupus	340.0	12.7	12.0	12.0	140	3.8	30.8	1.2
Chamaeleon-Musca	300.0	-15.0	16.0	16.0	160	2.3	29.7	1.3
Corona Australis (CrA)	0.0	-22.0	12.0	12.0	170	1.1	40.5	1.2
Aquila Rift	27.0	8.0	12.0	12.0	260	9.3	58.7	1.9
Perseus	159.0	-20.0	9.0	9.0	300	3.9	94.8	2.6
IC 5146	94.0	-5.5	5.0	5.0	400	3.7	22.6	1.0
Cepheus	110.0	15.0	16.0	16.0	440	4.2	21.3	1.2
Orion	212.0	-16.0	16.0	16.0	450	5.0	93.6	2.2

^a The estimates of distances are from: Schlafly et al. (2014) for Taurus, Ophiuchus, Perseus, IC 5146, Cepheus, and Orion; Knude & Hog (1998) for Lupus and CrA; Whittet et al. (1997) for Chamaeleon-Musca; and Straizys et al. (2003) for Aquila Rift.

^b Estimated from τ_{353} using Eq. (1) for the selected pixels defined in Appendix A.

^c Using the line integral W_{CO} over $-10 < v_{\parallel} / (\text{km s}^{-1}) < 10$ from the Dame et al. (2001) survey and $X_{\text{CO}} = 1.8 \times 10^{20} \text{ cm}^{-2} \text{ K}^{-1} \text{ km}^{-1} \text{ s}$.

Aquila Rift and Perseus; and (c) regions located at $d \approx 450$ pc, IC 5146, Cepheus, and Orion.

Among the clouds in the first group (all shown in Fig. 3, left column) are Ophiuchus and Lupus, which are two regions with different star-forming activities but are close neighbours within an environment disturbed by the Sco-Cen OB association (Wilking et al. 2008; Comerón 2008). Chamaeleon-Musca is a region evolving in isolation, and it is relatively unperturbed (Luhman 2008). Taurus (see also Fig. 1), a cloud with low-mass star formation, appears to be formed by the material swept up by an ancient superbubble centred on the Cas-Tau group (Kenyon et al. 2008). Finally, CrA is one of the nearest regions with recent intermediate- and low-mass star formation, possibly formed by

a high-velocity cloud impact on the Galactic plane (Neuhäuser & Forbrich 2008).

In the second group we consider Aquila Rift and Perseus, shown in Fig. 4 (left column). Aquila Rift is a large complex of dark clouds where star formation proceeds in isolated pockets (Eiroa et al. 2008; Prato et al. 2008). The Perseus MC is the most active site of on-going star formation within 300 pc of the Sun. It features a large velocity gradient and is located close to hot stars that might have impacted its structure (Bally et al. 2008).

In the third group are IC 5146, Cepheus, and Orion, shown in Fig. 5 (left column). IC 5146 is an MC complex in Cygnus. It includes an open cluster surrounded by a bright optical nebulaosity called the Cocoon nebula, and a region of embedded lower-

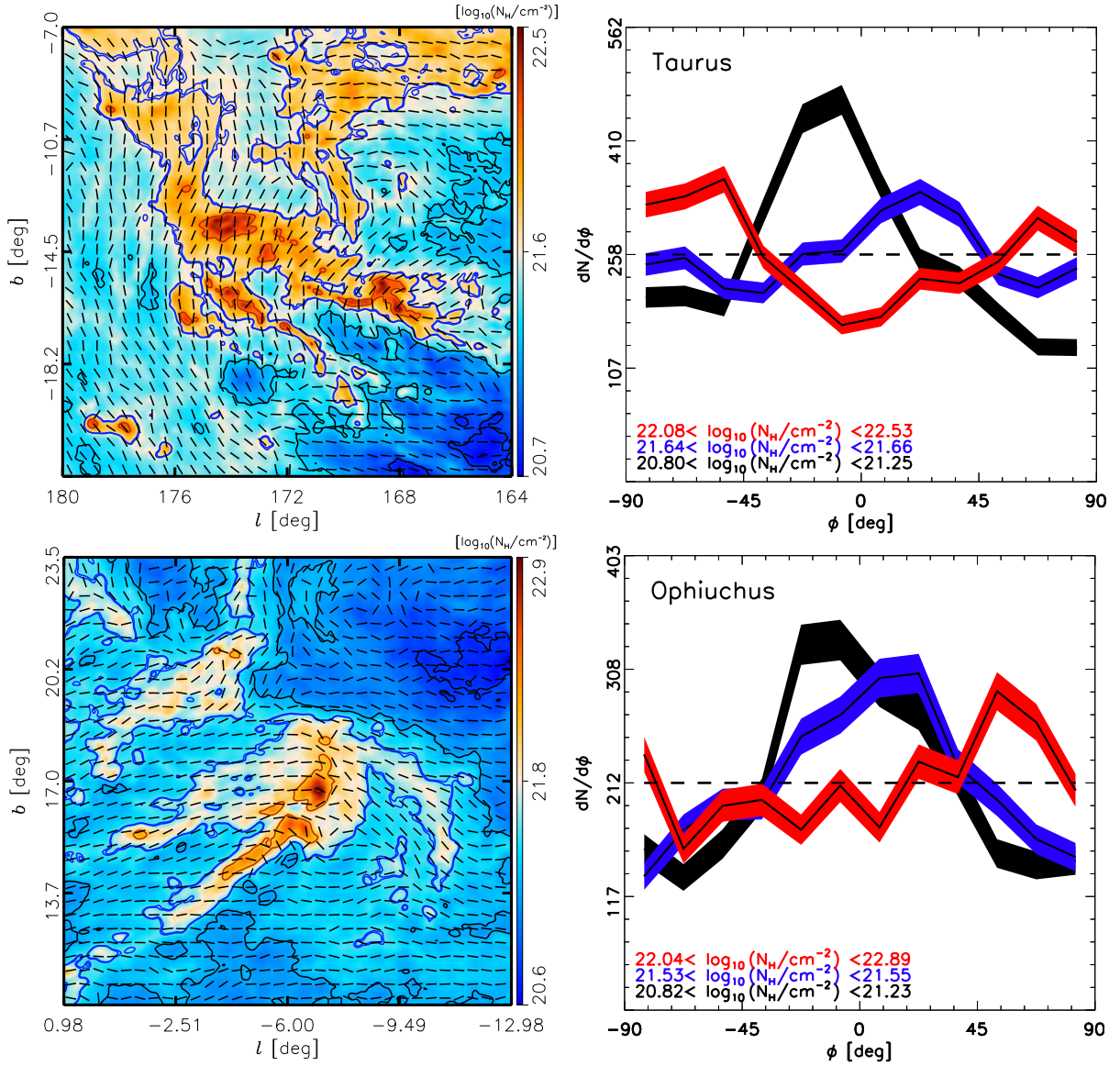


Fig. 3. *Left:* Column density map, $\log_{10}(N_H/\text{cm}^{-2})$, overlaid with magnetic field pseudo-vectors whose orientations are inferred from the *Planck* 353 GHz polarization observations. The length of the pseudo-vectors is normalized so does not reflect the polarization fraction. In this first group, the regions analysed are, from top to bottom, Taurus, Ophiuchus, Lupus, Chamaeleon-Musca, and CrA. *Right:* HROs for the lowest, an intermediate, and the highest N_H bin (black, blue, and red, respectively). For a given region, bins have equal numbers of selected pixels (see Sect. 4.1.1 and Appendix A) within the N_H ranges labelled. The intermediate bin corresponds to selected pixels near the blue contours in the column density images. The horizontal dashed line corresponds to the average per angle bin of 15° . The widths of the shaded areas for each histogram correspond to the $\pm 1 \sigma$ uncertainties related to the histogram binning operation. Histograms peaking at 0° correspond to \mathbf{B}_\perp predominantly aligned with iso- N_H contours. Histograms peaking at 90° and/or -90° correspond to \mathbf{B}_\perp predominantly perpendicular to iso- N_H contours.

mass star formation known as the IC 5146 Northern⁴ Streamer (Harvey et al. 2008). The Cepheus Flare, called simply Cepheus in this study, is a large complex of dark clouds that seems to belong to an even larger expanding shell from an old supernova remnant (Kun et al. 2008). Orion is a dark cloud complex with on-going high and low mass star formation, whose structure appears to be affected by multiple nearby hot stars (Bally 2008).

When taking background/foreground emission and noise within these regions into account, pixels are selected for analysis according to criteria for the gradient of the column density (Appendix A.2) and the polarization (Appendix A.2).

⁴ In equatorial coordinates.

4. Statistical study of the relative orientation of the magnetic field and column density structure

4.1. Methodology

4.1.1. Histogram of relative orientations

We quantify the relative orientation of the magnetic field with respect to the column density structures using the HRO (Soler et al. 2013). The column density structures are characterized by their gradients, which are by definition perpendicular to the iso-column density curves (see calculation in Appendix B.1). The gradient constitutes a vector field that we compare pixel by pixel

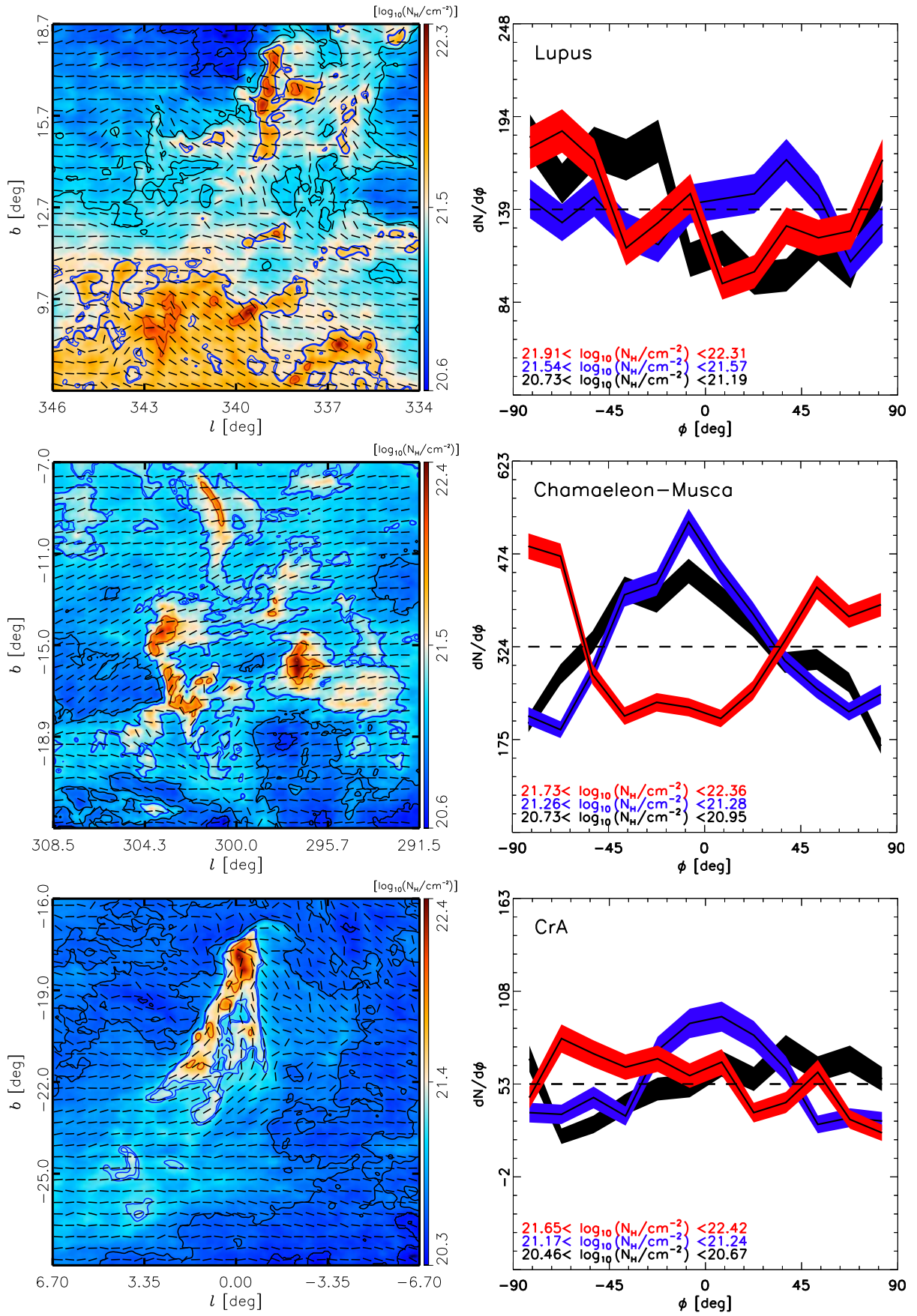


Fig. 3. (continued).

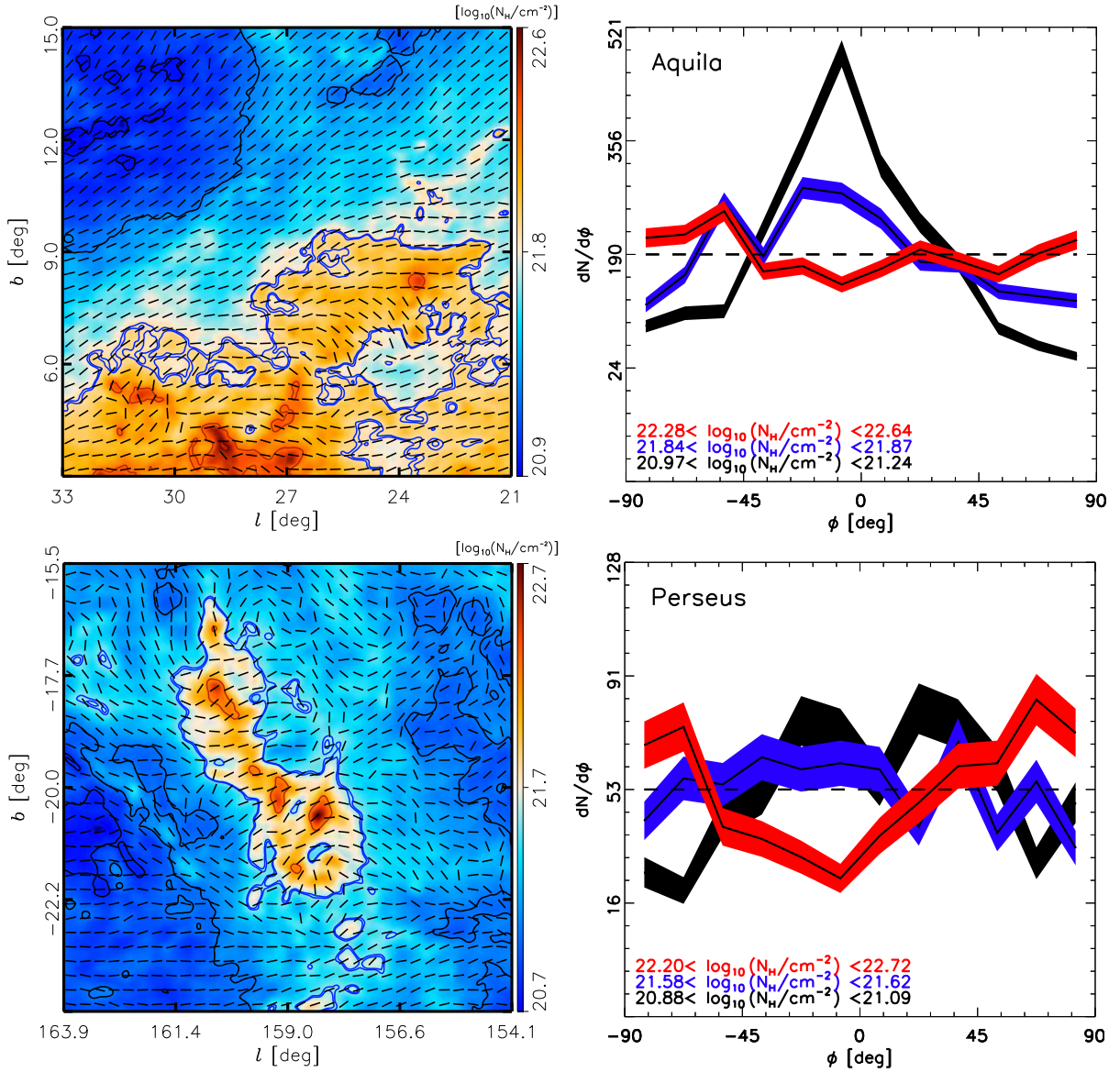


Fig. 4. Same as Fig. 3 for the second group, Aquila Rift and Perseus.

to the magnetic field orientation inferred from the polarization maps.

In practice we use τ_{353} as a proxy for N_H (Sect. 2.2). The angle ϕ between \mathbf{B}_\perp and the tangent to the τ_{353} contours is evaluated using⁵

$$\phi = \arctan\left(\frac{|\nabla \tau_{353} \times \hat{\mathbf{E}}|}{\nabla \tau_{353} \cdot \hat{\mathbf{E}}}\right), \quad (2)$$

where, as illustrated in Fig. 6, $\nabla \tau_{353}$ is perpendicular to the tangent of the iso- τ_{353} curves, the orientation of the unit polarization pseudo-vector $\hat{\mathbf{E}}$, perpendicular to \mathbf{B}_\perp , is characterized by the polarization angle

$$\psi = \frac{1}{2} \arctan(-U, Q), \quad (3)$$

and in Eq. (2), as implemented, the norm actually carries a sign when the range used for ϕ is between -90° and 90° .

⁵ In this paper we use the version of arctan with two signed arguments to resolve the π ambiguity in the orientation of pseudo-vectors (Planck Collaboration Int. XIX 2014).

The uncertainties in ϕ due to the variance of the τ_{353} map and the noise properties of Stokes Q and U at each pixel are characterized in Appendix B.

The gradient technique is one of multiple methods for characterizing the orientation of structures in a scalar field. Other methods, which include the Hessian matrix analysis (Molinari et al. 2011; Planck Collaboration Int. XXXII 2014) and the inertia matrix (Hennebelle 2013), are appropriate for measuring the orientation of ridges, i.e., the central regions of filamentary structures. The gradient technique is sensitive to contours and in that sense it is better suited to characterizing changes in the relative orientation in extended regions, not just on the crests of structures (Soler et al. 2013; Planck Collaboration Int. XXXII 2014). Additionally, the gradient technique can sample multiple scales by increasing the size of the vicinity of pixels used for its calculation (derivative kernel; see Appendix B.1). Previous studies that assign an average orientation of the cloud (Tassis et al. 2009; Li et al. 2013) are equivalent to studying the relative orientation using a derivative kernel close to the cloud size.

The selected pixels belong to the regions of each map where the magnitude of the gradient $|\nabla \tau_{353}|$ is greater than in a dif-

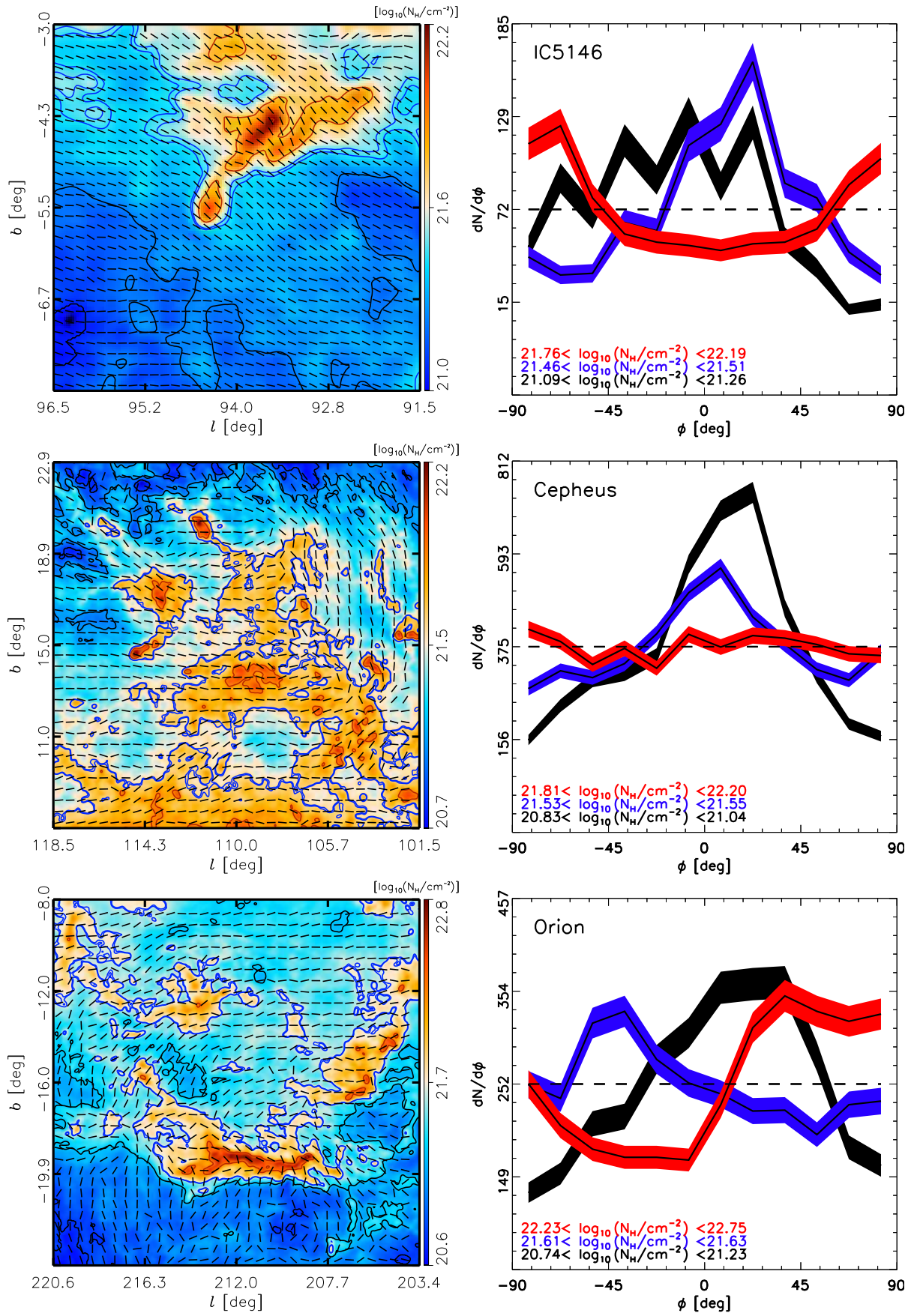


Fig. 5. Same as Fig. 3 for the third group, IC 5146, Cepheus, and Orion.

fuse reference field (Appendix A). This selection criterion aims at separating the structure of the cloud from the structure of the background using the reference field as a proxy. For each region the selected reference field is the region with the same size and Galactic latitude that has the lowest average N_H . See Appendix A.1.

In addition to the selection on $|\nabla\tau_{353}|$, we only consider pixels where the norms of the Stokes Q and U are larger than in the diffuse reference field, therefore minimizing the effect of background/foreground polarization external to the cloud. The relative orientation angle, ϕ , is computed by using polarization measurements with a high S/N in Stokes Q and U , i.e., only considering pixels with $|Q|/\sigma_Q$ or $|U|/\sigma_U > 3$. This selection allows the unambiguous definition of \hat{E} by constraining the uncertainty in the polarization angle (see Appendix A.2).

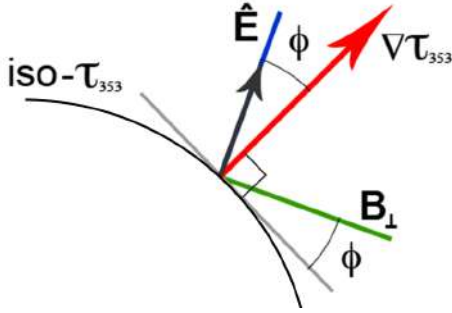


Fig. 6. Schematic of the vectors involved in the calculation of the relative orientation angle ϕ .

Once we have produced a map of relative orientations for selected pixels following Eq. (2), we divide the map into bins of N_H containing an equal number of pixels and generate a histogram of ϕ for each bin. The shape of the histogram is used to evaluate the preferred relative orientation in each bin directly. A concave histogram, peaking at 0° , corresponds to the preferred alignment of \mathbf{B}_\perp with the N_H contours. A convex histogram, peaking at 90° and/or -90° , corresponds to the preferred orientation of \mathbf{B}_\perp perpendicular to the N_H contours.

The HROs in each region are computed in 25 N_H bins having equal numbers of selected pixels (10 bins in two regions with fewer pixels, CrA and IC 5146). The number of N_H bins is determined by requiring enough bins to resolve the highest N_H regions and at the same time maintaining enough pixels per N_H bin to obtain significant statistics from each histogram. The typical number of pixels per bin of N_H ranges from approximately 600 in CrA to around 4 000 in Chamaeleon-Musca. We use 12 angle bins of width 15° .

The HROs of the first group of regions, the nearest at $d \approx 150$ pc, are shown in the right-hand column of Fig. 3. For the sake of clarity, we only present the histograms that correspond to three bins, namely the lowest and highest N_H and an intermediate N_H value. The intermediate bin is the 12th (sixth in two regions with fewer pixels, CrA and IC 5146), and it corresponds to pixels near the blue contour in the image in the left-hand column of Fig. 3. The widths of the shaded areas for each histogram correspond to the 1σ uncertainties related to the histogram binning operation, which are greater than the uncertainties produced by the variances of Q , U , and τ_{353} (Appendix B). The sharp and narrow features (“jitter”) in the HROs are independent of these variances. They are the product of sampling the spatial correlations in the magnetic field over a finite region of the sky together with

Table 2. Fit of ξ vs. $\log_{10}(N_H/\text{cm}^{-2})$.^a

Region	C_{HRO}	X_{HRO}
Taurus	−0.53	21.84
Ophiuchus	−0.22	22.70
Lupus	−0.28	21.72
Chamaeleon-Musca	−0.51	21.67
Corona Australia (CrA)	−0.11	24.14
Aquila Rift	−0.60	22.23
Perseus	−0.45	21.76
IC 5146	−0.68	21.79
Cepheus	−0.44	21.90
Orion	−0.28	21.88

^a See Eq. 6 and Fig. 7.

the histogram binning; these features average out when evaluating the relative orientation over larger portions of the sky (Planck Collaboration Int. XXXII 2014).

Although often asymmetric, most histograms reveal a change in the preferred relative orientation across N_H bins. The most significant feature in the HROs of Taurus, Ophiuchus, and Chamaeleon-Musca is the drastic change in relative orientation from parallel in the lowest N_H bin to perpendicular in the highest N_H bin. In Lupus the behaviour at low N_H is not clear, but at high N_H it is clearly perpendicular. In contrast, CrA tends to show \mathbf{B}_\perp as parallel in the intermediate N_H bin, but no preferred orientation in the other N_H bins.

The HROs of the clouds located at $d \approx 300$ pc, Aquila Rift and Perseus, are shown in the right-hand column of Fig. 4. They indicate that the relative orientation is usually parallel in the lowest N_H bins and perpendicular in the highest N_H bins.

The HROs of the third group, located at $d \approx 400 - 450$ pc, IC 5146, Cepheus, and Orion, are presented in the right-hand column of Fig. 5. In both IC 5146 and Orion the HROs for the highest N_H bins reveal a preferred orientation of the field perpendicular to the N_H contours (Orion is quite asymmetric), whereas the HROs corresponding to the low and intermediate N_H bins reveal a preferred alignment of the field with N_H structures. This trend is also present, but less pronounced, in the Cepheus region.

4.1.2. Histogram shape parameter ξ

The changes in the HROs are quantified using the histogram shape parameter ξ , defined as

$$\xi = \frac{A_c - A_e}{A_c + A_e}, \quad (4)$$

where A_c is the area in the centre of the histogram ($-22.5^\circ < \phi < 22.5^\circ$) and A_e the area in the extremes of the histogram ($-90^\circ < \phi < -67.5^\circ$ and $67.5^\circ < \phi < 90^\circ$). The value of ξ , the result of the integration of the histogram over 45° ranges, is independent of the number of bins selected to represent the histogram if the bin widths are smaller than the integration range.

A concave histogram corresponding to \mathbf{B}_\perp mostly aligned with N_H contours would have $\xi > 0$. A convex histogram corresponding to \mathbf{B}_\perp mostly perpendicular to N_H contours would have $\xi < 0$. A flat histogram corresponding to no preferred relative orientation would have $\xi \approx 0$.

The uncertainty in ξ , σ_ξ , is obtained from

$$\sigma_\xi^2 = \frac{4(A_c^2\sigma_{A_c}^2 + A_e^2\sigma_{A_e}^2)}{(A_c + A_e)^4}. \quad (5)$$

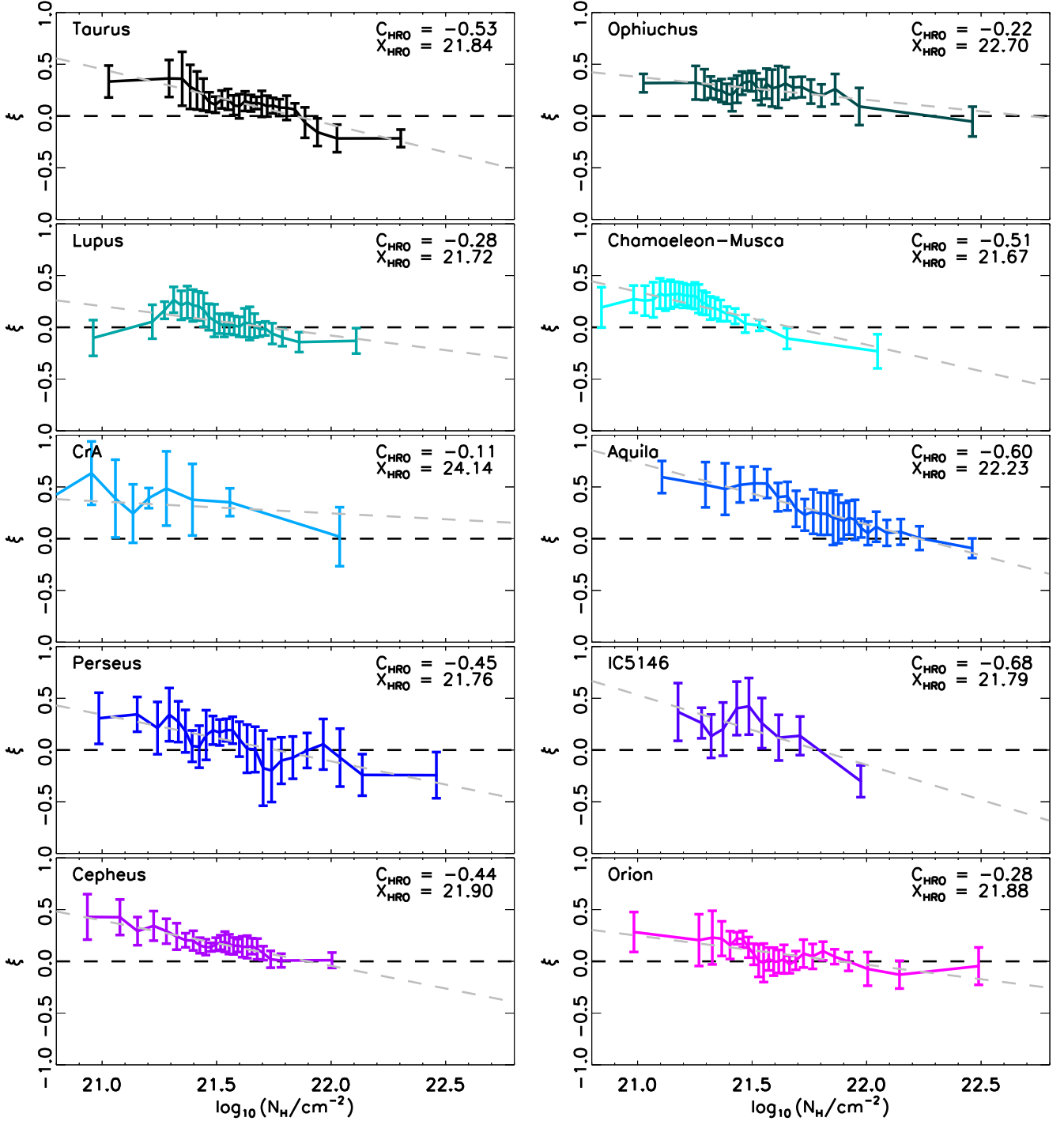


Fig. 7. Histogram shape parameter ξ (Eqs. 4 and 5) calculated for the different N_{H} bins in each region. The cases $\xi > 0$ and $\xi < 0$ correspond to the magnetic field oriented mostly parallel and perpendicular to the structure contours, respectively. For $\xi \approx 0$ there is no preferred orientation. The displayed values of C_{HRO} and X_{HRO} were calculated from Eq. (6) and correspond to the grey dashed line in each plot.

The variances of the areas, $\sigma_{A_e}^2$ and $\sigma_{A_c}^2$, characterize the jitter of the histograms. If the jitter is large, σ_{ξ} is large compared to $|\xi|$ and the relative orientation is indeterminate. The jitter depends on the number of bins in the histogram, but ξ does not.

Figure 7 illustrates the change in ξ as a function of $\log_{10}(N_{\text{H}}/\text{cm}^{-2})$ of each bin. For most of the clouds, ξ is positive in the lowest and intermediate N_{H} bins and negative or close to zero in the highest bins. The most pronounced changes

in ξ from positive to negative are seen in Taurus, Chamaeleon-Musca, Aquila Rift, Perseus, and IC 5146.

The trend in ξ vs. $\log_{10}(N_{\text{H}}/\text{cm}^{-2})$ can be fit roughly by a linear relation

$$\xi = C_{\text{HRO}} [\log_{10}(N_{\text{H}}/\text{cm}^{-2}) - X_{\text{HRO}}]. \quad (6)$$

The values of C_{HRO} and X_{HRO} in the regions analysed are summarized in Table 2. For the clouds with a pronounced change in relative orientation the slope C_{HRO} is steeper than about -0.5 ,

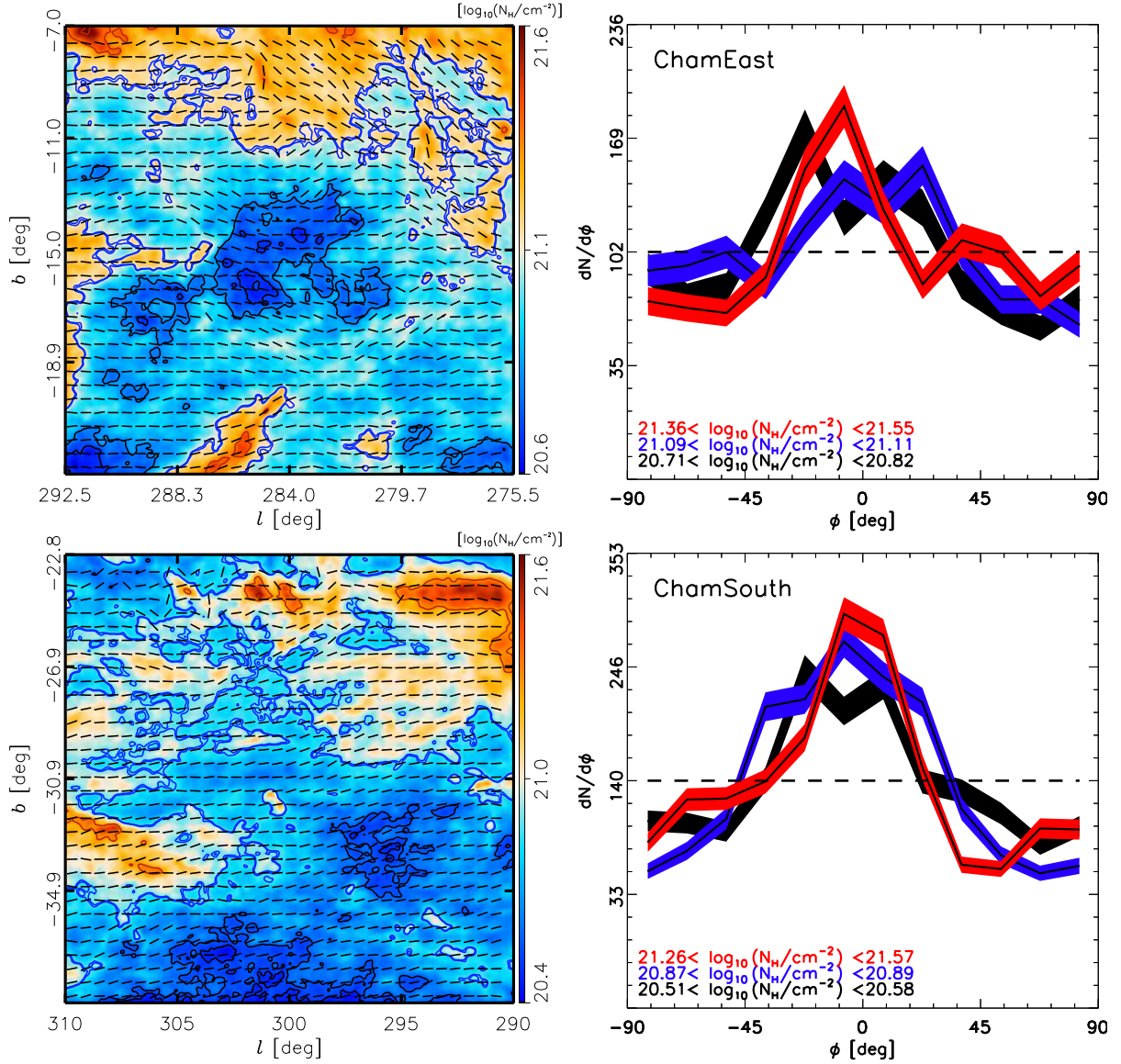


Fig. 8. Same as Fig. 3 for the two test regions located directly east (ChamEast) and south of Chamaeleon-Musca (ChamSouth).

and the value X_{HRO} for the $\log_{10}(N_H/\text{cm}^{-2})$ at which the relative orientation changes from parallel to perpendicular is greater than about 21.7. Ophiuchus, Lupus, Cepheus, and Orion are intermediate cases, where ξ definitely does not go negative in the data, but seems to do so by extrapolation; these tend to have a shallower C_{HRO} and/or a higher X_{HRO} .

The least pronounced change in ξ is seen in CrA, where ξ is consistently positive in all bins, and the slope is very flat. We applied the HRO analysis to a pair of test regions (Fig. 8) with even lower N_H values ($\log_{10}(N_H/\text{cm}^{-2}) < 21.6$; see also Fig. 11 below) located directly south and directly east of the Chamaeleon-Musca region. As in CrA, we find that \mathbf{B}_\perp is mostly parallel to the N_H contours, a fairly constant ξ , and no indication of predominantly perpendicular relative orientation.

4.2. Comparisons with previous studies

The above trends in relative orientation between \mathbf{B}_\perp and the N_H contours in targeted MCs, where \mathbf{B}_\perp tend to become perpendicular to the N_H contours at high N_H , agree with the results of the Hessian matrix analysis applied to *Planck* observations over the

whole sky, as reported in Fig. 15 of [Planck Collaboration Int. XXXII \(2014\)](#).

Evidence for preferential orientations in sections of some regions included in this study has been reported previously. The Taurus region has been the target of many studies. [Moneti et al. \(1984\)](#) and [Chapman et al. \(2011\)](#) find evidence using infrared polarization of background stars for a homogeneous magnetic field perpendicular to the embedded dense filamentary structure. High-resolution submillimetre observations of intensity with *Herschel* find evidence of faint filamentary structures (“striations”), which are well correlated with the magnetic field orientation inferred from starlight polarization ([Palmeirim et al. 2013](#)) and perpendicular to the filament B211. [Heyer et al. \(2008\)](#) report a velocity anisotropy aligned with the magnetic field, which can be interpreted as evidence of the channeling effect of the magnetic fields. But the magnetic field in B211 and the dense filamentary structures are not measured directly. As described above, using *Planck* polarization we find that \mathbf{B}_\perp is mostly aligned with the lowest N_H contours ($20.8 < \log_{10}(N_H/\text{cm}^{-2}) < 21.3$) (see also [Planck Collaboration Int. XXXIII 2014](#)), although the aligned structures do not correspond to the striations,

which are not resolved at $10'$ resolution. However, we also find that at higher N_H the relative orientation becomes perpendicular.

Similar studies in other regions have found evidence of striations correlated with the starlight-inferred magnetic field orientation and perpendicular to the densest filamentary structures. The regions studied include Serpens South (Sugitani et al. 2011), which is part of Aquila Rift in this study, Musca (Pereyra & Magalhães 2004), and the Northern Lupus cloud (Matthews et al. 2014). By studying *Planck* polarization in larger regions around the targets of these previous observations, we show that a systematic change in relative orientation is the prevailing statistical trend in clouds that reach $\log_{10}(N_H/\text{cm}^{-2}) \gtrsim 21.5$.

5. Discussion

5.1. The relative orientation between \mathbf{B}_\perp and N_H structures

5.1.1. Spatial distribution of the HRO signal

The maps obtained using Eq. (2) characterize the relative orientation in each region, without assuming an organization of the N_H structures in ridges or filaments; HROs basically just sample the orientation of N_H contours. However, the resulting maps of the relative orientation angle, shown for the Taurus region in Fig. 9, reveal that the regions that are mostly oriented parallel or perpendicular to the field form continuous patches, indicating that the HRO signal is not only coming from variations in the field or the N_H contours at the smallest scales in the map.

HRO analysis on larger scales in a map can be achieved by considering a larger vicinity of pixels for calculating the gradient $\nabla\tau_{353}$. This operation is equivalent to calculating the next-neighbour gradient on a map first smoothed to the scale of interest. The results for relative orientation after smoothing to resolutions of $15'$, $30'$, and $60'$ are illustrated for the Taurus region in Fig. 9. Figure 10 shows that the corresponding HROs have a similar behaviour for the three representative N_H values. These results confirm that the preferred relative orientation is not particular to the smallest scales in the map, but corresponds to coherent structures in N_H .

A study of the preferred orientation for the whole cloud would be possible by smoothing the column density and polarization maps to a scale comparable to the cloud size. The statistical significance of such a study would be limited to the number of clouds in the sample and would not be directly comparable to previous studies of relative orientation of clouds, where elongated structures were selected to characterize the mean orientation of each cloud (Li et al. 2013).

5.1.2. Statistical significance of the HRO signal

Our results reveal a systemic change of ξ with N_H , suggesting a systematic transition from magnetic field mostly parallel to N_H contours in the lowest N_H bins to mostly perpendicular in the highest N_H bins of the clouds studied. The statistical significance of this change can in principle be evaluated by considering the geometrical effects that influence this distribution. In Appendix C.1, using simulations of Q and U maps, we eliminate the possibility that this arises from random magnetic fields, random spatial correlations in the field, or the large scale structure of the field. In Appendix C.2 we simply displace the Q and U maps spatially and repeat the analysis, showing that the systemic trend of ξ vs. N_H disappears for displacements greater than 1° .

Using a set of Gaussian models, Planck Collaboration Int. XXXII (2014) estimated the statistical significance of this transition in terms of the relative orientation between two vectors in 3D and their projection in 2D. As these authors emphasized, two vectors that are close to parallel in 3D would be projected as parallel in 2D for almost all viewing angles for which the projections of both vectors have a non-negligible length, but on the other hand, the situation is more ambiguous seen in projection for two vectors that are perpendicular in 3D, because they can be projected as parallel in 2D depending on the angle of viewing. The quantitative effects are illustrated by the simulations in Appendix C.3, where we consider distributions of vectors in 3D that are mostly parallel, mostly perpendicular, or have no preferred orientation. The projection tends to make vector pairs look more parallel in 2D, but the distribution of relative orientations in 2D is quite similar though not identical to the distribution in 3D. In particular, the signal of perpendicular orientation is not erased and we can conclude that two projected vectors with non-negligible lengths that are close to perpendicular in 2D must also be perpendicular in 3D. This would apply to the mostly perpendicular orientation for the highest bin of N_H in the Taurus region.

5.2. Comparison with simulations of MHD turbulence

As a complement to observations, MHD simulations can be used to directly probe the actual 3D orientation of the magnetic field \mathbf{B} with respect to the density structures. The change in the relative orientation with N_H was previously studied in MHD simulations using the inertia matrix and the HRO analysis (Hennebelle 2013; Soler et al. 2013). Soler et al. (2013) showed that in 3D, the change in the relative orientation is related to the degree of magnetization. If the magnetic energy is above or comparable to the kinetic energy (turbulence that is sub-Alfvénic or close to equipartition), the less dense structures tend to be aligned with the magnetic field and the orientation progressively changes from parallel to perpendicular with increasing density. In the super-Alfvénic regime, where the magnetic energy is relatively low, there appears to be no change in relative orientation with increasing density, with \mathbf{B} and density structures being mostly parallel.

Soler et al. (2013) describe 2D synthetic observations of the MHD simulations. The synthetic observations are produced by integrating the simulation cubes along a direction perpendicular to the mean magnetic field and assuming a homogeneous dust grain alignment efficiency $\epsilon = 1.0$. The angular resolution of the simulation is obtained by assuming a distance $d = 150$ pc and convolving the projected map with a Gaussian beam of $10'$ full width at half maximum (FWHM). The trends in the relative orientation with N_H seen in 3D are also seen using these 2D synthetic observations. Given that sub-Alfvénic or close to Alfvénic turbulence does not significantly disturb the well-ordered mean magnetic field, the orientation of \mathbf{B} perpendicular to the iso-density contours is projected well for lines of sight that are not close to the mean magnetic field orientation. In contrast, the projected relative orientation produced by super-Alfvénic turbulence does not necessarily reflect the relative orientation in 3D as a result of the unorganized field structure.

The direct comparison between the HROs of the regions in this study and of the synthetic observations is presented in Fig. 11. The trends in the relative orientation parameter, ξ , show that the simulation with super-Alfvénic turbulence does not undergo a transition in relative orientation from parallel to perpendicular for $\log_{10}(N_H/\text{cm}^{-2}) < 23$. In contrast, most of the observed clouds show a decrease in ξ with increasing N_H , close

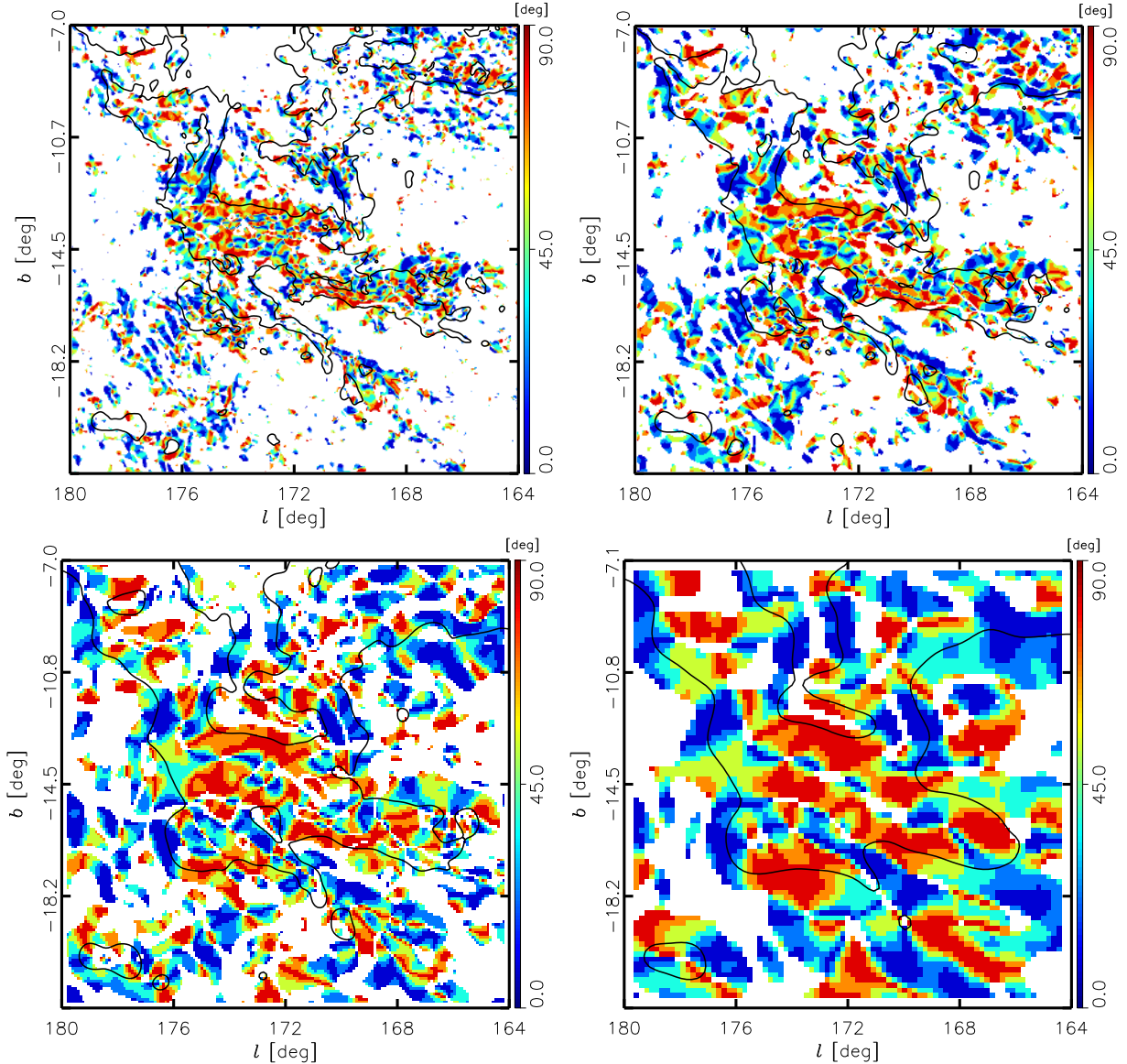


Fig. 9. Maps of the absolute value of the relative orientation angle, $|\phi|$, in the Taurus region. These maps are produced after smoothing the input maps to beam FWHMs of $10'$, $15'$, $30'$, and $60'$ and then resampling the grid to sample each beam FWHM with the same number of pixels. The regions in red correspond to \mathbf{B}_\perp close to perpendicular to N_H structures. The regions in blue correspond to \mathbf{B}_\perp close to parallel to N_H structures. The black contour, corresponding to the N_H value of the intermediate contour introduced in Fig. 3, provides a visual reference to the cloud structure.

to the trends seen from the simulations with Alfvénic or sub-Alfvénic turbulence for $\log_{10}(N_H/\text{cm}^{-2}) < 23$. Furthermore, X_{HRO} , the value of $\log_{10}(N_H/\text{cm}^{-2})$ where ξ goes through zero, is near 21.7, which is consistent with the behaviour seen in the simulations with super-Alfvénic or Alfvénic turbulence. Given that the physical conditions in the simulations ($\sigma_v = 2.0 \text{ km s}^{-1}$ and $n = 500 \text{ cm}^{-3}$) are typical of those in the selected regions (σ_{v_\parallel} is given in Table D.1), the similarities in the dependence of ξ on N_H suggest that the strength of the magnetic field in most of the regions analysed would be about the same as the mean magnetic fields in the Alfvénic and sub-Alfvénic turbulence simulations, which are 3.5 and $11 \mu\text{G}$, respectively. However, more precise estimates of the magnetic field strength coming directly from the HROs would require further sampling of the magnetization in the MHD simulations and detailed modelling of the effects of the line-of-sight integration.

Indirectly, the presence of a N_H threshold in the switch in preferred relative orientation between \mathbf{B}_\perp and the N_H structures hints that gravity plays a significant role. By contrast, for the regions with low average N_H (i.e., CrA and the two test regions; Fig. 11), there is little change in ξ and certainly no switch in the preferred relative orientation to perpendicular.

5.3. Physics of the relative orientation

The finding of dense structures mostly perpendicular to the magnetic field (and the small mass-to-flux ratios discussed in Appendix D.4) suggests that the magnetic field in most of the observed regions is significant for the structure and dynamics. However, discerning the underlying geometry is not obvious. As one guide, a frozen-in and strong interstellar magnetic field would naturally cause a self-gravitating, static cloud to become oblate, with its major axis perpendicular to the field lines, be-

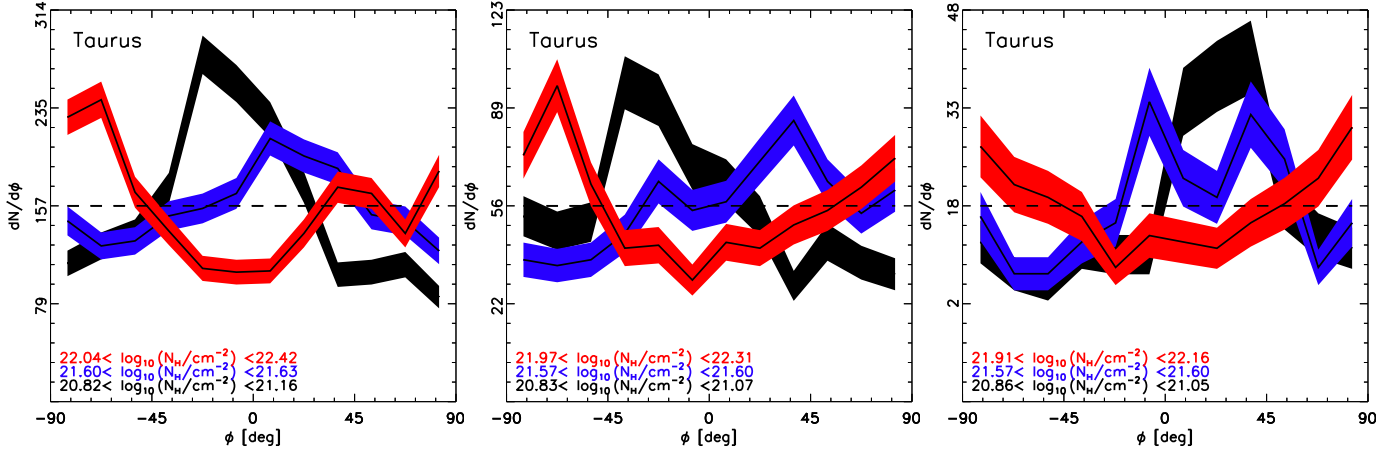


Fig. 10. HROs of the Taurus region after smoothing the input maps to beam FWHMs of 15', 30', and 60', shown from left to right, respectively.

cause gravitational collapse would be restricted to occurring along field lines (Mouschovias 1976a,b). In the case of less dense structures that are not self-gravitating, the velocity shear can stretch matter and field lines in the same direction, thereby producing aligned structures, as discussed in Hennebelle (2013) and Planck Collaboration Int. XXXII (2014).

If the MCs are isolated entities and the magnetic field is strong enough to set a preferred direction for the gravitational collapse, the condensations embedded in the cloud are not very likely to have higher column densities than their surroundings (Nakano 1998). This means that the formation of dense substructures, such as prestellar cores and stars, by gravitational collapse would be possible only if the matter decouples from the magnetic field. This is possible through the decoupling between neutral and ionized species (ambipolar diffusion, Mouschovias 1991; Li & Houde 2008) or through removal of magnetic flux from clouds via turbulent reconnection (Lazarian & Vishniac 1999; Santos-Lima et al. 2012).

Alternatively, if we regard MCs not as isolated entities but as the result of an accumulation of gas by large-scale flows (Ballesteros-Paredes et al. 1999; Hartmann et al. 2001; Koyama & Inutsuka 2002; Audit & Hennebelle 2005; Heitsch et al. 2006), the material swept up by colliding flows may eventually form a self-gravitating cloud. If the magnetic field is strong the accumulation of material is favoured along the magnetic field lines, thus producing dense structures that are mostly perpendicular to the magnetic field. The inflow of material might eventually increase the gravitational energy in parts of the cloud, thereby producing supercritical structures such as prestellar cores.

For supersonic turbulence in the ISM and MCs, density structures can be formed by gas compression in shocks. If the turbulence is strong with respect to the magnetic field (super-Alfvénic), gas compression by shocks is approximately isotropic; because magnetic flux is frozen into matter, field lines are dragged along with the gas, forming structures that tend to be aligned with the field. If the turbulence is weak with respect to the magnetic field (sub-Alfvénic), the fields produce a clear anisotropy in MHD turbulence (Sridhar & Goldreich 1994; Goldreich & Sridhar 1995; Mattheaus et al. 2008; Banerjee et al. 2009) and compression by shocks that is favored to occur along the magnetic field lines, creating structures perpendicular to the field. The cold phase gas that constitutes the cloud receives no information about the original flow direction because the mag-

netic field redistributes the kinetic energy of the inflows (Heitsch et al. 2009; Inoue & Inutsuka 2009; Burkhart et al. 2014). This seems to be the case in most of the observed regions, where the mostly perpendicular relative orientation between the magnetic field and the high column density structures is an indication of the anisotropy produced by the field.

The threshold of $\log_{10}(N_{\text{H}}/\text{cm}^{-2}) \approx 21.7$ above which the preferential orientation of B_{\perp} switches to being perpendicular to the N_{H} contours is intriguing. Is there a universal threshold column density that is independent of the particular MC environment and relevant in the context of star formation? In principle, this threshold might be related to the column density of filaments at which substructure forms, as reported in an analysis of *Herschel* observations (Arzoumanian et al. 2013), but the *Planck* polarization observations leading to B_{\perp} do not fully resolve such filamentary structures. In principle, this threshold might also be related to the column density at which the magnetic field starts scaling with density, according to the Zeeman effect observations of B_{\parallel} (Figure 7 in Crutcher 2012). However, establishing such relationships requires further studies with MHD simulations to identify what densities and scales influence the change in relative orientation between B_{\perp} and N_{H} structures and to model the potential imprint in B_{\parallel} observations and in B_{\perp} observations to be carried out at higher resolution.

5.4. Effect of dust grain alignment

Throughout this study we assume that the polarized emission observed by *Planck* at 353 GHz is representative of the projected morphology of the magnetic field in each region; i.e., we assume a constant dust grain alignment efficiency (ϵ) that is independent of the local environment. Indeed, observations and MHD simulations under this assumption (Planck Collaboration Int. XIX 2014; Planck Collaboration Int. XX 2014) indicate that depolarization effects at large and intermediate scales in MCs might arise from the random component of the magnetic field along the line of sight. On the other hand, the sharp drop in the polarization fraction at $N_{\text{H}} > 10^{22} \text{ cm}^{-2}$ (reported in Planck Collaboration Int. XIX 2014), when seen at small scales, might be interpreted in terms of a decrease of ϵ with increasing column density (Matthews et al. 2001; Whittet et al. 2008).

A leading theory for the process of dust grain alignment involves radiative torques by the incident radiation (Lazarian & Hoang 2007; Hoang & Lazarian 2009; Andersson 2015). A crit-

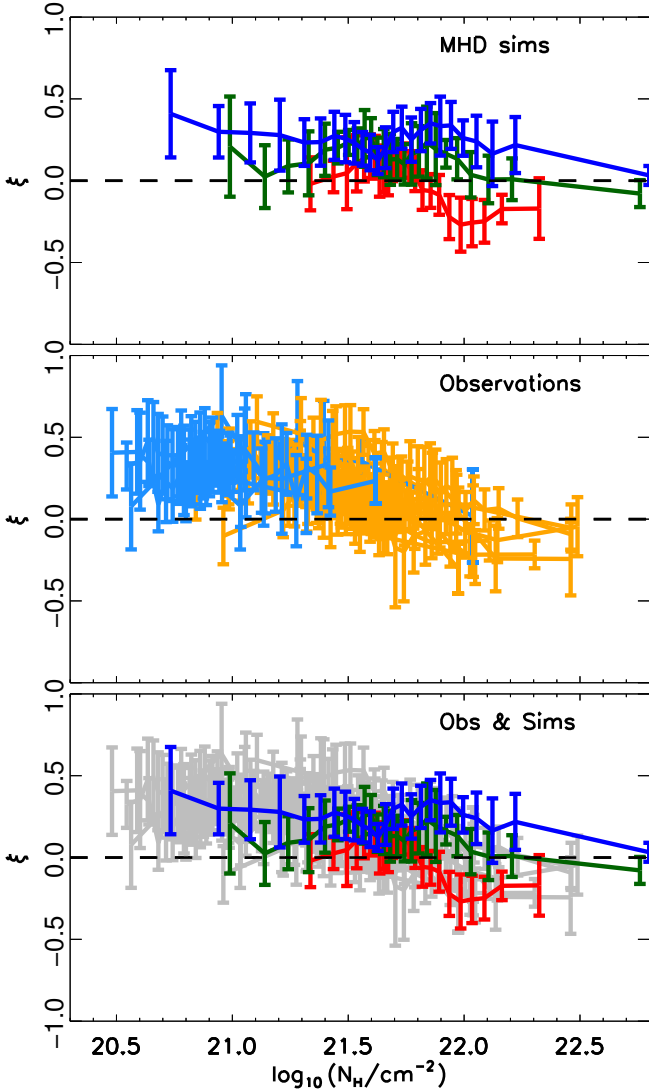


Fig. 11. Histogram shape parameter ξ (Eqs. 4 and 5) calculated for the different N_{H} bins in each region. *Top:* relative orientation in synthetic observations of simulations with super-Alfvénic (blue), Alfvénic (green), and sub-Alfvénic (red) turbulence, as detailed in Soler et al. (2013). *Middle:* relative orientation in the regions selected from the *Planck* all-sky observations, from Fig. 7. The blue data points correspond to the lowest N_{H} regions (CrA and the test regions in Fig. 8, ChamSouth and ChamEast) and the orange correspond to the rest of the clouds. *Bottom:* comparison between the trends in the synthetic observations (in colours) and the regions studied (grey). The observed smooth transition from mostly parallel ($\xi > 0$) to perpendicular ($\xi < 0$) is similar to the transition in the simulations for which the turbulence is Alfvénic or sub-Alfvénic.

ical parameter for this mechanism is the ratio between the dust grain size and the radiation wavelength. As the dust column density increases, only the longer wavelength radiation penetrates the cloud and the alignment decreases. Grains within a cloud (without embedded sources) should have lower ϵ than those at the periphery of the same cloud. There is evidence for this from near-infrared interstellar polarization and submillimetre polarization along lines of sight through starless cores (Jones et al. 2015), albeit on smaller scales and higher column densities than considered here. If ϵ inside the cloud is very low, the observed

polarized intensity would arise from the dust in the outer layers, tracing the magnetic field in the “skin” of the cloud. Then the observed orientation of \mathbf{B}_{\perp} is not necessarily correlated with the column density structure, which is seen in total intensity, or with the magnetic field deep in the cloud.

Soler et al. (2013) presented the results of HRO analysis on a series of synthetic observations produced using models of how ϵ might decrease with increasing density. They showed that with a steep decrease there is no visible correlation between the inferred magnetic field orientation and the high- N_{H} structure, corresponding to nearly flat HROs.

The HRO analysis of MCs carried out here reveals a correlation between the polarization orientation and the column density structure. This suggests that the dust polarized emission samples the magnetic field structure homogeneously on the scales being probed at the resolution of the *Planck* observations or, alternatively, that the field deep within high- N_{H} structures has the same orientation of the field in the skin.

6. Conclusions

We have presented a study of the relative orientation of the magnetic field projected on the plane of the sky (\mathbf{B}_{\perp}), as inferred from the *Planck* dust polarized thermal emission, with respect to structures detected in gas column density (N_{H}). The relative orientation study was performed by using the histogram of relative orientations (HRO), a novel statistical tool for characterizing extended polarization maps. With the unprecedented statistics of polarization observations in extended maps obtained by *Planck*, we analyze the HRO in regions with different column densities within ten nearby molecular clouds (MCs) and two test fields.

In most of the regions analysed we find that the relative orientation between \mathbf{B}_{\perp} and N_{H} structures changes systematically with N_{H} from being parallel in the lowest column density areas to perpendicular in the highest column density areas. The switch occurs at $\log_{10}(N_{\text{H}}/\text{cm}^{-2}) \approx 21.7$. This change in relative orientation is particularly significant given that projection tends to produce more parallel pseudo-vectors in 2D (the domain of observations) than exist in 3D.

The HROs in these MCs reveal that most of the high N_{H} structures in each cloud are mostly oriented perpendicular to the magnetic field, suggesting that they may have formed by material accumulation and gravitational collapse along the magnetic field lines. According to a similar study where the same method was applied to MHD simulations, this trend is only possible if the turbulence is Alfvénic or sub-Alfvénic. This implies that the magnetic field is significant for the gas dynamics on the scales sampled by *Planck*. The estimated mean magnetic field strength is about 4 and 12 μG for the case of Alfvénic and sub-Alfvénic turbulence, respectively.

We also estimate the magnetic field strength in the MCs studied using the DCF and DCF+SF methods. The estimates found seem consistent with the above values from the HRO analysis, but given the assumptions and systematic effects involved, we recommend that these rough estimates be treated with caution. According to these estimates the analysed regions appear to be magnetically sub-critical. This result is also consistent with the conclusions of the HRO analysis. Specific tools, such as the DCF and DCF+SF methods, are best suited to the scales and physical conditions in which their underlying assumptions are valid. The study of large polarization maps covering multiple scales calls for generic statistical tools, such as the HRO, for characterizing their properties and establishing a direct relation to the physical conditions included in MHD simulations.

The study of the structure on smaller scales is beyond the scope of this work, however, the presence of gravitationally bound structures within the MCs, such as prestellar cores and stars, suggests that the role of magnetic fields is changing on different scales. Even if the magnetic field is important in the accumulation of matter that leads to the formation of the cloud, effects such as matter decoupling from the magnetic field and the inflow of matter from the cloud environment lead to the formation of magnetically supercritical structures on smaller scales. Further studies will help to identify the dynamical processes that connect the MC structure with the process of star formation.

Acknowledgements. The development of *Planck* has been supported by: ESA; CNES and CNRS/INSU-IN2P3-INP (France); ASI, CNR, and INAF (Italy); NASA and DoE (USA); STFC and UKSA (UK); CSIC, MICINN, JA, and RES (Spain); Tekes, AoF, and CSC (Finland); DLR and MPG (Germany); CSA (Canada); DTU Space (Denmark); SER/SSO (Switzerland); RCN (Norway); SFI (Ireland); FCT/MCTES (Portugal); and PRACE (EU). A description of the Planck Collaboration and a list of its members, including the technical or scientific activities in which they have been involved, can be found at http://www.sciops.esa.int/index.php?project=planck&page=Planck_Collaboration. The research leading to these results has received funding from the European Research Council under the European Union's Seventh Framework Programme (FP7/2007-2013) / ERC grant agreement No. 267934.

References

- Andersson, B.-G. 2015, in *Astrophysics and Space Science Library*, Vol. 407, *Astrophysics and Space Science Library*, ed. A. Lazarian, E. M. de Gouveia Dal Pino, & C. Melioli, 59
- Arzoumanian, D., André, P., Peretto, N., & Könyves, V. 2013, *A&A*, 553, A119
- Audit, E. & Hennebelle, P. 2005, *A&A*, 433, 1
- Ballesteros-Paredes, J., Hartmann, L., & Vázquez-Semadeni, E. 1999, *ApJ*, 527, 285
- Bally, J. 2008, *Overview of the Orion Complex*, ed. B. Reipurth, 459
- Bally, J., Walawender, J., Johnstone, D., Kirk, H., & Goodman, A. 2008, *The Perseus Cloud*, ed. B. Reipurth, 308
- Banerjee, R., Vázquez-Semadeni, E., Hennebelle, P., & Klessen, R. S. 2009, *MNRAS*, 398, 1082
- Benoît, A., Ade, P., Amblard, A., et al. 2004, *A&A*, 424, 571
- Bergin, E. A. & Tafalla, M. 2007, *ARA&A*, 45, 339
- Bierman, E. M., Matsumura, T., Dowell, C. D., et al. 2011, *ApJ*, 741, 81
- Burkhart, B., Lazarian, A., Leão, I. C., de Medeiros, J. R., & Esquivel, A. 2014, *ApJ*, 790, 130
- Cabral, B. & Leedom, L. C. 1993, in *Special Interest Group on GRAPHics and Interactive Techniques Proceedings*, *Special Interest Group on GRAPHics and Interactive Techniques Proceedings*, 263–270
- Chandrasekhar, S. & Fermi, E. 1953, *ApJ*, 118, 113
- Chapman, N. L., Goldsmith, P. F., Pineda, J. L., et al. 2011, *ApJ*, 741, 21
- Comerón, F. 2008, *The Lupus Clouds*, ed. B. Reipurth, 295
- Crutcher, R. M. 2005, in *American Institute of Physics Conference Series*, Vol. 784, *Magnetic Fields in the Universe: From Laboratory and Stars to Primordial Structures*, ed. E. M. de Gouveia dal Pino, G. Lugones, & A. Lazarian, 129–139
- Crutcher, R. M. 2012, *ARA&A*, 50, 29
- Crutcher, R. M., Nutter, D. J., Ward-Thompson, D., & Kirk, J. M. 2004, *ApJ*, 600, 279
- Crutcher, R. M., Wandelt, B., Heiles, C., Falgarone, E., & Troland, T. H. 2010, *ApJ*, 725, 466
- Dame, T. M., Hartmann, D., & Thaddeus, P. 2001, *ApJ*, 547, 792
- Davis, L. 1951, *Physical Review*, 81, 890
- Davis, Jr., L. & Greenstein, J. L. 1951, *ApJ*, 114, 206
- Dotson, J. L. 1996, *ApJ*, 470, 566
- Dotson, J. L., Davidson, J., Dowell, C. D., Schleuning, D. A., & Hildebrand, R. H. 2000, *ApJS*, 128, 335
- Draine, B. T. 2011, *Physics of the Interstellar and Intergalactic Medium*
- Eiroa, C., Djupvik, A. A., & Casali, M. M. 2008, *The Serpens Molecular Cloud*, ed. B. Reipurth, 693
- Elmegreen, B. G. & Scalo, J. 2004, *ARA&A*, 42, 211
- Falseta-Gonçalves, D., Lazarian, A., & Kowal, G. 2008, *ApJ*, 679, 537
- Franco, G. A. P., Alves, F. O., & Girart, J. M. 2010, *ApJ*, 723, 146
- Goldreich, P. & Sridhar, S. 1995, *ApJ*, 438, 763
- Górski, K. M., Hivon, E., Banday, A. J., et al. 2005, *ApJ*, 622, 759
- Hartmann, L., Ballesteros-Paredes, J., & Bergin, E. A. 2001, *ApJ*, 562, 852
- Harvey, P. M., Huard, T. L., Jørgensen, J. K., et al. 2008, *ApJ*, 680, 495
- Heiles, C. & Haverkorn, M. 2012, *Space Sci. Rev.*, 166, 293
- Heitsch, F., Slyz, A. D., Devriendt, J. E. G., Hartmann, L. W., & Burkert, A. 2006, *ApJ*, 648, 1052
- Heitsch, F., Stone, J. M., & Hartmann, L. W. 2009, *ApJ*, 695, 248
- Heitsch, F., Zweibel, E. G., Mac Low, M.-M., Li, P., & Norman, M. L. 2001, *ApJ*, 561, 800
- Hennebelle, P. 2013, *A&A*, 556, A153
- Hennebelle, P. & Falgarone, E. 2012, *A&A Rev.*, 20, 55
- Heyer, M., Gong, H., Ostriker, E., & Brunt, C. 2008, *ApJ*, 680, 420
- Hildebrand, R. H. 1988, *QJRAS*, 29, 327
- Hildebrand, R. H., Kirby, L., Dotson, J. L., Houde, M., & Vaillancourt, J. E. 2009, *ApJ*, 696, 567
- Hiltner, W. A. 1949, *Science*, 109, 165
- Hoang, T. & Lazarian, A. 2009, *ApJ*, 697, 1316
- Houde, M., Fletcher, A., Beck, R., et al. 2013, *ApJ*, 766, 49
- Houde, M., Rao, R., Vaillancourt, J. E., & Hildebrand, R. H. 2011, *ApJ*, 733, 109
- Houde, M., Vaillancourt, J. E., Hildebrand, R. H., Chitsazzadeh, S., & Kirby, L. 2009, *ApJ*, 706, 1504
- Inoue, T. & Inutsuka, S.-i. 2009, *ApJ*, 704, 161
- Jones, T. J., Bagley, M., Krejny, M., Andersson, B.-G., & Bastien, P. 2015, *AJ*, 149, 31
- Kenyon, S. J., Gómez, M., & Whitney, B. A. 2008, *Low Mass Star Formation in the Taurus-Auriga Clouds*, ed. B. Reipurth, 405
- Knude, J. & Hog, E. 1998, *A&A*, 338, 897
- Kobulnicky, H. A., Molnar, L. A., & Jones, T. J. 1994, *AJ*, 107, 1433
- Koch, P. M., Tang, Y.-W., & Ho, P. T. P. 2013, *ApJ*, 775, 77
- Koyama, H. & Inutsuka, S.-i. 2002, *ApJ*, 564, L97
- Kun, M., Kiss, Z. T., & Balog, Z. 2008, *Star Forming Regions in Cepheus*, ed. B. Reipurth, 136
- Lamarre, J., Puget, J., Ade, P. A. R., et al. 2010, *A&A*, 520, A9
- Lazarian, A. & Hoang, T. 2007, *MNRAS*, 378, 910
- Lazarian, A. & Vishniac, E. T. 1999, *ApJ*, 517, 700
- Li, H., Griffin, G. S., Krejny, M., et al. 2006, *ApJ*, 648, 340
- Li, H.-b., Fang, M., Henning, T., & Kainulainen, J. 2013, *MNRAS*, 436, 3707
- Li, H.-b. & Houde, M. 2008, *ApJ*, 677, 1151
- Luhman, K. L. 2008, *Chamaeleon*, ed. B. Reipurth, 169
- Martin, P. G., Roy, A., Bontemps, S., et al. 2012, *ApJ*, 751, 28
- Matthaeus, W. H., Pouquet, A., Mininni, P. D., Dmitruk, P., & Breech, B. 2008, *Physical Review Letters*, 100, 085003
- Mathews, B. C., McPhee, C. A., Fissel, L. M., & Curran, R. L. 2009, *ApJS*, 182, 143
- Mathews, B. C., Wilson, C. D., & Fiege, J. D. 2001, *ApJ*, 562, 400
- Mathews, T. G., Ade, P. A. R., Angilè, F. E., et al. 2014, *ApJ*, 784, 116
- McKee, C. F. & Ostriker, E. C. 2007, *ARA&A*, 45, 565
- McKee, C. F., Zweibel, E. G., Goodman, A. A., & Heiles, C. 1993, in *Protostars and Planets III*, ed. E. H. Levy & J. I. Lunine, 327
- Molinari, S., Schisano, E., Faustini, F., et al. 2011, *A&A*, 530, A133
- Moneti, A., Pipher, J. L., Helfer, H. L., McMillan, R. S., & Perry, M. L. 1984, *ApJ*, 282, 508
- Montier, L., Plaszczyński, S., Levrier, F., et al. 2015, *A&A*, 574, A135
- Mouschovias, T. C. 1976a, *ApJ*, 206, 753
- Mouschovias, T. C. 1976b, *ApJ*, 207, 141
- Mouschovias, T. C. 1991, *ApJ*, 373, 169
- Myers, P. C. & Goodman, A. A. 1991, *ApJ*, 373, 509
- Nakano, T. 1998, *ApJ*, 494, 587
- Nakano, T. & Nakamura, T. 1978, *PASJ*, 30, 671
- Neuhäuser, R. & Forbrich, J. 2008, *The Corona Australis Star Forming Region*, ed. B. Reipurth, 735
- Ostriker, E. C., Stone, J. M., & Gammie, C. F. 2001, *ApJ*, 546, 980
- Palmeirim, P., André, P., Kirk, J., et al. 2013, *A&A*, 550, A38
- Paradis, D., Dobashi, K., Shimoikura, T., et al. 2012, *A&A*, 543, A103
- Pereyra, A. & Magalhães, A. M. 2004, *ApJ*, 603, 584
- Planck Collaboration XXIV. 2011, *A&A*, 536, A24
- Planck Collaboration I. 2014, *A&A*, 571, A1
- Planck Collaboration II. 2014, *A&A*, 571, A2
- Planck Collaboration V. 2014, *A&A*, 571, A5
- Planck Collaboration VI. 2014, *A&A*, 571, A6
- Planck Collaboration VIII. 2014, *A&A*, 571, A8
- Planck Collaboration XI. 2014, *A&A*, 571, A11
- Planck Collaboration Int. XIX. 2014, *A&A*, in press
- Planck Collaboration Int. XX. 2014, *A&A*, in press
- Planck Collaboration Int. XXI. 2014, *A&A*, in press
- Planck Collaboration Int. XXXII. 2014, *A&A*, submitted
- Planck Collaboration Int. XXXIII. 2014, *A&A*, submitted
- Poppel, W. 1997, *Fund. Cosmic Phys.*, 18, 1
- Prato, L., Rice, E. L., & Dame, T. M. 2008, *Where are all the Young Stars in*

- Aquila?, ed. B. Reipurth, 18
 Reipurth, B. 2008, Handbook of Star Forming Regions, Volume I: The Northern Sky
 Santos, F. P., Franco, G. A. P., Roman-Lopes, A., Reis, W., & Román-Zúñiga, C. G. 2014, ApJ, 783, 1
 Santos-Lima, R., de Gouveia Dal Pino, E. M., & Lazarian, A. 2012, ApJ, 747, 21
 Schlafly, E. F., Green, G., Finkbeiner, D. P., et al. 2014, ApJ, 786, 29
 Serkowski, K. 1958, Acta Astron., 8, 135
 Soler, J. D., Hennebelle, P., Martin, P. G., et al. 2013, ApJ, 774, 128
 Spitzer, Jr., L. 1968, Interscience Tracts on Physics and Astronomy, 28
 Sridhar, S. & Goldreich, P. 1994, ApJ, 432, 612
 Straizys, V., Černis, K., & Bartašūūtė, S. 2003, A&A, 405, 585
 Sugitani, K., Nakamura, F., Watanabe, M., et al. 2011, ApJ, 734, 63
 Tassis, K., Dowell, C. D., Hildebrand, R. H., Kirby, L., & Vaillancourt, J. E. 2009, MNRAS, 399, 1681
 Ward-Thompson, D., Kirk, J. M., Crutcher, R. M., et al. 2000, ApJ, 537, L135
 Whittet, D. C. B., Hough, J. H., Lazarian, A., & Hoang, T. 2008, ApJ, 674, 304
 Whittet, D. C. B., Prusti, T., Franco, G. A. P., et al. 1997, A&A, 327, 1194
 Wilking, B. A., Gagné, M., & Allen, L. E. 2008, Star Formation in the ρ Ophiuchi Molecular Cloud, ed. B. Reipurth, 351
 Zweibel, E. G. 1996, in Astronomical Society of the Pacific Conference Series, Vol. 97, Polarimetry of the Interstellar Medium, ed. W. G. Roberge & D. C. B. Whittet, 486

Appendix A: Selection of data

The HRO analysis is applied to each MC using common criteria for selecting the areas in which the relative orientation is to be assessed.

A.1. Gradient mask

The dust optical depth, τ_{353} , observed in each region, can be interpreted as

$$\tau_{353}^{\text{OBS}} = \tau_{353}^{\text{MC}} + \tau_{353}^{\text{BG}} + \delta_{\tau_{353}}, \quad (\text{A.1})$$

where τ_{353}^{MC} is the optical depth of the MC, τ_{353}^{BG} is the optical depth of the diffuse regions behind and/or in front of the cloud (background/foreground), and $\delta_{\tau_{353}}$ the noise in the optical depth map with variance $\sigma_{\tau_{353}}^2 = \delta_{\tau_{353}}^2$.

The gradient of the optical depth can be then written as

$$\nabla\tau_{353}^{\text{OBS}} = \nabla\tau_{353}^{\text{MC}} + \nabla(\tau_{353}^{\text{BG}} + \delta_{\tau_{353}}). \quad (\text{A.2})$$

We quantify the contribution of the background/foreground and the noise, $\nabla(\tau_{353}^{\text{BG}} + \delta_{\tau_{353}})$, by evaluating $\nabla\tau_{353}$ in a reference field with lower submillimetre emission. Given that the dominant contribution to the background/foreground gradient would come from the gradient in emission from the Galactic plane, for each of the regions analysed we chose a reference field of the same size at the same Galactic latitude and with the lowest average N_{H} in the corresponding latitude band. We compute the average of the gradient norm in the reference field, $\langle |\nabla\tau_{353}^{\text{REF}}| \rangle$, and use this value as a threshold for selecting the regions of the map where $\nabla\tau_{353}$ carries significant information about the structure of the cloud. We note that this threshold includes a contribution from the noise $\nabla\delta_{\tau_{353}}$. The HROs presented in this study correspond to regions in each field where $|\nabla\tau_{353}| > \langle |\nabla\tau_{353}^{\text{REF}}| \rangle$.

A.2. Polarization mask

The total Stokes parameters Q and U measured in each region can be interpreted as

$$Q^{\text{OBS}} = Q^{\text{MC}} + Q^{\text{BG}} + \delta_Q, \quad U^{\text{OBS}} = U^{\text{MC}} + U^{\text{BG}} + \delta_U, \quad (\text{A.3})$$

where Q^{MC} and U^{MC} correspond to the polarized emission from the MC, Q^{BG} and U^{BG} correspond to the polarized emission from the diffuse background/foreground, and δ_Q and δ_U are the noise contributions to the observations, such that the variances $\sigma_Q^2 = \overline{\delta_Q^2}$ and $\sigma_U^2 = \overline{\delta_U^2}$.

As in the treatment of the gradient, we estimate the contributions of the background/foreground polarized emission and the noise using the rms of the Stokes parameters in the same reference field, $Q_{\text{rms}}^{\text{REF}}$ and $U_{\text{rms}}^{\text{REF}}$. The HROs presented in this study correspond to pixels in each region where $|Q| > 2Q_{\text{rms}}^{\text{REF}}$ or $|U| > 2U_{\text{rms}}^{\text{REF}}$. The “or” conditional avoids biasing the selected values of polarization. This first selection criterion provides a similar sample to the alternative coordinate-independent criterion $\sqrt{Q^2 + U^2} > 2\sqrt{(Q_{\text{rms}}^{\text{REF}})^2 + (U_{\text{rms}}^{\text{REF}})^2}$. This first criterion aims to distinguish between the polarized emission coming from the cloud and the polarized emission coming from the background/foreground estimated in the reference regions.

Additionally, as a second criterion, our sample is restricted to polarization measurements where $|Q| > 3\sigma_Q$ or $|U| > 3\sigma_U$. This aims to select pixels where the uncertainty in the polarization angle is smaller than the size of the angle bins used for the constructions of the HRO (Serkowski 1958; Montier et al. 2015). In terms of the total polarized intensity, $P = \sqrt{Q^2 + U^2}$, and following equations B.4 and B.5 in Planck Collaboration Int. XIX (2014), the second criterion corresponds to $P/\sigma_P > 3$ and uncertainties in the polarized orientation angle $\sigma_\psi < 10^\circ$.

The fractions of pixels considered in each region, after applying the selection criteria described above, are summarized in Table A.1. The largest masked portions of the regions correspond to the gradient mask, which selects mostly those areas of column density above the mean column density of the background/foreground $\langle N_{\text{H}}^{\text{BG}} \rangle$. The polarization mask provides an independent criterion that is less restrictive. The intersection of these two masks selects the fraction of pixels considered for the HRO analysis.

Appendix B: Construction of the histogram of relative orientations and related uncertainties

The HROs were calculated for 25 column density bins having equal numbers of selected pixels (10 bins in two regions with fewer pixels, CrA and IC 5146). For each of these HROs we use 12 angle bins of width 15° (see Sect. 4.1.1).

B.1. Calculation of $\nabla\tau_{353}$ and the uncertainty of its orientation

The optical depth gradient ($\nabla\tau_{353}$) is calculated by convolving the τ_{353} map with a Gaussian derivative kernel (Soler et al. 2013), such that $\nabla\tau_{353}$ corresponds to

$$\nabla\tau_{353} = (G_x \otimes \tau_{353}) \hat{i} + (G_y \otimes \tau_{353}) \hat{j} = g_x \hat{i} + g_y \hat{j}, \quad (\text{B.1})$$

where G_x and G_y are the kernels calculated using the x - and y -derivatives of a symmetric two-dimensional Gaussian function. The orientation of the iso- τ_{353} contour is calculated from the components of the gradient vector,

$$\theta = \arctan(-g_x, g_y). \quad (\text{B.2})$$

Because the calculation of the gradient through convolution is a linear operation, the associated uncertainties can be calculated using the same operation, so that

$$\delta_{g_x} = G_x \otimes \delta_{\tau_{353}}; \quad \delta_{g_y} = G_y \otimes \delta_{\tau_{353}}, \quad (\text{B.3})$$

Table A.1. Selection of data^a.

Region	$\langle N_{\text{H}}^{\text{BG}} \rangle$ [10^{20} cm^{-2}]	f_{∇} [%]	f_{pol} [%]	f_{tot} [%]
Taurus	6.2	66	78	28
Ophiuchus	5.6	65	82	31
Lupus	9.6	65	67	24
Chamaeleon-Musca	6.3	49	83	31
Corona Australia (CrA)	5.4	34	40	4
Aquila Rift	18.4	48	96	32
Perseus	5.3	60	59	16
IC 5146	26.4	38	93	29
Cepheus	7.5	66	80	36
Orion	6.1	63	67	24
ChamEast	6.3	33	38	10
ChamSouth	4.9	36	42	13

^a Mean column density of the background/foreground for each region $\langle N_{\text{H}}^{\text{BG}} \rangle$ estimated from a reference field at the same Galactic latitude; percentage f_{∇} of all pixels where $|\nabla\tau_{353}| > \langle |\nabla\tau_{353}^{\text{REF}}| \rangle$; percentage f_{pol} of all pixels where $|Q| > 2Q_{\text{rms}}^{\text{REF}}$ or $|U| > 2U_{\text{rms}}^{\text{REF}}$ (first polarization criterion) and where $|Q| > 3\sigma_Q$ or $|U| > 3\sigma_U$ (second polarization criterion); and percentage f_{tot} of all pixels used for the HRO analysis.

from which we obtain the $\sigma_{g_x}^2 = \overline{\delta_{g_x}^2}$ and $\sigma_{g_y}^2 = \overline{\delta_{g_y}^2}$.

The standard deviation of the angle θ can be written as

$$\sigma_{\theta} = \sqrt{\left(\frac{\partial\theta}{\partial g_x}\right)^2 \sigma_{g_x}^2 + \left(\frac{\partial\theta}{\partial g_y}\right)^2 \sigma_{g_y}^2}, \quad (\text{B.4})$$

which corresponds to

$$\sigma_{\theta} = \frac{1}{g_x^2 + g_y^2} \sqrt{g_y^2 \sigma_{g_x}^2 + g_x^2 \sigma_{g_y}^2}. \quad (\text{B.5})$$

In the application discussed here, the standard deviations in the τ_{353} map within the selected areas are much less than a few percentage points, so their effect on the estimate of the orientation of the gradient is negligible.

B.2. Uncertainties affecting the characterization of relative orientations within MCs

B.2.1. Uncertainties in the construction of the histogram

To estimate the uncertainty associated with the noise in Stokes Q and U , we produce 1000 noise realizations, Q_r and U_r , using Monte Carlo sampling. We assume that the errors are normally distributed and are centred on the measured values Q and U with dispersions σ_Q and σ_U (Planck Collaboration II 2014; Planck Collaboration VI 2014; Planck Collaboration V 2014; Planck Collaboration VIII 2014). Given that σ_{QU} is smaller than σ_Q^2 and σ_U^2 , it is justified to generate Q_r and U_r independently of each other. We then introduce Q_r and U_r in the analysis pipeline and compute the HRO using the corresponding τ_{353} map in each region. The results, presented in Fig. B.1 for the Taurus region, show that the noise in Q and U does not critically affect the shape of the HROs or the trend in ξ . Together, the low noise in the maps of τ_{353} and the selection criteria for the polarization measurements ensure that the HRO is well determined.

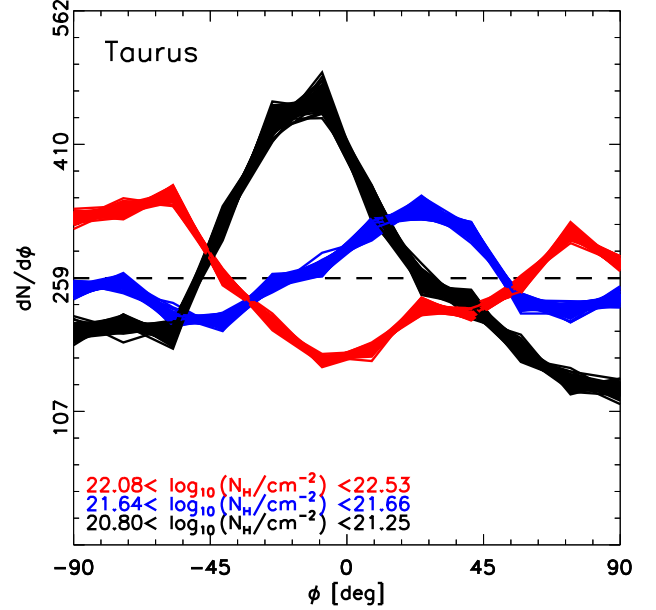


Fig. B.1. HROs in the Taurus region that correspond to the indicated N_{H} bins. The plotted values are obtained using the original τ_{353} map at $10'$ resolution and maps of the Stokes parameters Q_r and U_r , which correspond to 1000 random noise realizations. Each realization is generated using a Gaussian probability density function centred on the measured values Q and U with variances σ_Q^2 and σ_U^2 .

Another source of uncertainty in the HRO resides in the histogram binning process. The variance in the k th histogram bin is given by

$$\sigma_k^2 = h_k \left(1 - \frac{h_k}{h_{\text{tot}}}\right), \quad (\text{B.6})$$

where h_k is the number of samples in the k th bin, and h_{tot} is the total number of samples.

Of the two independent sources of uncertainty above, we find that the largest contribution comes from the binning process, so that these are the ones shown as the shaded uncertainty ranges in all figures of HROs, for example for the shaded uncertainty ranges in all figures of HROs, for example for the Taurus region in Fig. 3. Because of the large number of samples in each histogram bin, the uncertainties in the HRO do not significantly affect the results of this study.

B.2.2. Uncertainties in the histogram shape parameter ξ

As in the case of the HRO, the uncertainty in ξ , as defined in Eq. (4), can be quantified using the random realizations introduced in the previous section. Figure B.2 shows the dependence of ξ on $\log_{10} N_{\text{H}}$ obtained using Q_r and U_r for the Taurus region. The small variations around the trend line indicate that the uncertainties in Q and U do not significantly affect the trends discussed in this study, as expected from the behaviour of the histograms presented in Fig. B.1. The main source of uncertainty in the estimation of ξ is related to the histogram binning, characterized by the error bars calculated using Eq. (5). As seen in Fig. 7 and reproduced in Fig. C.1, these are much larger than the dispersion of the values of ξ in Fig. B.2.

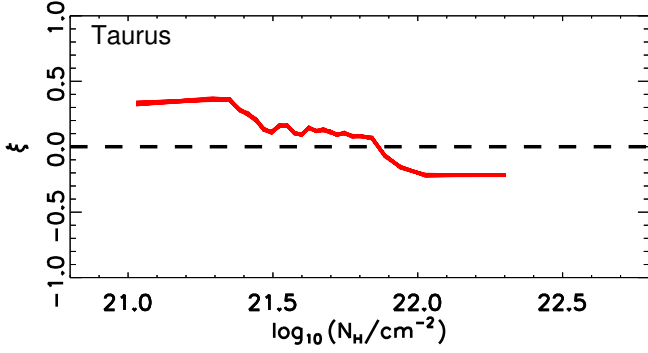


Fig. B.2. Histogram shape parameter, ξ , as a function of $\log_{10}(N_{\text{H}}/\text{cm}^{-2})$ in the Taurus region. The values are obtained using the τ_{353} map at $10'$ resolution and maps of the Stokes parameters Q_r and U_r that correspond to 1000 random-noise realizations. Each realization is generated using a Gaussian probability density function centred on the measured values Q and U with variances σ_Q^2 and σ_U^2 . By joining the values at each N_{H} bin, we find a trend very close to the black line in Fig. 7, with little dispersion from the noise; much larger are the uncertainties in evaluating ξ at each N_{H} bin, as given in Fig. 7 but not shown here.

Appendix C: Statistical significance of the HRO signal

C.1. A product of chance?

To investigate various potential sources of the signal found in the HROs we use the τ_{353} map at $10'$ resolution in each region in combination with Q and U maps that are produced with different recipes, each with 1000 realizations.

To eliminate random fields, we use Q and U maps produced with a random realization of ψ with a uniform distribution and with unit-length polarization pseudo-vectors. The results of this numerical experiment are shown in Fig. C.1 for the Taurus region. For each of the 1000 realizations, we join the values at each N_{H} bin to show the trend lines in order to compare with the lines in Fig. 7.

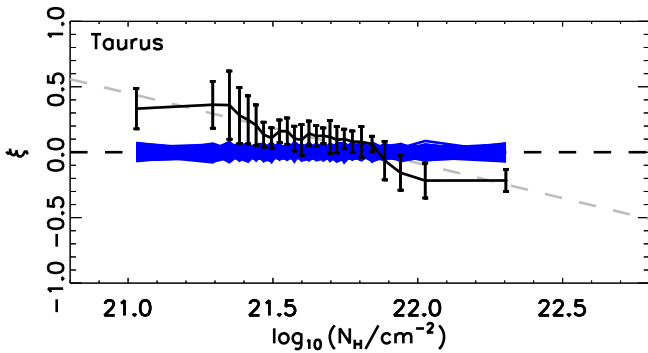


Fig. C.1. Histogram shape parameter, ξ , as a function of $\log_{10}(N_{\text{H}}/\text{cm}^{-2})$ in the Taurus region. Blue lines join the ξ values obtained using the τ_{353} map at $10'$ resolution and each of 1000 random realizations of Q and U maps corresponding to a uniform distribution of ψ . Results in black and grey are from the analysis of the *Planck* data, as reported in Fig. 7.

To eliminate the large-scale magnetic field as the source we use Q and U maps produced with random realizations of ψ with

a Gaussian distribution and unit-length polarization pseudo-vectors. The polarization angle distribution is centred at $\psi_0 = 0^\circ$ with a standard deviation $\varsigma_\psi = 45^\circ$. The results of this numerical experiment are shown in Fig. C.2 for the Taurus region.

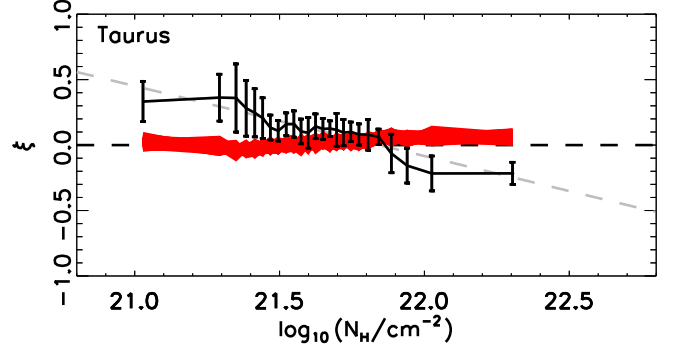


Fig. C.2. Like Fig. C.1 but for values of ξ (red) obtained using 1000 random realizations of Q and U maps corresponding to a Gaussian distribution of ψ centred on $\psi_0 = 0^\circ$ and with standard deviation $\varsigma_\psi = 45^\circ$.

To eliminate random spatial correlations, we use Q and U maps produced from random realizations with a power spectrum $P(k) \propto k^{\alpha_m}$. For the spectral indices we adopted, $\alpha_m = -1.5, -2.5,$ and -3.5 , correlations are introduced in the orientation of the polarization pseudo-vectors that are independent of the structure of matter. This test evaluates the statistical significance of the random sampling of spatial correlations in the magnetic field implied when we calculate the HROs in a finite region of the sky. The results of this numerical experiment are shown in Fig. C.3 for the Taurus region.

The results of these numerical experiments show that the trends with N_{H} found in the HROs and ξ do not arise by chance from these potential sources.

C.2. A product of random correlations in the polarization maps?

The random realizations of the magnetic field presented above are useful for characterizing the behaviour of ξ . However, they are bound to produce very different statistics compared to those in the real observations. In reality the orientations of \mathbf{B}_\perp have some non-trivial correlation structure in the map. In principle, the difference in the HROs might be due to the different correlations of the observed \mathbf{B}_\perp and of the random realizations of \mathbf{B}_\perp .

To evaluate whether the signal present in the HROs arises from an actual physical relationship between \mathbf{B}_\perp and τ_{353} , we introduce randomness by shifting the Stokes Q and U maps with respect to the τ_{353} map and then calculate the corresponding HROs and ξ as a function of $\log_{10}(N_{\text{H}}/\text{cm}^{-2})$. The intrinsic statistical properties of the two maps are unchanged because the two maps are unchanged, only shifted.

If the trend in ξ as a function of $\log_{10}(N_{\text{H}}/\text{cm}^{-2})$ were arising randomly, these trends would be unchanged even for significant shifts. Instead the results of this experiment, illustrated in Fig. C.4 for the Taurus region, show that the trends tend to disappear with increasing values of the size of the shift. For shifts of about 1° , the correlation between the magnetic field and the matter is still present, as expected from the results presented in Fig. 10, but for larger shifts the correlation is lost and the trend

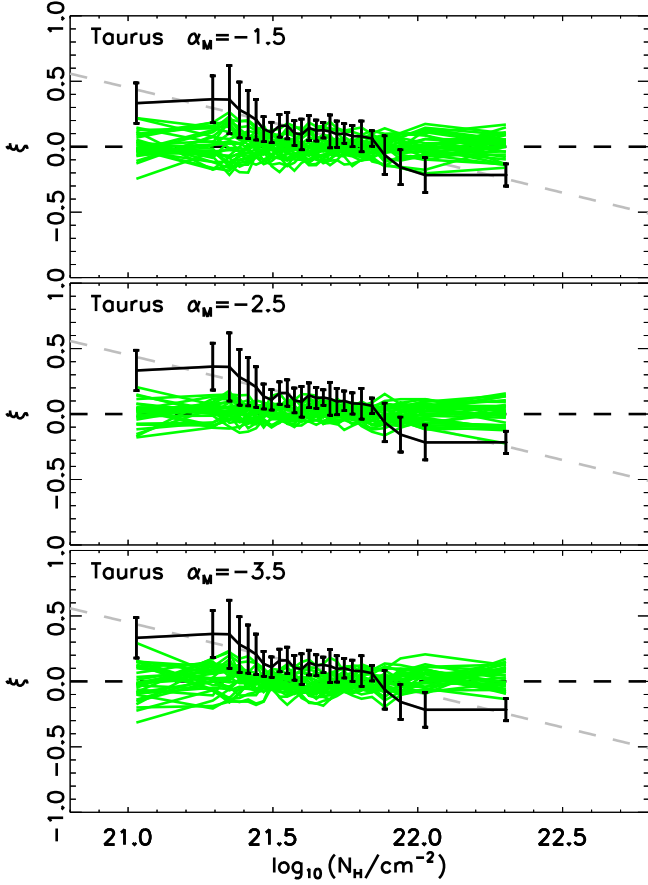


Fig. C.3. Like Fig. C.1 but for values of ξ (green) obtained using 1000 random realizations of Q and U maps corresponding to a power spectrum $P(k) \propto k^{\alpha_M}$, with $\alpha_M = -1.5, -2.5,$ and -3.5 .

does not survive. Over the many MCs studied, the nature of the trends at large shifts appears to be random.

C.3. Projection effects

We evaluate the statistical significance of the relative orientation between \mathbf{B}_\perp and $\nabla\tau_{353}$ by considering the distribution of relative orientations between two vectors in 3D space compared to the distribution of relative orientation between their projections in 2D.

The projection of a vector \mathbf{v} onto a plane normal to the unit vector $\hat{\mathbf{n}}$ can be written as

$$\mathbf{u} = \mathbf{v} - (\mathbf{v} \cdot \hat{\mathbf{n}}) \hat{\mathbf{n}}. \quad (\text{C.1})$$

Consider two unit vectors in 3D, \mathbf{v}_1 and \mathbf{v}_2 , separated by an angle α , such that

$$\cos \alpha = \mathbf{v}_1 \cdot \mathbf{v}_2. \quad (\text{C.2})$$

The angle β between the projections of these two vectors onto a plane normal to $\hat{\mathbf{n}}$, \mathbf{u}_1 , and \mathbf{u}_2 , can be written as

$$\begin{aligned} \cos \beta &= \frac{\mathbf{u}_1 \cdot \mathbf{u}_2}{|\mathbf{u}_1| |\mathbf{u}_2|} \\ &= \frac{(\mathbf{v}_1 \cdot \mathbf{v}_2 - (\mathbf{v}_1 \cdot \hat{\mathbf{n}})(\mathbf{v}_2 \cdot \hat{\mathbf{n}}))}{(\mathbf{v}_1 \cdot \mathbf{v}_1 - (\mathbf{v}_1 \cdot \hat{\mathbf{n}})^2)^{1/2} (\mathbf{v}_2 \cdot \mathbf{v}_2 - (\mathbf{v}_2 \cdot \hat{\mathbf{n}})^2)^{1/2}}. \end{aligned} \quad (\text{C.3})$$

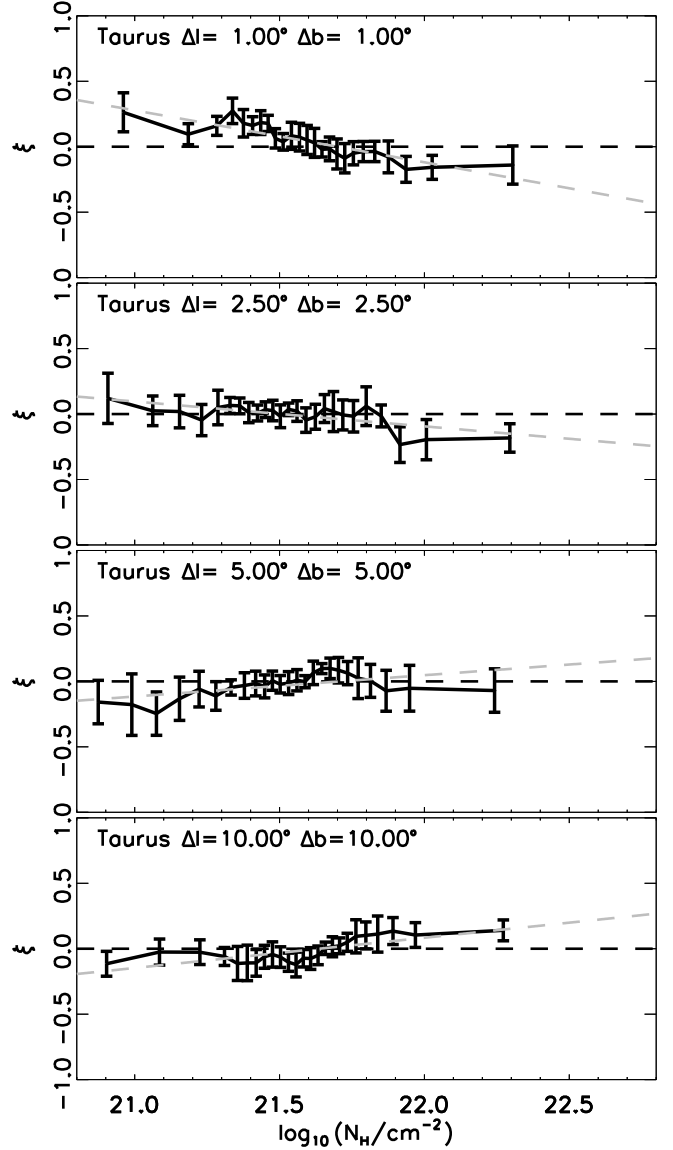


Fig. C.4. Histogram shape parameter, ξ , as a function of $\log_{10}(N_{\text{H}}/\text{cm}^{-2})$ calculated from the τ_{353} map at $10'$ resolution in the Taurus region and the Stokes Q and U maps shifted in Galactic longitude and latitude by the values indicated, for Δl and Δb , respectively.

Given a particular distribution of angles between the vectors \mathbf{v}_1 and \mathbf{v}_2 , this expression, which is solved numerically, is useful for evaluating the resulting distribution of angles between the projected vectors \mathbf{u}_1 and \mathbf{u}_2 . Without any loss of generality, we can assume that \mathbf{v}_1 is oriented along the axis of a spherical coordinate system, such that $\mathbf{v}_1 = \hat{\mathbf{k}}$, and that \mathbf{v}_2 is oriented at polar angle θ and azimuth ϕ , such that $\mathbf{v}_2 = \cos \phi \sin \theta \hat{\mathbf{i}} + \sin \phi \sin \theta \hat{\mathbf{j}} + \cos \theta \hat{\mathbf{k}}$. Then, we can simulate a distribution of $\cos \alpha$ by simulating a distribution of $\cos \theta$ and generating ϕ with a uniform distribution.

We thus generate a set of vectors \mathbf{v}_2 that follow a particular distribution of $\cos \alpha$. We choose three examples: a uniform distribution of relative orientation between \mathbf{v}_2 and \mathbf{v}_1 , \mathbf{v}_2 vectors that are mostly parallel to \mathbf{v}_1 , and \mathbf{v}_2 vectors that are mostly perpendicular to \mathbf{v}_1 . The last two are Gaussian distributions centred at $\cos \alpha = 0$ (for mostly parallel) or $\cos \alpha = \pm 1$ (for mostly perpendicular, given the periodicity of α) with a dispersion ζ_α .

These distributions are shown in the top panel of Fig. C.5 for three values of ζ_α .

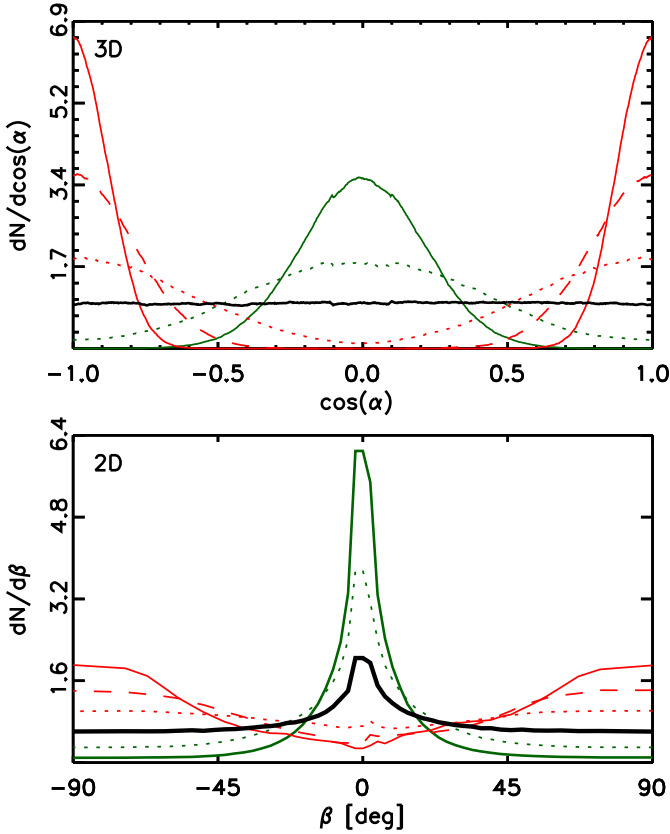


Fig. C.5. Normalized distributions of relative orientations of random vectors in 3D (top) and of their projections in 2D (bottom). The curves correspond to mostly perpendicular vectors (red), uniform distribution of relative orientations (black), and mostly parallel vectors (green). The solid, dashed, and dotted lines correspond to dispersions of the relative orientation angle $\zeta_\alpha = 18^\circ$, 36° , and 72° , respectively.

Using Eq. (C.3) we calculate the distribution of the angles between the projected vectors and the results are shown in the bottom panel of Fig. C.5. Projection generally tends to make vector pairs look more parallel in 2D than they are in 3D, regardless of the orientation in 3D, in agreement with the results of the Gaussian models presented in Planck Collaboration Int. XXXII (2014). Nevertheless, the distribution of relative orientations in 2D is qualitatively similar (though not identical) to the distribution in 3D. In particular, the signature of perpendicular orientation is not erased. We conclude that the observation in 2D of \mathbf{B}_\perp close to perpendicular to the column density structures is a direct indicator of the perpendicular configuration of \mathbf{B} with respect to the density structures in 3D. In contrast, the parallel alignment of \mathbf{B}_\perp with the structure, or no signs of preferential orientation, while suggestive of parallel orientation in 3D, does not unambiguously rule out the presence of some close-to-perpendicular orientations within the distribution in 3D.

Appendix D: Alternative estimates of magnetic field strength

Given the historic importance of the DCF method (Davis 1951; Chandrasekhar & Fermi 1953) and the related DCF+SF method

(Hildebrand et al. 2009), we have used them to estimate the magnetic field strength in each region. We also evaluated the mass-to-flux ratio, which is important in investigating the stability against gravitational collapse. We now provide a critical assessment of the applicability of these results.

D.1. Davis-Chandrasekhar-Fermi method

The DCF method estimates the strength of \mathbf{B}_\perp in a region using the dispersion of the polarization angles ζ_ψ . Assuming that the magnetic field is frozen into the gas and that the dispersion of the \mathbf{B}_\perp orientation angles (or equivalently ζ_ψ) is due to transverse incompressible Alfvén waves, then

$$B_\perp^{\text{DCF}} = \sqrt{4\pi\rho} \frac{\sigma_{v_\parallel}}{\zeta_\psi}, \quad (\text{D.1})$$

where σ_{v_\parallel} is the dispersion of the radial velocity of the gas (Appendix D.3) and ρ the gas mass density.

We calculate ζ_ψ directly from Stokes Q and U using

$$\zeta_\psi = \sqrt{\langle (\Delta\psi)^2 \rangle} \quad (\text{D.2})$$

and

$$\Delta\psi = \frac{1}{2} \arctan(Q\langle U \rangle - \langle Q \rangle U, Q\langle Q \rangle + \langle U \rangle U), \quad (\text{D.3})$$

where $\langle \dots \rangle$ denotes an average over the selected pixels in each map (Planck Collaboration Int. XIX 2014).

D.2. Davis-Chandrasekhar-Fermi plus structure function method

As described by Hildebrand et al. (2009), the DCF+SF method characterizes the magnetic field dispersion about local structured fields by considering the difference in angle, $\Delta\psi(\ell) = \psi(\mathbf{x}) - \psi(\mathbf{x} + \ell)$, between pairs of \mathbf{B}_\perp vectors separated by displacements ℓ in the plane of the sky. Assuming that the angle differences are statistically isotropic (i.e., they depend only on $\ell = |\ell|$ and not on the orientation of ℓ), they can be binned by distance, ℓ . From the $N(\ell)$ pairs of \mathbf{B}_\perp vectors for that bin, the square of the second-order structure function is

$$S_2^2(\ell) = \langle [\Delta\psi(\mathbf{x}, \ell)]^2 \rangle_x = \left\langle \frac{1}{N(\ell)} \sum_{i=1}^{N(\ell)} (\Delta\psi_{x,i})^2 \right\rangle_x, \quad (\text{D.4})$$

as introduced by Kobulnicky et al. (1994) and Falceta-Gonçalves et al. (2008). In terms of the Stokes parameters, each term in the sum can be written

$$\Delta\psi_{x,i} = \frac{1}{2} \arctan(Q_i U_x - Q_x U_i, Q_i Q_x + U_i U_x), \quad (\text{D.5})$$

where the subscripts x and i represent the central and displaced positions, respectively.

Hildebrand et al. (2009) assume that $\mathbf{B}(\mathbf{x})$ is composed of a large-scale structured field, $\mathbf{B}_0(\mathbf{x})$, and a random component, $\mathbf{B}_r(\mathbf{x})$, which are statistically independent of each other. Assuming that $\mathbf{B}_0(\mathbf{x})$ is a smoothly varying quantity, its contribution to $S_2^2(\ell)$ should increase in proportion to ℓ^2 for distances that are much smaller than the scales at which \mathbf{B}_0 itself fluctuates. Additionally, assuming that turbulence occurs on scales that are small enough to completely decorrelate \mathbf{B}_r for the range

Table D.1. Magnetic properties of the selected regions.^a

Region	$\sigma_{v_{\parallel}}$ [km s ⁻¹]	S_{ψ} [deg]	b [deg]	b [rad]	B_{\perp}^{DCF} [μG]	$B_{\perp}^{\text{DCF+SF}}$ [μG]	$\lambda_{\text{obs}}^{\text{DCF}}$	$\lambda_{\text{obs}}^{\text{DCF+SF}}$
Taurus	1.2±0.5	43±0.1	23±0.05	0.39±0.01	13±5	32±13	0.4±0.4	0.2±0.1
Ophiuchus	0.9±0.4	29±0.3	20±0.04	0.36±0.01	13±6	25±11	0.4±0.4	0.2±0.2
Lupus	1.5±0.6	46±0.7	30±0.06	0.52±0.01	14±5	29±11	0.3±0.2	0.2±0.1
Chamaeleon-Musca .	1.0±0.4	36±0.3	23±0.05	0.40±0.01	12±5	27±11	0.4±0.3	0.2±0.2
Corona Australis (CrA)	0.6±0.2	59±0.1	30±0.07	0.52±0.01	5±2	12± 5	0.9±0.9	0.3±0.3
Aquila Rift	1.9±0.6	43±0.5	23±0.09	0.40±0.01	20±6	50±15	0.3±0.2	0.1±0.1
Perseus	1.5±0.6	38±0.3	29±0.11	0.50±0.01	17±7	30±11	0.3±0.3	0.2±0.2
IC 5146	1.7±0.6	69±0.1	49±0.11	0.85±0.01	11±4	18± 6	0.5±0.3	0.3±0.2
Cepheus	1.6±0.6	43±0.2	20±0.04	0.35±0.01	16±6	47±18	0.3±0.1	0.1±0.0
Orion	1.7±0.6	36±0.1	26±0.06	0.45±0.01	20±7	38±14	0.3±0.3	0.2±0.2

^a Tabulated values are: the velocity dispersion, $\sigma_{v_{\parallel}}$; the dispersion of the polarization orientation angle, S_{ψ} ; the turbulent contribution to the angular dispersion, b , calculated from a linear fit to Eq (D.6); the magnetic field strengths, B_{\perp}^{DCF} and $B_{\perp}^{\text{DCF+SF}}$, calculated with the DCF method, of Eq. (D.1), and the DCF+SF method, of Eq. (D.10), with b values obtained from a fit to Eq. (D.6) in the range $50' \leq \ell \leq 200'$; and their corresponding observed mass-to-flux ratios, $\lambda_{\text{obs}}^{\text{DCF}}$ and $\lambda_{\text{obs}}^{\text{DCF+SF}}$. The reported uncertainties are from the appropriate propagation of errors.

of scales probed by the displacements ℓ , Hildebrand et al. (2009) derived the approximation

$$S_2^2(\ell) = b^2 + m^2 \ell^2, \quad (\text{D.6})$$

where the two terms on the right-hand side give the contributions from the random and large-scale magnetic fields, respectively. These assumptions are not necessarily valid for the range of scales in the *Planck* data.

Hildebrand et al. (2009) used Eq. (D.6) to estimate b^2 as the intercept and then related b to the ratio of the random to the large-scale magnetic field strength, both projected onto the plane of the sky, through

$$\frac{\langle B_{r,\perp}^2 \rangle^{1/2}}{B_{0,\perp}} = \frac{b}{\sqrt{2-b^2}}, \quad (\text{D.7})$$

where $\langle B_{r,\perp}^2 \rangle^{1/2}$ stands for the root mean square (rms) variations about the large-scale magnetic field, $B_{0,\perp}$. The same assumptions that result in Eq. (D.1) – i.e., considering only incompressible and isotropic turbulence, magnetic fields frozen into the gas, and dispersion of the B_{\perp} orientation originating in transverse incompressible Alfvén waves – lead to

$$\frac{\langle B_{r,\perp}^2 \rangle^{1/2}}{B_{0,\perp}} = \frac{\sigma_{v_{\parallel}}}{V_{A,\perp}}, \quad (\text{D.8})$$

where

$$V_{A,\perp} = \frac{B_{0,\perp}}{\sqrt{4\pi\rho}} \quad (\text{D.9})$$

is the speed of the transverse incompressible Alfvén waves. Combining Eqs. (D.7)–(D.9) results in

$$B_{\perp}^{\text{DCF+SF}} \equiv B_{0,\perp}^{\text{DCF+SF}} = \sqrt{4\pi\rho} \frac{\sigma_{v_{\parallel}} \sqrt{2-b^2}}{b}. \quad (\text{D.10})$$

D.3. Calculation

The estimates of velocity dispersion $\sigma_{v_{\parallel}}$ and mass density ρ are the same in the two methods (DCF and DCF+SF).

We obtain $\sigma_{v_{\parallel}}$ from the most complete CO emission-line survey of the Milky Way currently available, that of Dame et al.

(2001). This data set consists of 488 000 spectra that beam-sample (1/8°) a set of MCs and the Galactic plane over a strip from 4° to 10° wide in latitude. We find that material in the MCs has centroid velocities in the range $-10 < v_{\parallel}/(\text{km s}^{-1}) < 10$ in the first moment map. Furthermore, for the calculations below, we need to select pixels with sufficient S/N in the polarization observations and so use the second criterion described in Appendix A.2. This combination of cuts selects the areas illustrated in Fig. D.1. Over these areas we calculate the average of the velocity dispersion from the second moment map and use this value as $\sigma_{v_{\parallel}}$. This is tabulated along with other properties in Table D.1.

The mass density, $\rho = \mu n m_p$, is the product of the proton mass, m_p , the mean molecular weight per hydrogen molecule, $\mu = 2.8$, and the mean number density, n . We require a value of n , which for the discussions here we approximate to be 100 cm^{-3} . This is a typical value for MCs (Draine 2011) and in rough agreement with the column densities and cloud sizes presented in Table 1. In practice, n varies from one cloud to the next, and its estimation involves the assumption of a particular cloud geometry, resulting in additional uncertainties that are not considered in this study.

For the DCF method, the dispersion of the orientation angle S_{ψ} corresponds to the centred second moment of the ψ distribution evaluated in pixels within the selected region. Following the analysis presented in Planck Collaboration Int. XIX (2014) for $S(\ell)$, the variance on S_{ψ} can be expressed as

$$\sigma_{S_{\psi}}^2 = \frac{1}{N^2 S_{\psi}^2} \left[\left(\sum_{i=1}^N S_i \right)^2 \sigma_{\psi}^2 + \sum_{i=1}^N S_i^2 \sigma_{\psi_i}^2 \right], \quad (\text{D.11})$$

where ψ_i and σ_{ψ_i} are the orientation angle and uncertainty for each polarization pseudo-vector, N is the number of ψ measurements, $S_i = \psi_i - \langle \psi \rangle$, and $\langle \psi \rangle$ is the average orientation angle in each region. Like other quadratic functions, $\sigma_{S_{\psi}}^2$ is biased positively when noise is present, leading to an overestimation of this quantity. However, given that we limit our analysis to polarization measurements with high S/N and that the uncertainties in $\sigma_{v_{\parallel}}$ are considerably larger, the bias correction does not have a significant effect on our estimates. We apply Eq. (D.1) to estimate B_{\perp}^{DCF} and propagate the errors to obtain the values listed in Table D.1.

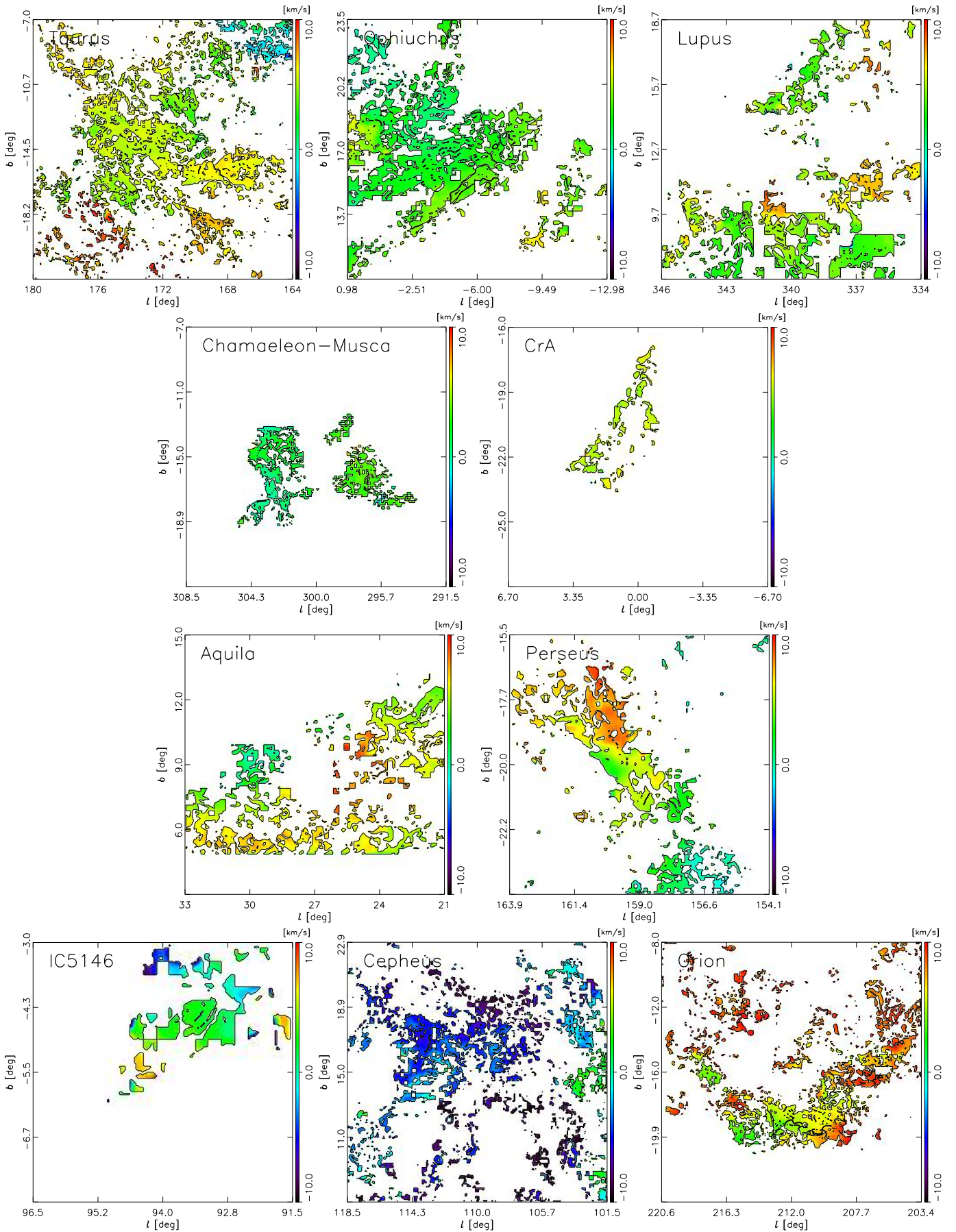


Fig. D.1. Line-of-sight centroid velocity $v_{||}$ maps inferred from CO emission (Dame et al. 2001). Areas shown have sufficient S/N in the polarization observations (second polarization criterion in Appendix A.2) for the DCF and DCF+SF analyses and lie in the range $-10 < v_{||}/(\text{km s}^{-1}) < 10$.

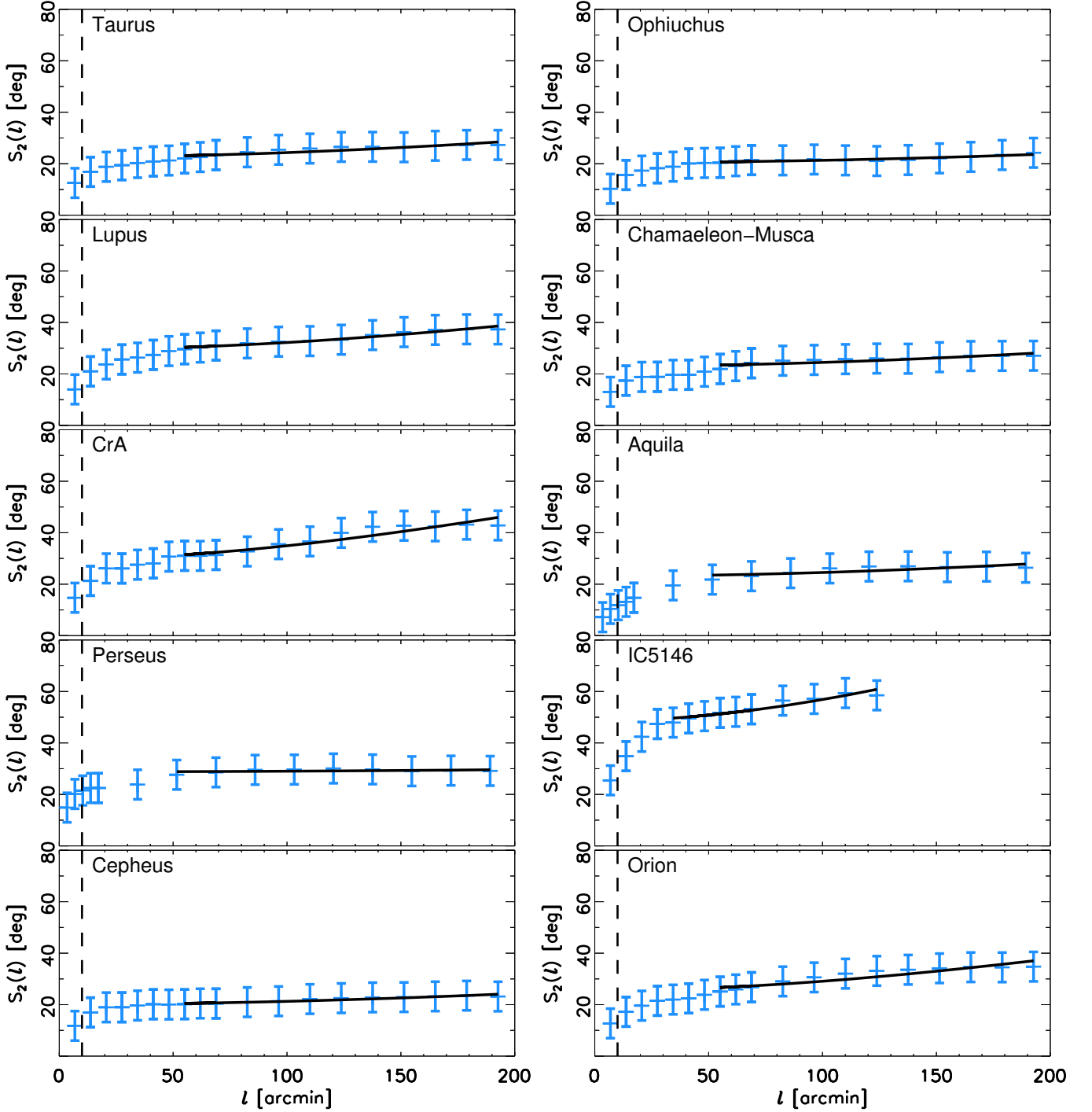


Fig. D.2. Structure function $S_2(\ell)$ calculated from the Q and U maps of the selected regions following Eq. (D.4). The black lines indicate the fits given by Eq. (D.6). The vertical dashed line marks the common $10'$ resolution of the data used in the analysis; the data are correlated for low values of ℓ causing the drop in $S_2(\ell)$.

For the DCF+SF method, to estimate the parameter b , we first calculate $S_2^2(\ell)$ for each of the regions. The resolution of the data used is $10'$. We evaluate $S_2^2(\ell)$ in steps of $3'.44$ for lags $0' < \ell < 34'.4$ and in steps of $34'.4$ for lags $40' < \ell < 200'$. For each considered lag ℓ , $\Delta\psi_{x,i}$ is evaluated pixel by pixel, considering all the pixels located in an annulus with radius ℓ . The term $\Delta\psi_{x,i}$ is only considered in the calculation of $S_2^2(\ell)$ if there are at least three pixels in the annulus. As anticipated, the model from Eq. (D.6) does not agree with the data on all sampled scales, so the range of scales considered is limited to ℓ above the resolu-

tion of the data and between $50'$ and $200'$, where the behaviour of $S_2^2(\ell)$ is approximately linear in ℓ^2 . We then make a linear fit of $S_2^2(\ell)$ using ℓ^2 as the independent variable and estimate the value of b and its uncertainty, σ_b . The results are plotted in Fig. D.2.

Using the calculated b values,⁶ we apply Eq. (D.10) to estimate $B_{\perp}^{\text{DCF+SF}}$, and the results are listed in Table D.1. As ex-

⁶ For Eq. (D.10) b is required to be in radians, and so those are also listed in Table D.1.

pected, the DCF+SF method produces estimates of B_{\perp} that are about twice as large as those obtained with the DCF method. However, it is worth noting that because of the discrepancy between the model and the observations, the value of b depends on the selected ℓ -range and so propagates into a different value of $B_{\perp}^{\text{DCF+SF}}$.

D.4. Mass-to-flux ratios

The critical value for the mass that can be supported against gravity by a magnetic flux Φ can be estimated to first order for a uniform disk from $(M/\Phi)_{\text{crit}} \equiv 1/(2\pi G^{1/2})$ (Nakano & Nakamura 1978). The precise value of the right-hand side changes for different geometries (e.g., Spitzer 1968; McKee et al. 1993). Stability can be assessed using

$$\lambda = \frac{(M/\Phi)}{(M/\Phi)_{\text{crit}}} = 7.6 \times 10^{-21} \frac{(N_{\text{H}_2}^{\text{mft}}/\text{cm}^{-2})}{(B^{\text{mft}}/\mu\text{G})}, \quad (\text{D.12})$$

where $N_{\text{H}_2}^{\text{mft}}$ and B^{mft} are the H_2 column density and magnetic field strength along a magnetic flux tube (Crutcher et al. 2004). A cloud is supercritical and prone to collapse under its own gravity, when $\lambda > 1$; otherwise, when $\lambda < 1$, the cloud is sub-critical, magnetically supported against gravitational collapse.

What is observable is λ_{obs} , in which $N_{\text{H}_2}^{\text{mft}}/B^{\text{mft}}$ is replaced by N_{H_2}/B_{\perp} . We evaluate λ_{obs} by combining the value of $\langle N_{\text{H}_2} \rangle$ computed from the integrated CO line emission and the conversion factor $X_{\text{CO}} = (1.8 \pm 0.3) \times 10^{20} \text{ cm}^{-2} \text{ K}^{-1} \text{ km}^{-1} \text{ s}$ (Dame et al. 2001) and B_{\perp} estimated with the DCF and DCF+SF methods. The X_{CO} factor may show cloud-to-cloud or regional variations (Draine 2011), but we consider that these are not significant in comparison to the uncertainties involved in the estimation of B_{\perp} . The calculated values of λ_{obs} are listed in Table D.1. They are consistent with being less than unity.

From this we might obtain λ by judicious deprojection, since

$$\lambda = (N_{\text{H}_2}^{\text{mft}}/N_{\text{H}_2})(B_{\perp}/B^{\text{mft}}) \times \lambda_{\text{obs}} \equiv f_{\text{dp}} \lambda_{\text{obs}}. \quad (\text{D.13})$$

Here, B_{\perp} is always less than B^{mft} , pushing f_{dp} below unity. The situation for column density depends on the geometry of the structure relative to the magnetic field. For a structure with the magnetic field along the short axis, $N_{\text{H}_2}^{\text{mft}} < N_{\text{H}_2}$, again lowering f_{dp} .

Statistically, the mean mass-to-flux ratio can be related to the observed value by assuming a particular geometry of the cloud, an ellipsoid with equatorial radius a and centre-to-pole distance c , and a magnetic field oriented along the polar axis of the ellipsoid. For an oblate spheroid, flattened perpendicular to the orientation of the magnetic field, $f_{\text{dp}} = 1/3$, yielding

$$\overline{M/\Phi} = \int_0^{\pi/2} \frac{M \cos \beta}{\Phi / \sin \beta} \sin \beta d\beta = \frac{1}{3}(M/\Phi)_{\text{obs}}, \quad (\text{D.14})$$

where β is the inclination angle with respect to the line of sight, and the $\sin \beta$ dependence in the flux comes from $B = B_{\perp} \sin \beta$ (Crutcher et al. 2004). For a sphere there is no $\cos \beta$ dependence and $f_{\text{dp}} = 1/2$. For a prolate spheroid elongated along the orientation of the field, the mass is multiplied by $\sin \beta$ instead of $\cos \beta$, resulting in $f_{\text{dp}} = 3/4$. Investigating which geometry, if any, is most relevant to the actual MCs and the magnetized structures detected within them is obviously important before firm conclusions can be drawn regarding gravitational instability.

D.5. Discussion

Our estimates of the magnetic field strengths in the MCs analysed and the mass-to-flux ratios, presented in Table D.1, stem from the classic calculation presented by Chandrasekhar & Fermi (1953) and an updated interpretation presented by Hildebrand et al. (2009). Both of these methods assume very specific conditions, so (as we discuss below) this limits the conclusions that can be drawn from these estimates of the magnetic field strength. The deduced mass-to-flux ratios suggest that the clouds are potentially magnetically sub-critical, but we again need to be cautious about drawing conclusions from this application of the DCF and DCF+SF analyses alone.

In the case of the DCF method, the values of B_{\perp}^{DCF} are obtained by assuming that the structure of the magnetic field is the product only of incompressible Alfvén waves, where the displacements are perpendicular to the direction of propagation. This is not the case for turbulence in MCs where the random component of the magnetic field can have any orientation. The dispersion measured about mean fields, assumed to be straight in DCF, may be much larger than should be attributed to MHD waves or turbulence, leading to an overestimation of ζ_{ψ} and to low values of B_{\perp} . Moreover true interstellar turbulence in MCs involves not only incompressible Alfvén waves, but also compressible magneto-sonic waves, which do not satisfy Eq. D.1. Furthermore, depending on the scales examined, the magnetic field may have structures due to effects such as differential rotation, gravitational collapse, or expanding HII regions.

In the case of the DCF+SF method, the values of $B_{\perp}^{\text{DCF+SF}}$ are obtained by assuming a very specific model of the magnetic field, which is in principle just a first-order approximation. First, this model assumes that the effect of the large-scale structured magnetic field, \mathbf{B}_0 , is to cause the square of the second-order structure function, $S_2^2(\ell)$, to increase as ℓ^2 . This corresponds to a very specific correlation function for \mathbf{B}_0 . Second, this model assumes that the dispersion of the random component of the field, \mathbf{B}_r , is scale-independent, which is not realistic for the range of scales probed by Planck (Elmegreen & Scalo 2004; Hennebelle & Falgarone 2012).

In addition, the magnetic field orientation deduced from the polarization angle in a particular direction is not generally that of the field at a single point along the line of sight. The observed polarization is the average of various field pseudo-vectors weighted by local dust emission along the line of sight. The net effect of the integration of multiple uncorrelated components along the line of sight is an observed dispersion of the polarization angle that is smaller than the true 3D dispersion of the magnetic field orientation, thus leading to an overestimation of B_{\perp} . Myers & Goodman (1991) presented an analysis of this effect in terms of the number of correlation lengths of the magnetic field along the line of sight through a cloud, which they calculated empirically.

Houde et al. (2009) presented an extension of the DCF+SF method that includes the effect of signal integration along the line of sight and across the area subtended by the telescope beam. The extended method, also implemented in Houde et al. (2011, 2013), is based on the identification of the magnetized turbulence correlation length (δ) by means of the structure function of the polarization angles. In the case of the Planck 353 GHz observations, the angular resolution is not sufficient to identify δ and the corrections would have to rely on rough estimates of this value and the depth of integration (Δ). Following equation 29 in Houde et al. (2009), rough estimates $\delta \approx 0.2 \text{ pc}$ and $\Delta \approx 10 \text{ pc}$ result in a few correlation lengths across the beam, corresponding to correction factors around 0.4. Coincidentally, such cor-

rection factors lead to values of $B_{\perp}^{\text{DCF+SF}}$ close to those of B_{\perp}^{DCF} in Table D.1. But note that this correction relies on specific assumptions on the nature of the turbulence correlation function, it does not circumvent the necessity to observe the dust polarized emission with higher angular resolution to fully characterize the magnetic field.

MHD simulations provide a potentially useful guide to what modifications might be introduced into the DCF formula to allow for inhomogeneity and line-of-sight averaging. Using synthetic observations of MHD simulations, Ostriker et al. (2001) showed that correcting Eq. (D.1) by a factor $C \approx 0.5$ provides a good approximation to the actual magnetic field strength in cases where $\zeta_{\psi} < 25^{\circ}$. However, the effect of nonlinear amplitudes is uncertain (Zweibel 1996), and the method fails for values of $\zeta_{\psi} > 25^{\circ}$, which is the case for all of the regions in this study (Table D.1). Falceta-Gonçalves et al. (2008) propose a method that is potentially valid for any value of ζ_{ψ} , based on a fit to the B_{\perp}^{DCF} values obtained from maps at different resolutions, again concluding that the field should be lower than estimated with Eq. (D.1). However, this approach was not tested in MHD simulations that include gravity, which is the critical process that we aim to evaluate by using the DCF method.

Another strong assumption is that the behaviour of the velocity and the magnetic field are represented well by the observed quantities $\sigma_{v_{\parallel}}$ and ζ_{ψ} for a particular set of scales, which might not necessarily be the case. Even if the power spectra of \mathbf{v} and \mathbf{B} are comparable in 3D, the integration along the line of sight is different for the two quantities. The dispersion $\sigma_{v_{\parallel}}$ is based on the emission-line profile v_{\parallel} tracing a gas species, and while the emission is directly integrated along the line of sight, the line profile is possibly affected by radiative transfer and excitation effects. The tracer of the magnetic field is the optically-thin polarized submillimetre emission of dust, and both the polarization and \mathbf{B}_{\perp} are projected and integrated along the line of sight as pseudo-vectors.

Finally, in the estimates of B_{\perp}^{DCF} and $B_{\perp}^{\text{DCF+SF}}$, a common mean density ρ has been adopted, while in practice ρ is different from cloud to cloud. Direct estimation of the values of ρ from the measured column densities $\langle N_{\text{H}} \rangle$ and $\langle N_{\text{H}_2} \rangle$ relies heavily on the geometrical modelling of the cloud and the filling factors of each species, introducing uncertainties that affect the calculated values of B_{\perp} .

Given the line-of-sight integration and the fact that $\zeta_{\psi} > 25^{\circ}$ uniformly, the calculated values could be considered as upper limits to the actual B_{\perp} . However, other shortcomings, such as the assumptions about the correlation structure and the uncertainties in the determination of the density, do not necessarily bias the estimate of the magnetic field strength towards high values. In conclusion, the values presented in Table D.1 should be viewed only as a reference and only applied with caution, given the many assumptions in both methods at the scales considered.

¹ APC, AstroParticule et Cosmologie, Université Paris Diderot, CNRS/IN2P3, CEA/Irfu, Observatoire de Paris, Sorbonne Paris Cité, 10, rue Alice Domon et Léonie Duquet, 75205 Paris Cedex 13, France

² African Institute for Mathematical Sciences, 6-8 Melrose Road, Muizenberg, Cape Town, South Africa

³ Agenzia Spaziale Italiana Science Data Center, Via del Politecnico snc, 00133, Roma, Italy

⁴ Aix Marseille Université, CNRS, LAM (Laboratoire d'Astrophysique de Marseille) UMR 7326, 13388, Marseille, France

⁵ Astrophysics Group, Cavendish Laboratory, University of Cambridge, J J Thomson Avenue, Cambridge CB3 0HE, U.K.

⁶ Astrophysics & Cosmology Research Unit, School of Mathematics, Statistics & Computer Science, University of KwaZulu-Natal, Westville Campus, Private Bag X54001, Durban 4000, South Africa

⁷ CITA, University of Toronto, 60 St. George St., Toronto, ON M5S 3H8, Canada

⁸ CNRS, IRAP, 9 Av. colonel Roche, BP 44346, F-31028 Toulouse cedex 4, France

⁹ California Institute of Technology, Pasadena, California, U.S.A.

¹⁰ Centro de Estudios de Física del Cosmos de Aragón (CEFCA), Plaza San Juan, 1, planta 2, E-44001, Teruel, Spain

¹¹ Computational Cosmology Center, Lawrence Berkeley National Laboratory, Berkeley, California, U.S.A.

¹² DSM/Irfu/SPP, CEA-Saclay, F-91191 Gif-sur-Yvette Cedex, France

¹³ DTU Space, National Space Institute, Technical University of Denmark, Elektrovej 327, DK-2800 Kgs. Lyngby, Denmark

¹⁴ Département de Physique Théorique, Université de Genève, 24, Quai E. Ansermet, 1211 Genève 4, Switzerland

¹⁵ Departamento de Astrofísica, Universidad de La Laguna (ULL), E-38206 La Laguna, Tenerife, Spain

¹⁶ Departamento de Física, Universidad de Oviedo, Avda. Calvo Sotelo s/n, Oviedo, Spain

¹⁷ Department of Astronomy and Astrophysics, University of Toronto, 50 Saint George Street, Toronto, Ontario, Canada

¹⁸ Department of Astrophysics/IMAPP, Radboud University Nijmegen, P.O. Box 9010, 6500 GL Nijmegen, The Netherlands

¹⁹ Department of Physics & Astronomy, University of British Columbia, 6224 Agricultural Road, Vancouver, British Columbia, Canada

²⁰ Department of Physics and Astronomy, Dana and David Dornsife College of Letter, Arts and Sciences, University of Southern California, Los Angeles, CA 90089, U.S.A.

²¹ Department of Physics and Astronomy, University College London, London WC1E 6BT, U.K.

²² Department of Physics, Florida State University, Keen Physics Building, 77 Chieftan Way, Tallahassee, Florida, U.S.A.

²³ Department of Physics, Gustaf Hällströmin katu 2a, University of Helsinki, Helsinki, Finland

²⁴ Department of Physics, Princeton University, Princeton, New Jersey, U.S.A.

²⁵ Department of Physics, University of California, Santa Barbara, California, U.S.A.

²⁶ Department of Physics, University of Illinois at Urbana-Champaign, 1110 West Green Street, Urbana, Illinois, U.S.A.

²⁷ Dipartimento di Fisica e Astronomia G. Galilei, Università degli Studi di Padova, via Marzolo 8, 35131 Padova, Italy

²⁸ Dipartimento di Fisica e Scienze della Terra, Università di Ferrara, Via Saragat 1, 44122 Ferrara, Italy

²⁹ Dipartimento di Fisica, Università La Sapienza, P. le A. Moro 2, Roma, Italy

³⁰ Dipartimento di Fisica, Università degli Studi di Milano, Via Celoria, 16, Milano, Italy

³¹ Dipartimento di Fisica, Università degli Studi di Trieste, via A. Valerio 2, Trieste, Italy

³² Dipartimento di Matematica, Università di Roma Tor Vergata, Via della Ricerca Scientifica, 1, Roma, Italy

³³ Discovery Center, Niels Bohr Institute, Blegdamsvej 17, Copenhagen, Denmark

³⁴ Escola de Artes, Ciências e Humanidades, Universidade de São Paulo, Rua Arlindo Bettio 1000, CEP 03828-000, São Paulo, Brazil

³⁵ European Space Agency, ESAC, Planck Science Office, Camino bajo del Castillo, s/n, Urbanización Villafranca del Castillo, Villanueva de la Cañada, Madrid, Spain

³⁶ European Space Agency, ESTEC, Keplerlaan 1, 2201 AZ Noordwijk, The Netherlands

³⁷ Facoltà di Ingegneria, Università degli Studi e-Campus, Via Isimbardi 10, Novedrate (CO), 22060, Italy

³⁸ Gran Sasso Science Institute, INFN, viale F. Crispi 7, 67100 L'Aquila, Italy

³⁹ HGSFP and University of Heidelberg, Theoretical Physics Department, Philosophenweg 16, 69120, Heidelberg, Germany

- ⁴⁰ Helsinki Institute of Physics, Gustaf Hällströmin katu 2, University of Helsinki, Helsinki, Finland
- ⁴¹ INAF - Osservatorio Astrofisico di Catania, Via S. Sofia 78, Catania, Italy
- ⁴² INAF - Osservatorio Astronomico di Padova, Vicolo dell'Osservatorio 5, Padova, Italy
- ⁴³ INAF - Osservatorio Astronomico di Roma, via di Frascati 33, Monte Porzio Catone, Italy
- ⁴⁴ INAF - Osservatorio Astronomico di Trieste, Via G.B. Tiepolo 11, Trieste, Italy
- ⁴⁵ INAF/IASF Bologna, Via Gobetti 101, Bologna, Italy
- ⁴⁶ INAF/IASF Milano, Via E. Bassini 15, Milano, Italy
- ⁴⁷ INFN, Sezione di Bologna, Via Inerio 46, I-40126, Bologna, Italy
- ⁴⁸ INFN, Sezione di Roma 1, Università di Roma Sapienza, Piazzale Aldo Moro 2, 00185, Roma, Italy
- ⁴⁹ INFN, Sezione di Roma 2, Università di Roma Tor Vergata, Via della Ricerca Scientifica, 1, Roma, Italy
- ⁵⁰ INFN/National Institute for Nuclear Physics, Via Valerio 2, I-34127 Trieste, Italy
- ⁵¹ IPAG: Institut de Planétologie et d'Astrophysique de Grenoble, Université Grenoble Alpes, IPAG, F-38000 Grenoble, France, CNRS, IPAG, F-38000 Grenoble, France
- ⁵² Imperial College London, Astrophysics group, Blackett Laboratory, Prince Consort Road, London, SW7 2AZ, U.K.
- ⁵³ Infrared Processing and Analysis Center, California Institute of Technology, Pasadena, CA 91125, U.S.A.
- ⁵⁴ Institut Néel, CNRS, Université Joseph Fourier Grenoble I, 25 rue des Martyrs, Grenoble, France
- ⁵⁵ Institut Universitaire de France, 103, bd Saint-Michel, 75005, Paris, France
- ⁵⁶ Institut d'Astrophysique Spatiale, CNRS (UMR8617) Université Paris-Sud 11, Bâtiment 121, Orsay, France
- ⁵⁷ Institut d'Astrophysique de Paris, CNRS (UMR7095), 98 bis Boulevard Arago, F-75014, Paris, France
- ⁵⁸ Institute of Astronomy, University of Cambridge, Madingley Road, Cambridge CB3 0HA, U.K.
- ⁵⁹ Institute of Theoretical Astrophysics, University of Oslo, Blindern, Oslo, Norway
- ⁶⁰ Instituto de Astrofísica de Canarias, C/Vía Láctea s/n, La Laguna, Tenerife, Spain
- ⁶¹ Instituto de Física de Cantabria (CSIC-Universidad de Cantabria), Avda. de los Castros s/n, Santander, Spain
- ⁶² Istituto Nazionale di Fisica Nucleare, Sezione di Padova, via Marzolo 8, I-35131 Padova, Italy
- ⁶³ Jet Propulsion Laboratory, California Institute of Technology, 4800 Oak Grove Drive, Pasadena, California, U.S.A.
- ⁶⁴ Jodrell Bank Centre for Astrophysics, Alan Turing Building, School of Physics and Astronomy, The University of Manchester, Oxford Road, Manchester, M13 9PL, U.K.
- ⁶⁵ Kavli Institute for Cosmological Physics, University of Chicago, Chicago, IL 60637, USA
- ⁶⁶ Kavli Institute for Cosmology Cambridge, Madingley Road, Cambridge, CB3 0HA, U.K.
- ⁶⁷ Kazan Federal University, 18 Kremlyovskaya St., Kazan, 420008, Russia
- ⁶⁸ LAL, Université Paris-Sud, CNRS/IN2P3, Orsay, France
- ⁶⁹ LERMA, CNRS, Observatoire de Paris, 61 Avenue de l'Observatoire, Paris, France
- ⁷⁰ Laboratoire AIM, IRFU/Service d'Astrophysique - CEA/DSM - CNRS - Université Paris Diderot, Bât. 709, CEA-Saclay, F-91191 Gif-sur-Yvette Cedex, France
- ⁷¹ Laboratoire Traitement et Communication de l'Information, CNRS (UMR 5141) and Télécom ParisTech, 46 rue Barrault F-75634 Paris Cedex 13, France
- ⁷² Laboratoire de Physique Subatomique et Cosmologie, Université Grenoble-Alpes, CNRS/IN2P3, 53, rue des Martyrs, 38026 Grenoble Cedex, France
- ⁷³ Laboratoire de Physique Théorique, Université Paris-Sud 11 & CNRS, Bâtiment 210, 91405 Orsay, France
- ⁷⁴ Lawrence Berkeley National Laboratory, Berkeley, California, U.S.A.
- ⁷⁵ Lebedev Physical Institute of the Russian Academy of Sciences, Astro Space Centre, 84/32 Profsoyuznaya st., Moscow, GSP-7, 117997, Russia
- ⁷⁶ Max-Planck-Institut für Astrophysik, Karl-Schwarzschild-Str. 1, 85741 Garching, Germany
- ⁷⁷ National University of Ireland, Department of Experimental Physics, Maynooth, Co. Kildare, Ireland
- ⁷⁸ Nicolaus Copernicus Astronomical Center, Bartycka 18, 00-716 Warsaw, Poland
- ⁷⁹ Niels Bohr Institute, Blegdamsvej 17, Copenhagen, Denmark
- ⁸⁰ Optical Science Laboratory, University College London, Gower Street, London, U.K.
- ⁸¹ SISSA, Astrophysics Sector, via Bonomea 265, 34136, Trieste, Italy
- ⁸² SUPA, Institute for Astronomy, University of Edinburgh, Royal Observatory, Blackford Hill, Edinburgh EH9 3HJ, U.K.
- ⁸³ School of Physics and Astronomy, Cardiff University, Queens Buildings, The Parade, Cardiff, CF24 3AA, U.K.
- ⁸⁴ Sorbonne Université-UPMC, UMR7095, Institut d'Astrophysique de Paris, 98 bis Boulevard Arago, F-75014, Paris, France
- ⁸⁵ Space Sciences Laboratory, University of California, Berkeley, California, U.S.A.
- ⁸⁶ Special Astrophysical Observatory, Russian Academy of Sciences, Nizhnij Arkhiz, Zelenchukskiy region, Karachai-Cherkessian Republic, 369167, Russia
- ⁸⁷ Sub-Department of Astrophysics, University of Oxford, Keble Road, Oxford OX1 3RH, U.K.
- ⁸⁸ UPMC Univ Paris 06, UMR7095, 98 bis Boulevard Arago, F-75014, Paris, France
- ⁸⁹ Université de Toulouse, UPS-OMP, IRAP, F-31028 Toulouse cedex 4, France
- ⁹⁰ University of Granada, Departamento de Física Teórica y del Cosmos, Facultad de Ciencias, Granada, Spain
- ⁹¹ University of Granada, Instituto Carlos I de Física Teórica y Computacional, Granada, Spain
- ⁹² Warsaw University Observatory, Aleje Ujazdowskie 4, 00-478 Warszawa, Poland

Note d'accompagnement

This document ("Note d'accompagnement") aims to highlight my personal contribution, as a "maître de conférences", both to the research effort undertaken by our group, our lab and within a broader international context, and to the formation of students, the collective life of the laboratory, and the organisation of academic studies, within ENS and beyond.

COLLABORATIVE RESEARCH ACTIVITIES

• Research within LRA / ENS / LERMA / Observatoire de Paris

Since my joining LERMA/LRA on a permanent position as "maître de conférences" in 2008, I have strived to collaborate as widely as possible with the other members of the group at ENS, including students, and other scientists within LERMA and other laboratories of Observatoire de Paris.

Among the contributions I made to collaborative research in this context, I should quote the work I did with Benoît Commerçon, published in Commerçon *et al.* (2012), in which I produced simulated ALMA dust emission maps from his MHD numerical simulations of collapsing dense cores.

I also led a work (Levrier *et al.*, 2012), in collaboration with several members of the group, to assess the effects of density fluctuations on the physical and chemical structures of interstellar clouds. This work also benefitted from a collaboration with the LUTH group developing the Meudon PDR code (Jacques Le Bourlot, Franck Le Petit, Evelyne Roueff), who have since joined LERMA.

I used this combined MHD-PDR approach in a further publication with Maryvonne Gerin (Gerin *et al.*, 2012), to establish observational constraints on the cosmic-ray ionization rate, using hydride spectroscopy. I have also participated in the work of Antoine Gusdorf¹, pertaining to the chemical diagnostics of shocks in the ISM, by providing him with versatile routines to run χ^2 analyses of results from numerous models of the Paris-Durham shock code applied to his observational data.

Finally, I have recently joined the team analyzing the line survey of the Orion B molecular cloud with the IRAM 30 m (PI : Jérôme Pety), in particular to advise Jan Orkisz (PhD student with Maryvonne Gerin and Jérôme Pety) in his analysis of turbulence in this cloud.

To emphasize this aspect of my research, I have been responsible since 2014 for leading the response of the ENS group focusing on the studies of the interstellar dynamics and chemistry to the call for proposals from "Programme National Physique et Chimie du Milieu Interstellaire (PCMI)". This involves gathering results from the various people involved in the proposal and their projects for the coming year, assessing the needs of the group in terms of travel expenses (conferences, collaboration with external groups), and writing a coherent grant request in accordance. We have benefitted from renewed support from PCMI each year, with constantly praising reports.

• Oxford SKA Collaboration

Just before my recruitment by ENS in 2008, I was a post-doctoral researcher at the University of Oxford, working with Steve Rawlings in the framework of the European FP7 program "Square Kilometer Array Design Studies (SKADS)". My role was to provide tools to build sky-maps from the mock source catalogues (S^3) designed by Richard Wilman and Danail Obreschkow (Wilman *et al.*, 2008 and Obreschkow *et al.*, 2009). After leaving Oxford, I kept maintaining these S^3 -Tools, which are hosted on my website², and I am still in contact with Danail Obreschkow (now at ICRAR, Australia) to provide constant access to the S^3 simulated catalogues.

• Planck collaboration

I have been a member of the *Planck* collaboration since 2011, as I joined the HFI Core Team at that time, to work on the analysis of the polarization data. I worked in close collaboration with scientists from ENS (Edith Falgarone), IAS Orsay (François Boulanger, Vincent Guillet), and IRAP (Jean-Philippe Bernard, Ludovic Montier) to provide the first sky maps of dust polarization, which were made public with the 2015 data release. I actively participated in much of the methodology work necessary to properly understand this data, which led to the publications of Montier *et al.* (2015a) and Montier *et al.* (2015b).

I also led the work on the paper *Planck* Int. XX (2015), which focused on the analysis of the statistics of dust polarization in nearby molecular clouds and other diffuse fields, with a strong emphasis on the comparison with simulated observations. As this paper was meant to be released simultaneously with

1. who was a long-time postdoc with LRA and has now been hired on a permanent CNRS position in our group

2. <http://www.lra.ens.fr/~levrier/Recherche/S3/>

Planck Int. XIX (2015), *Planck* Int. XXI (2015), and *Planck* Int. XXII (2015), the collaborative aspect of the work was paramount. After these papers were submitted in 2014, I became *Planck* scientist, and oversaw the writing of another paper, *Planck* Int. XXV (2016), which was in practice led by Juan Diego Soler, then post-doc at IAS with François Boulanger³.

I have also been involved in a fair number of other *Planck* papers concerning Galactic astrophysics, mostly as a reviewer for *Planck* Int. XXXII (2016), *Planck* Int. XXXIII (2016), and *Planck* Int. XLIV (2016). The *Planck* collaboration will release its final data products in the end of 2016. They will as before be accompanied by a series of papers, among which two will focus on the legacy of *Planck* with respect to dust polarization. The first one, led by François Boulanger, will focus on this emission as a foreground for cosmology, while the second, which I will lead, will focus on the astrophysical aspects of what *Planck* has taught us about Galactic dust and the Galactic magnetic field.

RESPONSIBILITIES WITHIN ENS AND LERMA

- **Health and safety representative**

Since september 2009, I have been appointed Health and Safety representative for the ENS team of LERMA. This primarily involves advising the group's director (Maryvonne Gerin, then Michel Pérault), regarding health and safety issues within the laboratory, and updating the corresponding document on a yearly basis.

- **CPER-2 Committee member**

Since may 2015, I have been a member of the committee overseeing the second phase of renovation works for the Physics Department of ENS. We have made propositions for the 30 M€ planned works aimed at renovating the "Grand Hall" section of the Physics department, in agreement with the personnel of the department.

- **LERMA Grid computation contact**

In the period 2010-2014, I was the official contact of the "Grilles de calcul" initiative for LERMA. This mainly involved ensuring that people requesting an account for grid computing with CNRS were legitimate in making such a request.

- **LERMA laboratory council member**

In january 2014, I was elected to the LERMA laboratory council ("conseil de laboratoire"). As such, I attend the regular meetings of the council (about 4 a year), to decide on the policies of LERMA regarding the laboratory's organization, rules, budget repartition, requests for association from external researchers and retirees.

NATIONAL AND INTERNATIONAL COMMITTEES

- **Conseil National des Universités (CNU)**

Since november 2015, I have been an appointed member of section 34 (astronomy & astrophysics) of "Conseil National des Universités" (CNU). As such, I am in charge of reviewing applications for "qualification", a necessary validating step before candidates can apply for positions as "maître de conférences". I also review applications for promotion and requests for sabbaticals.

- **IRAM Program Committee**

Since february 2016, I have been appointed to the Program Committee of Institut de Radio Astronomie Millimétrique (IRAM). This involves two-day meetings (two per year), to review the 70+ requests for observing time on the IRAM 30 m radiotelescope (Pico Veleta) and the NOEMA interferometer. Although very time-consuming, this duty is also a scientifically very gratifying one.

3. in the framework of the "MISTIC" ERC grant.

STUDENT AND POST-DOC SUPERVISION

Post-docs

- **Jérémy Neveu** [AGPR ENS Paris, 2014-2015]

Statistical analysis of polarized thermal dust emission maps from Galactic dust

In september 2014, Jérémy Neveu, who had just received his PhD from University Paris-Sud, joined our team at ENS as "agrégé-préparateur", to work with me on the statistical analysis of polarized thermal dust emission maps from Galactic dust observed by *Planck*, using a simple analytical model for the magnetized and turbulent interstellar medium. This work was presented at the IAU General Assembly in Honolulu in August 2015, and we are currently finishing the corresponding paper, to be submitted to *Astronomy & Astrophysics*. Jérémy Neveu was recruited on a permanent position as "maître de conférences" at University Paris-Sud in september 2015, and will pursue his research within LAL on the LSST project.

PhD students

- **Manuel Berthet** [PhD student ENS Paris, 2013-2017]

The interstellar web : filaments, turbulence and magnetic fields

Since september 2013, I am co-supervising Manuel Berthet's PhD thesis, with Edith Falgarone. This PhD work is in the continuation of the M2 internship work he did under my supervision in 2012 (see below). It consists in providing constraints for star formation models, via the study of the filamentary structures of matter within which, according to current models, prestellar dense cores form. The goal is in particular to understand the link between the distribution of matter and the magnetic field. To this end, we have at our disposal starlight polarization data taken with the "Beauty and the Beast" polarimeter at Mont-Mégantic Observatory, towards the Polaris Flare. These are compared to dust emission maps showing filamentary structures. Using algorithms to isolate these filamentary structures (**Disperse** by Thierry Sousbie), Manuel Berthet showed that the distribution of angles between starlight polarization and nearby filaments is not uniform, with a peak near 0° , consistent with the results of a similar study by Panopoulou *et al.* (2016). This work was published in *Highlights of Astronomy*, and is under review for publication in *Astronomy & Astrophysics*. Manuel Berthet is completing this work using other filament identification tools, such as RHT (Clark *et al.*, 2014), and studies the topology of the magnetic field, the velocity field, and structures of matter in numerical simulations of turbulent interstellar flows (with Eva Ntormousi and Patrick Hennebelle). Unfortunately, Manuel Berthet suffered from important health problems in 2015-2016, and his PhD work has been on hold since march 2016. He should be able to resume it in september 2016, for a defence in june 2017.

PhD jury member

- **Jean-François Robitaille** [Université Laval, Québec, 3 may 2014]

Multiscale analysis of dust emission in the Galactic Plane

I was a reviewing member of the jury. Jean-François Robitaille did his PhD under the supervision of Gilles Joncas (Université Laval) and Marc-Antoine Miville-Deschênes (IAS Orsay), working on multiscale analysis tools which he applied to dust thermal emission data (Hi-Gal), HI data (VGPS) and CO data (FCRAO). He showed how these can be used to separate Gaussian and non-Gaussian fluctuations, characterize their separate properties in terms of power spectra, and study the correlation between the dust distribution and neutral gaseous components in the ISM using complex wavelets.

Interns

- **Rémi Paulin** [M2 "Astronomie, Astrophysique et Ingénierie Spatiale", 2011, 2 months]

Lifetime of interstellar clouds

The goal of the internship was to characterize the coherence times of structures formed in magnetohydrodynamical numerical simulations of interstellar turbulence, especially comparing the cases of isothermal and multiphasic flows, with and without magnetic fields.

- **Manuel Berthet** [M2 “Astronomie, Astrophysique et Ingénierie Spatiale”, 2012, 2 months]
Orientation statistics of filaments and magnetic fields in the diffuse ISM

The goal of the internship was to compare the orientation of the magnetic field obtained by starlight polarization data in extinction, to those of filaments of matter observed with dust thermal emission, in the diffuse molecular cloud of the Polaris Flare.

- **Bilal Ladjelate** [M2 “Astronomie, Astrophysique et Ingénierie Spatiale”, 2013, 2 months]
Models of physico-chemical structures in interstellar molecular clouds

The goal of the internship was to perform a systematic study of the physical and chemical properties of realistic interstellar structures, taken as a sum of Gaussian clouds, using the Meudon PDR code ported on the EGEE grid for fast parallel computing of a large number of models.

- **Brice Poillot** [M1 “Physique de la Matière et ses Applications” (University Paris VII), 2011, 1 month]
Development of extragalactic simulations for SKA

The goal of the internship was to implement models of the radio continuum emission of galaxies (both total and linearly polarized intensities), according to their size, age and star formation rate (SFR), in the radio sky simulation tools which I had developed during my post-doctoral contract with the University of Oxford.

RESPONSIBILITIES IN A TEACHING CONTEXT

- **“Centre de préparation à l'agrégation de physique” (Deputy-director)**

The French education system has quite a few specificities. After high-school, many students choose to follow the competitive courses known as “classes préparatoires” (CPGE), instead of going to college. If the programs are basically the same as the first two years of college, the rhythm of studies is quite more intense. As a result, students are better prepared for the competitions organized by the “Grandes Écoles”, specialized schools delivering degrees after generally two to four years. Most of these schools deliver engineering degrees, but some, like the ENS, are meant to train scientists and teachers.

Another specificity of the French education system is the “agrégation”. It is a nationwide competition organised to recruit teachers at the high-school level and for the CPGE. There are many of these competitions, in French, history, geography, most foreign languages, and of course physics. The “agrégation” in physics includes some chemistry, and conversely the “agrégation” in chemistry includes some physics. The competition is made of a written part and an oral part. The written part takes place around april and is made up of two “compositions” and one “problème”. The “compositions”, one in physics, one in chemistry, test students on subjects they are bound to have seen during their training, while the “problème” treats questions which are beyond the scope of the program, to assess the candidate’s ability to face a new problem, to propose models and interpretations.

The oral part takes place around June and July, and is reserved for students who have passed the written part. It is made up of two “leçons” and one “montage”. The “leçons”, one in physics, one in chemistry, put the candidate in their future position of having to teach class on a well-defined subject, at a given level (usually high-school for chemistry and “classes préparatoires” for physics). The “montage” is the last, often dreaded, test : the candidate has to present and perform physics experiments illustrating a given subject, such as optical spectroscopy, fluid dynamics, physical constants, semiconductor devices, etc...

ENS Paris and Universities Paris VI and Paris XI have gathered forces to propose a year-long preparation to this competition, within the “Centre Interuniversitaire de préparation à l'agrégation externe de sciences physiques, option physique (Montrouge)”, for which I have been deputy-director since 2008, under Jean-Marc Berroir (now vice-president of the jury) and Jean-Michel Raimond.

A major overhaul of the teaching programs took place in recent years, leading to a strong decrease in the number of positions offered at the agrégation. The number of students at our Centre has decreased accordingly, from about 40 in 2008 to about 20 nowadays. I take care of recruiting these students, in agreement with Jean-Michel Raimond and representatives of Universities Paris VI and Paris XI. I establish yearly plannings for laboratory sessions, presentations of “leçons” and “montages”, blank written tests, etc... I organise academic meetings, and I encourage our staff to propose, design, and build new

experiments to illustrate the subjects of the competition. I also organize the transport of much of our experimental material, which serves for the national competition.

- **“Formation Interuniversitaire de Physique” (FIP)**

Since september 2008, like all other teachers at ENS, I am in charge of tutoring students of ENS (approximately one student each year). I oversee their study program (the courses they intend to follow), and I advise them regarding the specific fields of physics they wish to enter. I also act as a go-between for them when they search for internships, either in France or abroad, most notably for the long-term internships (6 months) which students of FIP have to undertake at the end of the second year. This was the case for Rémi Paulin (with Aris Karastergiou, Oxford, 2010), Sandrine Codis (Julien Devriendt, Oxford, 2010), Félix Driencourt-Mangin (Julien Devriendt, Oxford, 2014), Paul Caucal (Jo Dunkley, Oxford, 2015), and Jordan Philidet (Suzanne Aigrain, Oxford, 2016). I also am a regular jury member for these internships, as well as for the 1-month experimental internships of first-year students.

- **Master “Astronomie, Astrophysique et Ingénierie Spatiale”**

Since september 2012, I have been responsible, for ENS Paris, of the second year of the master “Astronomie, Astrophysique et Ingénierie Spatiale” (Universities UPMC, Paris-Diderot, Paris-Sud, Observatoire de Paris, ENS Paris). As such, and in collaboration with the other members of the bureau, I supervise the forty students a year that the master welcomes, especially in the choice of courses, their search for internship subjects and PhD grants. I also participate in a dozen internship juries a year.